Porous Semiconductors: A Symposium Held in Memory of Vitali Parkhutik and Volker Lehmann

Editors:

P. Schmuki
University of Erlangen
Erlangen, Germany

U. Goesele
MPI Halle
Halle, Germany

D. J. Lockwood
National Research Council of Canada
Ottawa, Ontario, Canada

H. Foell
University of Kiel
Kiel, Germany

J. J. Kelly
Utrecht University
Utrecht, The Netherlands

Y. H. Ogata
Kyoto University
Kyoto, Japan

Sponsoring Divisions:

Corrosion

Luminescence and Display Materials

Published by
The Electrochemical Society
65 South Main Street, Building D
Pennington, NJ 08534-2839, USA
tel 609 737 1902
fax 609 737 2743
www.electrochem.org

ecs transactions ™

Vol. 16 No. 3

Published by:

The Electrochemical Society
65 South Main Street
Pennington, New Jersey 08534-2839, USA

Telephone 609.737.1902
Fax 609.737.2743
e-mail: ecs@electrochem.org
Web: www.electrochem.org

ISSN 1938-6737 (online)
ISSN 1938-5862 (print)

ISBN 978-1-56677-649-3 (Hardcover)
ISBN 978-1-60768-002-4 (PDF)

Printed in the United States of America.

Preface

This issue of ECS *Transactions* contains more than 50 refereed papers from the talks presented over three days at the International Symposium on Porous Semiconductors held in Honolulu, Hawaii as part of the 214th Meeting of the Electrochemical Society, on October 12-17, 2008. The Symposium was held in Memory of Volker Lehmann and Vitali Parkhutik, two key scientists in the field of porous semiconductors who recently passed away.

The symposium was aimed at a more detailed understanding of growth mechanisms and the physical and chemical properties of all types of porous semiconductors. The symposium addressed research in the various subfields of porous semiconductors such as semiconductor electrochemistry, deposition into pores, matrix materials, optical spectroscopy, and transdisciplinary approaches to the topic. Moreover, the symposium included presentations on work relevant to the formation of advanced materials such as, for example, porous silicon, matrix composites and nanoclusters, and their applications such as chemical and biological sensors.

The symposium was a sequel to a series of symposia on "Pits & Pores" held in Montreal (1997), in Phoenix (2000), and in Honolulu (2004). These proceedings are anticipated to be beneficial not only for the tailored preparation of porous materials but also as a source of insights with respect to the origin and nature of localized dissolution processes. The papers were divided into oral sessions and a poster session and included two keynote talks and ten invited papers. These proceedings follow the order of presentation at the Symposium.

We wish to thank the session chairs and proceedings manuscript referees; Staff of the Electrochemical Society for their help in ensuring a successful Symposium; and Indhumati Paramasivam for administrative assistance. Finally, we thank all the participants for their valuable contributions to the Symposium and for promptly providing their manuscripts for these proceedings.

P. Schmuki
H. Foell
U. Goesele
J. J. Kelly
D. J. Lockwood
Y. H. Ogata

***ECS Transactions*, Volume 16, Issue 3**
Porous Semiconductors: A Symposium Held in Memory of Vitali Parhutik
and Volker Lehmann

Table of Contents

Chapter 1
Monday: Morning Session

Chapter 2
Monday: Afternoon Session

Chapter 3
Tuesday: Morning Session

Chapter 4
Tuesday: Afternoon Session

Chapter 5
Tuesday: Poster Session

Chapter 6
Wednesday: Morning Session

Chapter 7
Wednesday: Afternoon Session

Facts about ECS

The Electrochemical Society (ECS) is an international, nonprofit, scientific, educational organization founded for the advancement of the theory and practice of electrochemistry, electrothermics, electronics, and allied subjects. The Society was founded in Philadelphia in 1902 and incorporated in 1930. There are currently over 7,000 scientists and engineers from more than 70 countries who hold individual membership; the Society is also supported by more than 100 corporations through Corporate Memberships.

The technical activities of the Society are carried on by Divisions. Sections of the Society have been organized in a number of cities and regions. Major international meetings of the Society are held in the spring and fall of each year. At these meetings, the Divisions and Groups hold general sessions and sponsor symposia on specialized subjects.

The Society has an active publications program that includes the following.

Journal of The Electrochemical Society — JES is the peer-reviewed leader in the field of electrochemical and solid-state science and technology. Articles are posted online as soon as they become available for publication. This archival journal is also available in a paper edition, published monthly following electronic publication.

Electrochemical and Solid-State Letters — ESL is the first and only rapid-publication electronic journal covering the same technical areas as JES. Articles are posted online as soon as they become available for publication. This peer-reviewed, archival journal is also available in a paper edition, published monthly following electronic publication. It is a joint publication of ECS and the IEEE Electron Devices Society.

Interface — *Interface* is ECS's quarterly news magazine. It provides a forum for the lively exchange of ideas and news among members of ECS and the international scientific community at large. Published online (with free access to all) and in paper, issues highlight special features on the state of electrochemical and solid-state science and technology. The paper edition is automatically sent to all ECS members.

Meeting Abstracts (formerly Extended Abstracts) — Abstracts of the technical papers presented at the spring and fall meetings of the Society are published on CD-ROM.

ECS Transactions — This online database provides access to full-text articles presented at ECS and ECS-sponsored meetings. Content is available through individual articles, or as collections of articles representing entire symposia.

Monograph Volumes — The Society sponsors the publication of hardbound monograph volumes, which provide authoritative accounts of specific topics in electrochemistry, solid-state science, and related disciplines.

For more information on these and other Society activities, visit the ECS website:

www.electrochem.org

CHAPTER 1

MONDAY: MORNING SESSION

ECS Transactions, 16 (3) 3-5 (2008)
10.1149/1.2982537 ©The Electrochemical Society

VITALI PARKHUTIK : HIS CONTRIBUTIONS TO POROUS SEMICONDUCTOR SCIENCE AND TECHNOLOGY OVER 30 YEARS

Leigh Canham, Intrinsiq Materials Ltd, Malvern Hills Science Park, Geraldine Rd, Malvern, Worcs. WRI4 3SZ, UK.

Vitali Parkhutik conducted research into porous silicon from 1975 right up to when he died in 2006. Trained initially in semiconductor physics, he rapidly became fascinated by electrochemistry, and the etching processes via which mesoporous structures are created from metals (aluminium) and semiconductors (silicon). Significant research contributions include quantitative modelling of formation mechanisms and the development of both advanced hardware and software techniques for detailed characterization. Specific examples were automated anodisation equipment, FTIR spectra analysis and stochastic signal spectroscopy. One key technical advance was realizing the importance of hydrogen-induced stress and point defects in the silicon lattice, as a factor in pore creation from HF-based electrolytes. His passion for education was the inspiration for many of his students to begin careers in interdisciplinary materials science. He also played a key role in developing a truly international porous semiconductor R&D community through a very popular biannual series of conferences, and was a regular attendee of Electrochemical Society meetings.

Scientific Career

Vitali Parkhutik was born in Minsk, Bielorussia, on June 25th 1951. He finished secondary school in 1968 with a medal for outstanding academic achievements. One of his earliest hobbies was model construction, developing as he grew older into a passion for constructing and repairing all kinds of mechanical devices. He considered becoming an engineer, but chose instead a more theoretical career and entered the Physics Faculty of the Bielorussian State University. Specializing in semiconductor physics, he graduated in 1973 and a diploma with honours.

His first independent steps in science took place at the Minsk Radioengineering Institute, transformed after the breakup of the Soviet Union into the Bielorussian University of Informatics and Electronics. He started his doctoral studies there in 1975, the main topic of his research being the anodization of various metals, including aluminum and silicon. In this way, he first took interest in the formation and properties of porous silicon, a field that inspired most of his subsequent scientific activity. He defended his doctoral thesis in 1979, upgrading it to the level of Doctor Habilitus – the highest scientific degree in the Soviet Union – in 1991.

His first invitation to Spain in 1989 resulted in a post at the Madrid Autonomous University. The interest in porous silicon strengthened, and so did the personal ties. A year's fellowship led to an indefinite stay. His whole family came over and in 1992 Spain became his adopted country. Subsequent to Madrid, Valencia and its Polytechnic University, became Vitali´s scientific headquarters. He became a full Professor at the Department of Materials Science of the Technical University of Valencia (UPV) and Director of its R&D centre "Materials and Technologies of Microfabrication". In that capacity he founded and directed a number of regional and international collaborative R&D projects

Vitali Parkhutik´s research activities have been numerous and diverse, and this is reflected in his papers on various aspects and applications of porous silicon, and also porous TiO_2, silicides and alumina. A personal selection of those papers is given below (1-16). A survey of his major review paper (9) and full bibliography reveals his primary interests. He was always fascinated by the electrochemical etching process(1-4,6,7,11,12,15) but in the 1990's published novel work on electronic properties (8,10), and was just starting to publish data relevant to the biochemical applications (16).

A simple database search reveals the titles of more than a hundred indexed publications and the names of more than a hundred co-authors and collaborators. But Vitali has had much more depth to his character than is apparent from his published work. He was passionate about education (13) - he was an avid teacher who continued holding his classes when terminally ill.

Vitali is probably best known among the scientific community as the founder and promoter of the PSST (Porous Semiconductor Science & Technology) Conferences, born from his desire to bring people together and raise the profile of Valencia with regard international science. Throughout his three years of fighting colon cancer, he strived to maintain an absolutely normal, productive life. In his last months he worked actively preparing the 5th PSST Conference in Barcelona.

Vitali Parkhutik died on February 20th 2006, three weeks before his latest PSST meeting. He leaves his wife and co-author, Eugenia Matveeva, daughter and son. He will be missed and remembered in many ways, especially at our future conferences on electrochemistry and porous semiconductors.

Vitali Parkhutik : Selected References

1. V.P.Parkhutik, L.K.Glinenko and V.A.Labunov, Surface Technology **20**,265 (1983)
2. V.Parkhutik and V.Shershulsky. J.Phys.D.Appl.Phys. **19**, 623 (1986)
3. V.Parkhutik. Electrochim.Acta **36**,1611 (1991)

4. V.P.Parkhutik and V.I.Shershulsky, J.Phys.D.Appl.Phys**.25**,1258 (1992)
5. E.Matveeva, V.P.Parkhutik et al. J.Lumin**. 57**, 175 (1993)
6. Y.E.Makushok, V.P.Parkhutik et al. J.Phys.D.Appl.Phys. **27**,661 (1994)
7. V.Parkhutik et al. J.Surf.Interface Analysis 2**2**, 358 (1994)
8. V.Parkhutik. Thin Solid Films, **276**, 195 (1996)
9. V.P.Parkhutik. Solid State Electron, **43**, 1121 (1999)
10. V.P.Parkhutik and S.Timashev, J.Appl.Phys, **87**,7558 (2000)
11. V.Parkhutik et al. Mat.Sci.Engn.**B69/70**,53 (2000)
12. V.Parkhutik et al. Mat.Sci.Engn.**B69/70**, 553 (2000)
13. V.Parkhutik and L.T.Canham. Phys.Stat.Sol.(a) **182**,591 (2000)
14. V.Kytin,A.Petrov,V.Yu.Timoshenko,V.Parkhutik,P.K.Kashkarov,J.Weidman, F.Koch, and Th.Dittrich. Phys.Stat.Sol.(a) **197**,487 (2003)
15. V.Parkhutik,M.Udagawa and Y.Harima. Phys.Stat.Sol.(a) **202**, 1374 (2005)
16. V.Parkhutik, J.Curiel-Esparza,M.C.Millan and J.Abella. Phys.Stat.Sol.(a) **202**, 1576 (2005)
17. E.Pastor,E.Matveeva,V.Parkhutik et al. Phys.Stat.Sol.(c) **4**,2136 (2007)

ECS Transactions, 16 (3) 7-20 (2008)
10.1149/1.2982538 ©The Electrochemical Society

Volker Lehmann: An Unconventional Scientist

U. Gösele[a] and H. Föll[b]

[a] Max Planck Institute of Microstructure Physics, 06120 Halle, Germany
[b] Faculty of Engineering, Christian-Albrechts-University of Kiel, 24143 Kiel, Germany

It is generally known that Volker Lehmann has made numerous important contributions to the science and technology of the various forms of porous silicon. Less well known is that he started his education in the world of art and that he kept this interest alive, even after a professional career in engineering, materials science, physics and electrochemistry. In addition he was an athlete, enjoying all kinds of sports and physical challenges. The paper will be based upon the personal experience of the authors who worked directly with Volker Lehmann or in related fields of research for over two decades.

Introduction

The authors (U. G. and H. F. for short in the following) had the privilege to know and to work with Volker Lehmann for more than twenty years. As it turned out the two most cited publications of Volker Lehmann (1, 2) are also the most cited papers of the present authors showing the close intertwining of the respective research outputs. The purpose of this presentation is not to give an exhaustive overview of his life and scientific work but rather to highlight a few typical aspects and examples of his personality and his life as a scientist; touching also his way of doing research and combining science with art and sports. This presentation is a substantially enlarged version of a recent article in memory of Volker Lehmann by the present authors (3). The article will be structured along his CV with specific examples of his research accomplishments picked out to highlight his style of research and life in general. Sometimes less emphasis will be put on the science and more on the stories around his research and on his personality.

From Birth to Ph. D.

Volker Lehmann was born in December 1959 in Southern Germany in the city of Ulm. From 1976 – 1983 he studied Electrical Engineering at the RWTH Aachen, one of the best German universities devoted to engineering. In the spring of 1982 he did part of the required industrial internship at the then newly established “Solar” department of Siemens Central Research in Munich, Germany. Here he worked for one of the authors (H. F.) who introduced him to Si electrochemistry. The task was to assess the “solar cell quality” of various pieces of oddly shaped Si that were obtained in many novel and unusual ways (e.g. by sintering of Si powder, by melt spinning, or by coating carbon fiber nets with liquid Si) and it was decided to do this by measuring the cathodic photo current of the typically p-type samples via a solid-liquid junction. Everything was new and untried, calling for a “quick and dirty” approach. Volker Lehmann was perfectly suited for this kind of work. Already as an intern he quickly mastered the necessary background in the materials science of silicon and combined it with his training as an engineer and his uncanny ability to build complex machinery from various debris found in any lab. This first encounter with the electrochemistry of silicon as an undergraduate student proved to be decisive for his future research career. He would very successfully stay in this area of research with a passion for a hands-on approach and creative solutions for the rest of his professional life. Based on his positive internship experience, he returned to Siemens Central Research for doing his diploma thesis under the guidance of H. F. His thesis was well received at the University and lead to his first publication in the area of silicon electrochemistry, entitled "A high-speed characterization technique for solar silicon", unfortunately in a somewhat obscure proceedings (4).

Figure 1. Volker Lehmann

After an interruption of his education necessitated by compulsory civil service (in lieu of military service) he came back to Siemens in the summer of 1985 for a Ph. D. in physics, again under the direct supervision of H.F. but now in association with the University of Erlangen-Nürnberg (Prof. Helbig). Interestingly enough, Volker Lehmann decided to go for a Ph. D. in physics only after his application to the Munich School of Arts had been turned down. All his life he did not only like science and engineering but he also loved to produce works of art himself. Throughout his career he created pictures, lithographies, sculptures, and so on – every technique was of artistic interest to him. Figs. 2 and 3 give some impressions of his early art.

a)

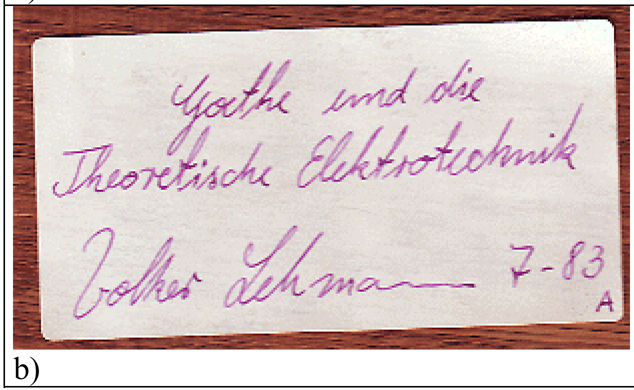

Goethe und die
Theoretische Elektrotechnik
Volker Lehmann 7-83
A

b)

Figure 2. a) Goethe und die Theoretische Elektrotechnik (Goethe and the theory of electrical engineering) by Volker Lehmann, 1983.
62 cm x 62 cm; metal foil from the necks of wine bottles over wood relief.

b) Proud signature on the back (first time he sold a piece of art).

Whatever the artistic value of the piece in Fig. 2 might be, Volker Lehmann met the most common definition for a professional artist: he actually sold that piece - to H. F. in 1983 for about € 500. The craftsmanship and the originality are certainly impeccable. As with most of his art (and to some extent science), one needs to take a second and third look to grasp the meaning and the details. While the piece appears to be just a symphony of letters, it actually carries meaning. Just start to read from the top left to the bottom right (counting the big "a" twice) and you find the sentence "Grau ist alle Theorie" (gray are all theories), which, as all literate Germans will know, is straight from Goethe's "Faust I", and explains not only the title of the piece but also Volker Lehmann's attitude to just theory. The quote goes on as follows: "the verdant tree of Life is green alone". The tree of life, symbolized by the grapevine and its time-honored bottled product, is also found in this piece: many metal wrappers from around the neck of wine bottles supplied the essential material.

Remarkably, any new technique he tried came out rather perfect from the very beginning. Figure 3 shows his first lithography, clearly influenced by Escher; technically perfect and artistically thought provoking, especially for those who feel that the pen in the end will be mightier than the sword.

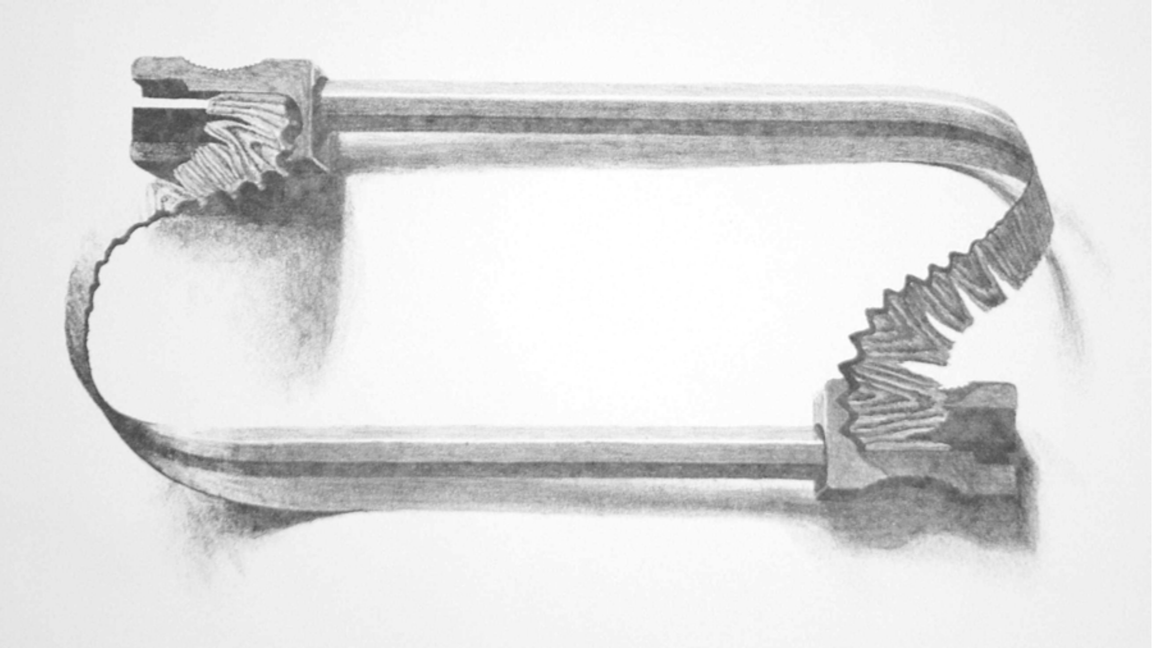

Figure 3. First attempt at lithography (here: printing from a cut flat stone).

After H. F. lend him an old book about "Perpetuum Mobiles" with illustrations of all the (needless to say: wrong) principles and designs that had come up through the centuries, he took that subject close to his heart and started to combine artistry and high-level engineering. Beautifully crafted and artful "Perpetuum Mobiles" emerged from his studio over many years – and they all worked! It took longer and longer, even for his scientifically and technically well trained colleagues and friends, to figure out where the energy was actually coming from, and where the tiny battery was hidden.

In his art, still found in many homes and offices, he lives on just as much as in his scientific contributions. But what was the loss to the artists' community has been the gain for materials science. In his research work for his Ph. D., which he defended in 1988, he put down the foundation for his successful scientific career.

Initially Volker extended his diploma work, dealing with ways for the electrochemical characterization of electronic properties of silicon. This lead to his first major discovery: the "ELYMAT" (ELectrolYtical MetAl Tracer) principle for lifetime mapping in silicon. In 1988 this lead to his second publication entitled "Minority-carrier diffusion length mapping in silicon wafers using a Si-electrolyte-contact", now suitably published in the Journal of the Electrochemical Society (5). Of course, working in the research department of a company, he filed a patent before publishing together with H. F. in 1987. The technique was licensed and produced some (little) money. It is still used, in particular for multi-crystalline solar Si, because it gives the best results and thus is the reference for other methods.

While originally the major interest was in measuring the cathodic photocurrent in p-type Si with frontside illumination (fsi) or, in the case of the ELYMAT, with backside illumination (bsi), his interest shifted gradually to basic questions of Si electrochemistry and to the peculiarities of n-type Si. The formation of what now is called "microporous Si" was of particular interest, and a lot of often quite involved experiments were done (e.g. Rutherford backscattering) and painstakingly written down in his famous Lab books. But no clear picture emerged, and no publications resulted from this early work.

With regard to n-type Si it was already clear that photocurrents etched these samples and that the structures obtained contained a lot of information about minority carriers (4). One day, however, something unexpected happened: after some anodic processing under fsi conditions, the piece of n-type Si under investigation came out looking pitch-black. The SEM quickly showed why (Fig. 4).

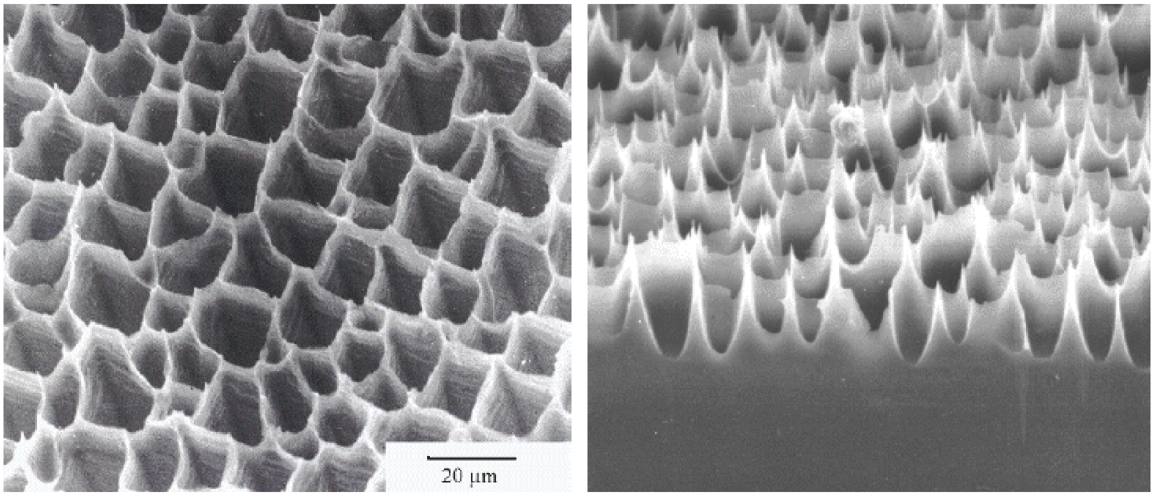

Figure 4. The structures ("fsi macropores") that caused the discovery of deep bsi macropores.

The astonishingly black surface triggered Volker's first patent in 1983 – a method to make cell-like structures for applications in solar cells and catalysts. The patent has long since expired, but the idea seems to get rediscovered every now and then. The big question of course was why such a structure forms in the first place, and the possible answer was because the bend space charge region around accidentally formed tips would capture holes, leading to a preferential growth of the tip. This lead to the prediction that backside illumination should promote "trench" growth, in particular if defined nucleation sites would be provided by lithography. Since H. F. (and thus Volker Lehmann, too) had meanwhile switched to microelectronic memory (DRAM) development, suitable samples from "trench capacitor" development were easy to come by, and the very first experiment in this direction produced the very first deep macropores in lightly doped n-type Si under backside illumination as reported in (1). Note that the microelectronic community for some undisclosed reason likes to misname things: trench instead of hole or pore, wafer fab instead of chip fab, and so on. The title of ref. (1) "Formation mechanism and properties of electrochemically etched trenches in n-type silicon" bears witness to this oddity. A long series of publications and of patents resulted from his work, establishing him early on as a leading researcher in the field of electrochemistry of silicon.

Doing research together with Volker during these times was fun and challenging. He held his own views of things and was not given to accept any scientific (or other) statement if he wasn't convinced of the truth himself. Just to do some experiment because his advisor told him so was not a good enough reason to march to the lab. However, whenever there was a difference of opinion, wagering a bet (usually for a case of beer) could to the trick. As an example, the IV characteristics for the illuminated case in Fig. 3.2 of his book (10) were the result of such a bet (and they are mentioned here because the topic addressed in these curves would bear some more investigation).

His athletic side, combined with an acute sense for killing two birds with one stone showed in the following anecdote: As a good friend he helped H. F. moving all and sundry to a new house and volunteered to do the laundry room in the basement. How not-so-tall Volker managed to bring a heavy washing machine etc. down a narrow staircase all by himself was not clear to those (= most) of us with less well developed athletic skills but neatly shows that he looked for and accepted challenges. That he used the opportunity to do his whole (bachelor) laundry on the side just showed his knack for making the best out of any situation.

Postdoc Time at Duke University

After finishing his Ph. D. Volker Lehmann joined one of the authors (U. G.) as a postdoc in the Department of Materials Science and Engineering at Duke University in North Carolina with his then girlfriend and later wife Judith. The paths of Volker Lehmann and U. G. had crossed earlier when U. G. had worked for a short period at Siemens Central Research in Munich as well, before accepting an offer as Professor of Materials Science at Duke University. In fact, U. G. came across the name of Volker Lehmann when he visited the house of H. F. and inquired about the special piece of art hanging there that is shown in Fig. 2.

At Duke only a one year postdoc position was waiting for him, whereas Siemens Corporation had offered him a "real job" and indicated that in one year's time such an opportunity would most likely not be available anymore. It was typical for Volker Lehmann that he made his decision based on his love and interest for research and new aspects in life and that he took the risk of possibly not getting a job when going back to Germany. As it turned out later, Siemens Corporation was still interested in hiring him after the one year postdoc period had passed.

His main job as a postdoc was to work on silicon wafer bonding and pushing the area of silicon-on-insulator (SOI) wafer fabrication, involving electrochemistry for etching back one of the bonded wafers down to the desired thin SOI layers. He wrote a number of well-cited papers in this area (6, 7). However, his scientific heart was still pounding for the electrochemistry of silicon. Therefore, parallel to the work on wafer bonding, he pursued discussions on the experiments on microporous silicon he had performed while still in Munich and that he had never published since they appeared to make no sense. The puzzling question was mainly which effect could possibly lead to the passivation of (2 – 5) nm silicon structures against further electrochemical etching. U. G. was just teaching a course in which quantum size effects played an essential role and these happened typically in this range of sizes. After some discussions a simplified back-of-the-envelope theoretical estimate showed that such sizes should indeed lead to a substantial increase in the bandgap of silicon, which would then explain the passivation by a quantum mechanical confinement effect. Obviously, such an increase in the bandgap of microporous silicon as compared to normal bulk crystalline silicon should be optically observable. Volker Lehmann immediately set out to do these experiments, "borrowing" the missing optical equipment from the nearby department of Physics. Within a very short time his experiments clearly showed the expected increase in the bandgap of porous silicon and consequently all his earlier experiments performed in Munich suddenly made sense. Lehmann later on sketched the basic effect of quantum confinement controlled etching as shown in Fig. 5.

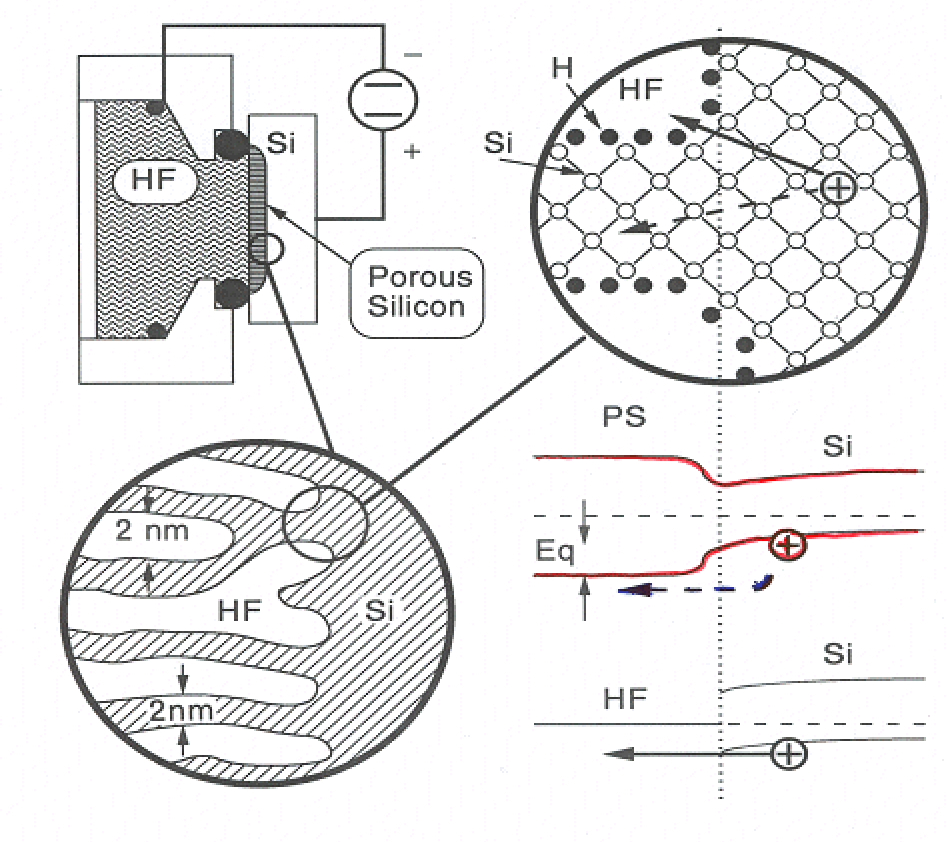

Figure 5. Schematics of the quantum confinement effect leading to the small crystallite sizes ("quantum wires") in microcrystalline silicon obtained by electrochemical etching in HF (8).

Immediately after the successful experiments a manuscript was written by him and submitted in March 1990 to Applied Physics Letters. Volker Lehmann was not in favor of flowery lyrics in research and therefore his manuscripts were always very short, sometimes to the extend that they were much too short even for a letters journal. This manuscript was no exception and submitted with the title "Porous silicon formation: A quantum wire effect", without any question mark at the end of the title. During the time the manuscript was reviewed he was already back at Siemens Corporation in Munich. Applied Physics Letters rejected the manuscript outright as shown in Fig. 6, to the utter disappointment of the authors.

The rejection was based on a long-winded review report basically stating that the authors were not capable of measuring properly and that the quantum confinement interpretation was ridiculous. The disappointment changed into disbelief and some anger when a Duke colleague, Prof. Hisham Massoud, pointed out a publication by L. Canham from a research center of the defense department in the UK, which had just appeared in Applied Physics Letters with the closely related title "Silicon quantum wire array fabrication by electrochemical and chemical dissolution of wafers" (9), which had been submitted in May 1990, months after the rejected manuscript.

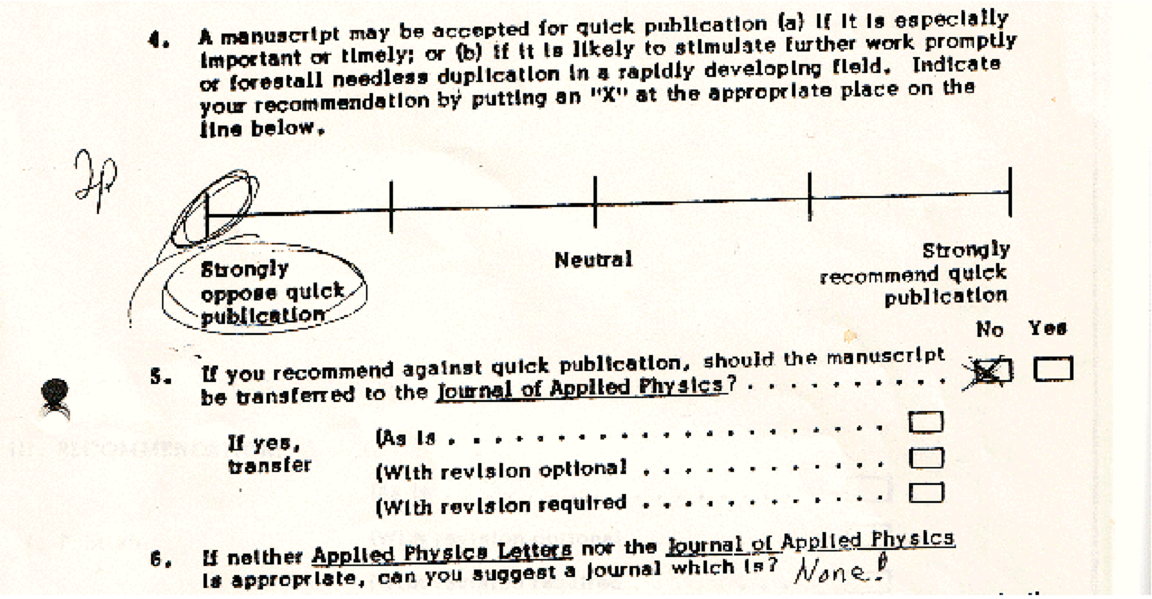

4. A manuscript may be accepted for quick publication (a) if it is especially important or timely; or (b) if it is likely to stimulate further work promptly or forestall needless duplication in a rapidly developing field. Indicate your recommendation by putting an "X" at the appropriate place on the line below.

[✓ Strongly oppose quick publication] — Neutral — Strongly recommend quick publication

5. If you recommend against quick publication, should the manuscript be transferred to the Journal of Applied Physics? . . . . No ☒ Yes ☐

If yes, transfer
(As is . . . . ☐
(With revision optional . . . . ☐
(With revision required . . . . ☐

6. If neither Applied Physics Letters nor the Journal of Applied Physics is appropriate, can you suggest a journal which is? None!

a)
b)

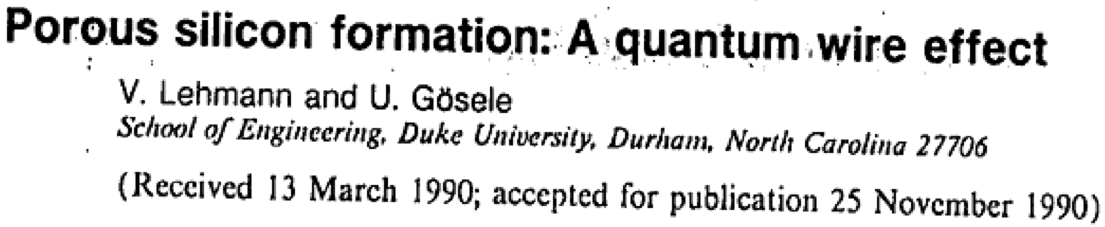

Porous silicon formation: A quantum wire effect

V. Lehmann and U. Gösele
School of Engineering, Duke University, Durham, North Carolina 27706

(Received 13 March 1990; accepted for publication 25 November 1990)

Figure 6. a) First referee judgement on (2), shown for the benefit and encouragement of younger readers: never give up if you are sure about your work! b) The paper as it appeared in the first September 1991 issue of Applied Physics Letters, showing the submission date of March 1990.

After a lengthy appeal process, Applied Physics Letters finally accepted the manuscript in the original form (2), without any citation of the Canham paper (9) that was submitted later, and with the original submission date of March 1990. Unfortunately, the appeal procedure took so long that the paper was finally published only in September 1991 and has therefore naturally been considered as the second paper proposing quantum size effects for porous silicon after the 1990 Canham paper. Nevertheless, the paper has received more than thousand citations and firmly established Volker Lehmann as one of the influential researchers in the porous silicon community.

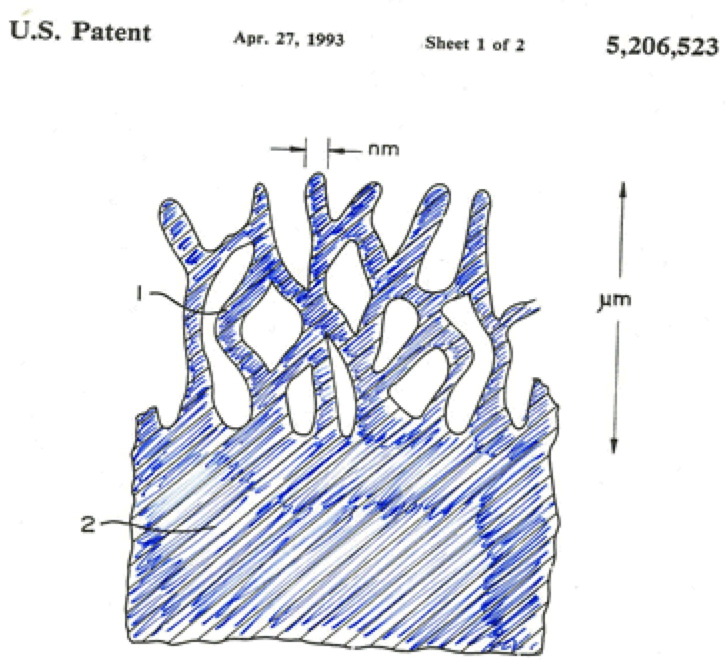

U.S. Patent Apr. 27, 1993 Sheet 1 of 2 5,206,523

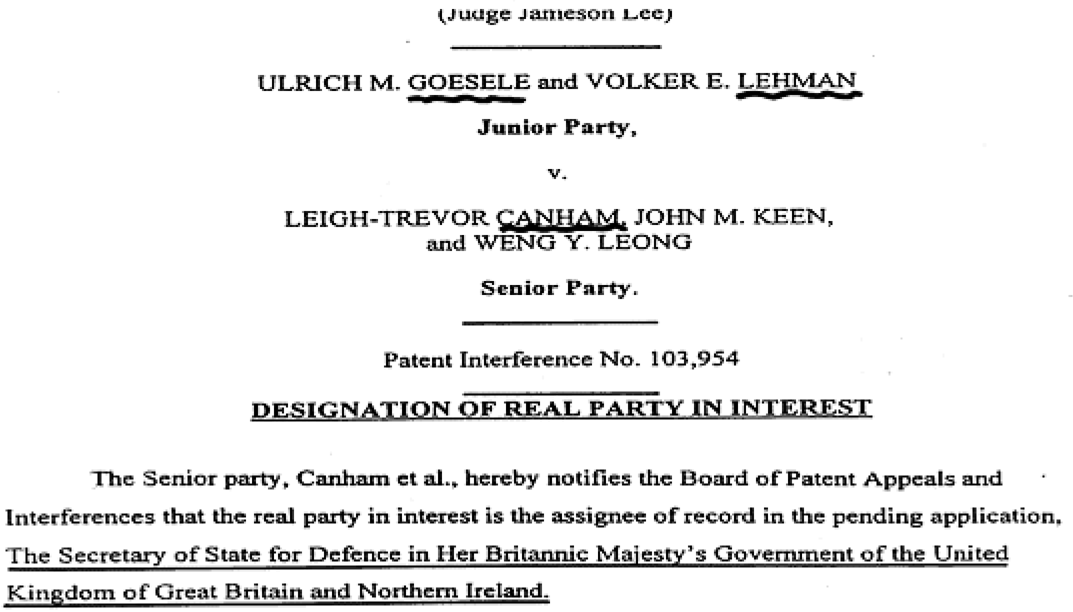

(Judge Jameson Lee)

ULRICH M. GOESELE and VOLKER E. LEHMAN

Junior Party,

v.

LEIGH-TREVOR CANHAM, JOHN M. KEEN,
and WENG Y. LEONG

Senior Party.

Patent Interference No. 103,954

DESIGNATION OF REAL PARTY IN INTEREST

The Senior party, Canham et al., hereby notifies the Board of Patent Appeals and Interferences that the real party in interest is the assignee of record in the pending application, The Secretary of State for Defence in Her Britannic Majesty's Government of the United Kingdom of Great Britain and Northern Ireland.

Figure 7. a) Schematics of the silicon "quantum sponge" as sketched in the above US Patent 5,206,523 which was later on given up in a patent interference procedure with the UK Ministry of Defence. b) Partial copy of legal interference document on porous silicon US Patent 5,206,523.
Shown for the benefit of younger readers: get out in time when science turns ugly, i.e. involves lawyers.

The quantum wire paper by Volker Lehmann (2) lead to a follow-up US patent in which for the first time a tandem cell silicon solar cell was suggested, based on a combination of bulk crystalline silicon and of microporous silicon with an appropriately higher bandgap. This concept of an all-silicon tandem cell making use of quantum confined silicon structures has just recently returned to active photovoltaics research, more than 15 years after the original suggestion. Already before the patent application was written, it became clear that the quantum wires were not at all straight as originally thought but formed an interconnected network (Fig. 7), which was then termed a “quantum sponge” in the US patent 5,206,523. Since Duke University was not interested in the patent it went personally to Volker Lehmann and U. G. It almost appears that Volker Lehmann divined the subsequent legal trouble - he got out of having to pay for getting the patent or any subsequent legal actions. Sure enough, the Ministry of Defense of the UK, a powerful entity (or more aptly put: enemy) that encompassed the research institution for which L. Canham worked, initiated a patent interference procedure (Fig. 7b). Suffice it to say that after a fairly unpleasant and lengthy period, in which the difference in the depth of the financial pocket of the UK Ministry of Defense and that of a Duke professor was the major consideration and decisive fact, the patent was given up in return for a check of $ 10.

Volker Lehmann always looked back at this patent issue more amused than really annoyed – it did not make any money in the end. It should finally be mentioned that during his time at Duke he was jogging regularly with U. G. and another faculty member, Prof. F. H. Cocks, who convinced Volker Lehmann at those numerous occasions that he should write a book on the electrochemistry of silicon. This would finally result in Lehmann’s classic book “Electrochemistry of Silicon” (10), finished more than ten years later in Munich.

Back in Munich

When Volker Lehmann came back to Siemens he joined the research arm of the semiconductor branch where he remained to the end, even after Siemens begot Infineon, and Infineon quite recently begot Qimonda. It is remarkable and reflects his passionate interest for science and research that for all this time he managed to convince his management that work on the electrochemistry of silicon was important and should be funded.

Early on in his industrial career Volker Lehmann, married in the meantime father of two sons, decided that he would not go for the rat race necessary for a management position. He wanted to have sufficient time for his family and for his other passions. Besides art he enjoyed many types of physical activities – e.g. judo, skiing, and going by bike every morning from his home on one side of Munich to the other side of Munich where Siemens Central Research was located. Consequently, he took advantage of a program by Siemens Corporation, which allowed employees to reduce their working hours to a four-day week with an appropriately reduced salary. It was obvious that this would not shift him up the ladder of a management career, but it allowed him to do experiments himself, something he valued far more than having power over some co-workers in a managerial position. Back at Siemens he kept in touch with H. F., now a dean and Professor in Kiel, U. G., and many other researchers he had met and collaborated with, and kept producing major papers in the field of Si electrochemistry.

After U. G. also had returned to Germany as director of a Max Planck Institute in previous East Germany with the mission of doing basic research, Volker Lehmann joked that in his special position in an industrial lab, he had more freedom to do the research he was interested in than U. G. at the helm of a Max Planck Institute, not to mention a Dean (H. F.) founding a new faculty at the University of Kiel. He even claimed that while Siemens Corporation had been shifting emphasis from one area to another with time constants of typically 1 – 2 years, he had always managed to do his beloved porous silicon research independent of all changes by just changing the labels and the association with various areas of applications. He was also proud of having designed a working device for checking whether liquids contained dangerous HF or rather just water. These HF testers he fabricated at home and sold them privately, thus increasing the safety in many chemical labs.

During his time in Munich Volker Lehmann did first class research spanning the range from fundamental investigations (e.g. on the oxidation of light-emitting porous silicon (11) or the topic of current-voltage oscillations at the silicon electrode (12)) to revenue generating products like “bio-chips” in the time leading up to 2006. In particular he was the first researcher showing that a deep understanding of electrochemical etching of macropores (13) allowed to obtain a beautiful periodic array of such macropores in silicon that could be used as an almost perfect photonic crystal (14), which may also be structured to contain waveguides and other photonic structures (15). He also convinced U. G. to go back into the area of porous silicon again – this time in macroporous silicon for photonic crystals after the endeavor into quantum wires in microporous silicon had ended somewhat disappointingly, at least concerning the patent involved. This lead to a period of cooperation between Volker Lehmann, H. F., and U. G. in the area of silicon based photonic crystals (16). An example of such a structure is shown in Fig. 8.

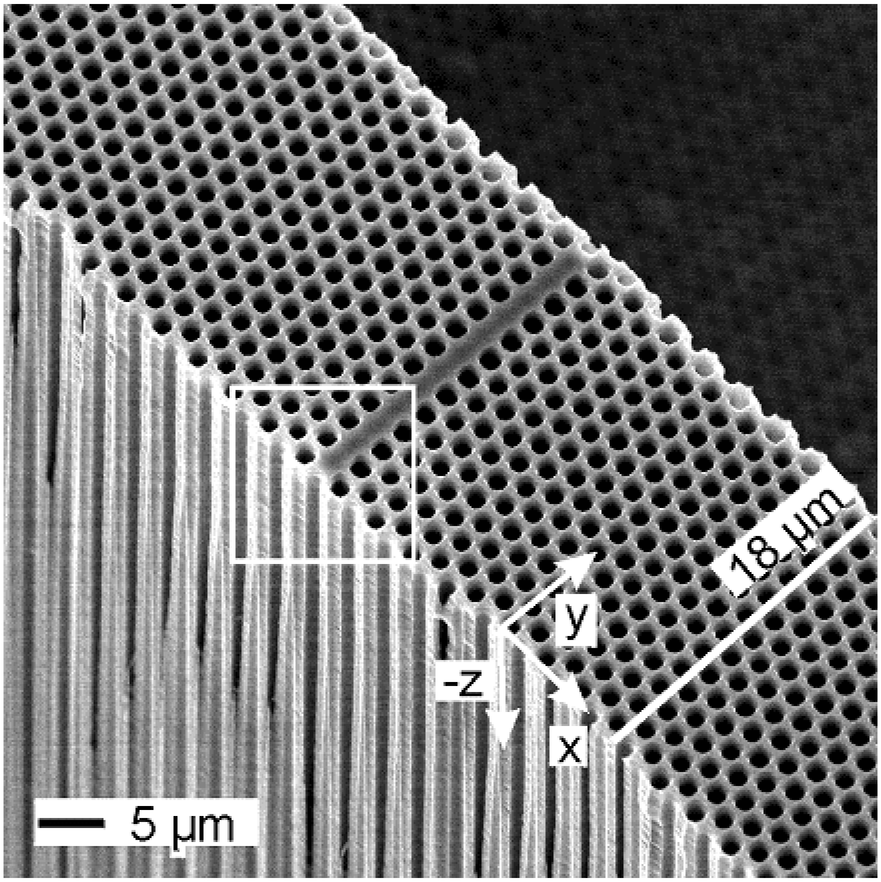

Figure 8. SEM picture of macroporous silicon ridge containing a waveguide the row with missing pores). Picture from (16).

Volker Lehmann tried hard to convince Siemens Corporation to use macroporous silicon as solid-state capacitor with superior properties (17). When management was not as excited as it should have been, concerning the prospects of such devices, he tried a somewhat unusual shock therapy. Together with another previous postdoc from the lab of U. G. at Duke University, who also had ended up working for Siemens Corporation, he prepared a copy of a well-known trade journal containing a short and faked news article, in which it was reported that a Japanese competitor of Siemens Corporation had started to produce solid state capacitors based on macroporous silicon with thousands of wafer starts per week. At April fools day this copy was brought to the attention of management, and the whole chain of command up to the very top fell for it! Only good fortune and a remaining sense of humor within management prevented a bad outcome of this attempt to get the product accepted by management.

During his time at Siemens Corporation and after U. G. had returned back to Germany it became a yearly custom that Volker, the other postdoc mentioned above, and U. G. went skiing together for an extended weekend. It was an opportunity to see how fast and efficient Volker was - not only in doing his science but also in doing sports. He was of the opinion that ski lifts and cable cars were not for him and his friends, and that walking up the mountains would increase the pleasure in finally skiing down the slopes. In the evenings after a tough day on the mountains during dinner in a restaurant, he typically got out his lab book from the backpack he always carried along with him, and started to discuss open questions concerning pore formation mechanisms in silicon - conveniently ignoring the fact that no non-disclosure agreement had been signed.

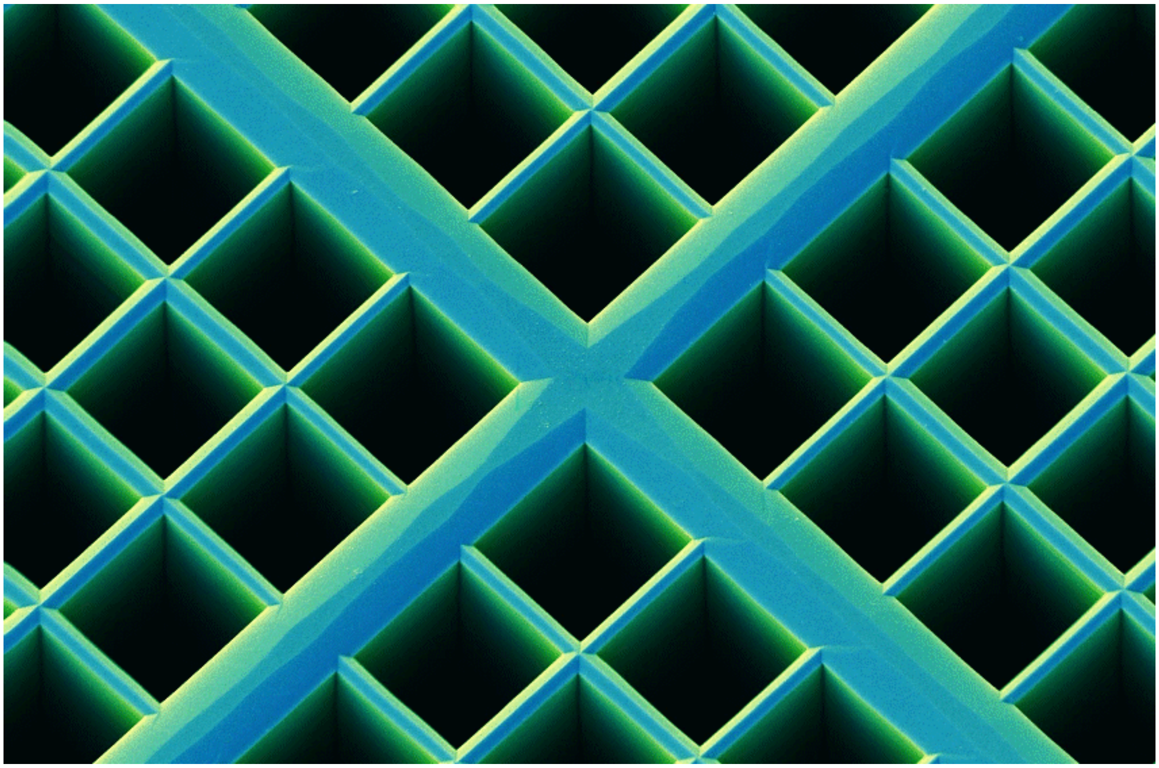

Figure 9. Macropores in Si after special KOH processing.

Similar things happened when the bi-annual “PSST” (Int. Conf. on Porous Semiconductor Science and Technology), a conference he never missed, took place in Tenerife in 2004. Hiking up the 12.000 feet tall volcano was a must (even so it was, theoretically, not allowed) with whoever went along. Porous rocks found along the way lead to discussions about porous semiconductors, and much progress in research and science resulted from these informal discussions during or after exertions.

His last contribution to science was an invited talk at the 2006 PSST; the picture in Fig. 9 is taken from this presentation. It illustrates once more two sides of a remarkable person: a scientist with unchallenged experience in porous silicon research and technology, and an artist who could find beauty wherever he looked.

Final Comments

Volker Lehmann was not only an outstanding scientist and accomplished artist, he was also a person with an extraordinary vitality, radiating good cheer and making friends easily. He was clearly enjoying life and consciously decided to do more research than management. He was always open and helpful and often the ringleader for extracurricular activities at workshops and conferences.

Volker Lehmann died unexpectedly and tragically on the 26th of May in 2006. He was married for 16 years and leaves a wife and two sons.

He has enriched the professional and private lives of many people. He will be missed and remembered. A picture showing him waiting for his friends to catch up with him is an appropriate ending to this article.

Figure 10. Volker Lehmann on one of his yearly skiing trips with one the authors (U. G.) being ahead of the crowd.

Acknowledgements

The authors acknowledge the hospitality of the Lehmann family over many years and discussions touching on the life of Volker Lehmann with various friends.

References

1. V. Lehmann and H. Föll, *J. Electrochem. Soc.*, **137**, 653 (1990).
2. V. Lehmann and U. Gösele, *Appl. Phys. Lett.*, **58**, 856 (1991).
3. H. Föll and U. Gösele, *Physica Status Solidi C*, **4**, 1881 (2007).
4. V. Lehmann, H. Föll, L. Bernewitz, J.G. Grabmaier, Proc. Flat Plate Solar Array Project Res. Forum on the High-Speed Growth and Characterization of Crystals for Solar Cells; Florida 1983 (JPL Publ. **84-23**), (1984) 527.
5. V. Lehmann and H. Föll, *J. Electrochem. Soc.*, **135**, 2831 (1988).
6. V. Lehmann, K. Mitani, R. Stengl, and U. Gösele, Jap. J. Appl. Phys. Part 2, Letters, **28**, L2141 (1989).
7. K. Mitani, V. Lehmann, R. Stengl, and U. Gösele, Jap. J. Appl. Phys. Part 1, **30**, 615 (1991).
8. U. Gösele and V. Lehmann, Adv. Materials, **4**, 114 (1992).
9. L. T. Canham, *Appl. Phys. Lett.*, **57**, 1046 (1990).
10. V. Lehmann, *Electrochemistry of Silicon*, Wiley-VCH, Weinheim (2002).
11. V. Petrova-Koch, T. Mushik, A. Kux, B. K. Meyer, F. Koch, and V. Lehmann, *Appl. Phys. Lett.*, **61**, 943 (1992).
12. V. Lehmann, *J. Electrochem. Soc.,* **143**, 1313 (1996).
13. V. Lehmann, *J. Electrochem. Soc.,* **140**, 2836 (1993).
14. U. Grüning, V. Lehmann and C. M. Engelhardt, *Appl. Phys. Lett.*, **66**, 3254 (1995).
15. S. Ottow, V. Lehmann, and H. Föll, *J. Electrochem. Soc.*, **143**, 385 (1996).
16. F. Müller, A. Birner, U. Gösele, V. Lehmann, S. Ottow, H. Föll, *J. Porous Materials*, **7**, 201 (2000).
17. V. Lehmann, W. Hönlein, H. Reisinger, H. Spitzer, H. Wendt, and J. Willer, *Solid State Technology*, **38**, 99 (1995).

ECS Transactions, 16 (3) 21-37 (2008)
10.1149/1.2982539 ©The Electrochemical Society

In-Situ Assessment of Macropore Growth in Low-Doped n-Type Silicon

J. Carstensen[a], A. Cojocaru[a], M. Leisner[a], and H. Föll[a]

[a] Institute for Materials Science, Christian-Albrechts-University of Kiel, Kaiserstrasse 2, 24143 Kiel, Germany

Understanding pore growth in semiconductors in detail needs some in-situ information about the processes occurring in a growing pore. It is shown that dual-mode in-situ FFT impedance spectroscopy can provide useful data for macropore etching in n-type Si under back side illumination. A new illumination mode is used alternating with the conventional current-voltage mode, and data evaluation is based on an advanced model developed for this kind of pore etching. The principles of the technique and the basics of the model are introduced and illustrated by a number of examples, some of which show new kinds of pore growth modes.

Introduction

In 1990 Lehmann and Föll published the first paper describing the formation of macropores in low-doped n-type Si by using back side illumination (bsi), aqueous HF-electrolytes, and lithographically defined nucleation – n-macro(aqu, bsi, litho) pores for short (1). The experiments performed were based on the prediction that the bent space charge region (SCR) around pore tips would focus holes diffusing around in the sample on the pore tips and thus enable pore growth. The initial experiment as well as many experiments performed since then (cf. e.g. (2 - 11) and the references therein) generally tended to confirm this "SCR-model" of n-macro(aqu, bsi) pores in Si, but also left a number of open questions, as did the discovery that very deep p-macro(org, (litho)) pores could also be obtained in (low-doped) p-type Si, if "organic electrolytes" were used (4, 11 - 15).

In this context it is interesting that the authors of (1) already filed a number of patent applications concerning the use of macropores. Many other groups have joined this quest for turning macropores in Si to some uses (cf. the overviews in (7, 11, 16); meanwhile some new applications like batteries (17, 18) or heat pipes (19) have emerged).

However, disregarding an n-macro(aqu, bsi, litho) based "biochip" fabricated in V. Lehmann's sphere of influence for a while, there is still no product based on macroporous Si on the market 18 years after the initial discovery. The reasons for this are variegated, complex, and not always known. Nevertheless, a few general points can be made. The slow etching speed of roughly 1 µm / min means processing times of many hours for deep pores – a cost factor not easily acceptable for mass products like fuel cell electrodes or optical filters. Moreover, restrictions on geometry (e.g. smallest pore size and distance) and morphology (e.g. systematic or random fluctuations of the pore diameter; pore wall roughness) may exceed the allowed bandwidth for some applications. Overcoming these problems proved to be difficult because the SCR model does not help much in this respect, and better models are not yet available. Large progress has been made empirically, e.g. with respect to geometry (5, 20, 21) and pore wall roughness (22) and lately for the first time also with respect to etching speed (23), but a more refined model for macropore etching would be helpful in this context.

The SCR model (like all other models) so far could only be checked by ex-situ or "post-mortem" analysis, i.e. by looking at the pore structure obtained after concluding an experiment; always destroying the sample. An in-situ observation of what is going on at the pore tips (and the pore walls) during etching would be of great help in understanding the finer points of pore etching and in constructing and evaluation models, but this task is quite difficult for obvious reasons: most methods are either not employable inside a pore or would change the etching conditions too much. Impedance spectroscopy (IS) emerged as the only tool that is presently capable of giving some in-situ information, and in the remainder of this paper we will focus on the possibilities and limits of this technique. It will be demonstrated that dual-mode in-situ IS, if done with a Fast Fourier Transform technique (FFT) and in a new mode in addition to the conventional one, is indeed capable to render useful information that is instrumental in overcoming some of the barriers to macropore employment in products.

Impedance Spectroscopy Applied to Pore Etching

General Points

The principle of IS is simple: Measure the impedance of the electrochemical cell, i.e. the complex resistance containing amplitudes and phases, as a function of the (circle) frequency ω. This can be done most easily by modulating the otherwise constant applied voltage U_0 in a potentiostatic experiment, i.e. $U_0(t) = U_0 + U_{\mathrm{mod}} \cdot \sin(\omega t)$ and by measuring the response with respect to amplitude and phase in the current individually for the desired frequencies. Basic conditions for successful experiments are linearity, usually obtained for small U_{mod}, steady state, and uniformity. Steady state simply means that the system does not change noticeably during the measurement, and this condition is not necessarily met during pore etching since conventional measurements take too long. Modulating with all frequencies simultaneously and extracting the response by an FFT technique can alleviate this problem. The price to pay are larger peak-to-peak amplitudes; requiring optimization with respect to linearity and signal-to-noise ratios. Of course, it is equally well possible to modulate the current in a galvanostatic experiment and to analyze the voltage response. This is the conventional voltage-current (UI) mode, hereafter referred to as "in-situ FFT UI IS".

The etching of n-macro(aqu, bsi) macropores generally is a branch of photo-electrochemistry and in this field "impedance" spectra can also be obtained by modulating the intensity of the illumination and measuring the response of the current and / or the voltage. Some work with respect to front side illumination ("fsi-IS") has been reported (24 - 29), but this fsi-IS mode has not yet been used during pore etching in semiconductors.

Modulating the intensity of back side illumination allows a third "bsi-IS" mode, which will be introduced here in the context of macropore etching as "in-situ FFT bsi IS".

The condition of uniformity is not easily met during pore etching experiments. Any IS records modulations of the total current and thus averages over (typically) millions of pore tips and whatever happens at the O-ring or at other unavoidable discontinuities in the current flow. Space prevents to go into details, suffice it to say that only after a dedicated FFT IS spectrometer had been built (by ET&TE), fully integrated into an etching system and with the capability to modulate the bsi illumination intensity, useful spectra can now be obtained routinely in the authors laboratory.

Evaluation of the bsi IS Data Obtained

A full understanding of n-macro(aqu, bsi) pore etching would mean that a quantitative expression for the current I flowing through the system as a function of all the variables like external voltage U_{ex}, illumination intensity P, temperature T, HF concentration c_{HF}, time t, circle frequency ω, and so on, would be known. The two impedances then would simply be given by $Z_{\text{U}} = (\mathrm{d}I/\mathrm{d}U)^{-1}$ for the UI mode and by $Z_{\text{bsi}} = (\mathrm{d}I/\mathrm{d}P)$. Note that while $[Z_{\text{U}}] = \Omega$, Z_{bsi} has an arbitrary dimension depending on how P is defined; and data are typically displayed in arbitrary units in what follows. No such complete model exists at present but as far as Z_{bsi} is concerned, major ingredients for a model have been established. **Fig. 1** shows a graphic model of the diffusion problem that has to be solved.

The light impinging on the sample back side generates electron-hole pairs at a density directly given by the light intensity P. The holes diffuse through the Si and recombine in the bulk; the diffusion length L describes this process. At some time t macropores have grown to a depth d_{Pore}, and in a first approximation, just mirroring the SCR-model for pore growth, it is assumed that all holes reaching a fictitious plane at depth d_{Pore} are consumed at the pore tips; this translates into a boundary condition for the recombination velocity $S_{\text{P}}(\text{z} = d_{\text{Pore}}) = \infty$. The current flowing through the pore tips then can be obtained by solving the diffusion equation for this problem; the result obtained for this first approximation is

$$Z_{\text{bsi-1}}(\omega, d_B, L) = \frac{\mathrm{d}j_{\text{sem}}(\omega, d_B, L)}{dP(\omega)} \propto \frac{1}{\cosh\left(d_{\text{B}}\sqrt{\dfrac{1}{L^2} + \dfrac{i\omega}{D}}\right)}. \qquad [1]$$

D is the (constant) diffusion coefficient of the holes.

Fitting measured Z_{bsi} spectra to Eq. [1] gives good results but not a perfect match.

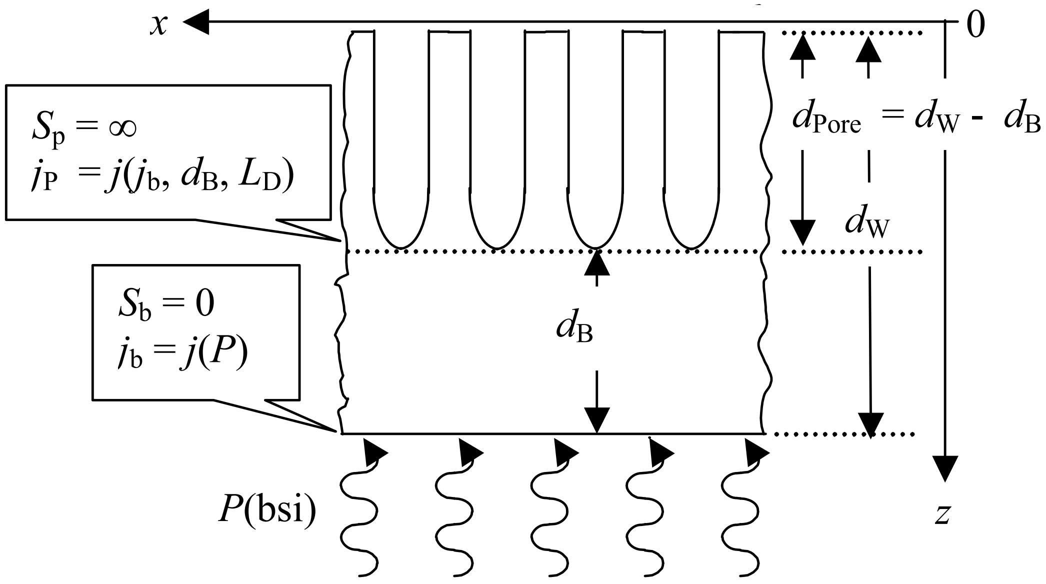

Figure 1. Parameter definition for etching n-Si-macropores(aqu, bsi).

This is shown in **Fig. 2** (curve A) for one spectrum printed in the conventional Nyquist plot, i.e. the (negative) imaginary part if the impedance is plotted vs. the real part. Note that one etching experiment yields several 1000 spectra and that the match shown is among the best one can get.

For sake of simplicity and clarity, Eq. [1] does not take into account the back side recombination velocity (i.e. $S_B = 0$ in **Fig. 1**) and the absorption constant α of the LASER light since this is not very important. However, for the fitting of the impedance data shown here, these parameters are included and the full (and quite lengthy equations) have been used with appropriate numbers for the two additional parameters. The problem of an imperfect match, however, still remains. In conclusion, the SCR-model for n-macro(bsi) pore growth is too simple and must be augmented.

At a next step of sophistication we now assume that some holes arriving at d_{Pore} do not contribute to the pore tip current but reach areas not very close to the pore tip. Mathematically this is expressed by changing the boundary condition $S_P = \infty$ in **Fig. 1** to a periodic expression where the recombination velocities between the pore tip and the point halfway between the pores differ by some ΔS_P. Taking this into account, the solution of this diffusion problem gives as a second approximation

$$Z_{\text{bsi}-2}(\omega, d_B, L, \Delta S_P) = A_1 Z_{\text{bsi}-1}(\omega, d_B, L) \left(\frac{\dfrac{1}{\sqrt{\dfrac{1}{L^2} + \dfrac{i\omega}{D}}}}{\dfrac{1}{\sqrt{\dfrac{1}{L^2} + \dfrac{i\omega}{D}}} + \Delta \dfrac{D}{S_P}} \right). \quad [2]$$

A_1 is some proportionality constant that will be discussed later in more detail. The match to the data point indeed improves (**Fig. 2**, curve B), but is still not perfect.

A perfect match can be obtained in a third approximation if one assumes that some fraction of the holes reaching the pore tip region is not immediately consumed at the tip but have to "wait" a bit, meanwhile diffusing around. In physical terms this means that oxide covered parts of the pore tip cannot process holes instantly but need to wait until the oxide thickness has been sufficiently reduced.

The proper term for this "waiting time" presently cannot be obtained from solving an appropriately changed diffusion equation but is taken introduced by adding a general diffusive term akin to what is known as "Warburg impedance" in UI IS. The quotation marks refer to the fact that "proper" impedances are measured in Ohm [Ω].

The complete model-based theoretical bsi IS, found sufficient to match huge numbers of spectra in many experiments rather perfectly, comes out to

$$Z_{\text{complete}}(\omega, d_B, L, \Delta S_P) = A_1 \left(Z_{\text{bsi}-1} + \frac{A_0}{\dfrac{1}{Z_{\text{bsi}-1}} + A_2\sqrt{i\omega}} \right) \left(\frac{\dfrac{1}{\sqrt{\dfrac{1}{L^2} + \dfrac{i\omega}{D}}}}{\dfrac{1}{\sqrt{\dfrac{1}{L^2} + \dfrac{i\omega}{D}}} + \Delta \dfrac{D}{S_p}} \right) \quad [3]$$

with the first bracket giving the Warburg-like diffusion term, and $Z_{\text{bsi-1}}$ as given by Eq. [1] or rather by the more complex equation not shown here that takes into account the effects mentioned above.

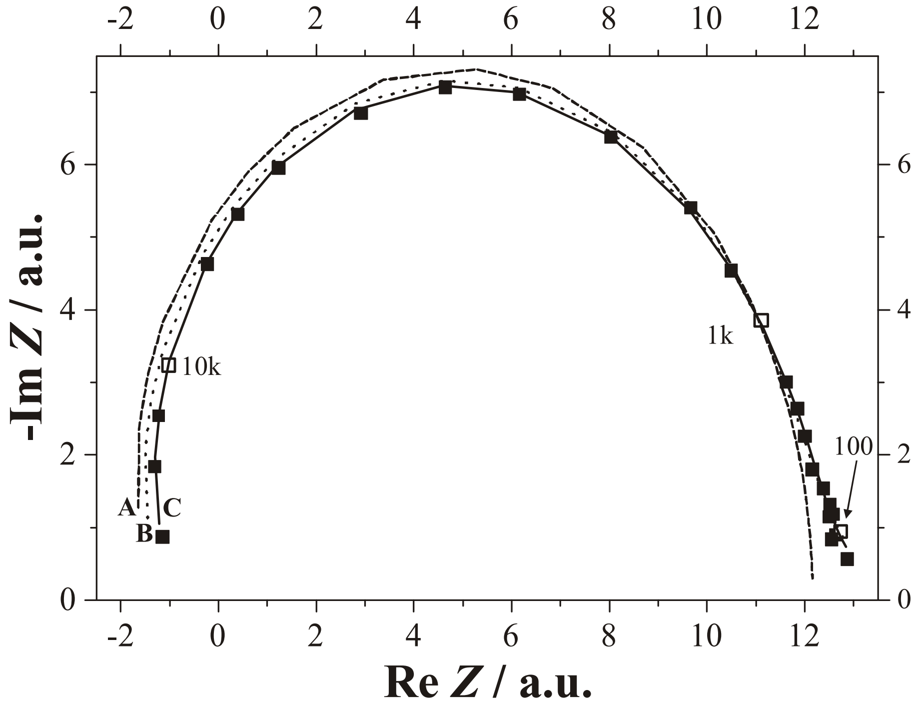

Figure 2. Fitting theory to measured in-situ bsi-IS data (black squares). Curve A results from Eq. [1] only. Curve B results from Eq. [2], and curve C is based on the complete impedance as given in Eq. [3]. Numbers indicate some of the 27 frequencies in Hz (total range 10 Hz - 40 kHz).

Besides the variables L, d_{pore}, ΔS_{P} (always found as D / S_{P}) and therefore expressed as $\Delta(D / S_{\mathrm{P}})$, two new parameters A_0, and A_2 emerge beside A_1 already mentioned above. It is easy to see that A_1 is a measure for the over-all etching area defined by the envelope of the pore tips, including the area of under-etching at the O-ring or under masks. The combination of A_0 and A_2 quantifies the fraction of and the collection efficiency for that part of the etching current that experiences the additional diffusion around the pore tips.

Evaluating the in-situ FFT bsi IS data thus should give in-situ information about the pore depth d_{Pore}, the diffusion length L, the total active area A_1 (essentially reflecting the degree of under etching), and the detailed current flow processes around the pore tips quantified by A_0, A_2, and $\Delta D/S_{\mathrm{P}}$. In addition, some "electrical" data about e.g. resistances and capacities are also obtained. Since L is a constant by definition, the numerical evaluation procedure determines L from the first few spectra and then takes it as constant, making subsequent data extraction easier and more precise.

Evaluation of the UI IS Data Obtained

As long as no closed (mathematical) model of the simple current-voltage characteristics of a Si electrode under any conditions exists, deriving theoretical UI impedances is not possible. In this case the general approach is to find the best fit to equivalent circuits expressed either in suitable circuit diagrams containing capacitances, resistors and Warburg impedances or, slightly more abstract but fully equivalent, by using model equations describing processes with as many time constants as needed. The equation, found in standard IS text books (30) that matches many thousands of in-situ FFT UI IS obtained so far rather well is

$$Z_U(\omega) = R_s + \frac{1}{\left(\frac{i\omega\tau}{(R_p + \Delta R_p)(1+i\omega\tau)} + \frac{1}{R_p(1+i\omega\tau)}\right) + i\omega C_p} . \qquad [4]$$

Following the standard interpretation of such a model equation, R_s describes the ohmic losses, C_p describes the capacitance of the interface, and R_p the chemical transfer resistance of the chemical dissolution process. The chemical dissolution splits up into two processes with different reaction rates characterized by the relaxation time τ of the slow process and the time constant R_pC_p of the fast process. The difference ΔR_p describes the increase in the chemical transfer resistance at higher frequencies. A similar approach has been used successfully for unraveling pore formation in InP, cf. (31, 32) for details.

The processes in question are current-driven direct dissolution of Si (typically occurring with a valence $n_{dd} = 2$), current-driven Si oxidation (valence $n_{Ox} = 4$), and purely chemical dissolution of the oxide. Assuming that direct Si dissolution is the "fast" process and that Si dissolution by oxide formation plus oxide dissolution is the "slow" process, it is possible to derive an equation for the over-all valence n (for a more detailed derivation see (33)

$$n = 2\beta + 4(1-\beta) = \frac{4}{2-F} = \frac{4}{2 - \frac{\Delta R_p}{R_p + \Delta R_p}} . \qquad [5]$$

It is known from numerous experiments that n-macro(aqu, bsi) pores in Si can only be obtained if the over-all post-mortem valence is $n \approx 2.7$. It is remarkable that an evaluation of in-situ FFT UI IS data with Eq. [4], as will be shown, does produce valence values rather close to this experimental finding, lending credibility to the approach chosen.

A full evaluation of in-situ FFT UI IS data thus provides as a function of time (or pore depth) the following parameters: R_s, R_p, C_p, τ, ΔR_p, and as a combination of those parameters the valence n calculated from Eq. [5]. It is beyond the scope of this paper to discuss in detail what kind of conclusion with respect to the pore etching process can be drawn from the 5 direct parameters; the examples given in the next section will provide some more information.

Cross Check of Impedance Data

Evaluation of IS data from the two modes described gives the (constant) diffusion length L (always close to the actual value as far as it is known), the direct time development of the 9 non-trivial parameters discussed above, and the time development of 2 derived parameters: the valence n as discussed above and the pore growth speed as simple derivation $d(d_{Pore})/dt$. To a small extent these numbers can be compared to numbers from a post-mortem analysis (e.g. d_{Pore} or (average) valence), but mostly no alternative cross-check is possible since no other methods can measure in-situ parameters. However, some comparison to external in-situ over-all data is possible. External in-situ data are simply the applied voltage U, the total current I flowing across the cell, and the illumination intensity P. In a typical n-macro(aqu, bsi) pore etching experiment the nominal current density $j = I$ / cell area is programmed to follow a specific, empirically determined function over time that takes into account that the HF concentration and the local potential at the pore tip drop as a function of pore depth and thus time. The voltage might also be programmed to follow a certain time dependence, and the only parameter that must be left free to adjust itself is the illumination intensity P. It is expected to drop for two reasons: First, since the current decreases with pore depth, fewer holes need to be produced. Second, since the distance between pore tip and the hole source (= back side) decreases, a larger percentage of the holes can reach the pore tip. The relation between the illumination intensity P and the external current is thus a quantity of interest; it is best recorded as $\ln(I / I_P)$ with I_P = maximum photo current injected; i.e. $I_P \propto P$, because a straight line could be expected from the recombination losses within the bulk silicon layer with thickness d because of $I / I_P \propto \exp(-d/L)$. As it turns out, $\ln(I / I_P)$ can be independently reconstructed from the impedance data, thus providing an additional cross-check.

Experimental Details

All experiments were run under the following general conditions. Specimen: n-type Si, doping 5 Ωcm, {100} oriented, implanted n^+ back side contact, mostly lithographically structured front side with a hexagonal or square array, lattice constant = 4.2 µm. Typically the sample size was 1 cm^2. ET&TE etching system ELYPOR 02 with full PC control of an LED array for illumination of the back side to ensure the desired etching current (and of all other parameters). FFT impedance spectrometer: ET&TE system for fully automated in-situ impedance data acquisition and analysis for UI IS and bsi IS.

Electrolytes used can be classified as i) standard 5 wt.% aqueous HF electrolyte, ii) acetic acid ("HAc") electrolytes, typically with high HF concentrations around (10 – 15) wt.% HF and 33 wt.% HAc, and iii) (5 – 15) wt.% HF "viscous" electrolytes (abbreviated "visc"), obtained by typically adding 0.42 – 0.83g/l of carboxymethylcellulose salt (CMC) to the electrolytes from above. Electrolyte ii) and iii) have been recently shown to allow for fast growth of qualitatively good pores (34) and are thus of large interest; they also open up new territories in parameter space that show a number of pore growth modes never seen before. Much simplified, we can state that "standard" electrolytes allow to etch "state-of-the-art" macropores, "viscous" electrolytes make for "better" pores in terms of e.g. pore wall roughness, and "HAc" pores allow for rapid pore etching to great depths far beyond the state-of-the-art. "Viscous HAc" electrolytes allow for good and fast pores with some limitations that need yet to be probed, cf. (34) for details.

Some Illustrative Results

Charting new territories in the parameter space of n-macropore etching under back side illumination

Given limits on space, it is not possible to discuss a large number of different etching experiments completely, i.e. by showing and discussing the time dependence of all 11 parameters extracted from IS data besides the diffusion length L, the $\ln(I / I_P)$ plot, scanning electron microscope (SEM) pictures of the pores obtained, atomic force microscope (AFM) pictures of the pore wall roughness, and so on. Instead we will focus on some selected experiments and parameters, in particular if they show unexpected behavior. The first example (**Fig. 3**) shows a standard n-macro (5 wt.%, 5 Ωcm, bsi, litho) experiment; i.e. macropore etching in 5 wt.% aqueous HF to a depth of approximately 100 µm under otherwise optimized conditions. Since the IS data yield the pore depth d_{Pore}, the data extracted have been rescaled from the originally measured time dependence and are printed as a function of d_{Pore} and directly matched to the SEM picture of the pores.

Without going into details, the 10 parameters shown develop as one might have expected. After some initial nucleation phase has ended, most parameters change slowly and smoothly with the pore depth. In particular, the valence n is rather constant around 2.8 (its average, however, would be somewhat smaller) and increases slightly. The growth speed v_{tip} of the tip is also rather constant (if somewhat noisy) around 0.8 µ/min, decreasing just a bit. The parameter $\Delta(D/S_P)$, after going through a maximum at a pore depth of about 15 µm, decreases smoothly thereafter. This is of some interest because it indicates a decreasing "focusing" efficiency of the pore tip with respect to the holes reaching it. The transfer resistance of the dissolution process increases smoothly, indicating diffusion-limited growth of the pore. The parameter A_1 increases continuously after nucleation, indicating that under etching continues and does not (yet) saturate. Generally, all parameters are well behaved and change smoothly with depth as would be expected for pore growth under these conditions to a relatively small depth. Note, however, that there is no "steady state" in the sense that transport parameters stay constant.

It is easier to discuss what follows if at this point the behavior of a pore tip will be considered in a highly simplified way as the result of a balance between driving and retarding "forces". A positive potential and molecules like HF or F^- at the pore tip promote Si dissolution and thus must be counted among the driving forces; a passivating species reaching the pore tip provides a retarding force (for more details of this concept see (35 - 38)). For the example given in **Fig. 3** it can be stated that this "force" balance allows pore growth and does not yet change very much with the pore depth. However, at some pore depth larger than that shown in **Fig. 3**, pore growth will invariable come to an end, meaning in the simple balance model introduced here, that the retarding forces or passivation always "wins" in the end.

The next example, shown in **Fig. 4**, demonstrates totally different behavior for pores that look very much like the ones shown in **Fig. 3**; they might even be classified as being of better quality. In essence, standard n-macro (5 wt.%, visc, 5 Ωcm, bsi, litho) pores were attempted with a "viscous" electrolyte, i.e. a standard 5 wt.% aqueous HF electrolyte with 0.83 g/l carboxymethylcellulose sodium salt (CMC) added for a considerable but unspecified increase of the electrolyte viscosity. As has been shown by Foca et al. (22) and Cojocaru et al. (34), viscous electrolytes provide for better pore quality without sacrificing growth speed and this is (somewhat surprisingly) still true for large growth speeds in more concentrated HF (34).

At least 5 out of 10 parameters now show very unruly behavior; there is a kind of periodic "pulsing", expressed, e.g., as sudden decreases in the valence n and (negative) peaks in the growth rate v_{tip}. In other words, roughly every 20 µm the pores stop to grow or at least become sluggish for a while, then they start growing again. Note that this kind of behavior does not show in the post-mortem pore picture and that without in-situ data it would be impossible to recognize this peculiar (or rather chaotic) behavior.

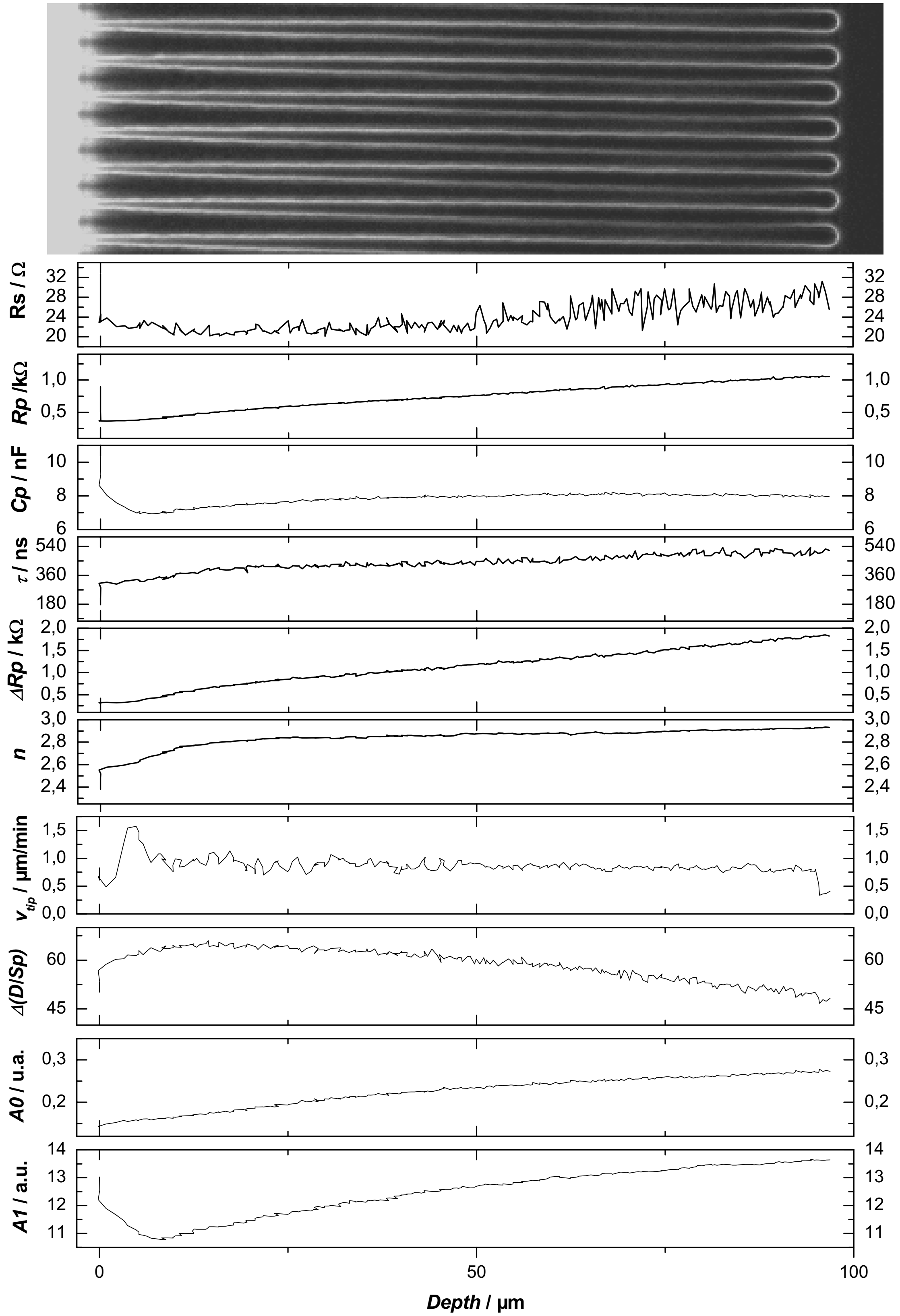

Figure 3. Impedance parameters vs. pore depth in direct comparison to the etched pore morphology. A standard aqueous electrolyte with an HF concentration of 5 wt.% was used. The applied voltage was 0.4 V, and the etching current decreased from 21 mA/cm^2 to 18 mA/ cm^2 during the total etching time of 126 min. Further data: $T = 20°C$, n-type Si, (100), 5 Ωcm, pre-structured by standard photolithography, hexagonal lattice $a = 4.2$ µm.

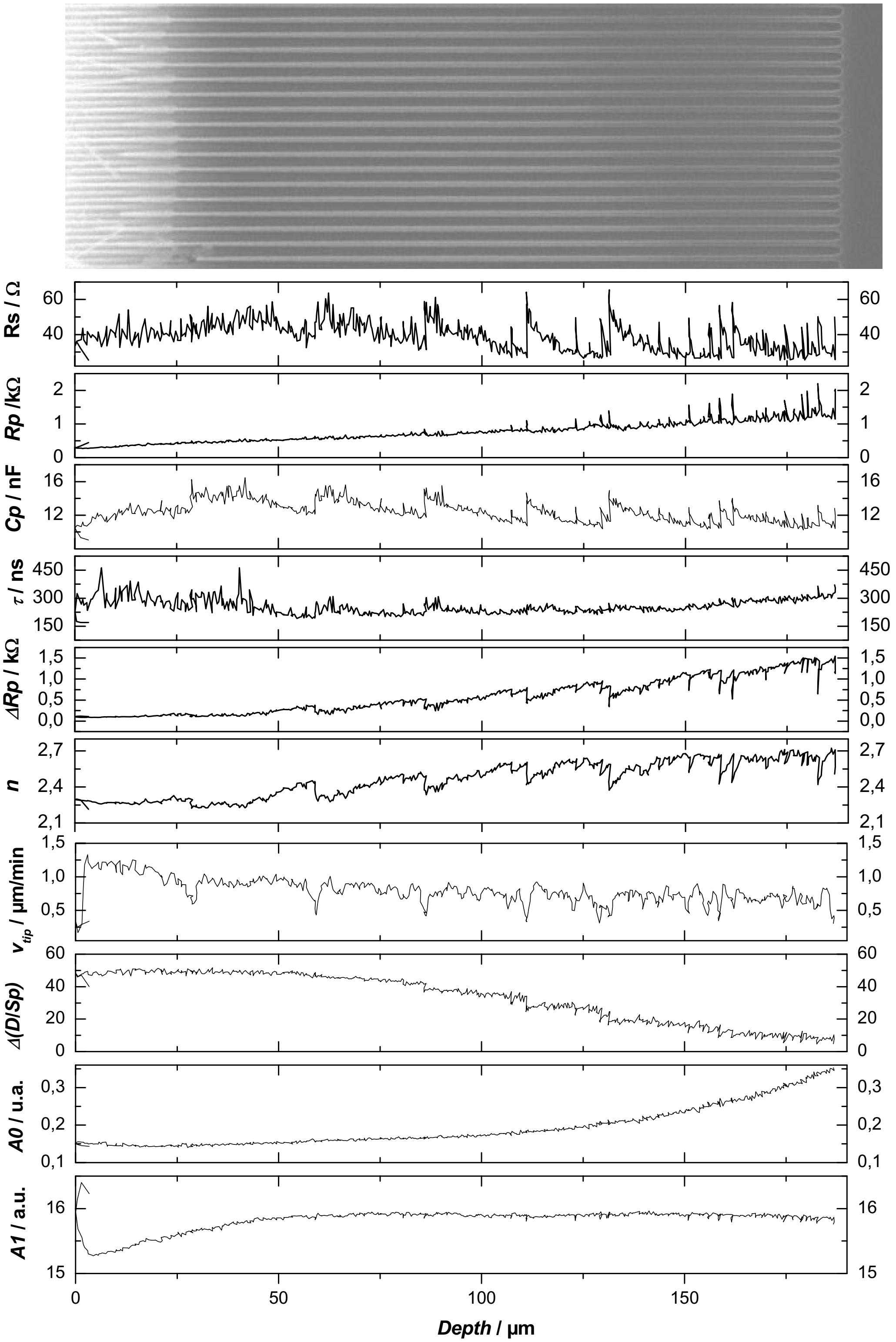

Figure 4. Impedance parameter vs. pore depth in direct comparison to the etched pore morphology. An aqueous electrolyte with an HF concentration of 5 wt.% and 0.83 g/l of CMC was used. The applied voltage was 0.7 V and the etching current decreased from 15 mA/cm^2 to 10 mA/ cm^2 during the total etching time of 295 min. Further data: $T = 20$°C, n-type Si, (100), 5 Ωcm, pre-structured by standard photolithography, hexagonal lattice $a = 4.2$ µm.

Looking at the data in **Fig. 4** and taking into account similar data from many comparable experiments not shown here, the first conclusion within the confines of the simple picture outlined above is that the balance of driving and retarding forces is fluctuating with some tendency to periodicity (indicating, perhaps, an intrinsically non-linear and thus chaotic system). In contrast, $\Delta(D/S_P)$ decreases smoothly, once more indicating that the "focusing" efficiency of the pore tip decreases. Interestingly, A_1 after some initial increase indicative for under-etching stays constant, allowing the conclusion that under-etching saturates after a while.

The next example shows n-macro (15 wt.% HF, HAc, visc, 5 Ωcm, bsi, litho) pores that show a rather unexpected and newly discovered behavior (34). The electrolyte used was based on 15 wt.% aqueous HF that does not produce good deep pores by itself but only in conjunction with additives like HAc; see (34) for more details.

At a pore depth of about 80 µm a so-called "growth mode transition", or "mode transition" (39) for short, occurs. Instead of the cavity formation expected for a neat 15 wt.% electrolyte and thus termination of the pore growth at about 100 µm (cf (34)), self-induced anti-phase diameter oscillations occur. In other words, every second pore stops growing for a while, passing its proper share of the (constant) current to one of its neighbors. Then the process reverses. Note that this structure for basic geometric reasons is only visible on one of the possible cleavage planes, but not on the others because anti-phase relationships cannot have a hexagonal symmetry (cf. (39) for more details) – we have a so-called frustrated arrangement. It is therefore entirely possible to miss this behavior in a post-mortem analysis.

Looking at the IS data, one first perceives a clear mode transition around 40 µm that is not quite obvious in the SEM picture and then the major mode transition taking place around 90 µm where the anti-phase oscillations start. That the data match well with the SEM picture, noting that d_{pore} is also obtained from these data, gives a rather clear indication that the measurements plus data extraction procedure are reliable.

The fact that the mode transition around 90 µm is not far more prominent than the one at 40 µm in the IS data as one might naively assume from the SEM picture is easy to understand: on average not much has changed. In fact, looking at the "electrical" parameters, in particular at the transfer resistance R_{p}, it appears that the system has achieved steady state for the first time.

The last example is taken from a set of experiments that were designed to amplify the mode transition behavior that are inherent in all n-macro(bsi) pore growth experiments and particularly clearly expressed at higher HF concentrations. In essence, the external current I, after some pore initiation time, was switched between some value I_0 and ½ I_0, forcefully switching a system hovering at some mode-transition limit into one mode or another. Noting that the system shown in **Fig. 5** has some internal frequency as expressed in time or pore depth by the diameter oscillations, the same conditions were chosen with a switching frequency matched to the internal one. The results are given in more detail in (39).

Some of the data clearly show the current switching; some do not, and this is already of some interest. The three mode transitions (outlined by arrows in the SEM picture) are visible in the IS data, too, but a detailed discussion would go beyond the scope of this paper. Note that replotting the IS data as a function of pore depth instead of time is more difficult here.

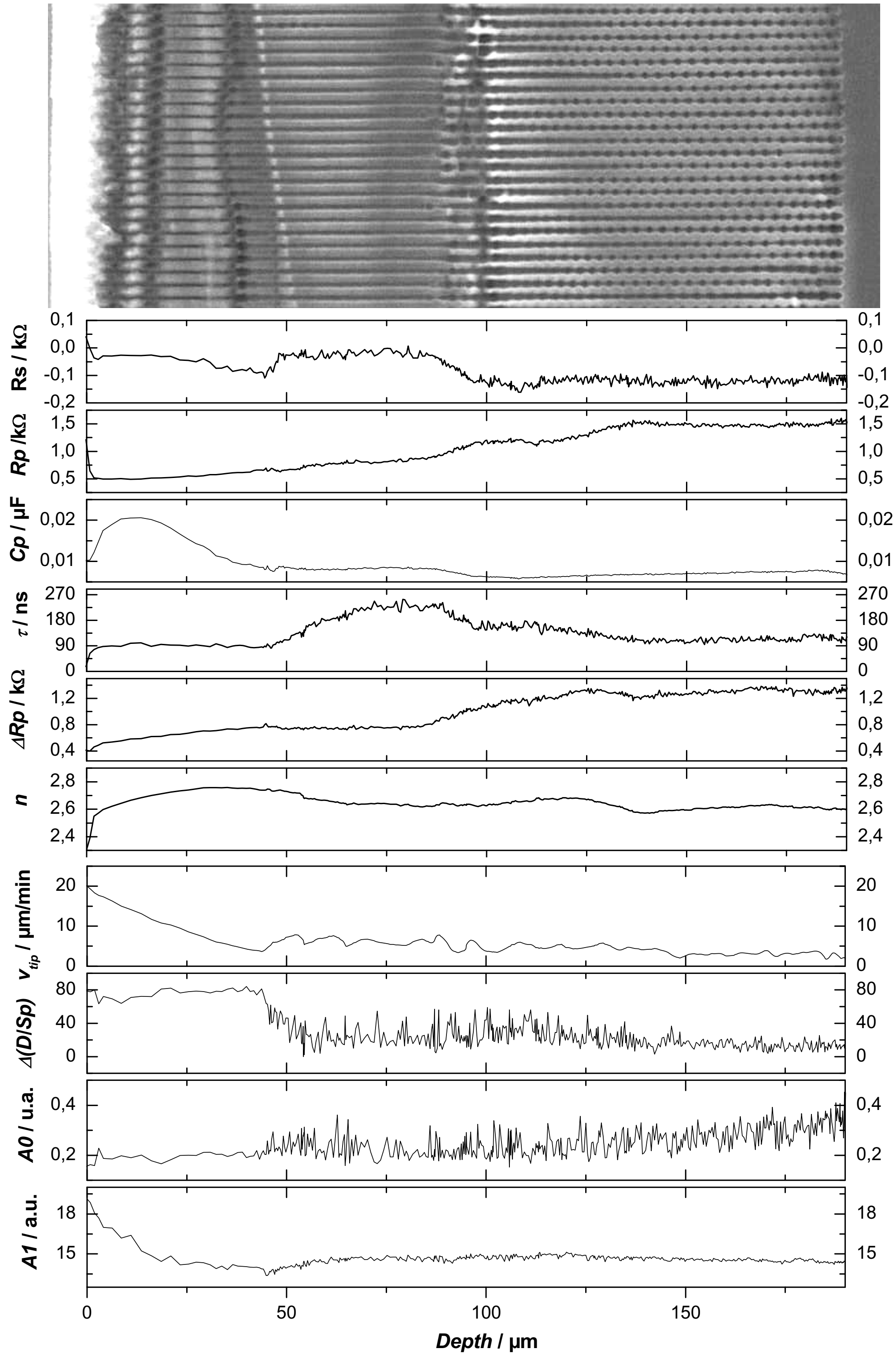

Figure 5. Impedance parameter vs. pore depth in direct comparison with the etched pore morphology. An aqueous electrolyte with an HF concentration of 15 wt.% and 0.42 g/l of CMC was used. The applied voltage was 1.0 V and the etching current decreased from 26 mA/cm^2 to 16 mA/ cm^2 during the total etching time of 117 min. Further data: $T = 20°C$; n-type Si, (100), 5 Ωcm, pre-structured by standard photolithography, hexagonal lattice $a = 4.2$ µm.

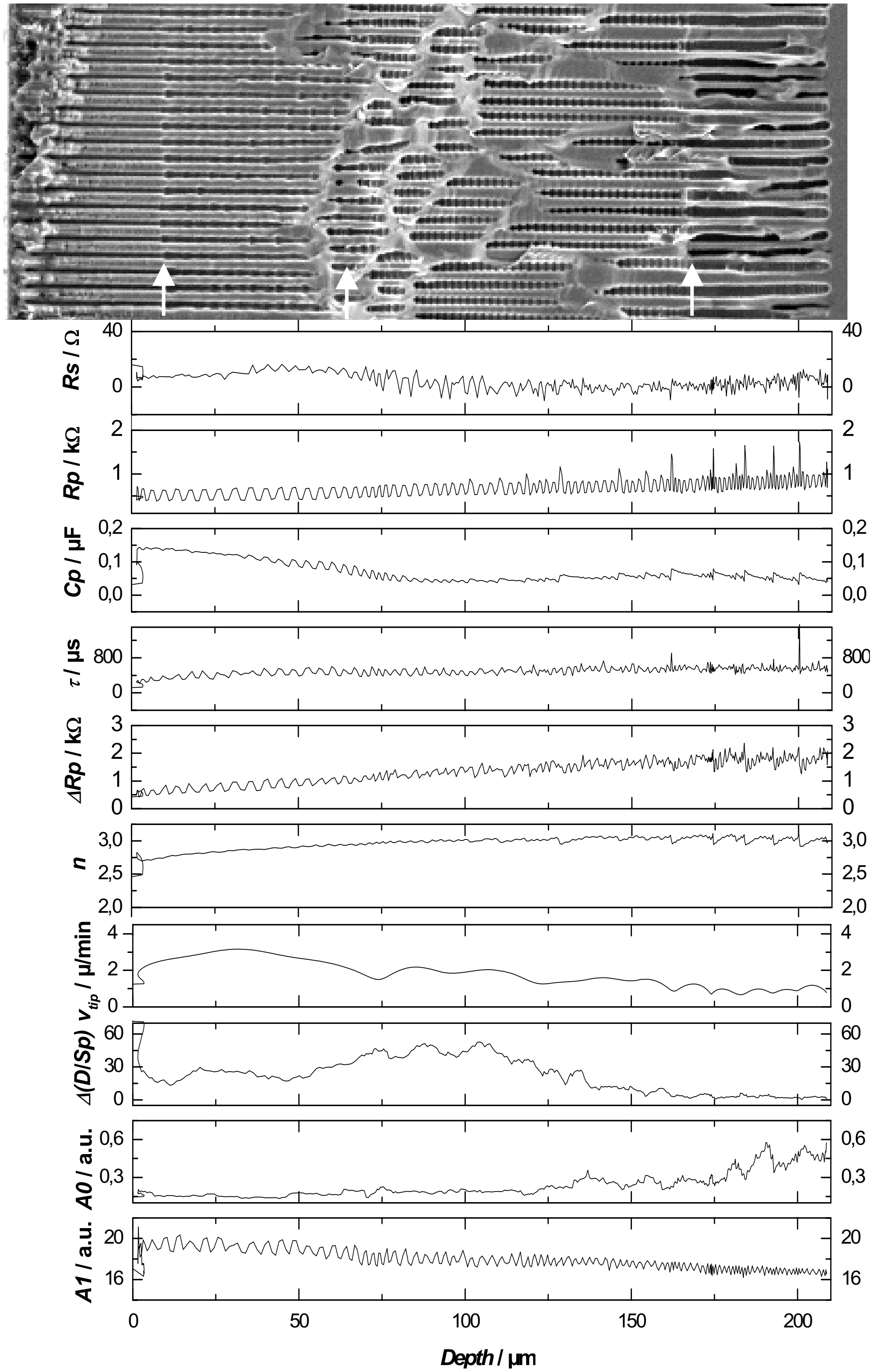

Figure 6. Impedance parameter vs. pore depth in direct comparison with the etched pore morphology. An aqueous electrolyte with an HF concentration of 15 wt.% with 0.83 g/l of CMC was used. A voltage of 1.0 V was applied. After 5 min. of constant current, the current was switched from 26 mA/cm^2 to 16 mA/ cm^2 and back with a period of 1 minute at each current value. The total etching time was 105 min. Further data: T = 20°C; n-type Si, (100), 5 Ωcm, pre-structured by standard photolithography, hexagonal lattice a = 4.2 µm.

The SEM picture also shows a particularly interesting effect: the pore diameter *increases* substantially upon halving the current; a closer look shows that the current density in the pore decreases by about a factor of > 6 instead of staying constant as expected in the naïve SCR model. In other words, instead of reducing the pore radius by a factor of $2^{1/2}$ as could be expected, the radius actually *increases*, contrary to what is known from standard 5 wt.% electrolytes. At the second mode transition around 80 µm the pore growth speed more or less suddenly slows down (with a concomitant increase in the average pore radius); the same thing happens once more at the third mode transition around 170 µm. Note that a 4th mode transition (to cavity formation) must occur by necessity if the experiments were to be continued.

Looking at the pore growth speed v_{tip} as deduced from the impedance data, these sudden changes of the speed seem to be absent. However, this is an artifact of the compressed diagram; if the data are "enlarged" the changes are clearly visible.

In this context it should be noted that the sharpness of growth mode transitions or other pore features in SEM pictures might be deceiving since they only show a small part of the pores. In consequence the SEM may show sharp structural transitions at a defined depth that are actually smeared-out in the full sample and thus not seen as sharp features by the impedance (or other averaging) techniques.

The amount of information contained in the IS data shown in **Figs. 3- 6** is quite large and not yet analyzed or understood in all details. Discussing those parts that are understood, or at least subjected to hypotheses, would go far beyond the scope of this paper; some more information can be found in (40).

Checking for Consistency

Since the etching current $I = j \cdot A_{sample}$ and the Laser intensity I_{P} are set or directly measured as a function of time, respectively, $\ln(I / I_{\mathrm{P}})$ can be plotted directly as a function of time (cf. curve C in **Fig. 7** for an experiment with an HF concentration of 10 wt.% aqueous HF + 33 wt.% HAc). For thick silicon layers recombination losses in the bulk silicon can simply be expressed as $I / I_{\mathrm{P}} = \exp(-d(t)/L) = \exp(-(d_0 - v_{tip} \cdot t)/L)$. For a constant growth speed v_{tip}, $\ln(I / I_{\mathrm{P}})$ therefore should be a straight line with a slope v_{tip}/L, which for larger etching times is visible in **Fig. 7**. Deviations from this straight line are mainly related to under-etching, i.e. an increase of the effective etching area, as can be seen from SEM pictures and also from a comparison with the impedance data. Since $d(t)$, L, and the etching area A_1 are parameters directly obtained from the impedance data, $\ln(I / I_{\mathrm{P}})$ can be calculated from the impedance data, too. Curve A in Fig. 7 represents $\ln(-d(t)/L)$ as expected without under-etching, which for larger times is in good agreement with curve C. Curve B in **Fig. 7** represents $\ln(-d(t)/L)+\ln(A_1)$, taking into account under-etching, and this curve reconstructs the directly measured curve C rather well.

The impedance data, as far as could be checked, have always been found to be fully consistent with independent measurements. The impedance data therefore may be used with some confidence to separate the various processes that electrochemically dissolve silicon in such a way that pores result. One might separate, for example, that part of the current that results in under-etching, or the leakage currents flowing through the pore walls. Curve A in this context shows the expected $\ln(I / P)$ curve as calculated mainly from d_{Si} / L (L: diffusion length as extracted from the impedance data) if no under etching would occur but this will be the topics for future investigations.

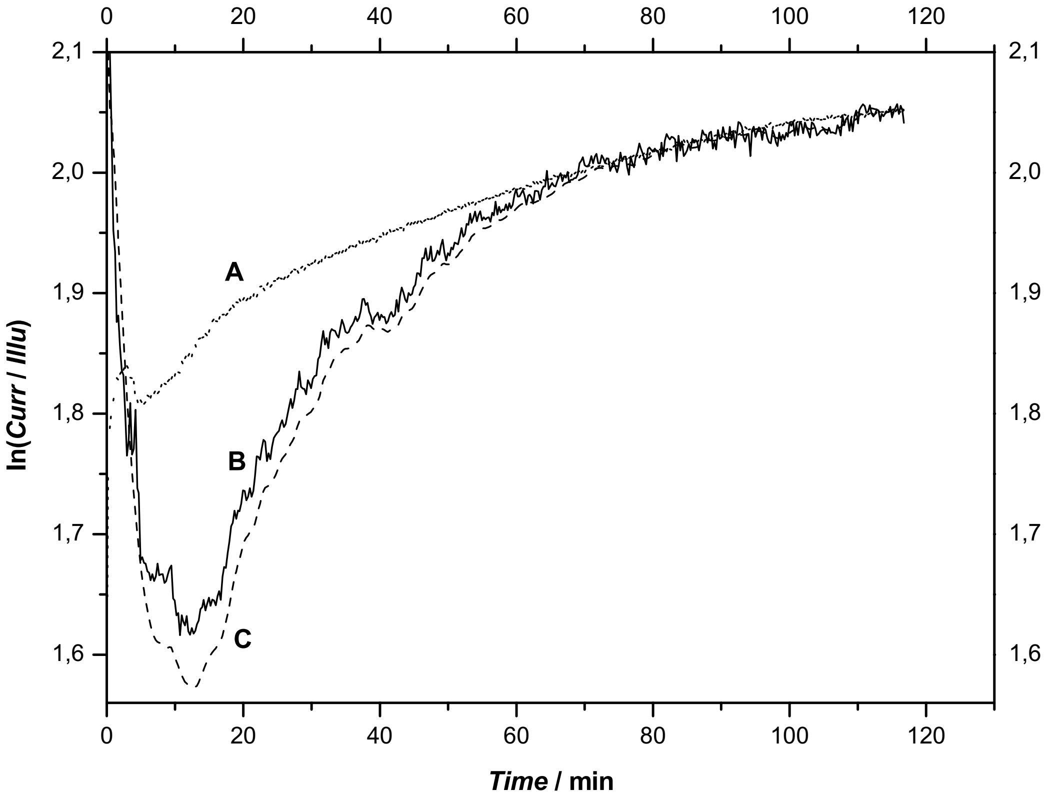

Figure 7. ln(I / P) curves for the experiment described. The dashed line C shows the directly measured curve (no impedance needed), the solid line B shows the curve as reconstructed from impedance data. The dotted line A reconstructs what one would obtain without under-etching. Aqueous electrolyte with an HF concentration of 10 wt.% + 33 wt.% of HAc; U = 0.4 V. The etching current decreased from 27 mA/cm^2 to 16 mA/ cm^2 Further data: T = 20°C; n-type Si, (100), 5 Ωcm, pre-structured by standard photolithography, the nucleation pattern has a hexagonal lattice a = 4.2 µm.

Summary / Conclusion

It has been shown that dual-mode in-situ FFT impedance spectroscopy can be used to obtain a large number of reliable in-situ data that allow unprecedented insights into the dynamics of pore growth in n-type Si under back side illumination. First experiments in a much larger parameter space with respect to the electrolyte composition than previously used provided a number of new results with respect to pore geometry, morphology and growth speed that can only be understood (in parts) by analyzing the IS data obtained in-situ.

It is clear from the data provided that an improved model of the pore etching process cannot possibly be found without reliable in-situ data and the results given must be seen as a first step in this direction. Immediate direct benefits include the possibility to etch better pores faster than the state-of-the-art after 18 year of pore research and development, and to monitor the process in-situ with the option of automating the process via a feedback loop.

In-situ FFT impedance spectroscopy is not limited to n-macro(bsi) pores but can be applied to all pore etching experiments in at least on mode. It can be expected that its application to, e.g., p-macro(org) pores (12, 13, 41) or to "crysto-curro" pores in InP (31, 32) will allow new insights into these pore etching processes, too.

Acknowledgement

Parts of this work have been supported by the Alexander von Humboldt foundation.

References

1. V. Lehmann and H. Föll, *J. Electrochem. Soc.* **137(2)**, 653 (1990).
2. V. Lehmann, *J. Electrochem. Soc.* **140(10)**, 2836 (1993).
3. V. Lehmann and S. Rönnebeck, *J. Electrochem. Soc.* **146(8)**, 2968 (1999).
4. V. Lehmann, *Electrochemistry of Silicon*, Wiley-VCH, Weinheim (2002).
5. S. Matthias, F. Müller, J. Schilling, and U. Gösele, *Appl. Phys. A* **80(7)**, 1391 (2005).
6. E.V. Astrova and A.A. Nechitailov, *phys. Stat. Sol. (a)*, to be published (2008).
7. H. Föll, M. Christophersen, J. Carstensen, and G. Hasse, *Mat. Sci. Eng. R* **39(4)**, 93 (2002).
8. X.Q. Bao, J.L. Lin, J.W. Jiao, and Y.L. Wang, *Electrochim. Acta* **53**, 823 (2007).
9. X.Q. Bao, J.W. Jiao, J. Zhou, and Y.L. Wang, *Electrochim. Acta* **52**, 6728 (2007).
10. M.S. Salem, M.J. Sailor, K. Fukami, T. Sakka, and Y.H. Ogata, *Phys. Stat. Sol. (a)*, to be published (2008).
11. V. Kochergin and H. Föll, *Mater. Sci. Eng. R* **52(4-6)**, 93 (2006).
12. E. Propst and P.A. Kohl, *J. Electrochem. Soc.* **140(5)**, L78 (1993).
13. E.A. Ponomarev and C. Levy-Clement, *Electrochem. Solid-State Lett.* **1(1)**, 42 (1998).
14. J.-N. Chazalviel, F. Ozanam, N. Gabouze, S. Fellah, and R.B. Wehrspohn, *J. Electrochem. Soc.* **149(10)**, c511 (2002).
15. J. Zheng, M. Christophersen, and P.L. Bergstrom, *Phys. Stat. Sol. (a)* **202(8)**, 1402 (2005).
16. H. Föll, J. Carstensen, and S. Frey, *J. of Nanomaterials: Nanoporous and Nanostructured Materials for Catalysis, Sensor, and Gas Separation Applications* **2006**, Article ID 91635 (2006).
17. W. Sun, N.P. Kherani, K.D. Hirschmann, L.L. Gadeken, and P.M. Fauchet, *Adv. Mater* **17**, 1230 (2005).
18. W. Sun, N.P. Kherani, K.D. Hirschmann, L.L. Gadeken, and P.M. Fauchet, *Mater. Res. Soc. Symp. Proc.* **836**, L8.3.1 (2005).
19. D. Cytrynowicz, M. Hamdan, P. Medis, H.T. Henderson, and F.M. Gerner, in *AIP Conference Proc.*, 227 (2003).
20. J. Schilling, F. Müller, S. Matthias, R.B. Wehrspohn, U. Gösele, and K. Busch, *Appl. Phys. Lett.* **78**, 1180 (2001).
21. S. Matthias, F. Müller, and U. Gösele, *J. Appl. Phys.* **98**, 023524-1 (2005).
22. E. Foca, J. Carstensen, M. Leisner, E. Ossei-Wusu, O. Riemenschneider, and H. Föll, *ECS Trans.* **6(2)**, 367 (2007).
23. A. Cojocaru, J. Carstensen, E.K. Ossei-Wusu, M. Leisner, O. Riemenschneider, and H. Föll, *PSST 2008*, submitted (2008).
24. J. Li and L.M. Peter, *J. Electroanal. Chem.* **193**, 27 (1985).

25. Y. Stricot, P. Clechet, and J.R. Martin, *Appl. Phys. Lett.* **49(1)**, 32 (1986).
26. J.-N. Chazalviel, *Electrochim. Acta* **33**, 461 (1988).
27. L.M. Peter, *Chem. Rev.* **90(5)**, 753 (1990).
28. A.R. de Wit, D. Vanmaekelbergh, and J.J. Kelly, *J. Electrochem. Soc.* **139(9)**, 2508 (1992).
29. S. Krause, W. Moritz, H. Talabani, M. Xu, A. Sabot, and G. Ensell, *Electrochimica Acta* **51**, 1423 (2006).
30. J.R. MacDonald, *Impedance spectroscopy*, John Wiley & Sons (1987).
31. M. Leisner, J. Carstensen, and H. Föll, *J. Electroanal. Chem.* **615(2)**, 124 (2008).
32. M. Leisner, J. Carstensen, A. Cojocaru, and H. Föll, *ECS Trans.* **()**, this proceedings (2008).
33. J. Carstensen, E. Foca, S. Keipert, H. Föll, M. Leisner, and A. Cojocaru, *Phys. Stat. Sol. (a)*, submitted (2008).
34. A. Cojocaru, J. Carstensen, M. Leisner, H. Föll, and I.M. Tiginyanu, *PSST 2008*, submitted (2008).
35. J. Carstensen, M. Christophersen, G. Hasse, and H. Föll, *Phys. Stat. Sol. (a)* **182(1)**, 63 (2000).
36. J. Carstensen, M. Christophersen, and H. Föll, *Mat. Sci. Eng. B* **69-70**, 23 (2000).
37. H. Föll, J. Carstensen, M. Christophersen, and G. Hasse, *Phys. Stat. Sol. (a)* **182(1)**, 7 (2000).
38. J. Carstensen, H. Föll, E. Foca, and C. Fang, *Solid State Phenomena* **121-123**, 1115 (2007).
39. A. Cojocaru, J. Carstensen, and H. Föll, *ECS Trans.* **()**, this proceedings (2008).
40. E. Foca, J. Carstensen, G. Popkirov, and H. Föll, *Phys. Stat. Sol. (a)* **204(5)**, 1378 (2007).
41. M. Christophersen, J. Carstensen, and H. Föll, *Phys. Stat. Sol. (a)* **182**, 601 (2000).

ECS Transactions, 16 (3) 39-51 (2008)
10.1149/1.2982540 ©The Electrochemical Society

A Three Pulse Electrochemical Regime as a Fabrication Platform for Nano-Structured Multifunctional Silicon Based Materials and Their Primary Prototypes

E. Matveeva, Y. Makushok[a], L. Bychto[b], and E. Pastor[a]

[a] Nanophotonics Technology Center, Technical University of Valencia
46071 Valencia, Spain
[b] Department of Electronics and Computer Sciences, Koszalin University of Technology,
75-453 Koszalin, Poland

Nano-Silicon is an extremely versatile material that can be structured at the level of its porosity, multi-film thicknesses or size of particles. Science's keen interest in these new nanomaterials is motivated by new fascinating properties and their tunability. Different forms of nano-Si primary prototypes can be made using a novel cyclic three-pulse electrochemical regime presented in this work. It consists of three pulses of different intensity: a working pulse when layer with determined thickness and porosity is formed; a cut pulse that introduces an embedded pre-partition between the layers; and an etch stop pulse when electrolyte is refreshed. An easy control by electrical means of overall morphology opens the possibility for large variations of nano-structuring in the obtained material. In-situ deposition of some metals simultaneously with layers formation through variation of the electrolyte composition and some parameters of the electrical regime is attainable as well.

Introduction

Silicon is a well known chemical element that just 50 years ago was one of the fundamental building blocks of the modern microelectronics. Nowadays its nanostructured forms are recognized to be valuable pieces in the creation of the fundaments of nanoscience and nanotechnology. The nanoworld is the essence of nature and life where the dissimilar elementary slabs (atoms and molecules) create new forms and acquire new properties under spontaneous ordering into diverse supra-molecular structures.

The nano-Silicon is an extremely versatile material that can be structured at the level of its porosity, multi-film thicknesses or size of particles. Nano silicon then demonstrates fascinating new characteristics that are dependable on the way of its nanostructuring. The most attractive detail is that those new properties are tunable. Together with biodegradability and biocompatibility, tunability explains modern science's keen interest in this new nanomaterial. Recently proposed applications of nano-Si range from electronics to medicine and different prototypes of new devices with diverse components made from nano-Si have been fabricated. A brief overview of those applications is summarized in the Scheme 1 below.

From the practical point of view, the fabrication route from the raw material (bulk Si, powders or wafers) to the final devices (products) could be divided into two main steps/levels. Firstly, primary nanostructured materials (prototypes) must be obtained (with stabilized surface properties and functionalized if necessary). Development of the final device is performed on the next level together with final adjustment and improvement of the material itself, product design, fabrication technology, etc., including development of an analytical instrumental platform and details of the final usage.

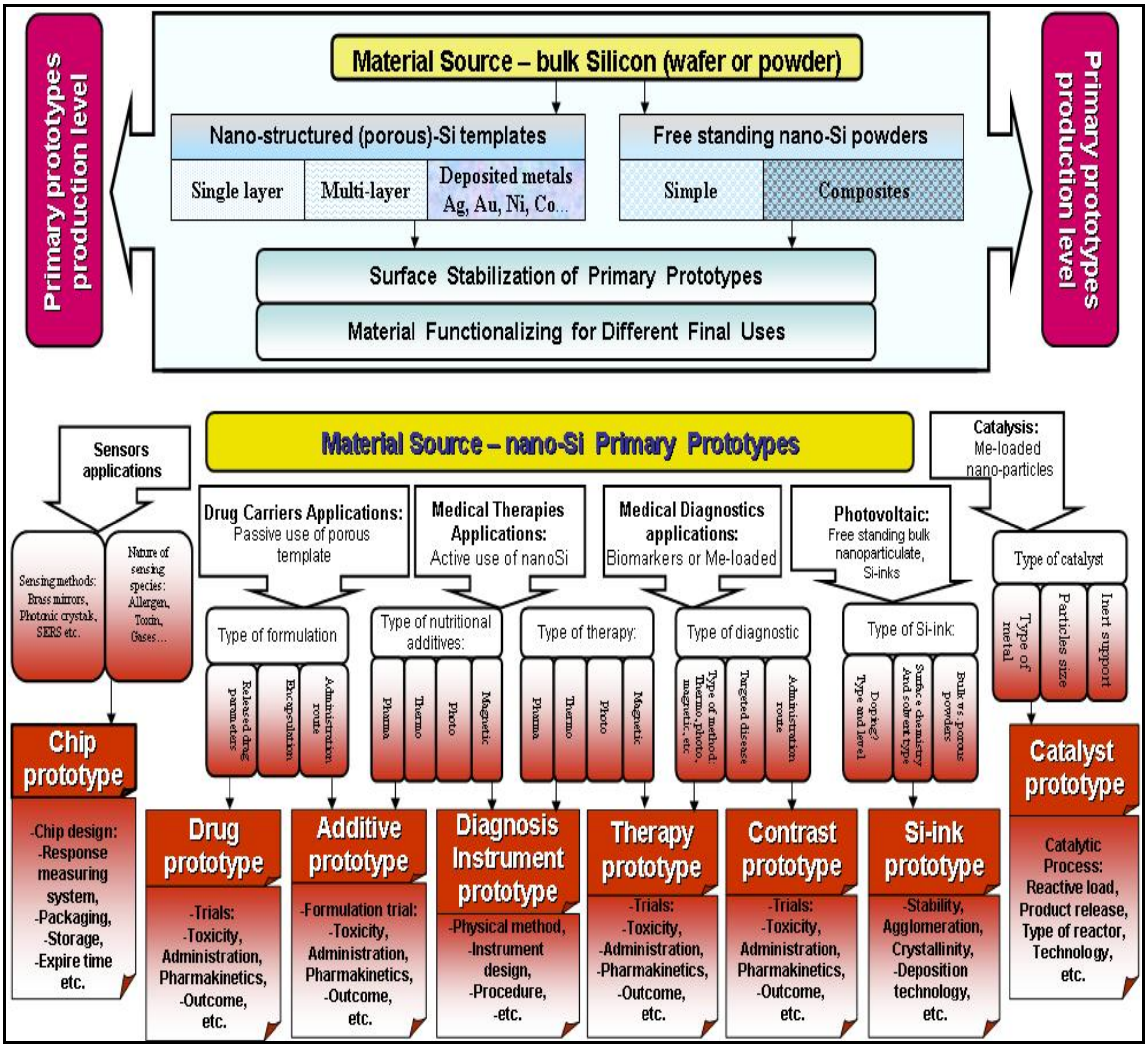

Scheme 1. An overview of the existing application of nanostructured silicon materials

As mentioned above, there are two basic presentations of nanostructured silicon materials or their primary prototypes:

- Powders ("free standing" particulates as an opposite to the compacted or pressed ones, the most representative form could be their dry aerosols or wet suspensions in different solvents); these primary prototypes with well defined structural, physical and chemical properties are potentially useful as drug carriers, in body imaging, biomedical, pharmaceutical, and catalytical applications;

- Specially designed in-plan structures with micrometer or smaller elements (and nanometer-sized porosity); these nanostructured forms are applicable for advanced photonic and lab-on-a-chip sensors applications, in controllable drug devices.

For a further use of nano-Si materials and development of the advanced technologies an easily accessible source of nanostructured primary nano-Silicon prototypes is required. Various methods were employed until now to fabricate them – from electrochemistry to laser ablation, also including a stain etching (chemical) method and wet energetic ball milling. The last three methods only can offer the possibility to produce powdered materials (bulk or porosified), though electrochemistry is able to yield all forms of nanostructured silicon.

In the Table 1 below some important characteristics of each mentioned fabrication methods and the materials obtained are summarized.

TABLE 1. Existing methods of fabrication of nanostructured silicon and characteristics of the material obtained

Method	Scalability	Grade of Silicon Used	Powders /layers	Porosification, surface area	Particle size distribution	Remarks (as ref. to medical applications)
Electro-chemistry	Medium	Wafers	Yes/Yes	Yes (throughout) >500m^2/g	Controlled Narrow	Numbers of works have been already published in drug delivery applications
Laser ablation	Low	Wafers	Yes/No	No, >20m^2/g	Controlled Narrow Uniform	Useful for in situ surface modification
Stain etching	Very high	Metallurgical	Yes/No	Yes (bulk Si core), 100m^2/g	Uncontrolled Wide	Me, N, F Impurities, Insufficient biodegradability
Ball milling	Very high	Metallurgical	Yes/No	No, 5-20m^2/g	Controlled Wide	Me impurities, Unknown surface chemistry (strong oxidation)

The strong points of the laser micro-processing method are the uniformity of the produced particles and its particular suitability for in-situ surface modification (control of the surface properties). On the other hand this method produces bulky (not porosified) materials with relatively low surface area, possesses a high ablation threshold and processes miniature area thus offering few possibilities for scalable production.

The stain etching method allows for larger-scale production and uses the cheapest polycrystalline Si powders of metallurgical grade [1]. Nevertheless it produces particles with wide size distribution and leaves a residual bulk Si core in each of them (of a few microns). This results in insufficient biodegradability of the obtained nano-Si materials making the method questionable for medical applications (drug delivery).

The wet energetic ball milling, even though it seemed very suitable for mass production, can only offer bulky powders with low surface area of unknown composition. The liquid solvents used for milling (normally water or alcohols) under energetic mechanical treatment uncontrollably modify (oxidize) the surface. The crystallinity of the sample can be destroyed as the time needed to achieve the sub-micron particles is very long (up to several hours, [2]). Even under the most favorable conditions the final particles size distribution is wide. This method is less studied than the others, and many improvements have to be done before it can be used for medical proposes.

The two forms of nanostructured primary nano-Si prototypes can be easily made by the electrochemical method. Using a novel cyclic three-pulse electrochemical regime presented in this work many, important parameters like porosity, pore diameter, thickness of the layer and their numbers can be controlled by simple electrical means [3, 4]. At the moment the only material processed by this method has been monocrystalline silicon (wafer) but there are indications that the compacted pressed polycrystalline Si tablets might be treated as well [5]. The biodegradability of the fabricated materials could be widely controlled as soon as it depends on morphology of the produced nano-Si particulates. The extremely high surface area (as a rule more then $500 m^2/g$) makes it appropriate for adsorption of a huge quantity of active molecules (drugs). Chemical modification opens the possibility for tuning the surface properties (first of all hydrophobicity) and adequating them to any candidate for loading (molecule, etc.) [6].

Electrochemical method and the three pulse cyclic regime for nano-Si prototypes fabrication

1. Complete electrochemical fabrication process.

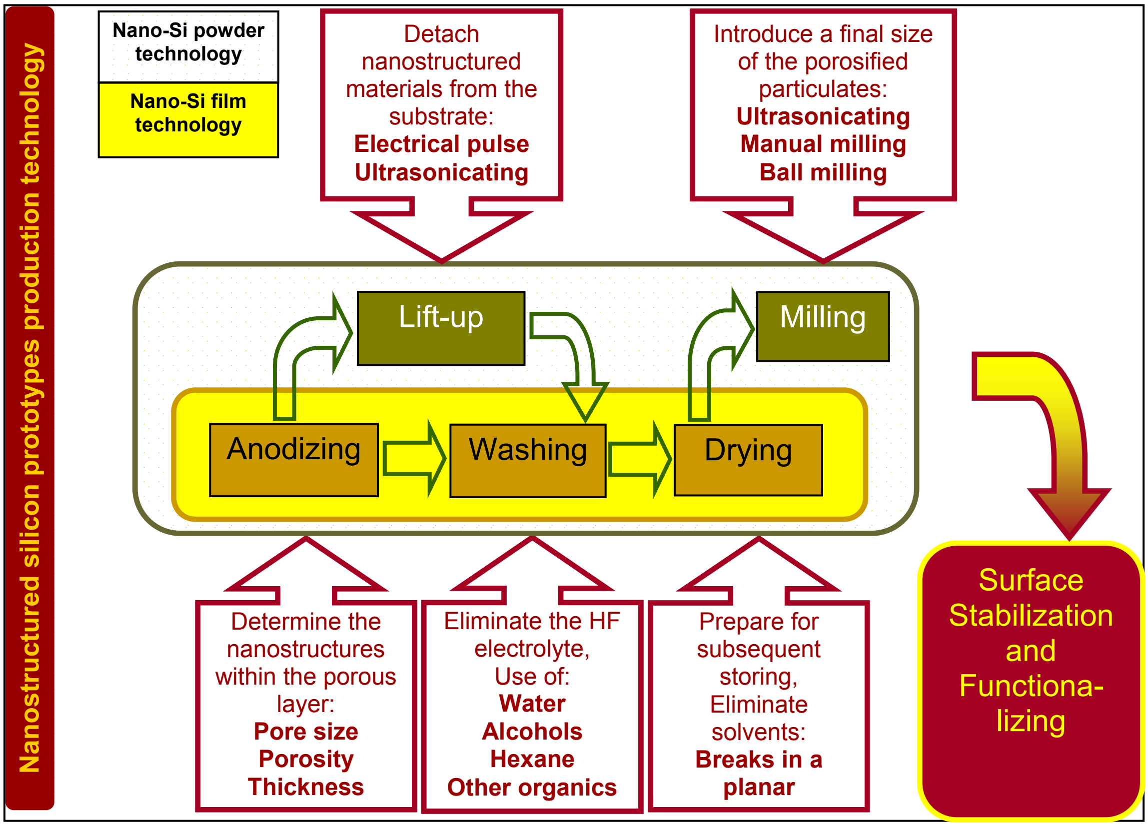

Scheme 2. The complete technological route for nano-Si production by the electrochemical method

The complete porous silicon fabrication process is performed in several steps, basically, anodization, rinsing and drying (Scheme 2). In cases when the powder is the ultimate product additional steps like lift-up and milling must be introduced. At the end of the complete production route surface stabilization (by controllable oxidation for instance) and bio-modification are needed.

The anodization step creates nano-structures within the growing porous silicon material/ film. A lot of experimental parameters can be varied (chosen) in order to obtain the predefined porSi nano-morphologies [7]. During the rinsing step the rests of electrolyte are removed from the pores with the help of distilled water or ethanol. Physical properties and morphology of material suffer very small variations on this step (in fact, they are often unobservable). On the other hand, the drying procedure does have a great influence on the physical properties of the produced material. Due to mechanical stresses developed while drying the porSi layer can be broken and its structuring destroyed [8, 9]. To avoid that, liquids with a low surface tension (pentane, etc.) are applied during the rising procedure.

Traditionally the most used and studied electrochemical regime for porSi formation was that of the constant current. The only perfect thin films formed on the top of Si wafer have been wanted and used in the numerous researches. Morphology, porosity and pore size of the obtained films can be easily controlled by varying the applied electrical conditions – current density and time [7]. Severe requisites to the homogeneity of the pore size distribution throughout the whole film thickness and the integrity of the entire film were mandatory. Only limited conditions (electrochemical and others over the complete fabrication route) yielded such an ideal quality film: electrolyte and current density were carefully chosen, as well as the washing and drying procedures´ parameters.

If an anodization is used for further porSi powder preparation (via subsequent grinding and milling) the wider experimental parameters could be applied for porosification and nanostructuring. More intensive drying procedure and ultra-sonication are used to lift the porSi film up from a substrate. Even a special electrochemical lift-up pulse (very high and short current at the end of the anodization step) was proposed for separation of the porosified materials from the wafer (substrate).

The last step of porSi powder fabrication is the stabilization of its properties. This procedure is required for both, the long-term storing of the material and/or to provide new functionalities to its surface. Generally, the term “modification” includes surface oxidation (thermal or chemical) as well as binding of new molecules and/or simple physical coverage by surfactants. Achieving the miscibility with water (in physiological conditions, for instance, by conversion of the native hydrophobic surface of porSi into hydrophilic one) is an important goal of such surface treatments [10, 11]. Any of those treatments involves a deep changing of the surface chemistry of silicon nanostructures (existence of the SiHx, SiOx, SiOH etc. surface groups and binding others functionalities) and could be widely adapted for any specific needs.

2. The overview of the electrochemical regimes

The porSi films prepared under a constant current can have heterogeneous in-depth morphology (pore size and porosity) if they are thicker than tens of microns. These two parameters depend on HF concentration, which is depleted during the growth of the porous layer. During the electrochemical treatment the HF is consumed (as H_2SiF_6), and a concentration gradient is developed along with the pores. Morphology of the entire film is then changed in depth. While working with a few micrometers layers (most common case) such inhomogeneity is not very high or crucial. Nevertheless, when applying this method for powder preparation and under deeper treatment (as large as possible, up to the etch-through of the entire wafer of 500 microns) the problem becomes essential. Morphology of the prepared film depends on thickness and is extremely unequal with the film depth. Powders obtained from such anodized silicon wafers are also inhomogeneous (varied porosity) and single particulates size is incontrollable.

The described problem was recognized time ago and some improvements to the electrochemical regime were proposed [12-14]. The most known method accepted by many researchers is an introduction of etch-stop periods during electrochemical treatment. Figure 1 depicts the two regimes: the most commonly used constant current Regime I, and the one using an etch-stop, Regime II. The last regime is in fact the cyclic one: to achieve a deeper treatment longer time (many cycles) should be applied.

In the Regime I the user defines the values of current density J_1 and time t_1. For given types of electrolyte and Si material (type of doping and its level) the J_1 value determines the obtained morphology (porosity and size of the pores) whereas the thickness of the produced film depends on anodization time t_1. There exists a limiting value of the applied current density, critical J_{PS}, above which the total dissolution of the Si wafer is observed – the so called electro-polishing region. To produce a porosified film these conditions must be avoided (also because of complications appearing during the drying step – spontaneous breaks in the porous layer are more probable in more porous films). When the method is applied to fabricate powder, larger current densities can be used (but always less then J_{PS}) because we do not need a perfect film. As well, the larger periods of time are used for deeper treatment.

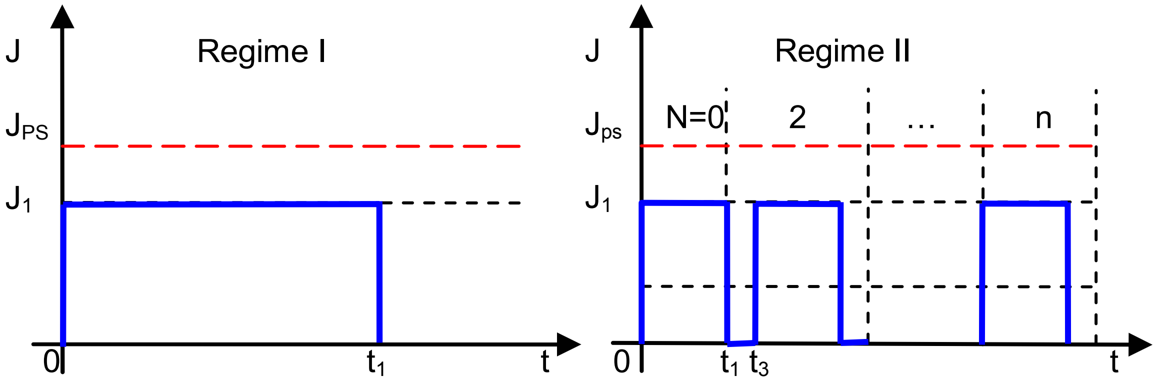

Figure 1. Description of Regimes I and II

In the Regime II the etch stop period, t_3, is introduced after some time of anodization, $t_{1,}$ that allows HF to be supplied to the reaction interface inside the porous layer. The Regime II is additionally characterized by parameters such as time of etch stop, t_3, and duration of one cycle (period) t_d=t_1+t_3. The regime is periodic (cyclic) in time and N cycles are applied for the total anodizing time $T=N\cdot t_d$. As to an applied currently density, it was demonstrated that, respect to ones applied in the Regime I, the overall porosity and the reaction rate are only slightly changed under these new conditions [3].

Fabrication of some optoelectronics devices on the basic of layered porous structures (interferometer biosensors for instance) was developed using a very similar regime with two (or more) levels of different anodization currents that yield layers of different porosity (and different refraction index). In these cases each current level is lower than the critical current density J_{PS}, Regime III, Figure 2. The description of this regime is the same as that of Regime II.

Recently we have proposed and studied the new three pulses Regime IV [4]. It uses the advantages of an etch stop period combining them with incomplete lift-up. This Regime IV is extremely suitable for fabrication of both types of nanostructured silicon materials, the layered films with different porosity in each layer and the nano-Si powders. We consider it as a platform for new production technology of the nanostructured silicon materials.

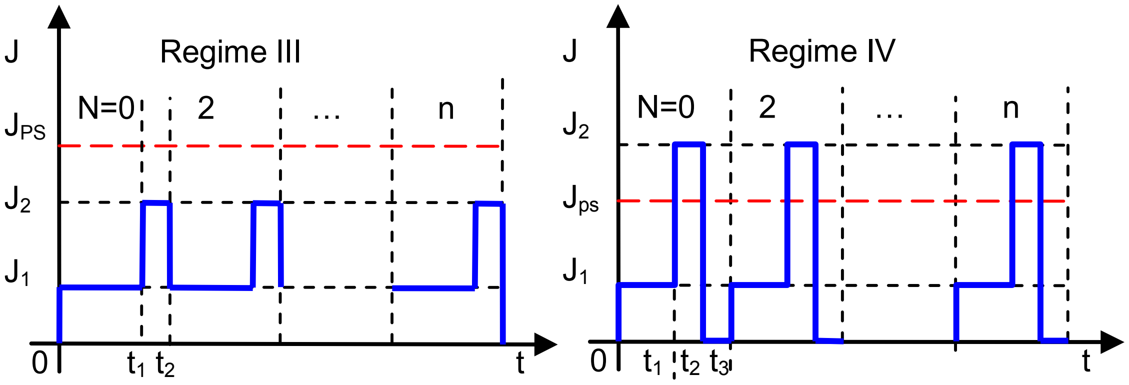

Figure 2. Description of regimes III and IV

The three pulse electrochemical Regime IV is a cyclic one similarly to the two pulses Regimes II or III and consists of three levels of different intensity (current density o voltage): a working pulse when a layer with determined thickness and porosity is formed; a cut pulse that introduces pre-partition into the entirely porosified film; and an etch stop pulse when electrolyte is supplied to the reaction site (refreshed) after its strong consumption. An easy control by electrical means of overall morphology opens the possibility for large variations of nano-structuring in the obtained material. The number of the layers grown within the entire film is determined by the numbers of the cycles applied.

Experimental results – some examples of primary prototypes obtained by the three pulse regimes

For the first time the three pulse method was presented elsewhere [4]. That work confirmed by the direct SEM measurements that the number of the formed layers is equal to the numbers of cycles applied. At the same time it was shown by using the gravimetric method that the dissolution valence and porosity of the porSi fabricated under the Regime II (with an etch stop) were slightly decreased (10-15%) but growth rate increased (25-

30%) respect to the constant current Regime I. This is a direct consequence of the lesser HF concentration gradient developed with time inside the pores. Using the etch-stop pulse with time ratio less then 10:1 (respect to the working pulse) a steady homogeneous concentration of HF was maintained in the pores during all period of the treatment (2-3 hours, achieved depth of 200-300 microns). Geometrical parameters within each cap (layer) formed under studied conditions followed the predicted (calculated) values.

In Figure 3 the SEM photos of one of the anodized samples are shown; the three pulse regime with 300 cycles was used. During the drying procedure and the preparative manipulations for SEM, some of the formed layers were joined in stocks as seen on the Figure 3A. More detailed view in Figure 3B and 3D revealed the fine structure of each stock. The single cap in Fig.3D is of 173nm, equal to the calculated for the applied anodizing conditions ($20mA/cm^2$ in a working pulse for 10s).

The surface plan of the sample in Figure 3C is not smooth showing that under the treatment the round shaped cells of 2-3 microns diameter have been formed. Most probably they are due to the gas (hydrogen) evolution from the anodized site (at the bottom of the pores). Under (beneath) each surface cell a tubular layered structure appeared. As we proposed in [4] it could be the path by which the H_2 gas escaped from the grown porous film.

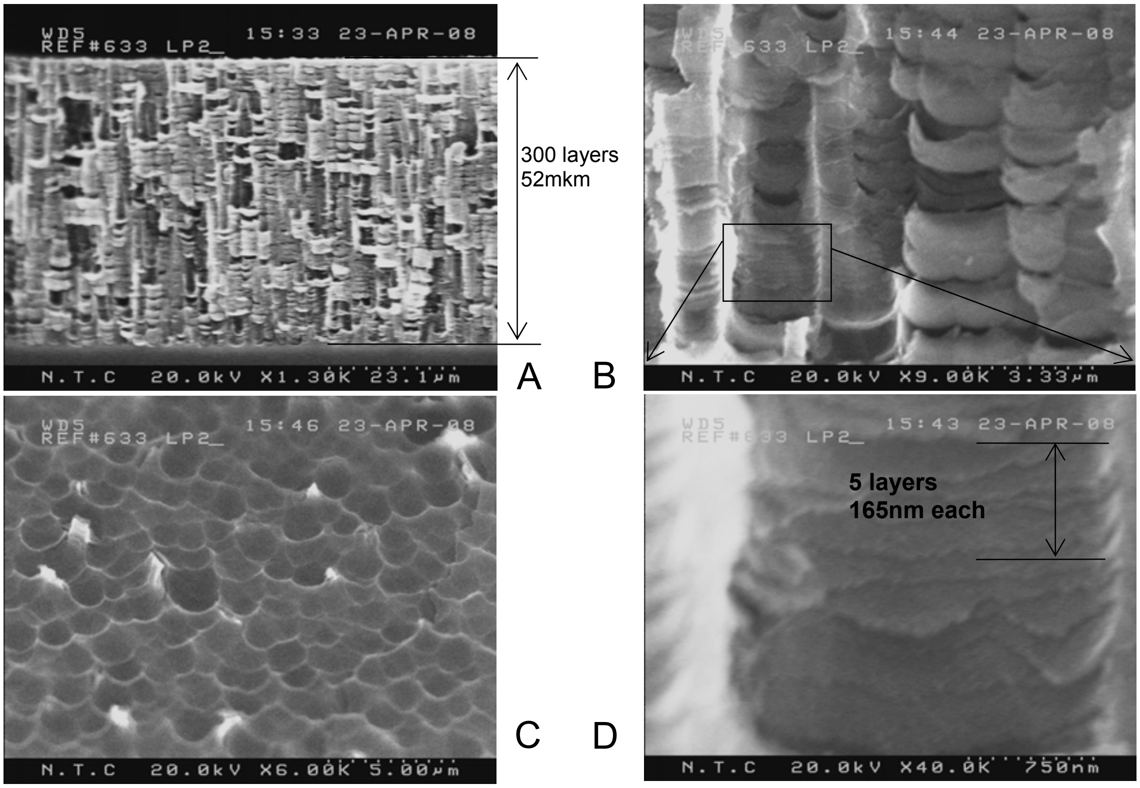

Figure 3. The layered structure formed in Boron doped Si (10-20Ohm·cm) the 1:1 HF (40%) ethanol electrolyte under the three pulse regime: $J_1= 20mA/cm^2$, $t_1=10s$; $J_2= 390mA/cm^2$, $t_2=0.5s$; $J_3= 0mA/cm^2$, $t_3=2s$; N= 300. Calculated single layer thickness is appr.175nm. A, B and C – the cross-section views of different magnifications, D – the surface view

The layered films obtained under the three pulse regime are extremely fragile. They were frequently broken when the Si wafer was still under electrochemical treatment (usually after the depth of treatment achieved more then 50-100 microns). The laminas of porosified material then floated in the electrolyte and could be collected manually. Later, even under short time ultrasonicating (few minutes) the totality of the anodized silicon was easily lifted-up from the Si wafer. The produced porous film was pulverized into particulates with preferred dimensions (of a single layer thickness).

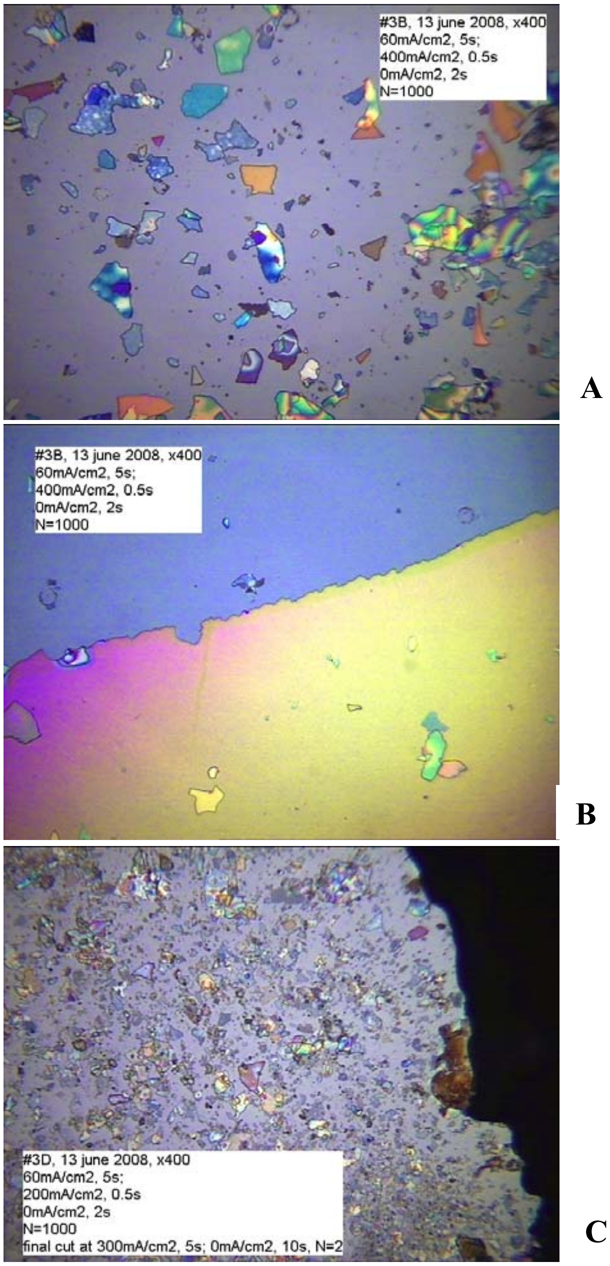

Figure 4. Optical photos of the Si wafer (Boron doped, 0.01-0.02Ohm·cm) after anodizing in three pulse regimes (see insets in the photos) and ultrasonicating of the substrates in hexane:
A – The upper view of the untreated portion of the Si wafer: the small planar parts of the broken porosified caps are deposited on it; single particles are of few microns dimensions in large with a thickness of appr.200nm (calculated from the experimental conditions);
B - The bottom part of the wafer: the very lasts caps (layers) formed under treatment are perfectly seen;
C – The micron sized particles of the porosified silicon deposited on the untreated part of the Si wafer (regime with an additional final lift-up).

In the optical photos shown in Figure 4A one can see the Si substrate after electrochemical treatment, washing and additional 3 minutes ultrasonicating in hexane. Deposited micro particles of a single layer thickness (170 nanometers) are perfectly seen. The remnants of the very last caps of the material not separated from the bottom of the wafer are well visible on the Figure 4B together with micron sized porosified particulates deposited on the bottom.

Intensity and duration of the cut pulse in the three pulse regime affected the detachment and partition of the layered film during electrochemical treatment and posterior ultrasonicating. Usually, application of a current density of 200mA/cm^2 for 1s was enough to achieve spontaneous detachment and make later grinding unproblematic. Nevertheless, even under the three pulse regime an additional final lift-up procedure was sometimes needed at the end of the whole treatment. We used to perform it after 200-400 cycles. This procedure was beneficial only for some types of the initial Si material (and mean porosity formed under anodizing) and the entire block of the porosified material was detached from the Si wafer, see Figure 4C.

To study the partition limit of porosified silicon additional grinding of the obtained powdered (and layered) materials was performed in the ball milling machine. Different solvents (water, alcohol and hexane) were used. Only a small number of publications on this method were previously available. Even less was published on Si; one of the works was done with polycrystalline bulk material of initial fineness of 4-10 microns [2]. This material was subjected to the energetic ball milling using water (or alcohol) as a solvent. It was reported that long time (several hours) was needed to get submicron pulverization (d_{97}<1 micron; means that 97% of the total product has dimension less then 1 micron). Very strong oxidation of the bulk Si by water and alcohol was also pointed out there. Our experiments with porosified Si material have confirmed the strong influence of the milling media on the chemical (surface) composition of the produced suspensions. Elimination of all the SiHx groups from the surface (with visible H_2 gas evolution) and oxidation of porous Si material was observed in case of using water or alcohol. In case of hexane used as milling media, the SiHx surface groups were preserved and no gases were evolved. The detailed report on these results is under preparation and will be published elsewhere.

In Figure 5 the SEM pictures of the milled porosified material are shown. The particles with less the 1micron were obtained after only 20 minutes of milling. They possess an irregular shape and the rests of pores of tens of nanometers are guessed in photos with larger magnification.

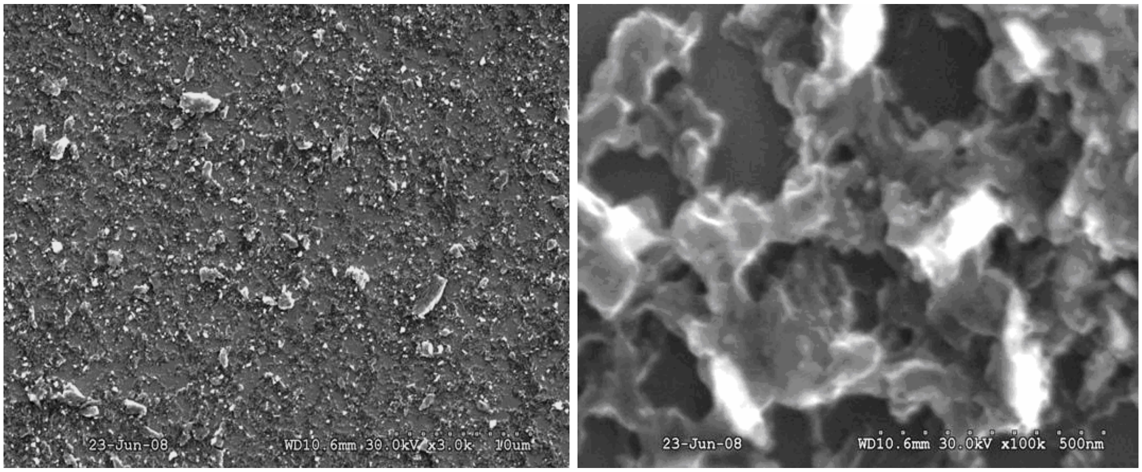

Figure 5. SEM photos of the ball milled porous silicon: time – 30 minutes, solvent - alcohol

In-situ deposition of some metals (noble or transitory) simultaneously with layers formation is easily attainable through variation of the electrolyte composition. By adjusting the parameters in the three pulse regime the fine control of size (and distribution) of the deposited metallic particles is possible as well.

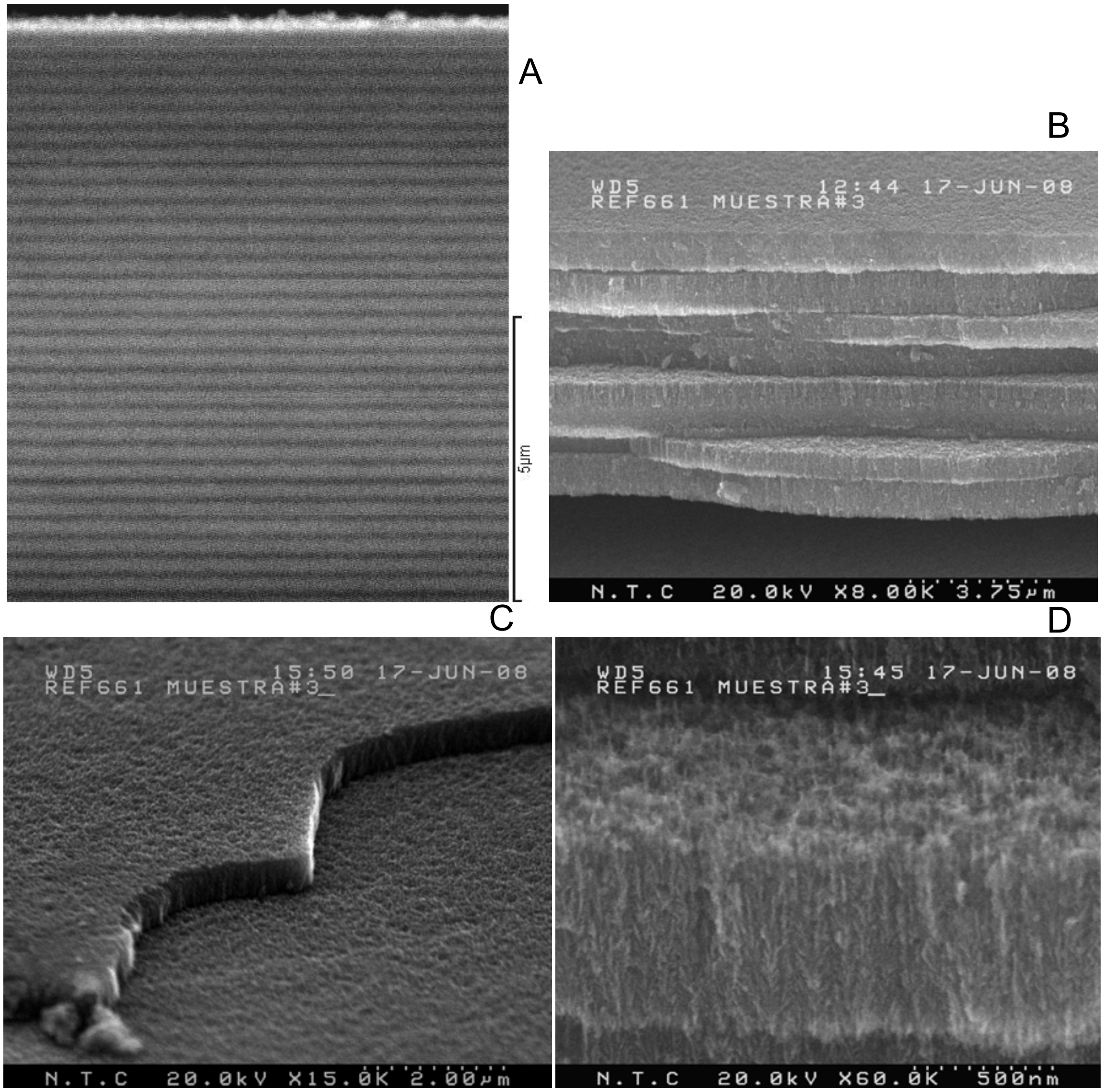

Figure 6. SEM photos of the porosified Si samples (0.01-0.02Ohm·cm, Boron doped) with Ag deposits obtained in the three pulse regime in the 1:1 HF (40%): EtOH electrolyte contained 10^{-3}M $AgNO_3$. A – J_1= 120mA/cm^2, t_1=2s; J_2=400mA/cm^2, t_2=0.5s; J_3=0mA/cm^2, t_3=1s. B,C and D - J_1= 120mA/cm^2, t_1=10s; J_2=400mA/cm^2, t_2=0.5s; J_3=0mA/cm^2, t_3=10s.

In Figure 6 the SEM images of the layered samples with Ag deposits are shown. In Figure 6A the Ag content is homogeneously distributed throughout the thickness of the entire film but periodic accumulation of metal in the layers formed under the working pulse (clearer ones in the picture) could be figured out. The atomic Si to Ag ratio is 150:1

there versus the 240:1 calculated for the thinner (darker) layers that were created under the cut pulses (results of the performed chemical analyses are not shown). The time of Ag deposition (during the etch stop pulse) was very short – 1s – in that experiment. In Figure 6B another sample prepared with different working and etch stop pulses is shown. The thickness of a single cap (formed under the working and cut pulses) is larger here (600nm) as well as the time available for Ag deposition (10s in an etch stop pulse). The Ag content is indeed increased (Si to Ag atomic ratio is 90:1) and metal accumulation in-between the thicker layers is appreciated (Fig.6D). More works are needed and are in progress in the laboratory with different metals (Cu, Pd, Ni among others).

As a conclusion, the proposed three pulse electrochemical regime can constitute a basic technology for production of primary prototypes of nanostructured silicon in their different presentations: layered films and fine powders (suspensions). In principle, there are no limits for preparation of ultra thin (100nm and less) porosified layers on a Si wafer. By using times during the working pulse in the range of 0.5-2s one should expect such dimensions. Further disintegration of material by mechanical means, ball milling or ultrasound, or even spontaneously during a highly energetic electrical treatment will produce nano-Si powders of finest quality (narrow size distribution). We expect that the main problem that will then occur will be the aggregation of single particles into assembles of much bigger sizes. This is a problem of great importance in a field of nanostructured materials that could possibly find its solution in the control of the surface properties of single particulates. Possibilities for embedding of metallic components and/or surface control and modification through the electrolyte or milling solvent composition are open as well. The only real limitation of this method is the availability of the special short-pulse power source/potentiostat suitable for processing of large surfaces (at least four-inch Si wafers with area of appr.80cm^2). This equipment (prototype unit is under development, [15]) is available at our laboratory and the results presented in this report were obtained through its use.

Acknowledgement

This work is a part of the project PSY-NANO-Si (NMP4-CT-2004-013875) financed by the European Community and co-financed by Ministry of Education and Science of Spain (MAT2006-27447-E) and Valencian Community (ACOMP06/016 and ACOMP/2007/209). The authors are thankful to Mr. J. Ayúcar for performing the SEM analyses and micro photographs. The help of Mr. B. Goller (Bath University, UK) in milling of the porosified silicon samples is acknowledged with gratitude. E.M. is thankful to Mr. K. Witt for fruitful discussion and encouragement.

References

1. M. Nahidia, K. W. Kolasinski, J. Electrochem. Soc., **153** (1), C19, (2006)
2. L. T. Canham, Nanotehcnology, 18, 1, (2007)
3. Spanish patent application, P200800037, December 2007
4. L. Bychto, Y. Makushok, V. Chirvony and E. Matveeva, Phys. Status Solidi, 2008, in press.
5. K. G. Barraclough, A. Loni, E. Caffull, L. T. Canham, Materials Letters, **61**, 485, (2007)

6. C. A. Prestige, T. J. Barnes, Ch.-H. Lau, C. Barnet, A. Loni, L. Canham, Expert opinion, Grug Delivery, **4**, 2, (2007)
7. V. Lehmann, Electrochemistry of Silicon, Willey-VCH, 2002
8. L.T. Canham, A. G. Cullis, C. Pickering, O. D. Dosser, T. I. Cos, T. P. Lynch, Nature, **368**, 133, (1994)
9. O. Belmont, D. Bellet, Y. Brechet, J. Appl. Phys., **79**, 7586, (1996)
10. M. P. Stewart, J. M. Buriak, Advanced Materials, **12**, 12, (2000)
11. V. Chirvony, A. Chyrvonaya, J. Ovejero, E. Matveeva, B. Goller, D. Kovalev, A. Huygens, P. de Witte, Adnamced Materials, **19**, 2967, (2007)
12. J. Ge, W. J. Yin, Y. F. Long, X. M. Ding and X. Y. Hou, Chin. Phys.Lett. 24, 5, 1361 (2007)
13. J. Ge, W. J. Yin, L. L. Ma, E. Obbard, X.M. Ding and X.Y. Hou, Semicond. Sci. Technol 22, 95 (2007)
14. R. Grover, K.L. Narasimhan and D.K Sharma, Journal of Porous Materials 7, 377 (2000)
15. Yu. Makushok, E. Matveeva, L. Fedorov, Materials of the 6th International Conference Porous Semiconductors – Science and Technology, Sa-Coma. Mallorca, Spain, 10-14 March 2008, Extended Abstract #P2-74, p. 458

CHAPTER 2

MONDAY: AFTERNOON SESSION

ECS Transactions, 16 (3) 55-59 (2008)
10.1149/1.2982541 ©The Electrochemical Society

Design and Fabrication of Extended-Bandwidth Rugate Filters Made of Porous Silicon

N. Ishikura[a], M. Fujii[a], K. Nishida[a], S. Hayashi[a], J. Diener[b], M. Mizuhata[c], S. Deki[c]

[a] Department of Electrical and Electronic Engineering, Graduate School of Engineering,
Kobe University, Rokkodai, Nada, Kobe 657-8501, Japan
[b] Physik-Department E16, Technische Universität München,
D-85747 Garching, Germany
[c] Department of Chemical Science and Engineering, Graduate School of Engineering,
Kobe University, Rokkodai, Nada, Kobe 657-8501, Japan

We designed and fabricated porous silicon-based broadband rugate filters by combining up to seven rugate structures. A near-infrared stop-band filter having a reflection band width of 1926 nm with no higher-order harmonics and very small sidelobes were realized. The suppression of higher-order harmonics and the reduction of sidelobes also allowed us to produce a high quality pass-band filter having three high transmittance regions consisting of broad stop-bands.

Introduction

A rugate filter is a kind of interference filter characterized by a continuous sinusoidal index variation in the direction perpendicular to the film plane (1). It shows a high reflectivity “stop-band” in a specific range of wavelength. Advantages of the rugate filter to discrete multilayer filters consisting of alternating high and low refractive indices layers are a smaller sensitivity to angle variation of incidence light (2) and a suppression of higher-order harmonics. The drawback is its difficulty in realizing the complex refractive index profile with a great accuracy. Usually, the complex refractive index profile is achieved by continuous variation in composition or the density of the filter material (3-6).

Porous silicon produced by electrochemical etching of a silicon wafer is a material of great interest for the fabrication of rugate filters. The refractive index of porous silicon can be controlled by the porosity, which is determined by the current density during the electrochemical etching process (7). The electrochemical etching proceeds only at the etching front and thus already etched layers are unaffected by subsequent etching. These properties make porous silicon an almost ideal system to realize one-dimensional smooth refractive index profiles. In fact, several types of porous silicon-based rugate filters have been reported so far (8-10).

Some applications of a rugate filter, e.g. pass-band, stop-band and edge filters, require wide stop-bands. The width of the stop-band depends on the contrast of the refractive index in a rugate filter. Since the refractive index contrast of a rugate filter made of porous silicon is limited in the range of about 1.3-2.3, it generally has a relatively narrow stop-band. The extension of the rugate stop-band is usually achieved either by a superposition of rugate profiles of different periodicity (4, 11) or by a serial growth of different rugate profiles (12). The combination of the superposition and the serial methods is also proposed by Southwell (13). The advantage of the combination method is the reduction of the total film thickness. By using the combination method, in a previous work (14), we have succeeded in realizing porous silicon-based broadband rugate filters. The bandwidth reached 1356 nm. This paper is an extension of the previous work. We demonstrate that further extension of the bandwidth is possible by properly controlling the preparation procedure. Furthermore, as an application of the broadband filter a pass-band filter having three transmittance bands is demonstrated.

Experiment

Porous silicon structures were produced by electrochemical etching of (100) oriented p^+ Si wafers (0.02 Ω cm). The etching solution was a 2:3 by volume mixture of HF (46 wt.% in water) and ethanol. The current density was changed from 5 mA/cm^2 to 109 mA/cm^2 with the minimum step of 0.5 mA/cm^2 by computer-controlled current source (Agilent 6612C). In this current density range, the refractive index of porous silicon was changed from 2.38 to 1.30 (at the wavelength of 2 μm). The refractive indices of porous silicon were obtained either from interference patters of uniform layers with known thicknesses or Bruggeman effective medium approximation (15). The total etching time was in the range of 10 to 60 min depending on the structure. During etching, the etching rate decreases slowly (7), i.e., about 1.5 % during the etching of 10 μm. This effect was compensated by controlling the etching time. When free-standing layers were required, porous silicon structures were detached from Si substrates by a high current pulse (400 mA/cm^2, 1.6 s) after finishing the etching procedure. Reflectance and transmittance spectra of porous silicon structures were measured by a UV-visible-NIR spectrophotometer (Shimadzu UV-3101PC) over the spectral range of 350 to 3200 nm with the spectral resolution of 1 nm. The incident angle for the reflectance measurements was 5°.

Results and Discussion

The rugate refractive index profile used in this letter is expressed as

$$n(x) = \exp\left[\frac{\ln n_H + \ln n_L}{2} + \frac{\ln n_H - \ln n_L}{2}\sin\left(\frac{4\pi x}{\lambda_0} + \varphi\right)\right] \qquad [1]$$

where x is the optical path length, n_H and n_L are maximum and minimum refractive indices used in the layer, λ_0 is the wavelength of the stop-band position, and φ is the phase angle (1, 8). To reduce sidelobes that appear on both sides of the stop-band, apodization is applied. We chose a quintic apodization function (16, 17), which shows significant sidelobes suppression properties. A half-apodization technique (18) is also used to reduce total etching time (8). Furthermore, to remove sidelobes caused by large refractive index mismatch between the rugate structure and the surrounding media, the quintic index-matching layers are added to the front and back of the filter. The refractive index profile of the quintic index-matching layer (17) that matches indices form n_1 to n_2 is expressed as

$$n(t) = n_1(n_2 - n_1)(10t^3 - 15t^4 + 6t^5) \qquad [2]$$

where *t* is the normalized layer thickness, which varies from 0 to 1. In this work, at the interface with air *t* is varied from 0 to 1, while at that with Si substrate, it is limited from 0 to 0.5 because a full quintic index-matching requires too long etching time when the refractive index of the surround media is very high (8).

Figure 1(a) shows the refractive index profile consisting of seven rugate profiles. To reduce the total film thickness, neighboring rugate profiles are partly overlapped. Each rugate profile consists of 30 periods with quintic apodization and the stop-bands are centered at 1217, 1400, 1610, 1852, 2129, 2449 and 2816 nm. The distances between neighboring stop-bands were determined to be as large as possible to extend the stop-band while keeping the high reflection intensity. Combination of rugate profiles cause optical density minima (dips) in the stop-band. Depths of these dips are usually uneven, but they can be made equal by adjusting the phase (φ) of the rugate profiles [15]. To equalize these dips, the phase is shifted by $\pi/6$ with respect to the neighboring rugate profile. In Fig. 1(b), calculated and measured reflectance spectra are compared. We can see a good agreement between calculated and measured spectra. The width of the stop-band (R>90%) is about 1926 nm. Because of the quintic apodization and indexmatching layers, the sidelobes are rather small.

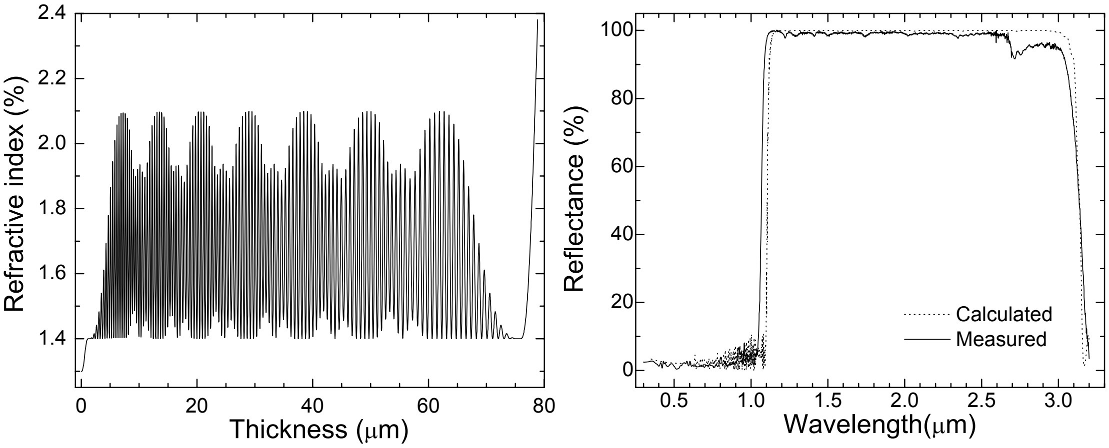

Figure 1. (a) Refractive index profile vs. physical depth and (b) calculated (dotted line) and measured (solid line) reflectance spectra of a rugate structure consisting of seven rugate profiles.

The small sidelobes and higher-order harmonics allow us to make pass-band filters with desired pass-band numbers, positions and widths. As a demonstration we made a pass-band filter with three wide stop-bands. The filter consists of six rugate structures (30 periods) with the stop-bands at 1170, 1346, 1547, 2046, 2353 and 3112 nm (Fig. 2(a)). The filter is detached from the substrate after etching. Fig. 2(b) shows the calculated and measured transmittance spectra. We can see three pass-bands centered at 900, 1780 and 2710 nm sandwiched by broad stop-bands. Note that the stop-band below 800 nm is due to silicon absorption. The pass-band position, width and number can be tailored simply by properly controlling the stop-band positions of rugate structures constructing the filter.

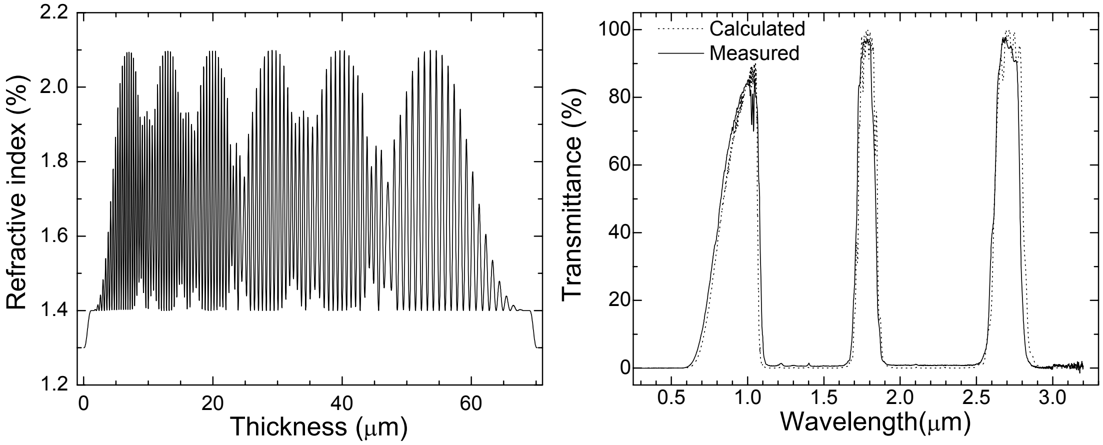

Figure 2. A pass-band filter consisting of six rugate profiles: (a) refractive index profile vs. physical depth and (b) calculated (dotted line) and measured (solid line) transmittance spectra.

Conclusion

By combining seven rugate refractive index profiles, we fabricated a stop-band filter that has a reflection band width of 1926 nm and high transmission region outside the stop-band. A pass-band filter that exhibits three high transmittance regions produced by three broad stop-bands was also demonstrated. The present results demonstrate that the porous silicon-based rugate structures allow us to realize higher-order harmonics free and sidelobes free high quality broadband optical devices by a simple and low-cost process.

Acknowledgments

This work is supported by a Grant-in-Aid for Scientific Research from the Ministry of Education, Culture, Sports, Science and Technology, Japan.

References

1. B. G. Bovard, *Appl. Opt.*, **32**, 5427 (1993).
2. W. H. Southwell, *J. Opt. Soc. Am. A*, **5**, 1558 (1988).
3. K. Kaminska, T. Brown, G. Beydaghyan, and K. Robbie, *Appl. Opt.*, **42**, 4212 (2003).
4. W. J. Gunning, R. L. Hall, F. J. Woodberry, W. H. Southwell, and N. S. Gluck, *Appl. Opt.*, **28**, 2945 (1989).
5. P. L. Swart, P. V. Bulkin, and B. M. Lacquet, *Opt. Eng.*, **36**, 1214 (1997).
6. K. Robbie, A. J. P. Hnatiw, M. J. Brett, R. I. MacDonald, and J. N. McMullin, *Electron. Lett.*, **33**, 1213 (1997).
7. A. G. Cullis, L. T. Canham, and P. D. J. Calcott, *J. Appl. Phys.*, **82**, 909 (1997).
8. E. Lorenzo, C. J. Oton, N. E. Capuj, M. Ghulinyan, D. Navarro-Urrios, Z. Gaburro, and L. Pavesi, *Appl. Opt.*, **44**, 5415 (2005).
9. S. Ilyas, T. Böcking, K. Kilian, P. J. Reece, J. Gooding, K. Gaus, and M. Gal, *Opt. Mater.*, **29**, 619 (2007).
10. M. S. Salem, M. J. Sailor, T. Sakka, and Y. H. Ogata, *J. Appl. Phys.*, **101**, 063503 (2007).

11. J. A. Dobrowolski, and D. Lowe, *Appl. Opt.*, **17**, 3039 (1978).
12. A. G. Imenes, and D. R. McKenzie, *Appl. Opt.*, **45**, 7841 (2006).
13. W. H. Southwell, *Appl. Opt.*, **36**, 314 (1997).
14. N. Ishikura, M. Fujii, K. Nishida, S. Hayashi, J. Diener, M. Mizuhata, and S. Deki, *Opt. Mater.*, to be published.
15. P. A. Snow, E. K. Squire, P. St. J. Russell, and L. T. Canham, *J. Appl. Phys.*, **86**, 1781 (1999).
16. W. H. Southwell, *Appl. Opt.*, **28**, 5091 (1989).
17. W. H. Southwell, *Opt. Lett.*, **8**, 584 (1983).
18. H. A. Abu-Safia, A. I. Al-Sharif, and I. O. Abu Alijarayesh, *Appl. Opt.*, **32**, 4831 (1993).

ECS Transactions, 16 (3) 61-67 (2008)
10.1149/1.2982542 ©The Electrochemical Society

Deep Trench Etching in Macroporous Silicon — Application to Photonic Crystal Gas Sensing

R. B. Wehrspohn[a], S. L. Schweizer[a], T. Geppert[a], and A. Lambrecht[b]

[a] Department of Physics, University of Halle, 06099 Halle, Germany
[b] Fraunhofer Institute for Physical Measurement, Heidenhofstr. 8, 79110 Freiburg, Germany

We present a method to create at the same time trenches and ordered macropore arrays during photo-electrochemical etching of n-type silicon. This novel method allows in situ separation of single devices with a submicrometer precision. The limits of this new process are simulated using electrostatic models and are verified experimentally. This new techniques enables new device structures in macroporous silicon in the areas of photonics, sensing and electronics, as an example an photonic crystal gas sensor is shown.

Introduction

Since the discovery of macroporous silicon in 1990 (1) and ordered macropore arrays in 1993 (2), numerous applications of this material system have emerged. Hexagonally arranged macropores were the first model system for two-dimensional photonic crystals. Lithographically defined waveguides and microresonators have been realized (3) and first applications such as a miniaturized gas absorption element have emerged (4). Recently, even three-dimensional photonic crystals have been obtained by modulation of the pore diameter with depth (5). Other applications are in the area of nanobiotechnology such as biochips or filters (6). In the area of microelectronics, these structures can be used as capacitors due to their high specific surface area, or in the area of fuel cells they can be used as gas-permeable electrodes (7). However, most of the current applications rely on pore formation only. Here, we present a method to create at the same time trenches and ordered pore arrays.

Theory of etching

The etching method used in this work to produce trenches and ordered arrays of macropores in Si is based on photo-electrochemical etching (PECE) of silicon by Lehmann (1, 2). While Si is easily etched in aqueous alkaline solutions, it is quite stable in most aqueous acids. However, hydrofluoric acid (HF) is an exception to this general observation. In the regime of cathodic currents the Schottky-like HF/*n*-Si contact is forward biased. The current is determined by the majority charge carriers, i.e. the electrons – independent of the illumination state – and leads to the reduction of the H^+ ions in the acidic solution followed by formation of molecular hydrogen (H2). The regime of anodic currents is the more interesting one. When the semiconductor Si is brought into contact with the electrolyte HF, the situation resembles a Schottky contact in which the rather conductive electrolyte represents the metal. The different chemical potentials of the aqueous HF and the Si will adapt. This leads to the formation of a Helmholtz double layer in the electrolyte and a surface charge resulting from the ionized donor atoms in the Si, from which a depletion of majority charge carriers (electrons in *n*-Si) at the HF/Si interface follows. Due to the mobile ions in the electrolyte, the width of the Helmholtz double layer is only a few nm while due to the stationary nature of the donors in Si the depletion region in *n*-Si is on the order of a few μm wide. If no illumination is applied to the *n*-Si, a small (anodic) dark current resulting from thermally generated holes is observed. If the Si is strongly illuminated, the HF/*n*-Si contact behaves like an HF/p-Si contact. An increase in applied voltage V leads to an increase in current across the HF/Si interface. For anodic currents below the critical current density j_{PS} and $V < V_{PS}$ divalent dissolution of Si occurs along with the formation of hydrogen. Here the etching current is limited by charge-carrier supply from the Si electrode and porous Si is formed. In aqueous HF electrolytes the critical current density j_{PS} was experimentally found to depend only on electrolyte concentration c_{HF} (in weight %) and electrolyte temperature T_{HF} and can be described by

$$j_{PS} = C c_{HF}^{3/2} e^{-E_a/(k_B T_{HF})}$$

with C being a constant of 3300 A/cm^2, E_a = 0.345 eV and kB being Boltzmann's constant (2). For anodic currents and $V > V_{PS}$ tetravalent dissolution of Si is observed. Here the current is limited by the chemical reaction rate during the removal of the SiO_2. As a consequence, the Si electrode is electropolished, i.e. all Si surface atoms are removed uniformly. Stable macropore growth is now possible for $j < j_{PS}$ and $V_{PS} < V$. The ratio j/j_{PS} only controls the average porosity p of the sample. The *x–y* positions as well as the diameters of individual pores show a random distribution under the constraint of the average porosity being $p = j/j_{PS}$. For ordered arrays of pores in the hexagonal or square lattice, a periodic pattern on top of the Si wafer is defined lithographically. By this procedure, so-called 'etchpits' in the form of inverse pyramids are generated which serve as starting points for the subsequent pore growth. The porosity of such an ordered macropore array is given by

$$p = \frac{j}{j_{PS}} = \frac{A_{Pores}}{A_{Sample}}$$

with A_{Pores} being the total pore area and A_{Sample} the total HF/Si interface area. The porosity of such an ordered array of macropores with radius r_{Pore}, e.g. arranged in a hexagonal lattice with lattice constant a, can be expressed as

$$p_{hex} = \frac{2\pi}{\sqrt{3}} \left(\frac{r_{Pore}}{a}\right)^2$$

Extension of the PECE Model of Lehmann to Trenches

For the realization of the trenches during PECE, it was necessary to extend the Model of Lehmann (8). A trench has to be etched in close proximity to an ordered array of macropores to prevent the formation of non-lithographically defined pores. Keeping in mind the design rule of constant porosity within a unit cell, the thin silicon layer between the last row of pores and the trench, called in the following the ARL, can be realized by lithographically defining a trench to be etched next to the last row of pores (Fig. 1a). The thickness t_{ARL} of the remaining ARL is given by the distance from the edge of the trench to the center of the adjacent pores. By lithography the x–y positions of the pores and the trench are fixed. But, the width of the etched trench depends on the r/a ratio chosen during PECE according to

$$t_{\text{trench}} = \frac{\pi \left(\frac{r}{a}\right)^2 (2t_{\text{ARL}} - 0.5)}{\sqrt{3} - 2\pi \left(\frac{r}{a}\right)^2}$$

with the symbols used in Fig. 1a. As a consequence, the intended r/a ratio has to be taken into account when defining the position of the trench on the lithography mask. Figure 1b depicts successfully etched, 450-μm-deep trenches next to arrays of hexagonally arranged macropores. Both the macropores as well as the trenches grow stably. Due to the observance of the before-stated design rules, stable trench-next-to-macropores growth could be achieved by using PECE parameters comparable to the parameter set used for the fabrication of pure macropore arrays. However, it is clear that constant porosity in bulk porous silicon and the ARL/trench regions is a necessary but not sufficient prerequisite to achieve stable macropore/trench growth. If the system is disturbed too much by, for example, creating too thick ARLs with $t_{\text{ARL}} > 1.0a$ the PECE process becomes unstable. As a result, dying out of trenches or branching of pores and trenches is observed.

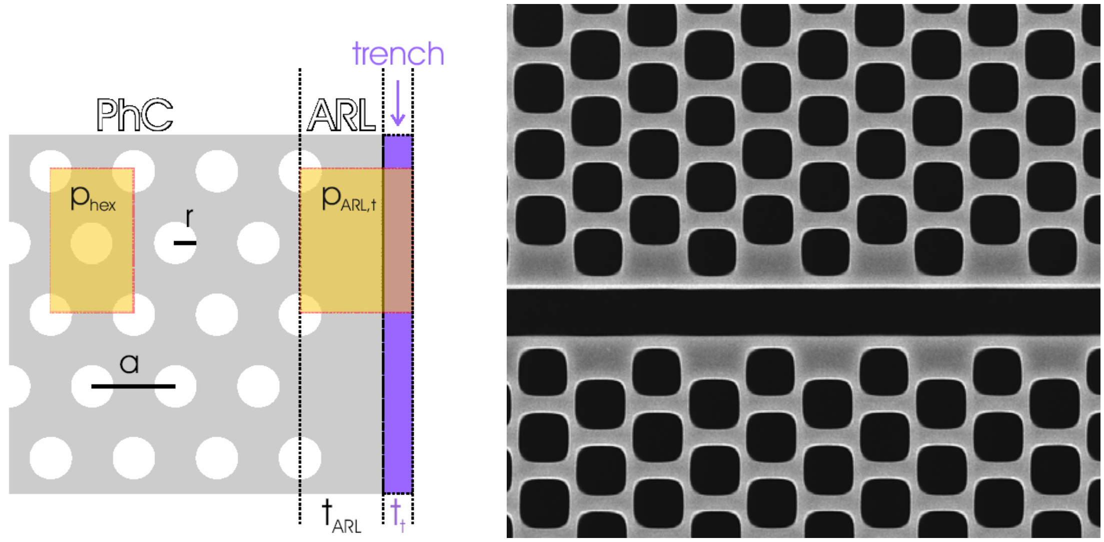

Figure 1. (a,left): Schematic diagram of the trench etching gas layout. (b, right): Scanning electron micrograph of PhC devices with etched trench in between (pore distance a=4,2μm).

The instability of the PECE process for thick ARL layers, can be understood by looking at Fig. 2 where the equipotential surfaces for the PhC/ARL geometries used are numerically calculated. When homogeneously distributed electronic holes created by illumination at the back side of the Si wafer approach the growth front, they are focussed onto the pore tips and the bottom of the trench, respectively, by the gradient of the potential. In the case of the thick ARL with $t_{\text{ARL}} = 1.0a$, a region with only a small potential gradient exists. Here only weak focussing of holes onto either the pore tips or the trench is achieved, resulting in an unstable PECE process. The increase in surface roughness of the ARL is a consequence of the disturbed potential distribution. At the beginning of pore growth the pore and trench locations are determined by lithography. But, the asymmetric potential leads to an inhomogeneous consumption of electronic holes. As a consequence, pore/trench shapes and positions gradually change with increasing depth. In regions where the pores are close to the ARL, the latter will be a little thicker than designed, while, in regions where the pores are further away from the ARL, the ARL can consume more electronic holes during growth and therefore will become slightly thinner than intended.

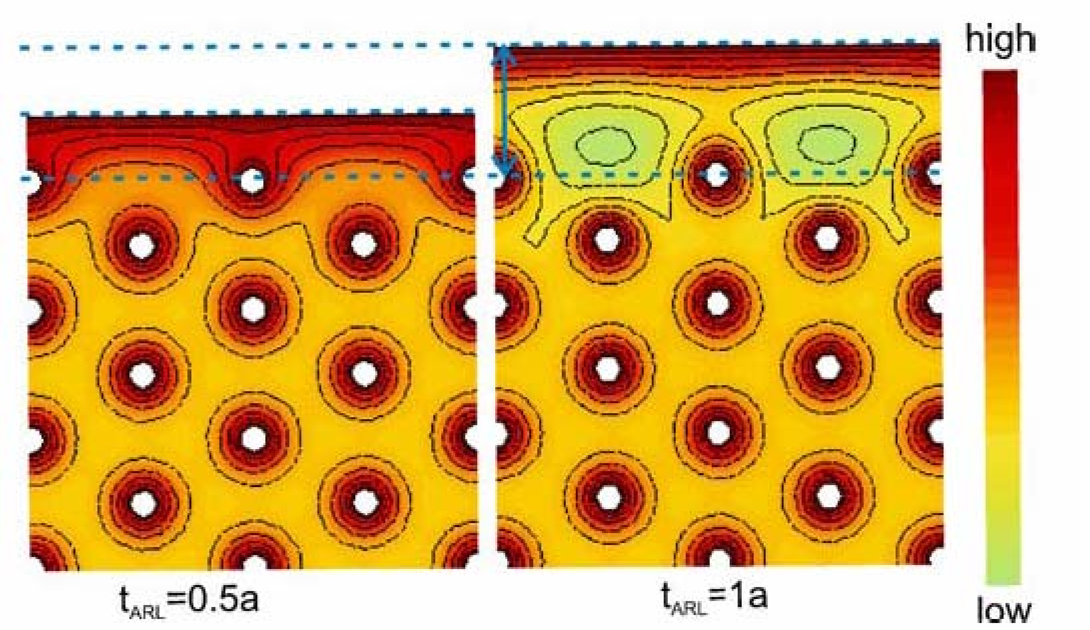

Figure 2: Numerically calculated equipotential surfaces for a regular hexagonal pore pattern and at a PhC ARL interface for two different ARL thicknesses during PECE.

PECE of trenches allows in addition the realization of novel, interesting structures. Figure 3a,c and d show how PECE trenches next to macropore arrays can be used to precisely define thin stripes of arbitrary numbers of pore rows with even waveguides. While this is shown for lattice constants of 2 μm and 4.2 μm in Fig. 3a and d, respectively, trench etching is expected to work in principle independent of the lattice constant of the macropore array. These thin stripes are generated during the PECE process without any post processing (except for cleaving using a pair of tweezers). By standard procedures, i.e. inscribing the Si with a diamond scribe and mechanical cleaving, such thin stripes cannot be realized. Figure 9b shows that PECE of trenches allows realization of well-defined hole structures in macropore arrays. The macropore array in the center of the hole can easily be removed after membrane fabrication by pushing with a small tip or blowing with pressurized air.

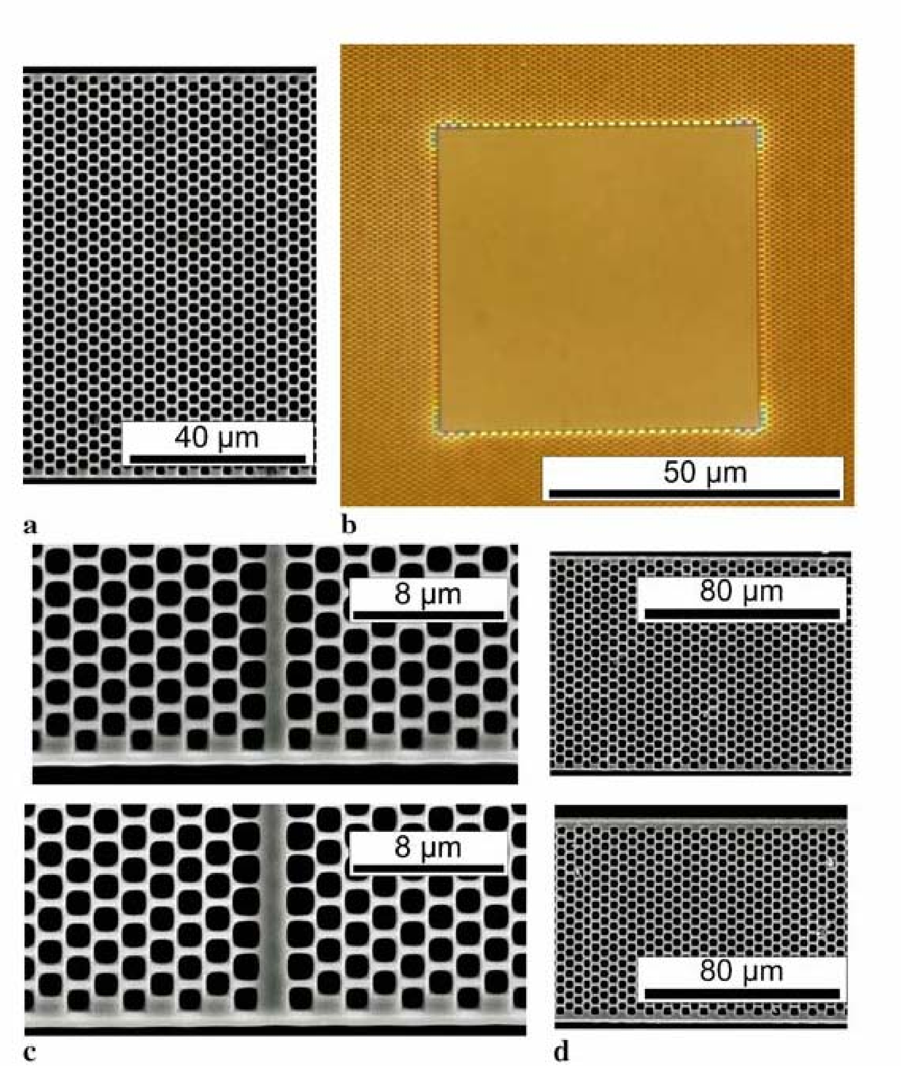

Figure 3: PECE trenches: (**a**) two trenches used to define a thin stripe of 61 pore rows (*a* = 2 μm); (**b**) trenches along a 100×100 μm^2 hole within a macropore array (*a* = 2 μm); (**c**) PhC waveguides, terminated with an ARL (*a* = 2 μm); (**d**) two trenches used to define thin stripes of 35 (*bottom*) and 39 (*top*) pore (*a* = 4.2 μm) (SEM: (**a**), (**c**), (**d**); optical microscope: (**b**))

Photonic crystal gas sensors

Photonic crystals (PhC) allow the tailoring of light such increased diffraction or slowing down of light in the region of low group velocities. If the pores of the photonic crystals are filled with an analyte such as gas, the interaction time t_{int} is increased and therefore the length of the interaction path l_{int} can be reduced while keeping the total interaction constant (4). As a consequence the fields of the scattered waves superimpose coherently and interact several times with the gas atoms and this gives the enhanced interaction. Following the technology described above, 2D-PhC samples with lengths from 100 µm to 1mm, an interpore spacing of 4.2 µm and a thickness of 330 µm were prepared. Transmission measurements indicate an optical attenuation of less than 2dB/mm showing the high quality of the structure. Losses are probably mainly due to residual scattering due to the pore diameter variation of 1-2 %. The PhC membranes were fixed between two BaF_2 light guiding rods (12mm x 1mm x 400 µm), which couple the IR radiation in and out of the PhC sample (Fig. 4a). A flat plastic top plate seals the setup airtight. Two tiny holes in the center at the position of the PhC enable a gas flow through the PhC sample. The assembled gas cell is mounted between a thermal radiation source and a pyrodetector with an IR bandpass filter centered at 4.24 µm for CO_2. The radiation intensity of the IR emitter was modulated via the operating voltage with a frequency of 10 Hz. The signal of the pyrodetector was measured using a digital lock-in amplifier with a time constant of 2s. The transmission of the PhC sample (length 200 pore rows i.e. 250 µm, thickness 330 µm) without gas is about 8,6% absolute. First measurements with other samples with 1 mm PhC length yield transmission values of approximately 4 %. In the course of the experiments the gas cell was filled with dry N_2, then filled with CO_2, and rinsed with N_2 again. This cycle was repeated several times. The results are shown in Figure 4b. The normalized data show that with the PhC the absorption by CO_2 is more than twice the value of the empty cell, taking into account the porosity of the sample, a factor of about 3.4 enhancement is obtained. This is the first evidence that in PhCs enhancement of absorption can be achieved.

To increase this enhancement factor to about 10 the quality of the PhC has to be further enhanced. Doping inhomogeneities of silicon wafers (striations) lead to pore diameter distribution resulting in scattering. NTD-silicon (neutron transmutation doped) is free of such doping striations and therefore a promising candidate for highest quality PhCs.

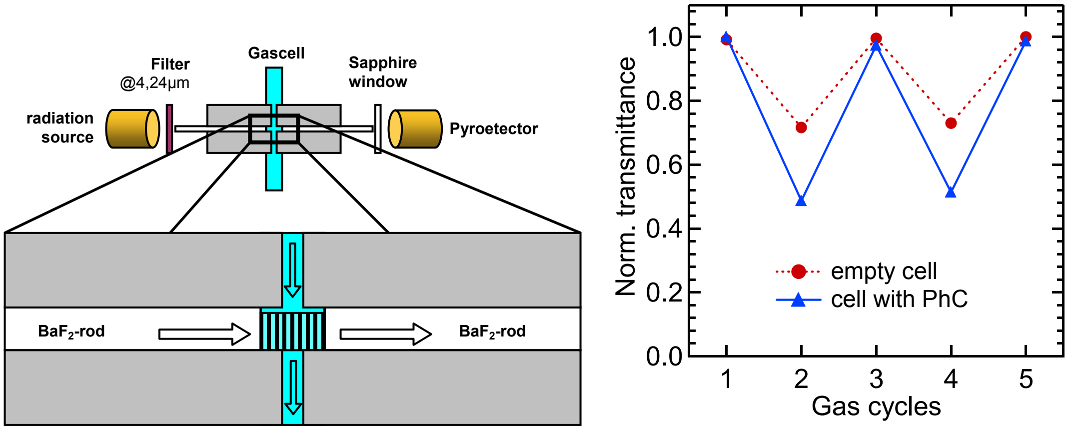

Figure 4. (a,left): Schematic diagram of the gas measurement setup. (b, right): Normalized absorption for gas cycles (CO_2, N_2, etc.) for the empty gas cell and the gas cell with PhC.

Conclusion

We presented a method to create at the same time trenches and ordered macropore arrays during photoelectrochemical etching of n-type silicon. Even very deep trenches of more than 400 µm have flat surfaces with an average roughness in the range of 100 nm. The remaining silicon thickness between the trenches and the pore arrays is limited to one inter-pore distance. For larger thicknesses, the trenches do not grow stably. This can be understood by analyzing the equipotential surface during electrochemical etching. This novel method allows in situ separation of single devices with a submicrometer precision. It also enables new device structures in macroporous silicon in the areas of photonics, sensing and electronics. As an example, a photonic crystal gas sensor is shown which performance is limited by the doping variations (striations) of the starting wafer.

Acknowledgments

The authors would like to acknowledge financial support by the BMBF and by Drägerwerk AG within the project PHOKISS (13N8525).

References

1. V. Lehmann, H. Föll, *J. Electrochem. Soc.*, **137**, 653 (1990).
2. V. Lehmann, *J. Electrochem. Soc.,* **140**, 2836 (1993).
3. A. Koenderink, R. Wüest, B. Buchler, S. Richter, P. Strasser, M. Kafesaki, A. Rogach, R. Wehrspohn, C. Soukoulis, D. Erni, F. Robin, H. Jäckel, V. Sandoghdar, *Photon. Nanostruct. Fundam. Appl.* **3**, 63 (2005)
4. A. Lambrecht, S. Hartwig, S. L. Schweizer, R. B. Wehrspohn, *Proc. of SPIE*, **6480**, 64800D-1 (2007).
5. S. Matthias, F. Müller, C. Jamois, R.B. Wehrspohn, U. Gösele, *Adv.Mater*. **16**, 2166 (2004)
6. V. Lehmann, *Nat. Mater*. **1**, 12 (2002)
7. P. French, in *Ordered Porous Nanostructures* (Springer, Heidelberg, 2005), Chap. 7
8. T. Geppert, S. L. Schweizer, U. Gösele, R. B. Wehrspohn, *Appl. Phys. A*, **84**, 237 (2006).

ECS Transactions, 16 (3) 69-75 (2008)
10.1149/1.2982543 ©The Electrochemical Society

Catalytic Activity of Hybrid Metal/Silicon and Metal/Silicon Dioxide Nanocomposites

S. Polisski[a], B. Goller[a], A. Lapkin[b], and D. Kovalev[a]

[a] Department of Physics, University of Bath, Claverton Down, Bath
BA2 7AY, United Kingdom
[b] Department of Chemical Engineering, University of Bath, Claverton Down, Bath
BA2 7AY, United Kingdom

Here we demonstrate that H-terminated porous silicon (PSi) powders and layers can be utilized as highly efficient reductive templates for noble metal salts. The metal salt reduction results in a metal nanoparticle (NP) formation in the porous matrix of PSi. Gold NP formation has been monitored *in-situ* by measuring the plasmon resonance response. Pt NPs, formed in the pores of PSi, were investigated by transmission electron microscopy (TEM) and energy-dispersive X-ray (EDX) analysis. Furthermore, hybrid Pt/PSi nanocomposites exhibit a high catalytic activity for CO oxidation. Some of the samples were oxidized to obtain Pt/PSiO$_x$ nanocomposites for comparison of catalytic activity.

Introduction

PSi nanostructures exhibit a very large (up to 500 m^2/cm^3) hydrogenated internal surface area and can be prepared in many different ways: electrochemically, by stain etching process and other (1). In this paper we demonstrate that these peculiar morphological properties of PSi result in a high reductive potential due to hydrogen termination. The groups of *Sham* and *Coulthard* have shown that noble metal salts, dissolved in water can be reduced on the surface of PSi layers (2). However, it was shown that the hydrogenated PSi surfaces are hydrophobic (1), and therefore, the large internal surface area of PSi is not accessible to metal salts $_{(aq)}$ and is not exploited.

In recent years the catalysis based on metal NPs has been widely developed (3). Scaled to nano sizes, metal particles are more efficient in catalysis due to the large extended surface area and exposed higher energetic surfaces. They promote chemical reactions which cannot be realized otherwise. The reason is most likely the new provided reaction sites and modified surface properties of the NPs (4). Nowadays NPs are not only competing, but frequently replacing up to date known homo- and heterogeneous catalysts (5).

Therefore, the reactive PSi templates open very promising possibilities for applications in nanometal-supported catalysis. Salts of Pt and Au were reduced on the internal Si nanocrystalline surface. The obtained metal NPs can be in the size range of 3 to 20 nm.

Hydrogen effusion experiments show that Si surfaces lacking H-termination are not able to act as reductive templates. This fact emphasises the crucial difference for metal NP formation between H-terminated PSi and in catalysis widely used chemically inactive templates. The catalytic activity of the developed Pt/PSi and oxidized Pt/PSiO$_x$ nanocomposites has been studied using a conversion of carbon monoxide (CO) to carbon dioxide (CO$_2$) in oxygen.

Experimental

Sample Preparation and Characterization

Free-standing PSi layers have been prepared via standard electrochemical etching of B-doped (100) Si substrates with a typical resistivity of 2–5 Ω cm (microporous Si, 70 % porosity) (1). To prepare nanocrystalline PSi powder we used metallurgical grade (Al doped) powder with a mean particle size of 4 μm. The stain etching was performed as described elsewhere (6). To obtain the surface area and the pore size distribution of an as-prepared PSi powder, adsorption–desorption isotherm of PSi for nitrogen at 77 K was measured. The internal surface area of the PSi was evaluated by the Brunauer, Emmett and Teller method (BET) (7), derived from the N_2 desorption isotherm. The pore size distribution was calculated by the Barrett, Joyner and Halenda calculation (BJH) (8).

For the preparation of the nanocomposites, the metal salts were first dissolved in ethanol. Then, PSi was immersed into metal salt solutions at different temperatures. To obtain oxidized hybrid nanocomposites, as-prepared M/PSi samples were heated to 1100 °C in air.

For the characterisation of the sample morphology, high resolution transmission electron microscopy measurements (HRTEM) of as-prepared PSi samples, metal/PSi (M/PSi) and M/$PSiO_x$ hybrid nanocomposites were performed using a JEM-2010 (JEOL) apparatus operated at 200 kV.

For plasma resonance experiments electrochemically etched PSi layers were utilized. These PSi samples were inserted in a quartz cuvette, containing solutions of Au salts in ethanol (10, 1 and 0.1 mM). Optical transmission spectra were then taken at regular time intervals of both the solution and the PSi samples.

Catalytic Activity Measurements

The catalytic activity of the metal NPs embedded in the PSi matrix was tested using the oxidation reaction of carbon monoxide in the absence of water and hydrogen. For this purpose a gas mixture of 1 % CO / 20 % O_2 (balanced in He) was used, providing a gas flow of 75 cm^3 min^{-1} through a quartz microreactor. In all experiments a mixture of catalyst sample with 40 % wt. of broken quartz (diameter approximately 10 μm) were used to assure a homogeneous gas flow distribution. The actual amount of metal was measured to determine its catalytic activity by X-Ray Photoelectron Spectroscopy (XPS). The reaction was monitored by a gas-sampling mass spectrometer to trace the CO_2 output.

Results and Discussion

Morphology of PSi Powder and M/PSi Nanocomposites

After the stain etching of Al-doped polycrystalline Si grain, a sponge-like network of Si nanocrystals in the nanometre range was obtained (see Fig. 1).

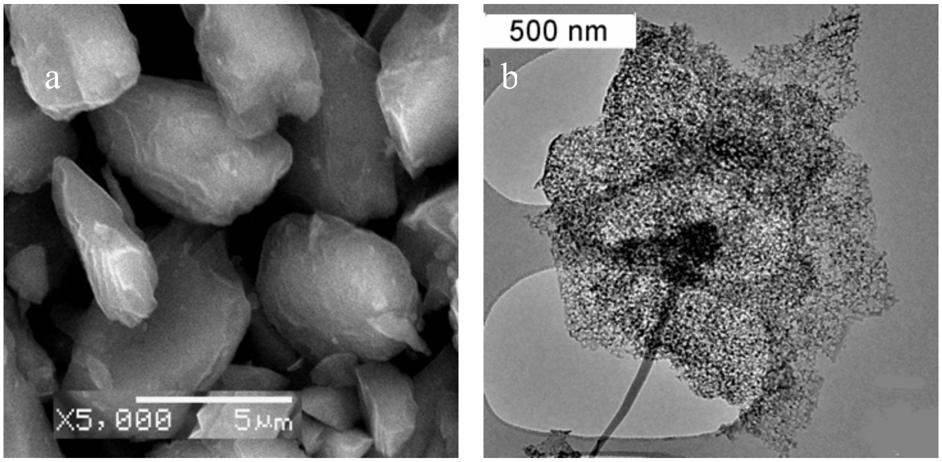

Figure 1. a. SEM image of the starting material: metallurgical grade Si grains. b. TEM image of PSi, called *Hawaiian flower*, indicating the sponge-like structure of stain etched Si grains.

Furthermore, we identified Si-H_x bonds (x = 1, 2 and 3) as the dominating surface groups on PSi using infrared absorption spectroscopy. To demonstrate the importance of hydrogen surface termination for the NP formation hydrogen desorption (effusion) experiments were performed by heating the samples up to 400 °C. Then, a noble metal salt was reduced in the matrix of PSi to compare both, an as-prepared and a thermally treated sample. While for the H-terminated samples an efficient metal NP formation was observed, no reductive activity under the same conditions was noticed for the pre-heated samples.

Hence, we conclude that the surface Si–H_x groups act as the main force for the reduction of noble metal salts in the PSi matrix. We found that the pore size of PSi support, the temperature during metal NP formation and the metal salt concentration in primary ethanol solutions are crucial in defining the overall morphology of the nanocomposites. HRTEM images of Au and Pt NPs, formed in the PSi matrix, is shown in Fig. 2. The mean particle size of Pt NPs determined by HRTEM technique is around 6 – 8 nm, which coincides with the average pore size. This evidences the pre-definition of the size of NPs by the pore size of the support and its porous structure.

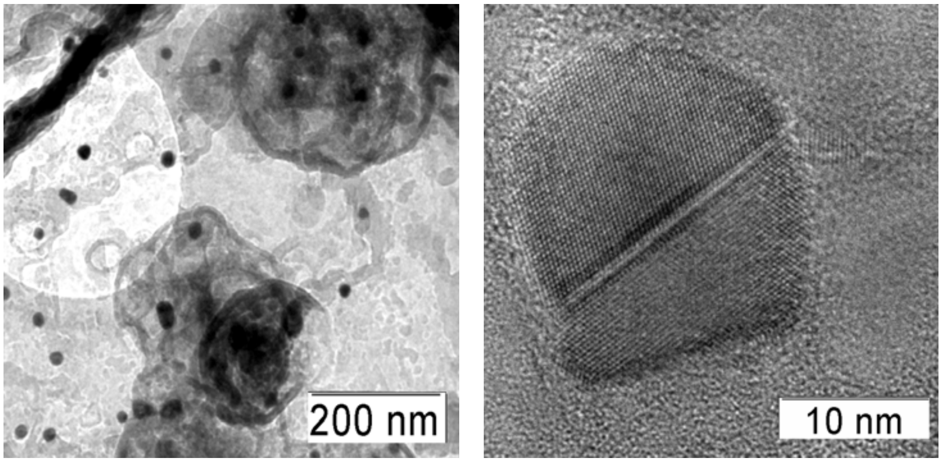

Figure 2. HRTEM images of Au NPs (left) and an interestingly twinned Pt nanoparticle (right) formed in PSi layers.

In-situ Plasma Resonance Monitoring of Metal NP's Formation

To observe Au NP formation in-situ, thin (up to 25 μm) free standing layers of PSi with pore sizes of 5–10 nm were employed. Time-dependent NP formation inside PSi matrix was studied by measuring the metal plasma oscillation frequency response with time. The plasma frequency of metal particles is dependent on their shape, size and the surrounding dielectric medium (9).

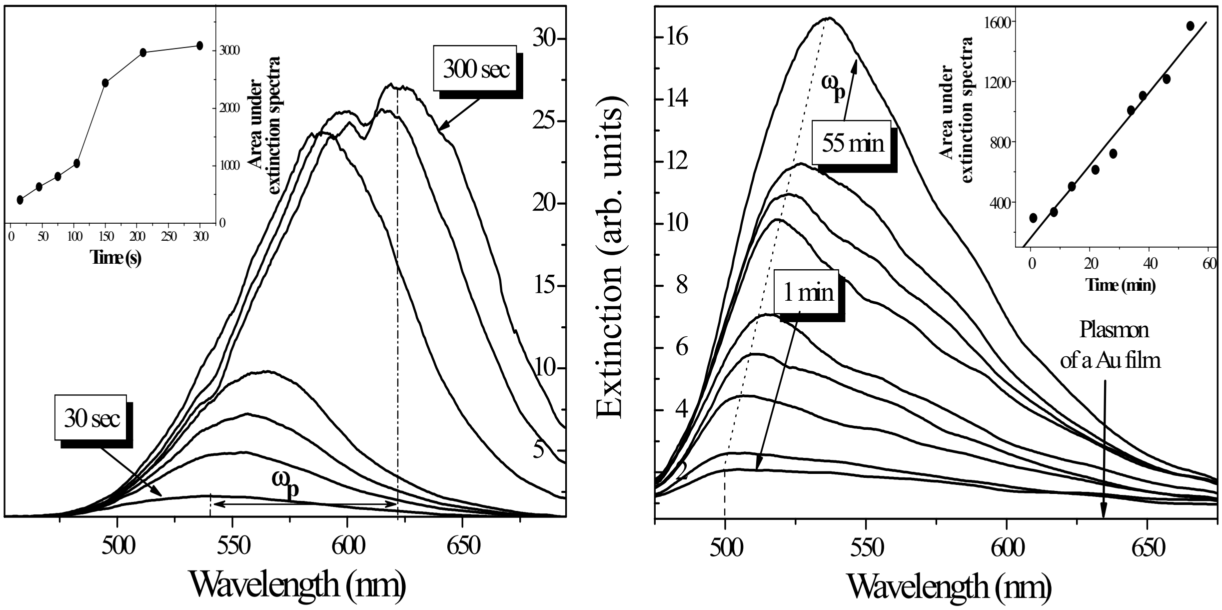

Figure 3. In-situ monitored plasma frequency of Au NPs forming in PSi.
Left: 10 mM concentrated $HAuCl_4$ solution. Right: 0.1 mM concentrated $HAuCl_4$ solution. Extinction spectra were recorded in periodic steps. Insets: Area under the extinction spectra versus time. The dotted lines are for eye guidance only.

Free standing PSi layers were exposed to two different enthanolic solutions of $HAuCl_4$ (0.1 and 10 mM). The continuous gold particle formation was traced *in-situ* via the measurement of the extinction spectra.

In solutions with a high $HAuCl_4$ concentration gold particle formation on the surface is observed already after several minutes (Fig.3, left). The extinction of the Au/PSi samples presents a strong red-shift and a higher value with longer reaction time (Fig. 3, left). The shift in the plasmon frequency ω of Au can be explained by the formation of larger/elongated particles within and on the outer surface of the PSi matrix. An explanation for the saturation of the extinction from gold NPs on PSi could be that no further Au ions can be reduced or the increasing Au particle size does not affect significantly the extinction of the sample. The saturation is reached here after 5 min, according to the area under the extinction spectra (inset of Fig.3, left).

In lower Au salt concentrations the area under extinction spectra rises linearly with time during the first hour of the reaction (inset of Fig. 3, right). Only after two hours, the extinction spectra reach their steady state. Nevertheless, even after two hours the plasmon frequency of the formed NPs (580 nm) is still far from the bulk value of 634 nm (10), indicated by the arrow in Fig. 3. For Au NPs it is in the visible range (λ = 550 nm). Pt has its plasmon resonance in the UV-range (~235 nm) (11), which makes the optical studies of Pt NP formation in PSi impossible, as PSi adsorbs very efficiently in this range. Plasmon resonance is a fingerprint of Au NP formation.

We assume that the amplitude of the integral area under the extinction spectra scales in the first approximation with the quantity of reduced particles. At concentrations of 10 mM the formation of micrometer-large particles has been detected. At lower concentrations gold particles are formed much slower and mostly inside PSi template. The Plasmon resonance of gold shifts only slightly to longer wavelengths with time, implying a nanometer particle size (Fig. 3, right). The area under extinction spectra rises linearly with time during the first hour of the reaction, showing that a uniform formation of small particles can be realized (inset of Fig. 3, right).

Catalysis on Pt/PSi Nanocomposites

CO oxidation reaction was selected to test the catalytic activity of prepared Pt/PSi hybrid nanocomposites. Different Pt/PSi powders (m = 0.35 g) were placed in to a so called continuous flow microreactor. A gas mixture (CO and O_2 in He) was passed through the microreactor during the experiment maintaining a flow of 75 cm^3min^{-1}. A complete CO conversion was achieved for every Pt weight loading shown in Figure 4. A Pt-free sample showed no activity (circles, Fig. 4) over the tested temperature range. A negligible conversion of CO was registered above 300 °C; which probably results from a hydrogen desorption taking place in the temperature range of 350 °C to 500 °C. Due to the presence of dangling bonds in the peripheral PSi sites, small amount of CO and O_2 molecules can be adsorbed at the free sites and reacts to carbon dioxide. Since almost no difference in catalytic activity for all Pt/PSi samples has been found, we believe that similar reaction sites are involved due to an equivalent particle size distribution. In Figure 4 a sharp step in the CO conversion is observed when the so called "light-off" temperature (T_L) is reached. At this temperature the catalyst starts to be highly active and the reaction product in respective amounts can be detected.

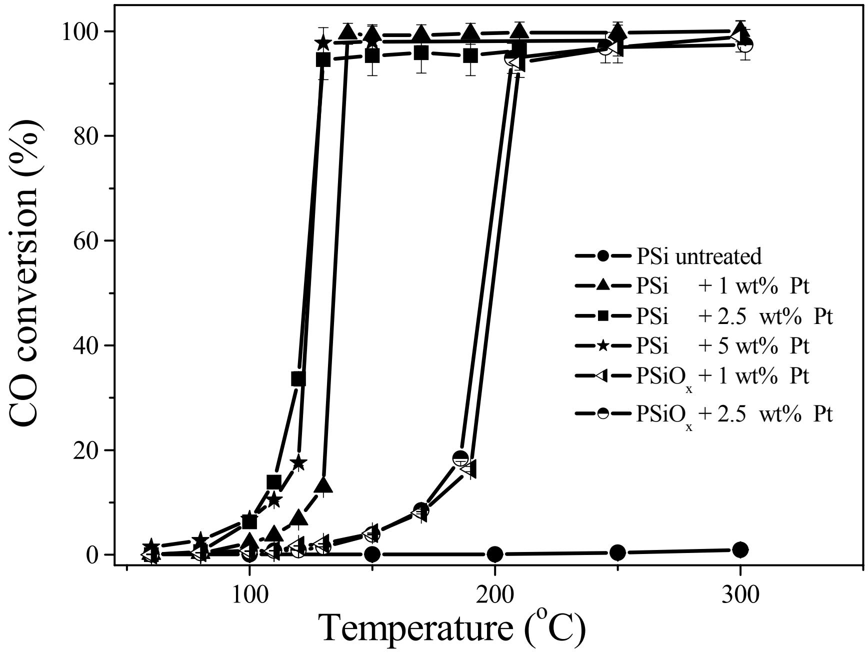

Figure 4. CO conversion by Pt/PSi and Pt/PSiO$_x$ catalysts. Gas flow rate is 75 cm^3 min^{-1}, mass of catalyst used: 350 mg. Light-off temperatures (T_L) are indicated by arrows.

Interestingly, the oxidized Pt/PSiO$_x$ samples are still stable and catalytically active even after a treatment at 1100 °C. They show higher light-off temperatures (180 - 190 °C) than their non-oxidized counterparts, implying the fact that the morphology of the catalysts has changed. Another explanation could be that the Pt NPs are not fully accessible after the oxidation. These aspects will be investigated in detail in future.

Conclusions

The PSi matrix is very different from other known and used support materials for catalysis. They present a high reductive ability by the extended H-terminated surface and a widely tuneable pore size. Furthermore, the pore morphology of PSi prevents agglomeration and leakage of formed NPs. The plasmon resonance seems to be a promising method to investigate the NP formation *in-situ*. By utilising this technique a controllable synthesis of NPs can be achieved.

Furthermore, we found that the NP formation is strongly dependent on the used metal salt concentration for the reduction and the exposure time to PSi layers. The CO oxidation experiments provide evidence for the high catalytic activity of Pt NPs embedded in PSi matrix even after high temperature treatment at 1100 °C. As presented, the conversion efficiency is dependent on the metal particle size, the used metal salt concentration in solution during deposition, the PSi morphology with the pore size distribution and the used gas flow rate, respectively. We think that much smaller metal loadings of an optimized catalyst, based on Pt/PSi hybrid nanocomposites, will be sufficient for high CO conversion.

Acknowledgements

S.P. wishes to thank his father G. Polisski and his mentor in organic chemistry G. Remennikov for their support and shared knowledge during his undergraduate studies in chemistry at the LMU Munich. This work was in part supported by Engineering and Physical Sciences Research Council via grant EP/E012183/1.

References

1. A. G. Cullis, L. T. Canham, and P. D. J. Calcott, *J. Appl. Phys.* **82**, 909 (1997).
2. I. Coulthard and T. K. Sham, *Solid State Commun.* **105**, 751 (1998).
3. D. Astruc, F. Lu, and R. Aranzaes Jaime, *Angew. Chem. Int. Ed.*, **44**, 7852 (2005).
4. A. S. K. Hashmi and J. Hutchings Graham, *Angew. Chem. Int. Ed.*, **45**, 7896 (2006).
5. G. P. Chiusoli and P. M. Maitlis (eds.), *Metal-Catalysis in Industrial Organic Processes* RSC Publishing, Cambridge (2006).
6. S. Limaye, S. Subramanian, B. Goller, J. Diener and D. Kovalev, *phys. stat. sol. (a)* **204**, 1297 (2007).
7. S. Brunauer, P. H. Emmett, and E. Teller, *J. Am. Chem. Soc.* **60**, 309 (1938).
8. E. P. Barrett, L. G. Joyner, and P. P. Halenda, *J. Am. Chem. Soc.* **73**, 373 (1951).
9. S. A. Maier, *Plasmonics: Fundamentals and Applications*, Springer Science + Business Media LLC, New York (2007).
10. E. D. Palik, *Handbook of Optical Constants of Solids,* p. 804., Academic Press, New York (1985).
11. S. Remita et al., *Radiat. Phys. Chem.* **54**, 463 (1999).

ECS Transactions, 16 (3) 77-81 (2008)
10.1149/1.2982544 ©The Electrochemical Society

Gas Sensing Property of Porous SnO_2 Layer Synthesized through Anodic Oxidation

Jeong-Hoon Jeun, Hyun-Sam Ryu, and Seong-Hyeon Hong

Department of Material Science and Engineering and Nano Systems Institute-National Core Research Center, Seoul National University, Seoul 151-742, Korea

SnO_2 porous structure was fabricated by anodic oxidation. The Sn coated SiO_2/Si wafer was used as an anode and it was anodized in 0.3 M oxalic acid aqueous solution using DC power supply. The phase of formed oxide was rutile and the morphology showed a porous structure. The porous SnO_2 with nano-channel was obtained at 6V and the pore diameter was approximately 20 nm. A post annealing was performed at 500 ℃ for 3 h to enhance the crystallinity. To evaluate the gas sensing properties, a comb like Pt pattern was deposited on the anodized and annealed specimen and its gas sensing properties were measured as a function of gas concentration and working temperature

Introduction

Tin oxide (SnO_2) is widely used as a solid state gas sensor material detecting inflammable and toxic gases. The gas adsorption and desorption on the surface of gas sensing material change its electric resistivity, which depends on the thickness of depletion layer. Therefore, a surface area is one of main factors to determine gas sensing performance such as sensitivity, response-recovery time and long-term stability, and many researchers have studied for applying nanostructures with large surface-volume ratio to solid state gas sensor in order to enhance gas sensing performance.

In this study, we focused on the synthesis of nano porous SnO_2 using anodizing process The anodizing process has been widely used for self-ordered porous oxide formation due to potential mass production at low cost. In spite of that advantage, a few materials such as Al and Ti have been mainly studied to form the porous structure [4, 5]. In previous study, the synthesis of SnO_2 via anodic oxidation has been reported once [6]. However, the anodic oxide formed on tin surface was stripped off during annealing for crystallization due to the low melting point of tin, 250 ℃. In this study we report the formation of porous tin oxide layer on silicon oxide through anodic oxidation to overcome previously reported problems and its gas-sensing properties were evaluated.

Experimental

Sample preparation

SiO_2(20000Å)/Si wafer (100) was cut into the rectangular shape of 20 mm x 10 mm dimension and rinsed 2~3 times with acetone, ethanol and rinsed 3~4 times with deionized water. The cut wafers were attached on 4 inches silicon wafer and loaded to thermal evaporator (MHS-1800) to form Sn film of 500 nm thickness. The tin shot

(Kojundo chemical, 99.999%) was used as the metal source and the deposition was performed with the deposition rate of 15 Å/s and 18 rpm rotation

Anodic oxidation

A carbon plate was used as a counter electrode for anodic oxidation. The distance between working electrode and counter electrode was 3 cm. The constant voltages of 4 ~ 8 V was applied to the electrode using a DC power supply (Fine-power, F-100) in 0.3 M oxalic acid (Sigma Aldrich) electrolyte solution at 15 ℃ for 15 - 60 s. Anodic oxidation was performed without stirring and N_2 bubbling. After anodization, the samples was rinsed with deionized water and annealed for crystallization at 500 ℃ for 3 h.

Measurement of gas-sensing property

A pair of comb-like Pt electrodes was formed by sputtering on the porous SnO_2 layer and a silver paste was used for attaching Au lead wire to them. Thereafter, the fabricated sensor was fired at 500 □ for 1 h in order to make the electrical contact between Au lead wire and silver paste. The gas sensing property was determined by measuring the resistivity changes between 100 and 1000 ppm H_2 balanced with air and pure air at the range of 300 – 400 ℃ and the electrical resistivity was measured through a multimeter (2000 multimeter, Keithley)

Characterization

The field emission scanning electron microscope (FESEM, JSM-7401F) was employed for the analysis of morphologies. The phase was determined by X-ray diffraction (XRD, M18XHF-SRA)

Result and Discussion

Morphology

There was a competition between film adhesion and formation of porous structure. The adhesion between anodic oxide and silicon oxide was getting poor as the reaction was more vigorous whereas the porosity was increased. We reduced the reaction rate in order to find the optimized condition to form porous structure and maintain oxide layer on tin surface. In order to control the reaction, temperature, applied voltage, time and electrolyte concentration was mainly adjusted.

The influence of electrolyte concentration during anodizing process was observed under the constant applied voltage (V) at 15 ℃. We found that a crack, not porous structure, on the surface was merely formed in 0.1 M oxalic acid electrolyte solution and the adhesion between silicon oxide and anodic oxide was enhanced with the decrease of electrolyte concentration from 0.5 M to 0.3 M during anodic oxidation.

In terms of applied voltage, a porous structure was not formed below 5 V. The SEM image of morphology (top view) of the anodized tin oxide formed at 6 V in 0.3 M oxalic acid electrolyte solution at 5 ℃ is shown in Fig. 1. The pore with irregular shape was approximately 20 nm of diameter and randomly distributed on the overall surface. Some samples in the early stage of reaction have a crack on the surface due to the oxygen evolution and relatively thin Sn coating thickness.

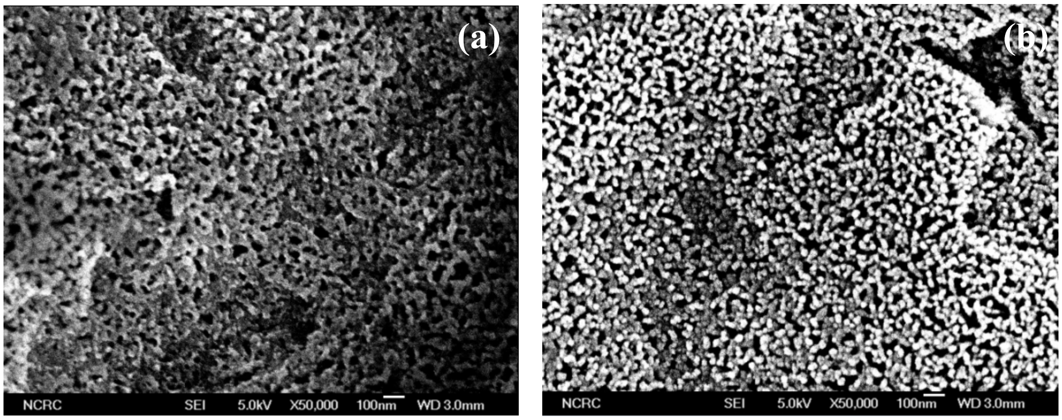

Fig. 1. SEM images of porous tin oxide synthesized by anodic oxidation for different periods of time at 5℃: (a) 1 min, (b) 1.5 min. The surface porosity increased with the anodizing time

The porosity of anodic oxide layer clearly increased with the anodizing time. The anodic oxide shown in Fig. 2 was synthesized in 0.3 M oxalic acid electrolyte at 15 ℃ and show the dependence of the porosity on the anodizing time. As compared with Fig. 1, the effect of enhanced oxide dissolution with increasing electrolyte temperature leads to a more porous oxide structure [7].

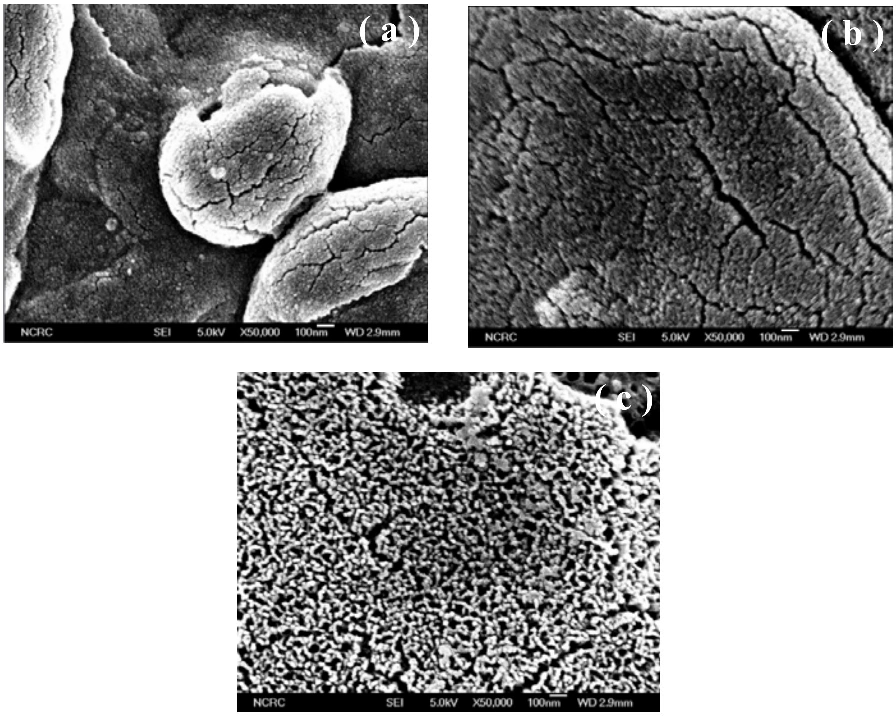

Fig. 2. SEM images of the anodic oxide formed in 0.3 M oxalic acid at 6 V with different anodizing time at 15℃: (a) 15 sec, (b) 30 sec, (c) 45 sec

Although the samples anodized at 5 ℃ takes the longer anodizing time in Fig. 1(a) the porosity is smaller than the oxide anodized at 15 ℃ in Fig. 2(c)

Fig. 3 shows nano-channels grown on the kink-step of surface and the vertical growth of anodic oxide were analyzed. The length of nano-channel is the range of 400~600 nm.

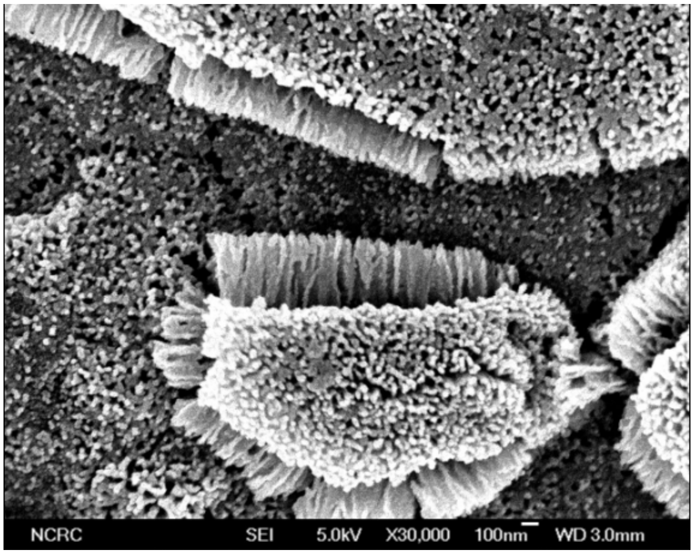

Fig. 3. The anodic oxide vertically grown on the kink-step of surface

Phase analysis

The anodic oxide appeared to be dark brown, signifying the remains of stannous oxide (SnO) on surface. [8] The surface color turned into white after annealing for crystallization, implying that stoichiometric stannic oxide (SnO_2) is obtained. [6] As shown in Fig. 4, the X-ray diffraction pattern indicate that amorphous tin oxide is crystallized to stannic oxide through annealing process at 500 ℃ for 3 h.

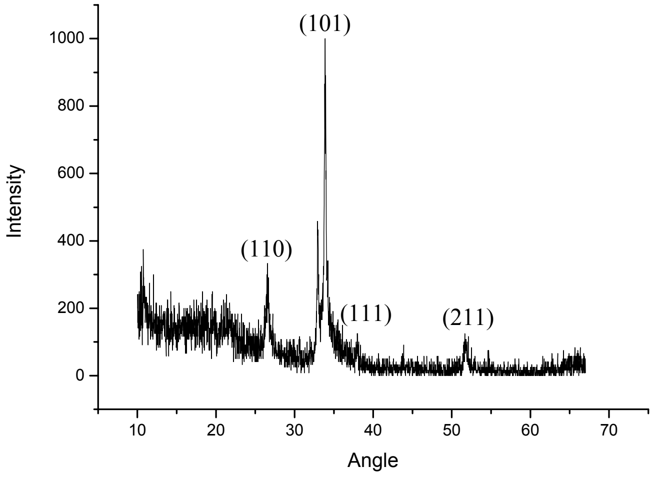

Fig. 4. X-ray diffractogram of the anodized tin oxide annealed at 500 ℃ for 3 h

Gas sensing properties

Fig. 5 is the response transient and sensing properties of the porous SnO_2 layer to H_2 gas. The resistance rapidly decreased by several orders of magnitude. The gas sensing performance was quite stable and reversible and the recovery-response time was relatively fast. The gas-sensing sensitivity increased with increasing temperature and H_2 concentration.

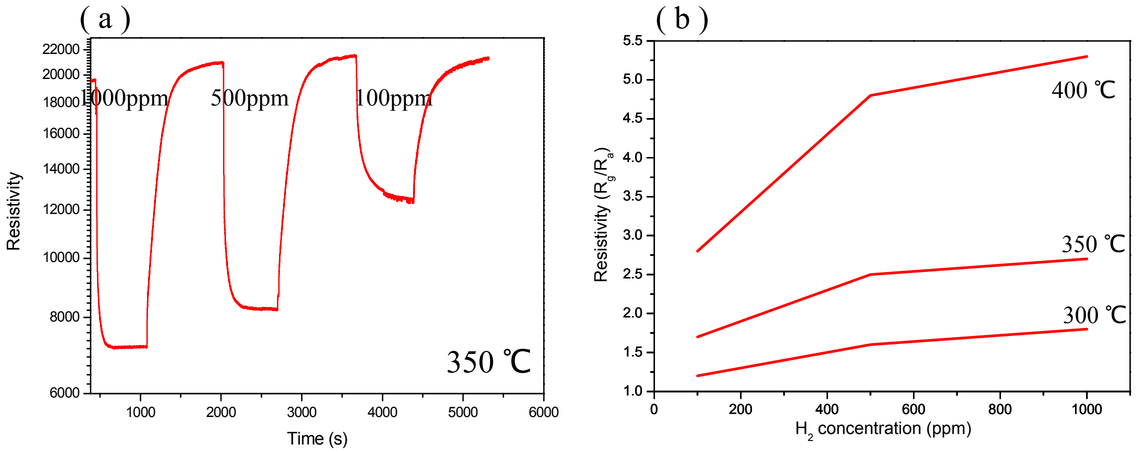

Fig. 5. (a) Response transient of the porous SnO_2 measured at 350 ℃ and (b) the sensitivity of gas-sensing with H_2 concentration and temperature

Acknowledgement

The authors acknowledge the support from Nano Systems Institute-National Core Research Center, Seoul National University, Korea

Reference

[1] M. Batzill and U. Diebold, *Prog. Surf. Sci.*, **2005**, *79*, 47-154,
[2] V. Brinzari, G. Korotchenkov, S. Dmitiev, *J. Electr. Technol.*, **2000**, *33*, 225,
[3] S.R. Morrison, *Sens. Actuators. B*, **1987**, *11*, 283,
[4] J. P. O’sullivan, G. C. *Wood, proc. R. Soc. London, Ser. A* **1970**, *317*, 511.
[5] D. Gong, C. A. Grimes, O. K. Varghese, W. Hu, R. S. Singh, Z. Chen, E. C. Dickey, *J. Mater. Res*. **2001**, *16*, 3331
[6] H. C. Shin, J. Dong and M. Liu, *Adv. Mater*. **2004**, *16*, 237
[7] T. Aerts, T. Dimogerontakis, I. D. Graeve, J. Fransaer, H. Terryn, *Surf. Coat. Technol.* **2007**, *201*, 7310
[8] L. Young, *Anodic Oxide Films*, Academic Press, London, New York, **1961**, p.326.

ECS Transactions, 16 (3) 83-89 (2008)
10.1149/1.2982545 ©The Electrochemical Society

Silicon/Metal Hybrid Nanosystem with Tailored Magnetic Properties in Two Characteristic Field Regions

K. Rumpf[a], P. Granitzer[a,b], P. Poelt[b], H. Krenn[a]

[a] Institute of Physics, Karl Franzens University Graz, Universitaetsplatz 5, A-8010 Graz, Austria
[b] Institute for Electron Microscopy, University of Technology Graz, Steyrergasse 17, A8010 Graz, Austria

Electrodeposition of ferromagnetic metal-nanostructures into a porous silicon (PS) matrix merges the electronic properties of a semiconductor and the ferromagnetic ones of the precipitated metal on one material level. The deposition is performed in using a metal salt solution as electrolyte and an applied pulsed current under cathodic conditions. The metal precipitation within a PS-template exhibiting unconnected mesopores with aspect ratios of about 1000 leads to nanostructures with a maximum elongation of a few microns (aspect ratio 100). The achieved hybrid system exhibits magnetic characteristics which drastically differ from the corresponding bulk materials. Magnetization measurements of this hybrid material show two characteristic field regions, one at magnetic fields below the saturation magnetization M_S of the deposited metals due to the spin-magnetism (e.g. M_S (Ni) = 0.62 T, M_S (Co) = 1.82 T) and another one at higher fields above M_S which is assigned to a novel, recently intensively investigated magnetic contribution likely caused by spin-orbit interaction.

Introduction

Magnetic nanostructures play a decisive role in today's basic research and nanotechnological applications. The fabrication of low dimensional structures is often carried out by nanopatterning using lithographic methods. On the other hand self-assembling techniques are of great interest due to the uncomplex and low-cost fabrication process. Quite common are nanoparticles grown on a substrate by self-organization. Also 3-dimensional arrays of nanostructures (nanowires, nanotubes) have been formed without prestructuring in using hexagonal arranged porous alumina as matrices (1). Magnetic properties of metal filled membranes (e.g. porous alumina, polycarbonate) are also under extensive investigation (2). Moreover magnetization reversal processes with the concomitant domain wall motion within the deposited metal nanostructures, the interactions among them (3), but also transport phenomena (4) like magnetoresistance in spin valves (5) are common topics in literature.

The merge of both, the ferromagnetic properties of a metal and the electronic properties of a semiconductor within one material is a great effort of today's research. One way to reach this aim would be the doping of a semiconductor with transition metals. Whereas we are working on the fabrication of ferromagnetic nanostructures embedded in a silicon substrate and introduce in this work an emerging hybrid system offering ferromagnetic properties at room temperature. This semiconductor/metal nanocomposite brings nanomagnetism and electronic properties together on large area samples and can be fabricated as a 3-dimensional quasi-regular arrangement of the precipitated nanostructures.

Experiments

The semiconductor/metal composite material is fabricated in two steps. First a highly n-doped silicon wafer is anodized in a hydrofluoric acid solution resulting in a porous structure and second the achieved matrix is filled with a metal (Ni, Co, NiCo, Fe) during a cathodic deposition process. The self-assembled porous silicon matrix exhibits oriented pores, grown perpendicular to the (100) wafer surface which are clearly separated from each other. The pore-arrangement is quasi-regular offering a four-fold symmetry considering the top-view of the specimens (6). The dimensions of the structures are in the transition region between meso and macropores. The oriented pores offer an additional growth of small dendrites which could not be suppressed completely so far. The main pores have small side-pores with lengths typically smaller than the pore-diameter. But the pores are not connected to each other due to the constraint length of the occurring side-pores. Porous silicon templates with a typical average pore-diameter of 60 nm and a pore-distance of about 50 nm are used in the following for deposition of a ferromagnetic metal. Most experience has been gained so far with Ni, Co and NiCo (6, 7). For the precipitation of Ni-structures a $NiCl_2$- or Watts-electrolyte ($NiCl_2$ and $NiSO_4$ solution) is used, Co is deposited from a $CoSO_4$-electrolyte and the NiCo-alloy is gained from a composition of Watts and $CoSO_4$-solution in the ratio of 2:1. The deposition is carried out under cathodic conditions by pulsing the applied current. A modification of the pulse duration of the current results in metal precipitations with distinct elongation. Figure 1 shows the relation between the elongation of deposited Ni-nanostructures and the pulse duration of the applied current.

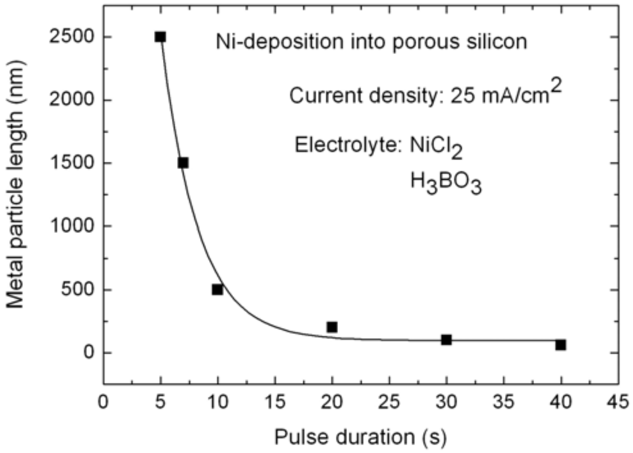

Figure 1: Relation between pulse duration of the deposition current and the resulting particle-length. A decrease of the pulse duration (40 s to 5 s) leads to an increase of the maximum length of the Ni-precipitations from ~ 50 nm up to 2.5 µm. For all specimens equivalent PS-matrices with an average pore-diameter of 50 nm ± 6 nm and a mean pore-distance of 45 nm ± 5 nm are used.

The geometry of the embedded metal nanostructures can be modified by altering the deposition conditions as current density, pulse duration of the applied current and electrolyte concentration. The shape varies between spheres, ellipsoides and wires. The maximum elongation of precipitated Ni-wires is a few microns reaching an aspect ratio up to 100. Figure 2 shows Ni-wires of about 1.5 µm in length embedded within a PS-matrix exhibiting an average pore-diameter of 50 nm.

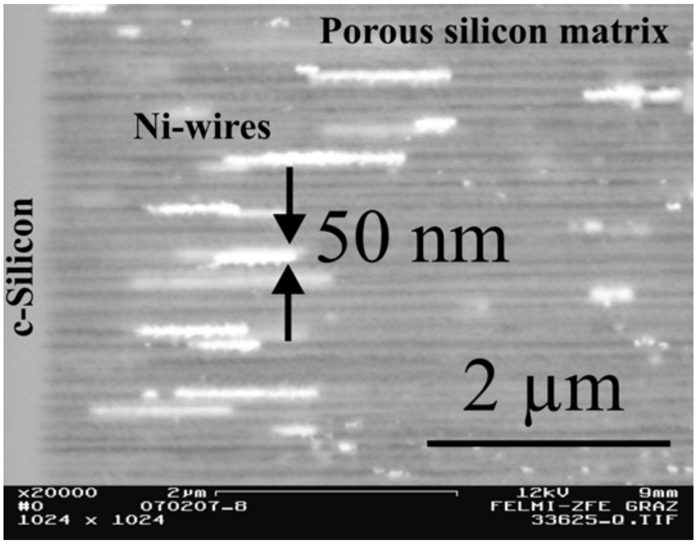

Figure 2: Typical self-organized porous silicon template exhibiting oriented pores grown perpendicular to the surface. The total length of the pores is about 35 µm and the precipitated Ni-wires show a length up to 1.5 µm and a diameter of about 50 nm, corresponding to the pore-diameter.

The electrochemical fabricated magnetic specimens are investigated by SQUID-magnetometry in a field range between ± 7 T and a temperature range varied from 4.2 K up to 310 K and a correlation between structural characteristics and magnetic properties is figured out.

Discussion

At low magnetic fields, smaller than the saturation magnetization (M_S) of the precipitated metal the magnetic behaviour is due to the spin-magnetism of the ferromagnetic precipitations and depends on the geometrical features of the deposited metal-structures as well as on the morphology of the silicon template. Thus the magnetic properties of the nanocomposite can be tailored by the process parameters of the template fabrication as well as the metal deposition. By modifying the deposition parameters the precipitations can be tuned in their shape (spheres, ellipsoids, wires) and in their spatial distribution within the PS-layer (near the surface, over the entire porous layer, near the pore-tips). Due to the correlation between process parameters and magnetic properties samples with desired coercivities, magnetic anisotropies and magnetic remanences can be fabricated. Figure 3 shows the hystereses loops of porous silicon samples of same morphology with embedded Ni-wires, reaching a length of a few microns and such with precipitated Ni-particles with a maximum elongation of a few hundred nanometers.

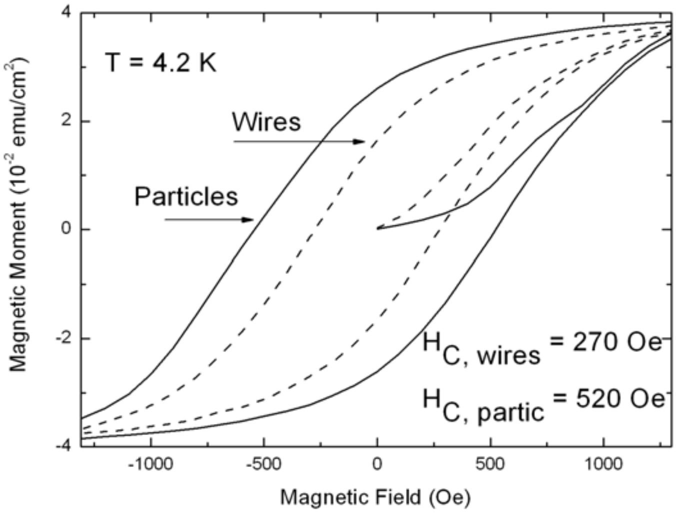

Figure 3: Magnetization curve of two porous silicon/Ni composite samples. The filling of one sample is dominated by Ni-wires (length of a few microns), whereas the other one contains mainly Ni-particles with a maximum elongation of a few hundred nanometers. The magnetic field is varied between ± 1500 Oe and is applied perpendicular to the sample surface which means parallel to the pores. It can be seen that the coercivity strongly depends on the geometry of the deposited metal-nanostructures.

Considering PS/Ni hybrid specimens with precipitated nanostructures of different shape the magnetic properties vary, especially in their coercivity. For PS-templates offering an equivalent morphology the coercivity H_C is always smaller if containing a high amount of embedded Ni-wires (aspect ratio > 10) than for those with preferentially deposited particles (elongation < 500 nm) caused by stronger demagnetizing effects of the needle-like structures which can be seen in equation 1.

$$H_C = \frac{2K}{\mu_0 M_S} + \left(N_\perp - N_{//}\right) M_S = H_{AN} + \left(N_\perp - N_{//}\right) M_S \qquad 1$$

Being:
K … anisotropy constant
M_S … saturation magnetization
$N_{//}$ … demagnetizing factor along z-direction
$N_\perp$ … demagnetizing factor along x,y-direction
H_{AN} … anisotropy field

The temperature dependence of the coercivity of two typical samples with incorporated wires and particles, respectively, is shown in figure 4.

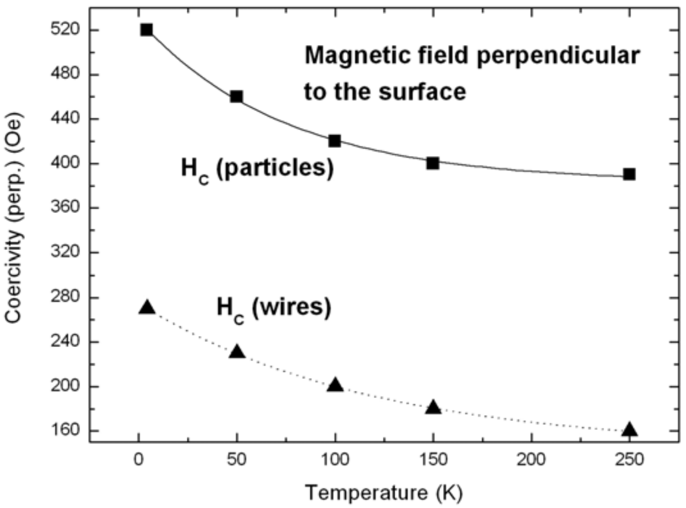

Figure 4: Coercivity in dependence on the temperature for two differently Ni-filled samples. One contains a high amount of precipitated Ni-wires (Fig 2), the other one contains mainly Ni-particles.

The magnetic anisotropy of the specimens is also strongly correlated with the shape of the metal precipitations within the pores. For external fields applied perpendicular to the surface (parallel to the pores) and parallel to the surface (perpendicular to the pores), respectively the coercivity varies about 50% in case of incorporated metal wires with an aspect ratio greater than 20, whereas samples with precipitated particles of an aspect ratio smaller than 10 show a difference of the coercivity of only 30% for the two magnetization directions.

At magnetic fields above the saturation magnetization of the deposited metal (measured for fields up to 7 T) a novel non-saturating term occurs (inset Fig. 5) which does not depend on the geometry of the deposited metal nanostructures but differs with the kind of used metal. This non-saturating term shows a temperature dependence. The magnetization measured at a certain field above M_S of the precipitated metal decreases with increasing temperature (measured between 4.2 K and 300 K) offering a paramagnetic behaviour which is verified by fitting the temperature dependent magnetization with the Curie-Weiss law.

In case of Ni this temperature dependent behaviour follows exactly the Curie-Weiss law (Fig. 5), whereas in case of Co precipitated within the PS-templates deviations between experiment and theoretical curve are observed.

At fields just below M_S where the contribution of the spin magnetism is not constant the magnetization behaviour is a mixing of both magnetic terms the ferromagnetic and paramagnetic one. Far below M_S the spin-magnetism overwhelms the paramagnetic contribution.

The non-saturating high-field term shows an enhancement with increasing magnetic field which is nearly linear, measured at temperatures above 80 K. The occurrence of this additional high-field contribution is not completely clarified yet but there are strong hints to be caused by orbital currents in the silicon skeleton (10).

A new kind of magnetism is also observed by some groups in usually diamagnetic systems as thiol capped gold-nanoparticles or thin gold layers (11) caused by a strong spin-orbit coupling due to a broken symmetry at the surface. An enhancement of the orbital moment and the magnetic anisotropy by a tetragonal distortion of the lattice of FeCo-alloy films is demonstrated by (12). Recently a unique kind of giant magnetic behaviour observed in organic monolayers is explained by bose condensation of the electrons into a single low angular momentum quantum state caused by triplet pairing (13). The occurring paramagnetism is explained by an internal angular momentum. Considering the PS/metal composite the occurrence of the non-saturating paramagnetic term can also be explained by an interface magnetism caused by triplet-pairing of carriers injected into the Si-skeleton. The resulting orbital moment leads to the paramagnetic behaviour of the specimens.

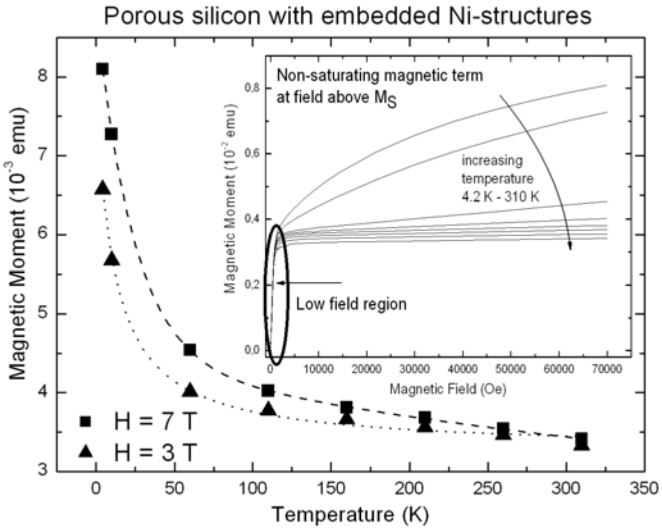

Figure 5: Temperature dependent magnetization measurements carried out at an applied magnetic field of H = 7 T and H = 3 T. The measured curves follow exactly the Curie Weiss law. Inset: Field dependent magnetization in a temperature range between T = 4.2 K and T = 310 K. The paramagnetic term decreases with increasing temperature.

Conclusion

The achieved ferromagnetic/paramagnetic composite material offers a broad range of characteristic features as a tunable ferromagnetic behaviour by electrochemical process parameters, a linearly decreasing paramagnetic term at high magnetic fields (> 2 T) as well as the merging of the electronic properties of a semiconductor and the magnetic ones of the deposited metal structures resulting in a hybrid system with distinct and specific properties. In the low field region where the ferromagnetic spin-magnetism is dominant the geometrical features and the spatial distribution of the precipitated metal-structures as well as the morphology of the PS-templates determine the magnetic characteristics of the nanocomposite. This enables low-cost fabrication of samples with tailored ferromagnetic properties compatible with today's microtechnology. At higher applied fields, far above the saturation magnetization of the deposited metal the fabricated hybrid systems show a non-saturating paramagnetic term which seems to be caused by a novel interface magnetism occurring from the orbital motion of the electrons leading to an enhanced non-saturating paramagnetic term. Due to this occurring linear high field behaviour the hybrid system is appropriate to be utilizable for magnetic high-field sensor applications.

Acknowledgments

The authors would like to thank Sanja Simic from the Institute of Electron Microscopy at the University of Technology Graz for her efforts in making scanning electron micrographs.

References

1. H. Masuda, H. Yamada, M. Satoh, H. Asoh, M. Nakao, T. Tamamura, Appl. Phys. Lett. **71**, 2770 (1997).
2. M. Vazquez, K. Pirota, J. Torrejon, D. Navas, M. Hernandez-Velez, J. Mag. Mag. Mat. **294**, 174 (2005).
3. L. Clime, P. Ciureanu, A. Yelon, J. Mag. Mag. Mat. **297**, 60 (2006).
4. F. Nasirpouri, P. Southern, M. Ghorbani, A. Irajizad, W. Schwarzacher, J. Mag. Mag. Mat. **308**, 35 (2007).
5. J. Nogues, J. Sort, V. Langlais, V. Skumryev, S. Surinach, J. S. Munoz, M. D. Baro, Physics Reports **422**, 65 (2005).
6. P. Granitzer, K. Rumpf, P. Pölt, S. Simic, H. Krenn, phys. Stat. Sol (a) **1-4** (2008).
7. K. Rumpf, P. Granitzer, P. Poelt, S. Simic, H. Krenn, phys. Stat.sol. (a), in press.
8. A. F. Gross, M. R. Diehl, K. C. Beverly,E. K. Richman, S. H. Tolbert, J. Phys. Chem. B **107**, 5475 (2003).
9. K. Rumpf, P. Granitzer, P. Pölt, S. Simic, H. Krenn, phys. stat. sol. (a) **1-4** (2008), DOI 10.1002/pssa 2007 78116.
10. S. D. Ganichev, E. L. Ivchenko, V. V. Belkov, S. A. Tarasenko, M. Solinger, D. Weiss, W. Wegscheider, W. Prettl, Nature **417**, 153 (2002).
11. A. Hernando, P. Crespo, M. A. Garcia, Phys. Rev. Lett. **96**, 057206 (2006).
12. F. Yildiz, F. Luo, C. Tieg, R. M. Abrudan, X. L. Fu, A. Winkelmann, M. Przybylski, J. Kirschner, Phys. Rev. Lett. **100**, 037205 (2007).
13. Z. Vager, R. Naaman, Phys. Rev. Lett. **92**, 087205 (2004).

ECS Transactions, 16 (3) 91-99 (2008)
10.1149/1.2982546 ©The Electrochemical Society

Porous silicon/Fe_3O_4-nanoparticle composite and its magnetic behaviour

P. Granitzer[a,c], K. Rumpf[a], A. G. Roca[b], M. P. Morales[b], P. Poelt[c]

[a] Institute of Physics, Karl Franzens University Graz, Universitaetsplatz 5, A-8010 Graz, Austria
[b] Instituto de Ciencia de Materiales de Madrid, CSIC, Sor Juana Ines de la Cruz 3, Cantoblanco, 28049 Madrid, Spain
[c] Institute for Electron Microscopy, University of Technology Graz, Steyrergasse 17, A8010 Graz, Austria

Porous silicon (PS) matrices with oriented pores grown perpendicular to the surface are used as template for the incorporation of magnetite nanoparticles. The Fe_3O_4-particles used for infiltration into the PS-template are coated with oleic acid in a hexane solution and exhibit an average diameter of 9 nm ±1 nm. The narrow size-distribution and the superparamagnetic behaviour at room temperatre are interesting features of these nanoparticles. Magnetite nanoparticles play a key role in medical applications but also the magnetic properties of such a nanoparticle/PS system are of technical interest due to the transition between superparamagnetic and ferromagnetic behaviour. Temperature dependent magnetization measurements are used to gain information about the magnetic interaction of the particles.

Introduction

The fabrication of low dimensional systems as ultrathin layers, nanowires, nanoparticles and nanodots is a key-trend in today's nanotechnology. Not only the change of the physical properties of low-dimensional materials compared to their bulk materials is of interest but also their applicability is a developing subject. Magnetic materials in the nanoscale range are utilized in magnetic data storage, GMR-devices but also in biological and medical applications magnetic particles are employed.

The fabrication of isolated magnetic nanoparticles is difficult to reach because the large surface areas oxidize easily when using metals and its tendency to agglomerate due to the magnetic interactions. A controlled passivation of the particles can be carried out but can also lead to interactions between the metal core and the passivating materials. Magnetic iron oxide such as magnetite has the advantage of being more stable. Recently, a new preparation method has been reported based on the decomposition at high temperature of an organic precursor in the presence of oleic acid, which leads to a monodisperse size-distribution of nanoparticles isolated by an oleic acid layer of around 2 nm (1-3).

The combination of nanostructured silicon and magnetite leads not only to interesting magnetic properties of the nanocomposite system but is also a good candidate for applications in biomedicine because both are biocompatible in biological systems due to their low toxicity and biodegradability (4, 5).

In the present work porous silicon fabricated in a selforganizing electrochemical procedure with dimensions in the mesoporous regime is used as matrix for very uniform Fe_3O_4-nanoparticles with an average size of 9 nm. Magnetic characterization of this composite material sheds light on the transition between ferromagnetic and superparamagnetic behaviour but also on the magnetic interaction between the particles.

Experiments

A porous silicon (PS) matrix, which acts as template for the impregnation of magnetite nanoparticles is fabricated by anodization in hydrofluoric acid solution (10 wt%) of a highly doped n-type silicon wafer (6). In applying a current density of 120 mA/cm^2 a porous structure with oriented pores grown perpendicular to the wafer surface is achieved. The average pore-diameter of these typical templates is 80 nm and the mean distance between the pores exhibits 40 nm (Figure 1). The thickness of the investigated PS-layer is about 40 µm. In this diameter range the growth of the main pores in (100)-direction is accompanied by the growth of additional side-pores in (111)-direction. The length of these dendrites can be minimized to a length in the range of the pore-diameter thus assuring the clear separation of the pores.

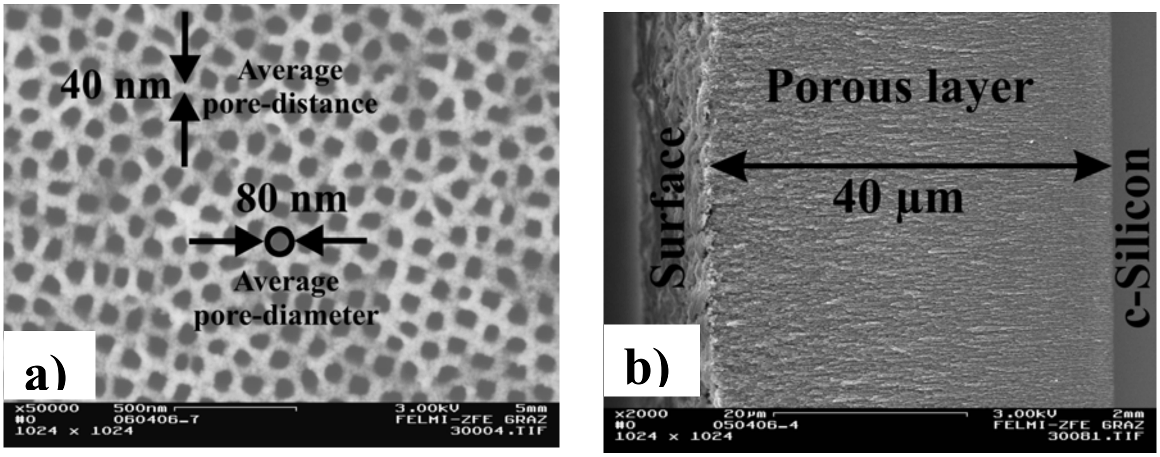

Figure 1: a) SEM-image of the top-view of a porous silicon matrix exhibiting an average pore-diameter of 80 nm and a mean pore-distance of 40 nm.
b) Cross-sectional micrograph showing the porous layer of about 40 µm with separated oriented pores.

Magnetite nanoparticles of an average size of 9 nm have been prepared by high temperature decomposition of iron organic precursors following previously reported works (2). Magnetite nanoparticles have been synthesized using iron acetylacetonate as precursor and phenyl ether as solvent. A mixture of 0.71 g of $Fe(acac)_3$ (2 mmol), 2.38 g of 1,2-hexadecanediol (10 mmol), 1.69 g of oleic acid (6 mmol), 1.60 g of oleylamine (6 mmol) and 20 ml of trioctylamine have been added to a three-neck flask. Then, the mixture reaction has been heated under mechanical stirring and a flow of nitrogen gas until a temperature of 200 ºC has been reached. This temperature has been kept constant for 120 min and then the solution has been heated to reflux (369 ºC) for 30 min in a nitrogen atmosphere. Finally, the solution has been cooled down to room temperature.

The powder was obtained by precipitation with ethanol, collected with a magnet and finally dried under nitrogen flow. A stable suspension of the powder could be obtained when nanoparticles have been mixed with 20 ml of hexane and 0.05 ml of oleic acid and sonicated for a time period of 5 minutes. The achieved particles show a quite monodisperse size-distribution (Figure 2b) of 9 nm obtained from TEM-images (Figure 2a) with a deviation of ± 1 nm.

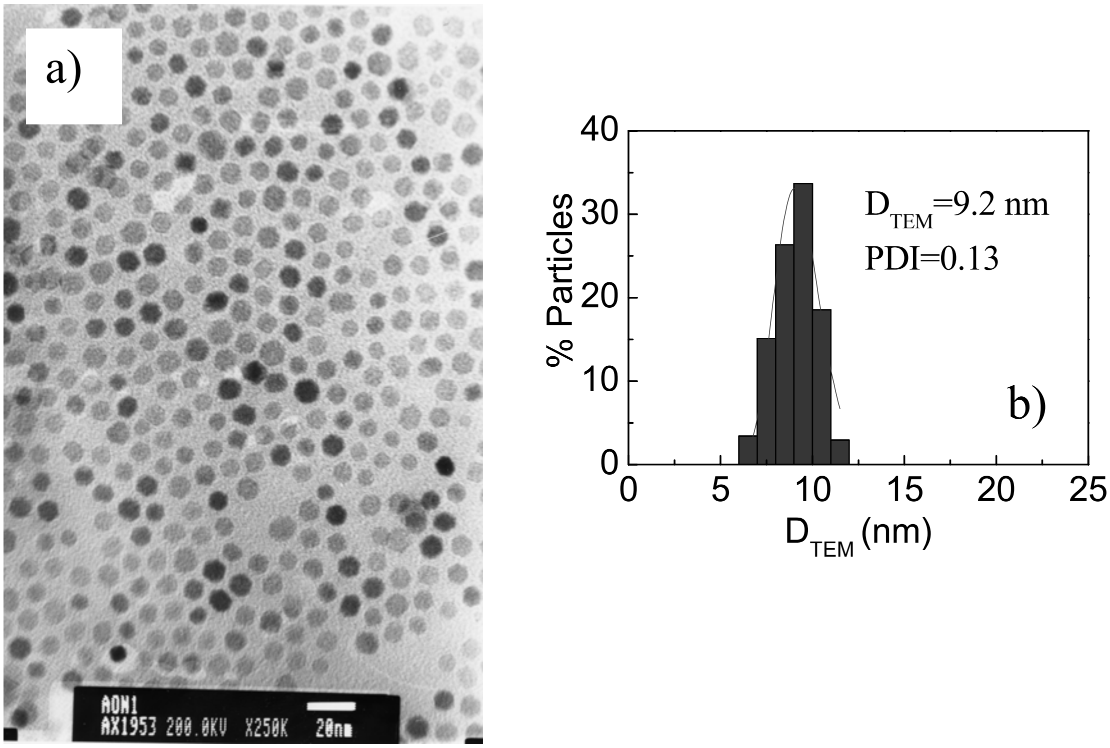

Figure 2: a) TEM-image of magnetite nanoparticles used for the infiltration into a porous silicon matrix which is shown in figure 1.
b) Histogram of the investigated Fe_3O_4 particles showing an average diameter of 9.2 nm with a deviation of ± 1 nm and a low polydispersity index of 0.13.

The suspension of magnetite nanoparticles in hexane solution has been infiltrated into the mesoporous silicon matrix. This immersion has been carried out under defined conditions (e.g. concentration, temperature). FTIR-spectroscopy has been performed to figure out the additional contribution of oleic acid and Fe-O to the absorption bands of porous silicon.

Magnetization measurements of magnetite nanoparticles in powder form and after infiltration within porous silicon have been performed by SQUID-magnetometry. The magnetic field has been applied between ± 1 T in two directions of magnetization, perpendicular and parallel to the sample surface, respectively and the temperature has been varied from 4.2 K up to room temperature. Zero field cooled (ZFC)/field cooled (FC) curves were registered at an applied field of 5 Oe.

Discussion and results

The Fe_3O_4-particles used for infiltration into the PS-template coated with oleic acid in a hexane solution exhibit an average diameter of 9 nm and only a distance of a few nanometers (~3 nm) between them (Fig. 2). The narrow size-distribution and the superparamagnetic behaviour at room temperature are interesting features of these nanoparticles.

A comparison of a porous silicon template and a PS/Fe_3O_4-sample has been figured out by FTIR-spectroscopy (figure 3). Additional to the Si-H stretching modes of the porous silicon, occurring in both samples, C-O stretching modes have been identified at 1530 cm^{-1} and 1625 cm^{-1} which is in agreement with IR-investigations of magnetite nanoparticles (7). The Fe-O modes at 430 cm^{-1} and 610 cm^{-1} could not be found because of the absorption edge of the silicon substrate at 1200 cm^{-1}. Additional peaks around 2260 cm^{-1} indicate oxidation of the PS-matrix (H-Si(O_3)-modes).

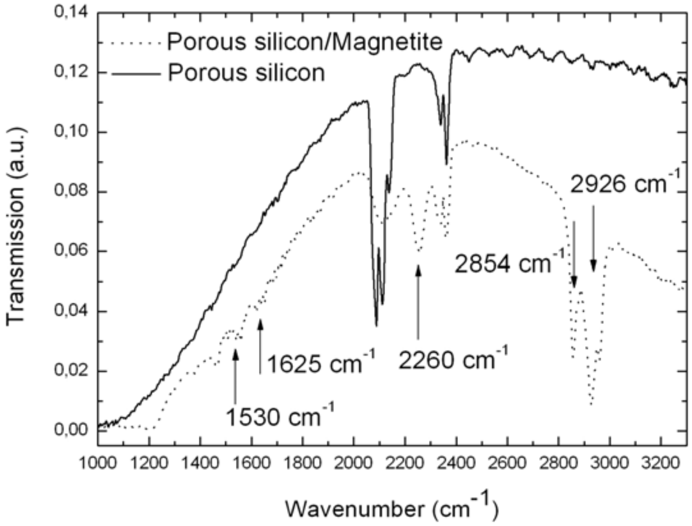

Figure 3: FTIR-spectroscopy performed on a bare porous silicon sample in comparison with a PS/magnetite specimen exhibiting additional absorption bands at 1625 cm^{-1} and 1530 cm^{-1} due to C-O stretching modes. At wavenumbers of 2854 cm^{-1} CH_2 modes appear and at 2926 cm^{-1} modifications of SiO_x-modes are observed. The Si-H stretching modes around 2100 cm^{-1} decrease and additional peaks around 2260 cm^{-1} occur which are due to the oxidation of the PS-matrix (H-Si(O_3)-modes).

The achieved magnetic system with porous silicon acting as substrate and infiltrated magnetite nanoparticles leading to a composite material shows a ferromagnetic behaviour at low temperatures ($T < T_B$) and superparamagnetism at higher temperatures ($T > T_B$). This transition temperature can be influenced by the particle size but also by the distance between the particles.

The superparamagnetic behaviour of the magnetite/porous silicon system above a blocking temperature T_B is shown by temperature dependent magnetization measurements. Zero field cooled (ZFC)/field cooled (FC) investigations performed at an applied field of 5 Oe show a rather high blocking temperature T_B at 135 K which indicates magnetic interactions between the particles (Figure 4). Furthermore a shift of the blocking temperature to lower temperatures with higher applied fields is observed (inset Fig. 4). This behaviour of superparamagnetic particles is known to be proportional to $H^{2/3}$ at high fields and proportional to H^2 for lower fields (8). The blocking temperatures determined for different applied magnetic fields are summarized in table 1.

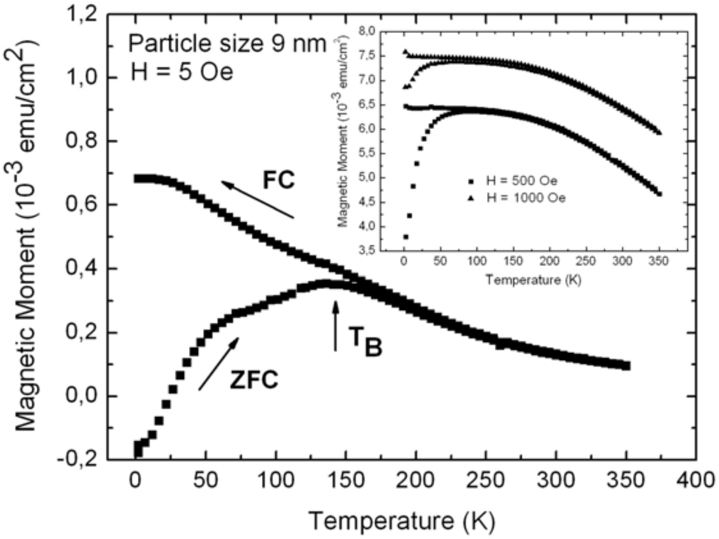

Figure 4: ZFC/FC measurements carried out at an applied magnetic field of 5 Oe and in a temperature range between 4.2 K and 360 K. The blocking temperature (maximum peak of the ZFC-branch) at 135 K indicates dipolar coupling between the particles.
Inset: Shift of T_B towards lower temperatures with increasing applied magnetic field.

Table 1: Blocking temperatures for magnetic fields between 5 Oe and 1000 Oe.

H [Oe]	5	500	1000
T_B [K]	135	75	55

Considering the ZFC/FC measurements one recognizes that the splitting temperature between the ZFC and the FC-branch differs from the blocking temperature which coincides with the maximum of the ZFC-curve. Such a behavior is observed in randomly dipolar coupled nanomagnet-systems. Also the width of the peak of the ZFC-branch can be attributed to dipolar coupling of the nanoparticles since the distribution of the particle-size is quite monodisperse proofed by TEM-images.
Using the thermal energy

$$25k_BT_B = KV\left(1 - \frac{\mu_0 M_S H_C}{2K}\right)^2 \qquad [1]$$

with
K … anisotropy constant
V… volume of the particle
M_S … saturation magnetization
H_C … coercive field
the critical diameter D_B for blocking at the threshold field H_C can be derivated as

$$D_B = \left(\frac{25 k_B T_B}{\alpha K} \right)^{1/3} \qquad [2]$$

α … shape factor (= 0.5236 for a sphere).
This leads to estimated values of D_B to be 20 nm which is far away from the diameter of the incorporated magnetite nanoparticles exhibiting an average size of 9 nm. Consequently it can be said that the particles of the investigated samples are superparamagnetic above a quite high blocking temperature of 135 K due to the presence of dipolar interactions.

Considering the magnetization curve of magnetite nanoparticles (size 9 nm) without PS-matrix one sees that the blocking temperature is 160 K and the bifurcation of the ZFC and FC branches takes place at 230 K (Figure 5).

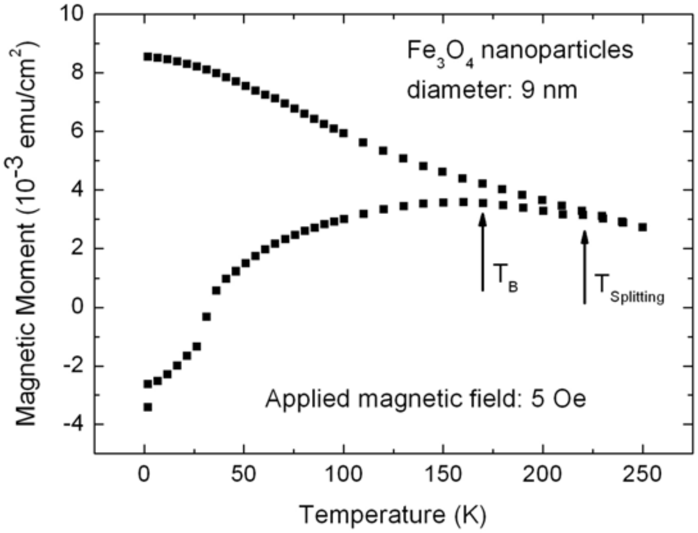

Figure 5: Temperature dependent magnetization measurements of Fe_3O_4-nanoparticles exhibiting a blocking temperature at 160 K and a bifurcation of the two branches (ZFC/FC) at 230 K.

These temperatures are higher than in case of magnetite nanoparticles embedded in PS. Given that in both cases the same particles are used, a reduction in the magnetic interaction seems to take place when the magnetite nanoparticles are incorporated within the PS-matrix, which could be caused by the morphology of the PS, exhibiting a pore-distance of about 60 nm. Thus the Fe_3O_4-nanoparticles can only interact in one direction, along the pores. Moreover, due to the presence of oleic acid coating of the particles, exchange interaction is discarded and the interaction is mainly dipolar.

It should be noted that an additional peak is observed in the ZFC curve for magnetite nanoparticles as synthesized and dispersed in the silicon matrix below 50 K which could be assigned to the Verwey transition (9).

Hystereses loops of a bare silicon wafer offering a surface covered with a suspension of Fe_3O_4-nanoparticles and a porous silicon matrix with magnetite-nanoparticles impregnated into the PS-layer are measured at T = 4.2 K. The magnetic field is applied perpendicular and parallel to the sample surface, respectively. The silicon wafer having the surface covered with the magnetite-solution shows a magnetic anisotropy between the two magnetization directions (figure 6) which is alike the behaviour of a magnetic thin film due to the dipolar coupling of the nanoparticles.

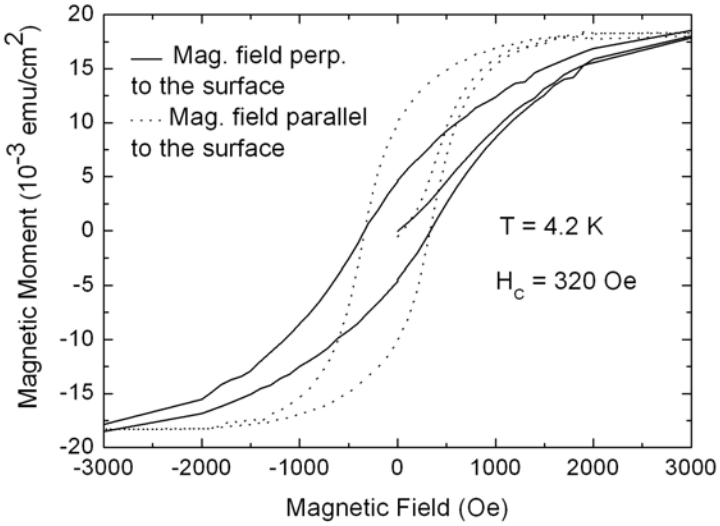

Figure 6: Magnetization measurements performed with the magnetic field applied perpendicular to the surface (full line) and parallel to the surface (dotted line), respectively. The obtained anisotropy is alike to the one of a magnetic film affirming that the Fe_3O_4-particles which form a thin layer interact dipolar.

Considering the hystereses loops of a porous silicon specimen infiltrated with the same magnetite-solution the magnetic anisotropy between the two magnetization directions is weak (figure 7) but it differs drastically from the magnetization curve of the surface covered bare silicon wafer. The coercivities obtained for the two different magnetization directions vary a little which shows that the particles are mainly incorporated within the pores and they do not accumulate on the surface of the PS-template.

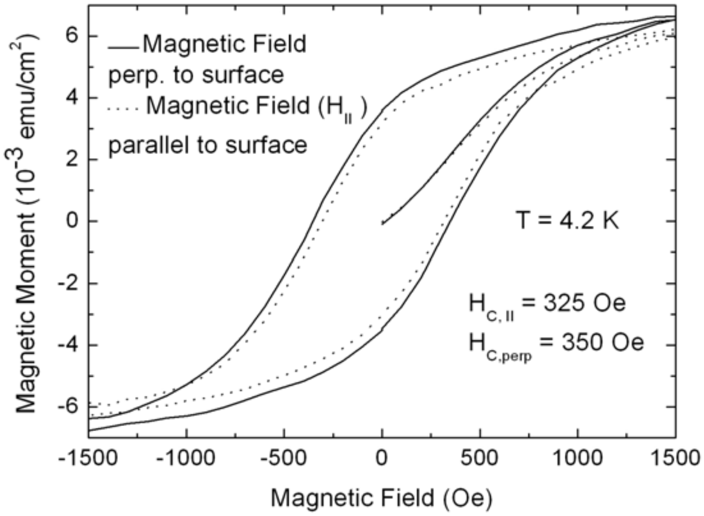

Figure 7: Hystereses loops of a PS-matrix impregnated with a magnetite-solution. The measurements have been carried out for two directions of magnetization, perpendicular (full line) and parallel (dotted line) to the sample surface. The small anisotropy is mainly caused by the morphology of the used PS-template leading to predetermined coupling of particles situated along one pore.

Magnetite is nowadays investigated because of its promising applications in nanomedicine for the location and diagnosis of tumors. Due to the biodegradability and biocompatibility of porous silicon (5) a combination of these two materials could be a promising candidate for medical in vivo applications. The magnetic properties of the nanoparticle/PS system are of interest due to the magnetic phase transition controlled by the strength of the magnetic interaction, which is determined by the distance between the particles and the direction, given by the matrix. Strongly interacting particles could lead to a blocking even at room temperature.

Conclusion

The immersed magnetite nanoparticles into the PS-matrix are superparamagnetic at room temperature and dipolar interactions are present. This behaviour explains the high blocking temperature obtained from ZFC/FC-measurements. Due to the infiltration of the particles into the pores of a porous silicon layer the interaction can only take place in one direction, reduced along the pores with respect to pure nanoparticles or a thin layer of particles formed on a wafer-surface. An influence of the PS-template can also be found in direction dependent magnetization measurements resulting in a magnetic anisotropy. The obtained composite material consisting of a PS-matrix and infiltrated Fe_3O_4-nanoparticles is an interesting system in nanotechnology applications due to the magnetic switching behaviour due to the transition between superparamagnetic and ferromagnetic behaviour which can be adjusted by modifying the distance between the particles. Moreover, the silicon substrate material is compatible with today's microtechnology. PS/magnetite systems could also be interesting for medical applications because of the low toxicity of both materials.

Acknowledgments

The authors would like to thank Sanja Simic from the Institute of Electron Microscopy at the University of Technology Graz for her efforts in making scanning electron micrographs. M.P. Morales and A.G. Roca work was supported by the Ministerio de Ciencia e Innovacion through NAN2004-08805-C04-01 project.

References

1. T. Hyeon, S. S. Lee, J. Park, Y. Chang, H. B. Na, J. Am. Chem. Soc. **123**, 12798 (2001).
2. S. Sun, H. Zeng, J. Am. Chem. Soc. **124**, 8204 (2002).
3. W. W. Yu, J. C. Falkner, C. T. Yavuz, V. L. Colvin, Chem. Commun. **20**, 2306 (2004).
4. M. P. Pileni, N. Feltin, N. Moumen, Nanosized ferrite particles – preparation characterization and magnetic properties, in: Scientific and clinical applications of magnetic carriers, Ed. U. Häfeli, W. Schütt, J. Teller, M. Zborowski, Plenum Press, NY, London 1997.
5. L. T. Canham, Biomedical applications of porous silicon, in: Properties of porous silicon, Ed. L. T. Canham, IEE Press London, 1997.

6. P. Granitzer, K. Rumpf, P. Poelt, A. Reichmann, H. Krenn, Physica E **38**, 205 (2007).
7. A. G. Roca, M. P. Morales, K. O'Grady, C. J. Serna, Nanotechnology **17**, 2783 (2006).
8. G. F. Goya, M.P. Morales, J. Metastable and Nanocrystalline Materials **20-21**, 673 (2004).
9. G. F. Goya, T. S. Berquo, F. C. Fonseca, M. P. Morales, J. Appl. Phys., Vol. **94**, 3520 (2003).

ECS Transactions, 16 (3) 101-106 (2008)
10.1149/1.2982547 ©The Electrochemical Society

Novel morphology dependent ferromagnetic behaviour of mesoporous silicon

P. Granitzer[a,b], K. Rumpf[a], P. Poelt[b]

[a] Institute of Physics, Karl Franzens University Graz, Universitaetsplatz 5, 8010 Graz, Austria
[b] Institute for Electron Microscopy, University of Technology Graz, Steyrergasse 17, 8010 Graz, Austria

Nanostructuring of a silicon wafer by etching in an HF-solution leads to a porous semiconductor which offers physical properties (e.g. optical, magnetic) drastically different from the ones of the according bulk material. A change of the magnetic behaviour from diamagnetic in case of bulk silicon to ferromagnetic has been observed in mesoporous samples. This ferromagnetism depends on the morphology (porosity) of the investigated samples, which can be modified by the electrochemical process parameters and/or the doping level of the used Si-substrate. The occurrence of this novel ferromagnetic behaviour is not completely clarified yet but has to be caused by surface-effects resulting in a new kind of interface-magnetism.

Introduction

In recent years nanostructuring of materials has become an important role in the research of many fields in physics, chemistry, biology and medicine. On the one hand due to the drastic change of the physical properties of the nanostructured material compared to their bulk behaviour and on the other hand following the demand of miniaturization in today's technology nanoscale materials are a developing topic. The nanostructuring of silicon by employing an electrochemical etching process leads to porous structures which are under intense investigation since the early '90s. Many investigations have been done to gain information about the mechanisms taking place in the porous material but also applications have been discussed (photoluminescence, waveguiding of multilayered PS-structures, optical detection of biomolecules, gas sensing and many more).

One way to achieve a nanostructured semiconductor which exhibits completely different properties compared to the bulk material is the anodization of a silicon wafer in hydrofluoric acid solution. For example microporous silicon offers light emitting properties in the visible which first has been discovered in 1990 by L. Canham. Furthermore porous silicon has to be found biodegradable and biocompatible (1, 2) which renders this versatile material a promising candidate for applications in medical and pharmaceutical nanotechnology.

The opportunity to manipulate the spin of electrons by an electric field would give rise to new applications in microtechnology and thus this quite new topic of so-called spintronic is under great investigation. Silicon as base material is a precondition to be integrable in today's process-technology. A further condition is the successful operation at room temperature, which is not reached yet in case of diluted magnetic semiconductors.

The investigated porous silicon shows an interesting magnetic behaviour which depends on the morphology of the template and even is present at room temperature which opens the opportunity of new applications.

Experiments

Porous silicon (PS) has been fabricated by anodization of an n^+-silicon wafer in hydrofluoric acid solution. Distinct morphologies with porosities between 20% and 80 % are achieved by varying the anodization current density between 50 mA/cm^2 and 125 mA/cm^2, whereas the electrolyte concentration has been the same (3). All of the samples offer oriented pores, grown perpendicular to the wafer surface with diameters between 25 nm up to 95 nm depending on the current density. The porosities have been estimated by image processing of top view images of scanning electron micrographs.

Magnetization measurements of the porous silicon samples have been performed by SQUID-magnetometry with an applied magnetic field varied between ±1 T and the temperature adjusted to 4.2 K, 100 K and 250 K, respectively. The investigated specimens have been mounted within the magnetometer with the applied magnetic field parallel to the pores of the PS-template (perpendicular to the sample surface). The modification of the PS-morphology has been achieved only by tuning the current density in utilizing the same electrolyte and the same wafer-substrate.

Discussion

The interface between Si/SiO_2 has been investigated by many authors according to the dangling bond of the silicon atom, the P_b-center which is the dominant paramagnetic defect in porous silicon (4). EPR-studies give information about these defects from analysis of g-tensors (5) and hyperfine data (6). In the case of the observed ferromagnetic behaviour the interface between Si/SiO_x is proposed to play a dominant role too, because the ferromagnetism is clearly present in investigating aged porous silicon samples whereas as-etched samples with a hydrogen terminated surface show a diamagnetic behaviour.

The magnetic behaviour of nanostructured n^+-silicon wafers with dimensions between 25 nm and 95 nm has been measured in a temperature range between 4.2 K and 250 K. The magnetism changes from a diamagnetic, in case of bulk silicon to a ferromagnetic behaviour simply by anodization of the substrate and subsequent aging in air.

Dependence of the magnetization on the morphology

The characteristics of the novel ferromagnetic behaviour (coercivity, remanence, saturation magnetization) have been observed to be dependent on the morphology of the PS-layer which can be tuned by the electrochemical process parameters and the doping density of the silicon substrate. Figure 1 shows the investigated morphologies of cross-sectional SEM-micrographs. In a temperature range from 4.2 K up to room temperature the ferromagnetic signal is not quenched as illustrated in figure 2b. The coercivity decreases with increasing temperature from $H_{C,\,4.2K} = 360$ Oe to $H_{C,\,250K} = 200$ Oe. The saturation magnetization decreases from $M_{S,\,4.2K} = 2.45 \cdot 10^{-4}$ emu/cm^2 to $M_{S,\,250K} = 1.95 \cdot 10^{-4}$ emu/cm^2, resulting in a squareness M_R/M_S (remanence/saturation magnetization) at T = 4.2 K of 0.09 and at T = 250 K of 0.08. In all magnetization curves the diamagnetic contribution of the substrate has to be taken into account.

Figure 1. Scanning electron images of the cross-section of porous silicon samples exhibiting different porosities varying between ~ 20% and ~ 80%.

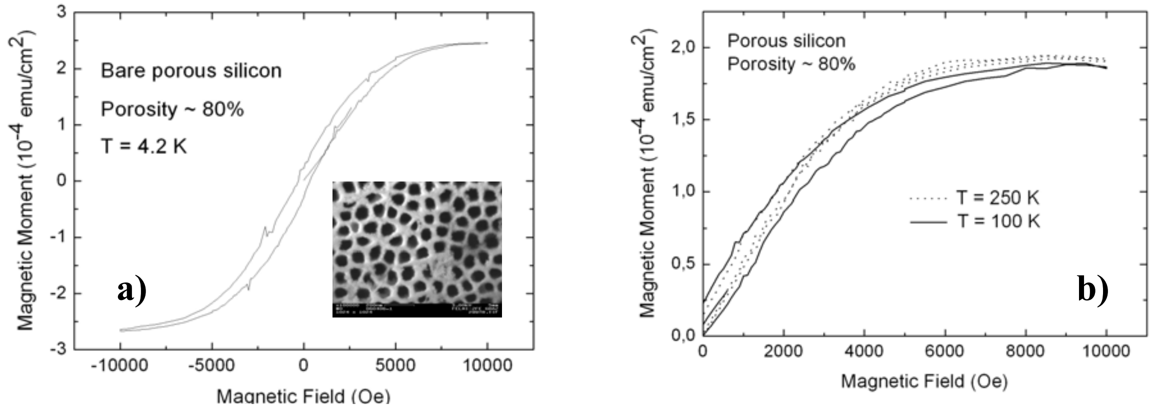

Figure 2. a) Hystereses loop of a porous silicon sample exhibiting an estimated porosity of 80% - 85% (average pore-diameter: 95 nm, average pore-distance: 45 nm). The coercivity $H_C = 360$ Oe and the magnetic remanence $M_R = 0.071 \cdot 10^{-5}$ emu.

b) Magnetization measured at T = 100 K (full line) and T = 250 K (dotted line), respectively.

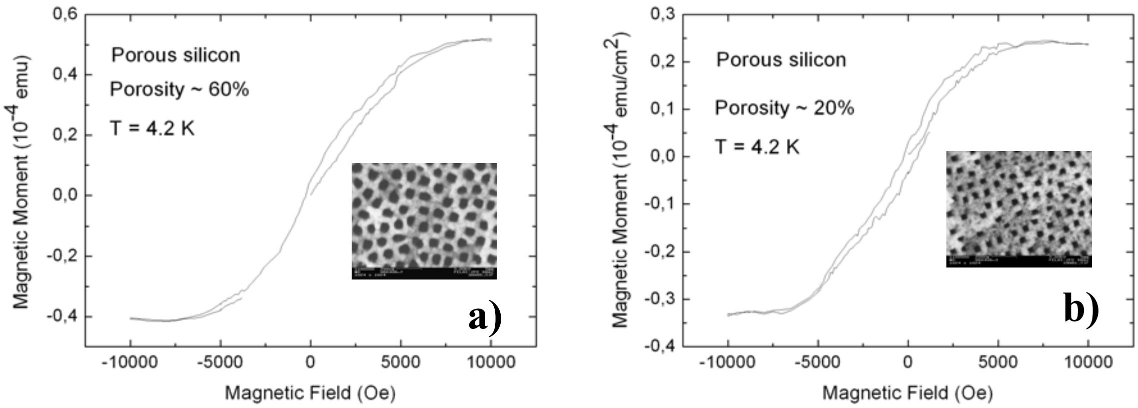

Figure 3. Magnetization curves of porous silicon samples with different porosities: a) p ~ 55% - 60%: pore-diameter ~ 60 nm, pore-distance ~ 40 nm and b) p ~ 20% - 25%: pore-diameter ~ 45 nm, pore-distance ~ 50 nm.

Previously released works also deal with the observation of a magnetic behaviour of porous silicon. The investigated porous silicon samples in these works have been of different morphologies and also the post-treatment has been of distinct manner to achieve the peculiar magnetic property of a nanostructured silicon wafer.

A magnetic behaviour of luminescent porous silicon has been reported by Laiho et al. (7). In this case the observed ferromagnetism has been attributed to the low dimensions of the material which exhibits dimensions in a similar range than the magnetic exchange interaction leading to ordering effects. For comparison the exchange length l_{ex} ($l_{ex} = \sqrt{\frac{2A}{\mu_0 M_S^2}}$, with A … exchange constant, M_S … saturation magnetization) of ferromagnetic metals as Fe, Co and Ni are between 3 nm and 10 nm.

Recently a magnetic behaviour observed on porous silicon samples which have been etched in an HF-solution and additionally treated with KOH has been attributed to an interface magnetism (8) which has also been observed on other diamagnetic materials as thin gold layers or thiol capped gold nanoparticles (9). A magnetic moment of the samples could not be observed by etching the silicon wafer in an HF or KOH solution only.

Another ferromagnetic behaviour has been reported using Si-ion and Ar-ion implantation into silicon as well as by neutron irradiation (10) and is explained by the unpaired spins of the dangling bonds which interact and offer the ferromagnetic contribution.

The ferromagnetic behaviour observed in the investigated mesoporous silicon samples shows a decreasing saturation magnetization with decreasing porosity, whereas very low porosities show only the diamagnetic contribution (M_{dia}(PS) = $1.35 \cdot 10^{-8}$ emu/cm^2). The ferromagnetic behaviour has been observed in a broad temperature range between 4.2 K and room temperature.

Considering the susceptibility of the investigated porous silicon sample which exhibits a porosity of about 80% one recognizes the clear ferromagnetic behaviour (figure 4).

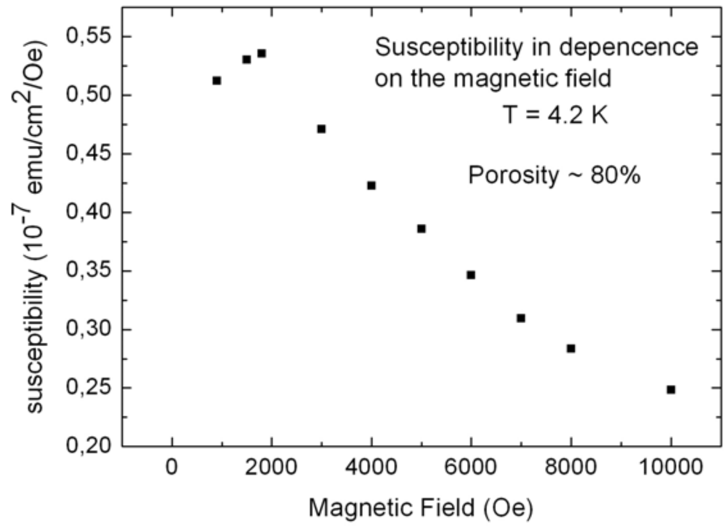

Figure 4: Magnetic field dependence of the susceptibility of a porous silicon specimen with an average porosity of 80%. The ferromagnetic behaviour can clearly be seen.

Due to the fact that the magnetization at a certain field and the saturation magnetization, respectively, decrease with lower surface-area this particular behaviour has to be caused by surface-effects. The investigated specimens are aged in ambient air and therefore covered by a native oxide-layer. As-etched porous silicon samples offering an equal morphology exhibit a hydrogen terminated surface and show a diamagnetic magnetization signal. A charge transfer between silicon and oxide-layer resulting in a novel kind of interface magnetism can be assumed to explain this ferromagnetic behaviour of nanostructured silicon. This phenomenon can not only be explained by spin-magnetism but also the orbital motion of the electrons has to be taken into account which leads to an enhancement of the orbital magnetic moment. Spin-orbit interaction due to a symmetry-breaking interface potential (9) can be assumed to be the driving force of this novel mechanism.

Conclusion

Porous silicon which is a versatile material utilizable in many fields of research as well as in many applications could become an encouraging nanomaterial with a magnetic future. The possibility to fabricate magnetic silicon simply by nanostructuring of a wafer in a common etching procedure opens great opportunities to use this novel magnetic behaviour for technological applications and it could play a role in the developing field of the so-called spintronic. The occurring magnetism observed in a temperature range between 4.2 K and room temperature is independent on the temperature. It strongly depends on the morphology as well as on the post-treatment after the fabrication process. Only specimens exhibiting an oxide layer caused by an aging effect show a ferromagnetic behaviour, whereas hydrogen terminated surfaces offer a diamagnetism comparable to the one of bulk-silicon. The appearance of the magnetism at room temperature is one important precondition to render the fabricated porous silicon as an interesting candidate for technological utilization.

Acknowledgments

The authors would like to thank Sanja Simic from the Institute of Electron Microscopy at the University of Technology Graz for her efforts in making scanning electron micrographs.

References

1. L. T. Canham, Applied Physic Letters, 57, 1046 (1990).
2. L. T. Canham, Advanced Materials, 7, 1033 (1995).
3. P. Granitzer, K. Rumpf, P. Pölt, A. Reichmann, H. Krenn, Physica E 38, 205 (2007).
4. J. L. Cantin, M. Schoisswohl, H.-J. von Bardeleben, chapter 14 in: Structural and optical properties of porous silicon nanostructures, edited by G. Amato, C. Delerue, H.-J. von Bardeleben, Gordon and Breach Science Publishers (1997).

5. J. L. Cantin, M. Schoisswohl, H.-J. von Bardeleben, N. Hadj Zoubir, M. Vergnat, Phys. Rev. B 52, R11599 (1995).
6. H.-J. von Bardeleben,J. L. Cantin, L. Ke, Y. Shishkin, R. P. Devaty, , W. J. Choyke, Materials Science Forum 483-485, 273 (2005).
7. R. Laiho, E. Lähderanta, L. Vlasenko, M. Vlasenko, M. Afanasiev, J. Luminescence 57, 197 (1993).
8. G. Kopnov, Z. Vager, R. Naaman, Adv. Mater. 19, 925 (2007).
9. Z. Vager, R. Naaman, Phys. Rev. Lett. 92, 087205, (2004).
10. T. Dubroca, J. Hack, R. E. Hummel, Appl. Phys. Lett. 88, 182504 (2006).

CHAPTER 3

TUESDAY: MORNING SESSION

ECS Transactions, 16 (3) 109-123 (2008)
10.1149/1.2982548 ©The Electrochemical Society

Etching Deep Macropores in n-Type Silicon in Short Times

E. K. Ossei-Wusu[a], A. Cojocaru[a], J. Carstensen[a], M. Leisner[a], and H. Föll[a]

[a] Institute for Materials Science, Christian-Albrechts-University of Kiel
Kaiserstrasse 2, 24143 Kiel, Germany

Etching deep macropores into n-type Si was limited for more than 15 years to maximal depth around 500 µm at processing times > 10 hrs, severely impeding the commercialization of many applications. It will be shown that substantial progress with respect to depth and speed is possible without losing pore quality if newly designed electrolytes are used in conjunction with in-situ data acquisition and analysis. Some new phenomena are encountered in some regions of the now vastly increased parameter space that will be briefly discussed.

Introduction

The discovery of an electrochemical process for etching deep macropores into n-type Si via back side illumination by Lehmann and Foell in 1990 (1) was already accompanied by proposals for possible uses and first patent applications. Since then many possible applications of these (and other) macropores in Si have been proposed and many R&D projects aiming at commercial products have been started (see e.g. (2) and references therein and (3)) Some progress was made towards the development of production technologies, e.g. uniform etching of large wafers (4); recent developments may even allow some degree of automation in the near future by implementing feed-back loops in an etching system (5). However, despite much progress, 18 years after the first macropores there is still no commercial product on the market that utilizes macropores in Si.

One reason for this deplorable fact is that the wafer processing time is too large. Etching n-macro(aqu, bsi) (aqu = aqueous electrolyte, bsi = back side illumination) pores to a (maximum) depth of 500 µm takes with the present state-of-the art process more than 10 hrs, and a depth of 300 µm require at least 4 hrs. Applications like, e.g., microelectrodes for fuel cells (6, 7), heat pipes for chip cooling (8) or optical filters of all kinds (9) require mass production. The etching of 100 000 wafers per year at processing times of 10 hrs per wafer would thus requires more than 100 etching stations running day and night. While this is not impossible in economic terms, it would be clearly very desirable to reduce the processing time without sacrificing pore "quality".

In principle, it is clear what needs to be done to increase the etching speed. According to the "Lehmann model" (10, 11), the ratio j / j_{PSL}, with j = current density flowing through the pore tips and j_{PSL} = first current peak in the current-voltage characteristics, is the decisive factor controlling the pore geometry. The dissolution rate is proportional to the current; higher growth rates of pores thus call for higher currents and concomitantly higher j_{PSL} values. Increasing j_{PSL} means increasing c_{HF}, the HF concentration of the electrolyte. The pore etching community, however, is fully aware of the experimentally established fact that at c_{HF} > 5 wt.% (always weight %) all kinds of problems start to emerge. Many attempts have been made to overcome the limitation to processing times inherent to this finding, and **Fig. 1** gives a good idea from our own efforts that are representative for the state-of-the-art. Note that these curves are the best that can be achieved after much optimizing of all parameters like, e.g., electrolyte flow conditions, addition of tensides, carefully adjusted voltage over time and so on. Curve "D" shows the effect of cooling down during etching – it is the best that can be achieved. There is some small progress compared to curve "B" obtained at constant temperature but defined cooling requires some non-trivial hardware developments if it is to be used for large area etching. **Fig. 1** and **Fig. 2** show the general trend quite clearly: Increasing the HF concentration leads to concomitant increases in the initial etching rates, but to an earlier termination of the etching process (usually by cavity formation). The reasons for this behavior are understood in principle (cf. V. Lehmann's book (4)) and are related to the continuous change of all parameters at the pore tip like the potential or the concentration of the HF, and the increasing "leakage" current, i.e. dark current flowing through the pore walls. These effects are routinely countered to some extent by running a suitable $j(t)$ and possible voltage $U(t)$ and temperature $T(t)$ profile. However, there is no particularly good reason why these measures work reasonably well at $c_{\mathrm{HF}} \approx 5$ wt.% but not at $c_{\mathrm{HF}} = 10$ wt.% or larger.

As will be shown here, the decisive process for obtaining higher growth rates may be summarized by the catchword "pore wall passivation", but there are still many open questions to be solved.

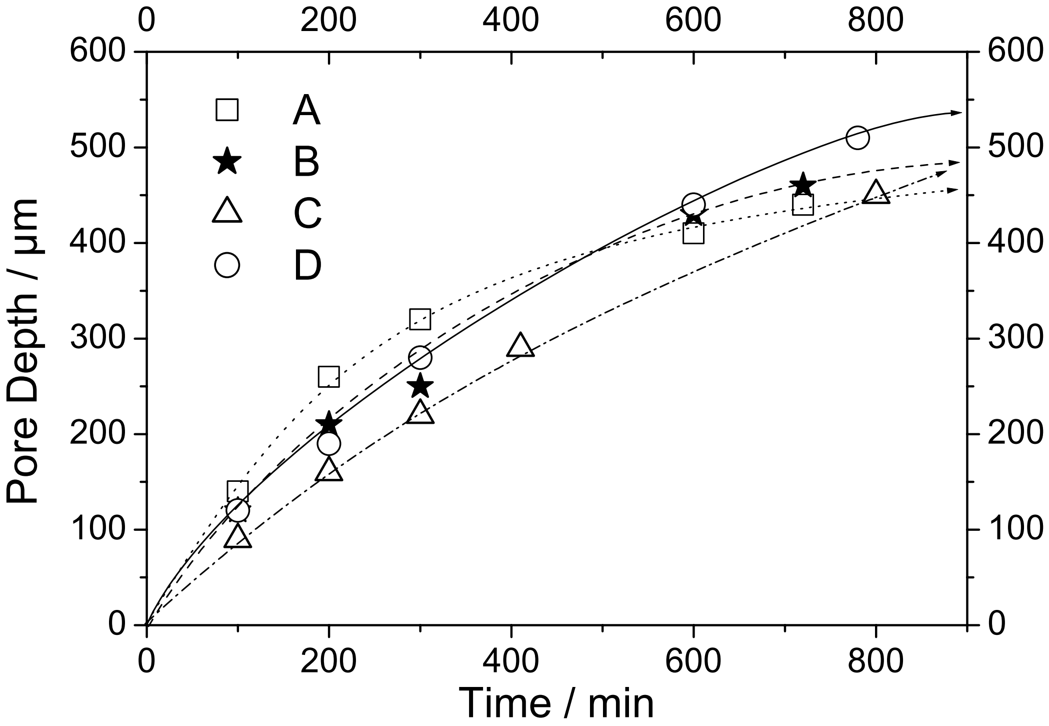

Figure 1 Optimized $d_{\mathrm{pore}}(t)$ curves showing the state-of-the-art of n-macro(aqu, bsi) pore etching around the "5 wt.% limit". Curve A: 6 wt.% HF (aqu), $T = 20$°C; curve B: 5 wt.% HF (aqu), $T = 20$ °C; curve C: 4 wt.% HF (aqu), $T = 20$ °C; curve D: 5 wt.% HF (aqu), $T = 20$ °C decreasing to 14 °C.

It should be noticed at this point that many experiments have been performed where “something” has been added to the typical 5 wt.% HF electrolyte – usually without much improvement and thus without publications. This is true, e.g. for additions of other acids like HCl or even acetic acid or by adjusting the pH value somehow. A noticeable exception is the addition of tensides – there is some improvement (12), but they must be used with care and not much seems to be published to this point.

In this paper we demonstrate that much higher pore growth rates as compared to the state-of-the-art can be achieved for n-macro(aqu, bsi) pores without sacrificing quality through optimization of the electrolyte composition in an HF – HAc – CMC system. HAc refers to acetic acid (CH_3COOH), CMC refers to a carboxymethylcellulose sodium salt; it increases the viscosity of the electrolyte. Electrolytes without the addition of either component will be termed “neat”, mixtures will be indicated by “viscous electrolyte” if CMC is added, “HF - HAc electrolyte”, or by using combinations of the abbreviations from above. Percentages given always refer to the HF concentration in wt.%.

Experimental Details

In most experiments low-doped (100) oriented n-type Si wafers with a resistivity of 20 Ωcm were used for etching the macropores. An implanted and annealed n^+ layer on the back side of the wafer provided the necessary good ohmic contact to the sample. The samples were pre-structured by standard photolithography (hexagonal lattice, a = 4.2 µm or 8 µm). Etching was performed at 20 °C in a fully integrated etching system of ET&TE GmbH with full control of all parameters including back side illumination (bsi) by an LED matrix, and an integrated fast Fourier transform (FFT) impedance spectrometer (IS) that took a complete spectrum every second, alternating between the (classical) current-voltage mode and a new bsi mode. From the impedance spectra 10 in-situ parameters including the actual pore depth, the valence of the dissolution process, or the instantaneous growth rate were extracted and displayed in real time; cf. (13) for some details. Electrolytes are always of the basic constitution mentioned above; details will be given (in obvious “short-hand”) in the context of the experiments.

Results

General Results

The following general points (which must be taken with a grain of salt, considering the rather large and complex parameter space) can be made:

i) At HF concentrations up to 15 wt.% a viscous electrolyte generally seems to improve the pore quality (as measured, e.g., by the surface wall roughness) and enhances pore stability somewhat (i.e. it is easier to etch very deep pores) without significantly changing the growth speed; this is shown in **Fig. 2** which also shows the “neat 5 wt.%” curve “B” from **Fig. 1** for comparison. Note the early pore growth termination around 100 µm for both 10 wt.% electrolytes). Note also that viscous electrolytes make large pore depths easier to achieve even so this is not directly obvious from **Fig. 2**.

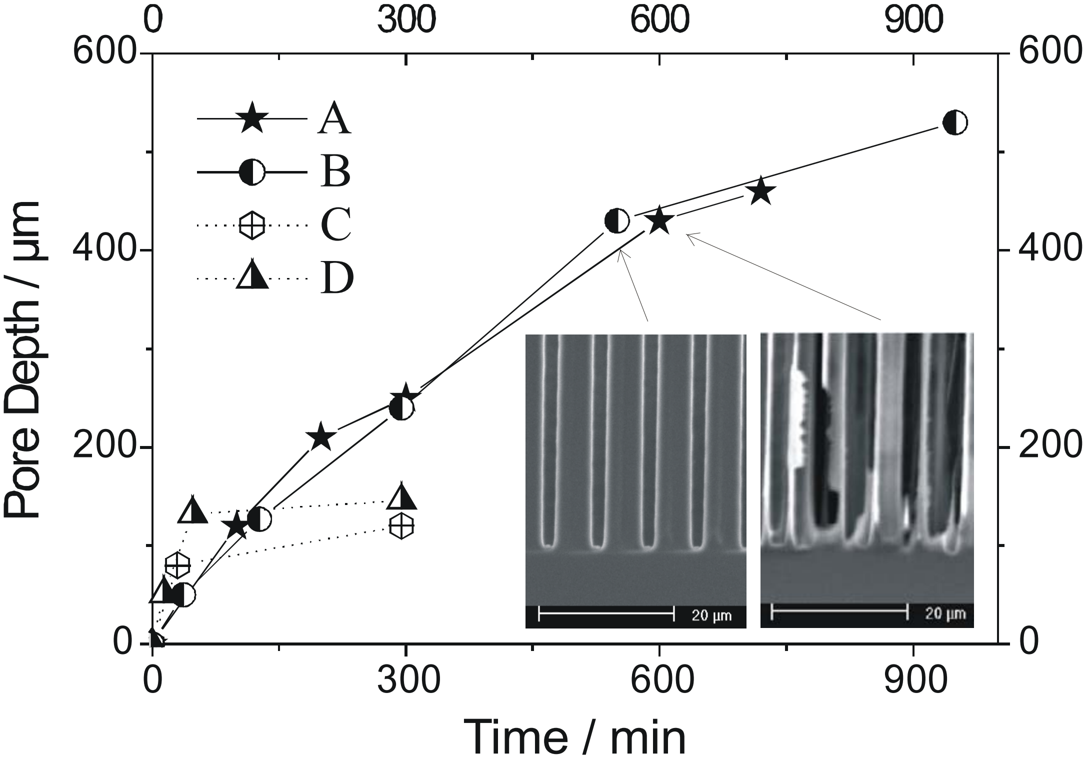

Figure 2 Comparison of viscous and neat 5 wt.% and 10 wt.% electrolytes with d_{pore} (t) curves; at T = 20 °C. Curve A: 5 wt.% HF (aqu); curve B: 5 wt.% HF (aqu + 0.83 g / l CMC); curve C: 10 wt.% HF (aqu); curve D: 10 wt.% HF (aqu + 0.83g / l CMC). Insets: SEM images of pore tips for the experiments marked by the arrows.

ii) An optimized HF – HAc electrolyte allows for growing qualitatively good pores far faster and deeper than before as shown by the curve in **Fig. 3** (also showing the "5 wt.% neat" curve from **Fig. 1** for comparison).

iii) Viscous HF – HAc electrolytes enable good pore qualities at high growth rates only somewhat lower than HF – HAc electrolytes. This is also summarily shown in **Fig. 3**.

At this point it should be mentioned that the use of acetic acid as growth speed promoter is less trivial than it might appear. Acetic acid has been tried (as a matter of course) as an additive to the 5 wt.% standard HF electrolyte – but no significant advantage was found. That HAc additions "work" at higher HF concentration was neither predictable nor expected. Contrariwise, adding other acids like HCl to 10 wt.% electrolytes tends to make etching worse. Using viscous electrolytes is also counterintuitive to some extent because all diffusion is slowed down; it could have been expected that etching rates slow down. However, "viscous" electrolytes have been found useful for producing better TiO_2 nanotubes in anodic oxidation experiments (14) giving a vague hint that increased viscosity could be helpful. A systematic study of Foca et al. (15), successfully undertaken with the aim to decrease the pore wall roughness of n-macro(5 wt.% aqu, bsi) pores, did indeed show that viscous electrolytes are beneficial in this respect without any obvious negative effects.

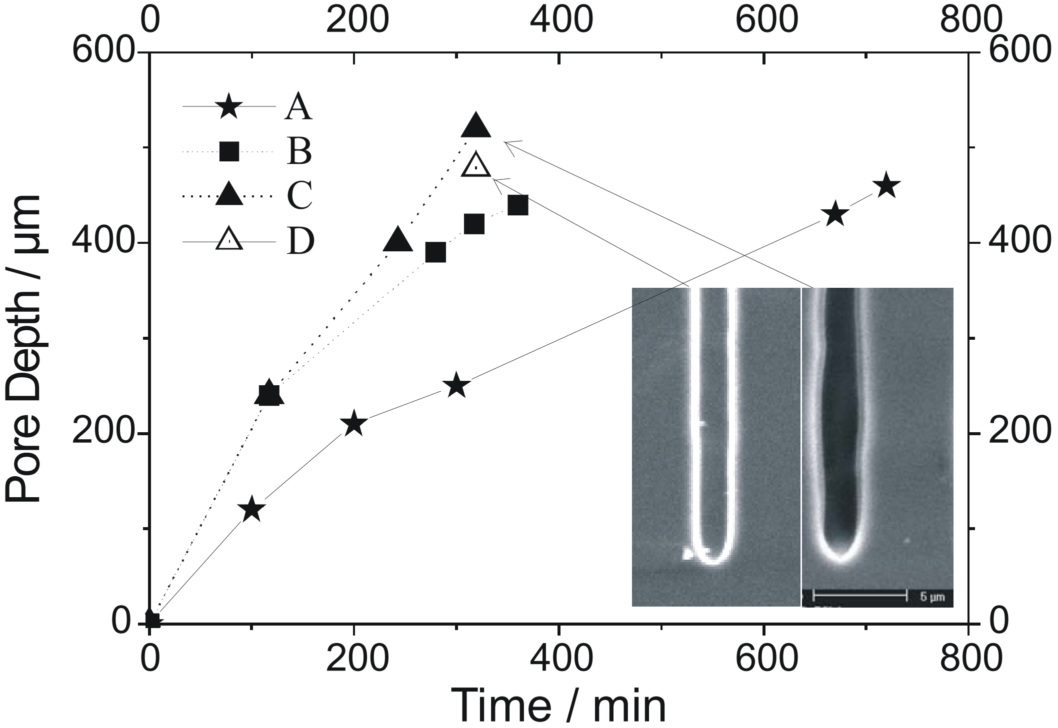

Figure 3 The pore depth d_{pore} (t) for the three basic 10 wt.% electrolytes. Curve A: 5 wt.% HF (aqu), 5 Ωcm; curve B: 10 wt.% HF + 33 wt.% HAc + CMC, 5 Ωcm; curve C: 10 wt.% HF + 33 wt.% HAc, 30 Ωcm; point D: 10 wt.% HF + 33 wt.% HAc + CMC, 30 Ωcm. Insets: SEM images of pore tips for the experiments marked by the arrows.

Given these first findings, the course of action is obvious: Try all kinds of mixtures of the three basic ingredients for HF concentrations between 5 wt.% and 25 wt.%, then substitute the acetic acid by other acids of this family (e.g. formic acid HCOOH, propionic acid C_2H_5COOH, butyric acid C_3H_7COOH), then repeat at different temperatures, doping levels and pore geometries – we have the outline of a rather extensive work program. While the parameter space described above has not yet been probed in great detail, a few generalizations from a number of experiments can be made.

There is, for example, a certain concentration of acetic acid for a given HF concentration that optimizes growth speed and pore quality. For 5 wt.% HF, it is rather close to zero while for 10 wt.% HF it is around 50 wt.% for growth speed only as shown in **Fig. 4** and around 35 wt.% if the pore quality is considered, too. **Fig. 5** shows pores obtained in this way. Note that a pore depth of 520 µm is very difficult if not impossible to obtain with neat 5 wt.% electrolytes and that etching times would be at least 900 min instead of 325 min.

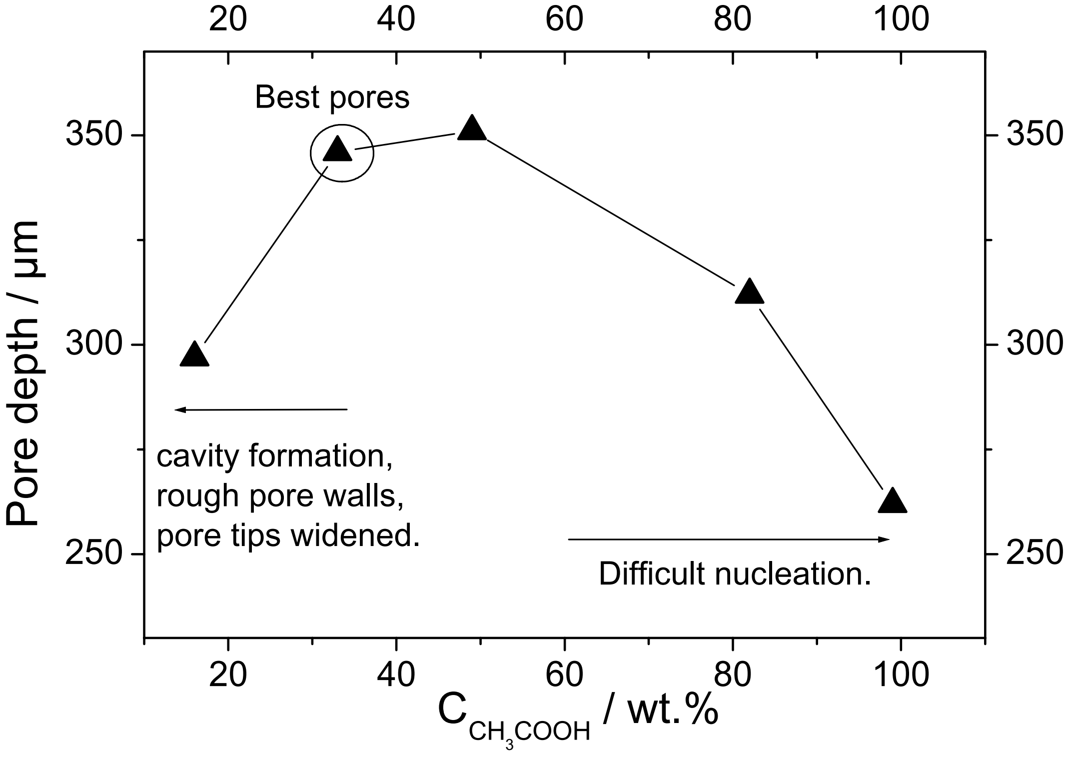

Figure 4 Influence of the acetic acid concentration on pore depths and quality for a 10 wt.% HF electrolyte.

The term "pore quality" together with the term "pore stability" in this context describes pore parameters that are easily assessed by looking at SEM picture in a qualitative way and hard to express quantitatively in numbers. Lumped together are issues like i) pore wall roughness (the only easily parameter accessible via atomic force microscopy (AFM), cf. (15), ii) destruction of the original surface, iii) side pore formation, iv) general straightness of pores and systematic or random diameter variations, v) self induced diameter oscillations (often observed in the new electrolytes introduced here, cf. (16)), vi) coating with microporous Si, and vii) straightness of pore tip front and individual pore defects.

As far as the other carboxylic acids are concerned; the ones tried so far (propionic acid and butyric acid) at 10 wt.% HF concentration give results similar to acetic acid with respect to the growth rate. Going to HF concentrations in excess of 10 wt.% plus carboxylic acids (including HAc) allows for even higher growth rates and far larger depths as compared to the "straight" electrolytes in some respects but produces a host of new phenomena and quality problems; a few relevant data points are shown in **Fig. 6**.

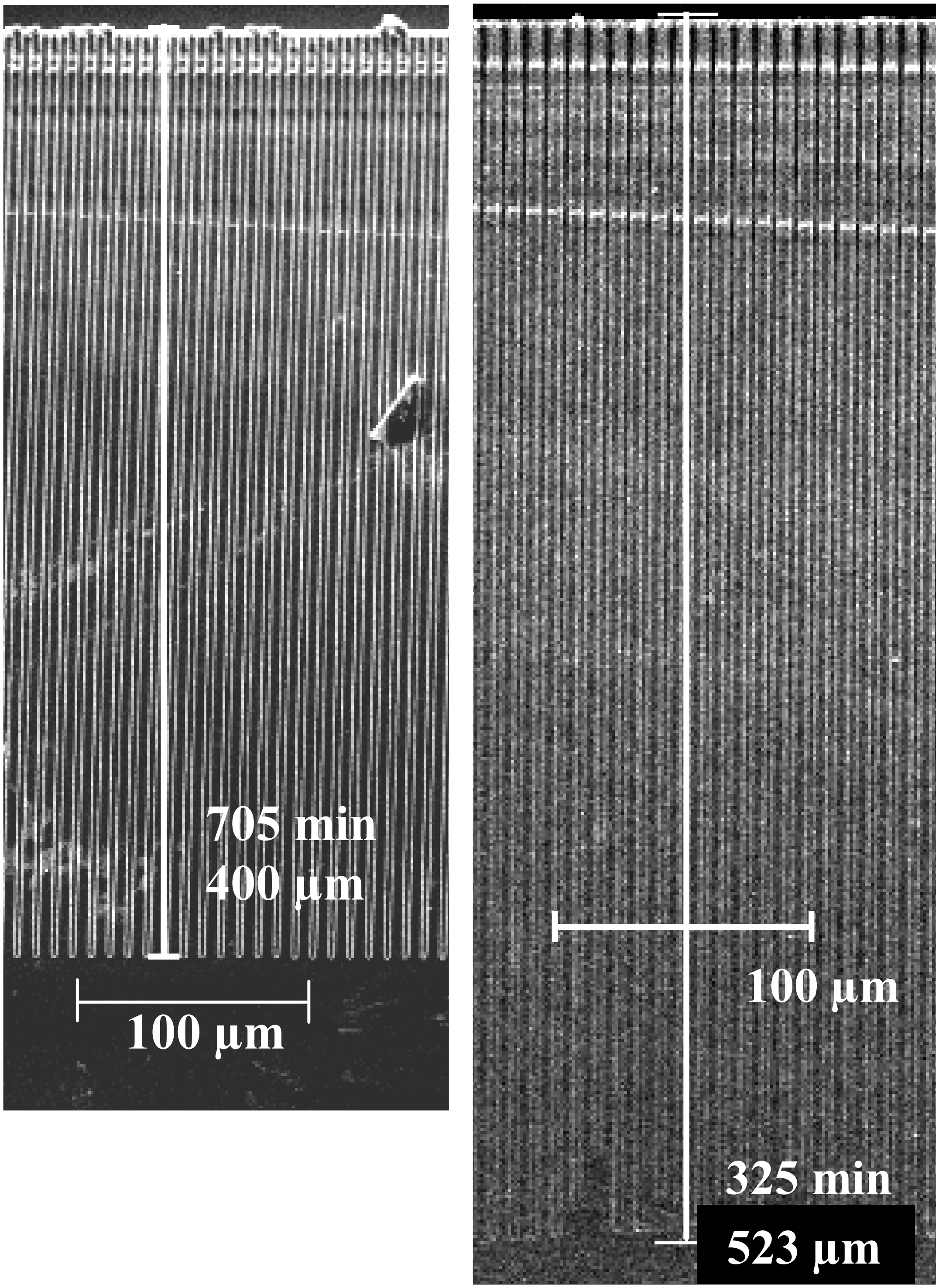

Figure 5 Comparison of deep, good-quality pores obtained in a standard neat 5 wt.% electrolyte (left) and in a 10 wt.% HF + 33 wt.% HAc electrolyte (right).

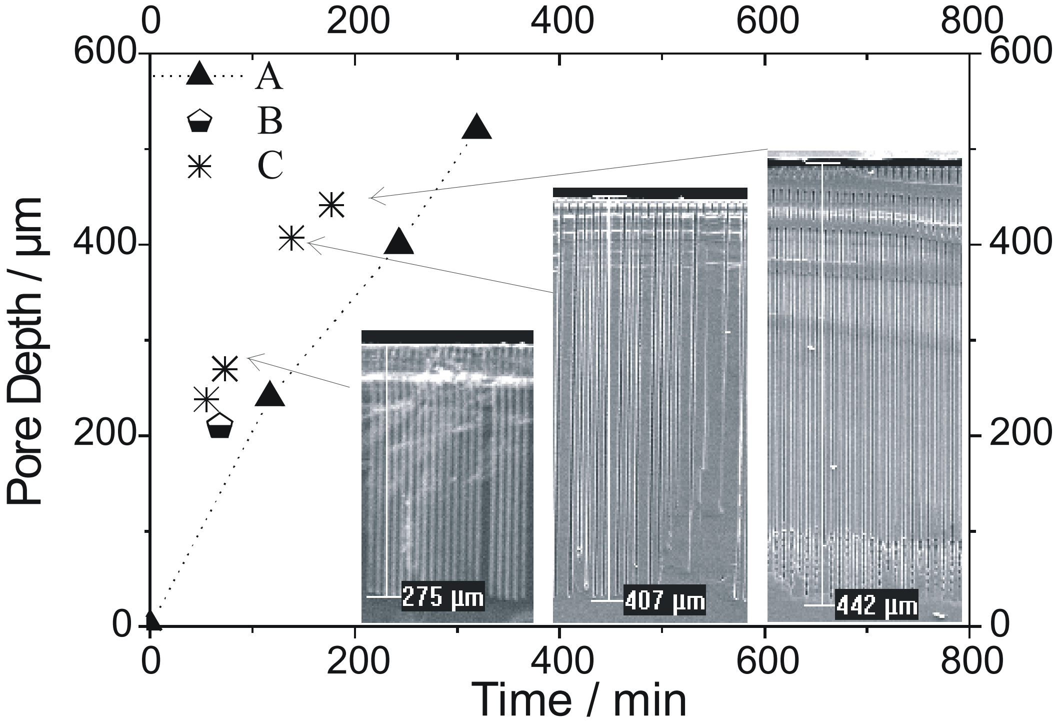

Figure 6 The pore depth $d_{pore}(t)$ for some other electrolytes including very high HF concentrations. A: 10 wt.% HF + 33 wt.% HAc; B: 15 wt.% HF + 33 wt.% HAc; C: 20 wt.% HF + 18 wt.% Butyric acid. Insets: SEM images of pores for the experiments marked by the arrows. Regarding the pore diameter oscillations in the third picture cf. (17).

From many results not shown here a few general points for etching with carboxylic acid based electrolytes at 15 wt.% or higher HF concentrations can be made:

i) It is very likely that conditions can be found that allow etching good macropores even faster as indicated by curve "B" in **Figs. 3** and **5** to some considerable depth.

ii) Realizing that potential needs detailed optimization, taking into account more parameters like the pore diameter and the doping. For example, the maximum pore depth obtainable seems to depend far more on the pore diameter than in the 5 wt.% range since the growth mode may change as detailed below, reducing the pore quality (an effect rarely seen at 5 wt.%) and this is influenced strongly by the chosen pore diameter.

iii) A host of new phenomena is encountered in this part of parameter space, in particular if CMC is added, too. Examples are self-induced anti-phase pore diameter oscillations, several new pore types (e.g. branched pores growing in steeply inclined <113> directions) and various kinds of pore linings with probably microporous Si; cf. (4) for details. Some of these new pore types or morphologies are reminiscent of pore structures and phenomena observed in III-V semiconductors (18), indicating that there are some general underlying principles that do not depend on the detailed reaction mechanisms governing the dissolution of semiconductors at pore tips.

Since no further drastic improvement of macropore etching for $c_{HF} > 10$ wt.% with high quality standards was found right away, semi-random probing of the large parameter space described above has been abandoned for the time being in favor of some more systematic experiments with a 10 wt.% HF – 33 wt.% HAc electrolyte. In a first working hypothesis it was assumed that HAc acts roughly like a tenside, with HAc^- coating the pore walls and reducing leakage currents. This would indicate that shifting the dissociation balance $[H^+]$ $[Ac^-]$ ↔ [HAc] (about 1 : 1 in aqueous environment) would increase or decrease the passivating action of the HAc. Adding (aqueous) NH_3 would increase the concentration of Ac^- and thus increase the passivation efficiency of the HAc (eventually leading to overpassivation) while adding NH_4F should do the opposite. Results are shown in **Fig. 7**, they clearly support the hypothesis made.

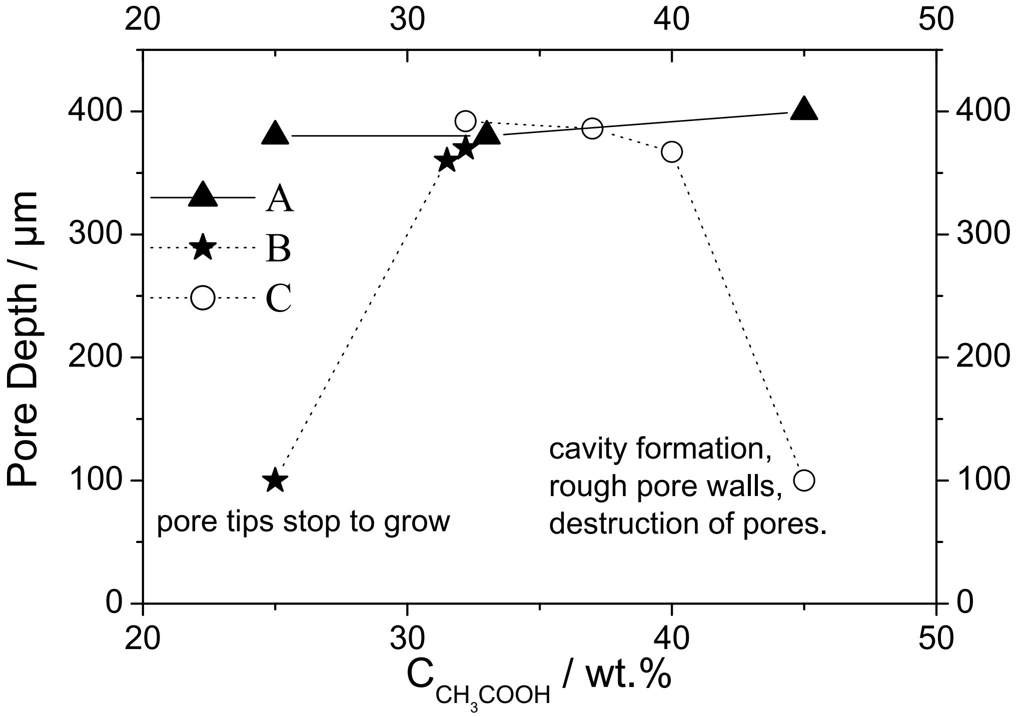

Figure 7 Pore depths in various electrolytes; curve A: 10 wt.% HF + HAc in different concentration; curve B: 10 wt.% HF + (33 - *x*) wt.% HAc + *x* wt.% NH_3; curve B: 10 wt.% HF + (33 + *x*) wt.% HAc + *x* wt. % NH_4F.

Shown is a more detailed view of the curve in **Fig. 4** for the HAc concentration range 25 wt.% – 45 wt.% and the effect of adding NH_3 or NH_4F, respectively. Note that the curve for no additions comes from a set of measurements independent of the ones shown in **Fig. 4**, confirming reproducibility but giving somewhat different absolute numbers. It is clear that the additions essentially shift the curve in **Fig. 4** to higher or lower HAc concentrations as was expected and amplify the effects outside the optimum HAc concentration.

More than 10^5 impedance spectra have been obtained in the course of the experiments described above, providing a plethora of quantitative data. While it is impossible to go into any details of the information gathered by evaluating these spectra as outlined in more detail in (5, 19), a few highlights are shown in **Figs. 8** and **9**.

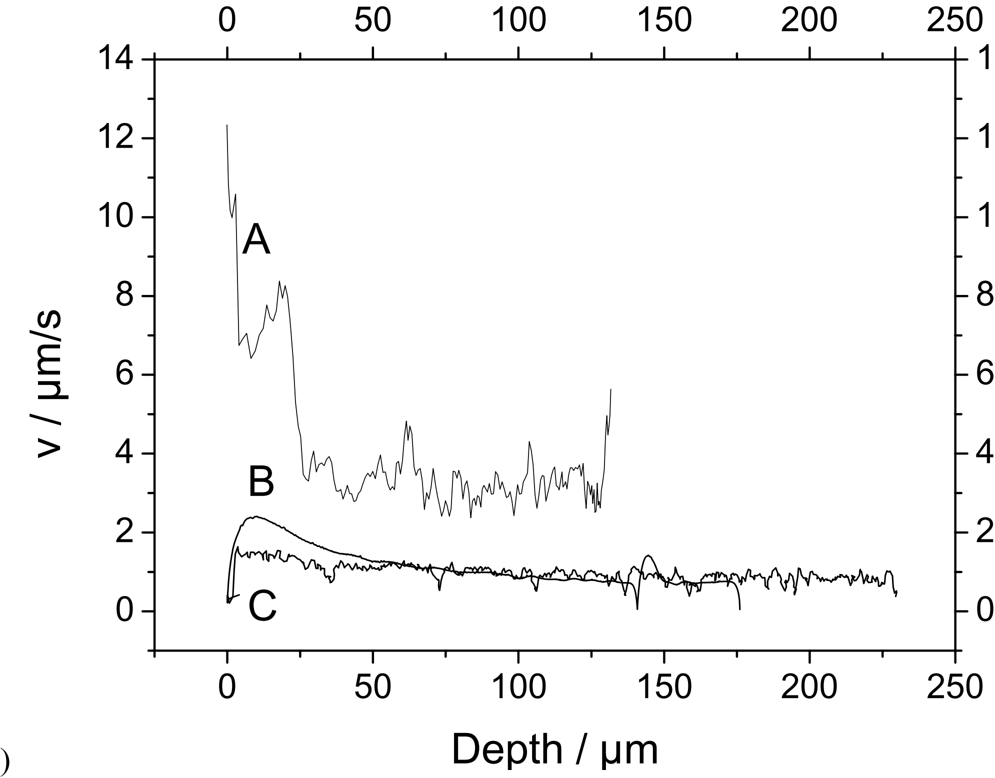
v / µm/s
Depth / µm
A
B
C
0
50
100
150
200
250
0
2
4
6
8
10
12
14

a)

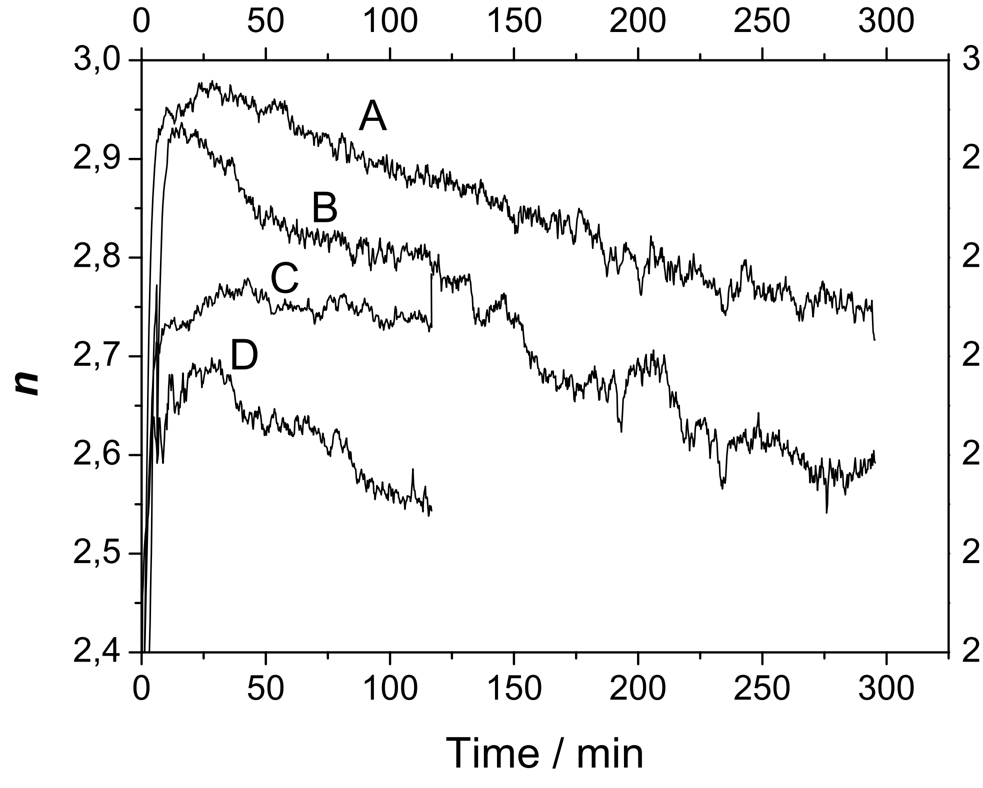
n
Time / min
A
B
C
D
0
50
100
150
200
250
300
2,4
2,5
2,6
2,7
2,8
2,9
3,0

b)

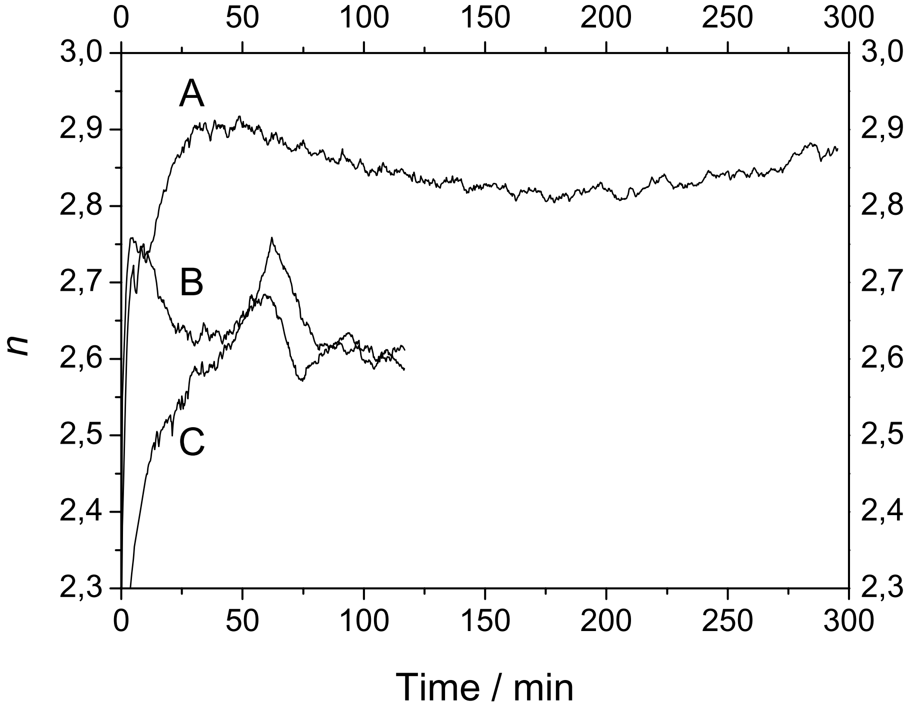

c)

Figure 8 Some selected data from in-situ impedance spectra.
a) Pore growth speed for some typical electrolytes vs. pore depth; A: 10 wt.% HF + 0.83 g/l CMC (1V), B: 5 wt.% HF + 33 wt.% HAc (1 V constant), C: 5 wt.% HF + 0.83 g/l CMC (0.7 V);
b) Valence *n* vs. time; A: 5 wt.% HF + 33 wt.% HAc (0.7 V), B: 5 wt.% HF +33 wt.% HAc (1.0 V), C: 10 wt.% HF + 33 wt.% HAc (0.7 V constant), D: 10 wt.% HF + 33 wt.% HAc (1.0 V).
c) Valence *n* vs. time for experiments with and without cavity formation; A: 5 % HF + 0.83 g/l CMC (1.0 V), B: 10 wt.% HF + 0.83 g/l CMC (1 V), C: 15 wt.% HF + 0.83 g/l CMC (1 V) (total current 50 %).

While ten parameters are obtained in-situ, only a few will be shown here. **Fig. 8a)** shows the pore growth speed as a function of pore depth or etching time, respectively, for some electrolytes and demonstrates that the growth speeds can be properly assessed in-situ with IS and that there is indeed little difference between regular and viscous electrolytes. The "noise" in curves A and C is actually real, i.e. the growth speed is not constant on small time scales. Together with many similar findings (see (17) for more results) these data once more demonstrate that pore etching is a stochastic process with some tendency to chaos or order, depending on the conditions, as first proposed in (20 - 22).

Fig. 8b) shows a comparison of the dissolution valence *n* for 5 wt.% and 10 wt.% electrolytes with HAc addition as a function of the (constant) external voltage and with etching times chosen to yield similar pore depths. It has long been known that the growth of macropores requires $n \approx 2.7$ (4) but so far *n* could only be measured ex-situ as an average over the whole etching process. Note that *n* tends to decrease with time (and thus pore depth) except for the case of 10 wt.% - low voltage. A decrease of *n* signifies that the balance between dissolution via oxidation ($n = 4$) and direct dissolution ($n \approx 2$) is shifted towards direct dissolution, indicating that leakage currents become more prominent. At this point it becomes clear that the etching process is far more sensitive to the applied potential (as known by all practitioners in the field) as could be expected from the SCR (space charge region) model. In fact, the optimizations of the 5 wt.% curves in **Fig. 1** always included suitable (small) changes of the potential as a function of time, something that has not yet been tried with the more advanced electrolytes presented here.

Fig. 8 c) gives another set of $n(t)$ curves that show growth mode transitions from pore growth to cavity formation again illustrating that in-situ FFT IS allows to monitor the growth process quite accurately. Cavity formation is indicated by a steep increase of the valence n. Since cavity formation is a direct consequence of a strong diffusion limitation which again drastically increases with increasing current density and pore depth no cavity formation is found at low HF concentration even for long etching times and correspondingly deep pores (curve A in Fig. 8c)). Using 15 wt.% HF and thus applying the highest current densities leads to the strongest diffusion limitation as indicated by the steepest increase of n in curve C in Fig. 8c).

Note for all curves in **Fig. 8** that the IS data by necessity show averages over all (10^6 or so) pores plus whatever happens at the O-ring or other boundaries in contrast to SEM pictures that show a minute fraction of all the pores and typically the best ones. IS data thus can never show transitions as sharply as SEM pictures; i.e. the change of the valence indicating cavity formation cannot be a sharp step in the $n(t)$ curves. On the other hand, the relative sharpness of IS data give an indication about the uniformity of the process.

Discussion

It has been shown that many new effects can be found in the parameter space introduced here, including not only faster and deeper pores at good quality but a large number of new structures in both pore geometry / morphology and in-situ IS data; see also (16). It must be expected that even more new results will emerge in the near future and it is thus too early to attempt an all-inclusive model for macropore growth with back side illuminated low-doped n-type Si that contains not only the new findings but also the relevant and undisputed facts of the existing SCR and "Lehmann" models. In what follows only some guidelines, partially speculative, towards an understanding will be offered.

The key to many of the new effects is the reduction of leakage currents (= currents flowing in the dark through the pore walls and dissolving Si) by a better pore wall "passivation". The reason for this is rather simple: a pore grows into the depth only via the current j_{tip} flowing through its tip, and its radius r_{pore} is (roughly) given by (4)

$$\frac{j_{tip}}{j_{PSL}} = \frac{\pi r^2}{a^2} \qquad [1]$$

where a is the pitch for a simple cubic lattice of pore nuclei.

The critical current density j_{PSL} is a simple function of the HF concentration c_{HF} and thus decreases with pore depth because c_{HF} at a pore tip will always be smaller than in the volume electrolyte. In any etching experiment attempting to generate deep pores, the total (external) current density j_{ex} must be decreased in such a way as to keep $j_{\mathrm{tip}} / j_{\mathrm{PSL}} = \mathrm{const.}$ As long as there are no leakage currents, this is not very difficult to do. Pores would grow "forever", but the growth speed $v_{\mathrm{pore}} \propto j_{\mathrm{tip}}$ decreases with pore depth to arbitrarily small values. However, if there is a certain leakage current density j_{leak}, a second current $I_{leak} = j_{leak} \cdot A_{pore\,wall}$ will flow through the pore in addition to the current $I_{tip} = j_{tip} \cdot A_{tip}$. Since the pore wall area continuously increases with increasing pore length this additional current will lead to an additional, continuously increasing diffusion limitation at the pore tips, i.e. at some depth the reduction of the HF concentration at the pore tip will not allow for further pore growth into the depth, i.e. j_{tip}, $v_{\mathrm{pore}} \rightarrow 0$ in this case. This effect will be more pronounced at high currents $I_{tip} + I_{leak}$ and for deep pores. Since for fixed pore geometries Eq. [1] implies a large j_{tip} for higher HF concentration, diffusion limitations will become more severe for the higher HF concentrations used here. Since $A_{tip} / A_{pore\ wall} \propto r_{\mathrm{pore}}$ diffusion limitations will also be more pronounced in thin pores.

The diffusion limitations as briefly addressed here are essential for the understanding of several pore morphologies in Si and III-V compounds (cf. e.g. (23, 24) for more details).

Assuming that HAc (and the other carboxylic acids) increases the pore wall passivation and thus decreases the leakage currents is necessary but not yet sufficient to explain the $d_{\mathrm{pore}}(t)$ curves for these conditions. What must be taken into account is that these ingredients do not only passivate the pore walls much better but also the pore tip area. In other words, the system might be "over-passivated", making not only current flow through the pore walls difficult, but also through the pore tip. Since under galvanostatic conditions current must flow, the system responds by transitions to growth modes not observed otherwise (17).

A second aspect that must be considered here is the selectivity of passivation, i.e. the difference in passivation kinetics for (slowly) dissolving pore walls and (quickly) dissolving pore tips, which will also be influenced by the crystal orientation of pore walls and pore tips. The results in Fig. 7b), showing even better pore qualities by adding some NH_3, can be qualitatively understood in this context: the pore wall passivation is increased without significantly increasing the pore tip passivation.

Without going into more details, adding "over-passivation" to the model developed so far will be sufficient to understand the results presented here with respect to the optimum relation between HF and HAc for growth speed and achievable pore depth. In addition, over-passivation and selectivity contains the seeds for some of the growth mode transitions observed, too.

However, considering passivation and over-passivation is not yet sufficient to explain all features observed, like all growth mode changes or the dependence of many parameters on the pore radius r_{pore}, and a few points will be made to this. First, it is necessary to note that the simple Eq. [1] for r_{pore} given above has some limits. First of all, the maximal pore radius r_{max} is not as implied in Eq. [1] given by $r_{\mathrm{max}} \approx a/2$ but at best by $r_{\mathrm{max}} \approx a/2 - d_{\mathrm{SCR}}$ (d_{SCR} = width of the space charge region) as is well known. Moreover, there is also a minimal radius r_{min} that is determined either by avalanche breakdown of "sharp" tips with a concomitantly large electrical field, or by the minimum size of so-called domains as postulated in the so-called "current burst model" (CBM) and detailed in (20, 21). Note that the CBM also justifies Eq. [1], which is otherwise just an empirical relation. The results shown here (and in (16)) strongly imply that there is also an "optimal" pore radius r_{opt}, envisioned most simply as the system-immanent pore radius that the system would adopt free of the constraints defined by the lithographically given lattice constant a. In the growth mode transitions: "lithographically defined pores" - "cavity"- "renewed pore growth" detailed in (16)), the pores formed after the cavity directly express r_{opt}. So far only the CBM provides a framework for r_{opt}; it is given by the size of "synchronized domains", which in turn is a function of the oxide properties covering the pore tip most of the time during dissolution. For details see (20 - 22). While for pores grown at low HF concentrations the actual radius r_{pore} and r_{opt} can be more or less identical for a large part of the pore depth, the differences become more pronounced in the parameter space dealt with here. Large deviations from the requirement $r_{\text{opt}} / r_{\text{pore}} = 1$ will trigger growth mode changes of various kinds.

The above enumeration of parameters that need to be considered in the context of an attempt to understand fast and deep pore etching in n-type Si under backside illumination allows three essential conclusions:

i) The goal of constructing a quantitative and complete model for just this part of pore etching in Si will not be an easy task.

ii) Reaching this goal without in-situ data (i.e. just by ex-situ analysis of the pore structure obtained) will be exceedingly difficult if not impossible.

iii) An increasing number of close similarities concerning basic mechanisms of pore formation in semiconductors emerges, strongly suggesting that a basic framework exists that covers many aspects of on general principles that do not depend on the specific detailed chemistry.

Summary / Conclusion

The addition of 30 wt.% acetic acid to a 10 wt.% HF electrolyte allows to etch qualitatively good macropores at more than twice the speed and far deeper than the prior state-of-the-art. Making the electrolyte viscous increases the quality of the pores with only small losses of growth speed.

The huge and mostly unexplored parameter space defined by the ternary system HF – HAc (or other carbonic acids) - CMC (or other viscosity reducers) will most likely contain conditions that allow even faster and deeper pores, but will require detailed process optimization.

Many new effects found demonstrate that the chemical side of macropore etching in Si is not yet sufficiently well understood. Extensions of the “space-charge region” model are required; in particular the role of “leakage currents”, system immanent pore sizes, and diffusion limitations must be assessed.

Some of the pore structures obtained show distinct similarities to pore structures observed in other semiconductors and indicate that there are some general, not yet fully understood principles that govern pore formation in semiconductors.

The results allow decreasing processing costs dramatically and thus having immediate bearing on the economy of pore etching.

Acknowledgements

The contribution of Dr. G. Popkirov, who was instrumental in developing the FFT impedance spectroscope, is gratefully acknowledged. This work has not been supported by the DFG. Parts of this work have been supported by the Alexander von Humboldt foundation.

References

1. V. Lehmann and H. Föll, *J. Electrochem. Soc.* **137(2)**, 653 (1990).
2. L.T. Canham, A. Nassiopoulou, and V. Parkhutik (Eds.), *Phys. Stat. Sol. (a)* **202(8)** (2005).
3. H. Föll, M. Christophersen, J. Carstensen, and G. Hasse, *Mat. Sci. Eng. R* **39(4)**, 93 (2002).

4. V. Lehmann, *Electrochemistry of Silicon*, Wiley-VCH, Weinheim (2002).
5. E. Foca, J. Carstensen, G. Popkirov, and H. Föll, *Phys. Stat. Sol. (a)* **204(5)**, 1378 (2007).
6. NEAH power systems, *http://www.neahpower.com*.
7. L. Ohlsen, A.M. Cooke, J. Mallari, C.M. Chan, and G. Rice, *U.S. Patent Application* **12386 20020419** (2002).
8. D. Cytrynowicz, M. Hamdan, P. Medis, H.T. Henderson, and F.M. Gerner, in *AIP Conference Proc.*, 227 (2003).
9. V. Kochergin and H. Föll, *Mater. Sci. Eng. R* **52(4-6)**, 93 (2006).
10. V. Lehmann, *J. Electrochem. Soc.* **140(10)**, 2836 (1993).
11. V. Lehmann, *Thin Solid Films* **225**, 1 (1995).
12. S. Schweizer, R.B. Wehrspohn, and J. Schilling, *203rd meeting of the Electrochem. Soc., Paris*, Abstract 2747 (2003).
13. J. Carstensen, E. Foca, S. Keipert, H. Föll, M. Leisner, and A. Cojocaru, *Phys. Stat. Sol. (a)*, submitted (2008).
14. E. Balaur, J.M. Macak, H. Tsuchiya, and P. Schmuki, *J. Mat. Chem.* **15**, 4488 (2005).
15. E. Foca, J. Carstensen, M. Leisner, E. Ossei-Wusu, O. Riemenschneider, and H. Föll, *ECS Trans.* **6(2)**, 367 (2007).
16. A. Cojocaru, J. Carstensen, M. Leisner, H. Föll, and I.M. Tiginyanu, *PSST 2008*, submitted (2008).
17. A. Cojocaru, J. Carstensen, and H. Föll, *ECS Trans.*, this proceedings (2008).
18. H. Föll, S. Langa, J. Carstensen, M. Christophersen, and I.M. Tiginyanu, *III-Vs Review* **16(7)**, 42 (2003).
19. E. Foca, J. Carstensen, G. Popkirov, and H. Föll, *ECS Trans.* **6(2)**, 345 (2007).
20. J. Carstensen, M. Christophersen, G. Hasse, and H. Föll, *Phys. Stat. Sol. (a)* **182(1)**, 63 (2000).
21. J. Carstensen, M. Christophersen, and H. Föll, *Mat. Sci. Eng. B* **69-70**, 23 (2000).
22. H. Föll, J. Carstensen, M. Christophersen, and G. Hasse, *Phys. Stat. Sol. (a)* **182(1)**, 7 (2000).
23. S. Lölkes, M. Christophersen, S. Langa, J. Carstensen, and H. Föll, *Mat. Sci. Eng. B* **101**, 159 (2003).
24. S. Langa, J. Carstensen, I.M. Tiginyanu, M. Christophersen, and H. Föll, in *Ordered Porous Nanostructures and Applications*, ed. R.B. Wehrspohn, 57 (2005).

ECS Transactions, 16 (3) 125-132 (2008)
10.1149/1.2982549 ©The Electrochemical Society

Formation Mechanism of Porous Silicon with Medium Pores: The Role of $KMnO_4$

K. Fukami[a], H. Kamakura[a], T. Sakka[a], and Y. H. Ogata[a]

[a] Institute of Advanced Energy, Kyoto University, Uji, Kyoto 611-0011, JAPAN

We investigated the medium pore formation in the presence of $KMnO_4$, H_2O_2 or HNO_3 in an HF solution. The time development of pore formation showed a crystallographically oriented etching with $KMnO_4$, while a less-oriented etching in the presence of H_2O_2 or HNO_3 or in the absence of the oxidants. In current vs. potential curves, the positive shift in the critical potential, above which uniform electropolishing occurs, was clearly observed in the presence of $KMnO_4$, while the critical potential increased a bit with H_2O_2 or HNO_3. The increase of the critical potential enabled to apply a higher current than that at the original critical potential, resulting in the formation of much wider pores.

Introduction

Porous silicon is formed via electrochemical anodization of silicon in HF solution. The pore sizes can be easily tuned from a few nanometers to several micrometers width by changing experimental conditions such as applied potential, current density and solution (1). The wide range of pore width has led to many applications based on porous silicon, for instance, sensors, templates, catalysts and photovoltaic devices (2-8). However, few studies were reported about the formation of pores from 50 to 300 nm width, so called medium pores. A systematic study on the formation of medium pores will lead to novel applications based on porous silicon.

There are three major approaches to fabricate medium pores. The first approach is metal particle assisted pore formation in silicon (9-11). The pore size basically depends on the size of metal particles in this system. Many researchers studied the issue by electroless etching in the presence of an oxidant, for instance, hydrogen peroxide, while the pores can be also formed and easily controlled under polarization in the absence of the oxidant (11). The second approach is medium pore formation by applying a high current density with highly doped p-type silicon (12, 13). Lehmann first reported the approach, then Janshoff et al. followed the approach and obtained medium pores, the diameters of which were highly controlled by the applied current density (13). The third approach is the anodization of silicon in the presence of an oxidizing reagent (14-17). Föll et al. achieved the formation of medium pores by adding CrO_3 in a HF solution based on the "current burst model" (14). Ouyang et al. reported microcavity formation with medium pores in the presence of CrO_3 or in the absence of an oxidant (15, 16). We also find that medium pores can be formed in the presence of $KMnO_4$ (17). However, the mechanism of medium pore formation is unclear although many trials with an oxidant have been reported. In the present paper, we investigated the formation of medium pores in the presence of an oxidant such as H_2O_2, $KMnO_4$ and HNO_3, focusing on the role of the oxidants for pore widening. The surface observation and the electrochemical measurements indicate that the equilibrium potentials of the oxidants are not important for pore widening but the oriented etching, which causes the positive shift in the potential, influences the widening.

Experimental

A highly doped *n*-type (n^+) silicon (100) with resistivity 0.010-0.018 Ω cm was mainly used as a substrate. A highly doped p-type silicon with resistivity of 0.0045-0.0060 Ω cm was also used for comparison. The substrate was rinsed in ultra pure water and acetone under ultrasonic irradiation for 5 minutes. Before the formation of porous silicon, the native oxide layer was removed in 5 wt% HF aqueous solution. The preparation of porous silicon was carried out under current controlled condition in an HF aqueous solution with a two-electrode cell. The Si substrate (0.79 cm^2) and a Pt rod (1 mmϕ × 1 cm) were used as the working electrode (WE) and the counter electrode (CE), respectively. The basic solution was 6 wt% HF + 3000 ppm of NCW-1001 (surfactant) + oxidant ($KMnO_4$, HNO_3 or H_2O_2). The concentration of the oxidants was 0, 2, 4 and 8 mM. The electrolyte with 1 or 3 wt% HF aqueous solutions was also used. The value of the applied current was 1, 10 and 25 mA for 1 and 6 wt% HF, respectively. I-E characteristics were measured with a potentiostat (Hokuto Denko, HZ3000). The I-E measurements were carried out with a three-electrode cell, the reference electrode of which was a Ag|AgCl with saturated KCl. The samples were observed by a field emission-type scanning electron microscope (JEOL FE-6500, SEM).

Results

Figure 1 shows the time development of plan views during the pore formation in the HF solution with $KMnO_4$, and a cross-sectional view of medium pores. At the initial stage of the anodization, the surface is covered with small inverse pyramids. The pore diameter increases with time, and the crystallographically oriented etching observed in

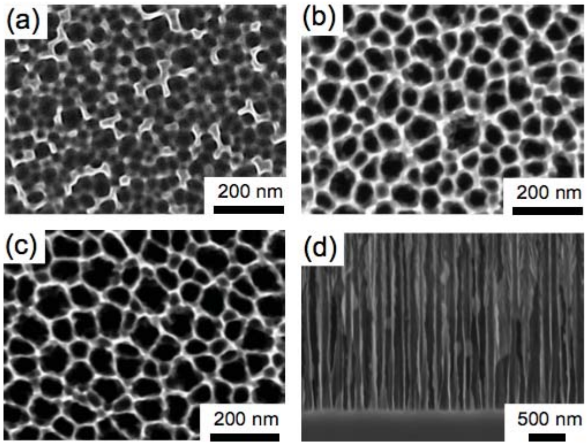

Figure 1. (a-c) Time development of pore formation in 6 wt% HF + 8 mM $KMnO_4$ + 3000 ppm NCW solution with n^+ silicon. The applied current was 25 mA. The anodization times were 10, 50 and 100 s for (a), (b) and (c), respectively. (d) A cross-sectional view of typical pores formed in the solution after 100 s anodization.

Fig. 1a gradually disappears. Finally, the pores with about 150 nm width are formed. The pore width is almost constant from the bottom to the opening. The pore formation without $KMnO_4$ in the solution is completely different as shown in Figure 2. In the absence of $KMnO_4$, the oriented etching as in Fig. 1a is not observed even at the initial stage of the anodization. With increasing the anodization time, the surface morphologies do not change so much. The surface after the formation of medium pores without $KMnO_4$ is scabby. The thin layer of scabs exists very near the surface of porous silicon. However, the cross-sectional view shows that the medium pores are formed almost uniformly from the bottom to the opening except the scabby part. The same result was reported by Ouyaung et al. (16). In a lower concentration of HF, the pore morphology is also completely different from the results shown above. Figure 3 shows the time development of the plan views and a cross-sectional view of pores obtained in 1 wt% HF with $KMnO_4$. The pores show inverse square pyramids, the sizes of which are from 20 nm at the initial stage to over 10 μm after the 6 hour anodization. Pores with high aspect ratio were not obtained, and they did not grow toward the bulk silicon but grew laterally. When the specimen was dipped into the solution overnight without polarization, the surface was roughened but such macropores with 10 μm width were not obtained. It should be noted that the tips of the inverse pyramids are not sharp but relatively flat as shown in Figure 3d. If silicon is etched in an alkaline solution chemically, the surface shows inverse pyramids with sharp tips. According to these results, the pores with low aspect ratio obtained in the present experiment should be induced by electrochemical dissolution.

It is clear that $KMnO_4$ affects the etching of silicon. We investigated the pore formation in the presence of the other oxidant such as H_2O_2 or HNO_3. Figure 4 shows the pores formed in the presence of H_2O_2 or HNO_3. The equilibrium potentials of H_2O_2, $KMnO_4$ and HNO_3 in the present system are 1.85, 1.77 and 1.02 V vs. Ag|AgCl sat. KCl, respectively. The pores do not show crystallographically oriented etching even in the presence of H_2O_2, which has a more positive equilibrium potential than $KMnO_4$. However, the pore bottom is relatively wide (~ 100 nm) when the applied current is set at a value very near the critical current, while much wider pores as in Figure 3 were not

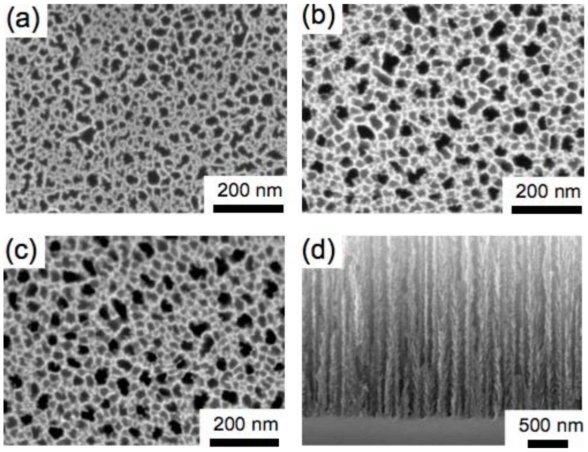

Figure 2. (a-c) Time development of pore formation in 6 wt% HF + 3000 ppm NCW solution with n^+ silicon. The applied current was 10 mA. The anodization times were 10, 50 and 100 s for (a), (b) and (c), respectively. (d) A cross-sectional view of typical pores formed in the solution after 100 s anodization.

obtained with H_2O_2 or HNO_3 even in 1 wt% HF solution. In order to understand the difference among the oxidants, I-E characteristics were measured. First, we measured I-E curves in the absence of oxidants with various concentrations of HF. As shown in Figure 5a, critical potentials exist in the curves, above which electropolishing uniformly occurs on the whole electrode surface. Thus, we focus on the potential and current range below the critical values. The critical potential shifts to positive with decreasing the concentration of HF together with the decrease of the critical current. Figure 5b shows that the critical potential also shifts to positive when the concentration of $KMnO_4$ increases. In contrast, Figure 5c and d show that the positive potential shifts are little with the 2 mM addition of H_2O_2 or HNO_3, but there is no large difference between the 2 and 4 mM addition of the oxidants.

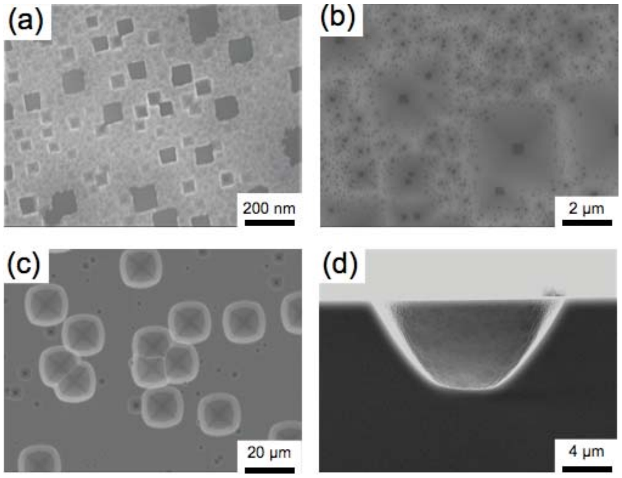

Figure 3. (a-c) Time development of pore formation in 1 wt% HF + 8 mM $KMnO_4$ + 3000 ppm NCW solution with n^+ silicon. The applied current was 1 mA. The anodization times were 0.5, 1.5 and 6 hours for (a), (b) and (c), respectively. (d) A cross-sectional view of typical pores formed in the solution after 6 hour anodization.

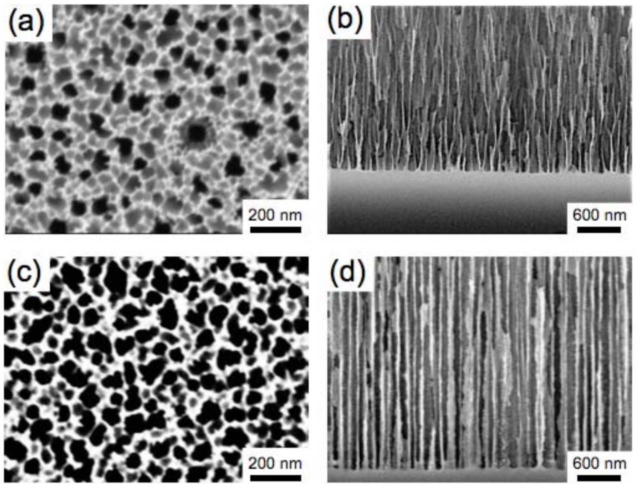

Figure 4. Plan (a) and cross-sectional (b) views of pores formed in 6 wt% HF + 8 mM H_2O_2 + 3000 ppm NCW with n^+ silicon. Plan (c) and cross-sectional (d) views of pores formed in 6 wt% HF + 8 mM HNO_3 + 3000 ppm NCW with n^+ silicon. The anodization times were 100 s. The applied current was 10 mA.

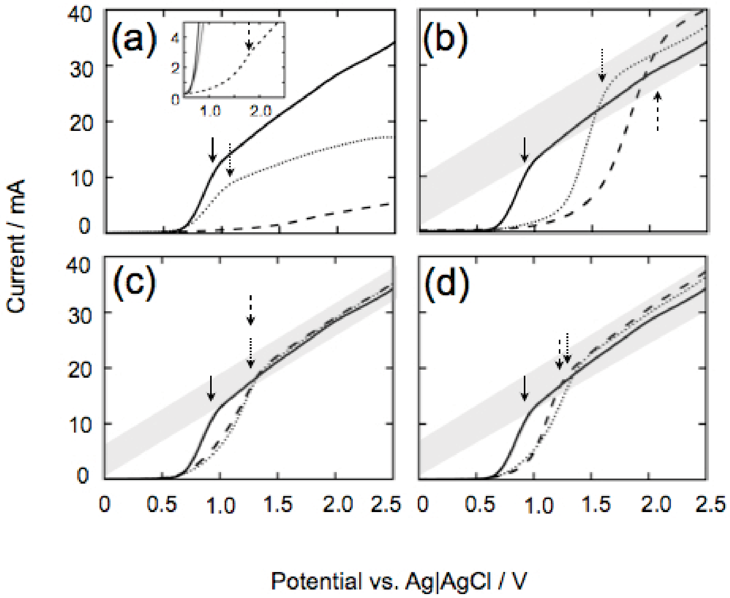

Figure 5. (a) I-E curves measured in the absence of oxidants. The solid, dotted and dashed lines indicate the I-E curves in 6, 3 and 1 wt% HF + 3000 ppm NCW. (b-d) I-E curves measured with the different concentration of an oxidant. The solid, dotted and dashed lines indicate the I-E curves in 0, 2 and 4 mM oxidant + 6 wt % HF + 3000 ppm NCW. The oxidant was $KMnO_4$, H_2O_2 and HNO_3 for (b), (c) and (d), respectively. The scan rates were 50 mV s^{-1}. The gray regions in (b), (c) and (d) indicate the I-E slope of electropolishing reaction. The solid, dotted and dashed arrows indicate the critical potentials for each curve.

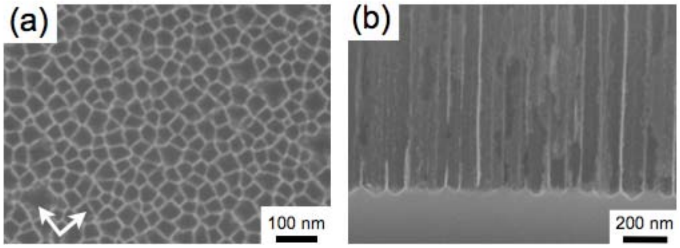

Figure 6. Plan (a) and cross-sectional (b) views of pores formed in 6 wt% HF + 8 mM H_2O_2 + 3000 ppm NCW with p^+ silicon. The anodization times were 100 s. The applied current was 25 mA. The white arrows in (a) indicate the preferential orientation of pore walls.

The formation of medium pores was also investigated with p^+ silicon. Figure 6 shows the pores obtained from p^+ silicon. Medium pores are formed, and show relatively crystallographically oriented pores. The pore wall is straight from the bottom to the opening as observed in n^+ silicon. However the optimal condition is very narrow, and the medium pores are difficult to form uniformly on the whole electrode surface.

Discussion

In general, the pore size increases with increasing the applied potential or current. However, this generality often has a limit because of electropolishing. Electropolishing occurs uniformly at a potential or current above the critical point. Therefore, the continuous widening of pores from mesopore to macropore is often difficult by simply changing the applied potential or current. The onset of uniform electropolishing can be detected electrochemically by measuring the I-E characteristics. If the critical point is tunable toward a more positive potential and a higher current, we can apply a more positive potential or a much higher current, and expect the formation of much wider pores. In this study, we found that the critical potential shifted with the addition of $KMnO_4$ in the HF solution together with the increase of the critical current. As written in Experimental section, the pore formation was carried out under current controlled condition, thus we could apply a higher current than the original critical current measured in the absence of $KMnO_4$, and then obtained much wider pores.

On the basis of the above discussion, an important point is the reason why the critical potential shifts to positive together with the increase of critical current in the solution with $KMnO_4$. First, let us consider the effect of the equilibrium potentials. The equilibrium potential of H_2O_2/H_2O (1.85 V) is positive compared with $KMnO_4/MnO_2$ (1.77 V), while that of HNO_3/HNO_2 (1.02 V) is negative. According to the relation, equilibrium potential of the oxidant is not important. Another factor should exist to induce the shift of the critical point. It should be mentioned here that oxidation process not only by $KMnO_4$, H_2O_2 or HNO_3 but also by water itself must be essentially important for medium pore formation as described by Föll et al. (14). If one simply aims to increase the critical potential or current, the porosification should be performed in a concentrated HF solution. However, the porosification in 10 wt% HF solution always resulted in the formation of mesopores. Therefore the oxidation by water might be basically important, but we hereafter focus on the activation of pore widening by another factor in the presence of $KMnO_4$.

Then what is another factor? The surface morphologies give additional information. The time development of pore morphologies in the presence of $KMnO_4$ shows that the crystallographically oriented dissolution exposing small inverse pyramids proceeds at the beginning of the etching. In contrast, the preferential orientation is not observed in the absence of $KMnO_4$ or in the presence of H_2O_2 or HNO_3. This classification is very related to the shift of the critical current in the I-E characteristics. Thus the oriented etching seems to be an important factor. How does the oriented etching affect the positive shift in the potential and the increase of the critical current? The oriented etching shows inverse pyramids, which means the exposed surfaces are (111) plane. The (111) plane should be more stable than the (100) or high index planes because the (111) is terminated by monohydride. This stability of the plane results in a lower etching rate on the (111) than on the other planes. This means that a larger overpotential is necessary to achieve the same etching rate on the (111) predominant porous silicon as on the surface with other planes. The higher overpotential means the positive shift in the potential, thus the potential shifts to positive with the addition of $KMnO_4$. On the other hand, At a potential or current above the critical point, the dissolution of silicon proceeds uniformly, and the I-E curves show monotonic increases as highlighted with gray regions in Figure 5. The electropolishing reaction always shows a constant slope in the I-E curves, but the actual current is not always the same in all the solutions because the measured currents depend on the surface roughness. In the solution with $KMnO_4$, a higher overpotential is necessary for the porosification as discussed above. This in turn leads to the increase of the critical current in order to reach the current to the gray (electropolishing) region. As a result, a higher current can be applied, and wider pores can be obtained. In the case of solutions with H_2O_2 or HNO_3, the surface morphologies showed less-oriented pores. The clear increase of the overpotential and the critical current is not expected in the solutions. Therefore the tunable range of the applied potential or current via the addition of the oxidants is limited compared to the solution with $KMnO_4$. Note that the etching by $KMnO_4$ is a local electroless reaction, thus it does not depend on the type of doping. Föll et al. also reported that medium pores were formed in an HF solution with CrO_3 (14). A solution containing CrO_3 in HF is a famous etchant for silicon, for example, so called Sirtl etching (18). The etchant is known that the silicon surface often shows oriented etching. On the other hand, an HF solution containing HNO_3 with acetic acid is also famous etchant exhibiting less-oriented etching (19). In the present case, $KMnO_4$ also shows the same oriented etching as CrO_3, while HNO_3 shows less-oriented etching. We think that the solution containing CrO_3 should also show the same tendencies of critical potential shift and oriented etching although we have not tried the reagent yet.

The effect of $KMnO_4$ might strongly depend on the concentration of HF because the balance of the etching rate by electrochemical reaction at the bottom and local electroless reaction on the pore wall depends on the concentration of HF and $KMnO_4$. In 1wt% HF solution, the preferential orientation became remarkable leading to the pores with low aspect ratio, while pores with a higher aspect ratio can be formed with 2 wt% HF (not shown here). Therefore a critical concentration of HF seems to exist between 1 and 2 wt%. According to the above discussion, an optimal concentration of HF and $KMnO_4$ for much wider medium pore or macropore having a higher aspect ratio with n^+ silicon should be found.

Conclusion

We investigated the medium pore formation in the presence of an oxidizing reagent. According to the current burst model, oxidants such as H_2O_2, $KMnO_4$ and HNO_3 expected to form medium pores (14). However, the pore widening is much easier and wider with $KMnO_4$ than with the others. The difference seems to be strongly based on the oriented etching of silicon with $KMnO_4$. The oriented etching leads to the stabilization of the pore surface, which enables to apply a more positive potential or a much higher current than that without $KMnO_4$. Etching at a higher current density results in the formation of wider pores that are not realized with H_2O_2 or HNO_3, but with $KMnO_4$ or CrO_3. The understanding of medium pore formation will lead to the precise size control of medium pores and novel applications based on the medium pore sizes.

Acknowledgments

This work was partially supported by the Grant-in-Aid from the Japan Society of Promotion of Science for Scientific Research (B) under Grant No. 18350107 and for Young Scientists (Start-up) under Grant No. 19850012.

References

1. V. Lehmann, *Electrochemistry of Silicon, Instrumentation, Science, Materials and Applications*, Wiley-VCH, Weinheim (2002).
2. R. M. L. Van de Leur, and A. Van der Waal, *Synth. Met.*, **102**, 1330 (1999).
3. J. C. Vidal, E. Garcia, and J. R. Castillo, *Anal. Chim. Acta*, **381**, 213 (1999).
4. V. Vrkoslav, I. Jelinek, G. Broncova, V. Kral, and J. Dian, *Mater. Sci. Eng. C*, **26**, 1072 (2006).
5. K. Fukami, K. Kobayashi, T. Matsumoto, Y. L. Kawamura, T. Sakka, and Y. H. Ogata, *J. Electrochem. Soc.*, **155**, D443 (2008).
6. T. Matsumoto, K. Kobayashi, K. Fukami, T. Sakka, and Y. H. Ogata, *submitted for publication*.
7. K. Fukami, F. A. Harraz, T. Yamauchi, T. Sakka, and Y. H. Ogata, *Electrochem. Commun.*, **10**, 56 (2008).
8. S. Radhakrishnan, and P. Somani, *Mater. Lett.*, **37**, 192 (1998).
9. K. Tsujino and M. Matsumura, *Adv. Mater.*, **17**, 1045 (2005).
10. S. Yae, Y. Kawamoto, H. Tanaka, N. Fukumuro, and H. Matsuda, *Electrochem. Commun.*, **5**, 632 (2003).
11. Y. L. Kawamura, K. Fukami, T. Sakka, and Y. H. Ogata, *Electrochem. Commun.*, **10**, 346 (2008).
12. R. Herino, *Properties of Porous Silicon, (ed. L. Canham)*, INSPEC, Exeter, p. 89 (1997).
13. A. Janshoff, K. S. Dancil, C. Steinem, D. P. Greiner, V. S. –Y. Lin, C. Gurtner, K. Motesharei, M. J. Sailor, and M. R. Ghadiri, *J. Am. Chem. Soc.*, **120**, 12108 (1998).
14. H. Föll, J. Carstensen, M. Christophersen, and G. Hasse, *Phys. Status Solidi A*, **182**, 7 (2000).
15. H. Ouyang, M. Christophersen, and P. M. Fauchet, *Phys. Status Solidi A*, **202**, 1396 (2005).
16. H. Ouyang, M. Christophersen, R. Viard, B. L. Miller, and P. M. Fauchet, *Adv. Funct. Mater.*, **15**, 1851 (2005).
17. Y. H. Ogata, A. Koyama, F. A. Harraz, M. S. Salem, and T. Sakka, *Electrochemistry*, **75**, 270 (2007).
18. R. B. Heimann, *J. Mater. Sci.*, 19, 1314 (1984).
19. C. T. Seo, C. H. Bae, D. S. Eun, J. K. Shin, and J. H. Lee, *Jpn. J. Appl. Phys.*, 43, 7773 (2004).

ECS Transactions, 16 (3) 133-142 (2008)
10.1149/1.2982550 ©The Electrochemical Society

In-Situ FFT Impedance Spectroscopy during the Growth of n-type InP "Crysto Pores"

M. Leisner[a], J. Carstensen[a], A. Cojocaru[a], and H. Föll[a]

[a] Institute for Materials Science, University of Kiel, 24143 Kiel, Germany

In this work the growth of crystallographically oriented pores in n-type InP is studied. The evolution of the pore structure with time is outlined in detail. It is found that growth and branching of these pores in different crystallographic directions depend on the etching time. Besides an ex-situ evaluation of the pore structure by microscopy, in-situ FFT impedance spectroscopy measurements have been performed. A model has been found which fits the data consistently. First steps towards a physico-chemical understanding of the processes underlying the pore growth have been made, yielding a qualitative view of pore growth.

Introduction

For the electrochemical formation of pores in n-type InP mostly aqueous HCl based electrolytes (1 - 6) have been employed, but more recently also liquid ammonia (7) or KOH were used (8). At least the pores obtained in the HCl experiments can be classified into two different types with respect to their growth mechanism and their concomitant morphology. At lower current densities, so-called crystallographically oriented pores ("Crystos") are observed. They always grow into the <111>B directions of the single-crystalline semiconductor, independent of the initial surface orientation. They tend to have a triangular cross-section and their pore walls and tips show a pronounced crystallography as well (9). At higher current densities so-called current-line oriented pores ("Curros") form. These pores show a more circular cross-section and they always grow perpendicular to the equipotential lines, i.e. in the direction of the local current flow and thus usually perpendicular to the sample's surface. The "crysto" pore growth mode may be changed to the "curro" pore growth mode by external causes, e.g. upon increasing the current or even in a self-organized way (6).

These facts raise the immediate question of what exactly happens in the system that leads to such drastic changes in the pore growth mode? To elucidate this question, an understanding of the sub-processes constituting pore growth as a function of time is mandatory. The problem is that in-situ data about the on-going reactions in a pore-growing system are not easily accessible since the most important reactions occur at the pore tip deep inside the sample. Any interpretation of pore formation thus is usually only based on analyzing the final pore morphology and the external current and / or voltage measurements. This does not provide enough data and thus no undisputed model for pore growth in InP (or most other semiconductors) exists.

The approach of this work is to measure and evaluate in-situ data obtained during the pore growth in n-type InP through in-situ Fast Fourier Transform (FFT) Impedance Spectroscopy (IS) (10, 11). Classical ex-situ IS measurements have been performed in the n-type InP / HCl system (12 - 14), but the techniques used are not applicable in-situ during the pore etching, since stable measurements take too long in relation to system dynamics where a pore tip may move with a speed of up to 20 µm / min. FFT IS allows for shorter measurement times and thus can follow relatively fast-changing reactions while still yielding stable measurements. FFT IS has already yielded new insights into the growth of macropores in n-type silicon (15) and first measurements during the growth of curro pores in n-type InP have been performed and evaluated as well (16). The next step towards a more general understanding of pore growth on n-type InP will be taken in this work, applying FFT IS to the growth of crysto pores. A comparison with the results obtained for curro pores will be made. An analysis leading to an understanding of the crysto-curro switchover mechanism is the basic goal of this study.

Experimental

All samples have been cut from single-crystalline (100)-oriented single-side polished n-type InP wafers with a doping concentration of $N_D = 1\ 10^{17}$ cm^{-3}. All experiments have been performed in an electrochemical double-cell described in detail in (17). Aqueous HCl with a concentration of 5 wt.% (= 1.4 M) has been used as electrolyte. All experiments have been performed in the galvanostatic mode at a rather low current density of j = 0.4 mA/cm^2 on a sample area of A = 0.25 cm^2 and at a constant temperature of 20 °C. To achieve a better pore nucleation, experiments were started by a current pulse of 40 mA/cm^2 for 1 s. Several experiments have been performed for different etching times between 5 min and 360 min. The resulting pore structures have been investigated by scanning electron microscopy (SEM).

The in-situ FFT IS measurements have been performed with a signal consisting of 27 frequencies distributed between 20 Hz and 15 kHz; the total signal amplitude was 70 mV. The frequency spectrum of the response signal around the applied discrete frequencies has been continuously measured to check for measurement artifacts, e.g. second harmonics, that might have been induced by the rather high total amplitude as compared to conventional IS measurements, where only one frequency is used at a time (18). Only results without those artifacts have been evaluated, ensuring that only linear response was observed.

Results

Pore morphology vs. time

Pore etching experiments under closely controlled and nominally identical conditions have been conducted for differing etching times while recording a complete FFT IS every 1.5 s. After the experiments, the samples were cleaved and analyzed in cross-sectional view using a Philips XL30 SEM.

In the first 5 minutes a nucleation layer forms that consists of inhomogeneously distributed holes with diameters between 0.5 µm and 1 µm and that appears to be situated right below the surface. These holes are the nucleation sites for the subsequently formed first crysto pores. These pores begin to grow into the two <111>B directions pointing downwards from the <100> surface. This mode of pore growth continues for about 15 to 20 minutes. An example for this pore structure can be seen in **Fig. 1a** where the structure after a 10 min experiment is shown. Note that both <111>B directions pointing downwards are lying in the <110> cleavage plane of the crystal shown here, i.e. the pores are visible as straight lines. Quite often the pores branch at the tips and subsequently grow into both downward pointing <111>B directions.

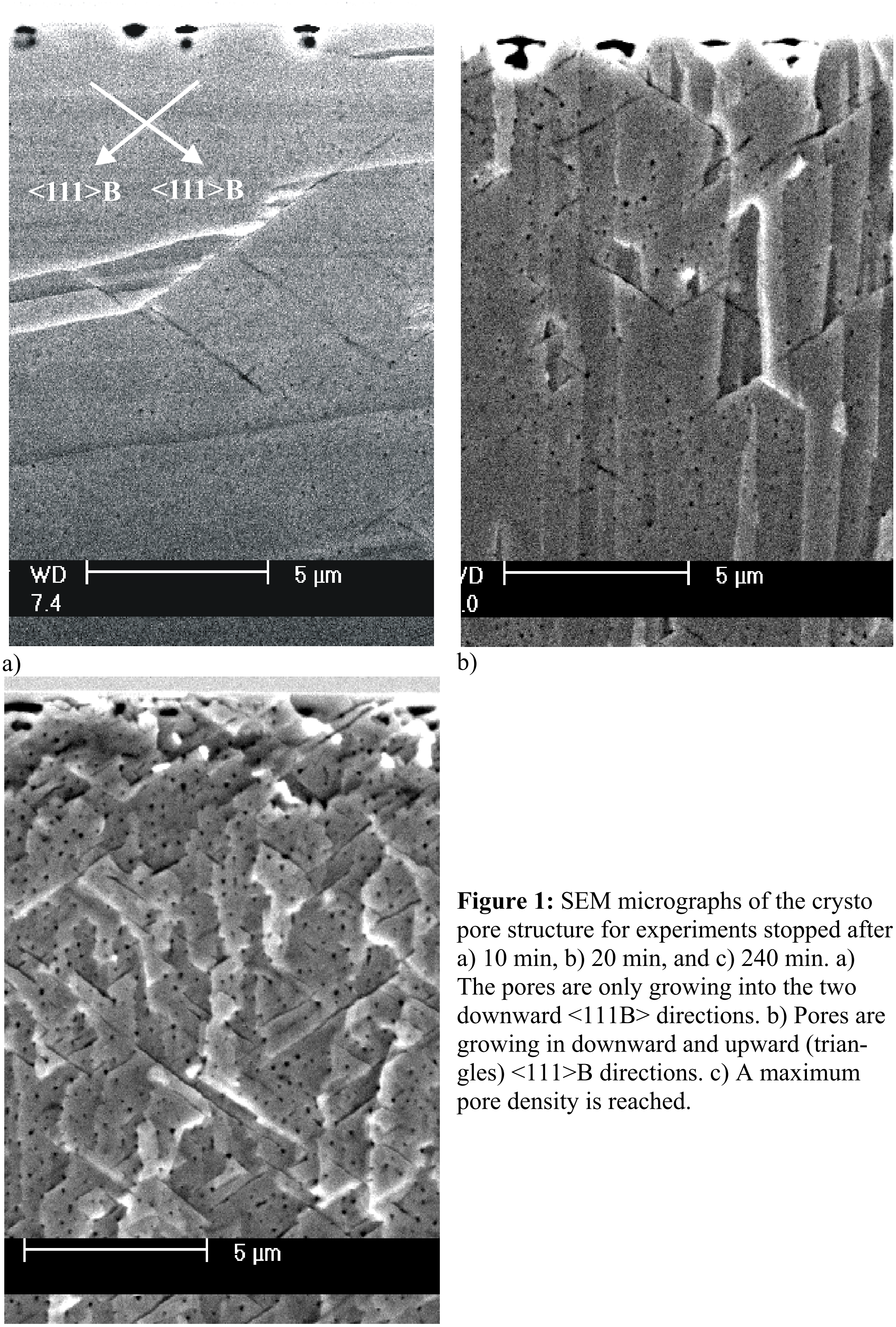

a)

b)

c)

Figure 1: SEM micrographs of the crysto pore structure for experiments stopped after a) 10 min, b) 20 min, and c) 240 min. a) The pores are only growing into the two downward <111B> directions. b) Pores are growing in downward and upward (triangles) <111>B directions. c) A maximum pore density is reached.

After etching 15 or 20 minutes the pores start to branch out of the pore walls into the <111>B directions pointing upwards. In the <110> cleavage plane these upward growing pores show up as small triangles in the SEM micrographs. These directions are crossing the cleavage plane and thus are only leaving the "imprint" of the pore cross-section. **Fig. 1b** illustrates this phenomenon. It can be seen that the branching of the downward growing pores is stronger than before and that upward growing pores are observed as well.

All pores, growing into the upward or downward <111>B directions, show the same behavior. They can either branch at the tips into the other same direction ((up → up) or (down → down)), or pores can branch out of the pore walls into the opposite direction ((up → down) or (down → up)) (6, 9, 19). Both processes can be attributed with a probability P_{tips} resp. P_{walls}, which will be used in the discussion part.

For longer etching times, the downward growth as well as both kinds of branching continue until the bulk is nearly completely filled with pores with a minimum distance of about 300 nm, yielding a maximum pore density. This state is reached in the surface near region first, whereas the pore density is reduced with increasing distance to the surface. **Fig. 1c** shows an example for such a most dense pore structure after 240 minutes of etching.

Note that the pore structure in contrast to most other pore types does not show a straight pore front at a constant depth. Branching into the two upward <111>B directions only occurs to a certain pore depth, followed by a smaller layer of pores only growing into the downward <111>B directions.

Accordingly, when plotting the pore depth vs. the etching time (cf. **Fig. 2**), two pore depths can be distinguished. The depth to the end of the layer containing four growth directions $d_{\text{pore 1}}$, given by the closed squares, and the depth to the end of the proceeding two -direction layer $d_{\text{pore 2}}$, given by the open diamonds.

It can be clearly seen from **Fig. 2** that in the beginning the pore depth is related to the etching time by a logarithmic growth law, i.e.

$$d_{\text{pore}} \propto \ln t\,. \qquad [1]$$

Note that this functionality does not yield a pore depth of zero for $t = 0$ min and thus is only valid for times > about 10 min. From **Fig. 2** it can be seen that both lines intersect at $t = 7$ min with a corresponding pore depth $d_{\text{pore}} = 0$ µm. This phenomenon can be understood, because pore growth will start delayed by a nucleation time and the zero point in time is actually around 10 min later relative to the experimental time.

For etching times > 120 min the experimental data can be fitted by a logarithmic growth law or a linear growth law. Neither can be ruled out from the small number of data points.

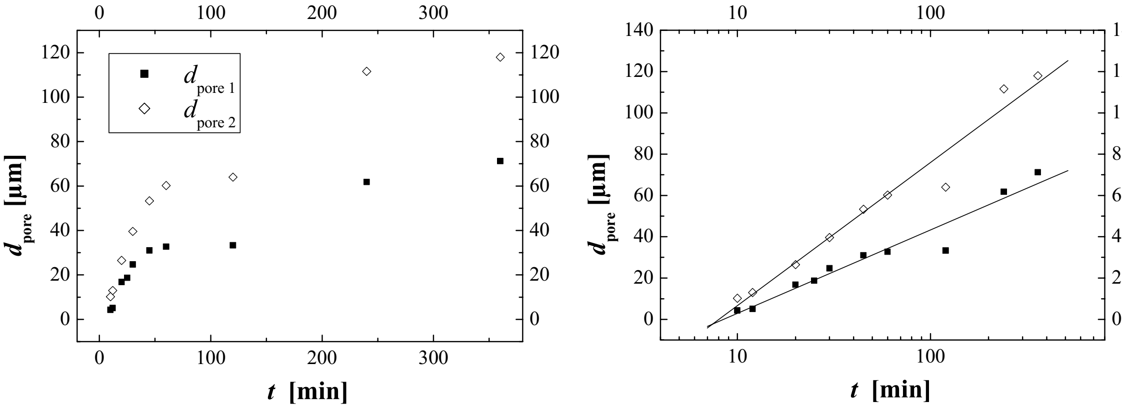

a) b)

Figure 2: a) The pore depth d_{pore} as a function of the etching time. The closed squares represent the depth $d_{\text{pore 1}}$ of the four-directions layer, the open diamonds the depth $d_{\text{pore 2}}$ of the two-directions layer. b) Same data in logarithmic coordinate representation. The lines represent a linear fit of the two data sets. For details see the text.

FFT Impedance Spectroscopy

Some representative results of the measured FFT IS data are presented in **Fig. 3**. They show the Nyquist- and Bode-plots at $t = 7$ min and $t = 75$ min during a 360 minutes experiment. It can be seen that the data can be very well fitted in this example, and this is also true for the ≈ 15.000 spectra measured in the whole experiment. The fit function used for the measured impedance is

$$Z(\omega) = R_S + \frac{1}{\frac{1}{R_1} + i\omega C_1 + \left(R_2 + \frac{1}{i\omega C_2}\right)^{-1}} + \frac{R_3}{1 + i\omega R_3 C_3}, \qquad [2]$$

corresponding to the equivalent circuit shown in **Fig. 3e**. This model function contains 7 parameters, the serial resistance R_S, the chemical transfer resistances R_1, R_2, and R_3, as well as the corresponding capacitances C_1, C_2, and C_3. Several other standard models for the fit function have been tried, especially those with less fitting parameters, but only unsatisfactory results were obtained. The three $R_i - C_i$ circuits encode three (chemical) processes with time constants $\tau_i = R_i C_i$ that will be referred to as "process i" in what follows.

The time dependence of the fitting parameters over the course of an experiment is plotted in **Fig. 4**. In addition to the 7 fitting parameters, the voltage U is shown, as well as the three time constants $\tau_1 = R_1 C_1$, $\tau_2 = R_2 C_2$, and $\tau_3 = R_3 C_3$.

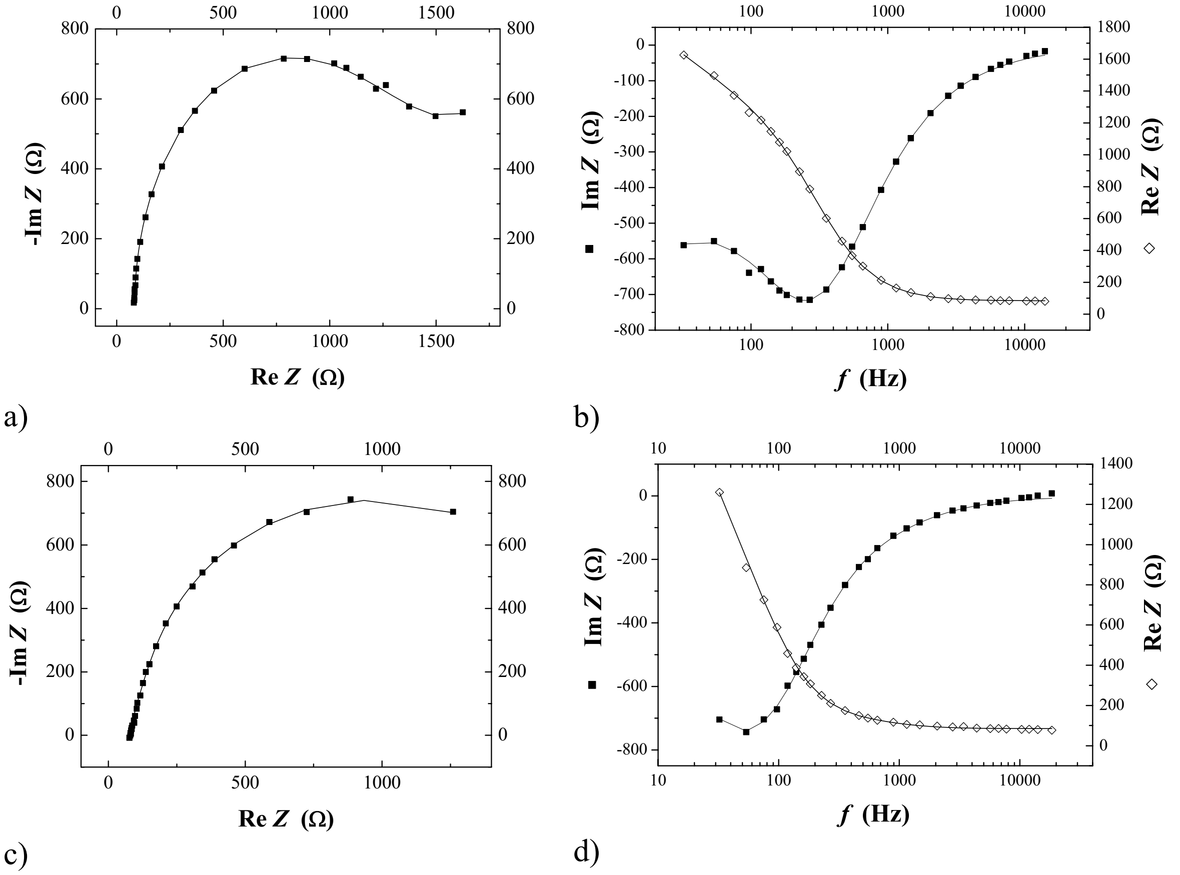

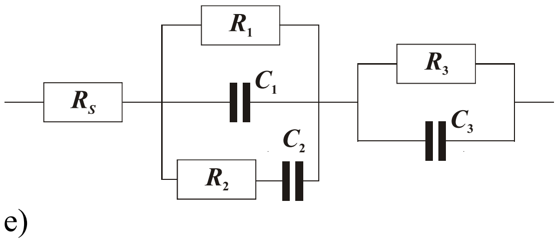

Figure 3: a) Nyquist plot and b) the corresponding Bode plots measured during the experiment at $t = 7$ min. c) Nyquist plot and d) the corresponding Bode plots measured during the experiment at $t = 75$ min. The squares represent the measured data, the lines the fit according to Eq. [2]. e) The equivalent circuit of the fitting model described in Eq. [2], which has been employed to fit the IS data.

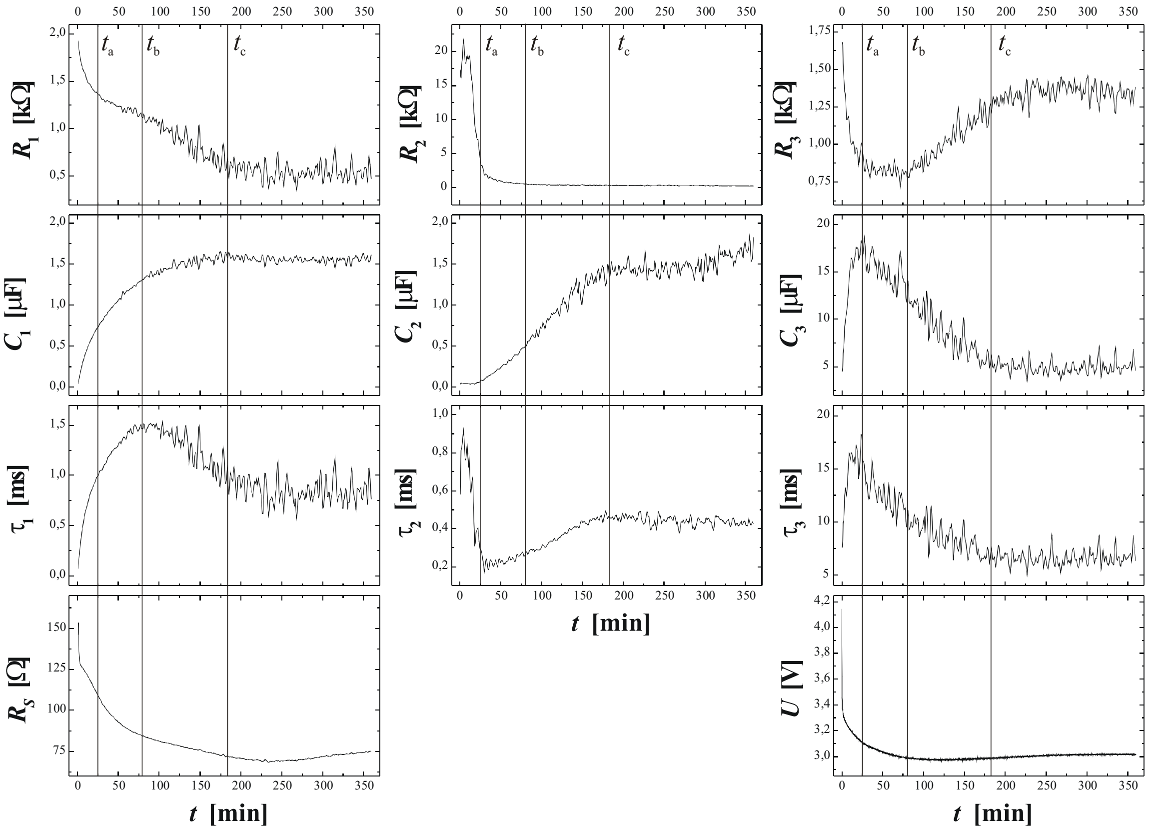

Figure 4: Time dependence of the fitting parameters contained in Eq. [2] and the voltage $U(t)$. The time constants τ_i result as the product of the respective resistance R_i and capacitance C_i. For a detailed discussion of the meaning of the times t_a, t_b, and t_c, see the text.

Discussion

The time dependence of the fitting parameters in the model Eq. [2] allows to indicate three characteristic times, which are marked in **Fig. 4**. The first time t_a at roughly 20 min coincides well with the time where upwards growing pores have been first found in the SEM images. Moreover, at the time t_a the slopes of the three resistances $R_1 - R_3$ decrease substantially and extrema for the time constants τ_1 and τ_3 are found. The second-most significant time t_c is reached after 180 minutes: From that time on most of the curves do not change significantly anymore and thus stay constant. This indicates that pore growth has reached a steady-state, i.e. the pore structure is qualitatively the same between the depth of the pore tips and the depth of the top layer with the highest density. These two layers relating to pore fronts as described above move deeper into the substrate with time, increasing the thickness of the layer with the high pore density. The slight linear increase of R_S is in good agreement with these results, since in a steady-state of pore growth only d_{pore} changes, and thus the linear change in R_S can be attributed to the linearly increasing ohmic losses. As a consequence of this steady state the distance between the two pore fronts should stay constant and a linear increase of both $d_{pore\ 1}$ and $d_{pore\ 2}$ should be expected, reflecting the speed of the pore tips. This is in good agreement with the results in **Fig. 2a** for etching times larger than 200 min.

A third transition time t_b after roughly 80 min is also clearly visible for the curves R_3, R_1, and τ_1. It is quite obvious that when a certain pore density is reached the pores growing upwards must grow into regions where already many pores have been growing downwards. These pores thus will have to stop growing since there is simply no space left into which they could continue; this phenomenon has also been found for GaAs (6, 19). The time t_b could well be related to this process, i.e. it indicates a time when a significant number of upward growing pores stop, thus getting closer to steady state.

One characteristic of the crystallographic pore growth mode is that nucleation on the free sample surface is extremely difficult (6, 20) and commences at a few sites only. High densities of pores are reached by the successive branching of pore tips. The logarithmic curve of pore depth vs. time in **Fig. 2** can be explained from three simple assumptions for the kinetics of branching:

i) The valence during pore growth is constant. Thus, the pore growth velocity v of the pores is proportional to the current density j in the pore.

ii) Branching occurs predominantly at the pore tip, i.e. $P_{\text{tips}} >> P_{\text{walls}}$.

iii) The probability P_{branch} for the branching of a pore tip in a time period Δt is proportional to the current density j at this pore tip.

Obviously the etching area A, i.e. the sum of all pore tip areas, increases by branching, i.e.

$$\frac{dA}{dt} \propto A P_{\text{tips}} \propto A\, j\,. \tag{3}$$

Applying a constant current I we get

$$\frac{dA}{dt} \propto A\, j = A\frac{I}{A} = I = const., \tag{4}$$

i.e.

$$A = A_0 t\,. \tag{5}$$

The pore depth d_{pore} can thus be calculated from the simple relations

$$j = qnv, \text{ and } d_{\text{pore}}(t) = \int v \mathrm{d}t\,, \tag{6}$$

yielding

$$d_{\text{pore}}(t) = \int v \mathrm{d}t = \frac{I}{A_0 \mathrm{q} n}\cos\alpha \int t^{-1}\mathrm{d}t = \frac{I\cos\alpha}{A_0 \mathrm{q} n}\ln t + C\,, \tag{7}$$

taking into account the slanted pore growth with respect to the surface by the angle α. This result is in perfect agreement with the experimentally determined growth law described in **Fig. 2**.

The time dependence of the capacitance C_1 shows a logarithmic growth law from the beginning of the experiment until t_c is reached. The functionality is not changed at the characteristic times t_a and t_b. These facts might indicate that process 1 describes the reaction at all pore tips (downward and upward growing) and that the logarithmic growth law not only reflects the linear increase in the area, but also a correspondingly changed electrolyte concentration and a potential drop at the tips with increasing pore depth.

For process 2 the resistance R_2 is large and C_2 is constant and close to zero until t_a is reached. Then C_2 drastically increases until a steady-state at t_c is reached, whereas R_2

slightly decreases between t_a and t_b and stays almost constant after t_b. As mentioned before, the time t_b coincides with the beginning of upward branching, thus it is highly probable that process 2 is linked to the upward branching of pores starting at pore walls.

According to the equivalent circuit in **Fig. 3e** the resistances R_1 and R_2 represent processes occurring in parallel during pore formation, the process 3 is in series to both process 1 and 2. The resistance R_3 shows a more complex time behavior. It could describe a subsequent electrochemical reaction or it could be related to a transport process.

To identify the electrochemical reactions and physico-chemical processes related to the processes 1 to 3, more experiments with parameter variations are necessary, but the points made above allow already to draw some conclusions about the growth of crystallographically oriented pores in n-type InP. Nearly all changes in the impedance data could be related to changes in the morphology of the assembly of the crystallographically oriented pores, while the valence at the pore tips seems to be constant. This is in good agreement e.g. with TEM analysis (9): the shape of a crystographically oriented pore does not change significantly if the pore is growing upwards or downwards, if it is growing near the sample surface or deep in the substrate. This indicates that for all crystallographically oriented pores the reactions at the pore tips, and the subsequent reactions that form the crystallographically oriented pore walls, do not change significantly. Such stable crysto pore growth only exists when small current densities are applied. At medium and high current densities a continuous transition to current line oriented pores is found, with of course quite different reaction kinetics (16). Taking into account the small diameter and the extreme length of crystallographically oriented pores, and the correspondingly large problems related to the transport of reaction products and educts through these pores, the stability of the “crysto” pore growth mode is quite astonishing. For pores with comparable aspect ratios, e.g. in Si, all resistances extracted from impedance data show a continuous increase (15). It might be inferred that a self-organized stabilizing mechanism exists which allows such stable growth of the crystallographically oriented pores.

Summary and Conclusion

The evolution of the pore structure for crystallographically oriented pores in n-type InP has been studied in detail. Pore growth starts by the formation of a nucleation layer. Subsequently pores start to grow in the downward <111>B directions and branch at the tips; with some delay branching out of pore walls and growth into the upward directions follows. After reaching a maximum pore density in the top regions, pore growth proceeds more slowly into the depth. Until this maximum pore density is reached the pore depths follows a logarithmic growth law.

The in-situ FFT impedance spectroscopy measurements could be very well fitted by the model shown in **Fig. 3e**. A qualitative interpretation of the time dependence of its parameters in terms of processes occurring during pore growth has been given.

All results could be consistently understood by a model for the kinetics of pore branching based on the assumptions that the branching probability is proportional to the current density at the pore tips, and that the valence of the dissolution is constant.

References

1. T. Takizawa, S. Arai, and M. Nakahara, *Japan J. Appl. Phys.* **33(2, 5A)**, L643 (1994).
2. A. Hamamatsu, C. Kaneshiro, H. Fujikura, and H. Hasegawa, *J. Electroanal. Chem.* **473**, 223 (1999).
3. H. Hasegawa and T. Sato, *Electrochim. Acta* **50**, 3015 (2005).
4. H. Tsuchiya, M. Hueppe, T. Djenizian, and P. Schmuki, *Surface Science* **547(3)**, 268 (2003).
5. L. Santinacci, A.-M. Goncalves, C. David, A. Eb, C. Mathieu, M. Herlem, and A. Etcheberry, *Phys. Stat. Sol. (c)* **4(6)**, 1898 (2007).
6. H. Föll, S. Langa, J. Carstensen, S. Lölkes, M. Christophersen, and I.M. Tiginyanu, *Adv. Mat.* **15(3)**, 183 (2003).
7. A.M. Gonçalves, L. Santinacci, A. Eb, I. Gerard, C. Mathieu, and A. Etcheberry, *Electrochem. Solid-State Lett.* **10(4)**, D35 (2007).
8. C. O'Dwyer, D.N. Buckley, D. Sutton, and S.B. Newcomb, *J. Electrochem. Soc.* **153(12)**, G1039 (2006).
9. E. Spiecker, M. Rudel, W. Jäger, M. Leisner, and H. Föll, *Phys. Stat. Sol. (a)* **202(15)**, 2950 (2005).
10. G.S. Popkirov and R.N. Schindler, *Rev. Sci. Instrum.* **63**, 5366 (1992).
11. G.S. Popkirov, *Electrochimica Acta* **41(7/8)**, 1023 (1996).
12. Z. Hens and W.P. Gomes, *Phys. Chem. Chem. Phys.* **1**, 3607 (1999).
13. Z. Hens and W.P. Gomes, *Phys. Chem. Chem. Phys.* **1**, 3617 (1999).
14. Z. Hens and W.P. Gomes, *J. Phys. Chem. B* **104**, 7725 (2000).
15. J. Carstensen, E. Foca, S. Keipert, H. Föll, M. Leisner, and A. Cojocaru, *Phys. Stat. Sol. (a)* , accepted (2008).
16. M. Leisner, J. Carstensen, A. Cojocaru, and H. Föll, *PSST 2008*, submitted (2008).
17. S. Langa, I.M. Tiginyanu, J. Carstensen, M. Christophersen, and H. Föll, *Electrochem. Solid-State Lett.* **3(11)**, 514 (2000).
18. G.S. Popkirov and R.N. Schindler, *Electrochim. Acta* **39(13)**, 2025 (1994).
19. S. Langa, J. Carstensen, M. Christophersen, H. Föll, and I.M. Tiginyanu, *Appl. Phys. Lett.* **78(8)**, 1074 (2001).
20. S. Langa, I.M. Tiginyanu, J. Carstensen, M. Christophersen, and H. Föll, *Appl. Phys. Lett.* **82(2)**, 278 (2003).

ECS Transactions, 16 (3) 143-155 (2008)
10.1149/1.2982551 ©The Electrochemical Society

Electric Field Effects on the Formation of Isolated Macro Porous Silicon

L. K. Vanga[a], M. K. Oisten[a], T. L. Ritzdorf[b], and P. L. Bergstrom[a]

[a] Department of Electrical and Computer Engineering, Michigan Technological University, Houghton, Michigan 49931, USA
[b] Semitool, Inc., Kalispell, Montana 59901, USA

In this paper, we discuss some of the challenges involved in the formation of isolated vertical pores, thereby describing the electric field effects on the pore formation. The diameters of the pore features under investigation range from 5µm to 20µm. A variety of experiments have been conducted, which include exploration of features with large pyramidal pits, large patterned features with an array of pyramidal pits, and patterned features using a metal mask or a dielectrically isolated etch mask. Macroporous silicon is explored under these parameters for *p*-type (100) and *p*-type (111) silicon substrates using electrochemical anodization. Electric field effects on the pore profile and formation will be discussed using the experimental anodization results and electric field and process modeling analysis related to the formation of isolated pores.

1 Introduction

The dimensions of device features in an integrated circuit are shrinking so as to increase the significance of the dimensions and resulting delays associated with the interconnect (1). Improperly scaled interconnects introduce signal delays that can drastically affect the integrated system performance. With increasingly integrated microelectronic systems, through-wafer interconnect technologies are a promising option to reduce the signal delays between substrates that are integrated in three dimensions (1). Various techniques have been implemented in the past to achieve through-wafer vias with small diameters while maintaining a high aspect ratio. Some of these techniques include Deep Reactive Ion Etching (DRIE), Laser Machining and Electro-Discharge Machining (EDM). However, these techniques are limited by sidewall scalloping, low aspect ratios, machining tailing or reaction byproducts, and micro cracks (2).

Porous silicon has been of great interest because of its demonstrated application in sensing, photonic systems, and as an enabling technology for micromachining (3). Significant background research has built an understanding of the many aspects of the formation of porous semiconductors. These studies include effects on pore formation ranging from parameters like the applied current densities, crystal orientation, masking materials, electrolytic concentration and the impact of doping of the semiconductor substrate. A detailed explanation of the formation of porous silicon is explained elsewhere (4). Most of the studies involving the fabrication of micro- and nanoscaled porous silicon have been performed on anodization regions that are millimeters or larger in scale. We are investigating the fabrication aspects of localized porous silicon with patterned anodization features that are in the microscale.

In general, porous silicon is formed on various substrate types, which include *p*-type, p^+, *n,* and n^+ with crystalline orientations primarily in (100) and (111) substrates. In the case of *p* type substrates for the fabrication of highly vertical and uniform pores, lithographically patterned and chemically etched pore initiation sites are preferred and often necessary. These pore initiation sites are typically the inverted pyramidal pit with sharp tips associated with anisotropic etching of silicon in a suitable etchant. The formation of uniform pores along the <100> direction occurs when positive holes accumulate at the tip of the inverted pyramidal pit due to the reduced radius of curvature, resulting in the decrease of the space charge region (SCR), hence allowing a larger hole current to flow, contributing to the pore propagation. The dimension of this tip must be significantly smaller than the surface roughness of walls of the pit to achieve the geometrical field enhancement at the tip (5, 6).

In our study, we have investigated the formation of porous silicon in features with sizes ranging from 5–20 um that are anisotropically etched, and 5–20 um features that are pre-patterned with an array of much smaller features and anisotropically etched. Both Cr/Au and silicon nitride masking layers were used to selectively form porous silicon on the substrate. Masking materials for defining porous silicon (PS) regions on a silicon substrate can be formed using insulators, metals, or implanted impurities (1, 2, 14). Dielectric masks such as silicon nitride or silicon dioxide are widely used throughout the literature (7, 8, 9). No dielectric material has been demonstrated to uniformly control the formation of porous regions under the mask edge. Metallic masking materials have been recently explored to determine their impact in PS anodization to control the electric field orientation near the mask edge and modulate the direction of current flow through the sample. Pore growth is controlled in part by the direction of the hole current in the substrate. With an insulating masking layer, the total current in the substrate is constrained by the area exposed to the electrolyte, resulting in higher current density at the periphery of each feature than at the center of the feature (8). Current crowding increases the depth of the pores at the edges of the mask compared to those located at the center of the feature, and results in the lateral growth of pores under the mask edge with current-directed or crystallographically-controlled orientations. Silicon nitride masking has the advantage that it is highly resistant to liquid HF etching compared to an Au mask. Sputter deposited gold is prone to pin hole defects that will cause undesired pore formation in the masked areas and will result in mask peeling during the electrochemical anodization experiment.

2 Experimental details

The experiment utilized boron doped *p*-type (100) and *p*-type (111) substrates with resistivity of 10–20 Ω-cm and a thickness of 525 ± 25μm. Isolated pore sites of 5μm, 10μm, 15μm, and 20μm diameter features were lithographically defined in a sputter deposited Cr/Au or Si_3N_4 masking layer on the silicon substrate. All the *p*-type (100) samples were electrochemically etched in an aqueous electrolyte consisting of 10^{-3}M cetyltrimethylammonium chloride (CTAC) and HF (49%), ethanol, and de-ionized water at a volume ratio of 1:2:3. The *p*-type (111) substrates were electrochemically etched in an electrolyte consisting of HF and DMSO (dimethylsulphoxide) at a volume ratio of 5:35.

Galvanostatic setup was employed for all the electrochemical etch experiments. The electrochemical anodization configuration is shown in Fig. 1. The samples were anodized in an electrolyte with a 1:2:3 ratio of 49% HF, ethanol, and deionized water, respectively. Cetyltrimethylammonium chloride (CTAC) at 10^{-3}M was used as a surfactant. The sample fixture was configured to allow isolated electrical connection directly to the metal mask layer. For the first set of experiments the Cr/Au mask was biased using a Keithley 2400 Sourcemeter and referenced to the anode.

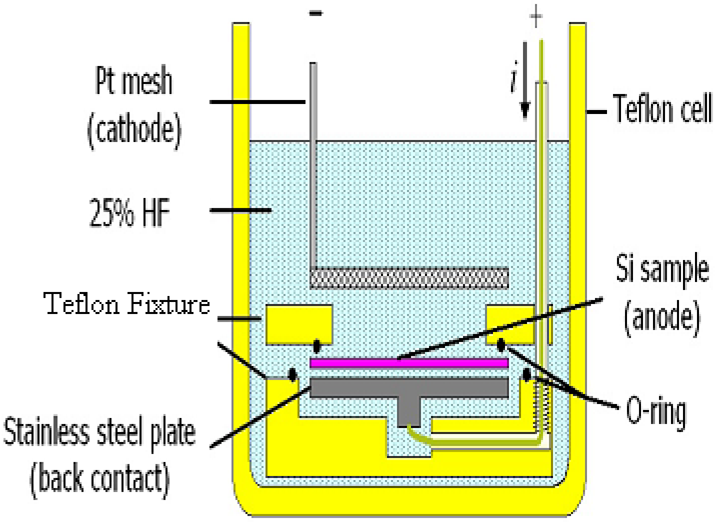

Figure 1. Electrochemical etching cell used in the fabrication of porous silicon.

A typical electrochemically anodized sample is shown in Fig. 2. The sample is exposed to the electrolyte that encompasses the O-ring with an inner diameter of 0.8 cm

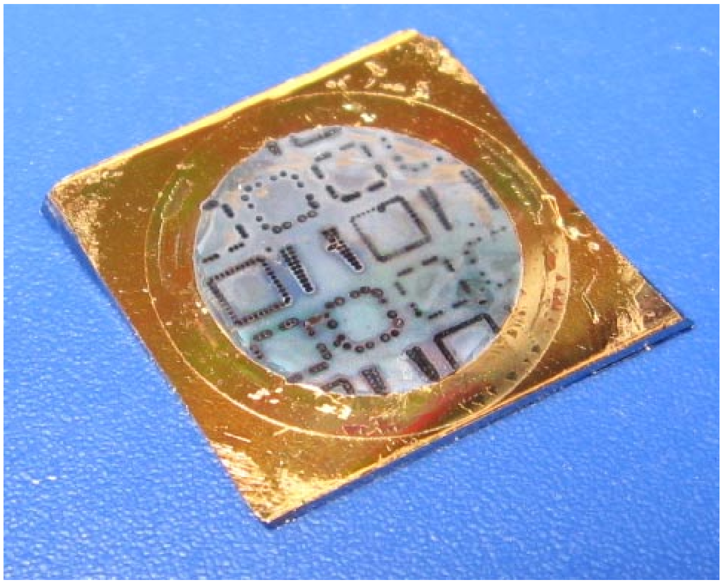

Figure 2. A characteristic electrochemically etched silicon sample with Cr/Au mask.

2.1 Sample configurations utilized in the experiments.

1) ***Sample 1***: This sample consisted of lithographically defined 5–20 um feature sites as shown in Fig. 3. Chromium and gold thin film masking layers 20nm and 250nm thick, respectively, were sequentially deposited using a Perkin Elmer 2400–6J parallel plate RF sputter deposition system and lithographically patterned. The feature sites were chemically etched to expose the silicon substrate surface to the subsequent electrochemical etch process.

2) ***Sample 2***: Isolated inverted pyramidal pits of 5 μm, 10 μm, 15 μm, and 20 μm diameters were produced as shown in the image in Fig. 4. A 200 nm Si_3N_4 masking layer was deposited on the *p*-type (100) silicon substrate in a Perkin Elmer 2400–6J parallel plate RF sputter deposition system. The silicon nitride was lithographically patterned and etched in an oxygen/fluorine plasma chemistry in a Trion Phantom III RIE/ICP etch system. Arrays of inverted pyramidal pits were then formed using anisotropic wet chemical etching techniques.

3) ***Sample 3***: These samples had an array of 2 μm pyramidal pits formed in the larger 5 - 20 μm feature sites as shown in Fig. 5. An array of pyramidal pits is first formed in silicon through a silicon dioxide mask. The silicon dioxide mask layer is RF sputter deposited using a Perkin Elmer 2400–6J parallel plate RF sputter deposition system. When the array of pits is formed, the silicon dioxide layer is stripped from the substrate in BHF solution to allow ohmic contact between the conducting mask layer and the substrate. A 20nm layer of chromium and a 250nm layer of gold were deposited using RF sputter deposition in a Perkin Elmer 2400–6J parallel plate RF sputter deposition system. The lithographically patterned features are then etched in gold etchant and chromium etchant to expose the silicon features for the electrochemical etch processing.

4) ***Sample 4:*** Two experiments are conducted using this sample configuration. A first experiment was performed on a *p* (111) sample with a feature size of 800 μm defined using a shadow mask. A 20nm layer of chromium and a 100nm layer of gold was deposited using RF sputter deposition in a Perkin Elmer 2400–6J parallel plate RF sputter deposition system. The lithographically patterned features are etched in gold etchant and chromium etchant to expose the silicon features to the electrochemical etch processing. A second experiment was performed on the smaller feature sizes of 5-20 μm. A sputter deposited Si_3N_4 layer is used as the masking material. The patterned silicon features are exposed using reactive ion etching in a Trion RIE/ICP plasma etching system.

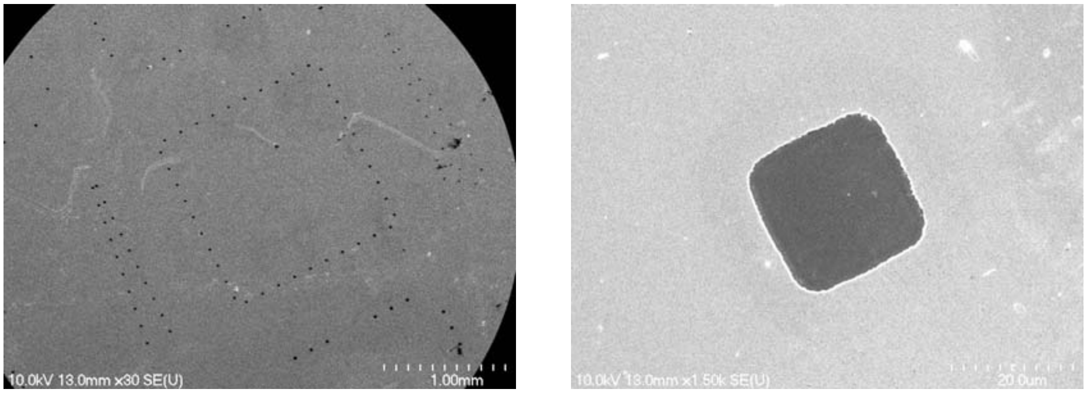

Figure 3. Features on the Cr/Au mask layer. left) Top view of the array of pore features at low magnification; right) single pore site at higher magnification.

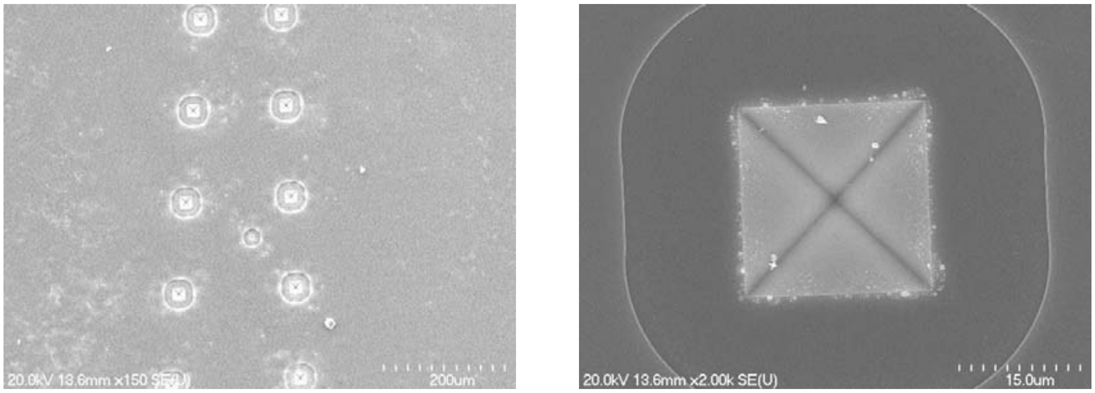

Figure 4. Top view of the 5-20 μm array of large pyramidal pits used in Sample 1 experiments. left) Features at a low magnification; right) a 20 μm isolated pore site at a low magnification.

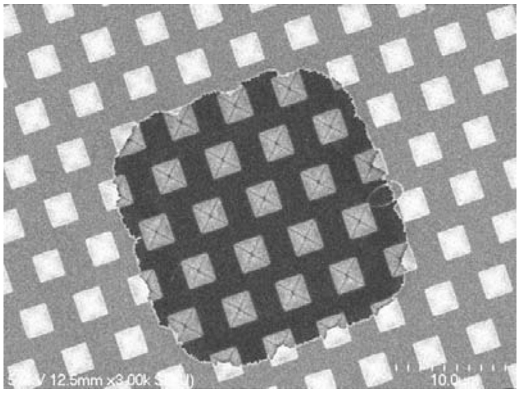

Figure 5. Top view of the 20 μm features patterned with a 2 μm array of pyramidal pits.

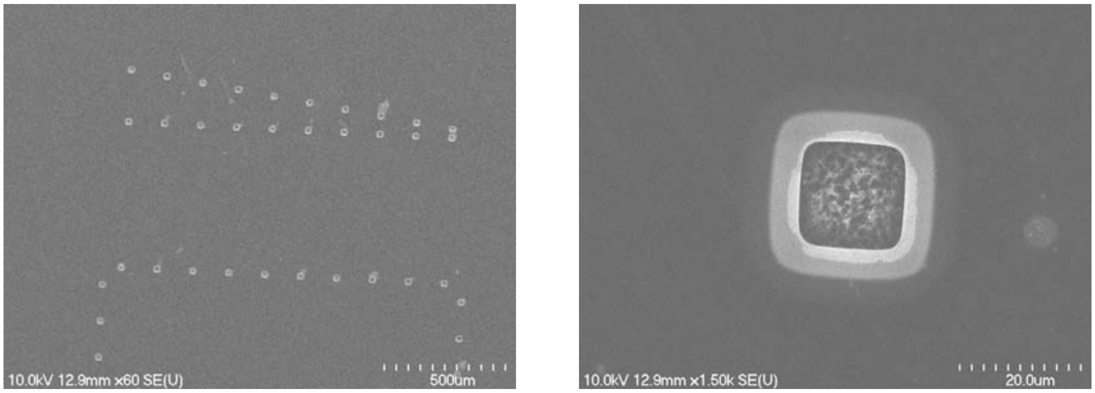

Figure 6. A 2 µm array of pyramidal pits formed in the 5-20 µm feature sites in Sample 2.

The experimental electrochemical anodization conditions are listed in the Table I:

TABLE I. Experimental Parameters used in the formation of porous silicon.

Sample	Applied Current/Current Density(mA/cm^2)/ Etch Time	Vdc (Electrode Potential)
Sample 1	0.2 mA/280/4hours	High 0.4, Low 0.36
Sample 2	0.9 mA/1260/ 3hours	High 4.0, Low 2.5
Sample 3	1.0 mA/1400/3hours	High 2.0, Low 0.48
Sample 4	0.1 mA/140/9 hours	High 0.8, Low 0.7

3 Results/Discussion

The different electrochemically anodized samples are shown in the images below. It is observed that during all of the electrochemical anodization experiments, the electrode potential across the substrate started at a high value and then dropped to a lower value in first few minutes of the experiment. The electrode potential then stabilized and remained constant throughout the experiment. This drop of electrode potential is believed to be characteristic of the pore initiation period. Once a stable pore is formed, the electrode potential remained constant.

3.1 Electrochemically anodized samples.

Sample 1: This sample was electrochemically anodized at a current of 0.2mA.

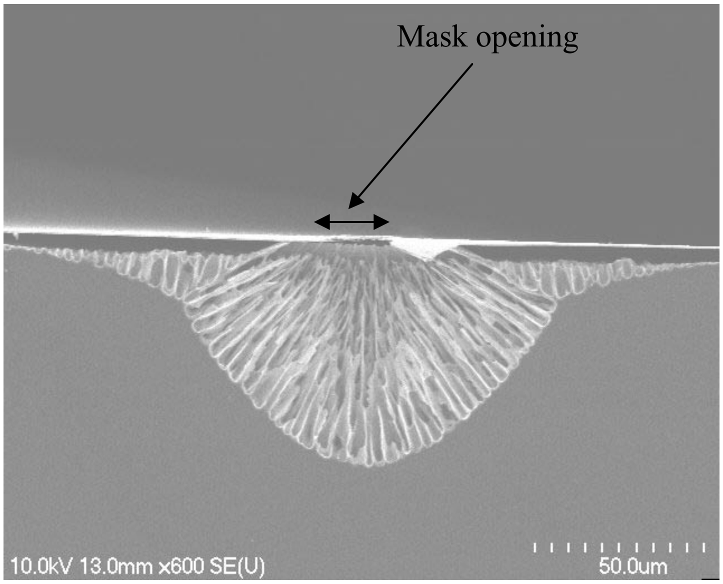

Figure 7. A 20 µm etched feature characteristic for Sample 1.

The results of electrochemical etching in the sample demonstrated considerable etching in the <100> and <111> crystallographic directions, as shown in Fig. 7. The etch rate in the <100> direction was 0.3 µm/minute compared to 0.22 µm/minute along the <111> direction. The low etch rate along <100> and <111> directions is primarily due to the low applied current density that is being used during the electrochemically anodization. From the figure, it can be seen that there is mask undercut, resulting in the formation of macro porous silicon under the mask edge. This mask undercut is appreciable compared to the size of the feature opening. This undercut is primarily due to the undesired etching of the chromium adhesion layer during anodization (10).

The formation of macro porous silicon under the mask is dependent on the electric field distribution across the mask opening and under the mask edge. High electric field at the mask opening compared to the mask edge contributed higher etch rate of macroporous silicon under the mask opening. The low electric field distribution under the mask edge caused to form random pores of significantly lower depths. Current crowding is not significant in the case of a metal mask compared to a dielectric mask. A detailed study on using alternative etch masking layers is discussed elsewhere (11).

Dissolution of silicon occurs in the presence of electronic holes (h+), which are supplied from the anode. Any defect site that is available (in the patterned region of the substrate) will serve as a nucleation site. In the case of Sample 1, the primary nucleation site contribution comes from the surface roughness of the silicon under the feature site or in the mask opening. Hole current will traverse the mask opening from all directions, causing the dissolution of silicon more isotropically.

Sample 2: Figure 8 shows the FE-SEM images of the electrochemically-etched Sample 2. Similar etch profiles were observed by other authors (12, 13) for larger pores.

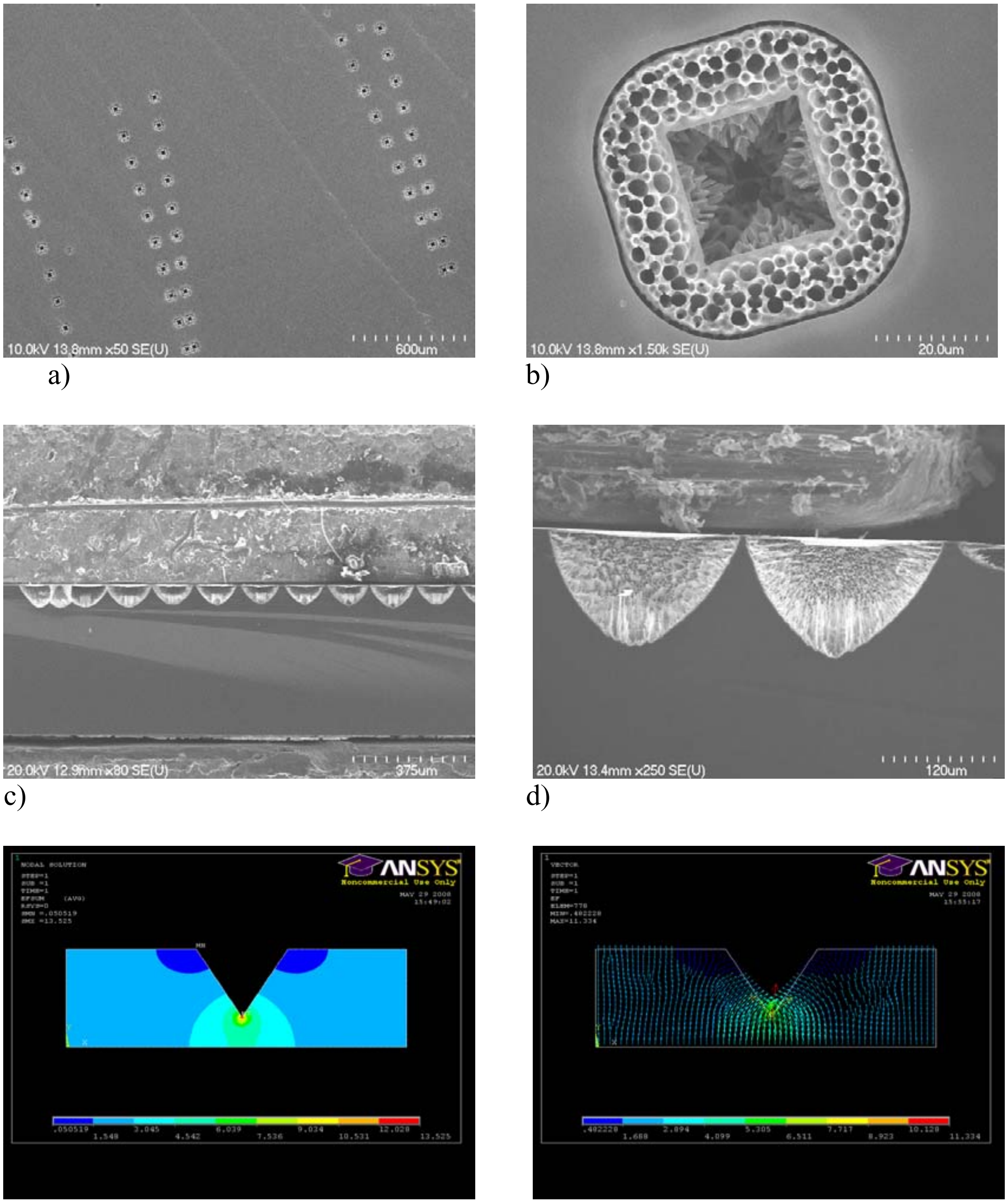

a) b) c) d) e) f)

Figure 8. Electrochemical anodization performed on 5- 20 μm pyramidal pits. a) Top view of array of sites that are electrochemically etched; b) zoomed in top view image of a isolated pore; c) cross-sectional view of anodized region; d) close up view of the pores; e) electric field strength model for a single 20 μm pore; f) electric field direction vectors for a single 20 μm pore.

The results demonstrate considerable etching at the tip and vertices where the (111) planes in the pyramidal pits intersect due to the strong field enhancement in these regions. The combination of the large surface area of the walls along with surface defects serve as undesirable nucleation sites where pore formation occurred as shown in Fig. 8b. The formation of uniform vertical pores is dependent on the pore size and their density in a given region. The pyramidal pits used in the experiment are relatively large with low density, resulting in pores with isotropic etch profile as shown in Fig. 8c and 8d. FESEM cross-sectional images of the pores are shown in Fig. 8c and Fig. 8d. The dimension of this tip has to be significantly smaller compared to the surface roughness of walls of the pit to achieve the geometrical field enhancement at the tip. These walls with surface defects or surface roughness comparable to the dimension of the tip of the pit will serve as an undesirable nucleation site. During the electrochemical anodization, a high concentration of positive holes converge at the tip and also at the vertices, causing the silicon to dissolve. The contribution of these two effects result in the dissolution of the silicon in a nearly isotropic profile as observed. From Fig. 8d, it can be seen that the pore propagates equally in vertical and lateral directions. This is an undesirable result in realizing pores with very high aspect ratio.

For this experiment, the hole current density is too high, so some of these holes reach the relatively low field points under the mask causing the formation of porous silicon and undesirable under etching of the mask. Simple electric field distribution for an isolated pore is modeled using Finite Element Modeling software ANSYS. The electric field distribution of Sample 2 is shown in Fig. 8e. Figure 8f shows the vector plot of the current flow of charge carriers to the tip of the pyramidal pit and also to the vertices of the pit.

Sample 3: Figure 9 shows results for the electrochemical anodization of Sample 3.

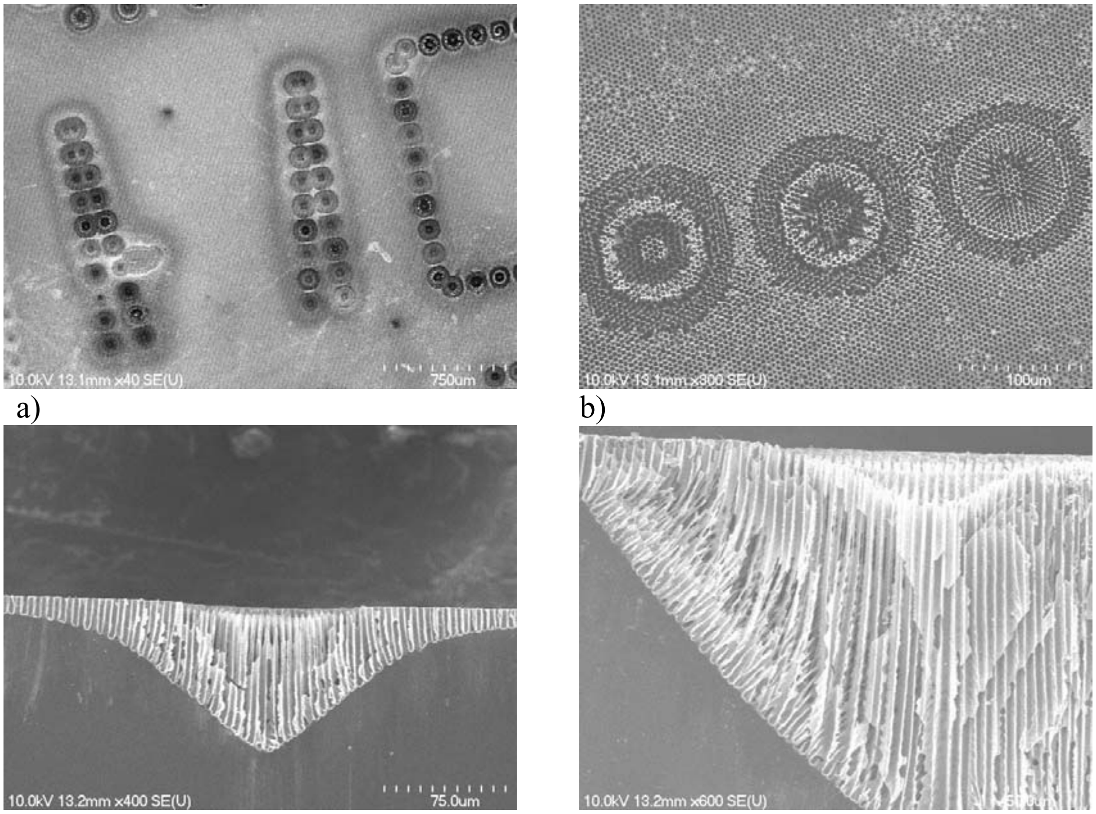

a) b) c) d)

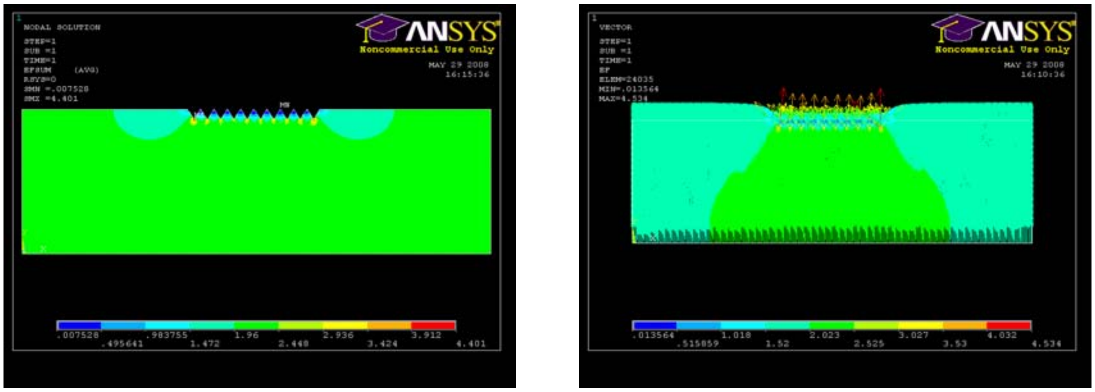

e) f)

Figure 9. Electrochemically anodized samples. a) Top view of array of sites that are electrochemically etched; b) Top view of isolated pore; c) Cross section of isolated pore; d) Zoomed in view of the cross section of isolated pore. e) Electric field strength model for ten 1µm pores; f) electric field direction vectors for for ten 1µm pores.

Sample 3 has 5-20 µm features with pre-patterned 2 µm pore initiation sites. As can be seen from the cross-sectional FE-SEM images, the pore diameters are uniform and highly anisotropic in the <100> direction compared to the etch in the <111> direction. The orientation of the highly vertical pores closer to the mask opening change from the <100> direction to the <111> direction away from the mask opening. This is primarily due to the flow of charge carriers that preferentially travel to the mask opening instead of traversing through the mask. There is a significantly lower but definite etching under the mask edge.

The process configurations for Sample 2 and Sample 3 are modeled using ANSYS. For the case of Sample 2, a 10 µm feature is modeled and for the case of Sample 3, an array of ten densely packed 1 µm pits is modeled. The electric field distribution of Sample 3 is shown in Fig. 9e. Fig. 9f shows the vector plot of the current flow of charge carriers to tips of the pyramidal pits. In the case of a 10 µm isolated pit, the hole current is primarily focused at the tip of the pit, but there are charge carriers that flow to the side walls and vertices due to the current crowding effect, contributing to the etching both in the <100> and <111> direction. In the case of ten 1 µm pits, there are more distributed high field sites for the carriers in the mask opening, resulting in less current crowding and contributing to macroporous silicon formation more uniformly in the <100> direction.

During electrochemical anodization, there is a much higher concentration of electronic holes that reach these high field points causing the dissolution of silicon uniformly (14). From the modeling results, we can see that there is a smaller electric field distribution under the mask edge. Any holes that are attracted to this point will again cause pore formation. In this case, since the substrate was prestructured with pits evenly over the substrate, the pores that are formed are vertical, but with much smaller depths compared to the pore depths under the mask opening.

Sample 4: Figure 10 shows the images of electrochemically anodized Sample 4.

One additional experiment was performed on a relatively large pore site. A 400 µm pore site is patterned on a *p* (111) substrate using a Cr/Au shadow mask. The sample was electrochemically anodized at a current of 0.5 mA.

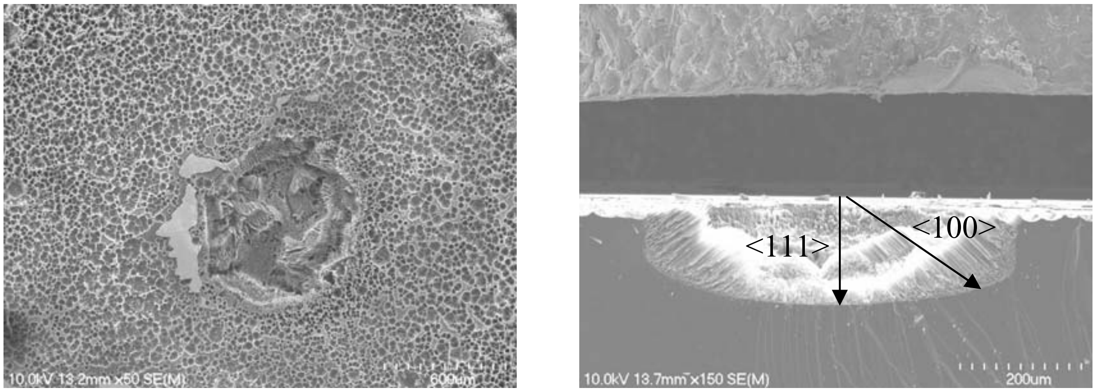

a) b)

Figure 10. Electrochemically anodized *p* (111) sample a) Top view of the electrochemically etched pore site; b) Cross-sectional FE-SEM image of the pore.

The top and cross-sectional view of the electrochemically anodized sample is shown in the images in Fig. 10. In general, porous silicon on *p* (111) can be fabricated with pore dependence on either crystallographic orientation or current dependence. As can be seen in the cross sectional image in Fig. 10a, the pores propagate in the <100> direction and <111> directions. The etch rates along the <111>, <100> and lateral <110> directions are 0.48 µm/minute, 0.66 µm/minute, and 0.83 µm/minute respectively. As can be seen in Fig. 10b, the etch rate along the <100> direction is greater than the <111> direction resulting in greater lateral pore growth than vertical growth. Again, from the modeling results we see that the electric field is much higher at the mask opening compared to the region just under the mask near the opening. We can see that there is pore formation under the mask near the opening due to the high etch rate in the <100> direction. A cumulative result of these two effects is a more uniform pore profile as can been seen in the figure. In order to realize high aspect ratio pores, the electric field distribution in the opening needs to be modulated in such a way that there is a significantly larger electric field at the center of the mask opening compared to edges of the mask opening.

A similar experiment to that just described was performed on features of sizes 5-20 µm. Images in Fig. 11 show the top and cross-sectional view of a sample that was electrochemically anodized.

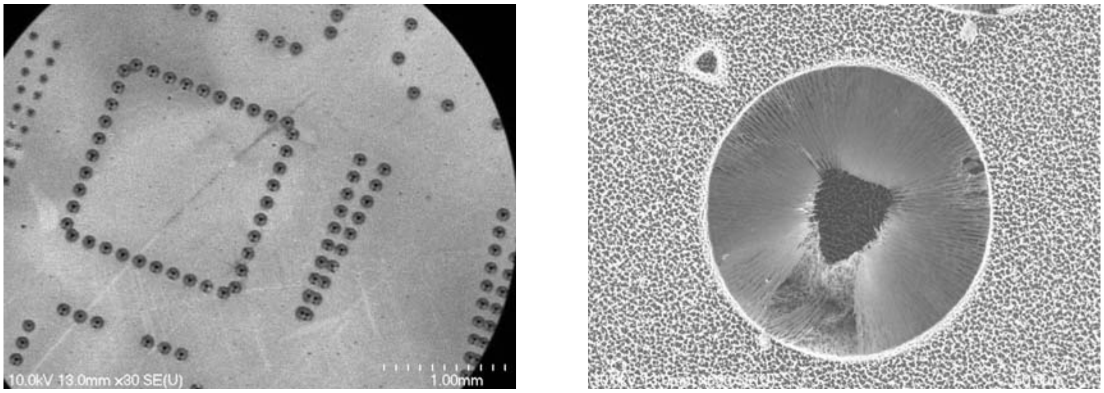

a) b)

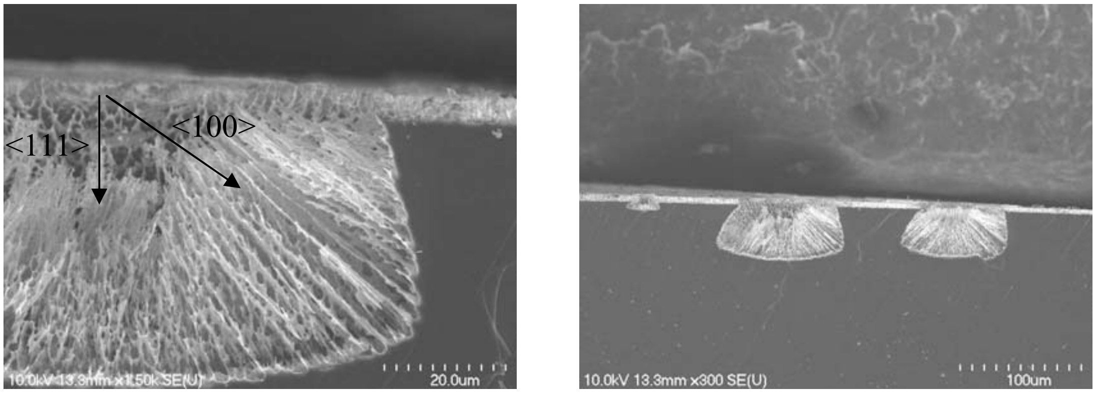

c) d)

Figure 11. Porous silicon formation in *p* (111) silicon. a) Top view FE-SEM image of features patterned in *p* (111) silicon; b) top view of an electrochemically etched feature; c) Cross-sectional FESEM image showing vertical versus lateral pore growth; d) low magnification FESEM image of the cross section showing greater pore growth rate in the <100> direction compared to the vertical (111) direction.

From the image in Fig. 11c, it can be seen that pore formation is in the <100> crystallographic direction as well as in the <111> direction. The pore growth in the *p* (111) substrates is always much lower than for *p* (100) samples (12). Cross-sectional images in Fig. 11c and 11d show the pore depth profile. The pore formation is primarily crystal orientation dependent. The etch rate along the <100> and <111> direction is approximately 0.12 μm/min and 0.09 μm/min respectively. The pore growth along the <100> in general is higher than <111>, and this ratio helps explain the governing parameters associated with the particular etch conditions. The depth of the pore is approximately 53 μm and the width of the pore at the base is approximately 100 μm. The lateral etch at the top of the pore, near the mask opening is approximately 44 μm. The lateral width at the bottom of the pore is approximately 100 μm. From the profile of the porous region, we can see that the sidewalls of the pore are relatively vertical when compared to experiments performed on the *p* (100) samples.

Conclusions

From the experiments on the large pyramidal pits, we conclude that it is difficult to directly achieve isolated pores with high aspect ratio. Formation of porous silicon on features that are patterned with an array of pyramidal pits give better results compared to the larger isolated pyramidal pits. This alternate process gives more uniform results due to the high density of pore initiation sites compared to the isolated pore. Dissolution of porous silicon to achieve large pores with uniformity and high aspect ratio is promising. Experiments on *p* (111) samples gave more vertical sidewalls for the porous region at the expense of significantly lower etch rates than for *p* (100) substrates and significant increase in lateral dimension of the resulting porous region. The realization of individual and isolated pores remains an elusive challenge since field dependence is not the sole processing parameter defining the formation and orientation of pores. The studies reported do indicate that proper management of electric field profiles can improve the anisotropy of pore formation in a region and under a mask edge.

Acknowledgements

The authors would like to acknowledge support from the Engineering Research Centers Program of the National Science Foundation under Award Number EEC-9986866.

References

1. Akinobu Satoh, *Jpn J. Appl. Phys*. **39**, 378-386 (2000).
2. Shuji Tanaka, Satoshi Fujimoto, Osamu Ito, Seong-Hun Choe and Masayoshi Esashi, *J. Micromech. Microeng*. **17**, 597–602 (2007).
3. Ponomarev E.A.1; Lévy-Clément C. Journal of Porous Materials, Volume 7, Number 1-3, , pp. 51-56(6), January 2000
4. R.L. Smith and S.D. Collins, J. Appl. Phys., pp. R1–R22, 71 (1992)
5. V. Lehmann and H. Föll, *J. Electrochem. Soc*., **137**, 653-659 (1990).
6. Akinobu Satoh, *Jpn J. Appl. Phys*. **39**, 1612-1621 (2000).
7. J. Zheng, M. Christophersen and P. L. Bergstrom, phys. stat.sol. (a) 202, 1402, (2005).
8. K. Grigoras, S. Franssila, T. Sikunen, T. Kotiaho, R.Kostiainen, phys. stat. sol. (a) 202, 1624 (2005).
9. M. Christophersen, P. Merz, J. Quenzer, J. Cartensen, H.Föll, phys. stat. sol. (a) 182, 561 (2000).
10. Bien D.C.S.; Rainey P.V.; Mitchell S.J.N.; Gamble H.S. J. Micromech. Microeng., S34–S40, 13 (2003)
11. Bell T.E.; Gennissen P.T.J.2; DeMunter D.2; Kuhl M.3, Journal of Micromechanics and Microengineering, Volume 6, pp. 361-369(9), Number 4, 1996
12. M. Guendouz [a] , P. Joubert[a], M. Sarret[b] Material Science and Engineering 43-47, B69-70 (2000)
13. V. V. Starkov, phys. stat. sol. (a) 197, No. 1, 22– 26 (2003)
14. Yi Tao, Masayoshi Esashi, J. Micromech. Microeng., 1411–1415, 14 (2004)

ECS Transactions, 16 (3) 157-172 (2008)
10.1149/1.2982552 ©The Electrochemical Society

Growth Modes of Macropores in n-Type Silicon

A. Cojocaru[a], J. Carstensen[a], and H. Föll[a]

[a] Institute for Materials Science, Christian-Albrechts-University of Kiel, Kaiserstrasse 2, 24143 Kiel, Germany

The growth of macropores in Silicon under galvanostatic conditions always terminates at some maximum depth by some growth mode transition, e.g. from pore growth to cavity formation. It will be shown that macropore growth in lightly doped n-type Si under back side illumination may experience several different kinds of growth mode transitions, including some new ones; in particular if new and improved electrolytes are used. Existing models of macropore growth cannot account for these mode transitions and need to be augmented.

Introduction

There is an astonishing diversity of pores in semiconductors, cf. for example the overviews given in (1 - 6). From a purely geometric point of view one finds micropores, mesopores and macropores, i.e. pore diameters span the range from 1 nm to > 10 µm. Pores with the same geometry may have distinctly different morphologies ranging from straight cylinders to heavily branched or random sponge configurations. Next, pores may grow in preferred crystallographic directions ("crysto" pores), including unusual ones like <113> in Si, or they may grow in current flow direction ("curro pores"), i.e. perpendicular to equipotential planes (7 - 9). Moreover, pores may express strong self-organization issues, be it in the form of self-induced current oscillations inside the pore, or in geometric arrangements showing some degree of order in one, two or even three dimensions, including fully expressed pore single crystals (10).

In any suitable experiment some species of pores will grow that can be characterized by the criteria given above, and these pores then express one possible pore growth mode of the semiconductor-electrolyte system investigated. The necessary conditions to induce a certain selected growth mode are known to some extent and most easily expressed in the self-explaining shorthand notation introduced in (2). In Si, we have for example the classical n-macro(bsi, aqu) pores, i.e. straight cylindrical macropores obtained under back side illumination in aqueous HF-based electrolytes. It is implicitly understood that these pores, obtained in low doped {100} substrates, are crysto pores, and not given to self-organization of any kind. However, just looking at SEM pictures of typical n-macro(bsi, aqu) pores, it is not possible to tell if one has <100> crysto or curro pores because both types would grow perpendicular to the surface. Only after the work of Rönnebeck et al. (11) we can state with confidence that usually we have n-macro(bsi, aqu, crysto) pores, at least for most of the parameter space explored so far. With the same kind of reasoning, finding straight pores in a random (if closely packed) arrangement in the case of n-macro(bsi, aqu, avalanche breakdown, random nucleation) pores does not prove that there are no self-organization issues to be found in the respective pore growth mode – demonstrations to the opposite have been made in (12). It is perfectly possible, for example, that even in a galvanostatic experiment the current flowing through just one pore shows strong self-induced oscillations, since without synchronization of the current phases between the typically > 1 million pores produced in one experiment the external current would average to a rather constant value. In conclusion, it is not clear (and actually rather unlikely) that all parameters inherent in some growth mode that produces pores in semiconductors are actually known, and it is perfectly possible that completely different growth modes result in similar pore structures. The lack of detailed knowledge about growth modes stems from a lack of in-situ data – nobody until recently could know what exactly is going on at the tip (and at the walls) of a growing pore.

Generally speaking, until recently all data that characterize a certain pore growth mode came from monitoring external quantities (e.g. current $I(t)$, voltage $U(t)$, illumination intensity $P(t)$, and temperature $T(t)$), from knowing certain basic chemical and system properties (reaction equations, *IU* characteristics, …), and from "post-mortem" or ex-situ analysis of the pores obtained. Recently the situation has changed with the advent of model-based in-situ FFT impedance spectroscopy (IS) in two different modes as described in (13). In-situ direct pore data as, for example, the dissolution valence n, the pore depth d_{pore}, the instantaneous growth speed $v_{\text{pore}} = \mathrm{d}(d_{\text{pore}})/\mathrm{d}t$ can now be obtained routinely (together with 7 more in-situ parameters) during n-macro(bsi, aqu) etching experiments. In-situ FFT IS "raw" data can now be obtained during any pore etching experiment (some examples are given in (13 - 16)), but only for n-macro(bsi, aqu) pores is modeling advanced enough to allow extraction of the important direct parameters from the raw impedance data as detailed above.

The new tool has been applied to etching n-macro(bsi, aqu) pores in a far larger than usual parameter space that can be described by i) going far above the usual HF-concentration limit of $c_{\text{HF}} < 5$ wt.% and ii) by adding carboxylic acids (mostly acetic acid (HAc); and / or carboxymethylcellulose sodium salt (CMC)) in various concentrations to the electrolyte. CMC makes the electrolyte viscous; in shorthand it will be denoted as "visc".

All together this describes a huge extension of the parameter space and it has not yet been fully explored. Nevertheless, remarkable results have already been obtained, e.g. a new growth mode that allows growing macropores much faster than before (17) and completely new self-organization issues as expressed in the ex-situ pore morphology. Generalizing, it was found that there is more than one distinctive growth mode for n-macro(bsi, aqu. HF, HAc, visc.) pores, and that there are clear transitions between different growth modes that may or may not affect the macroscopic pore geometry and morphology.

Growth mode transitions, or mode transitions for short, are nothing new in semiconductor pore etching research. They may occur as a result of external "switching", e.g. by abruptly changing current or voltage, or as intrinsic or self-induced transitions. Examples for the former include the well-known technique of increasing the current to disattach a layer of micropores in Si (1), the structures observed with n-macro(org., breakdown) pores in (12), or the switching back-and-forth between <111> crysto pores and curro pores in {100} n-type InP (7, 18, 19). Note that this crysto-curro transition can also be induced in {111} n-type InP (20) but that it is hardly visible in an ex-situ analysis since both pore types look pretty much the same. Self-induced mode transitions are also quite common – the termination of standard n-macro(bsi, aqu) pore growth at some depth by cavity formation may be seen as such a mode transition. More subtle, perhaps, are self-induced or externally triggered transitions between a "straight pore" growth mode and the "pore with diameter oscillation" mode observed in InP; see for example (21). It stands to reason that mode transitions have occurred and may occur without being recognized as such by ex-situ analysis, and that a better understanding of this topic will lead to a better understanding of pore etching in semiconductors.

This paper deals with some pronounced mode transitions found during the etching of n-macro(bsi, (5 – 20) wt.% HF aqu., HAc, visc.) pores. While some findings are unique, some of the results (and the explanations offered) must be seen as tentative; much more research is needed to exhaust the issue raised here.

Experimental Details and Framework for Establishing Pore Geometries

In most experiments low-doped (100) oriented n-type Si wafers with a resistivity of 5 Ωcm were used for etching the macropores. An implanted and annealed n^+ layer on the back side of the wafer provided the necessary good ohmic contact to the sample. The samples were pre-structured by standard photolithography (hexagonal lattice, lattice constant a = 4.2 µm). Etching was performed at 20 °C in a fully integrated etching station from ET&TE GmbH with full control of all parameters including back side illumination (bsi) by an LED matrix and an integrated fast dual-mode Fourier transform (FFT) impedance spectrometer (IS) that took a complete spectrum every second, alternating between the (classical) current-voltage mode and the new bsi illumination mode. From the impedance spectra 10 in-situ parameters, including the actual pore depth, the valence of the dissolution process, or the instantaneous growth rate, were extracted and displayed in real time; cf. (13, 22) for some details. Electrolytes were always of the constitution mentioned above; details will be given (in obvious "short-hand") in the context of the experiments.

Given the seed lattice geometry expressed by a lattice constant a, the pore diameter r_{Pore} (r_{Pore} = pore radius) for the hexagonal geometry is expected to follow (1)

$$r_{\text{pore}} \approx 0.91\ a\ (j_{\text{tip}} / j_{\text{PSL}})^{1/2}, \qquad [1]$$

with j_{tip} = current density at the pore tip (referenced to the pore across-sectional area), j_{PSL} is the current density the first peak in the IU characteristics. Eq. [1] allows to define a range of r_{pore} values and current densities j_{tip} that go with it. However, already at this point we introduce an "optimal" pore radius r_{opt} and a concomitant "optimal current density" j_{opt} that are necessary for particularly stable pore growth. In a first approximation, the optimal radius r_{opt} is just the maximal radius allowed at the beginning of the experiment, taking into account that the pore wall thickness cannot be smaller than twice the space charge region thickness d_{SCR}, i.e.

$$r_{\text{opt}} = r_{\max} = a/2 - d_{\text{SCR}}. \qquad [2]$$

The existence of such an optimal current is also demanded by the so-called "current burst model" (CBM) as outlined in (2, 23, 24); it gives the same r_{opt} as defined above for the beginning of the experiment.

As the pore grows into the depth, the empirical relation that the current density j_{PSL} of the so-called PSL peak in the IV characteristics is given as $j_{\text{PSL}} \sim \text{const.}\ (c_{\text{HF}})^{1.5}$ (1) must be taken into account, and $j_{\text{tip}}\ (t)$ must be chosen accordingly. However, the galvanostat can only be programmed to run a certain $I(t)$ profile. The relation between $I(t)$ and $j_{\text{tip}}(t)$ is quite complex since some of the current will be leakage current (i.e current flowing through the pore walls) and the areas to which the current density is referenced may change with the pore depth because of, e.g., under-etching at the O-ring or mask, and because the pores may change in geometry and morphology with depth. As a consequence, r_{opt} as defined by Eq. [2] and by the CBM may no longer be identical with increasing pore depth, and this dichotomy is amplified at large HF concentration (and thus current densities). The existence of some r_{opt} (and in parallel some j_{opt} for the current density at the pore tip) is an almost unavoidable conclusion form the experiments reported here and in (17, 25, 22).

This framework is introduced already at this point to facilitate the description of the results presented below. However, given the uncertainties inherent in all of the parameters discussed above for the types of electrolyte discussed here, j_{opt} is not (yet) an exact number but only a guideline for the discussion of what follows.

Results

Self-Induced Anti-Phase Diameter Oscillations

The most spectacular (and unexpected) finding in the parameter space described was a mode transition from “straight pores” to pores with self-induced anti-phase diameter oscillations as shown in **Fig. 1**. This kind of behavior will always be found if the basic pore growth mode is governed by diffusion limitations *and* if the current chosen is close to $j_{\text{opt}}/2$ giving pores with radius $\approx r_{opt}/\sqrt{2}$.

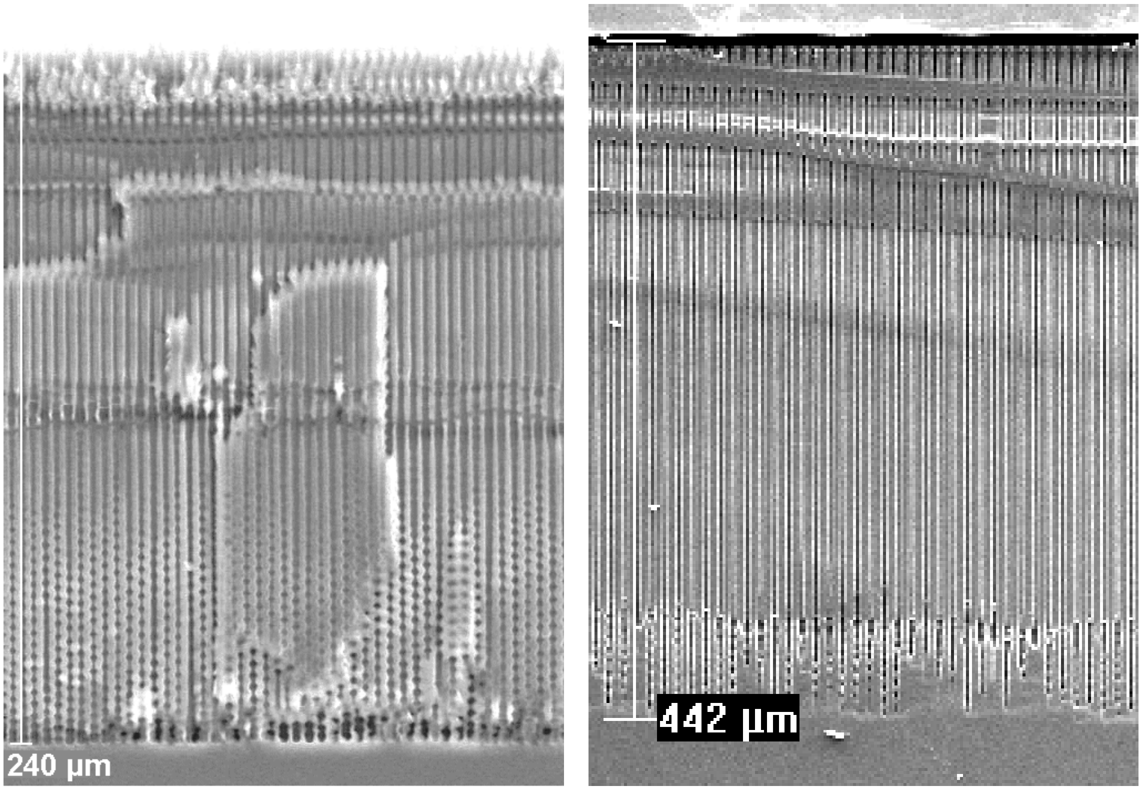

a) b)

Figure 1. a) Self-induced “anti-phase” pore diameter oscillations in macropores in n-type Si. a) 15 wt.% HF aqu. + 0.42 g/l CMC - electrolyte, b) 20 wt.% HF aqu. + 18 wt.% butyric acid. Note that pore growth would have terminated around 130 µm without the addition of the organic acids (17).

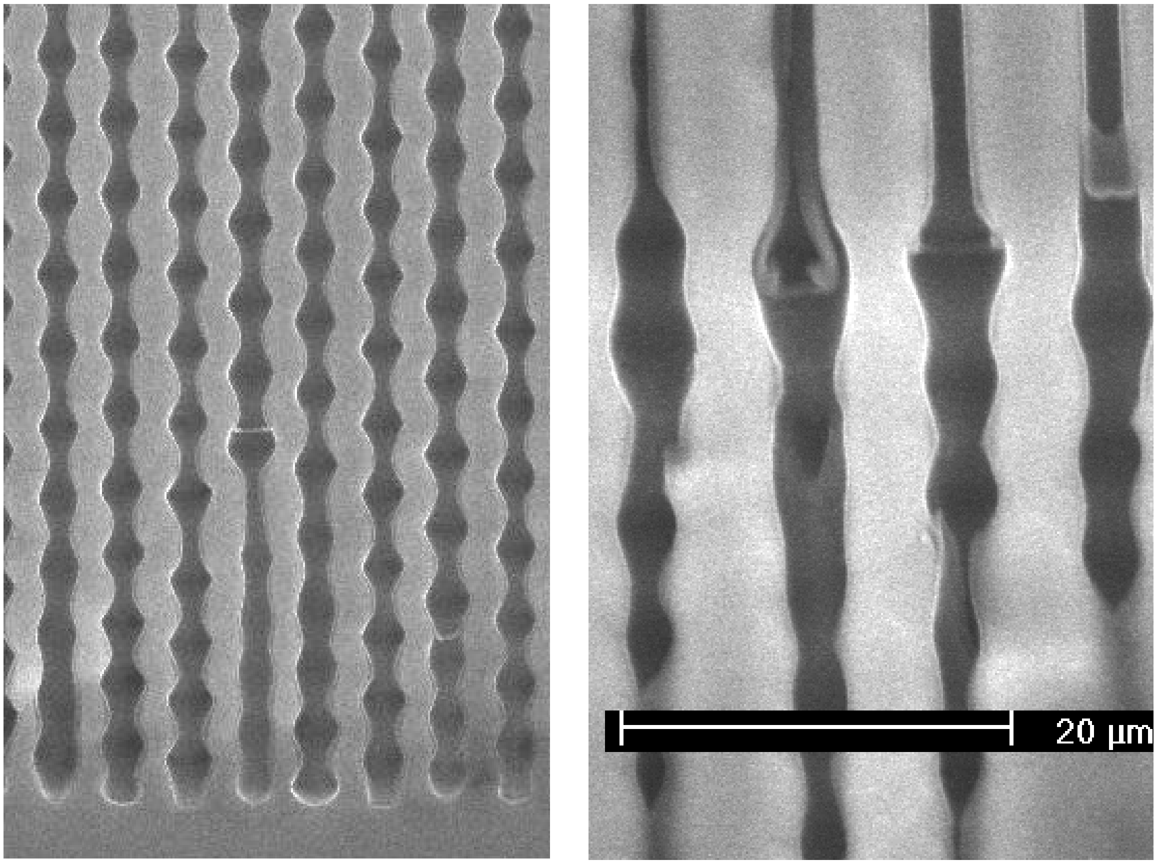

a) b)

Figure 2. a) Details from the sample in **Fig. 1** a). b) Details from the sample in **Fig. 1** b).

The two pictures serve to illustrate that the phenomenon occurs not just at a single point in parameter space; by now we have observed it >10 times. In **Fig. 1** a) the mode transition occurs about half way down; the onset of the oscillations starts right away in some parts of the sample and apparently somewhat delayed in other parts. It is interesting to note that **Fig. 9.19** in Lehmann's book shows what might be the onset of anti-phase oscillations at a 15 wt.% HF aqu. electrolyte at a depth of about 80 µm (1).

Fig. 2 a) shows some details of the pore arrays given in **Fig. 1**. In **Fig. 2** a) it becomes clear that the mode transition also means a transition in the lining of the pores, which most likely consists of microporous Si.

It is worthwhile to note in this context that the anti-phase structure shown in **Figs. 1** and **2** cannot have the hexagonal symmetry of the pore array for the simple geometric reasons outlined in **Fig. 3**. In other words, a cut at right angles to the {110} Si plane realized in **Figs. 1** and **2** cannot show anti-phase diameter oscillations.

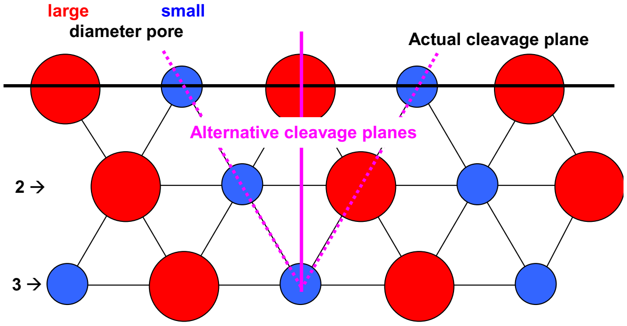

Figure 3.
The impossibility of having anti-phase diameter oscillations in a hexagonal symmetry. The cleavage plane indicated by a bold black line would show anti-phase oscillations, all other possible cleavage plane will either show constant diameters or some succession of "thin" and "thick" pores.

Of course, on the second and third {1 -1 0 0} plane of the hexagonal lattice the large and small pores could be interchanged, allowing several possible "frustrated" structures. If the anti-phase diameter oscillations as shown in **Fig. 1** will be observed in an ex-situ SEM picture, typically obtained from specimens "randomly" cleaved, may thus be a bit accidental. This particular mode transition is also found in the dual-mode in-situ FFT IS data, **Fig. 4** gives an example.

Since dual-mode in-situ FFT IS allows to extract the actual pore depth $d_{\mathrm{pore}}(t)$, all other parameters (originally measured as a function of time) can be displayed as a function of pore depth as demonstrated in **Fig. 4**. How the data are extracted and exactly how they are defined is detailed in (25); here we focus on the first curve showing the actual pore tip speed v_{tip} in µm/min; the second curve showing the collection efficiency of a pore tip in terms of the difference of recombination velocity S_{P} between pore tip and in between pore tips (expressed as $\Delta(D/S_{\mathrm{P}})$; D = diffusion coefficient of holes); and the last curve showing the valence n of the dissolution process. The other curves show parameters like resistances, capacities, time constants and hole diffusion properties; all with a well-defined meaning outlined in (13, 25 - 27). Looking just at the v_{tip} curve one notes pronounced minima at about 40 µm, 90 µm and 100 µm – all announcing mode transitions. In fact, looking closely at the SEM picture in **Fig. 1** and **Fig. 4**, the mode transitions at 40 µm and 90 µm can be seen in addition to the prominent transition to anti-phase oscillations around 100 µm. Note that the mode transition to self-induced or intrinsic oscillations of pore diameters and pore current is very prominent in the SEM pictures but not in the IS data. This is as it should be because the average over millions of pores as measured by IS did not change for many of the parameters recorded. In fact, looking e.g. at the so-called transfer resistance R_{P} (and some other parameters) it becomes evident that a true steady-state is only reached at a pore depth of about 140 µm when the anti-phase oscillations have fully developed. This is easy to understand in the light of the j_{opt} discussion from above. In the region of the anti-phase oscillations only one half of the pores grows at any instant in time, the other half is dormant. The actual current density in a pore now reaches j_{opt} as long as it is active, promoting more stable growth in (average) steady state.

At this point the IS results just serve to demonstrate that large deviations from a generally expected (slowly and smoothly) changing steady-state may be encountered during macropore growth in n-type Si, some but not all of which might be expressed in visible mode transitions of the pore growth. More examples to this point are given in (25).

Externally Induced Mode Transitions

Mode transitions, in a general way of reasoning, happen because the current at the pore tip deviates too much from a system-immanent optimal value with increasing pore depth, forcing the pores to "do" something about it. Options for "doing" are, e.g., switching the current periodically between subsets of pores as in the example above, changing the pore diameter and therefore the current density concomitant with appropriate changes of the growth speed, and changing the valence, i.e. the mix of dissolution processes within a (at present somewhat unclear) bandwidth.

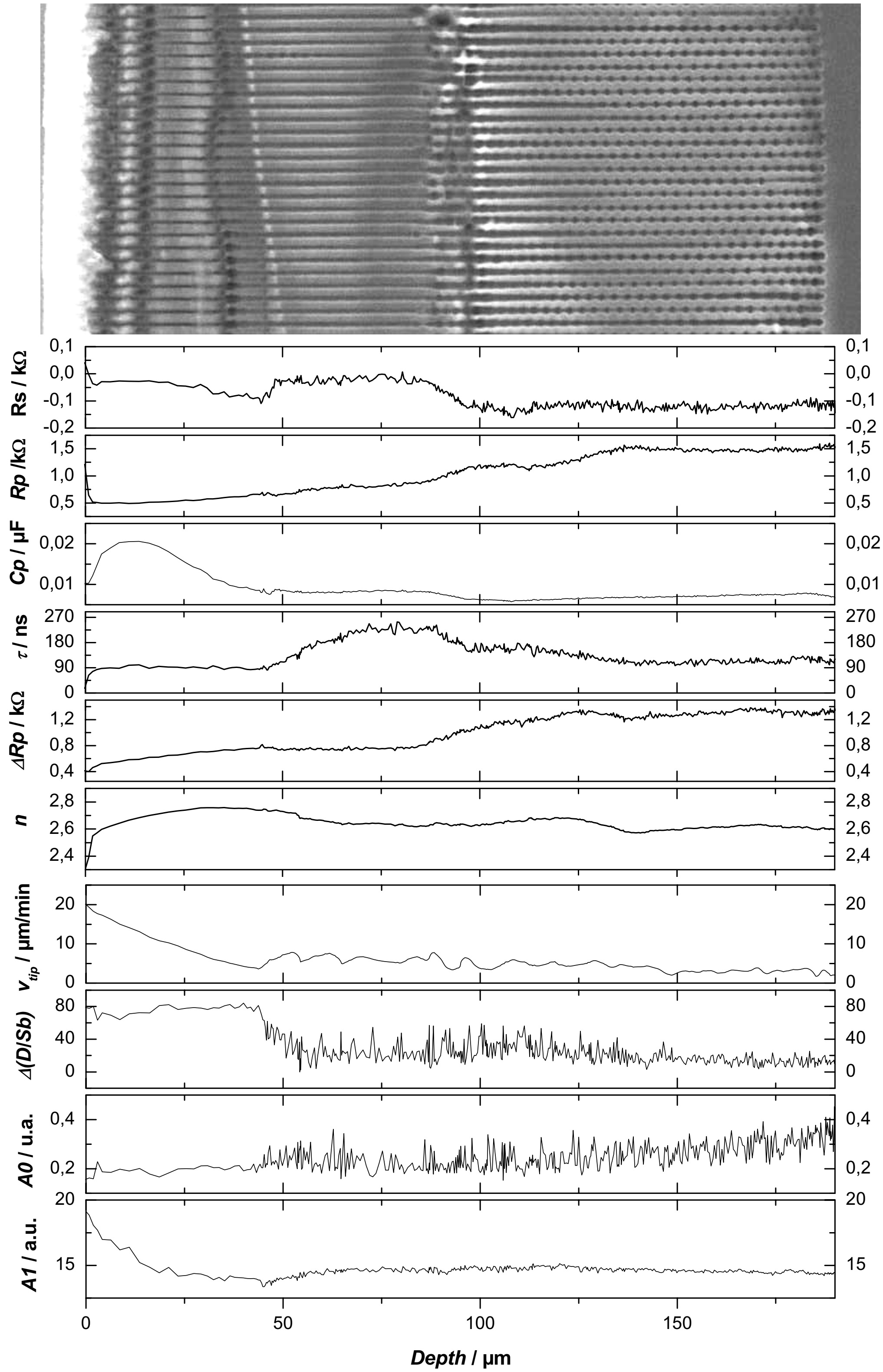

Figure 4. Impedance parameters vs. pore depth in direct comparison with the etched pore morphology. An aqueous electrolyte with an HF concentration of 15 wt.% aqu. and 0.42 g/l of CMC was used. The applied voltage was 1.0 V and the etching current decreased from 26 mA/cm^2 to 16 mA/ cm^2 during the total etching time of 117 min. Further data: $T = 20°C$; n-type Si, (100), 5 Ωcm, pre-structured by standard photolithography, hexagonal lattice $a = 4.2$ µm.

The mode transitions achieving the desired result may occur suddenly or gradually; depending on general etching uniformity and on some self-amplifying mechanism (like the one that tends to keep the pore front straight; cf. (28)). All in-situ measurements (including FFT IS) average over all pores and it must be expected that even if rather sharp transitions occur in some small part of the specimen (as seen in a SEM picture) they might be smeared out in data averaged over the whole specimen area (and the always deviating parts around the O-ring). As shown most clearly in InP (20), intrinsically occurring but often somewhat “blurred” transitions can be made quite sharp by “shuttling” the system between two states, e.g. by switching the current periodically between two distinct values. **Fig. 5** shows what one obtains with this technique under conditions that would otherwise lead to self-induced anti-phase diameter oscillations as shown above. The only difference to **Fig. 1** a) is that the current I_0, after an initializing period of 5 min., corresponding to a pore depth $d_{\text{pore}} \approx 35$ µm, is switched between I_0 and $I_0/2$ every 1 min, i.e. with about the same frequency as found previously for the self-induced oscillations. Both, upper and lower current then decrease smoothly according to the “Lehmann model” to compensate for diffusion. Note the first mode transition at the onset of the current switching (arrow 1) and the two following transitions marked by arrows 2 and 3 where the growth mode changes without changes in any external parameter.

The result of this experiment is remarkable for several reasons. First, the experiment is started at the high current density value, at the onset of the current switching the current is decreased by 50 %. The pore diameters, however, *increase* by a substantial amount as can be clearly seen in **Fig. 4** b). This is completely unexpected because the standard macropore growth model couples the diameter to the current via Eq. [1]. As shown in many experiments by the Halle group (29, 30), while the relation between current density and pore diameter is more complex than what is expressed in Eq. [1] for standard 5 % electrolytes, the *sign* of the diameter variation is always the same as that of the current variation, and the resulting pore diameter variations then do not indicate mode transitions but just the bandwidth of one basic pore growth mode. The large *decrease* of the current density in the experiment shown here thus signals a true growth mode transition by definition.

Second, the system undergoes two more mode transitions as the pores grow into the depth of the sample. At the position indicated by arrow 3, the growth speed decreases suddenly by a factor of about 3, clearly indicated by the shorter “wavelength” (**Fig. 5** b)). At the position indicated by arrow 3, the growth speed drops sharply once more; the wavelength is now so short that it is hardly visible in **Fig. 5** a) but clearly seen in the detailed picture in **Fig. 5** d). It also should be noted that a continuation of the experiment would produce yet another mode transition – most likely cavity formation and thus termination of pore growth.

As in the case of the pores with self-induced anti-phase diameter oscillations, the results are reproducible and this behavior is found in a large (but not yet fully specified) area in the “viscous – large c_{HF}” region of the parameter space.

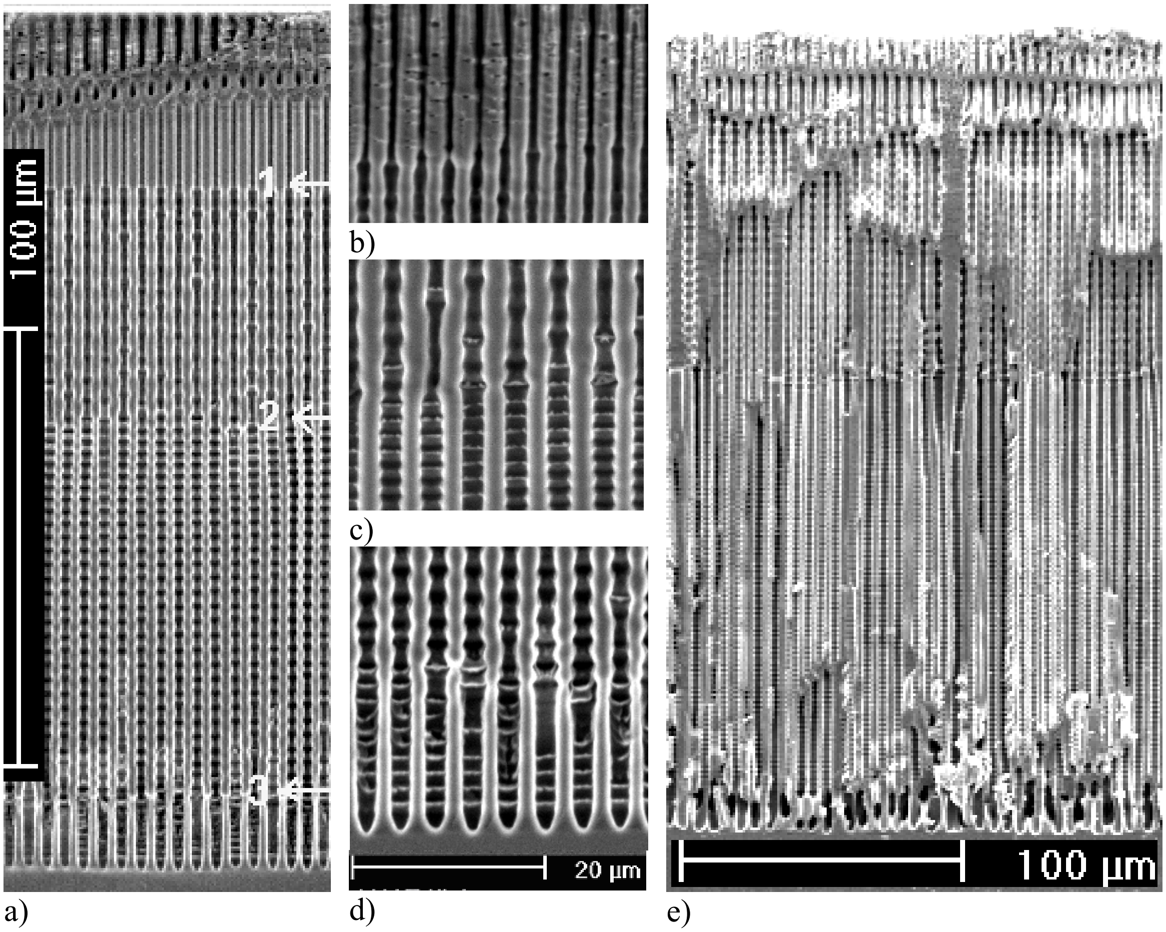

Figure 5. a) Macropores in n-type Si; 15 wt.% HF aqu. + 0.83 g/l CMC electrolyte; 1.0 V applied voltage. After 5 min. of constant current, the current was stepwise modulated from 26 mA/cm^2 to 16 mA/ cm^2 with a period of 2 minutes during the total etching time of 105 min. T = 20°C; n-type Si, (100), 5 Ωcm, pre-structured by standard photolithography, hexagonal lattice with lattice constant a = 4.2 µm.
b), c), d) show details at the boundaries indicated by arrows 1, 2, and 3, respectively.
e) The same etching parameters as in a) except for a 15 wt.% HF aqu + 0.42 g/l CMC electrolyte, and an etching time of 245 min.

The post-mortem data contained in the SEM pictures shown in **Fig. 5** (and in many similar pictures not shown here) provide much input for speculations about mechanisms but will hardly be sufficient to allow unambiguous conclusion and process modeling. It is thus of interest to correlate the ex-situ SEM analysis with multi-mode in-situ FFT IS. **Fig. 6** shows the result of one experiment presented in the same way as discussed for **Fig. 4**. It would be precocious to claim that the wealth of information contained in the data has been fully evaluated and understood, but a few points can be made. First, the external current swings are seen in some but not all the parameters measured; this could be expected to some extent. The valence n, for example is little affected by the external input but starts some periodic variations on its own (like some of the other parameters) towards the end of the experiment that are reminiscent of the behavior observed for “viscous” electrolytes, see (17, 28) for more details. The in-situ measured growth speed shows the sudden decreases (especially if plotted with an expanded scale) but also some more details not seen in the SEM picture.

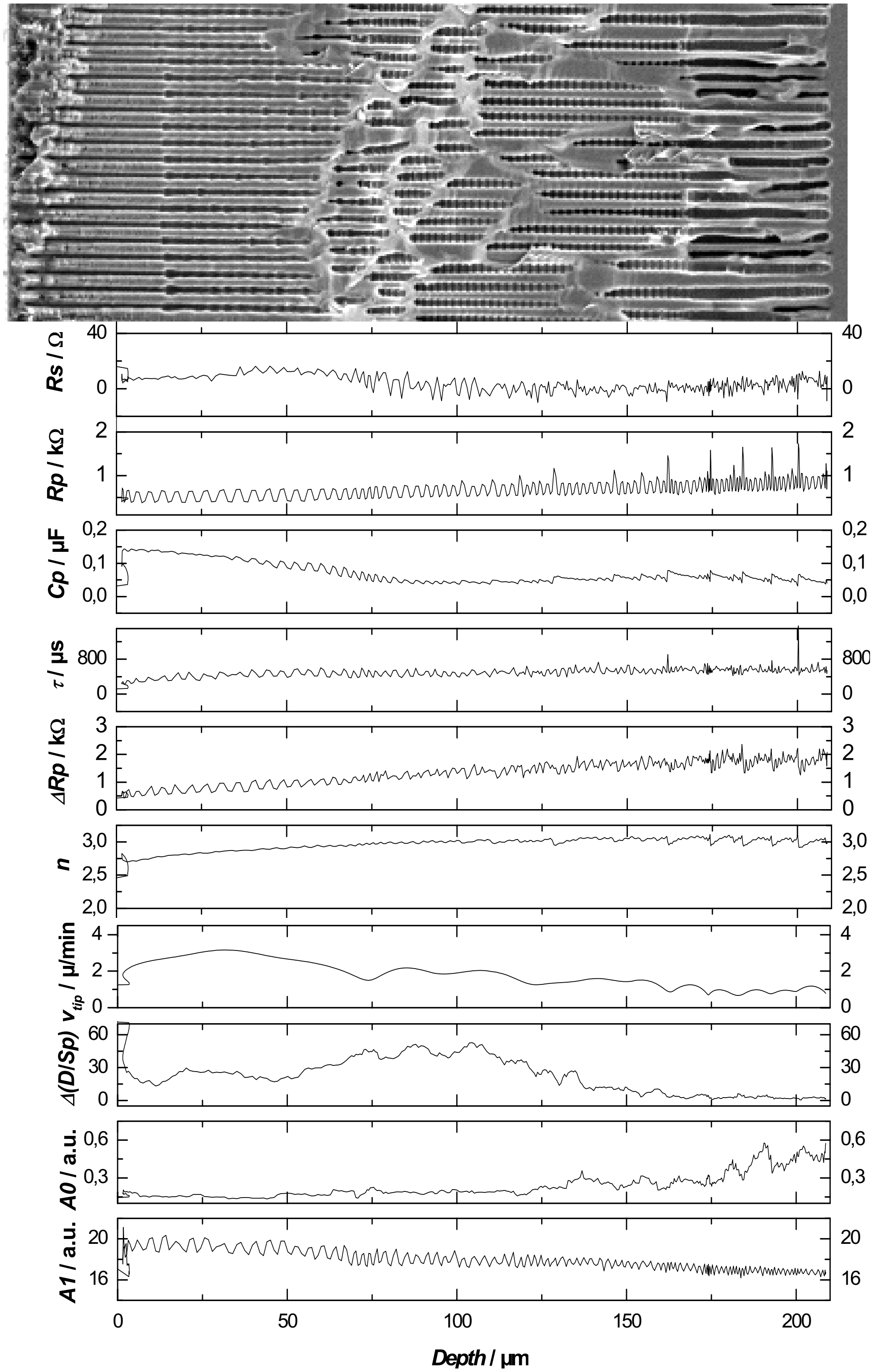

Figure 6. Impedance parameters vs. pore depth in direct comparison with the etched pore morphology. An aqueous electrolyte with an HF concentration of 15 wt.% HF aqu. + 0.83 g/l of CMC was used. The applied voltage was 1.0 V. After 5 min. of constant current, the current was switched from 26 mA/cm^2 to 16 mA/ cm^2 with a period of 2 min. during the total etching time of 105 min. T = 20°C; n-type Si, (100), 5 Ωcm, prestructured by standard photolithography; hexagonal lattice with lattice constant a = 4.2 µm.

At this point the calculation of pore depth is somewhat problematic for the first part of the experiment (and therefore omitted in the curves in **Fig. 6**). This is a consequence of the model-based approach (22) and thus expected. In fact, obvious deviations of the system under investigation from the model inherent in the data evaluation provide clues for what it going on just as much as model-consistent behavior.

Cavity Formation plus Continued Pore Growth

The mode transitions introduced above occur instead of the cavity formation that usually terminates pore growth in standard 5 % electrolytes (the only obvious mode transition in these cases). As an intermediate effect between anti-phase oscillations and cavity formation one might find a cavity followed by newly nucleated pores at the bottom of a cavity. These pores then do not retain the original order induced by lithography but are invariable larger and less densely spaced than their progenitors; **Fig. 7** shows an example. The effect has also been seen and described by Bao et al. in (31, 32). This indicates simply that the actual pore radius r_{pore} is too small compared to r_{opt} as introduced above.

Cavity formation is often described as an increase of r_{pore} to values of $> a/2$ and thus as an effect inherent in the basic growth mode and not a mode transition, but this is not really the case.

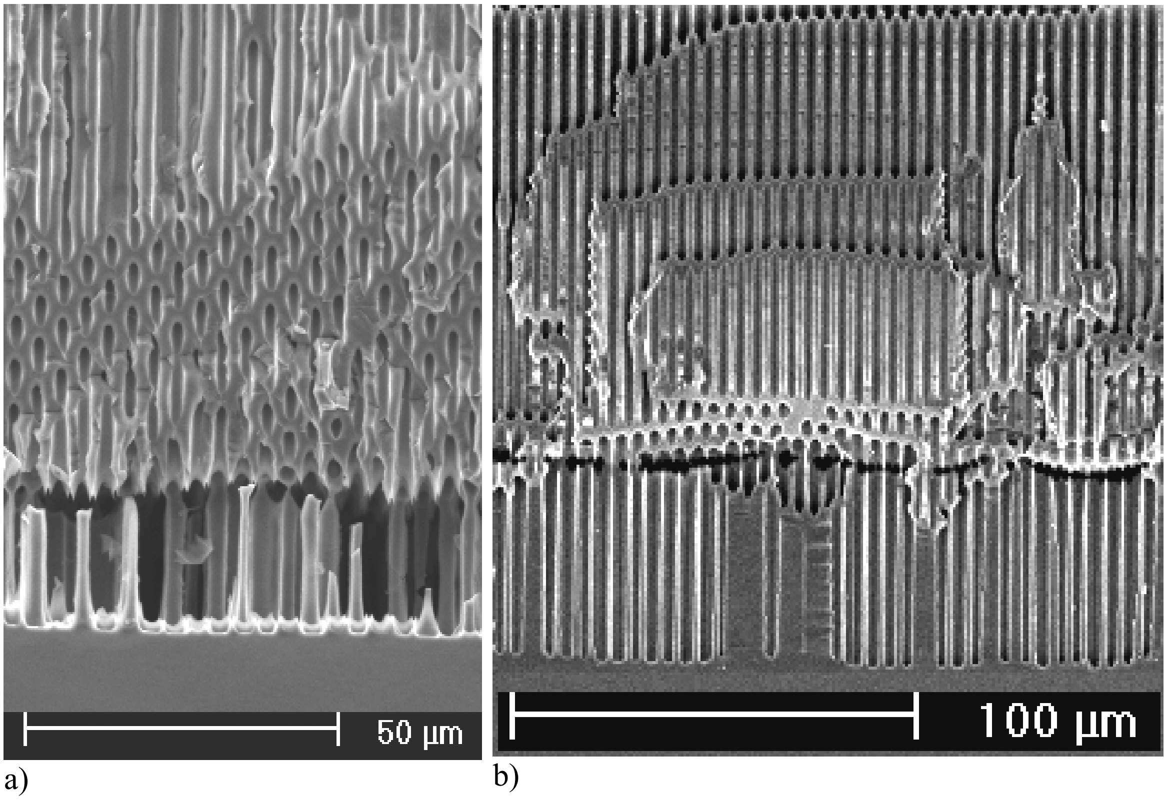

a) b)

Figure 7. Cavity formation and subsequent pore growth. An aqueous electrolyte with an HF concentration of 15 wt.% and 0.83 g/l of CMC was used. The etching current decreased from 27 mA/cm^2 to 16 mA/ cm^2 during the total etching time of 117 min. **a)** The applied voltage was 1.0 V for 50 min then increased to 1.5 V. **b)** The applied voltage was 0.7 V for 50 min then increased to 1.0 V. Further data: $T = 20°\text{C}$; *n*-type Si, (100), 5 Ωcm, pre-structured by standard photolithography, hexagonal lattice, $a = 4.2$ µm.

First of all, this should be a gradual and not a rather sudden process, and secondly, there would be no reason to commence pore growth again. Cavity formation is thus better described as a true mode transition that reconfigures the system (a cavity, e.g. may act as a buffer for the concentration of an electrolyte species).

It may be added that repeated cavity formation with subsequent pore growth is rather common in n-macro(org, breakdown) pores, i.e. macropores in n-type Si produced under avalanche breakdown conditions in the dark in an "organic" electrolyte (12), where staggered systems with many layers of cavities – pores have been observed; **Fig. 8** b) shows an example.

"Exotic" Mode Transitions

In general, large HF concentrations combined with the then possible very large current densities seem to enable pore structures in Si that are similar to structures obtained in InP at high current densities including specific mode transitions and to Si n-macro(org) pores. Most remarkably, perhaps, is the transition from obviously <113> oriented steeply inclined "crysto" pores (never observed before in {100} Si samples) to <100> oriented pores as shown in **Fig. 8** a). The picture looks quite similar to the familiar crysto – curro transitions from InP (7) or the less familiar crysto-curro transition observed with n-macro(org, dark, {111}) pores in Si (12). Note that the picture shown in **Fig. 8** a) is just one particularly clear example of new pore morphologies found in that area of parameter space that can be described as "very large HF concentration + carbonic acids + plus very high current densities".

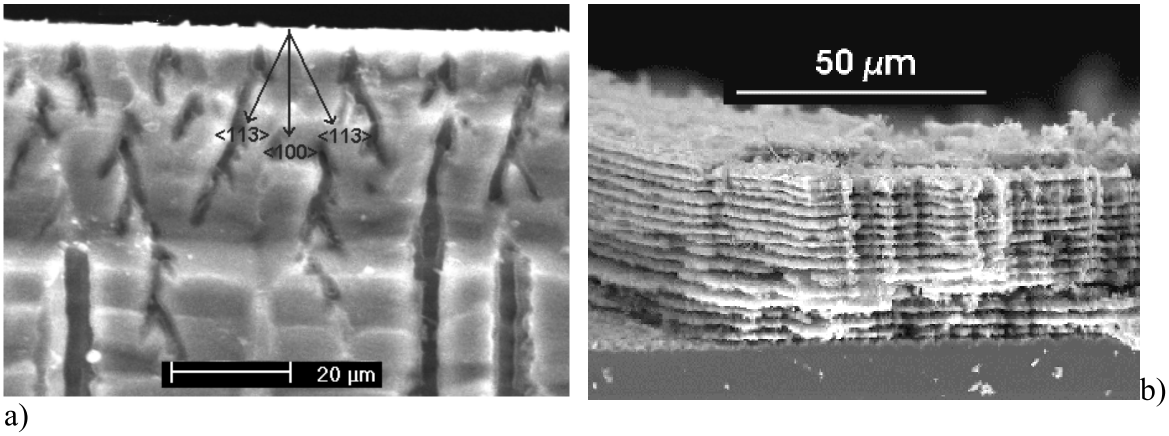

Figure 8. a) Transition from <113> oriented crysto pores to <100> oriented crysto or curro pores in {100} n-type Si under backside illumination.
b) "Puff pastry" structure of repeated pore - cavity – pore - mode transitions in n-macro(org. electrolyte, breakdown) pores.
For details see text.

Discussion

It is well known that taking only into account ohmic losses ΔU from the pore tips to the surface, according to the Nernst equation the concentration c_{tip} of, e.g., HF near the pore tips should be reduced by $c_{\text{tip}}/c_0 = \exp(-\Delta U/kT)$. Keeping ΔU small needs high conductivities and thus concentrations. The HF concentration, however, cannot be increased just to reduce ohmic losses because it also determines reaction rates. There is simply no way to prevent a significant reduction of the concentration of reactants near the pore tips, which in consequence with increase the ohmic losses for current flow through the pore, without interfering too much with the pore growth mode. Due to the strong nonlinear coupling between concentration and voltage losses the concentration of reactants near the pore tip will change strongly as a function of pore depth. The reduced concentration will slow down the reaction rates at the pore tips, leading to a decrease of pore tip speed v_{tip}. In order to obtain constant pore diameters the current through the pores must be reduced as a function of time proportional to the reduction of v_{tip}. The tip current thus is always "diffusion limited" at some depth. A correct reduction of the external etching current would in principle allow for a continuous pore growth albeit with a monotonous decrease of speed, and this is the reason why the etching current is always decreased during a pore etching experiment.

Taking into account leakage currents through the pore walls drastically changes the situation. Most of the leakage current is not strongly diffusion limited because it is generated far away from the pore tips. While the etching current at the pore tip must decrease as a function of pore depth, the leakage current continuously increases (nearly proportional to the pore wall area). This additional leakage current through the pores reduces the concentration of reactants at the pore tips even more and will finally disallow pore growth. The relation between parameters like concentration, current, and voltage is extremely non-linear allowing the self-organization features outlined above, e.g. oscillatory behavior of the reactions at the pore tips.

Sometimes these oscillations are visible in the pore morphology as is true for nearly all examples in this paper (e.g. as diameter modulation ore periodical lift off as shown in **Fig. 8** b)). But often these (stochastic) oscillations are only visible in the impedance data; e.g. the step-like changes of the valance n for pore depth larger than 100 µm in **Fig. 6**. Similar behavior, expressed also in the capacitance C_{p}, the resistance ΔR_{p}, or in the spikes in R_{p}, is found in many experiments but is not always visible in the etched pore morphologies (c.f. e.g. Fig. 4 in (25)). Of course, these "oscillations" of the reaction at the pore tips are a consequence of the non-linear coupling between concentration, current, and voltage but as often in nonlinear systems they can also be the reason for "spontaneous" switching of the pore growth mode. If the reactions at the pore tips would take place in a steady-state mode just with a continuous decrease of dissolution rate, further pore growth would always be possible (if ever so slow); but if the reaction rates oscillates stochastically, a critical dissolution rate may occur, at which the pore growth mode instantly switches. Enhancing these intrinsic oscillations or fluctuations by externally imposed parameter changes may thus amplify the generally more or less stochastic mode transition behavior.

The observation that the pore diameter strongly increases upon decreasing the current in the experiments shown here, while always decreasing in standard "5 %" experiments can be understood qualitatively within this framework. In the first case we have strong passivation of the pore walls, allowing the pore tip to draw a large current. Upon reducing the pore-tip current, the now too high concentrations of reactants passivate the pore tip to a point where it has to switch its growth mode and increases its area to be able to process the current still impressed on the system by the galvanostat. For 5 % electrolytes and the concomitant smaller current, this effect is not yet felt for not-so-deep-pores and the pores stay within one growth mode; the diameter essentially following the current. However, the results for this mode (in particular the results of the Halle group (33, 34)) are far from showing a linear relationship between current and pore diameter; it is also noteworthy that direct pore diameter modulations by in-phase current modulations appear not to be possible at large pore depth. In fact, within the reasoning given here, it must be expected that pores in standard 5 % electrolytes would also tend to increase their diameters as a response to a current reduction at large depths.

It is too early to attempt explanations going beyond of what has already been briefly outlined above or is given in two related papers (13, 25). Staying within a very general way of reasoning, one might note that the behavior of a pore tip can always be seen as the result of balancing a driving and a retarding "force". A positive potential and molecules like HF or F^- at the pore tip drive Si dissolution; a passivating species at the pore tip retards it. Steady state implies force equilibrium, but the steady-state growth mode is rarely established as the impedance data seem to imply. If steady state is not present, the (highly non-linear) system may behave more or less chaotically with respect to internal parameters while still showing constant behavior in some others. If the time development of the driving and retarding forces is different, mode transitions occur as soon as something akin to a "bifurcation" point is reached. The addition of HAc clearly improves passivation of the pore walls, i.e. reduces leakage currents and thus allows for larger pore tip current at significant pore depths. However, the higher concentrations of electrolyte ingredients and the concomitant higher currents render the system more "chaotic" in the sense outlined above and enable a range of mode transition never seen before. Some more details to this point of view can be found in (2, 13, 23 - 25).

There is a clear message encoded in the data shown here, in particular in the mode transition shown in **Fig. 8** (and other pictures not shown here): If one looks at the details of etching macropores in lightly doped Si under back side illumination, it turns out to be even more complex then has been known so far. However, if one looks at the general situation or etching all kinds of pores in all kinds of semiconductors, pore etching in semiconductors becomes less complex. There are clearly some common features found by now in many semiconductors that go beyond considering the semiconductor part (i.e. space charge region effects and hole supply issues) and the detailed chemistry (detailed reaction equations an so on) but address some "general" part, since these common features cannot depend on the details enumerated. Clearly, some more general principles must be at work. One such common principles could be the stochastic nature of the dissolution process as proposed in (23, 24, 35), another one could be the geometry of "diffusion limitation", i.e. the fact that the supply of chemical species to the pore tip (and the pore wall) of pores of comparable geometry is subject to the same geometrical restrictions and comparable conditions for enabling current flow in all circumstances.

Summary / Conclusion

Extending the parameter space of n-macro(bsi, aqu HF) pore etching to HF concentrations far larger than the typical 5 wt.% used so far as by adding carboxylic acids (and viscosity promoters) shows that growth mode transitions are rather common in the full parameter space but rarely expressed beyond cavity formation at the $c_{\mathrm{HF}} < 5$ wt % corner that was mainly probed so far. Higher current densities under geometrical restrictions defined by the macropore "amplify" effects tied to diffusion limitations and the general stochastic natures of the detailed dissolution process.

While a detailed model is still lacking, it is clear from the results given that in-situ data acquisition is essential for an understanding of the generally non-linear (or chaotic) processes that produce pores and the plethora of self-organization and mode transitions that come with it. It has been shown that dual-mode in-situ FFT impedance spectroscopy can deliver at least some of the necessary data, and that a first evaluation tends to confirm the assumptions made. The results strongly imply that there are some common principles that apply to pore formation in most semiconductors.

Acknowledgement

Parts of this work have been supported by the Alexander von Humboldt foundation.

References

1. V. Lehmann, *Electrochemistry of Silicon*, Wiley-VCH, Weinheim (2002).
2. H. Föll, M. Christophersen, J. Carstensen, and G. Hasse, *Mat. Sci. Eng. R* **39(4)**, 93 (2002).
3. X.G. Zhang, *J. Electrochem. Soc.* **151(1)**, C69-C80 (2004).
4. H. Föll, J. Carstensen, and S. Frey, in *Sensor, and Gas Separation Applications*, eds. S.W. Lu, H. Hahn, J. Weissmuller, and J.L. Gole, R12.1, Mater. Res. Soc. Symp. Proc., Warrendale, PA (2005).
5. C. Fang, H. Föll, and J. Carstensen, *J. Electroanal. Chem.* **589**, 259 (2006).
6. C. Fang, J. Carstensen, and H. Föll, *Solid State Phenomena* **121-123**, 37 (2007).
7. S. Langa, M. Christophersen, J. Carstensen, I.M. Tiginyanu, and H. Föll, *Phys. Stat. Sol. (a)* **197(1)**, 77 (2003).
8. S. Langa, J. Carstensen, I.M. Tiginyanu, M. Christophersen, and H. Föll, in *Ordered Porous Nanostructures and Applications*, ed. R.B. Wehrspohn, 57 (2005).
9. S. Langa, S. Frey, J. Carstensen, H. Föll, I.M. Tiginyanu, M. Hermann, and G. Böttger, *Electrochem. Sol. State Lett.* **8(2)**, C30 (2005).
10. H. Föll, J. Carstensen, and E. Foca, *Int. J. Mat. Res.* **2006(7)** (2006).
11. S. Rönnebeck, J. Carstensen, S. Ottow, and H. Föll, *Electrochem. Solid-State Lett.* **2(3)**, 126 (1999).
12. S. Frey, M. Kemell, J. Carstensen, S. Langa, and H. Föll, *Phys. Stat. Sol. (a)* **202(8)**, 1369 (2005).
13. J. Carstensen, E. Foca, S. Keipert, H. Föll, M. Leisner, and A. Cojocaru, *Phys. Stat. Sol. (a)*, submitted (2008).
14. M. Leisner, J. Carstensen, A. Cojocaru, and H. Föll, *PSST 2008*, submitted (2008).
15. M. Leisner, J. Carstensen, and H. Föll, *J. Electroanal. Chem.* **615(2)**, 124 (2008).
16. M. Leisner, J. Carstensen, A. Cojocaru, and H. Föll, *ECS Trans.*, this proceedings (2008).
17. A. Cojocaru, J. Carstensen, E.K. Ossei-Wusu, M. Leisner, O. Riemenschneider, and H. Föll, *PSST 2008*, submitted (2008).
18. T. Takizawa, S. Arai, and M. Nakahara, *Japan J. Appl. Phys.* **33(2, 5A)**, L643 (1994).
19. A. Hamamatsu, C. Kaneshiro, H. Fujikura, and H. Hasegawa, *J. Electroanal. Chem.* **473**, 223 (1999).
20. H. Föll, S. Langa, J. Carstensen, S. Lölkes, M. Christophersen, and I.M. Tiginyanu, *Adv. Mat.* **15(3)**, 183 (2003).
21. S. Langa, J. Carstensen, I.M. Tiginyanu, M. Christophersen, and H. Föll, *Electrochem. Solid-State Lett.* **4(6)**, G50 (2001).
22. A. Cojocaru, J. Carstensen, and H. Föll, *ECS Trans.*, this proceedings (2008).

23. J. Carstensen, M. Christophersen, G. Hasse, and H. Föll, *Phys. Stat. Sol. (a)* **182(1)**, 63 (2000).
24. J. Carstensen, M. Christophersen, and H. Föll, *Mat. Sci. Eng. B* **69-70**, 23 (2000).
25. J. Carstensen, A. Cojocaru, M. Leisner, and H. Föll, *ECS Trans.*, this proceedings (2008).
26. E. Foca, J. Carstensen, G. Popkirov, and H. Föll, *Phys. Stat. Sol. (a)* **204(5)**, 1378 (2007).
27. E. Foca, J. Carstensen, G. Popkirov, and H. Föll, *ECS Trans.* **6(2)**, 345 (2007).
28. A. Cojocaru, J. Carstensen, M. Leisner, H. Föll, and I.M. Tiginyanu, *PSST 2008*, submitted (2008).
29. J. Schilling, F. Müller, S. Matthias, R.B. Wehrspohn, U. Gösele, and K. Busch, *Appl. Phys. Lett.* **78**, 1180 (2001).
30. S. Matthias, F. Müller, J. Schilling, and U. Gösele, *Appl. Phys. A* **80(7)**, 1391 (2005).
31. X.Q. Bao, J.W. Jiao, J. Zhou, and Y.L. Wang, *Electrochim. Acta* **52**, 6728 (2007).
32. X.Q. Bao, J.W. Jiao, F. Duan, Y.L. Wang, K.W. Na, and H. Choi, *Electroch. Comm.* **9**, 1689 (2007).
33. A. Birner, K. Busch, and F. Müller, *Phys. Bl.* **55(4)**, 27 (1999).
34. S. Matthias and F. Müller, *Nature* **424**, 53 (2003).
35. E. Foca, J. Carstensen, and H. Föll, *J. Electroanal. Chem.* **603**, 175 (2007).

ECS Transactions, 16 (3) 173-180 (2008)
10.1149/1.2982553 ©The Electrochemical Society

Model for Current Oscillations at the Si/Electrolyte Contact: Extension to Spatial Resolution

J. Grzanna[a], T. Notz[b], and H. J. Lewerenz[a]

[a] Hahn-Meitner-Institut GmbH, Glienicker Str. 100, 14109 Berlin, Germany
[b] Max Planck Institute for Gravitational Physics (Albert Einstein Institute),
Am Mühlenberg 1, D-14476 Golm, Germany

A morphological model is given for the anodic oxidation of n-type silicon in fluoride containing solution in a potentiostatic arrangement. An earlier introduced macroscopic version of the model is extended from temporal to spatio-temporal resolution using a cellular automate. The prediction of the macroscopic model that lattice mismatch between silicon and its oxide leads to stress and stress leads to two types of oxides in the case of photocurrent oscillation is approved by the cellular automate model. The oxide types differ in stability against the etching process. Both oxide types are arranged in clusters which alternate at the electrode surface. Each cluster is in the size of 80-100 nm.

Introduction

The anodic oxidation of n-type silicon in fluoride containing solution is analyzed. At anode potentials of about 6 V, photocurrent oscillations that are in the maximum of the oscillation amplitude in dilute NH_4F solutions are observed. They are characterized by a fixed phase relation to a cyclic increase and decrease of the mean oxide thickness (1). Self-oscillating domains (2) in the size of 100 nm (3) were discussed as the origin of the oscillations. Later ref. (4) advocated that the volume difference between silicon and its oxide introduces defects and leads to nanopores in the structure. Stress has been measured during oscillations (5) and two types of oxide (6) were detected. For p-type Si, the current burst model (7,8) was developed and the role of stress and percolation effects of charged ionic species inside pores on the anodic silicon growth mechanism have been discussed (9). In refs. (10-14), the mentioned phenomena are unified in a morphological model for current oscillations at the silicon electrolyte contact. A macroscopic model (10-13) was introduced which describes the oxide thickness evolution with means without exact spatial resolution. Later a microscopic (spatio-temporal resolved) model was given (14) which is based on a cellular automate.

The Morphological Model

The model describes the cyclic oxidation and oxide etching process at silicon surfaces. At the beginning of the anodization process, the bare silicon surface is oxidized until a potential- and etching rate dependent maximum oxide thickness is reached. This oxidation process results from an excess minority carrier induced current which is proportional to the increase in oxide thickness. After reaching the maximum oxide thickness, the electrode is passivated and no further oxide grows. Simultaneously, the current-less etching process reduces the oxide thickness until a minimum value is reached at which electrical contact between electrolyte and silicon is made locally and the cycle starts again. During each cycle, a silicon layer of constant thickness *d* is consumed by oxidation and dissolution (15). The oxide thickness oscillation, however, proceeds not uniformly at the whole electrode surface. Local effects (such as stress due to lattice mismatch between silicon and its oxide that induces cracks and nanopores) lead to a dynamical behavior of the oxide thickness at the electrode. Hence the oxidation and etching process is in different stages at different locations at the same time. Accordingly, cracks and nanopores in the oxide lead locally to a de-synchronization of the process. In the case of randomly distributed cracks and nanopores in the oxide, the de-synchronization process dominates resulting in a constant current and a rougher oxide surface. It will be shown below that this de-synchronization process can be stopped if two types of oxides exist (Fig. 1) with a different area density of cracks and nanopores. Earlier grown oxide (oxide I) in a layer with less cracks and nanopores per area unit is more stable against etching whereas later grown oxide II, grown into compressively stressed silicon, has more structural defects and hence etches faster in a more three-dimensional manner. Both oxide types lead to a synchronization of the process that result in sustained current oscillations and a smoother oxide surface. Synchronization is reached when cluster of oxide I and II alternate both at the electrode surface within a layer and at the electrode surface from layer to layer (Fig. 2). Increasing stress in silicon between two growing oxide I islands in a layer leads to the intermediate later grown oxide II. In order to obtain photocurrent oscillations, the oxide growth and oxide etch rate has to be chosen such that the resulting maximum oxide thickness is large enough for an acting stress in silicon between two neighboring growing oxide I islands (for instance for a potential of 6V vs. SCE and a pH of 4.2). In other cases (for instance for a potential of less than 3V or a smaller pH value) the maximum oxide thickness is not sufficient. Then the formed oxide has rather randomly distributed cracks and nanopores, leading to damped oscillations and a rougher oxide surface.

The Macroscopic Model

The macroscopic model (10-13) describes the oxide thickness evolution using the so-called (oxide) thickness oscillators. Each point at the electrode surface is related to one thickness oscillator which describes the oxide thickness during the cycles. Two functions are used:

(i) the synchronization state function $p_i(t)$ that denotes the (differential) number of oxide thickness oscillators which reach their minimum thickness at the *i-th* time at the time *t*. p_i reflects the quality of the synchronization at the so called snap-shoot planes which are imaginary planes (with equal distances *d*) located in the electrode volume parallel to the bare silicon electrode surface. Hence at the snap-shoot planes, the oxide thickness is always at its minimum during the evolution process. In the case of synchronization, the p_i's are functions with one peak of constant height and the peaks are located sequentially with a spacing of the oscillation period. In the case of de-synchronization, the height of the peaks scales down for increasing cycle numbers and likewise p_i is more and more broadened;

(ii) the probability distribution function $q_{i,s}(t-s)$ for the periods $t-s$ of the oxide thickness oscillators which start their *i.-th* cycle at the time s. $q_{i,s}$ describes the lifetime of one oxide layer between two neighboring snap-shoot planes.

The temporal and a part of the spatial information of thickness oscillators are reflected in each function. Expressed more precisely, $p_i(t)$ defines for the time *t* and $q_{i,s}(t-s)$ for the relative time $t-s$ a determined (differential) number of points of the electrode surface. The points are connected one to one with the corresponding thickness oscillators. Only the exact location of the thickness oscillators is lost in $p_i(t)$ respectively $q_{i,s}$ but their (differential) number remain. Both time dependent functions are connected by the Markov process

$$p_i(t) = \int p_{i-1}(s)\, q_{i,s}(t-s)\, ds \qquad [1]$$

The current resulting from the *i-th* cycle is given by

$$I_i(t) = \int p_i(s)\, E_i(t-s)\, ds \qquad [2]$$

where $E_i(t)$ denotes the so-called elementary current peak resulting from one thickness oscillator during the oxide growth phase. Hence the total current of the electrochemical process results from

$$I(t) = \sum_i I_i(t) \qquad [3]$$

The model describes the process macroscopically and uses spatio-temporal means, that are the functions $q_{i,s}$, for the evolution of real domains. The real domains are domains of oxide located around nanopores. Measured from the location of the nanopore the boundary of a real domain is determined by the half nanopore distance to neighboring nanopores. The evolution of a real domain is characterized essentially by the etching behavior and the etching time depends on the size of the real domain. The smaller the size of the real domains is the smaller is the etching time because the (horizontal measured) half oxide thickness between two neighboring nanopores becomes smaller

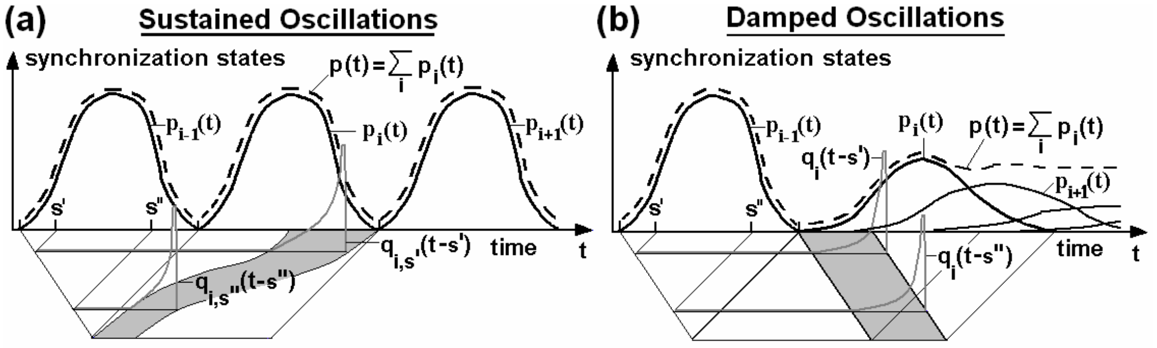

Figure 1. (a) Synchronization mechanism reflected in the macroscopic model by two types of oxide: $q_{i,s'}(t-s')$ corresponds to oxide I and $q_{i,s''}(t-s'')$ to oxide II. (b) De-synchronization mechanism based on a constant shape of q_i corresponding to only one type of oxide.

than the (vertical measured) maximum oxide thickness. The back transformation (to a spatiotemporal resolved representation) of $q_{i,s}$ is called the characteristic domain which gives information about the mean distance between cracks and nanopores inside the oxide starting their growth at the time *s* at the cycle *i*.

The primary finding of the macroscopic model is that two types of oxide (Fig. 1a) are mandatory to obtain current oscillations. We suppose that stress in the silicon (resulting from initially grown oxide I islands in a layer) increases the number of cracks and nanopores in the later grown oxide II. The synchronization mechanism results from the two types of oxide: earlier grown oxide I in a layer (less cracks and nanopores, more stable against oxide etching, longer life time) and later grown oxide II (more cracks and nanopores, less stable against oxide etching, shorter life time). In the case of de-synchronization (Fig. 1b) the prevalence of only one type of oxide leads to a broadening of the next synchronization state because Eq. [1] degenerates to a convolution operation with the constant kernel $q_i(t-s)$.

The Microscopic Model

In the microscopic model (14), the oxide thickness is described in time and in space. A one-dimensional cellular automate (16) is used that represents the values of the oxide thickness and the maximum stress in silicon at equidistant grid points along a line at the electrode in vector form: $(d_1^j, d_2^j, ..., d_n^j)$ for the oxide thickness and $(s_1^j, s_2^j, ..., s_n^j)$ for the maximum stress in silicon. The lower index represents the cell number and the upper index *j* the time $j\,\Delta t$. The used grid has a spatial resolution of $\Delta x = 1/2\, mm$ and a temporal resolution of $\Delta t = 1\, s$. A set of rule-based transition functions for the oxide growth phase, the calculation of the maximum stress in silicon caused by the firstly grown oxide in the layer, the stochastic calculation of the location of cracks in the just grown oxide in dependence on the prior stress in the silicon, and the oxide etching phase is used. As a result, a temporal oscillation of the oxide thickness (constant amplitude, different periods) is obtained at each cell per cycle. In the case of current oscillations, the spatial oscillation of the maximum stress along the considered line at the silicon electrode results from initially grown oxide I islands. That results in two types of oxide (see Fig. 2: oxide I in domains with a prior small stress in silicon and oxide II in domains with a prior large stress). The transition functions are formally given by

$$\begin{aligned} d_k^{j+1} &= f_k(d_1^j, d_2^j, ..., d_n^j; s_1^j, s_2^j, ..., s_n^j) \\ s_k^{j+1} &= g_k(d_1^j, d_2^j, ..., d_n^j; s_1^j, s_2^j, ..., s_n^j) \end{aligned} \qquad [4]$$

for *k=1,2,...,n*. More precisely,

$$d_k^j = d_k^{j,i,phase} \quad \text{and} \quad s_k^j = s_k^{j,i} \qquad [5]$$

that means each oxide thickness is connected with a cycle (or layer) number *i* and the information whether the oxide grows (phase: "growth") or is etched (phase: "etch"). The stress is connected with the cycle number *i* only. Eq. [4] could be interpreted as a discretized solution of a hitherto unknown stochastic differential equation that describes the oxide thickness dynamics continuously and spatio-temporally. In the following the transition functions f_k and g_k of the cellular automate are described.

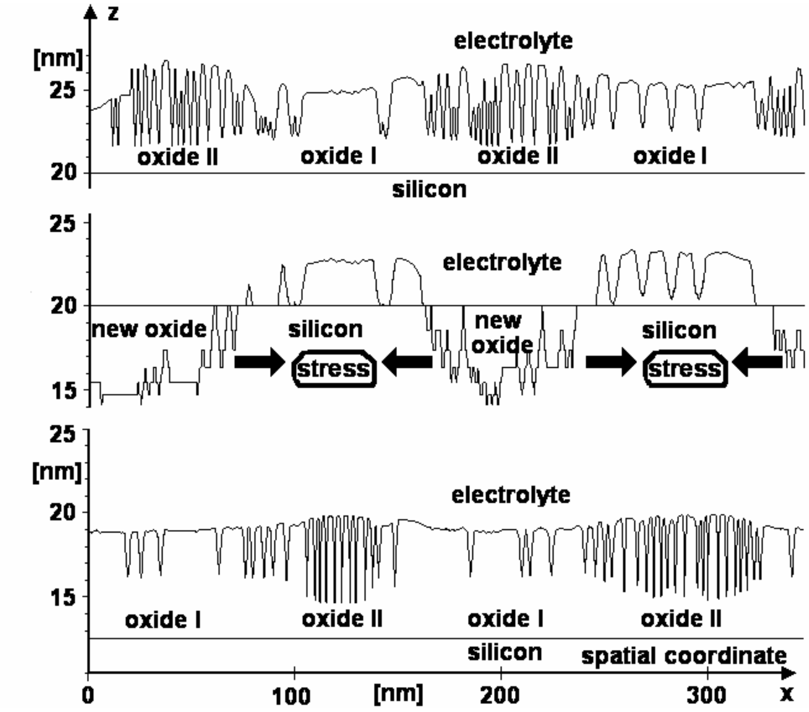

Figure 2. Synchronization mechanism reflected in the microscopic model: stress and two types of oxide during one current oscillation.

Oxide Growth Phase. After the minimum oxide thickness (here assumed to be zero) of the previous etching phase is reached at cell *k*, say at the time $j_0 \ \Delta t$, the oxide growth curve is given by

$$d_k^{j,i,growth} = \frac{d^{high}}{(j^{high})^3}(j - j_0)^3 + d^{high} \qquad \text{for} \qquad j_0 \le j \le j_0 + j^{high} \qquad [6]$$

where d^{high} denotes the maximum oxide thickness and $j^{high} \ \Delta t$ the oxide growth time, both depending on the potential and the etching rate. Eq. [6] is in accordance with (17) and reflects the increasing passivating behavior of the growing oxide thickness. It should be noted that j_0 depends on *k* and *i*, reflecting the dynamics of the oxidation and etching process. During the same cycle, the oxidation process beginns at different cells *k* at different times. The oxide growth curve has always the same shape and when the maximum oxide thickness has been reached, the growth phase ends. The oxide is now passivating the Si electrode. At that time, only etching takes place until the minimum oxide thickness is reached.

Stress in Silicon. During oxide island growth in a layer, compressive stress into the not yet oxidized silicon is induced. The linear stress contribution [18] originating from one cell *k* acting on cell *l* is defined by

$$S_k^{j,i}(l) = f(b)\,\left(-\frac{d^{high}}{(w/\Delta x)}|k-l| + d_k^{j,i,growth}\right) \qquad [7]$$

where w denotes the maximum impact length of stress, Δx is the local resolution, b is the diameter of grown oxide island to which the cell k belongs, f is a function reflecting the two-dimensional stress influence of the indicated oxide island on the cell l, and the stress $S_k^{j,i}(l)$ is set to zero for a negative value of the right side of Eq. [7]. At the end of the oxide growth phase, the maximum stress acted on cell l is given by

$$s_l^{j_0+j^{high},i} = \max_{j \le j_0+j^{high}} \sum_k S_k^{j,i}(l) \qquad [8]$$

Cracks in Oxide. The basic assumption of the model is that the maximum stress is proportional to the probability to find a crack in the just grown oxide. In the following the transition from the calculated maximum stress in silicon to a calculated distribution of cracks in the just grown oxide is described. First, the probability q_{crack} to find a crack in the just grown oxide at cell l is defined by

$$q_{crack} = \frac{(h_{\max} - h_{\min})}{(S_{\max} - S_{\min})}\left(s_l^{j^{high},i} - S_{\min}\right) + h_{\min} \qquad [9]$$

where $h_{\min}$ and $h_{\max}$ with $0 \le h_{\min} < h_{\max} \le 1$ denote the given minimum respectively the maximum number of cracks per nanometer and $S_{\min}$, $S_{\max}$ describe the minimum and the maximum value of the stress, respectively. A crack is generated at cell l, when $r < q_{crack}\,\Delta x$ is fulfilled where r is a uniformly distributed random number with $0 \le r \le 1$. The singular and probabilistic reduction of the oxide thickness from d^{high} to d_{crack} at a cell representing a crack is given by

$$d_{crack} = d_{\max} - \frac{(d_{\max} - d_{\min})}{(h_{\max} - h_{\min})}(q_{crack} - h_{\min}) \qquad [10]$$

where $d_{\max}$, $d_{\min}$ denote the given maximum and minimum oxide thickness at a crack, respectively with $0 \le d_{\min} < d_{\max} \le d^{high}$.

Oxide Etching Phase. The etching acts always perpendicular to the tangential plane of the oxide surface. Hence the gradient a of the oxide surface is needed at the cell k which is approximated by

$$a = \frac{(d_{k+1}^{j,i,etch} - d_{k-1}^{j,i,etch})}{2\,\Delta x} \qquad [11]$$

The effective ablation Δd_a^{eff} of oxide (measured perpendicular to the geometric electrode surface) per time step Δt including the geometrical ablation $\sqrt{1+a^2}\,\gamma\,\Delta t$ and a local increase of the etching rate $\gamma(a) = \frac{(4\left|a\right|+1)}{\sqrt{1+a^2}}\gamma$ close to the oxidation process is given by

$$\Delta d_a^{eff} = (4\left|a\right|+1)\,\gamma\,\Delta t \tag{12}$$

where γ denotes the nominal etching rate. The new oxide thickness at cell *k* is given by

$$d_k^{j+1,i,etch} = d_k^{j,i,etch} - \Delta d_a^{eff} \tag{13}$$

If the new oxide thickness is smaller than zero then it is set to zero and the etching phase ends. After it a new cycle starts with the oxide growth phase.

Conclusions

The cellular automate concept allows the calculation of the oxide thickness dynamics, the stress in silicon, and a locally varying etching rate at a 1mm long line at the silicon electrode with a resolution of 0.5 nm and 1 second. During photocurrent oscillations oxide cluster of type I (earlier grown, less cracks and more stable against etching) and type II (later grown, more cracks and unstable) are detected with a size of 80-100 nm. The transition from stress to a special crack distribution is of probabilistic nature. Hence as measurements show, the oxide thickness dynamics is not reproducible at the microscopic scale for two different processes in contrast to the macroscopic scale where the process is reproducible (current, mean oxide thickness, mean oxide roughness).

References

1. J. Lewerenz, *J. Phys. Chem. B*, **101**, 2421 (1997).
2. J.-N. Chazalviel and F. Ozanam, *J. Electrochem. Soc.*, **139**, 2501 (1992).
3. F. Ozanam, N. Blanchard and J.-N. Chazalviel, *Electrochimica Acta*, **38**, 1627 (1993).
4. H. J. Lewerenz and M. Aggour, *J. Electroanal. Chem.*, **351**, 159 (1993).
5. V. Lehmann, *J. Electrochem. Soc.*, **143**, 1313 (1996).
6. J.-N. Chazalviel, C. da Fonseca and F. Ozanam, *J. Electrochem. Soc.*, **145**, 964 (1998).
7. J. Carstensen, R. Prange, G. S. Popkirov and H. Föll, *Appl. Phys. A*, **67**, 459 (1998).
8. E. Foca, J. Carstensen and H. Föll, *J. Electroanal. Chem.*, **603**, 175 (2007).
9. R. Fenollosa, V. Parkhutik, B. J. Garcia and R. M. Almazan, *phys. stat. sol. (a)*, **182**, 79 (2000).
10. J. Grzanna, H. Jungblut and H. J. Lewerenz, *J. Electroanal. Chem.*, **486**, 181 (2000).
11. J. Grzanna, H. Jungblut and H. J. Lewerenz, *J. Electroanal. Chem.*, **486**, 190 (2000).
12. J. Grzanna, H. Jungblut and H. J. Lewerenz, *AIP Conf. Proc.*, **780**, 635 (2005).

13. J. Grzanna, H. Jungblut and H. J. Lewerenz, *phys. stat. sol. (a)*, **204**, 1245 (2007).
14. J. Grzanna, T. Notz and H. J. Lewerenz, "Stress-induced 1-dimensional model for current oscillations at the Si/electrolyte contact", submitted to *phys. stat. sol. (a)*.
15. J. Jakubowicz, *Cryst. Res. Techn.*, **38**, 313 (2003).
16. S. Wolfram, "Theory and Application of Cellular Automata", World Scientific 1986.
17. S. Ya. Elovich and C. M. Zhabrova, Zhur. Fiz. Khim. USSR, **13**, 1761 (1939).
18. K. Simon, Mechanics, Addison-Wesley, Reading. MA USA 1971.

ECS Transactions, 16 (3) 181-188 (2008)
10.1149/1.2982554 ©The Electrochemical Society

OCP Oscillation of Silicon in Solution Containing Oxidizing Species

Yukio H. Ogata, Takamasa Itoh, Mohamed L. Chourou,
Kazuhiro Fukami, and Tetsuo Sakka

Institute of Advanced Energy, Kyoto University, Uji, Kyoto 611-0011, Japan

Oscillation behavior of p-type Si(100) was investigated in an aqueous solution containing HF and oxidizing agents at its open-circuit state. The presence of Cu^{2+} ions gives a regular and sustained oscillation of the open-circuit potential (OCP). Change in the solution pH does not affect the amplitude noticeably, but the period becomes long at low pH. The OCP oscillation appears also in a solution containing Ag^+ while the condition is limited and the amplitude is small compared with the Cu^{2+} system. On the other hand, no oscillation is observed in a solution containing NO_3^-, the redox potential is high enough to oxidize the Si surface. These results indicate that the oscillation takes place at a surface spatially confined with deposits. A model for the OCP oscillation of Si is proposed based on local and inhomogeneous oxide formation at a Si surface in a confined space and its repair.

Introduction

Current or potential oscillation behavior has been extensively studied during the anodic polarization of Si in fluoride-containing solutions (1-4). If a Si sample, where the n-type needs illumination, is anodized in a fluoride-containing solution, oscillation appears in the potential or current. The oscillation behavior is affected by many parameters: concentration of fluoride ions, temperature, solution conductivity, and so on. Two typical oscillation modes have been distinguished: damped oscillations and sustained oscillation (5), where it is interestingly shown that the mode can be changed by adding a series resistance in the system. Some models explaining the behavior have been proposed (2, 4, 6-8). These models are based on formation of oxides with different characteristics: dense and less-dense oxides with different properties, variation of thickness, or local irregularity of the oxides or pores. All the models are premised on a high polarization condition, bringing about a high electric field, accelerating migration of ions and the presence of a large voltage drop in each phase.

The potential oscillation, which is spontaneous and regular, can be also seen at its open-circuit state or without external power supply. The phenomenon is clearly observed when a mildly doped p-type Si in HF solution containing Cu^{2+} ions (9). The condition partially resembles that of the oscillation under high polarization because Cu^{2+} ions function as an oxidant, leading to the oxidation of Si; however, the influence of the electric field over the oxide is quite different. When a sample is externally polarized, the high electric field can bring about a morphological change in the formed oxides and their breakdown that could be the cause of oscillation. Meanwhile, open-circuit potential (OCP) oscillation does not need a high electric field. The behavior has been explained by a simple model (10, 11) where reduction of Cu^{2+} ions promotes oxidation of the Si surface leading to a positive shift of the OCP, and then the formed oxides are attacked and dissolved in the presence of HF and the relating species resulting in the recovery of the OCP. The breakdown-and-repair of the oxidized surface continues and gives the sustained oscillation. The model can explain the basic oscillation behavior such as the HF concentration dependence. However, further refinement is necessary for the model to explain the complicated features. We here investigate the oscillation behavior under various conditions to collect more information to improve the model.

Experimental

A p-type Si (100) wafer, the resistivity of which was 3.2-4.8 Ωcm, was used as the specimen. The wafer received Al vapor deposition on the backside and was annealed at 450 °C in vacuum for 30 min to obtain good electric contact. The surface was pretreated by rinsing with acetone and then immersion in 3 M HF for 5 min. A cell made of poly(chlorotrifluoroethylene) was used for electrolysis. The Si wafer was mounted at the cell bottom with a Cu current collector using an O-ring. The effective area exposed to the solution was about 0.8 cm^2, and a Pt spiral was used as the counter electrode.

The sample was immersed in 10 mM $CuSO_4$ + 60 mM HF solution. The solution pH was adjusted to 2.7, 1.0 and 0.5 with H_2SO_4. Deaeration was not usually performed. However, the solution was deaerated with Ar bubbling prior to and during the measurement in the experiments when the effects of dissolved oxygen were investigated. The OCP was measured against a Cu reference electrode. The potential values are referenced to the Ag/AgCl (3.3 M KCl). The oxidizing agents other than Cu^{2+}, Ag^+ ions and NO_3^- ions using Ag_2SO_4 and $NaNO_3$, respectively, were also investigated. The basic solution was 60 mM HF and pH 2.7. The Ag_2SO_4 concentration was varied from 0.5 mM to 5 mM, where the concentration range was limited because of the low solubility in aqueous solution. An Ag rod was used as the reference electrode in the Ag^+ system; the potential values are converted to the ones with respect to the Ag/AgCl (3.3 M KCl) again. In the NO_3^- system, the concentration of $NaNO_3$ was varied in 10 to 100 mM, and a Pt wire was used as the indicator electrode. The potential values were used as they were because the electrode functions only as an indicator electrode.

The surface morphology after the immersion was investigated using a field-emission type scanning electron microscope (FE-SEM, JEOL JSM-9500FE).

Results

The OCP variations of Si were measured in solutions of pH 2.7, 1.0 and 0.5 without deaeration. The OCP oscillated in all the pH examined (Fig. 1). The surface morphologies after the OCP measurements are shown in Fig. 2. The amount of Cu deposition decreases with lowering the pH. This is partially because of the competition against the hydrogen evolution reaction, which becomes favorable at low pH when applied potential is fixed. An appreciable amount of the deposits is not observed at pH 0.5, but the OCP keeps oscillating. The oscillation amplitude does not change significantly but the period becomes long, 2.8 s, 4.0 s and 7.1 s at the three pH values, respectively, and the induction is pronounced. It is worth noting that the oscillation wave is not symmetrical but shows fast positive shift and slow negative shift.

Deoxygenation from the solution affects the Cu deposition. It prevents redissolution of deposited Cu (9), and therefore the effective deposition is expected. Figure 3 shows the OCP oscillation in the deaerated solution. The morphologies after immersion are shown in Fig. 4. Cu is deposited at all pH and development of crystallites is distinct compared with the deposits from a solution without deoxygenation. The deposition is observed even at pH 0.5 although the coverage was low. The oscillation at pH 2.7 changes greatly from the solution without deaeration (Fig. 5). It is instable at the early stage and damps after 5000 s of the immersion; however, regular oscillation continues but with a small amplitude and the wave comes to be symmetrical.

The oscillation had been investigated in the solution containing Cu^{2+} ions (10, 11). If the oscillation would result from the formation of oxides on the Si surface and the dissolution, the behavior should appear also in the other systems. OCP measurement of a p-type Si was performed in the solution containing Ag^+ ions (Fig. 6). The OCP oscillates in the Ag^+ solution when the concentration is higher than 3 mM. The oscillation is irregular and small, and exhibits a long induction period compared with the Cu^{2+} system. The deposition looked adhering solidly to the Si surface. The similar oscillation behavior was observed also on n-type Si (10-20 Ωcm), where the surface was illuminated.

The NO_3^-/HNO_2 couple has a positive redox potential as well as the Ag^+/Ag system, the E_o values are +0.94 V (+0.67 V at pH 3) and +0.80 V vs. SHE, respectively. Reduction of the system, of course, does not cause metal deposition but accompanies the oxidation of Si. Results of the OCP measurement are shown in Fig. 7. Only irregular and intermittent spikes are observed in the OCP during the immersion of Si in the system when the $NaNO_3$ concentration is higher than 50 mM.

Discussion

OCP measured in the present work is a mixed potential determined by possible cathodic and anodic reactions without polarization. In the present system, the possible anodic reaction is the oxidation of Si, and the possible cathodic reactions are the reduction of oxidizing agents and H^+ ions, while reduction of dissolved oxygen is also possible in the solution without deaeration. Considering the concentrations of the oxidizing agents and pH values employed, the reduction of the oxidizing agents would be dominant. Therefore, the following reaction couple determines the OCP.

$$Si + 2H_2O = SiO_2 + 4H^+ + 4e^- \qquad [1]$$

$$Ox + ne^- = Red \qquad [2]$$

We have explained the oscillation behavior of the Cu^{2+} system as follows (10). When the Si surface is oxidized as a counter reaction of the reduction of Cu^{2+} ions, area of the bare or slightly oxidized Si surface, which is electrochemically active, decreases and the OCP shifts toward the noble direction and finally settles at the potential of the electrochemically inactive surface. The oxide layer is inhomogeneous and the local breakdown by HF (Reaction 3) exposes a part of the electrochemically active surface, resulting in the recovery of the OCP. The breakdown and repair continue and give the sustained oscillation.

$$SiO_2 + 6HF = SiF_6^{2-} + 2H^+ + 2H_2O \qquad [3]$$

A noticeable feature in the oscillation, which was not discussed before, is the asymmetry in the positive and negative shifts. A slow excursion of the OCP toward the negative potential and the rapid recovery are always observed in the oscillation. They are attributed to the slow chemical attack by HF and the fast recovery by the oxidation accompanied by the reduction of Cu^{2+} ions, respectively. The chemical dissolution reaction is slow because the HF concentration is small under the present conditions. Meanwhile, recovery of the oxidized surface are electrochemically driven by coupled reactions of the oxidation of Si and the reduction of Cu^{2+} ions. This is a fast process. The different rates make the oscillation asymmetric. The asymmetric wave in the oscillation also supports the mechanism based on the formation-and-dissolution of the surface oxides.

The OCP variations of a p-type Si were measured in solutions of pH 2.7, 1.0 and 0.5 without deaeration. The OCP oscillates in all the pH as shown in Fig. 1. The oscillation amplitude does not change noticeably but the period becomes long at low pH. A bare Si surface is oxidized accompanying the reduction of Cu^{2+} ions. If the electrochemically active area is common for the cathodic and anodic sites, we cannot expect the OCP shift because cathodic and anodic currents similarly shift in the partial current-potential curves with the change of the area. The active anodic area is limited to the bare surface, but the active cathodic area is extended also to the deposited metal surface. Electrons produced by Reaction 1 migrate through Si, reach the deposited metal surface, and the cathodic reaction proceeds (12), where the reaction would be predominant over on the Si surface because the electrochemical activity is higher on Cu than on Si. As a result, the OCP is mainly controlled by the area of the bare surface where the anodic reaction proceeds. The reduction of the bare surface area leads to a positive shift in the OCP. After the surface is completely oxidized, the electrochemical process stops. Then chemical dissolution of the oxides follows. Recovery of the bare surface induces an appearance of the cathodically active site, but the formation of H^+ ions according to Reaction 3 inhibits the reduction of Cu^{2+} ions. Inhibition of Cu deposition at low pH is seen in Fig. 2. The process makes a negative shift in the OCP. The negative shift enhances the cathodic reactivity, and finally returns to the Cu^{2+} reduction and oxide formation step. Observed pH dependence of the oscillation can be interpreted in this context. Low pH retards the oxide dissolution reaction (Reaction 3) and also inhibits the metal deposition, leading to the long period.

How the oxide formation and the dissolution can make a synchronized OCP oscillation should be addressed. A very attractive and persuasive model, the current burst model, has been proposed by Föll and his coworkers to explain the electrochemical oscillation behavior and macropore formation in Si (8, 13). They treated the Si under polarization, and hence, the model cannot be applied directly to the present system. We here consider a simple model which explains the oscillation behavior. The oxide formation and dissolution process proceed locally on a Si substrate. Once the surface is covered by the oxides, it becomes passive or the surface cannot participate in the determination of the OCP. Only the bare surface or slightly oxidized surface can determine the potential. The active surface is limited to a small area in the system. If the active area is small, the local event can determine the potential and the potential determines the surface state. Thus the local event spreads globally into similar sites and results in the synchronization. To realize this condition an appropriate environment at the surface is required. If deposits solidly cover the Si surface, the solution cannot reach the interface to dissolve the formed oxides. The solid deposition would be a factor to suppress the oscillation. The Ag^+ system has a more positive redox potential than the Cu^{2+} system, and hence the easier deposition is expected at the open circuit state. The Cu^{2+} system with removing dissolved oxygen gives a firm adherence of deposits compared with the system in the presence of dissolved oxygen because the presence causes redissolution of deposited Cu (9). In the two cases, we find damping or suppression of the OCP oscillation. This implies that penetration of the solution is necessary for the oscillation. Furthermore, the penetration should take place locally. It is considered that a percolated structure of deposits is necessary for the regular OCP oscillation (11). Indeed, no oscillation appears in the NO_3^- system, where the whole oxidized surface is exposed to the solution, and hence the surface tends to undergo a uniform oxide formation and dissolution in the absence of deposits. If the area to be oxidized and then dissolved is not spatially confined, the oxidizing agents need high concentration for the surface oxidation and the following breakdown of formed oxides becomes stochastic. As a results, the OCP oscillation starts from the higher concentration of oxidizing species, 50 mM of $NaNO_3$, and it is irregular and intermittent. These results tell us that metal deposition having appropriate contact with Si yields the OCP oscillation.

In summary, a local oxide formation and repair model can explain the OCP oscillation of Si in solution containing oxidizing agents, although some incomprehensible questions remain. Asymmetry of the OCP oscillation wave is induced by the model. The synchronization may be discussed based on that the reaction sites are confined.

Acknowledgment

This work was done in memory of Prof. Vitali Parkhutik, with whom we collaborated on the OCP oscillation studies.

References

1. V. P. Parkhutik, *Electrochim. Acta*, **36**, 1611 (1991).
2. V. Lehmann, *J. Electrochem. Soc.*, **143**, 1313 (1996).
3. M. Aggour, M. Giersig, and H. J. Lewerenz, *J. Electroanal. Chem.*, **383**, 67 (1995).
4. H. J. Lewerenz, *J. Phys. Chem. B*, **101**, 2421 (1997).
5. J. -N. Chazalviel, F. Ozanam, M. Etman, F. Paolucci, L. M. Peter, and J. Stumper, *J. Electroanal. Chem.*, **327**, 343 (1992).
6. J. -N. Chazalviel and F. Ozanam, *J. Electrochem. Soc.*, **139**, 25014 (1992).
7. S. Cattarin, J. -N. Chazalviel, C. Da Fonseca, F. Ozanam, L. M. Peter, G. Schlichthöl, and J. Stumper, *J. Electrochem. Soc.*, **145**, 498 (1998).
8. J. Carstensen, R. Prang, and H. Föll, *J. Electrochem. Soc.*, **146**, 1134 (1999).

9. J. Sasano, R. Murota, Y. Yamauchi, T. Sakka, and Y.H. Ogata, *J. Electroanal. Chem.*, **559**, 125 (2003).
10. Y. H. Ogata, J. Sasano, T. Itoh, T. Sakka, E. Rayón, E. Pastor, and V. Parkhutik, *J. Electrochem. Soc.*, **152**, C537 (2005).
11. T. Nagai, S. Nakanishi, Y. Mukouyama, Y. H. Ogata, and Y. Nakato, *Chaos*, **16**, 037106 (2006).
12. F. A. Harraz, T. Tsuboi, J. Sasano, T. Sakka, and Y. H. Ogata, *J. Electrochem. Soc.*, **152**, C456 (2002).
13. H. Föll, J. Carstensen, M. Christophersen, and G. Hasse, *Phys. Status Solidi A*, **182**, 7 (2000).

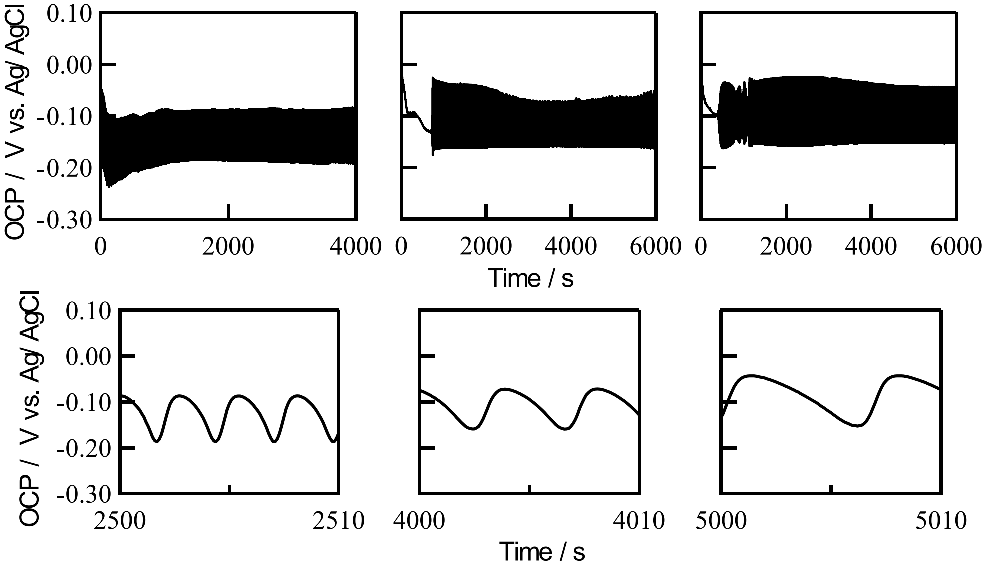

(A) (B) (C)

Figure 1. OCP oscillation of Si in 10 mM $CuSO_4$ + 60 mM HF solution, (A) pH 2.7 and (B) pH 1.0 and (C) pH 0.5.

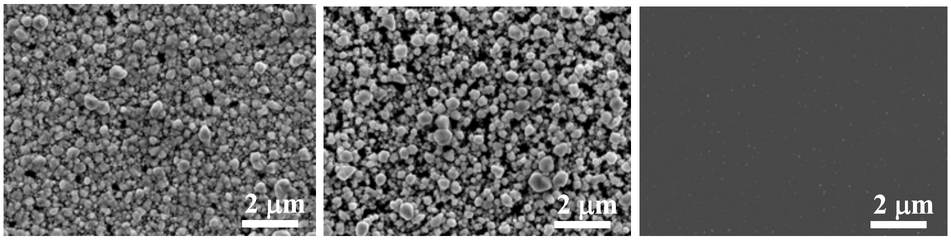

(A) (B) (C)

Figure 2. SEM plan views of Si samples after immersion in 10 mM $CuSO_4$ + 60 mM HF solution, (A) pH 2.7 and (B) pH 1.0 and (C) pH 0.5.

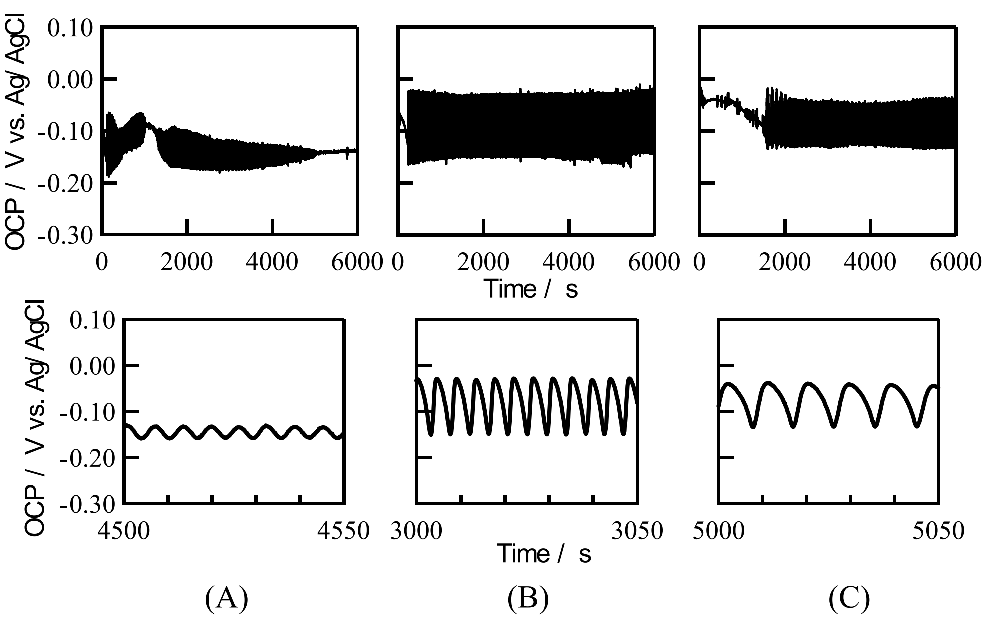

Figure 3. OCP oscillation of Si in 10 mM $CuSO_4$ + 60 mM HF solution with deaeration, (A) pH 2.7 and (B) pH 1.0 and (C) pH 0.5.

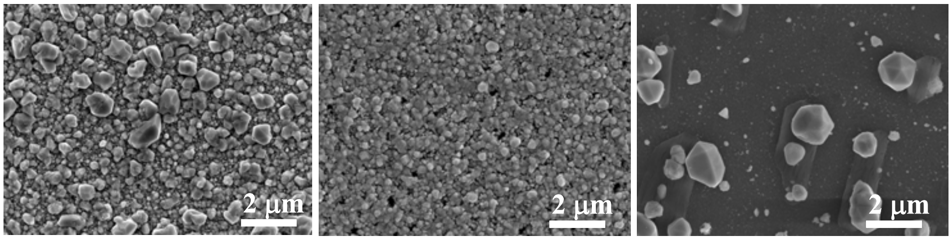

(A) (B) (C)

Figure 4. SEM plan views of Si samples after immersion in 10 mM $CuSO_4$ + 60 mM HF solution with deaeration, (A) pH 2.7 and (B) pH 1.0 and (C) pH 0.5.

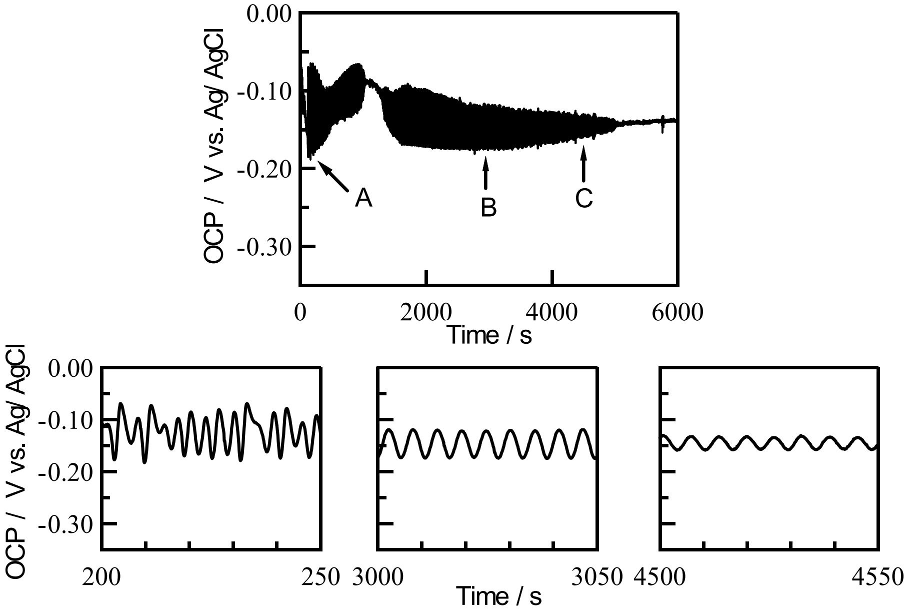

(A) (B) (C)

Figure 5. Temporal change of the OCP oscillation in 10 mM $CuSO_4$ + 60 mM HF solution with deaeration at pH 2.7.

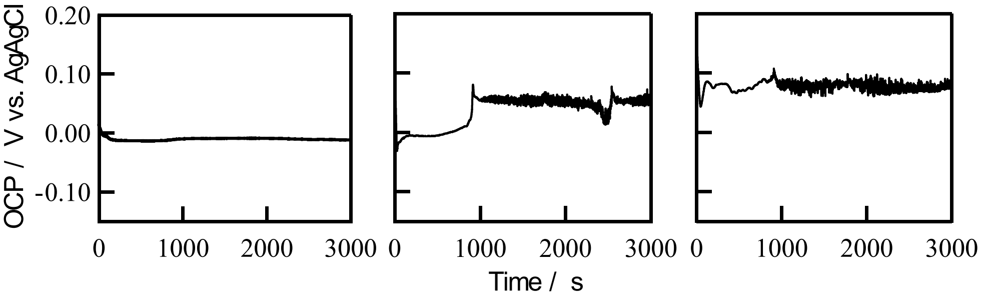

(A) (B) (C)

Figure 6. OCP oscillation of Si in Ag_2SO_4 + 60 mM HF solution, (A) 2 mM and (B) 3 mM and (C) 5 mM of Ag_2SO_4 concentration.

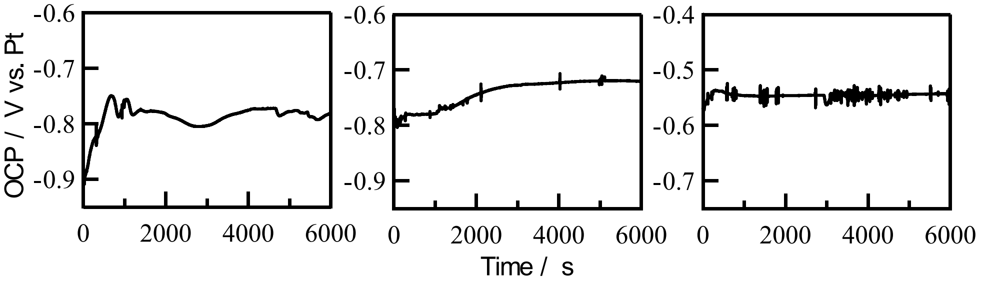

(A) (B) (C)

Figure 7. OCP oscillation of Si in $NaNO_3$ + 60 mM HF solution, (A) 10 mM and (B) 50 mM and (C) 100 mM of $NaNO_3$ concentration.

ECS Transactions, 16 (3) 189-194 (2008)
10.1149/1.2982555 ©The Electrochemical Society

Are the Oscillations During the Anodic Dissolution of Si in Dilute Fluoride Electrolyte Damped or Sustained?

J.-N. Chazalviel and F. Ozanam

Physique de la Matière Condensée, École Polytechnique, CNRS, 91128 Palaiseau, France

The current oscillations observed under potentiostatic conditions during the anodic dissolution of silicon in a fluoride electrolyte have been reexamined. This phenomenon, originating from an oscillation of the oxide thickness on the local scale, can be observed as a macroscopic oscillation only if the phase of the local oscillators is synchronized over the whole electrode surface. In the absence of an external excitation, theoretical modeling indicates that such a synchronization can hardly be obtained from a short-range interaction between the local oscillators. Experimental analysis of the oscillation damping suggests that such an interaction is either absent or extremely weak. We conclude that the synchronization observed in some instances is most plausibly due to global coupling through the uncompensated series resistances of the electrode, its back-contacts, and the electrolyte.

Introduction

In the last 20 years, there has been much excitement about the oscillatory behavior observed during the anodic dissolution of silicon in fluoride electrolytes, in the electropolishing regime (1-7). The origin of this intriguing behavior, associated with an oscillation of the thickness of the interfacial oxide layer, has led to different hypotheses, some of which have been turned into detailed mathematical models (8-10). However, there remains an unresolved controversy about the self-oscillatory character of the current under potentiostatic control. Some investigators claim that a self-oscillatory behavior can be observed (4). Others say that the self-oscillatory behavior is induced by global coupling, typically through the series resistance of the electrolyte (3). According to these authors, the self-oscillatory behavior is present on the local (microscopic) scale, but the macroscopic behavior is only resonant: oscillations can be externally triggered, for example by a potential step, but they are damped because a steady state is reached, for which the phase of the oscillation is distributed over the electrode surface, and only the (constant) average value of the current is observed (11-13).

Here we have readdressed this problem from a theoretical and an experimental viewpoint. On the theoretical side, we have examined whether or not coupling between neighboring surface locations can lead to oscillator synchronization over the whole electrode surface. On the experimental side, we have chosen systems where a self-oscillatory behavior has been reported, and we have investigated the time-behavior of the oscillation amplitude under stringent experimental conditions. The driving idea of these investigations is that, in the absence of interaction between the local oscillators, the oscillation can be triggered by a potential step, but an exponential damping of the oscillation amplitude is expected to follow. The presence of a synchronizing interaction should yield a deviation from this behavior, namely a lowering of the damping rate and the reaching of a steady-state amplitude if the oscillations can be sustained. The theory is aimed at predicting some bounds to this behavior, which can be quantitatively tested by the experiments.

Theory

The electrode surface is modeled as a collection of local oscillators, whose associated current can be written in the form:

$$I_i(t) = \sum_k f\left(t-kT-\Delta t_i^k\right), \qquad [1]$$

where the index i refers to the oscillator under consideration (i=1 to N), $f(t-t_0)$ represents a current "burst" (9) around time t_0, T is the oscillation period, k an integer, and Δt_i^k is a "jitter" time responsible for the phase loss in the absence of interaction between the oscillators. An interaction between neighboring oscillators can be modeled by assuming that the recursion relation between Δt_i^{k-1} and Δt_i^k is non-local, e.g.,

$$\Delta t_i^k = \Delta t_i^{k-1} + \Delta\tau_i^k + b\sum_l \left(\Delta t_l^{k-1} - \Delta t_i^{k-1}\right), \qquad [2]$$

where $\Delta\tau_i^k$ is a random time of zero mean, the summation is extended over the nearest neighbors l of i, and b is a positive dimensionless parameter characterizing the force of the synchronizing interaction.

The evolution of the system can be predicted from this model starting from the perfectly synchronized state ($\Delta t_i^0 = 0, \forall i$), either by numerical simulation or by analytical derivation. The detail of the analytical derivation will appear elsewhere (14). In brief, Δt_i^k can be considered as the i^{th} component of an N-dimensional vector Δt^k (i=1 to N); Equation [2] then appears as an affine transform from the vector Δt^{k-1} to the vector Δt^k, which can be diagonalized by using a discrete Fourier transform over space (indexes i and l). For a realistic electrode, this is a 2D-Fourier transform. Introducing the discrete Fourier transforms of Δt_i^k and $\Delta\tau_i^k$ as g_{q_x,q_y}^k and γ_{q_x,q_y}^k , respectively (q_x, q_y=0 to $n-1$, with $n=N^{1/2}$, the electrode being taken as a square), Equation [2] becomes

$$g_{q_x,q_y}^k = \gamma_{q_x,q_y}^k + g_{q_x,q_y}^{k-1}\left[1+2b\left(\cos\frac{2\pi q_x}{n}+\cos\frac{2\pi q_y}{n}-2\right)\right]. \qquad [3]$$

We can take as the initial condition g_{q_x,q_y}^0 = 0 (except for $q_x=q_y=0$) (perfect synchronism). The variance Δ^2 of Δt_i^k can then be derived using Parseval's theorem:

$$\Delta^2 = \left\langle {\Delta t_i^k}^2 \right\rangle = \frac{\delta^2}{n^2}\sum_{q_x,q_y}\sum_{k'=0}^{k-1}\left[1+2b\left(\cos\frac{2\pi q_x}{n}+\cos\frac{2\pi q_y}{n}-2\right)\right]^{2k'}, \qquad [4]$$

where δ is the rms value of $\Delta\tau_i^k$ (assumed independent of i and k). Expression [4] can be approximated in three limiting regimes for k (effective time): At small times ($8\pi bk \ll 1$), it is asymptotically equivalent to $\delta^2 k$. This is equivalent to the simple case with no interaction between the elementary domains. For $k > 1/8\pi b$, the interaction starts to play a role, and a new approximation of Expression [4] is $(\delta^2/8\pi b)[1+\ln(8\pi bk)]$. Finally, for infinite time ($8\pi bk \gg N$), a steady-state value is obtained as $(\delta^2/4b)\times 0.33\ln n$. Figure 1 shows results of this approximate analytical derivation, together with the results from Monte Carlo simulations for an electrode with $n=100$. As expected, the presence of a synchronizing interaction (increasing b values) limits the increase of the jitter-time distribution over the surface, thus slowing down the desynchronization between the local oscillators.

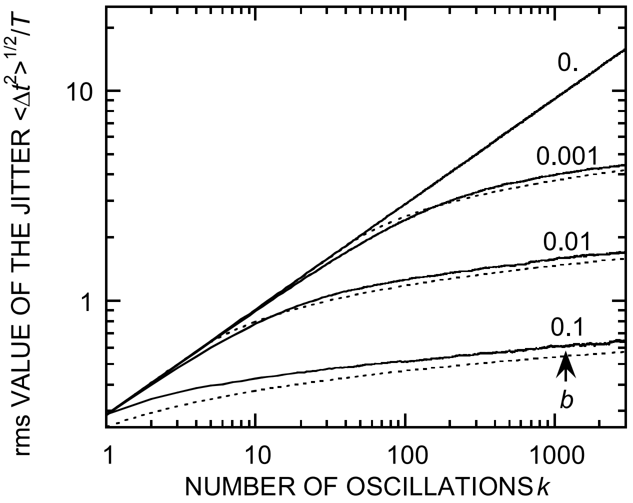

Figure 1. rms width of the jitter-time distribution, as a function of effective time $k=t/T$, for $\delta/T=0.29$ and several values of the interaction parameter b. The full lines are the averaged result of several Monte Carlo simulations. The dotted lines are the result of the approximate analytical resolution of Equation [4].

The oscillation amplitude is expected to decrease when the rms value of Δt_i^k increases. Namely, if we limit our consideration to the amplitude a_1 of the first Fourier component of the oscillation (i.e., the component at the fundamental frequency $1/T$), this quantity can be calculated by assuming that the distribution of Δt_i^k is Gaussian; hence,

$$a_1 \propto \int_{-\infty}^{+\infty} e^{2i\pi(\Delta t)/T}\left[\frac{1}{\Delta\sqrt{2\pi}}\, e^{-(\Delta t)^2/2\Delta^2}\right] d(\Delta t) = e^{-2\pi^2\Delta^2/T^2} \qquad [5]$$

From the above three regimes of variation of Δ^2, it results that the variation of a_1 is initially exponential with a characteristic damping time $T^3/2\pi^2\delta^2$. For times on the order of $T/8\pi b$, it switches to a slower decay of a power-law form $t^{-\alpha}$, with an exponent $\alpha=\pi\delta^2/4bT^2$. At very large times ($\sim NT/8\pi b$), a constant value ($\sim N^{-\alpha}$) is finally predicted. Note that this value is sizable only if $\alpha \sim \delta^2/bT^2 \ll 1$.

Experiment

p-Si rotating-disk electrodes were prepared from 1 Ωcm wafers, back-contacted with a diffused contact and soldered on a brass substrate with indium solder, in order to minimize series resistance. For the same reason, the electrolytes were brought to 1M ionic strength using NH_4Cl as a supporting salt, and the reference electrode was placed behind the working electrode plane. Two electrolytes where sustained oscillations have been reported were used (c_F=0.05M, pH 3 and c_F=0.1M, pH 4.5). The oscillation was triggered by a potential step from +1.5 V to a potential in the range where oscillations have been reported (typically between +3 and +8 V). Subsequently, the potential was held fixed and the variation of the oscillation amplitude and shape was recorded as a function of time t or oscillation number k.

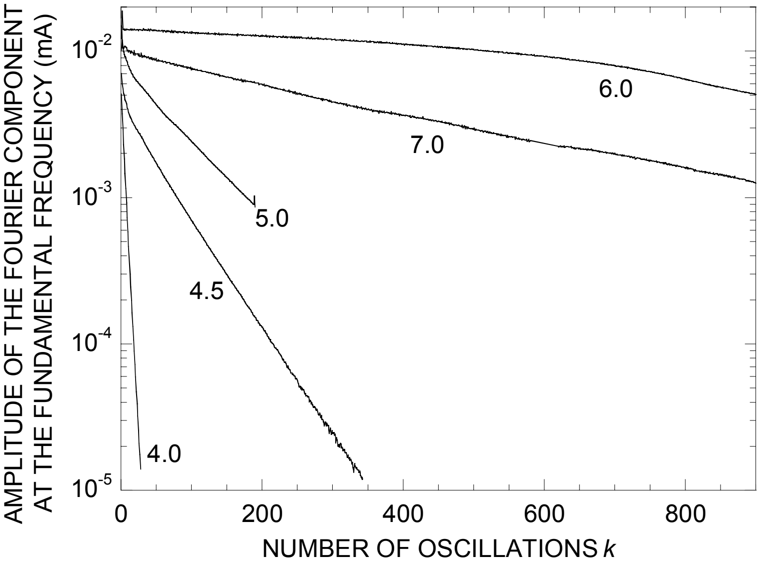

Figure 2. Typical experimental decay curves of the fundamental-frequency amplitude a_1 for the (c_F=0.1M, pH 4.5) electrolyte, and various potentials. Rotating disk electrode 4 mm diameter, 1500 rpm. The non-exponential behavior at 6.0 V is due to inhomogeneous damping (T~300 s: these experiments last several days!).

Typical results are shown in Figure 2. The oscillations generally exhibit an exponential damping. In no case did we observe sustained oscillations, though the characteristic damping time may occasionally be extremely long. In such cases, the damping generally deviates from exponential behavior at long times (see the curve for 6 V potential in Figure 2), but in contrast to the predictions from the above model, these deviations consist in an acceleration, rather than a slowing down, of the damping. Such deviations can be attributed to imperfections in the electrode geometry and the uniform accessibility of the electrode surface: the regions of the surface experiencing a slower (respectively faster) renewal of the electrolyte exhibit a slightly lower (respectively higher) current density. Since the oscillation frequency at a given potential is proportional to the current density, the oscillation frequency becomes distributed over the electrode surface, leading to inhomogeneous damping of the oscillation (15). We have tried to minimize this effect by carefully polishing the electrode. However, the geometry cannot be perfectly controlled, since the electrode is under dissolution conditions. Also, the current density is affected by the presence of polishing damage, and some dissolution is necessary in order to remove these defects. Figure 2 represents the best that we have been able to obtain. The exponential shape (linear in the semi-log plot of Figure 2) appears to be the limiting shape of the decay curves when inhomogeneous damping is minimized. In some cases, we have been able to observe a very slight lowering of the damping rate at long times. However, these deviations occurred at long times, just before the oscillation amplitude reached the noise level. If meaningful at all, noting that the change of exponential to power-law damping is expected to occur for $k \sim 1/8\pi b$, these observations suggest an upper value for b on the order of 10^{-4}. The characteristic damping time can then be identified to $T^3/2\pi^2\delta^2$. This leads to values of δ/T which can be as low as 10^{-2}.

The very small value found for the interaction parameter b may lead one to wonder whether such a "synchronizing interaction" is present at all. The above theory cannot be transposed to the case of a desynchronizing interaction ($b<0$), because in such a case the linear approximation subtending Equation [2] would hold no more. All in all, it appears plausible that there is no synchronizing interaction between the elementary domains, but rather a "desynchronizing interaction", as assumed indeed by Foca et al (9). However, even in the presence of a synchronizing interaction, our analysis indicates that a sustained oscillation can be observed in practice only if $(\delta^2/4b) \times 0.33 \ln n \ll 1$, a rather stringent condition in practice, especially given the large value $n \sim 10^5$ for practical electrodes.

Conclusion

Careful analysis of the oscillatory behavior of the p-Si fluoride interface confirms our earlier conclusion that the oscillations are damped (11). A theoretical examination indicates that a short-range synchronizing interaction between the local oscillating domains can bring a sustained oscillation only for values of the parameters ($\delta^2/bT^2 \ll 1$) that are not reached in practice. It seems plausible that no synchronizing interaction is present at all, and the sustained oscillations which have been reported in the literature probably arose from global coupling through the uncompensated series resistance of the electrolyte, electrode, and back-contacts.

Acknowledgments

We are indebted to Prof. H. Föll and J. Grzanna for many stimulating discussions.

References

1. H. Gerischer and M. Lübke, *Ber. Bunsenges. Phys. Chem.*, **92**, 573 (1988).
2. V. Lehmann and H. Föll, *J. Electrochem. Soc.*, **137**, 653 (1990).
3. F. Ozanam, J.-N. Chazalviel, A. Radi, and M. Etman, *Ber. Bunsenges. Phys. Chem.*, **95**, 98 (1991).
4. H.J. Lewerenz and M. Aggour, *J. Electroanal. Chem.*, **351**, 159 (1993).
5. J. Carstensen, R. Prange, G.S. Popkirov, and H. Föll, *Appl. Phys. A*, **67**, 459 (1998).
6. S. Cattarin, F. Decker, D. Dini, and B. Margesin, *J. Electroanal. Chem.*, **474**, 182 (1999).
7. V.P. Parkhutik and E. Matveeva, *Electrochem. Solid-State Lett.*, **2**, 371 (1999).
8. J. Carstensen, R. Prange, and H. Föll, *J. Electrochem. Soc.*, **146**, 1134 (1999).
9. E. Foca, J. Carstensen, and H. Föll, *J. Electroanal. Chem.*, **603**, 175 (2007).

10. J. Grzanna, H. Jungblut, and H.J. Lewerenz, *J. Electroanal. Chem*., **486**, 181 (2000); *ibid*., **486**, 190 (2000).
11. J.-N. Chazalviel, F. Ozanam, M. Etman, F. Paolucci, L.M. Peter, and J. Stumper, *J. Electroanal. Chem*., **327**, 343 (1992).
12. J.-N. Chazalviel and F. Ozanam, *J. Electrochem. Soc*., **139**, 2501 (1992).
13. F. Ozanam, J.-N. Chazalviel, A. Radi, and M. Etman, *J. Electrochem. Soc*., **139**, 2491 (1992).
14. J.-N. Chazalviel and F. Ozanam, *Electrochim. Acta* (submitted).
15. F. Ozanam, N. Blanchard, and J.-N. Chazalviel, *Electrochim. Acta*, **38**, 1627 (1993).

ECS Transactions, 16 (3) 195-200 (2008)
10.1149/1.2982556 ©The Electrochemical Society

Enhanced Controllability of Periodic Silicon Nanostructures by Magnetic Field Anodization

B. Gelloz, M. Masunaga, T. Shirasawa, R. Mentek, T. Ohta, and N. Koshida

Graduate School of Eng., Tokyo University of Agriculture and Technology, 2-24-16,
Nakacho, Koganei, Tokyo 184-8588, Japan.

The presence of a magnetic field during anodization of Si in HF solution can drastically influence the resulting porous Si morphology. The effect of the strength of the magnetic field was investigated. The magnetic field enables the realization of non-percolating straight pores of diameters from 100 nm with n^+-type Si to several micrometers for p-type Si, through depths as large as 100 μm, without any lithographic or pore initiation process. There is a clear enhancement of the pore aspect ratio when increasing the magnetic field strength, which enhances the collection of holes at the pore tips with respect to lateral pore walls. Thick, well-defined free-standing membranes can also been fabricated for applications such as bio-scaffold and filters.

Introduction

The morphology of porous silicon (PS), produced by electrochemical etching of bulk Si in HF solution, strongly depends on the anodization parameters (substrate resistivity, crystal orientation, conduction type, HF concentration, current density, temperature, illumination condition (1), and external magnetic field (MF)) (2, 3).

Periodic silicon nanostructures are attractive for example as photonic band crystals or sensors (1). Regular arrays of micrometer-size straight macropores in Si have been obtained using a pore initiation technique requiring a lithography step. In n-type Si, this technique requires back-side illumination (1).

As previously reported (3), structures consisting of arrays of sub-micrometer-size straight pores can be fabricated in heavily doped n-type Si using MF-assisted anodization (in the range 0-1.9 T) without any supplementary techniques such as lithography and illumination.

These structures consisting of either macropores or sub-micrometer size straight pores can be used in chemical or bio sensing. Monolithic integration of the various functions of PS (optoelectronic, bio, etc.) would be very valuable, technologically as well as environmentally, for example for lab-on-chip devices. Therefore, the understanding and optimization of the diverse properties of PS are of great importance.

In a view to optimize and get a deeper understanding of magnetic field assisted anodization, we have studied the effect of a strong magnetic field, from 0 to 4 T, on the morphology of the pores of n- and p-type PS. This technique was applied to fabrication of self-standing membranes consisting of sub-micrometer straight pores.

Experimental

Low-resistivity (4-6 Ω.cm) p-type (100)-oriented silicon samples were anodized in HF:DMF (dimethylformamide)=34:210 under 10 mA/cm^2. Heavily doped n-type (100)-

oriented silicon samples were anodized in $HF:H_2O:C_2H_5OH=80:140:220$ under 40 mA/cm^2. Anodization was carried out in the dark. The anodization temperature was set to 0ºC. The magnetic field was varied from 0 to 4 T using a superconducting apparatus. Figure 1 shows a cross-sectional view of the anodization setup. The morphology of PS pores was studied using a scanning electron microscope (SEM).

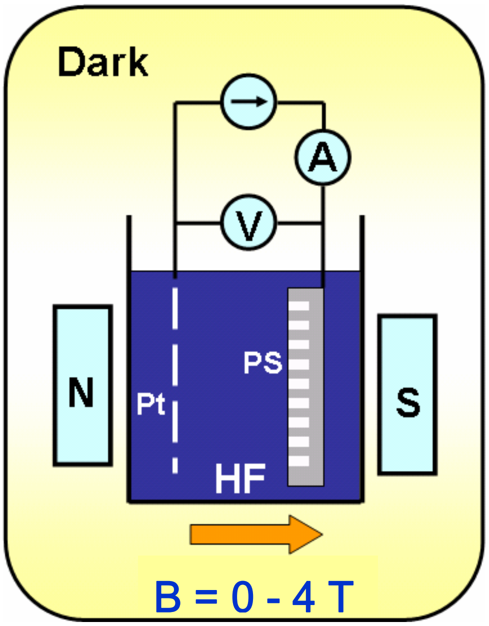

Figure 1. Schematic representation of the magnetic filed assisted anodization setup. The south (S) and north (N) poles of the magnet are represented.

Results and Discussion

Magnetic field-assisted anodization of p-type Si

Figure 2 shows SEM pictures of pores formed in p-type Si for 20 min, under two different MF strengths. At the highest MF (4 T), the pores exhibit no percolation and their diameter remains rather uniform through the PS depth. In contrast, as the MF is lowered, a deterioration of the in-depth uniformity of the pore diameter is noticeable, and some pore walls have been etched resulting in straight pore propagation with smooth inside walls.

The mean diameter of pores is not strongly affected by the magnetic field in the range of 2 to 4 T, while the pores diameter tends to decrease with increasing magnetic field in the range of 0-2 T. Another effect of a high magnetic field application is to suppress the outside top surface etching during the pore growth as suggested from the SEM photographs in Fig. 2. This results in an increase of both the pores aspect ratio and the PS layer thickness at higher MF intensity. Actually deep pores are uniformly fabricated at 4 T in comparison to the case of 2 T under the same anodization time.

Figure 3 shows higher magnification SEM pictures of the PS/substrate interface along with corresponding values of the pore tip curvature radius, PS formation rate and cyclotron diameter. As the MF increases, the pore tips become sharper. The comparison of the cyclotron diameter with pore tip curvature radius suggests an effective confinement of the holes at the pore tips.

The effect of the MF can be understood qualitatively. The MF promotes the supply of holes with a thermal velocity component normal to the substrate surface. It tends to prevent holes with different thermal velocity direction from contributing to silicon dissolution by confining them in the plane parallel to the substrate surface until a collision changes their thermal velocity. Meanwhile, the electric field concentrated at the pore tips still attracts holes towards them. The propagation of the pores in the vertical direction is then promoted by preferential charge exchange at the pore tips, leading to self-regulated formation of non-percolating high aspect ratio pores.

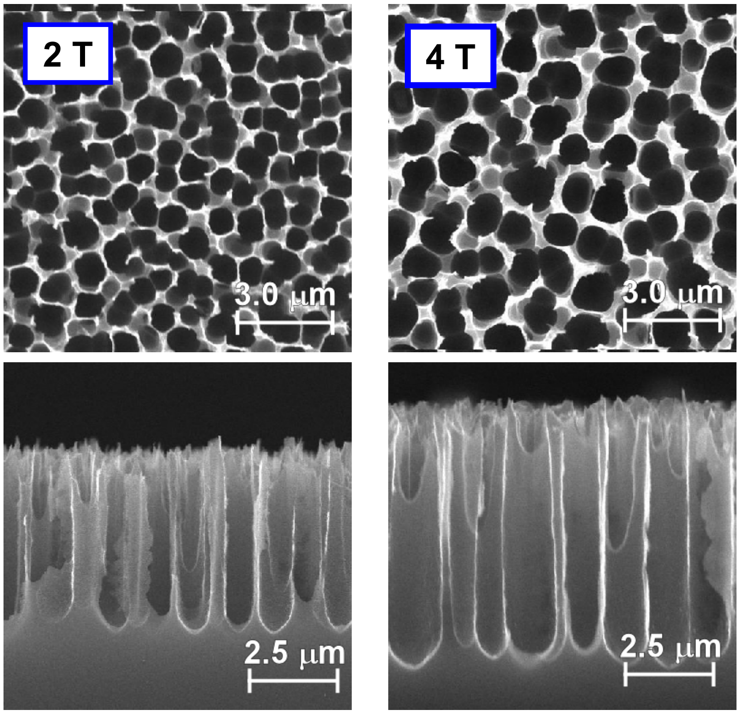

Figure 2. SEM pictures of p-type Si anodized under two different indicated MFs. The upper row shows top views of the resulting PS layers whereas the lower row shows cross-sections of the PS layers.

Magnetic field-assisted anodization of n^+-type Si

We have also investigated heavily doped n-type Si. Illumination is not necessary for its anodization since holes can be supplied by tunneling through the space charge region at the PS/substrate interface. Sub-micrometer size (~100 nm in diameter) straight pores were successfully realized, as shown in the SEM pictures of Fig. 4. The application of the magnetic field results in the suppression of pore percolation, even for PS thicknesses over 100 μm, and very high aspect ratios of the pores. Increasing the MF strength also results in smaller pore diameters and significant narrowing of their distribution.

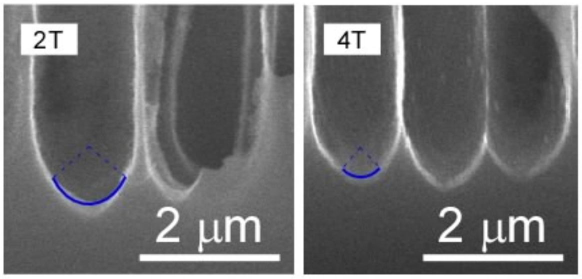

Pore tip curvature radius (nm)	*364*	*214*
Formation rate (μm/min)	*0.25*	*0.35*
Cyclotron diameter (nm)	*480*	*240*

Figure 3. SEM photographs of p-type Si anodized at two different MFs. The pore tips become sharper as the magnetic field is increased, as illustrated by the curvature section added into each picture. The corresponding pore tip curvature radius, formation rates, and cyclotron radius are also shown.

Fabrication of self-standing membranes

The MF-assisted anodization has been used to fabricate 100 μm-thick self-standing membranes including pores that propagate throughout them perpendicularly to the membrane surface without any dendritic percolation. The pores are straight, exhibit very high aspect ratio, and are 100 nm in diameter.

Figure 4 shows the fabrication process flow as well some SEM pictures of the surface and cross-section of such membrane. Heavily doped Si was used. The anodization conditions were those given in the experimental section. The MF was 0.45 T and the temperature 5ºC. After anodization, dry etching, using the conditions shown in Fig. 4, was used to remove surface fragments on the front and backsides of the samples. The backside was etched in order to ensure that all pores were opened on that side. The front side was also etched to remove a thin transient PS layer whose pores do not match well those underneath which propagate throughout the sample.

Those membranes have several applications. If electrodes are deposited on the front and backsides, they could be used as micro channel plates. They could also be used as bio-filters or bio-reactors.

Conclusion

The influence of the strength of a MF used during anodization was investigated. The MF enables non-percolating straight pores of dimensions from 100 nm with n^+-type Si to several micrometers for p-type Si without any lithographic or pore initiation process. There is a clear enhancement of the pores characteristics when increasing the MF strength. This fact results from enhanced collection of holes at the pore tips with respect to lateral pore walls.

The MF-assisted anodization allows the realization of thick well-defined nanostructures. Self-standing membranes can also been fabricated for applications such as bio-scaffold and filters.

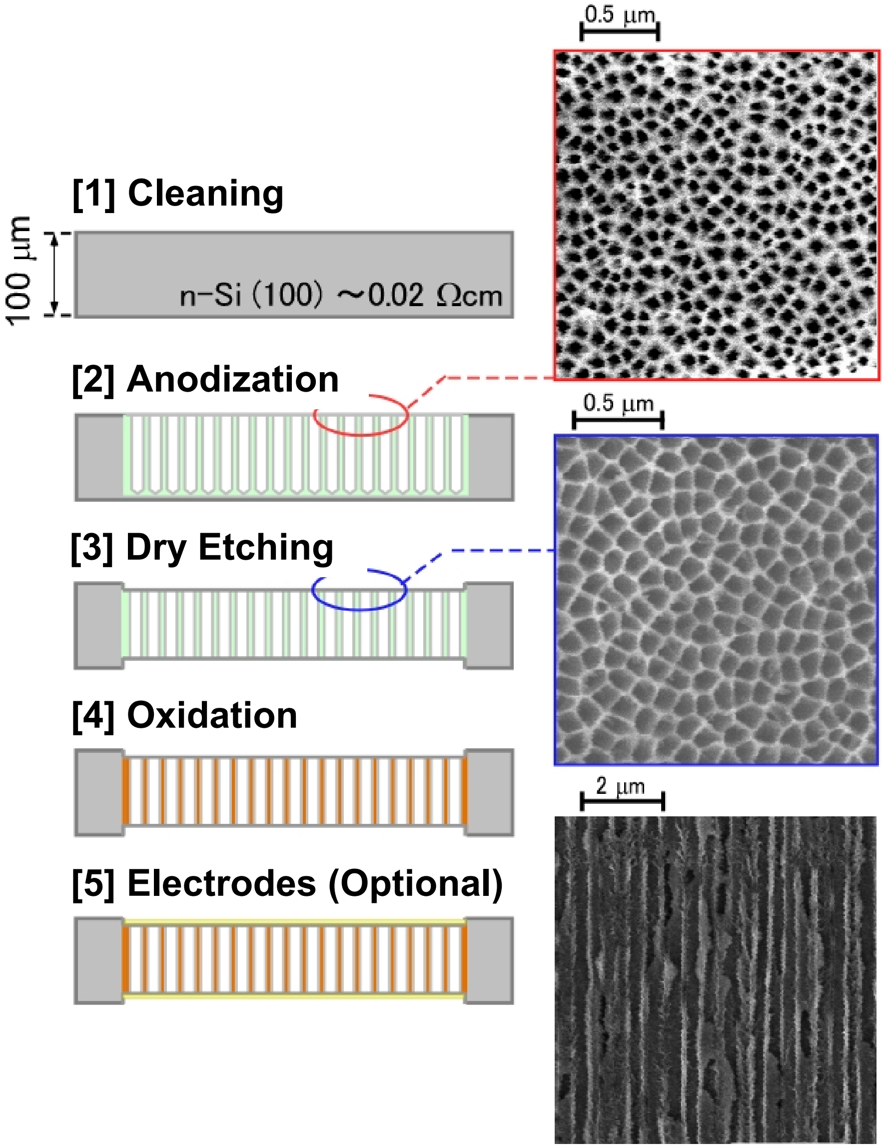

Figure 4. Process flow for fabrication of a self-standing PS membrane and the corresponding SEM photographs. After cleaning [1] and subsequent magnetic anodization [2], dry etching [3] was performed in $CF_4/O_2 = 20/3.2$ sccm at 150 W for 300 min. Plan view SEM photographs of the surface at the stages [2] and [3] are shown on the top-right corner. A cross-sectional SEM photograph of a fabricated membrane is shown on the bottom-right corner. Optional oxidation of the structure [4] can be performed by conventional thermal annealing in O_2 at 500-1000ºC. Optional electrodes [5] could be deposited for example by evaporation of gold or sputtering of gold or indium tin oxide.

Acknowledgments

This work was partially supported by a Grant-in-Aid for Scientific Research from the Ministry of Education and Science of Japan (MEXT) and from Japan Society for Promotion of Science (JSPS).

References

1. V. Lehmann, *Electrochemistry of Silicon: Instrumentation, Science, Materials and Applications* (Wiley-VCH, Weinheim, 2002).
2. T. Nakagawa, H. Koyama and N. Koshida, *Appl. Phys. Lett.*, **69**, 3206 (1996).
3. Ｔ. Nakagawa, H. Sugiyama and N. Koshida, *Jpn. J. Appl. Phys., Part 1*, **37**, 7186 (1998).

ECS Transactions, 16 (3) 201-207 (2008)
10.1149/1.2982557 ©The Electrochemical Society

Electrochemical Formation of Self-Positioned Nano-Sized Pores on Oxidized Porous Silicon Substrate

D. H. Ge, J. W. Jiao, X. Q. Bao, S. Zhang, P. Zhou, Y. L. Wang, S. L. Feng

State Key Laboratories of Transducer Technology, Shanghai Institute of Microsystem and Information Technology, Chinese Academy of Sciences, Shanghai 200050, China

This paper reports on recent improvements in the fabrication of self-positioned nano-sized pore array with a dimension of around 200 nm on the partly oxidized porous silicon (POPS) substrate. The fabrication process is based on photoelectrochemical etching, combined with steps of oxidation, CMP and KOH etching. Moreover, the dependency of a single pore diameter on the configuration of the partly oxidized micro-trenches with varied widths has been investigated. A simple model, based on the depletion effect, is proposed to explain the experimental phenomena.

Electrochemical silicon etching in HF (hydrofluoric acid) -based electrolytes is a well known technique to produce porous silicon (1). Depending on the silicon doping, the type of the anodized substrate and the etching parameters, different pore morphologies can be obtained. By illumination from the backside of the n-Si wafer, macroporous silicon can be formed via the electrochemical etching in HF (2). In particular, regular macropore array can be obtained from n-Si wafer by pre-patterning and back-side illumination (3). The formation mechanism requires a steady state condition between mass transport in the electrolyte and charge supply from the electrode at the pore tip (4). The pore aspect ratio can reach up to 250, grown on a whole wafer (5) and throughout the wafer thickness (6). Numerous applications of this porous silicon structure have emerged, such as photonic crystals (7), IR filters (8), fuel cells (9) and biosensors (10).

A very important application of porous silicon is the formation of thick silicon dioxide layer by thermal oxidation of porous silicon. It is a simple and low cost method for the growth of thermal silicon dioxide films with thickness of several tens of microns (11). Many applications utilizing this oxidized porous silicon (OPS) have been reported, such as the gas sensors (12), bulk micromachining (13), RF circuits (14) and biomedical microsensors (15). However, the electrochemical etching on the partly oxidized porous silicon (POPS) substrate, which can monolithically integrate micro- and nano-structures in order to facilitate novel applications, has not been well studied to date.

In this paper, we present a novel method to fabricate self-positioned nano-sized pore array with a dimension of around 200 nm on the POPS substrate. The fabrication process is based on photoelectrochemical etching combined with steps of oxidation, CMP and KOH etching. A simple model, based on the depletion effect, is proposed to explain the experimental phenomena.

Experimental

N-type (100) silicon wafer with electrical resistivity in the range of 3-8 Ω cm was used in our experiments. Figure 1 illustrates our procedure for the electrochemical formation of self-positioned nano-sized pore array. A silicon nitride film (500 nm thick) was grown on the wafer as a mask via PECVD (plasma enhanced chemical vapor deposition) (Fig. 1a). A triangular pattern of circular holes at a pitch of 3 µm was defined using a standard photolithographic process. Initial pits were finally formed after removing the silicon nitride in the patterned area via ion-beam bombard (Fig. 1b).

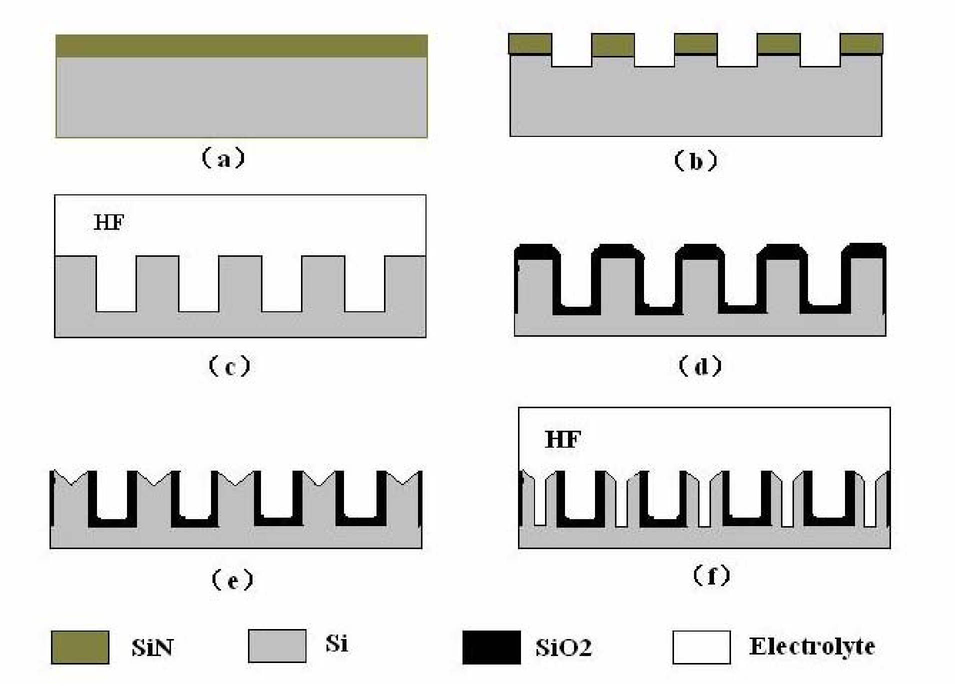

Figure 1. Nano-sized pore array fabrication process.

<u>POPS substrate formation</u>

All samples were anodized on an electrochemical etching platform in a decontamination chamber at room temperature. The electrochemical cell is made of polytetrafluoroethylene (PTFE). The anodization electrolyte was based on a mixture of 48 wt.% HF acid and deionized water in a 1:19 volume ratio. The area of the sample exposed to the electrolyte was about 1 cm^2 and had a circular shape. A power-controlled 50 W halogen lamp was kept 12 cm from the back-side of the sample to generate the illumination, through a circular window in a metal foil used to provide the electrical contact to the back side of the sample. A network-like platinum electrode (as cathode) was placed 5 mm away from the front side of the sample. Anodization voltage of 2 V was applied from an Agilent constant-voltage power-source to the samples during 20 min and about 8 µm thick macroporous Si layer was obtained. The diameters of the etched pores were around 2 µm (Fig. 1c).

The macropore sample was pre-oxidized at low temperature (300 ℃) under atmospheric pressure for 10min to grow a few oxide monolayers and avoid texture coarsening (16). A steam thermal oxidation was then performed at 1100 ℃ for 4 h, followed by an additional 10 min dry oxidation step. The POPS substrate was formed with the width (lateral thickness) of the produced silicon dioxide layer around 800 nm (Fig. 1d).

Nano-pores formation

The POPS substrate was subjected to a CMP (chemically-mechanically polish) process to both smooth the top surface of the sample and expose the remaining silicon among the oxidized primary pore array. The secondary self-positioned initial pits were created by KOH anisotropic etching through the patterned silicon dioxide on POPS substrate. The etch time was long enough to obtain full inverse pyramidal pits for the secondary macropore array formation (Fig. 1e).

A second electrochemical anodization step was performed on the same electrochemical etching platform mentioned above, with the same electrolyte, illumination and temperature, while the anodization voltage of 3 V was applied for 30 min. Nano-sized secondary pore array was successfully achieved along the secondary self-positioned initial pits, surrounded by the oxidized primary macropore array (Fig. 1f).

The pores produced were investigated with a field-emission scanning electron microscope (FESEM : Hitachi S-4700). Plan view micrographs show the (100) plane, whereas after cleaving the samples, cross-section view micrographs show the pores in the (110) cleavage planes.

Results and Discussion

Secondary self-positioned initial pits

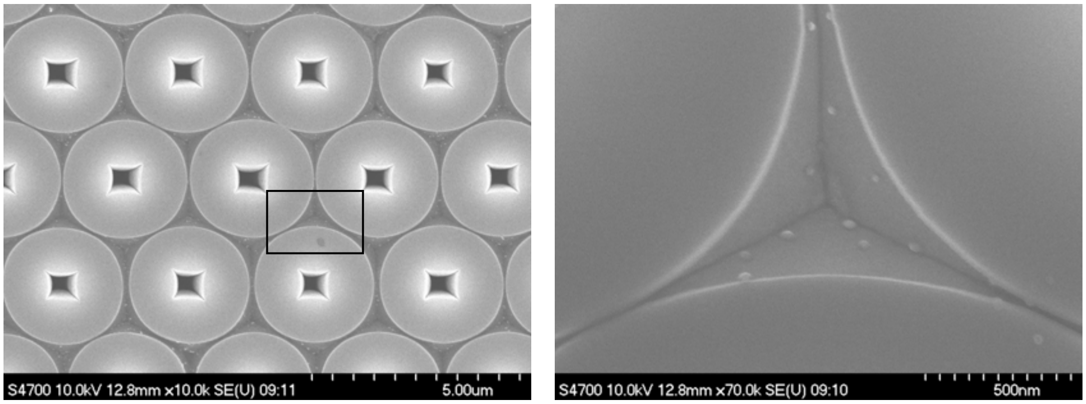

Figure 2. SEM top views of the oxidized macropore array with the secondary self-positioned initial pits at the center of three nearby oxidized pores forming equilateral triangle.

Patterned pores with the pitch of 3 μm were fabricated starting with the aforementioned silicon substrate, using the above detailed process. The primary macropores are about 8 μm deep and 2 μm in diameter, corresponding to 20 min of etching time. After the optimized oxidation process mentioned above the POPS substrate was formed, followed by a CMP process to expose the remaining silicon among the oxidized primary pore array. In Fig. 2 the SEM top views of the oxidized primary macropore array with the secondary self-positioned initial pits is shown. Lateral thickness of the silicon dioxide walls in the surface of POPS substrate is about 1 μm. The exposed silicon area was then etched by KOH to define the secondary initial pits at the center of three nearby oxidized pores forming equilateral triangle. The initial pits were used for the secondary pore array formation.

Nano-sized secondary pore array

SEM picture in Fig. 3 shows the cross section of the oxidized primary and secondary pore arrays after the second electrochemical etching on the POPS substrate. The nano-sized secondary pores were formed following the secondary self-positioned initial pits, and thus quite precisely positioned at the center of three nearby oxidized macropores forming the equilateral triangle. The secondary pores are of the dimension of 200 nm and depth of 4 μm, corresponding to 30 min of etching time, with the aspect ratio about 20:1.

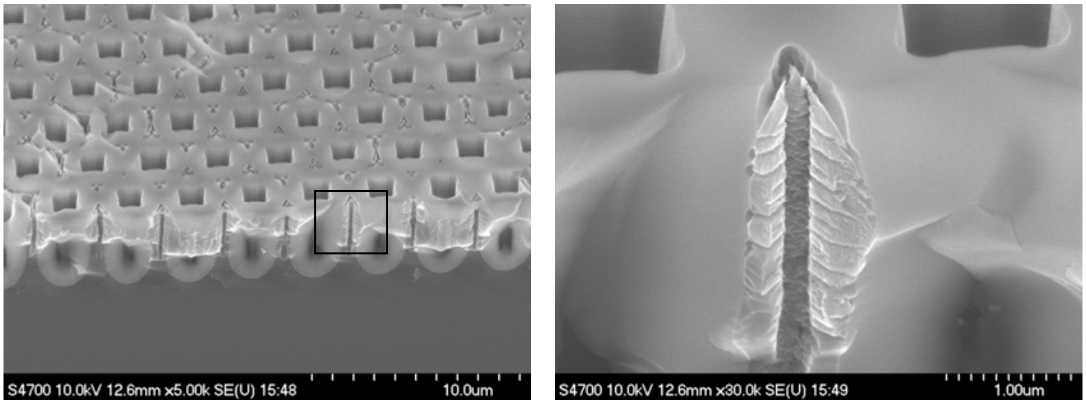

Figure 3. SEM cross section of the oxidized primary and secondary pore arrays after the second electrochemical etching.

It is commonly accepted (4) that the macropore growth process is ruled by the width of the space charge region (SCR), which is potential and doping dependent. The SCR width w for the electrochemical system can be estimated from the Schottky contact theory (17)

$$\mathrm{w} \approx (2\varepsilon\varepsilon_0 V / eN_D)^{1/2} \qquad [1]$$

ε = the dielectric constant of Si, ε_0 = the vacuum permittivity, V = junction voltage, e = elementary charge, N_D = doping density. If the substrate is not artificially oxidized, the SCR width is around 1.4 μm with anodization voltage of 3V and doping density of 2×10^{15} cm^{-3}, assuming that all the anodization voltage drops at the silicon-electrolyte interface. Thus the width of the silicon wall is no more than twice that of the SCR. If without the oxidizing process, too few holes, according to SCR model, can penetrate in the silicon wall and no secondary pores grow in the silicon between adjacent ones.

In our experiments, the width of silicon wall between two oxide layers on POPS substrate is around 800 nm, much smaller than that of the SCR. However the nano-sized secondary pores were still formed in the second electrochemical etching process, which could hardly be realized on lowly doped silicon substrate (3-8 Ω cm) according to the SCR model. Thus we suggest a depletion model to explain our experimental results, taking into account of the potential drop on the Si/SiO$_2$ interface around the primary macropores, which plays the dominant role in this phenomenon.

Due to the existence of a thin silicon oxide layer around the primary macropores, the electric field on the silicon-silicon dioxide interface became much higher when the anodization voltage was applied. Thus a depletion layer was formed near the silicon dioxide layer, with its width dependent on the oxide thickness, anodization voltage and the doping density. The depletion layer width d can be estimated (18)

$$d \approx \sqrt{(\frac{\varepsilon_{si}}{\varepsilon_{OX}} d_{OX})^2 + \frac{2\varepsilon_0 \varepsilon_{si} V}{\mathrm{e} N_D}} - \frac{\varepsilon_{si}}{\varepsilon_{OX}} d_{OX} \qquad [2]$$

$\varepsilon_{\mathrm{si}}$ = the dielectric constant of Si, $\varepsilon_{\mathrm{OX}}$ = the dielectric constant of oxide, ε_0 = the vacuum permittivity, V = anodization voltage, d_{OX} = oxide thickness, e = elementary charge, N_D = doping density.

Given the anodization voltage of 3V, doping density of 2×10^{15} cm^{-3} and oxide thickness of 800nm, the depletion width is about 300 nm, which is much smaller than the width of the space charge region (SCR) defined by the commonly accepted SCR model. As the width of silicon wall between two oxide layers on POPS substrate is more than twice that of the depletion layer, most of the holes, coming from the substrate, can diffuse into the silicon walls and finally drift to the HF/Si interface where they react with the electrolyte giving rise to the growth of secondary pores, due to the localized enhanced electric field (19) around the sharp tips. We obtain an estimation of the secondary pore diameter about 200 nm through simple subtraction operation, which is in excellent agreement with the experimental results. In other words, nano-sized pore array with larger pitch can be formed on low doped POPS substrate with our specially designed process flow.

Nano-sized pores among trench array

With almost the same process, we fabricated the nano-sized pores between oxidized trenches with bottle-like varied widths as shown in Fig. 4. The primary array of trenches is about 10 μm deep and with trench width bottle-like varied ranging between 0.5 μm and 2.5 μm by illumination modulation, corresponding to 30 min of etching time. The trench array was then oxidized, polished and etched in KOH to form secondary self-positioned initial seeds. A second electrochemical etching was performed at last to form the nano-sized secondary pore array.

The diameter of every single pore near the bottle neck is about 300 nm but gradually increases to 1.5 μm below the neck, which demonstrates the significant shift from the above depletion mechanism to the conventional SCR model. However, there's an interesting experimental phenomenon that the pore diameter above the neck till the initial defect remains uniform, independent of the variation of wall width. The possible reason maybe that the depletion effect near the neck strictly limits the amount of holes that can pass the neck. Only those holes, which can diffuse through the neck, can reach the Si-HF interface and thus determine the diameter of the pores. Fig. 5 schematically shows the mechanism, indicating the depletion layer and the holes' motion paths.

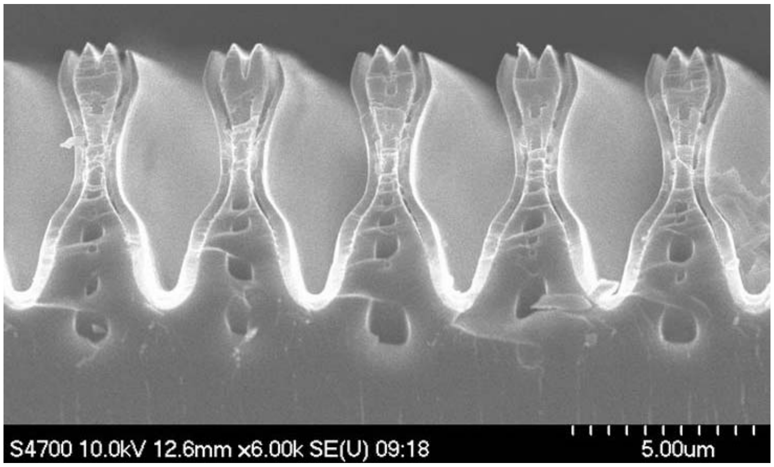

Figure 4. SEM cross section of nano-sized pores formed between oxidized trenches with bottle-like varied widths.

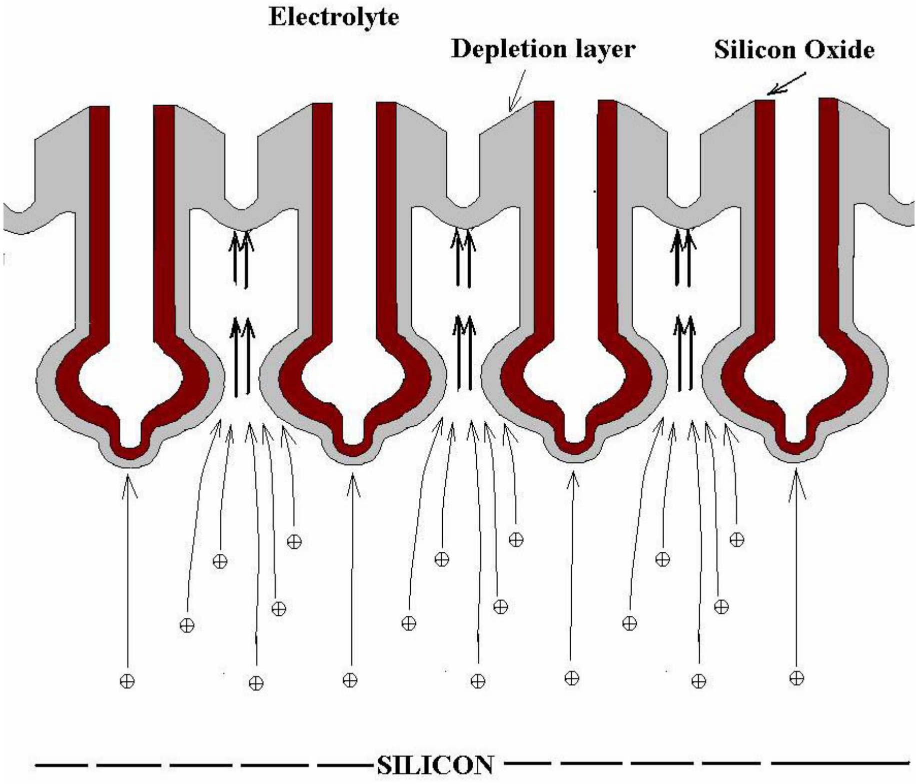

Figure 5. Schematic diagram of the depletion layer and the holes' motion paths.

Conclusions

In this paper a study of the photoelectrochemical formation of self-positioned nano-sized pore array with a dimension of around 200 nm on the POPS substrate is reported. A simple physical model, based on the depletion effect, is proposed to explain the experimental phenomena. Furthermore, the dependency of a single pore diameter on the configuration of the oxidized micro-trenches with varied widths has been carefully investigated. This novel hybrid micro-nano-sized porous structure has shown its possible applications of the photoelectrochemical etching technique in the fabrication of such as fuel cells.

Acknowledgments

This work was supported by Chinese National “863” (No.: 2006AA04Z312) and “973” (No.: 2006CB300403) Project and National Natural Science Foundation of China (NSFC) (No. 60772030).

References

1. R. L. Smith, S. D. Collins, *J. Appl. Phys.*, **71** R1 (1992).
2. H. Föll, M. Christophersen, J. Carstensen, and G. Hasse, *Mater. Sci. Eng. R,* **39** 93 (2002).
3. V. Lehmann and H. Föll, *J. Electrochem. Soc.,* **137**, 653 (1990).
4. V. Lehmann, *J. Electrochem. Soc.,* **140**, 2836 (1993).
5. H. Ohji, S. Izuo, P. J. French, K. Tsutumi, *Sens. Actuators A*, **92** 384 (2001).
6. P. Y. Kan, S. E. Foss, T. G. Finstad, *Mater. Sci. Eng. B,* **137** 63 (2007).
7. S. Matthias, F. Müller, C. Jamois, *Adv. Mater.*, **16** 2166 (2004).
8. V. Lehmann, R. Stengl, H. Reisinger, *Appl. Phys. Lett.*, **78** 589 (2001).
9. M. Hayase, T. Kawase, T. Hatsuzawa, *Electrochem. Solid-State Lett.*, **7**, A231 (2004).
10. A. Benilov, M. Cabrera, V. Skryshevsky, *Mater. Sci. Eng. B,* **139** 221 (2007).
11. G. Barillaro, A. Diligenti, A. Nannini, *Sens. Actuators A*, **107** 279 (2003).
12. P. Fürjes, G. Légrádi, A. Aszódi, *Sens. Actuators A*, **115** 417 (2004).
13. H. Ji-song, T. Kadowaki, K. Sato, *Sens. Actuators A*, **100** 114 (2002).
14. J. Y. Park, J. H. Lee, *Mater. Chem. Phys.*, **82** 134 (2003).
15. J. Salonen, V. Lehto, J. *Chem. Eng.,* **137** 162 (2008).
16. J. J. Yon, K. Barla, R. Herino, G. Bomchil, *J. Appl. Phys.*, **62** 1042 (1987).
17. E. H. Roderick and R. H. Williams, *Metal-Semiconductor Contacts*, 2nd ed., Oxford Science, New York (1987).
18. A. S. Grove, *Physics and Technology of Semiconductor Devices*, J. Wiley and Sons, Inc., (1967).
19. X. Q. Bao, J. W. Jiao, Y. L. Wang, *Electrochem. Commun.*, **9** 1491 (2007).

CHAPTER 4

TUESDAY: AFTERNOON SESSION

ECS Transactions, 16 (3) 211-219 (2008)
10.1149/1.2982558 ©The Electrochemical Society

Stabilization of Porous Silicon Free-Standing Coupled Optical Microcavities by Surface Chemical Modification

B. Gelloz[a], K. Murata[a], T. Ohta[a], M. Ghulinyan[b], L. Pavesi[c], D J. Lockwood[d] and N. Koshida[a]

[a] Graduate School of Eng., Tokyo Univ. of Agriculture and Technology, Koganei, Tokyo 184-8588, Japan
[b] Micro-Technology Lab., FBK - Inst. Sci. Res. & Technol., 38050 Povo (Trento), Italy
[c] INFM and Dipartimento di Fisica, University of Trento, 38050 Povo (Trento), Italy
[d] National Research Council of Canada, Ottawa, Ontario, K1A 0R6, Canada

As-anodized porous Si photonic structures experience drifts of their optical properties upon prolonged exposure to air due to spontaneous oxidation of the metastabe Si-H bonds terminating the pores surface. This is a critical limitation in the case of optical coupled optical microcavities, where both long term usage and stable nanometer resolution are required. With a view to stabilizing these structures, the surface of porous Si was chemically modified by hydrosilylation. The resulting surfaces are protected by stable Si-C bonds and by a steric hinderance mechanism. The modified photonic structures are stable for many months.

Introduction

Nanocrystalline porous silicon (PS), produced by electrochemical etching of bulk Si in HF solution, is a promising material for enabling various optoelectronic device applications based on Si (1,2). Significantly efficient and stable electroluminescence has recently been achieved by appropriate surface termination (3).

In spite of the structural inhomogeneities at the nanoscale, for visible and infrared light, PS shows optical properties typical of a dielectric material with an effective refractive index *n* lower than that of Si. Moreover, *n* can be continuously varied over a relatively wide range (~1.1-3) by varying the PS porosity, which is controlled by the anodization current density. Changing the current density during etching allows the fabrication of various types of one dimensional (1D) photonic crystals, such as distributed Bragg reflectors (DBRs), Fabry-Perot optical microcavities (MCs) and rugate filters (4-6).

A DBR is a periodic multilayer structure (also referred to as a 1D photonic crystal). With PS, the period (LH) could consist of a low porosity PS layer (L) stacked onto a high porosity PS layer (H). The total structure of a DBR including k periods, lying on a Si substrate and placed in air, would then be represented as Air/$(LH)_k$/Si/Air. Each H and L layer has an optical path of $\lambda_0/4$, where λ_0 is the central wavelength of the reflector. DBRs exhibit a spectral zone (centered at λ_0) where optical propagation is forbidden (photonic bandgap). As a consequence, a DBR acts as a reflector for optical waves whose wavelengths lie within this photonic bandgap.

A MC includes a $\lambda_1/2$ optical layer sandwiched between two distributed Bragg reflectors. This layer acts as a defect in the otherwise perfect photonic crystal, allowing optical transmission at λ_1, which is located inside the DBR bandgap. Therefore, a MC can act as a highly selective wavelength filter. With PS, this function is available for the important telecommunication window, in the 1.55 µm region. If $\lambda_1 = \lambda_0$, it is possible to produce MCs like the $(LH)_k/H_2/(LH)_k$ structure.

Several identical MCs can be coupled in a single 1D structure called coupled MCs (CMC). A typical CMC including 5 coupled MCs can be represented as a $[(LH)_k/H]_5/(LH)_k/L$ structure. Such structures can easily be produced with PS (7). The particular interest of CMCs is in the splitting of the MCs degeneracy, leading to fine structures packed around λ_1.

The physical properties of as-anodized PS drift upon ageing. This is due to the unstable Si-H bonds terminating the huge PS inner surface. The PS surface becomes progressively oxidized and/or contaminated by impurities it captures from air. Since the inner surface of PS is very large (typically 300 m^2/cm^3), a very small change in its chemistry is enough to induce a significant change of the optical properties of the PS layer (8). As a result, the characteristics of photonic structures progressively shift over time. In particular, the resonance of MCs and CMCs continuously drifts upon storage or operation. This is particularly problematic when high resolution (nanometer range) operation of the MCs is necessary. As an example, 30 min exposure of an MC to air was enough to induce a 1 nanometer shift in resonance peak position (7).

Two chemical stabilization methods have been proven efficient for PS. Recently, high-pressure water vapor annealing has been shown to efficiently stabilize PS photoluminescence (9,10), electroluminescence (3) and DBRs (11). This treatment performed on as-anodized PS leads to PS partial oxidation, thus affecting the original PS characteristics. However, PS can be prepared such that the desired properties are obtained after the treatment. Another promising approach is the chemical modification of PS surface using the reaction of hydrosilylation (12-15). This technique efficiently stabilizes PS photoluminescence (14) and electroluminescence (16), without affecting much the PS optical properties.

In order to stabilize MCs and CMCs, we have modified the chemistry of the PS surface using thermally induced hydrosilylation. Thus, metastable Si-H bonds were changed into stable Si-C bonds. The effects of both ageing and PS chemical modification on CMCs optical characteristics have been investigated.

Experimental

The samples have been grown by controlled electrochemical etching of heavily doped (0.01 Ω.cm) p-type (100)-oriented silicon in ethanoic HF. The electrolyte was a mixture of 30% volumetric fraction of aqueous HF (48 wt.%) with ethanol. It was continuously stirred during anodization to improve electrolyte exchange. High porosity layers (H layers; refractive index $n_H = 1.5$) and low porosity layers (L layers; refractive index $n_L = 2.1$) were prepared under a current density of 50 and 7 mA/cm^2, respectively. The thicknesses of the PS layers were adjusted by controlling the etching time.

CMCs represented by a $[(LH)_5/H]_5/(LH)_5/L$ structure were fabricated. They include 5 coupled MCs. For these PS structures, the natural refractive index drifts, which usually occur in relatively thick PS layers, can be compensated by adjusting the etching times of the layers in order to maintain the optical path constant to a first order approximation. In our case, to a first order approximation, a 12% difference between the thickness of the top (d_{top}) and bottom (d_{bottom}) layers was introduced [$(d_{top}-d_{bottom})/d_{bottom} = 0.12$] (6,7).

To obtain self-standing CMCs, an electropolishing current pulse was applied at the end of the PS formation process. This step leads to detachment of the PS structure from the substrate.

For chemical modification, PS was kept for 3 hours at 90 °C in 1-decene solution (15). Ar gas was flowed into the solution in order to minimize the content of dissolved oxygen in the organic solution. Transmission and reflectance spectra of the samples were measured from 800 to 2200 nm by a spectrophotometer (Hitachi U-4100).

Results and Discussion

Ageing of as-anodized PS photonic structures

Figure 1 shows the reflectivity of an as-anodized DBR whose structure was $(HL)_{10}$. After storage for 19 months in air, its optical characteristics have been significantly altered. A relatively large blue-shift of the reflectivity (about 50 nm) is apparent. This phenomenon is the result of progressive oxidation of the pores surface in the PS structure.

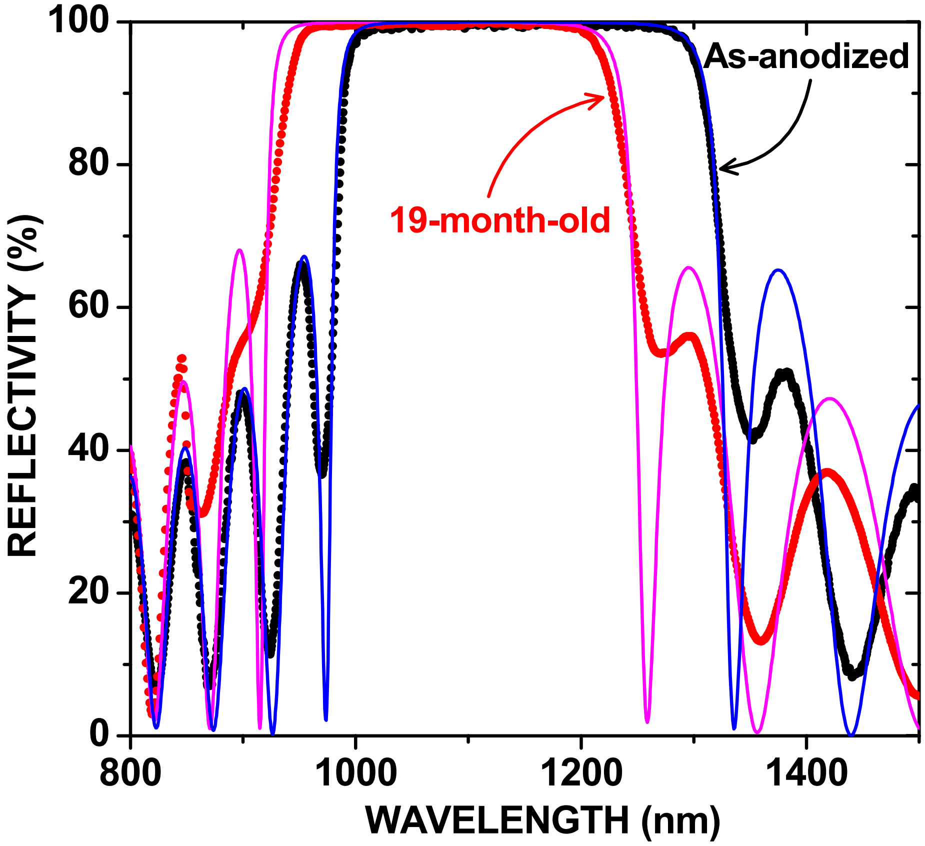

Figure 1. Reflectivity spectra of a ten-period DBR (structure: $(HL)_{10}$), as-anodized and after 19 months storage in air (scattered curves). Line curves represent best fits using transfer matrix analysis.

Both spectra in Fig. 1 were fitted using the standard transfer-matrix formalism. The calculated spectrum for the as-anodized sample fits very well the experimental data. From this modeling, the real physical thicknesses of the various layers were extracted, and they were then used to fit the spectrum of the aged sample. To do this, it was necessary to add an additional component, that of Si oxide, when calculating the effective refractive indices. The model considers that some fraction x of Si in PS has been oxidized, resulting in SiO_2 coating the pores surface. The fraction x was found to depend on PS porosity, as intuitively expected from the different surface areas and Si content (x increases with porosity). Thus, two different fractions x_H and x_L were introduced in the model for layers H and L, respectively. A good fit of the aged sample spectrum led to reliable estimates of $x_H \approx 21\%$ and $x_L \approx 10\%$.

In order to assess the impact of ageing on the optical properties of our self-supported CMCs, the theoretical evolution of the transmission spectrum upon oxidation has been calculated in the resonance spectral region. **Figure 2** shows the calculated transmission spectrum of a freshly prepared CMC. It includes 5 resonance peaks resulting from the coupling of the 5 MCs. The other spectrum in Fig. 2 has been obtained by assuming that the CMC has been oxidized similarly to the DBR shown in Fig. 1 (the fractions x_H and x_L obtained for the DBR were used in the calculation). This spectrum represents a theoretical ageing of 19 months in air.

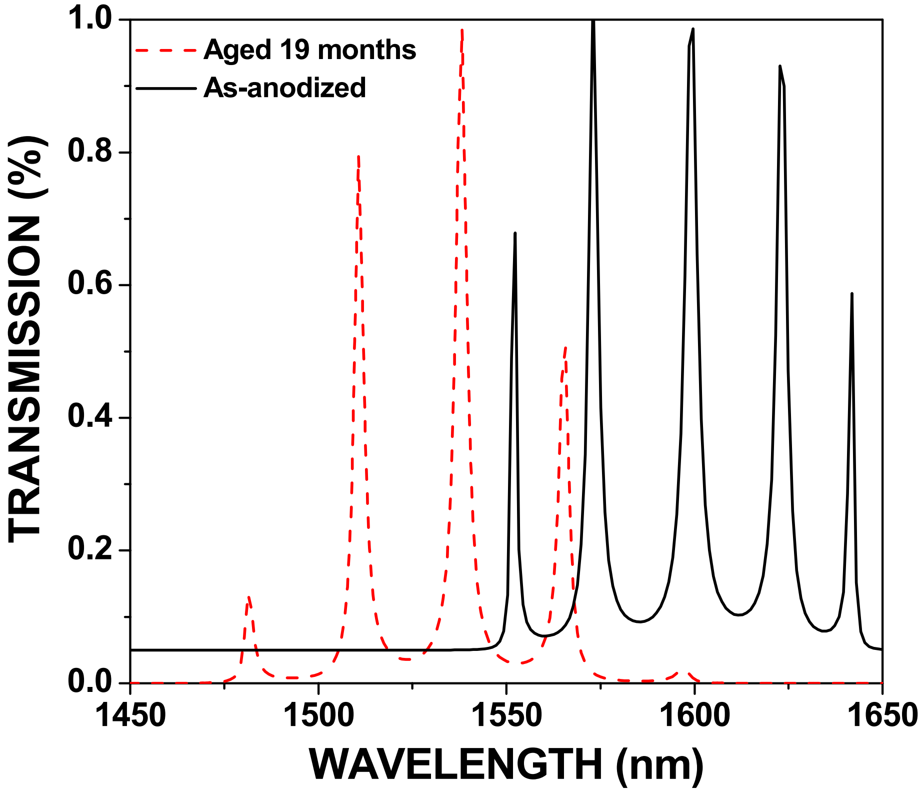

Figure 2. Calculated transmission spectra of a CMC including 5 MCs, freshly prepared (solid curve) and after 19 months storage in air (dashed curve), assuming the same ageing process as that experimentally obtained for the DBR of Fig. 1.

Ageing drastically modifies the resonance peaks. They are blue-shifted by about 70 nm due to the changes of refractive indices by oxidation. On the other hand, the resonance band is significantly deformed. This is due to three phenomena. First, the lowered index contrast between the H and L layers results in worsening of the reflectivity of coupling DBRs and thus less confinement of cavity modes. Second, the perfect condition of cavity resonance of individual MCs is lost due to the effect of oxidation on the refractive index, leading to lowered intensity of the resonance band. Third, because oxidation affects differently the H and L layers (the fractions x_H and x_L are different), the index compensation introduced in order to get a good coupling of the 5 MCs is partially lost, also leading to lowered intensity of the resonance band.

From the large modification of the resonance band upon ageing forecast by this calculation, it appears necessary to stabilize the PS photonic structures in order to be able to use them.

Ageing of chemically modified PS photonic structures

In order to stabilize the CMCs, chemical modification of the PS surface was implemented. First, a self-supported CMC was studied. **Figure 3** shows the transmission measurements performed on a CMC in its as-anodized state and after it was chemically modified. The effect of ageing in air for 5 and 9 months on the transmission was studied for the modified sample.

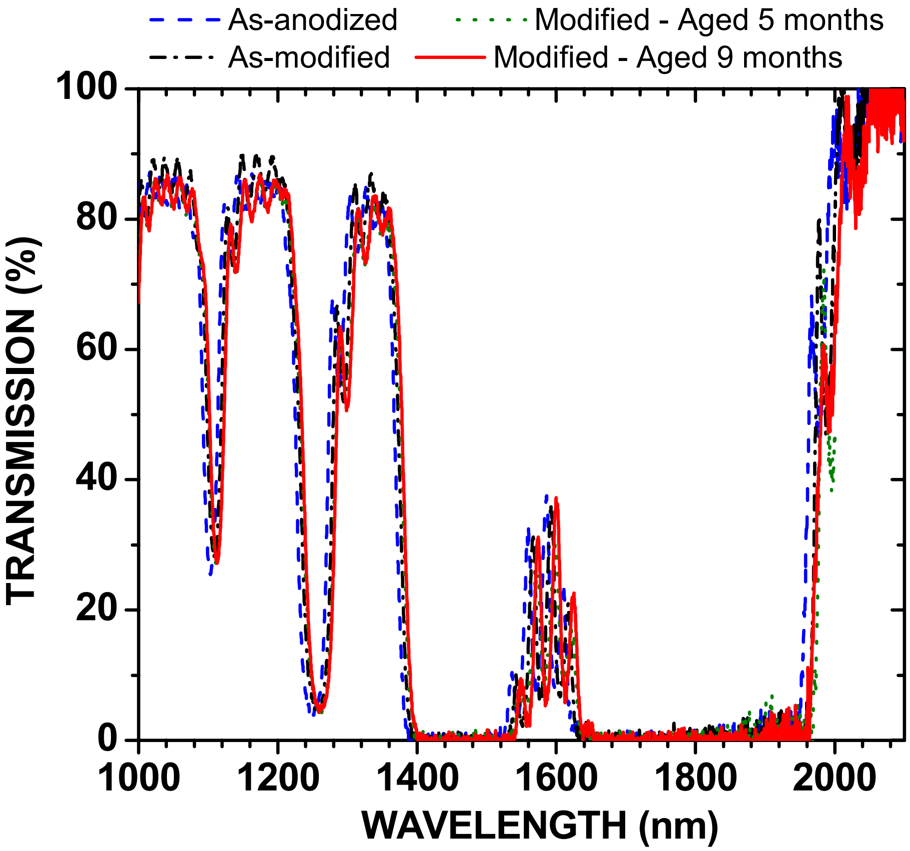

Figure 3. Transmission spectra of a self-supported CMC, as-anodized, as-modified, and as-modified after 5 and 9 months storage in air.

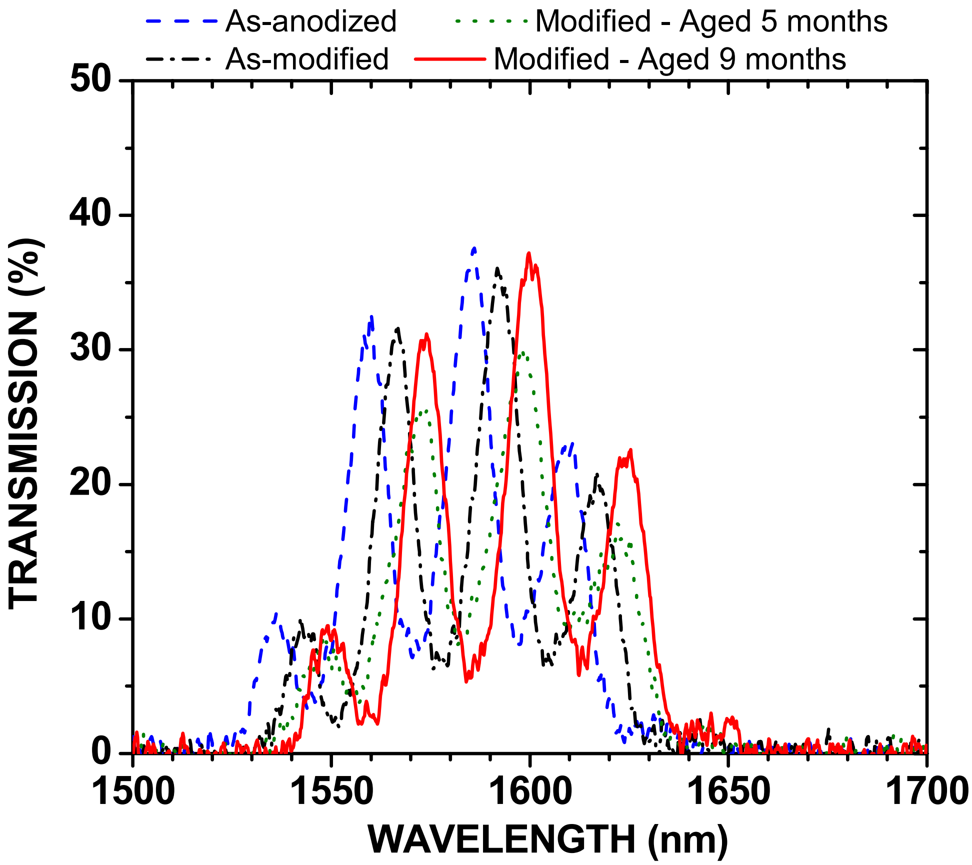

Figure 4. Same transmission spectra as in Fig. 3 but focusing on the CMC resonance spectral region.

As expected, a fine structure is experimentally observed in the resonance region (1500-1650 nm), resulting from the splitting of the MCs resonance. The resonance band can be seen more clearly in **Fig. 4**.

The chemical treatment led to a small red-shift of the resonance due to a small change of refractive index induced by the presence of alkyl groups in the PS pores. Considering the modified sample, only a minor further red-shift in the transmission spectrum was observed after 5 months. The measurement performed 9 months after modification did not show any further shift. Therefore, the CMC was effectively stabilized by the chemical modification. This absence of noticeable spectral shift contrasts with the large blue-shift systematically experienced by as-anodized superlattices upon ageing, as illustrated for a DBR in Fig. 1 and a CMC in Fig. 2.

A CMC lying on its Si substrate was also studied. In this case, only the reflectivity could be studied since the CMC was not self-supported. **Figure 5** shows the reflectivity spectra of a chemically modified CMC after 12, 21 and 36 months storage in air. **Figure 6** shows the resonance band in the 1400-1550 nm spectral range in greater detail. The CMC is extremely stable. No shift at all could be noticed on this modified sample. This result confirms the effectiveness of the chemical modification for the stabilization of 1D PS photonic crystals.

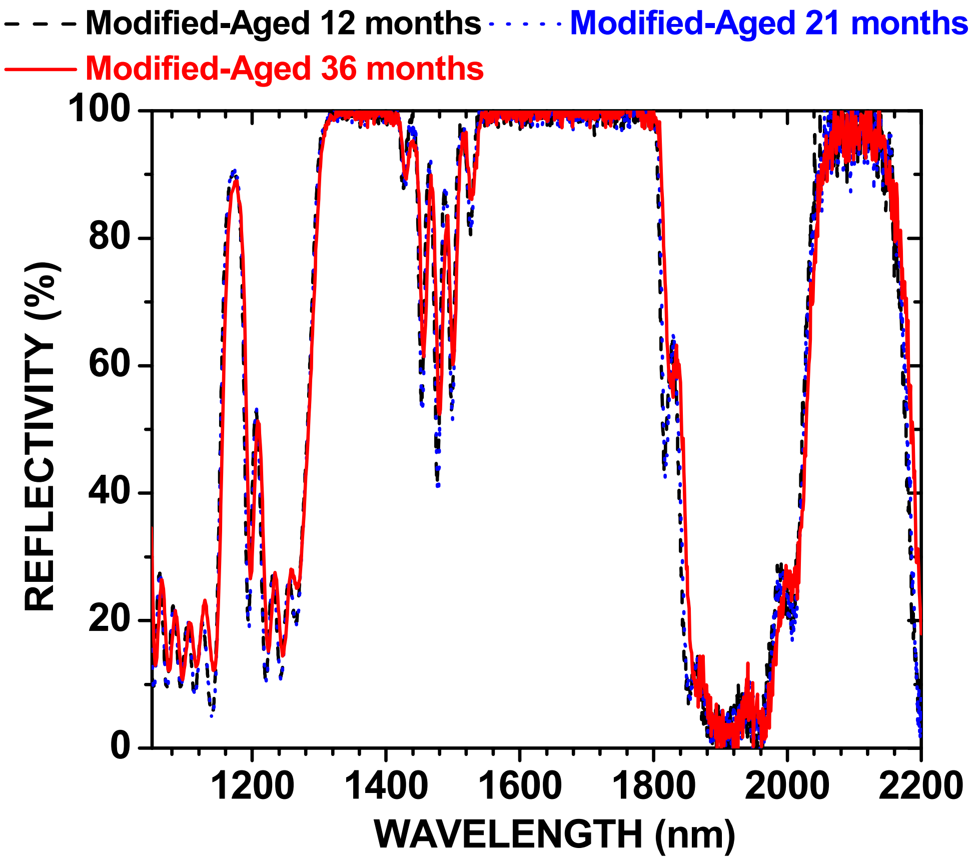

Figure 5. Reflectivity spectra of a chemically modified CMC on a Si substrate, after 12, 21 and 36 months storage in air.

The origin of the stabilization by chemical modification of the PS surface is two-fold. First, a large proportion of the easily oxidizable Si-H bonds covering the surface of as-anodized PS were replaced by much more stable Si-C covalent bonds by hydrosilylation reactions. Second, the large amount of decyl groups attached to the PS surface creates a physical protective barrier resulting from steric hinderance. This barrier tends to prevent the access of molecules in the air to the pores surface inside the PS structure. Moreover, due to the hydrophobic nature of the alkyl groups, water, a significant vector of Si oxidation, is efficiently repelled from the PS surface.

Conclusion

In order to stabilize PS based photonic structures, chemical modification of the surface of PS pores was carried out using a hydrosilylation reaction. The modification is very effective for PS superlattice refractive index stabilization, even when nanometer resolution is necessary.

The Si-C covalent bonds formed at the PS surface provide a very efficient surface passivation compared to the metastable Si-H bonds terminating the as-anodized PS surface. The long alkyl chains attached to the PS surface also generate a good protection of the PS surface by steric hinderance and hydrophobic mechanisms.

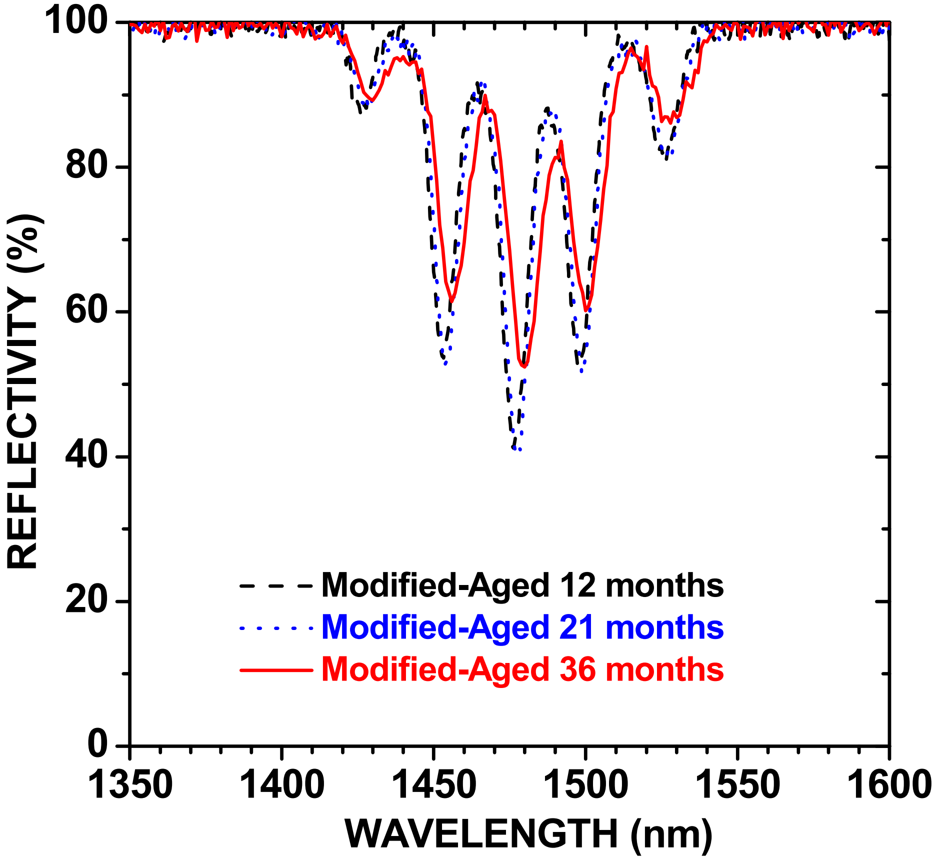

Figure 6. The same reflectivity spectra as in Fig. 5, but focusing on the CMC resonance spectral region.

Acknowledgments

This work was partially supported by a Grant-in-Aid for Scientific Research from the Ministry of Education, Science and Sport of Japan (MEXT) and from the Japan Society for Promotion of Science (JSPS). The authors wish to thank R. Boukherroub for his suggestions about the chemical modification process.

References

1. O. Bisi, S. Ossicini and L. Pavesi, *Surf. Sci. Rep.*, **38**, 5 (2000).
2. N. Koshida and N. Matsumoto, *Materials Science & Engineering R-Reports*, **40**, 169 (2003).
3. B. Gelloz, T. Shibata and N. Koshida, *Appl. Phys. Lett.*, **89**, 191103 (2006).

4. W. Theiss, *Surf. Sci. Rep.*, **29**, 95 (1997).
5. E. Lorenzo, C. J. Oton, N. E. Capuj, M. Ghulinyan, D. Navarro-Urrios, Z. Gaburro and L. Pavesi, *Appl. Opt.*, **44**, 5415 (2005).
6. M. Ghulinyan, C. J. Oton, Z. Gaburro, P. Bettotti and L. Pavesi, *Appl. Phys. Lett.*, **82**, 1550 (2003).
7. M. Ghulinyan, C. J. Oton, G. Bonetti, Z. Gaburro and L. Pavesi, *J. Appl. Phys.*, **93**, 9724 (2003).
8. W. Theiss, M. Arntzen, S. Hilbrich, H. Wernke, R. Arensfischer and M. G. Berger, *Phys. Status Solidi B*, **190**, 15 (1995).
9. B. Gelloz, A. Kojima and N. Koshida, *Appl. Phys. Lett.*, **87**, 031107 (2005).
10. B. Gelloz and N. Koshida, *J. Appl. Phys.*, **98**, 123509 (2005).
11. B. Gelloz, S. T., M. R. and N. Koshida, *Mater. Res. Soc. Symp. Proc.*, **958**, 227 (2007).
12. J. M. Buriak, *Chem. Rev.*, **102**, 1271 (2002).
13. R. Boukherroub, D. D. M. Wayner, D. J. Lockwood and L. T. Canham, *J. Electrochem. Soc.*, **148**, H91 (2001).
14. R. Boukherroub, D. D. M. Wayner and D. J. Lockwood, *Appl. Phys. Lett.*, **81**, 601 (2002).
15. R. Boukherroub, S. Morin, D. D. M. Wayner and D. J. Lockwood, *Phys. Status Solidi A*, **182**, 117 (2000).
16. B. Gelloz, H. Sano, R. Boukherroub, D. D. M. Wayner, D. J. Lockwood and N. Koshida, *Appl. Phys. Lett.*, **83**, 2342 (2003).

ECS Transactions, 16 (3) 221-229 (2008)
10.1149/1.2982559 ©The Electrochemical Society

Ellipsometric Porosimetry : Fast and Non Destructive Technique for Characterization of Porous Low-K ; Highlights on Plasma Damage and Water Effect on Treated Materials

A.Bourgeois[a],A.Bondaz[b], L.Kitzinger[b], and C.Defranoux[a]

[a] SOPRA SA, 26 rue Pierre Joigneaux, 92270 Bois Colombes , France
[b] SOPRA Inc, 407 S.California Ave, #11, Palo Alto, CA 94306, USA

Ellipsometric porosimetry (EP) is a non contact, non destructive approach based on a spectroscopic ellipsometric (SE) measurement which allows the precise determination of the refractive indices and thicknesses of the porous films. EP combined spectroscopic ellipsometric technique with a suitably adapted adsorption chamber. EP accords the great advantage of performing an in situ fast spectroscopic ellipsometric measurement at each stabilized pressure interval. From this combination, we can obtain morphological information such as open and closed porosity, pore size distribution, etc for thin films with an excellent sensitivity.

In this paper we will focus on a SiOCH porous low-K sample. Using EP we will demonstrate that it is a porous hydrophobic material.We will then study the effect of plasma treatment on the material. The damaged layer will be characterized.

By using water as an absorptive, we will be able to demonstrate the water degradation effect on treated materials.

Introduction

Ellipsometric Porosimetry (EP), first reported by Baklanov et al. in 2000 (1), is a very powerful technique for micro and mesopores characterization of porous thin films. This technique consists of plotting an adsorption-desorption isotherm from the variations of film refractive index induced by the change of partial pressure of an organic solvent above a film. The device is usually based on the coupling of a pressure controlled chamber (conventional in gas volumetry characterization devices) and a spectroscopic ellipsometer. Pore size distribution of micro and mesopores of the film can then be directly obtained via porosimetry models usually based on the Kelvin equation for the determination of mesopores sizes or different models such as the Dubinin Raduchkevich (DR) model for the determination of micropores sizes.

In 2004, SOPRA signed an exclusive licence agreement on IMEC's (Interuniversity MicroElectronics Centre, Leuven, Belgium**)** patented EP technique which leads to a system mainly dedicated to semiconductor industry for the low-K application.

In 2006, SOPRA had a collaboration work done with Pr Sanchez Laboratory of Condensed Matter Chemistry (LCMC / Paris 6 University) in order to use water as a probe molecule. Using this technique, it is possible to characterize in terms of porosity and pore size distribution oxide thin films. These are widely used in the photocatalysis and photovoltaic industries.

EP Technique

Measurement Principle

The wafer is placed in a vacuum chamber where an organic solvent is released. During the adsorption cycle, the pressure increases and the solvent fills the pores as illustrated in Fig 1. At each pressure step, an ellipsometric measurement gives the thickness and the refractive index and extinction coefficient of the ultra-low-K (ULK). During the desorption cycle the solvent is released from the pores. At each pressure step, EP measures the volume of solvent inside the material. The distribution of pore size is calculated using these isotherms for each pressure step.

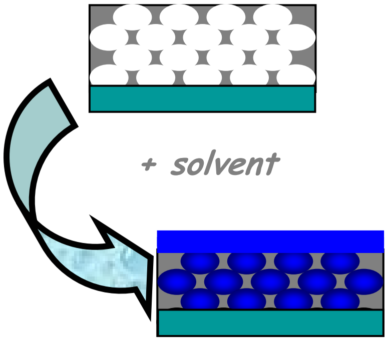

Figure 1. Adsorption of solvent changes optical properties of the porous material

Measurement of Porosity

The ellipsometric spectra are analyzed with standard dispersion laws. For each partial pressure, the thickness and refractive index are calculated.

Adsorbed volume is obtained using Lorentz-Lorentz equations.

$$V = \left(\frac{n_{eff}^2 - 1}{n_{eff}^2 + 2} - \frac{n_{init}^2 - 1}{n_{init}^2 + 2} \right) \Big/ \left(\frac{n_{ads}^2 - 1}{n_{ads}^2 + 2} \right) \quad [1]$$

Both isotherms (adsorption and desorption) for the adsorbed volume are displayed below in Fig 2. From these isotherms, we calculate the accessible void (porous) volume.

The porosity of the material is calculated at saturation point that is graphically visible by the presence of a plateau in the isotherms. The material used in Fig 2. is 35% porous.

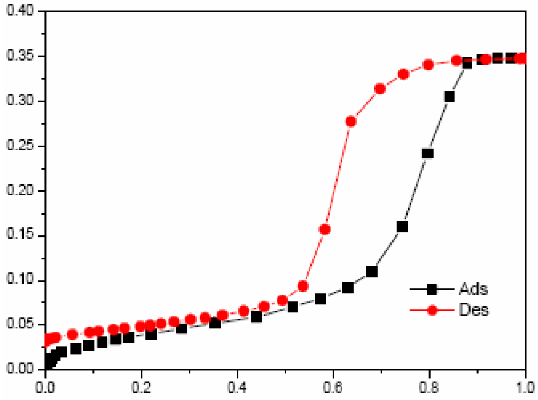

Figure 2. Typical hysteresis loop of solvent absorbed volume in a porous material versus relative pressure

Average Pore Size and Distribution

EP uses standard porosimetry equations for calculation of pore size. For meso pores (pore size from 2nm to 50nm from International Union of Pure and Applied Chemistry (IUPAC) classification) we use the Kelvin model. Boissiere et al. (2)

$$r = \frac{2\gamma V_L}{RT \ln(P/P_0)} \cos\theta \qquad [2]$$

Po : equibrium vapor pressure
P/Po: relative equilibrium vapor
g : Surface tension of adsorptive
V_L : molar volume of adsorptive
r_k: mean radius of curvature
Ø: wetting angle
r: kelvin radius

Applied to the volume adsorbed isotherms Kelvin model provide the pore radius distribution as shown in Fig 3.

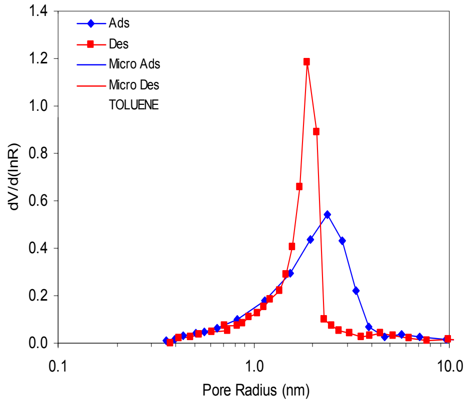

Figure 3. Pore radius distribution for mesoporous materials obtained using Kelvin model

Adsorption isotherm gives information on pore size while desorption isotherm gives information on the interconnections between the pores.

For micro pores (pore size below 2nm IUPAC classification) we use the Dubinin-Radushkevich model.

$$\log_{10}\left(\frac{V^{DR}}{V_0^{DR}}\right) = -D\log_{10}^2\left(\frac{p_0}{p}\right) \qquad [3]$$

Applied to the volume adsorbed isotherms DR model provide the pore radius distribution as shown in Fig 4.

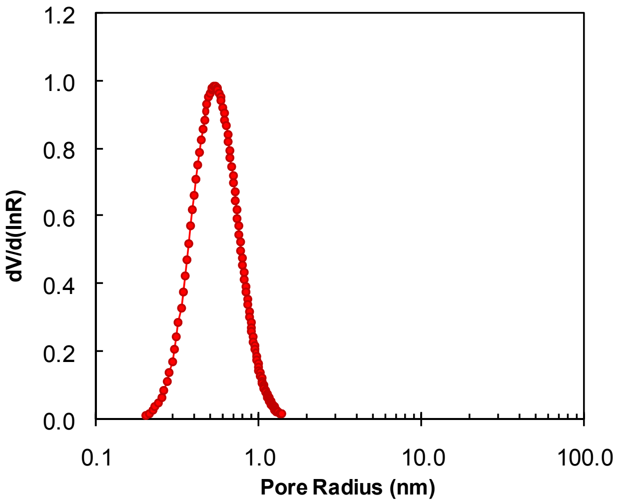

Figure 4. Pore radius distribution for microporous materials using DR model

Using EP to Characterize Materials

Material Description

The experiments described below were performed using a SiOCH porous low-K sample. This sample has been prepared by a spin coated process (sol-gel) using a pre-polymer Methylated-Hydrogen Silsesquoxane (MSQ) solution in Propylene Glycol Methyl Ether Acetate (PGMEA) followed by a thermal treatment at 400-450°C.

Hydrophobicity of SiOCH Porous Low-K

As shown in Fig 5. when using water as a solvent, we note that there is no water absorption in the film as the SE spectrums are the same at the beginning and at the end of the absorption sequence. The first measurement is displayed in pink (barely visible as it is exactly the same as the other measurements), the measurement at the end of the adsorption cycle is in green and the last measurement, after the desorption cycle, is in blue. Two interpretations are possible. Either the film is not porous either it is hydrophobic.

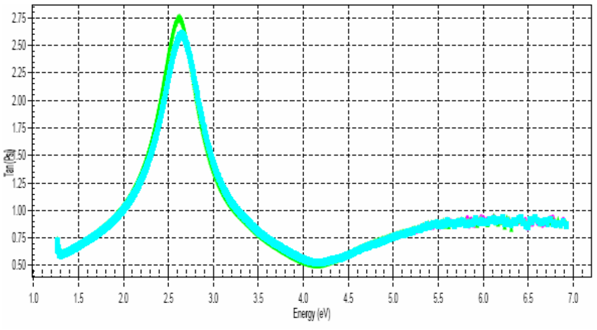

Figure 5. SE spectrums taken during EP experiment on SiOCH using water as the solvent

In order to determine which interpretation is the right one, we perform another experiment using toluene as a solvent as shown in Fig 6. The first point to note is that the first curve (pink) before adsorption and the last curve (blue) after desorption are identical. This means that we completely remove the solvent in the film and that we don't damage or modify the material during the experiment. Secondly, the curve taken at the end of the adsorption cycle (green) is very different from the initial one : some absorption of toluene is detected. The material is porous.
Then it's easy to conclude that the sample is hydrophobic.

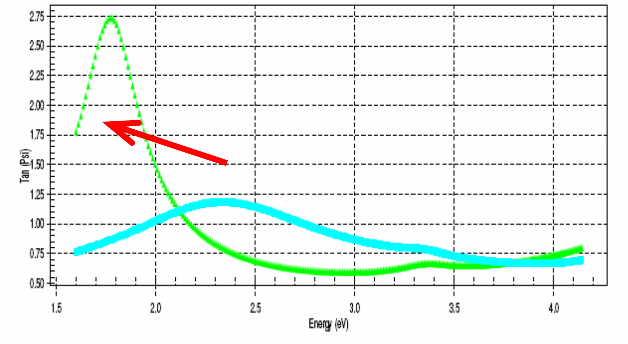

Figure 6. SE spectrums taken during EP experiment on SiOCH using toluene as the solvent

Plasma treatment of the SiOCH porous low-K

For integration, this low-K has to be sealed to avoid diffusion. A sealing technique consists of applying post N_2O plasma treatment on this material. The previous SiOCH sample will be treated by plasma and will then be characterized with EP using ethanol as solvent. To have a reference, the SiOCH before treatment will also be characterized with EP using ethanol as solvent.

Reference. SiOCH porous low-K is characterized with EP using ethanol as a solvent. The isotherms taken on the refractive index (n) during this experiment shown in Fig 7. shows that the material is not damaged or modify. Indeed, n at the end of the experiment is the same as n at the beginning.

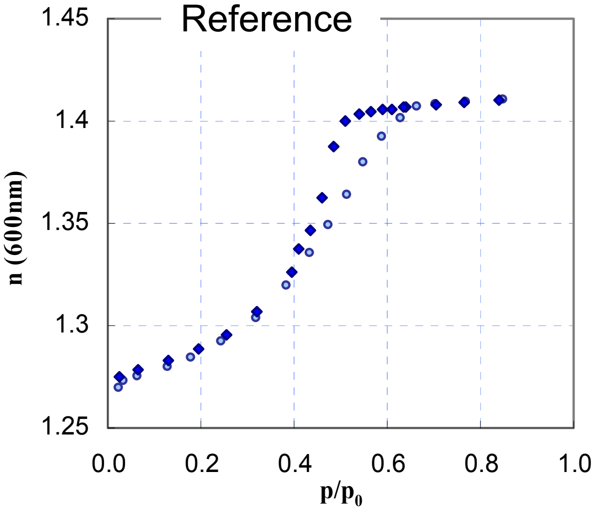

Figure 7. Refractive index of SiOCH characterized in EP with ethanol

Characterization after treatment with Ethanol. After N_2O treatment sample is characterized with EP using ethanol as a solvent as shown in Fig 8.

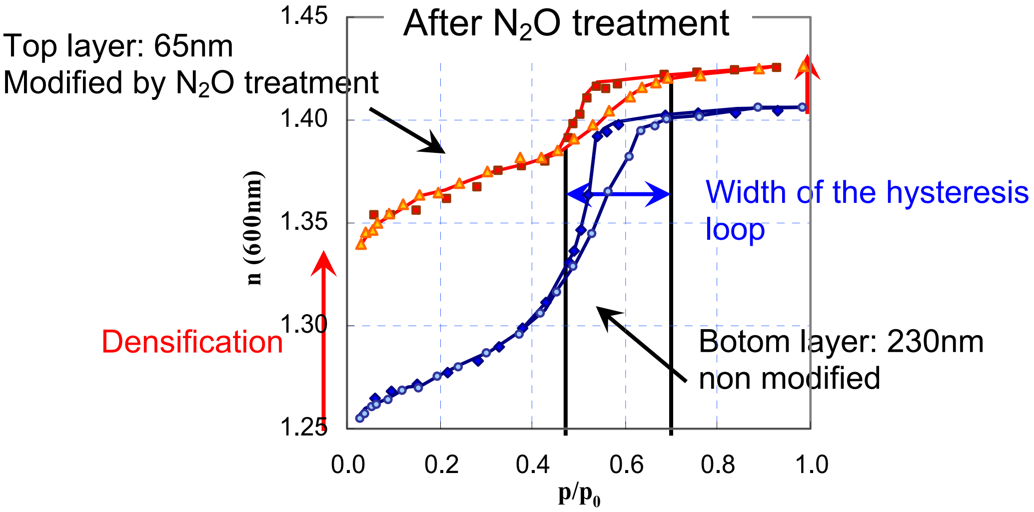

Figure 8. Refractive index of plasma treated SiOCH characterized in EP with ethanol

This experiment shows that a new layer is formed on top of the porous low-K material. Refractive index of this top layer increases which means that porosity decreases: there is a densification of the material. By comparison with the reference, the bottom layer is not modified. A closer look to the hysteresis loops shows an identical width for both layers which means that the pore size is not modified by the treatment.

Characterization after treatment with water. After N_2O treatment sample is characterized with EP using water as a solvent

Contrary to the previous experiments and as shown in Fig 9. after the adsorption / desorption cycle, the refractive index of the top layer in not coming back to its initial value. There is chemisorption: water is reacting with the treated material. A reasonable conclusion would be that the top layer becomes hydrophilic.

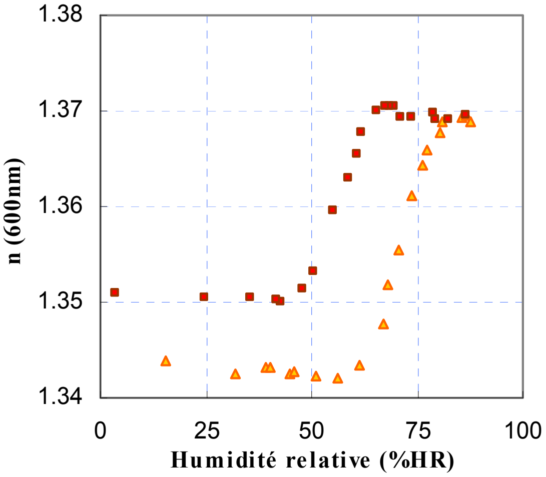

Figure 9. Top layer of treated SiOCH characterized with water

This conclusion is confirmed by a contact angle measurement showing a contact angle of 10 degrees after treatment versus a contact angle of 105 degrees before treatment. Also, as illustrated in Fig 10., an FTIR measurement shows the substitution of $Si\text{-}CH_3$ bond from the untreated SiOCH (blue curve) by Si-OH bond on the treated material (red curve)

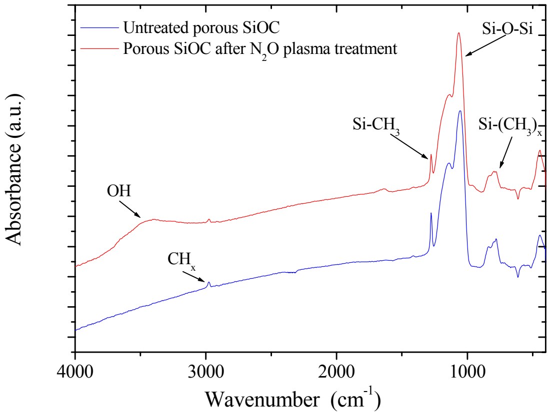

Figure 10. Top layer of treated SiOCH characterized with FTIR

Water Degradation of Treated Materials

As noticed in the previous experiment water is adsorbed by the treated material. We are now performing several adsorption / desorption sequences in order to study the evolution of the treated material after longer exposition time to water.

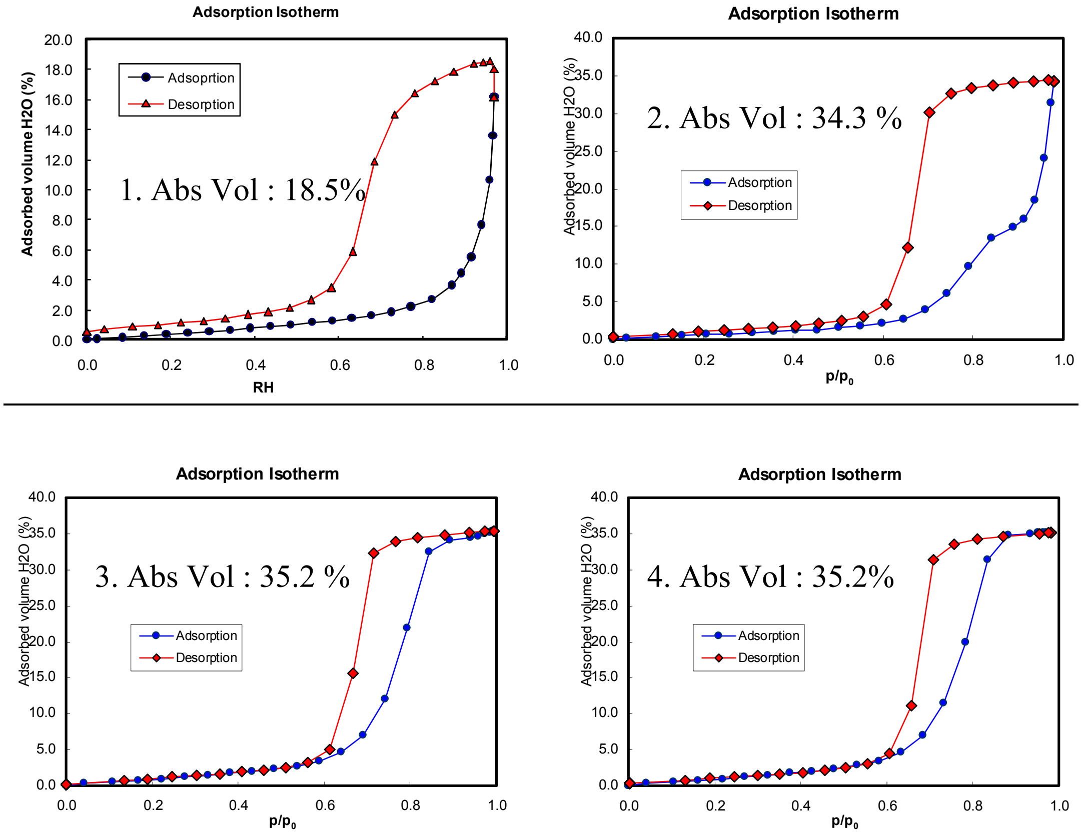

Figure 11. Multiple water absorption on treated material

Through the successive water absorptions sequences, we can notice that the shape of the isoterm is changing. In the end becomes similar to the shape of the reference sample. All the isotherms measured after cycle 4 are similar.

This experiment clearly shows that the treated material is degraded by water.

Conclusion

In this paper we have shown that SOPRA EP system can be used to characterize the effect of plasma treatment on porous low K as well as to characterize the effect of water on treated materials.

Plasma treatment of porous SiOCH which is a hydrophobic material induces the production of a densified top layer which is hydrophilic.

Finally, we were able to demonstrate that water degrades plasma treated materials which is critical information as many materials are getting into contact with water during immersion lithography for example.

References

1. Baklanov, M.R., Mogilnikov, K.P., Polovinkin, V.G., and Dultsev, F.N., J. Vac. Sci. Technol. B, **18**, 1385 (2000).
2. Boissière, C., Grosso, D., Lepoutre, S., Nicole, L., Brunet-Bruneau, A., Sanchez, C., Langmuir **21(26)**, 12362 (2005).

ECS Transactions, 16 (3) 231-235 (2008)
10.1149/1.2982560 ©The Electrochemical Society

Formation of Porous Noble Metal Layer by Displacement Reactions with Porous Silicon

M. Hayase[a], T. Matsuzaka[a], and J. G. A. Brito-Neto[b]

[a] Department of Mechanical Engineering, Faculty of Science and Technology
Tokyo University of Science, Noda, Chiba 227-8510, JAPAN
[b] Centro de Ciências Naturais e Humanas, Universidade Federal do ABC
Santo André, SP 09090-400, Brazil

Porous Pd layer was synthesized on a Si wafer using anodized porous Si as a starting material. In the immersion plating, Pd replaced Si and porous Pd layer was formed. Pt was deposited on the porous Pd layer by galvanic displacement reaction. It was demonstrated that fabrication process of our micro fuel cell electrode was applicable.

Introduction

Porous metal layers have important applications(1,2) in catalysis, separations, and sensing because of their high surface-to-volume ratios. Recently, there are some reports that porous Pt, Au and Ru layers were successfully synthesized by immersion plating performed on porous Si layers(3,4). Using the porous Pt layers as a catalyst layer, MEMS-based micro fuel cells are now under development in our group and a prototype cell showed relatively high output(5,6). However, in the fuel cell study, the amount of Pt used for the catalyst is large and it is not practical. In the previous study(7), we reported formation of Ru porous layer. In the study, Pt was deposited on the porous Ru layer by galvanic displacement reaction and the obtained Ru-Pt alloy showed catalytic activity to methanol oxidation. Pd is a less expensive material compared to Pt and Pd-Pt alloy can be a candidate for catalyst of the MEMS based fuel cells.

In this study, porous Pd formation was attempted. In the initial trial, $PdCl_2$ was simply used and large agglomerates were formed on the porous Si layer. Then using organic complex ion with ethylene diamine in similar way to porous Au formation, porous Pd layer was attempted to be formed. Formation of thicker porous Pd layer was attempted and the possibility as catalyst for the fuel cell was investigated.

Experimental

The silicon wafers used in this work were n-type, mirror-polished,(100)-oriented. Two doping levels were used: 0.007-0.02 Ωcm resistivity (medium-doping ones from now on) and 0.001-0.005 Ωcm (high-doping ones from now on). The plating bath was prepared by mixing the Pd(II) precursor solution ($[Pd(en)_2]^{2+}$ or $[PdCl_4]^{2-}$) solution with a 600 mM, neutralized (pH=3) HF in 1:1 volume ratio (the final Pd concentration is 20 mM). The bis (ethylenediamine) Pd(II) complex ($[Pd(en)_2]^{2+}$) was prepared simply by dissolving an appropriate amount of the $PdCl_2$ salt in a calculated volume of 1 M ethylenediamine solution in water. The actual metalization solutions contained 450 mM HF and had their pH adjusted to 3.

Porous Si Formation

The anodization electrolyte was prepared by mixing concentrated hydrofluoric acid (46%), ultrapure water, and ethanol in a 3:5:2 mass ratios. The anodization apparatus has been described elsewhere(3)(4). In brief, it consists of a poly-trifuloroethylene vessel, in which the anodized area is defined by an O-ring (9.93 mm diameter). Various anodization currents were tested. There is a tendency that deep part of porous layer becomes fragile after the metallization. Therefore, applied current was reduced along time to obtain porous Si layer with less porosity in deep area.

Immersion Plating

It is known that small pore region is formed on the top of the porous Si layer. Therefore, before immersion plating, dilute KOH etching was performed to eliminate the small pore region. Then, immersion plating was performed in the same vessel, also at 283K. Around 3 ml of plating solution was poured into the cell. The plating solution was allowed to remain in contact with the sample for different lengths of time from 5 up to 75 min. After plating the samples were rinsed with acetone, removed from the vessel, and dried under air.

In order to explore the possibility as a fuel cell catalyst, Pt deposition was also performed after the Pd plating by just immersing the samples into a bath consisting of 20mM H2PtCl6 and 1 M sulfuric acid.

Observation

A S4200 field emission scanning electron microscope (Hitachi, Japan) equipped with an energy dispersive x-ray spectrum analyzer (EDAX, USA) was used for obtaining cross-sectional images and elemental analysis. A JCM-5100 scanning electron microscope (JEOL, Japan) was also used for observation.

BET Analysis

Krypton adsorption isotherms were measured with a ASAP2010 gas adsorption analyzer (Micromeritics, USA). The porous layers formed on 5 chips under identical conditions were scratched away for insertion in the measurement cell. The isotherm data were analyzed through BET theory to estimate the total surface area of the sample.

Results and Discussion

Figure 1 shows cross-sectional SEM images of medium-doping porous Si samples anodized under similar conditions and exposed for 15 minutes to reaction baths containing 20 mM $[Pd(en)_2]^{2+}$ or $[PdCl_4]^{2-}$. Both samples exhibit a somewhat similar structure, consisting of an upper region containing a globular deposit, which EDS analysis identifies as Pd, and a lower, Si-rich region, where the original straight-pore morphology of porous Si can still be seen. In the sample treated with $[PdCl_4]^{2-}$, large agglomerates was observed and the surface was quite rough, while relatively smooth surface was observed in the sample treated with $[Pd(en)_2]^{2+}$. Therefore, we decided to use the $[Pd(en)_2]^{2+}$ plating bath for synthesizing porous Pd layer.

For using the Pd layer in our micro fuel cells, thicker porous layer was desired. Figure 2 shows the typical cross-sectional view after the immersion plating. Though thicker porous Si was prepared and the plating time was extended, but we could not obtain thicker porous Pd layer with medium doping Si wafer. Then, high-doping Si wafer was tested and we could have thicker porous Pd layer as shown in figure 3. BET analysis was performed with the specimens synthesized by identical conditions to that in figure 3. Surface area was estimated at $77m^2/cm^3$, which was very close to the surface area, 80 m^2/cm^3, obtained with porous Pt synthesized by similar way. At this point, it is not clear that it is just coincidence or any characteristic nature.

Pt deposition on the porous Pd layer was performed by 5 min immersion plating. Figure 4 shows the EDS analysis on the cross section. Quantitative analysis was performed on a spot close to the top surface as shown in figure 4. Specimens made with identical condition were observed before and after the Pt deposition. It showed that Pt was certainly deposited on the porous Pd layer. Further study about catalyst activity will be needed.

As described above, porous Pd-Pt layer was successfully fabricated and it was examined whether the fabrication process of our micro fuel cell electrodes(6) could be applied to the porous Pd-Pt layer. Figure 5 shows the cross-sectional image after the plasma etching. It was found that free-standing through-chip porous Pd-Pt layer was formed and the process could be applicable to the porous layer.

Conclusion

Porous Pd layers were synthesized on Si substrates by a galvanic displacement reaction on porous Si in buffered fluoride medium. Two metal precursors were employed: $[PdCl_4]^{2-}$ and $[Pd(en)_2]^{2+}$. The porous metal layers obtained with both of them have qualitatively similar particle morphologies, but the porous layer surface with $[PdCl_4]^{2-}$ was much rough than with $[Pd(en)_2]^{2+}$. Thick porous Pd layer was obtained with high-doping wafers and Pt deposition on the porous Pd layer was demonstrated by just immersing the Pd layer into the Pt plating bath. It was found that our micro fuel cell fabrication process was applicable to the porous Pd-Pt layer. Further study to build the micro fuel cells will be performed.

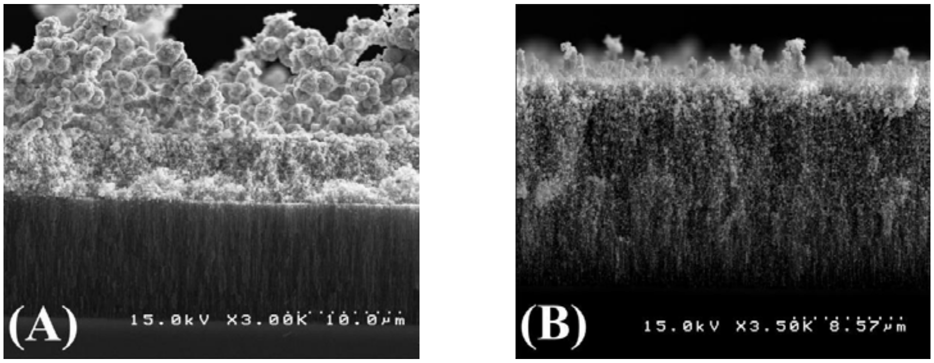

Figure 1. Cross-sectional SEM images of porous Pd samples prepared on medium-doping Si substrates; (A) deposition with 20 mM $[PdCl_4]^{2-}$;(B) deposition with 20 mM $[Pd(en)_2]^{2+}$; deposition time was 15 min and both solutions contained buffered HF/F- 300 mM with pH=3.

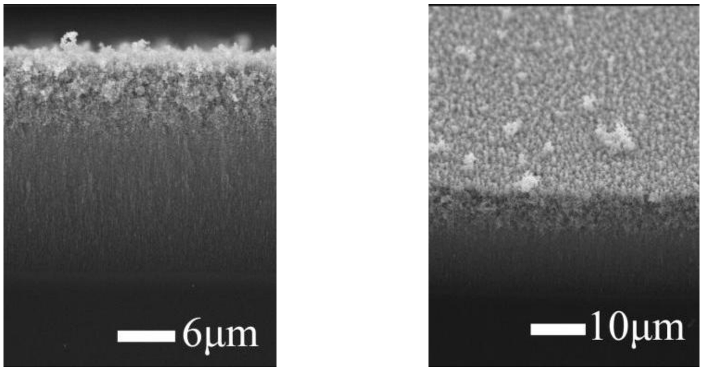

Figure 2. Cross-sectional view with extended immersion plating time using thicker porous Si layer

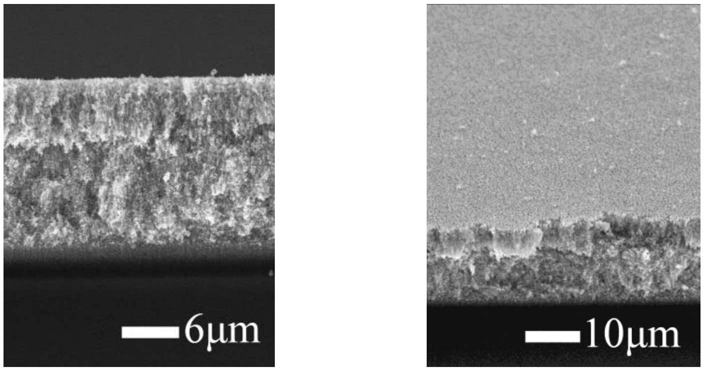

Figure 3. Cross-sectional SEM images of porous Pd samples prepared on high-doping Si substrates. Initial anodization current was 60 mA/cm^2 and reduced to 0mA/cm^2 along anodization time. Pd deposition with 20 mM $[Pd(en)_2]^{2+}$;deposition time was 15 min and both solutions contained buffered HF/F- 300 mM with pH=3.

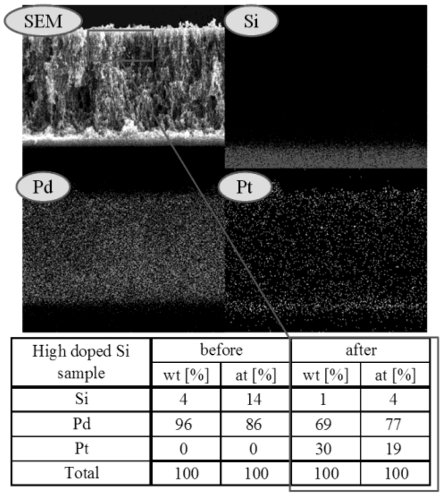

High doped Si sample	before		after	
	wt [%]	at [%]	wt [%]	at [%]
Si	4	14	1	4
Pd	96	86	69	77
Pt	0	0	30	19
Total	100	100	100	100

Figure 4. Cross-sectional view and EDS analysis of the porous Pd layer after 5 min of immersion Pt plating.

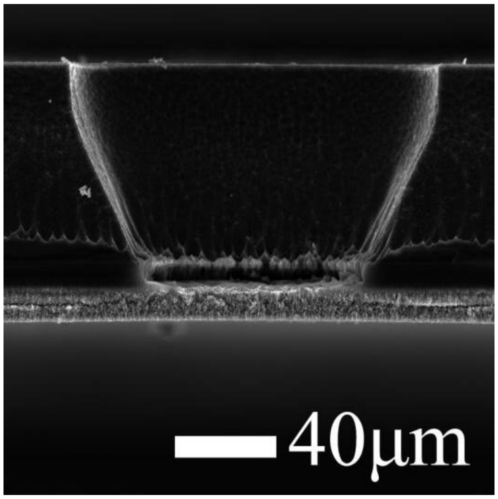

Figure 5. Cross-sectional view after the plasma etching from the back side of the porous layer.

Acknowledgments

This study was partly supported by NEDO of Japan, JST and JSPS post-doctoral fellowship program.

References

1. R. S. Jayashree, J. S. Spendelow, J. Yeom, C. Rastogi, M. A. Shannon, and P. J. A. Kenis, *Electrochim. Acta*, **50**, 4674 (2005).
2. J. Zhang, Y. Mo, M. B. Vukmirovic, R. Klie, K. Sasaki, and R. R. Adzic, *J. Phys. Chem. B*, **108**, 10955 (2004).
3. J. G. A. Brito-Neto, S. Araki, and M. Hayase, *J. Electrochem. Soc.*, **153**, C741 (2006).
4. J. G. A. Brito-Neto, K. Kondo, and M. Hayase, *J. Electrochem. Soc.*, **155**, D78 (2008).
5. M. Hayase, T. Kawase, and T. Hatsuzawa, *Electrochem. Solid-State Lett.*, **7**, A231 (2004).
6. 6. T. Fujii, J. G. A. Brito-Neto, M. Hayase, *7th intl. workshop PowerMEMS 2007*, pp.169-172 (2007.11).
7. M. Hayase, Y. Saito, K. Kondo, J. G. A. Brito-Neto, *212th Meeting Abstracts of the Electrochemical Society*, No.1365 (2007).

ECS Transactions, 16 (3) 237-244 (2008)
10.1149/1.2982561 ©The Electrochemical Society

Integration and Application of Electrochemically-Etched Silicon Nanowires

W. Xu and J. Flake
Department of Chemical Engineering
Louisiana State University, Baton Rouge, LA 70803, USA

Silicon nanowires (SiNW) are fabricated through electroless etching of single crystal silicon. The nanowires are separated from substrate, deposited onto electrodes and annealed. Nanowire silicidation methods and analysis of silicides including electrical characterization, SEM, TEM and sputter XPS, and XANES are considered.

Introduction

In recent years, silicon nanowires (SiNW) have attracted attention for applications in high-performance transistors, biosensors with femtomolar detection limits or ultra-high capacity Li battery anodes (1-3). Various fabrication methods of SiNWs have been reported, including Vapor-Liquid-Solid growth (4), solution synthesis (5), thermal-evaporation oxide assisted growth (6), and lithography patterning and etching (7). In addition to those additive methods, electrochemical etching methods to form large-area of SiNWs arrays have also been reported by Qui et al (8-10). These etching methods and mechanisms are similar to those used porous silicon formation (Lehman et al.), which enjoy the advantages of large scale, low cost and simplicity(11).

Electrical contacts between semiconductors and metals have always played a significant role in microelectronics devices. Metal contacts to silicon may form either rectifying or ohmic contacts (i.e. linear current-voltage characteristics), which can be used to make contacts to doped regions (12). In typical CMOS integrations, Ni or Co-silicides are used to provide electrical contact to source, drain, and gate electrodes prior to tungsten contact deposition. Silicides can be formed by either a solid-state reaction between a metal and Si, or by co-depositing the metal and Si. The solid-state reaction method is used in a salicide process (self-aligned silicide process), whereas the co-deposition method is commonly used in a polycide process (13).

Various metal silicides have been studied for potential improvement in CMOS microelectronics, including Ti, W, Mo, Co, Pt, and Ni. Among metal silicide materials, there has been great interest in nickel silicide (NiSi) to form low-resistance electrical contacts. The resistivity of NiSi (1:1 phase) is comparatively low (~14 $\mu\Omega\cdot$cm) with other phases of Ni silicides and other silicides. The other main advantage of NiSi is that less Si in consumed compared with other silicides, hence reducing the risk of “spiking” under shallow junctions (14).

NiSi can be formed by decomposition of silane on nickel surfaces or in a series of procedures including deposition of nickel on single crystal silicon wafer or nanowires followed by thermal annealing treatment and removal of excessive metal by wet etching (15, 16). In the same sense, the NiSi phase can also be formed with silicon nanowires by annealing single silicon nanowire with Ni reservoirs so that Ni can diffuse axially into the silicon nanowire (17).

In this work, SiNWs are grown via electroless etching in a HF solution. The nanowires are separated from parent substrate, deposited onto interdigitated electrodes (IDEs) followed by thermal annealing process. Electrical measurements show the resistivity drop after deposition and the formation of a stable NiSi phase in silicon nanowires is confirmed via sputter-XPS and synchrotron-source XANES analysis.

Experiment

Electroless etching of single crystal silicon is applied to form large arrays of silicon nanowires. 4 in. p-type, boron doped silicon wafer with resistivity 1-5 Ω·cm was first cleaned by acetone to degrease the Si wafer, followed by s standard RCA cleaning step to remove any surface contamination. Then the cleaned silicon wafer was etched in a 5.0 mol/L HF solution containing 0.02 mol/L silver nitrate at 50ºC for 30 min. After the etching process, the any silver deposit on the sample can be detached, followed by rinsing with de-ionized water and dried in air. The fabricated silicon nanowires were separated from the parent wafer by sonication in a transfer solvent with ultrasonic cleaner. Then the silicon nanowires were deposited onto electrodes, and the annealing process was carried out at 450ºC for 30 min in reducing atmosphere.

In addition to silicidation of single nanowires, silicidation of arrays of nanowires was used to characterize the process. In this method, a layer of nickel more than 100 nm was deposited on an array of silicon nanowires on parent substrate. Then the sample went through the same thermal annealing process at 450ºC for 30 min in reducing atmosphere, excessive nickel was stripped by wet etching afterwards. The morphology and composition of the samples were characterized by Scanning Electron Microscope (SEM), Transmission Electron Microscope (TEM), X-ray photoelectron spectroscopy (XPS) and X-ray absorption analysis. Electrical properties of the samples were studied by using a source probe.

Result and Discussion

Figure 1 is the SEM image of silicon nanowires on substrate. The silicon nanowires were fabricated by electroless etching, separated from parenting substrate, and deposited on bare silicon wafer. The average size of fabricated silicon nanowires is approximately 50-100 nm in diameter, and 10-20 μm in length.

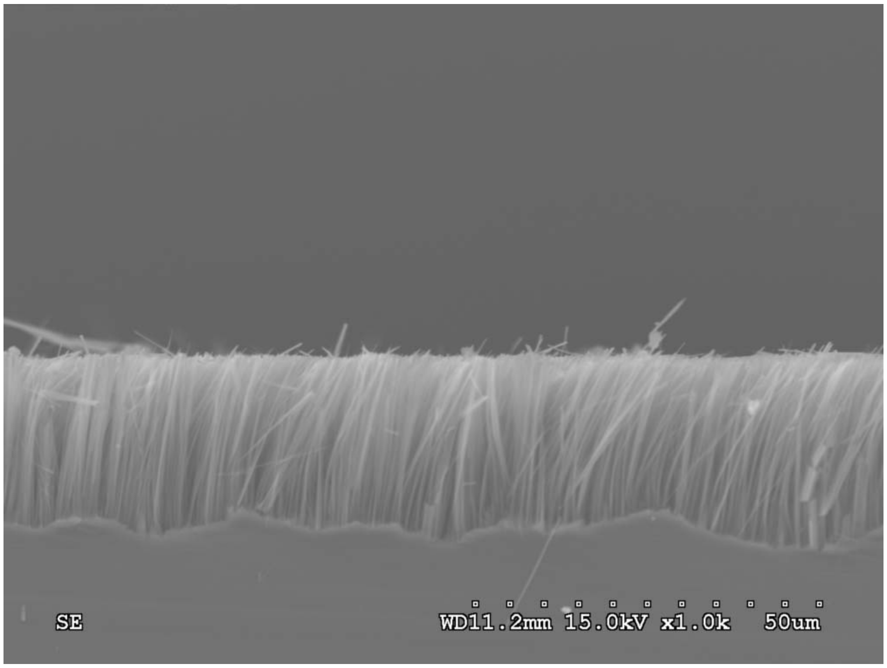

Figure 1. SEM image of the cross-section of silicon nanowire arrays on substrate.

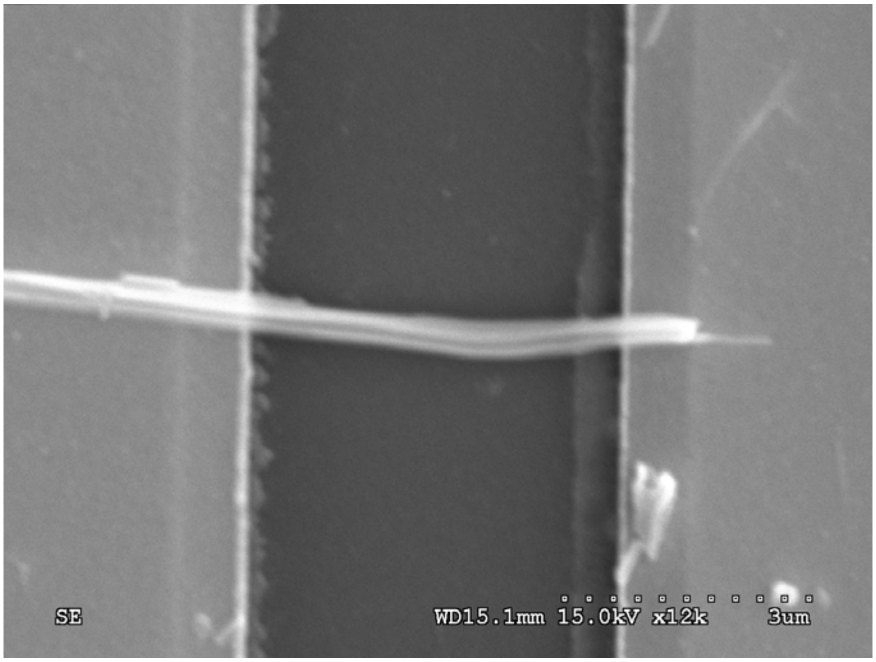

Figure 2. SEM image of transferred SiNW on electrode.

As shown in Figure 2, silicon nanowires were deposited on a commercial micro-electrode. The total length of the micro-electrode is 45mm with 5 micron wide metal electrodes and 5 micron spaces. In this experiment, there are approximately 200 nanowires across the interdigitated electrodes. Resistances of the electrodes before and after SiNW deposition, and before and after silicidation annealing were measured using a source probe. The electrical measurement results were listed in Fig. 3.

It is shown that before deposited with silicon nanowire, the resistance indicates an open circuit (>1·10^9Ω) on for the bare microelectrodes. After deposited with SiNW, the resistance of the electrodes decreased significantly (8.51·10^3Ω) suggesting conductive nanowires or ionic contamination from the carrier solution. Following SiNW deposition, electrodes with SiNWs were annealed in reducing atmosphere. Post anneal resistance shows a decrease of approximately seven orders of magnitudes from the bare electrodes (2.76·10^2Ω) Following anneal, resistance values remained constant after the electrode was washed by de-ionized water the suggesting that stable connection of nickel silicides between electrodes and silicon nanowires.

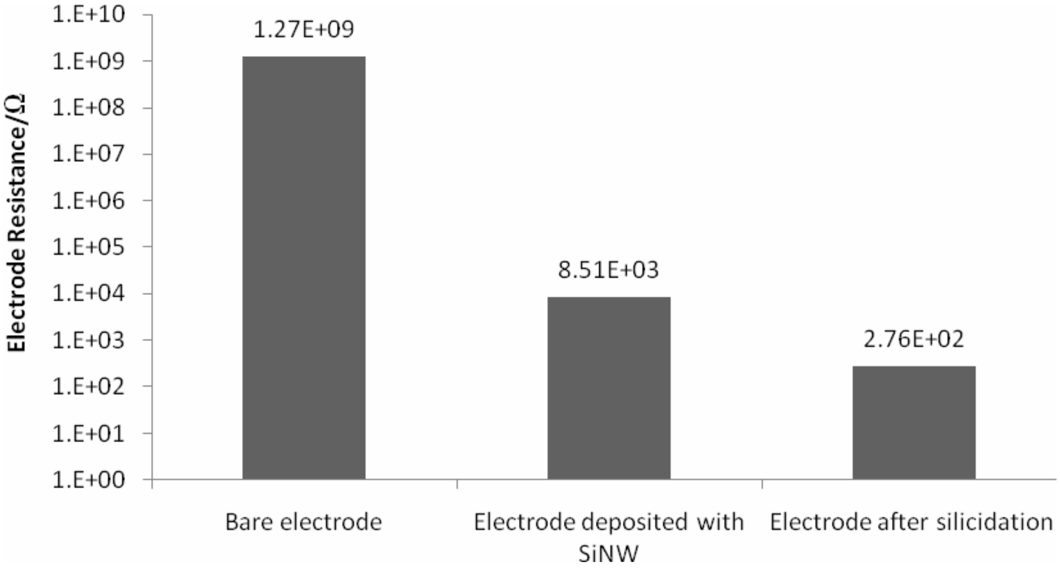

Figure 3. Resistance measurement of electrode deposited with SiNW.

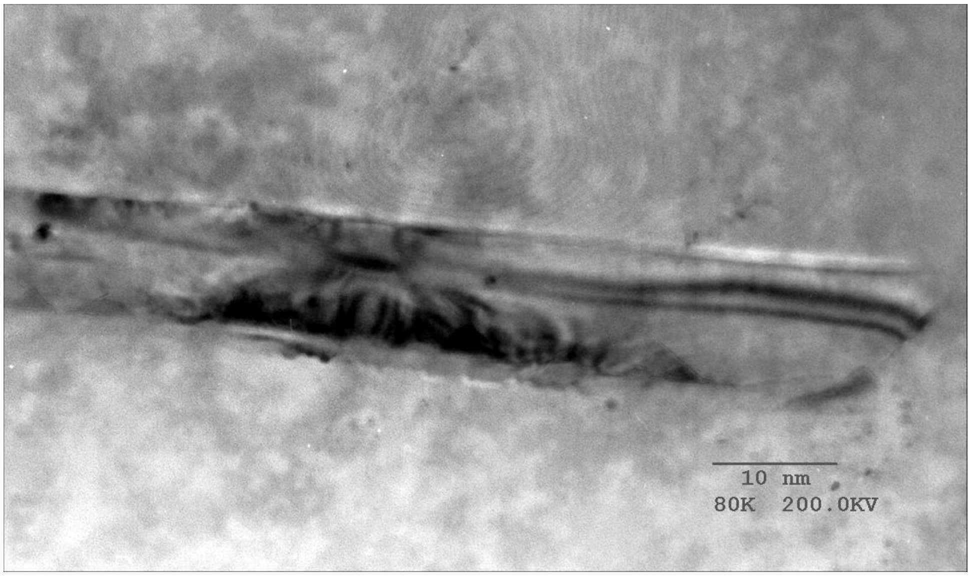

Figure 4. TEM images of SiNW with formed nickel silicide.

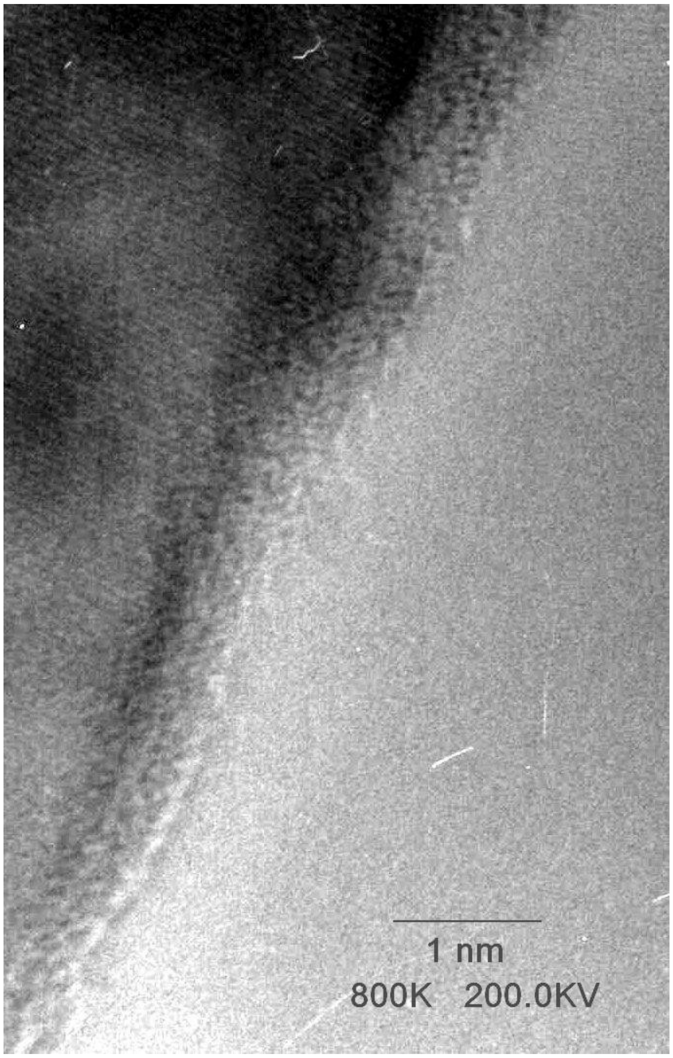

Figure 5. TEM images of SiNW with formed nickel silicide.

Fig.4 and Fig. 5 are the TEM images of a SiNW with formed nickel silicides. The dark and amorphous region indicates the formation of nickel silicides.

XPS was used to obtain compositional information about the sample. For depth profiling analysis, Ar^+ ion gun was used. As shown in Fig. 6, the atomic concentration of the sample changes from pure nickel to a ratio that nickel and silicon were almost 1:1 as the sputter time increased, indicating the low-resistance phase of nickel silicides with 1:1 atomic ratio.

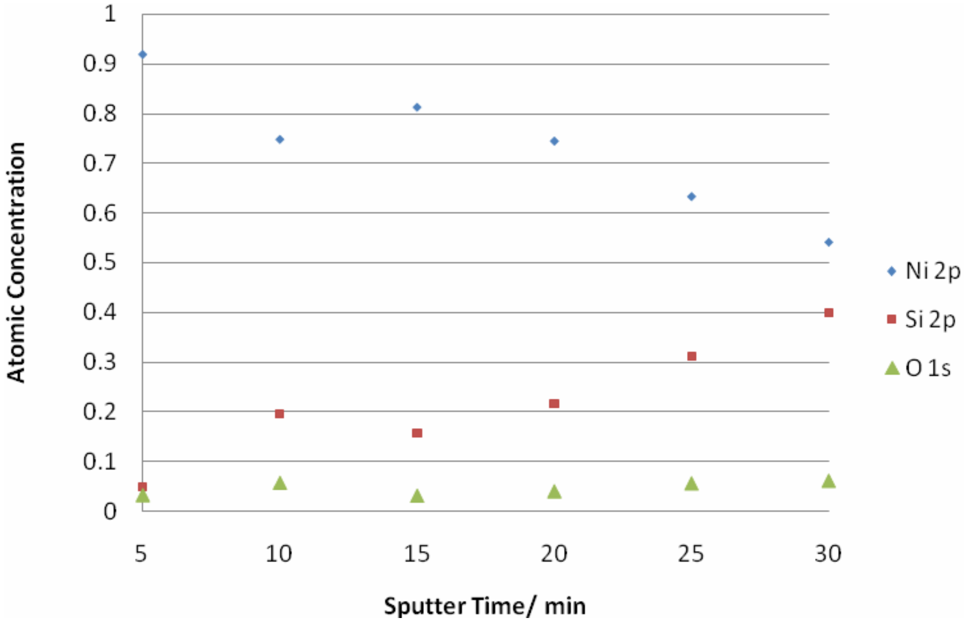

Figure 6. Sputter XPS data of formed nickel silicides on silicon nanowires.

In addition to XPS analysis, XANES analysis of Si and Ni was performed to further examine the silicide. Formation of the NiSi phase was verified using Ni and Si *K*-edge XANES analysis in TEY mode. The Si K-edge XANES results show little difference for the NiSi sample relative to unreacted Si since the photon might go beyond the nickel silicide phase. This is consistent with the work of Naftel indicating the penetrating depth of photon at Si K-edge is considerably larger than that at Ni K-edge (14).

The K-edge for Ni provides more conclusive results showing reacted nickel remaining with the sample following the nickel strip. Fig. 7 shows the Ni K-edge XANES of annealed sample of nickel on SiNW, together with nickel on silicon wafer and nickel foil in TEY mode. Compared with nickel foil, the Ni K-edge for both samples of nickel on silicon wafer and SiNW have shown a small shift of the initial peak (~2 eV), and a disappearance of the second peak (~8385 eV), indicating the formation of the NiSi phase. The peak at 8355 eV for the SiNW sample is relatively broader compared to the film with silicon wafer. The broadening might be due to a deeper NiSi phase and deeper photon penetrating depth in SiNW sample.

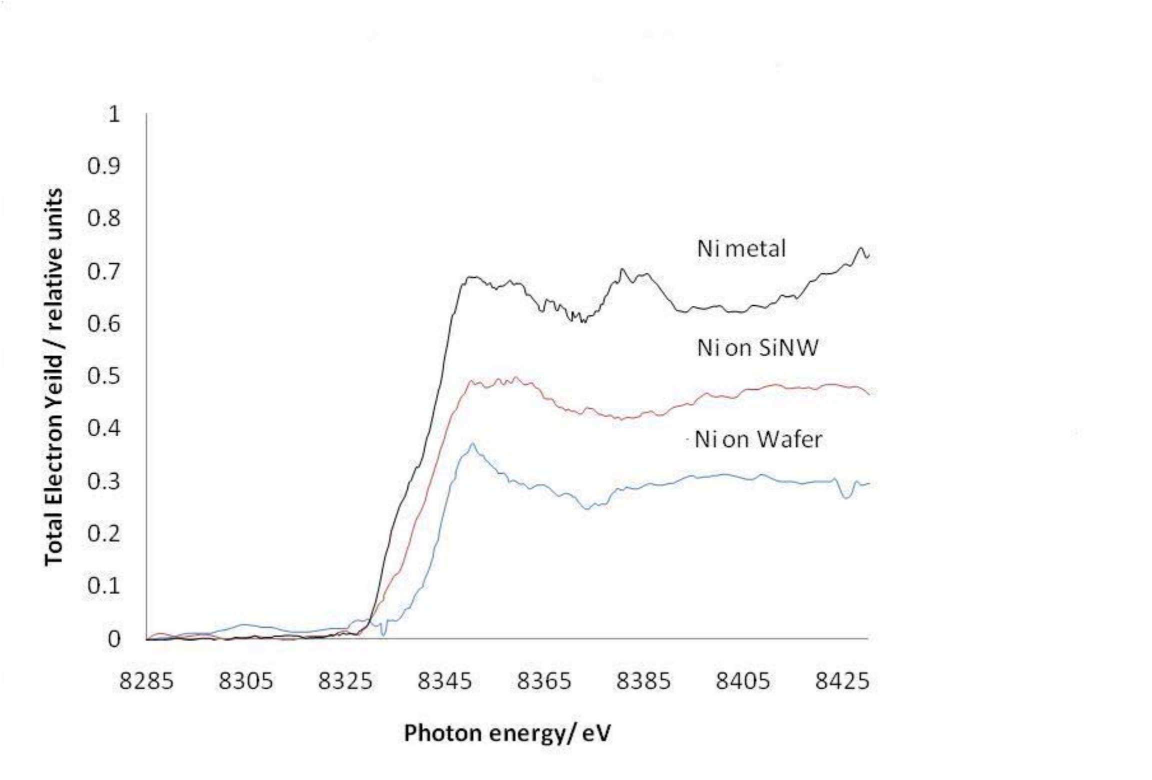

Figure 7. Nickel K-edge XANES (TEY) for annealed silicon nanowires, silicon wafer, and nickel foil.

Conclusion

These experimental results demonstrate significant reduction in resistance for SiNWs in contact with nickel electrodes following anneal. Both TEM, Sputter-XPS results show 1:1 NiSi formation in SiNWs in a similar fashion as bulk silicon samples treated with PVD nickel. XANES analysis also shows a NiSi phase is formed after anneal. The Ni K-edge spectra for unetched silicon wafers and SiNWs are different; however, this may be due to the penetration depth and size/porosity of the nanowire array relative to the unetched sample. The results indicate NiSi nanowire contacts can be used for the integration of electrochemically-formed SiNWs in microelectronic devices or battery anodes. In addition to the relatively simple silicidation process, electrochemically fabricated nanowires also benefit from the potential for large-scale and low cost fabrication.

References

1. Y. Cui, Z. H. Zhong, D. L. Wang, W. U. Wang and C. M. Lieber, *Nano Lett.* , **3**, 149 (2003).
2. Y. Cui, Q. Q. Wei, H. K. Park and C. M. Lieber, *Science*, **293**, 1289 (2001).
3. C. K. Chan, H. L. Peng, G. Liu, K. McIlwrath, X. F. Zhang, R. A. Huggins and Y. Cui, *Nat. Nanotechnol.* , **3**, 31 (2008).
4. Y. Y. Wu and P. D. Yang, *J. Am. Chem. Soc.*, **123**, 3165 (2001).
5. J. D. Holmes, K. P. Johnston, R. C. Doty and B. A. Korgel, *Science*, **287**, 1471 (2000).
6. A. Colli, S. Hofmann, A. Fasoli, A. C. Ferrari, C. Ducati, R. E. Dunin-Borkowski and J. Robertson, *Appl. Phys. A-Mater.* , **85**, 247 (2006).
7. K. M. Chang, K. S. You, J. H. Lin and J. T. Sheu, *J. Electrochem. Soc.* , **151**, G679 (2004).
8. T. Qiu, X. L. Wu, X. Yang, G. S. Huang and Z. Y. Zhang, *Appl. Phys. Lett.* , **84**, 3867 (2004).
9. T. Qiu, X. L. Wu, Y. F. Mei, P. K. Chu and G. G. Siu, *Appl. Phys. A-Mater.* , **81**, 669 (2005).
10. T. Qiu, X. L. Wu, Y. F. Mei, G. J. Wan, P. K. Chu and G. G. Siu, *J. Cryst. Growth*, **277**, 143 (2005).
11. V. Lehmann and H. Foll, *J. Electrochem. Soc.* , **137**, 653 (1990).
12. F. Deng, R. A. Johnson, P. M. Asbeck, S. S. Lau, W. B. Dubbelday, T. Hsiao and J. Woo, *J. Appl. Phys.* , **81**, 8047 (1997).
13. J. P. Gambino and E. G. Colgan, *Mater. Chem. Phys.* , **52**, 99 (1998).
14. S. J. Naftel, I. Coulthard, T. K. Sham, S. R. Das and D. X. Xu, *Physical Review B*, **57**, 9179 (1998).
15. B. Bokhonov and M. Korchagin, *J. Alloys Compd.* , **319**, 187 (2001).
16. C. J. Choi, S. Y. Chang, Y. W. Ok, T. Y. Seong, H. Gan, G. Z. Pan and K. N. Tu, *J. Electron. Mater.* , **32**, 1072 (2003).
17. Y. Wu, J. Xiang, C. Yang, W. Lu and C. M. Lieber, *Nature*, **430**, 61 (2004).

ECS Transactions, 16 (3) 245-252 (2008)
10.1149/1.2982562 ©The Electrochemical Society

Formation of Si Nanowire Arrays by Metal-Assisted Chemical Etching

C. Benoit, S. Bastide, C. Lévy-Clément*

Institut de Chimie et Matériaux de Paris-Est, CNRS, UMR 7182, 94320 Thiais, France
* levy-clement@icmpe.cnrs.fr

Formation of Si nanowire (SiNW) arrays using top-down methods based on metal-assisted chemical etching of Si is reported. Three different approaches were tested: i) a two-step process consisting in the electroless deposition of Ag nanoparticles followed by HF/H_2O_2 etching; ii) simultaneous electroless Ag deposition and etching in HF and highly concentrated $AgNO_3$; iii) a multi-step process using an Au replica mask obtained by Au evaporation on Si samples covered with polystyrene spheres, followed by HF/H_2O_2 etching. The morphologies of the Si structures obtained in each case are discussed in terms of the influence of different parameters. The third approach led to well controlled etching. Depending on the polystyrene sphere size, Si pillars 1 μm or SiNWs 200 nm in diameter could be obtained.

Introduction

Nanowire (NW) a new morphology exhibited by silicon (Si) is very attractive for various applications in Si based nanotechnology. The majority of Si nanowires (SiNWs) are produced by the vapor-liquid-solid (VLS) method, a versatile technique compatible with various types of substrates, offering good control over the NW features (diameter, length). However, using top-down methods like chemical etching is an interesting alternative with specific advantages. It is for instance possible to start by processing a device using conventional techniques and wafers (e.g. p/n junction diffusion), then etch it into SiNWs, all displaying the initial device structure. Control of the SiNW doping level seems easier, at least in theory, by simply choosing the appropriate substrate rather than by diffusing dopants in already made SiNWs. Contamination of the SiNWs by metallic impurities, especially Au in the VLS technique, is not an issue with chemical etching at ambient temperature.

In an ongoing effort to make SiNW based solar cells, we are developing top-down methods based on metal-assisted chemical etching of bulk Si. A few years ago, it has been shown that nanoparticles of noble metals (Ag, Au, Pt) deposited on a Si surface can act as catalysts for highly localized Si etching in HF solutions containing an oxidizing agent (e.g. H_2O_2) (1, 2). Etching only occurs at the level of the metal nanoparticles that sink into bulk Si, forming well-defined mesopores (10-100 nm in diameter). Because etching is localized at the level of few nanometers, it is possible to use it to form SiNWs.

Here, we report on 3 different approaches. The first approach consisted in using the well known HF/H_2O_2 system and Ag nanoparticles as catalysts, to dig mesopores with high surface density and in between SiNWs. It is a two-step method including (i) the deposition of Ag nanoparticles on Si surface using HF-$AgNO_3$, (ii) followed by etching in HF-H_2O_2. As a second option, we used step (i) as the sole etching process, allowing Ag^+ (from $AgNO_3$ at high concentration) to be the oxidizing specie (instead of H_2O_2) (1, 3-4). This method leads to large amounts of Ag deposition which have a strong influence on the morphology of the Si left after etching. Because significant amount of SiNWs could be obtained with this simple one step method, we studied the influence of several etching parameters ($AgNO_3$ and HF concentrations, etching time, bath temperature) on the SiNW morphology. These results led us to improve our etching system toward a third approach in which we added a step consisting in masking the Si surface by polystyrene spheres assembled by spin-coating prior depositing a metal either Ag by electroless deposition (leading to nanoparticles) or gold (Au) by evaporation to form a Au replica mask). Si samples coated with an Ag or Au replica mask were then dipped in a HF-H_2O_2 solution for Si etching. This last technique resembles that developed with electroless deposition by Asoh et al (5-6) or with thermal evaporation by Huang et al. using polystyrene beads (7) and Peng et al. using silica beads (8).

Experimental

1x1 cm^2 Si samples were cut from p-type (100) oriented Si wafers with a resistivity ~ 1-3 Ω.cm.

All chemicals were purchased from Prolabo. The solutions were prepared from 40 wt.% HF, 30 wt.% H_2O_2, $AgNO_3$ (Rectapur) and 18.2 MΩ.cm ultra-pure H_2O. Ag deposition and etching were performed under carefully controlled temperature using a Huber Ministat 240 cryothermostat.

Polystyrene spheres were deposited by spin coating with a Spin150 from APT. The Si surface was made hydrophilic as followed: Si wafers were washed in acetone and ethanol, then ultrasonicated for 10 minutes in piranha solution (4:1 (v/v) H_2SO_4/H_2O_2). Colloidal dispersions of spheres (1 µm and 200 nm in diameter) were prepared from Alfa Aesar commercial solutions (2.5 wt.%). 1µm sphere dispersions were centrifuged and re-diluted to obtain the following composition: 10/60/15/15 (v/v/v/v) of polystyrene/EtOH/H_2O/ethylene glycol. An ordered monolayer of 1 µm polystyrene spheres was obtained by spreading 50 µL of a prepared dispersion on a 1 x 1 cm² Si substrate and rotating at ω = 3000 rpm. An ordered monolayer of 200 nm polystyrene spheres was obtained by spreading 50 µL of the commercial dispersion (2.5 wt %) on a 1 x 1 cm² Si substrate and rotating at ω = 1500 rpm.

The Si surface morphology was investigated using a Leo 1530 Scanning Electron Microscope (SEM) with a GEMINI field emission electron gun.

Results and Discussion

Dissolution Mechanism

Metal assisted etching is based on a galvanostatic reaction between an oxidizing agent and Si. In our experimental conditions, the cathodic reaction is the reduction of H_2O_2 or Ag^+, according to:

$$H_2O_2 + 2H^+ \rightarrow 2H_2O + 2\,h^+ \qquad E_0 = +\,1.76\ \text{V/NHE}$$
$$Ag^+ \rightarrow Ag + h^+ \qquad E_0 = +\,0.79\ \text{V/NHE}$$

The anodic reaction is the chemical dissolution of Si which can be presented in the following general form:

$$Si + 6HF + nh^+ \rightarrow H_2SiF_6 + nH^+ + \left(\frac{4-n}{2}\right)H_2$$

where *n* is the number of holes per dissolved Si atom.

Depending on the experimental conditions, the dissolution regime and *n* can change. At low HF concentration or high oxidizing agent concentration, SiO_2 forms at the surface and is slowly solubilized by HF, $n = 4$ with no H_2 evolution (polishing regime). At high HF concentration or low oxidizing agent concentration, dissolution occurs with $n = 2$ to 3, corresponding to 1 to 0.5 H_2 evolved per dissolved Si atom (porous Si formation regime) (9,10).

Electroless Ag deposition is based on this galvanostatic reaction. Due to the more positive redox level of Ag/Ag^+ than Si/Si^{4+}, reduction of Ag^+ into Ag^0 nanoparticles occurs on the Si surface.

The localization of etching originates from the fact that H_2O_2 reduction is catalyzed on noble metals. In the absence of metal, Si etching in HF/H_2O_2 is extremely slow. In the same way, when Ag^+ is used instead of H_2O_2, it is more easily reduce on already deposited Ag than on Si. In both cases, holes are injected into Si at the Si/Ag interface; hence, Si atoms are mainly oxidized (and then dissolved) close to the metal sites (10).

NW Formation by Si Etching Catalyzed with Ag Nanoparticles

In this first approach, the chemical formation of SiNWs is divided in 2 steps: (i) electroless deposition of Ag nanoparticles at room temperature in $HF/AgNO_3$ (0.15 M/ 0.5 mM) during 3 minutes; (ii) Ag catalyzed Si dissolution in HF/H_2O_2 (4.6 M / 0.44 M) during 5 minutes. Figure 1 shows SEM images of the Si surface after (a) Ag deposition and (b) etching.

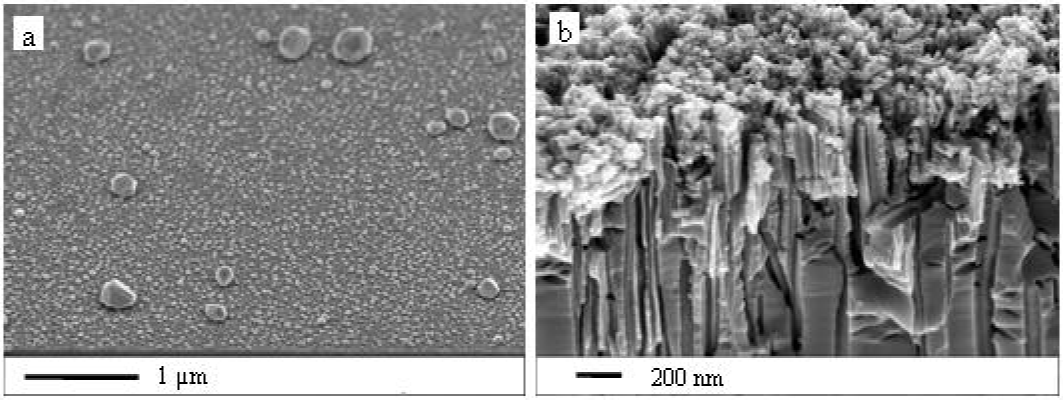

Figure 1. SEM images of the Si surface after (a) Ag deposition for 3 min and (b) HF/H_2O_2 etching.

Under these conditions, well defined individual Ag nanoparticles ~ 50 nm in diameter are obtained (some larger particles are also visible) that lead to the formation of a mesoporous Si layer by etching in HF/H_2O_2.

It is clear that SiNWs can only be formed if Ag nanoparticles form a continuous network, i.e. for a much higher Ag nanoparticle surface density. We therefore increased the Ag deposition time up to 30 min. Fig. 2a shows that the resulting Ag particles are larger, 100 to 200 nm in diameter, and that some are connected to each other.

After HF/H_2O_2 etching, a few μm thick highly structured Si layer is obtained, as shown by the SEM images in cross section of Fig. 2b (detail of the top of the layer in insert). The Si structures are actually closer to corrugated Si walls than to SiNWs. The Si walls are ~ 80 to 200 nm thick with shapes obviously defined by the mesopores.

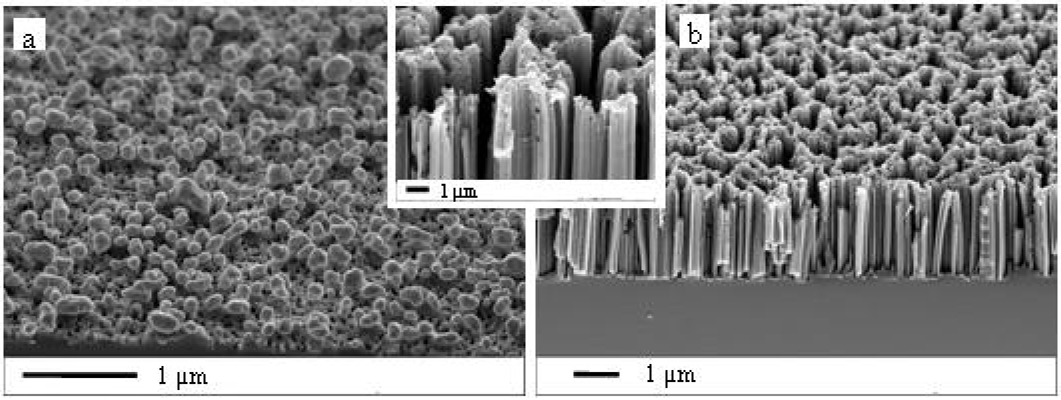

Figure 2. SEM images of the Si surface after (a) Ag deposition for 30 min and (a) HF/H_2O_2 etching.

At the top of the wires, small pores are visible and are probably due to the random migration of Ag particles at the beginning of etching. Normally, Ag nanoparticles dissolve Si preferentially in the <100> direction, i.e. dig pores perpendicular to (100) oriented surfaces. However, nanoparticles with odd shapes display helical or hieratic trajectories. This might be an additional problem for a well defined etching with nanoparticles.

SiNW Formation by Si Etching Catalyzed with a Ag/$AgNO_3$

To favor the formation of SiNWs, we had the option to further increase the Ag deposition time or to increase the $AgNO_3$ concentration. With a highly concentrated $AgNO_3$ solution in presence of HF, Ag is readily deposited in large amounts. Actually, an Ag foam forms all over the Si sample (simply removed by rinsing and sonication in ultra-pure water) and a significant quantity of Si is dissolved since Ag acts as a catalyst and Ag^+ as the oxidizing specie. Hence, the two step process described before can be simplified in a single step method in which Ag^+ replaces H_2O_2.

The initial conditions were 5 M HF, 0.02 M $AgNO_3$, 1 hour at 50°C (4). The resulting SiNWs are 35 µm long and 30 to 100 nm in diameter, as shown in Fig. 3a.

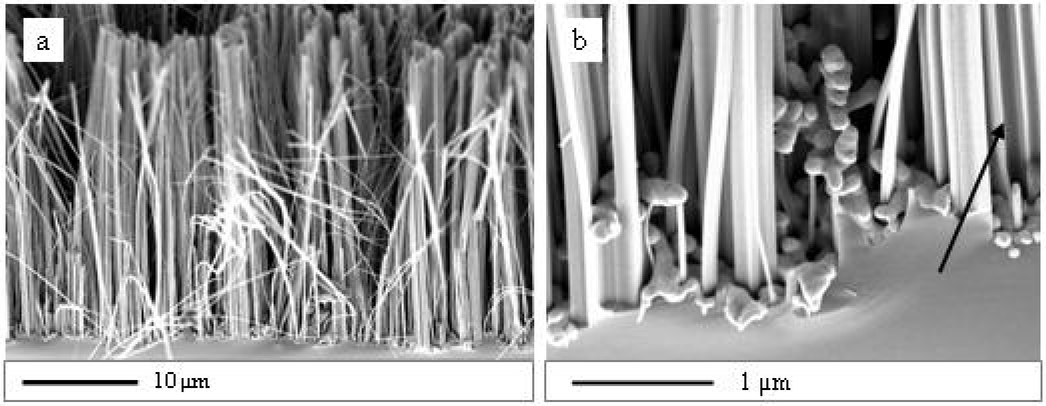

Figure 3: (a) SEM image of SiNWs obtained by a single step etching process in $HF/AgNO_3$; (b) higher magnification SEM image of the bottom of the SiNWs.

SEM observations, at higher magnification, of the bottom of the layer (Fig. 3b) reveal the existence of a Ag network made of connected nanoparticles. We assume that at the beginning of the process, individual Ag nanoparticles are formed as observed in low $AgNO_3$ concentration solutions after a short time (Fig. 1a). Because Ag deposition continues, the nanoparticles grow (Fig. 2a) and eventually merge in a Ag network. As etching proceeds further, the Ag network penetrates into bulk Si bulk.

A close look also confirms how effective is the Ag deposit in localizing the etching at the level of a few nanometers, with a "perfect" match between the SiNWs and Ag deposit shape. We also observe in many cases the existence of bundles of undetached SiNWs (indicated by an arrow in Fig. 3b).

Changes in etching conditions (HF concentration, temperature, time) affect the SiNW length, but only slightly the diameter. In all cases, bundles of SiNWs are observed.

SiNW Formation by Si Etching Catalyzed with a Metal Replica Mask

To fully benefit from the catalytic effect of the Ag network, it was necessary to develop a more regular metal pattern and hence to protect some Si areas where Ag deposition had to be avoided.

For that purpose, we assembled polystyrene spheres on the surface of Si substrates by spin coating, playing the role of a mask. We adjusted the spin coating conditions in order to get a monolayer of spheres or less. The spheres were often assembled into a hexagonal compact arrangement. Ag deposition was then performed by the electroless method with HF and $AgNO_3$.

As expected, Ag nanoparticles are deposited between the spheres where the Si surface is uncovered. This is illustrated by the SEM image of Fig. 4a. Unfortunately, we could not control further the Ag deposition into a metal homogeneous replica mask because this would detach the spheres from the surface. As a result, etching in HF/H_2O_2 led to the formation of mesopores, like in the first approach, instead of a full dissolution of the areas between the spheres. Additionally, a significant proportion of mesopores was not perpendicular to the surface (horizontal migration or change in direction) and partial etching under protected areas occurred (i.e. under the spheres), as shown in Fig. 4b and its insert.

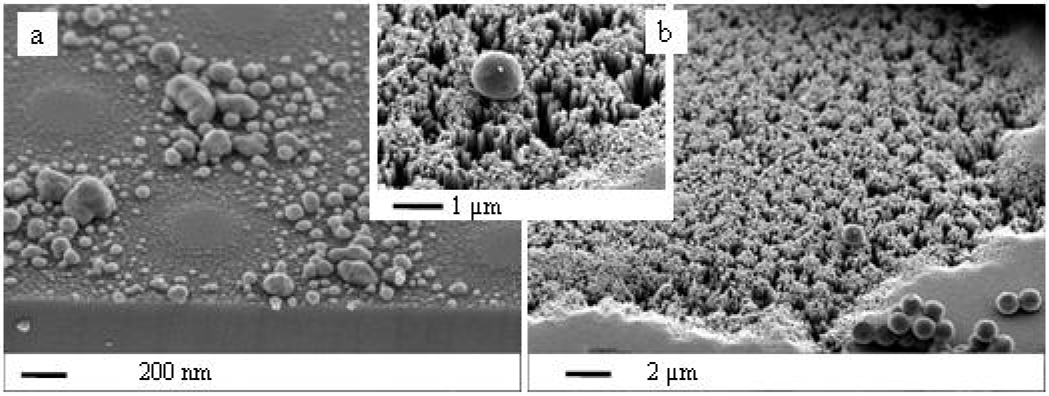

Figure 4. SEM images of Si surface after (a) Ag electroless deposition and (b) HF/H_2O_2 etching.

This clearly indicates that a homogeneous and cohesive metal replica mask is required to avoid any mesopore formation or unwanted lateral etching. Instead of the electroless deposition technique, we used thermal evaporation of Au on samples covered with the spheres to obtain such a mask. SEM images of a Si sample Au coated according to this procedure are shown in Fig. 5.

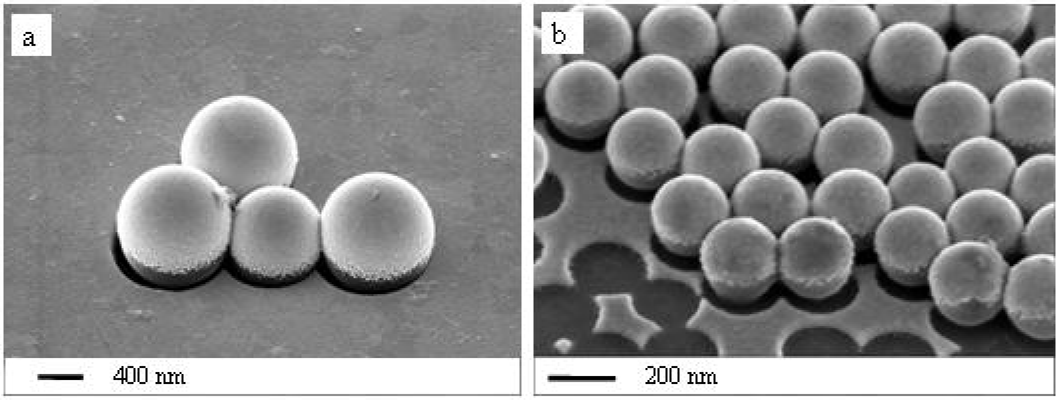

Figure 5. SEM images of Au coated Si surfaces with (a) polystyrene spheres 1 µm in diameter and a 15 nm thick evaporated Au layer; (b) polystyrene spheres 200 nm in diameter and a 45 nm thick evaporated Au layer.

The polystyrene spheres are not affected by the thermal evaporation. The Au mask is well defined, free of holes and has sharp edges. However, there is no Au between the spheres if there are too closely packed.

A Au layer 15 nm thick was deposited on a Si sample covered with 1 µm spheres (Fig. 5a). Etching in HF/H_2O_2 using the Au replica mask as a catalyst was then performed as described for the first method. Fig. 6 shows the surface after etching in 2.5 M HF and 0.63 M H_2O_2 during 5 min. Si pillars are obtained below the spheres, with approximately the same diameter as that of the sphere. The pillars are perpendicular to the (100) oriented Si surface.

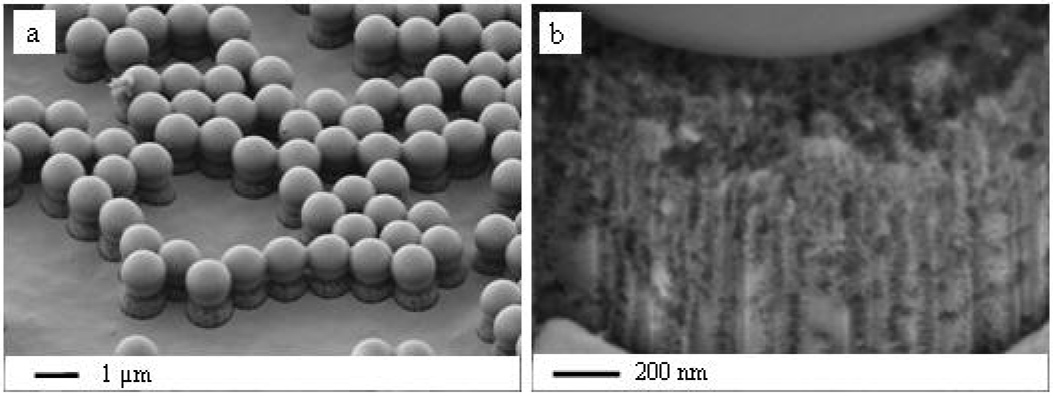

Figure 6. SEM images corresponding to the Si sample shown in Fig. 5a (1 µm polystyrene sphere) after etching in HF/H_2O_2: (a) view at low magnification and (b) detail of the top of a Si pillar.

The same results are obtained using smaller spheres (200 nm in diameter), as shown in Fig. 7. In this case, the thickness of the Au layer was 45 nm and etching was performed in 2.5 M HF and 0.28 M H_2O_2.

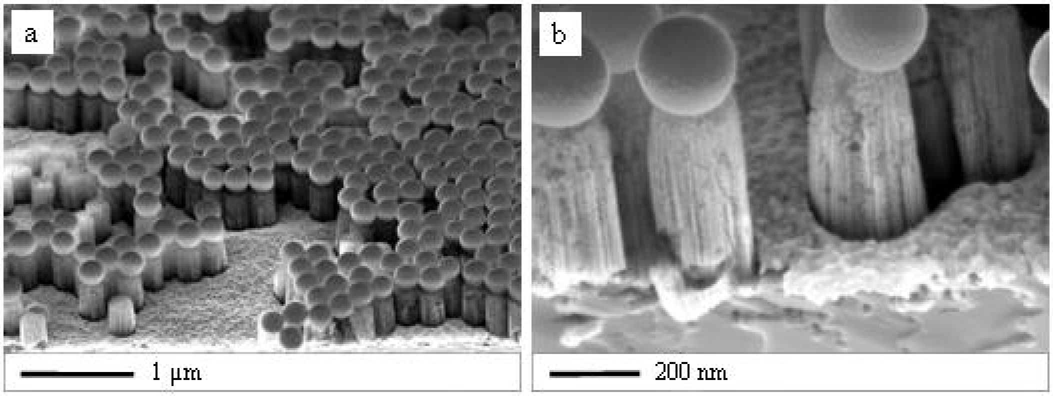

Figure 7. SEM images of the Si sample shown in Fig. 5b (200 nm sphere) after etching in HF/H_2O_2: (a) view at low magnification and (b) view at high magnification of the SiNWs.

Well defined SiNWs, 200 nm in diameter, are obtained. On the high magnification image (Fig. 7b) the NW walls appear rough, especially at their top. This is probably due to the grainy nature of the evaporated Au layer. The Au replica mask edges may release some Au nanoparticles that induce lateral etching within the SiNW. We consider that the rougher aspect of the SiNW at its top is the result of the longer etching time it experiences.

Conclusion

Metal assisted Si chemical etching was performed using 3 different approaches to form SiNWs. The first one, consisting of of an electroless deposition of Ag nanoparticles and subsequent etching in HF/H_2O_2 resulted in the formation of joint Si nanopillars at best. The second one, a single step process using a solution with HF and $AgNO_3$ at high concentration led to the deposition of a random Ag network that allowed Si to be etched into SiNWs and SiNW bundles of various size and shape. Control over the shape and the diameter of the SiNWs was however not possible but the interest of highly localized Si etching for SiNW formation was demonstrated. We therefore in the third approach use a multi-step process in which formation of a metal replica mask allowed a uniform catalyzed etching. The replica mask was obtained by thermal evaporation of Au on Si samples previously spin coated with a monolayer of polystyrene spheres. Etching was well defined in this way and Si pillars (1 µm in diameter) or SiNWs (200 nm in diameter) could be obtained depending on the polystyrene sphere dimensions.

Acknowledgments

This work was partially funded by CNRS and ANR within the DUOSIL project.

References

1. K.Q. Peng, J.J. Hu, Y.J. Yan, Y. Wu, H. Fang, Y. Xu, S.T. Lee, J. Zhu, *Adv. Funct. Mater.* **16** (2006) 387
2. K. Tsujino, M. Matsumura, *Adv. Mater.* **17**, 1045 (2005)
3. T. Qiu X.L. Wu, Y.F. Mei, G.J. Wan, Paul K. Chu, G.G. Siu, *J. of Cristal Growth*, **277**, 143-148 (2005)
4. K.Q. Peng, Y.J. Yan, S.P. Gao, J. Zhu, *Adv. Mater.* **14**, 1164 (2002)

5. H. Asoh, A. Oide, S. Ono, *Electrochem. Commun*., 8(12), 1817 (2006)
6. H. Asoh, F. Arai, S. Ono, *Electrochem. Commun*., 9(4), 535 (2007)
7. Z. Huang, H. Fang, J. Zhu, *Adv. Mater* **19**, 744-748 (2007)
8. K.Q. Peng, M. Zhang, A. Lu, N.B. Wong, R. Zhang and S.T. Lee, *Appl. Phys. Lett.* **90**, 163123 (2007)
9. E.S. Kooij, K. Butter and J.J. Kelly, *Electrochem. and Solid-State Lett.* **2(4)** 178-180 (1999)
10. C. Chartier, S. Bastide, C. Lévy-Clément, *Electrochim. Acta* **53** (2008) 5509-5516

ECS Transactions, 16 (3) 253-258 (2008)
10.1149/1.2982563 ©The Electrochemical Society

GaAs Microarrays by Noble-Metal Assisted Chemical Etching

Y. Yasukawa[a], H. Asoh[a,b], and S. Ono[a,b]

[a] Research Institute for Science and Technology, Kogakuin University
[b] Department of Applied Chemistry, Faculty of Engineering, Kogakuin University
2665-1 Nakano, Hachioji, Tokyo 192-0015, Japan

Microarrays of *n*-GaAs were fabricated for both (100) and (111) by colloidal crystal templating, ion sputtering and chemical etching using nanosized Au particles as the etching catalyst. Since self-organized polystyrene spheres were used as a mask, Au particles were selectively deposited at sites resulting in the formation of Au honeycomb pattern on GaAs. Microsized GaAs column arrays were achieved by chemical etching of GaAs, where the honeycomb-patterned Au metals were deposited. Although ordered column structures were obtained for both planes, different anisotropic etching patterns were observed by Au-assisted chemical etching between *n*-GaAs (100) and (111). The crystal-face orientation strongly affects the etching morphology and the rate of metal-assisted chemical etching.

Introduction

Metal-assisted chemical etching was proposed as a simple and effective technique (1, 2) to fabricate porous Si, which utilizes the catalytic ability of noble-metal particles in hydrofluoric-acid (HF) based etchant. Various metal sources have been investigated for the metal-assisted chemical etching of *p*-Si (100) substrates such as Au, Pt, Ag and Pd (2, 3). Also, porous GaN was fabricated through the metal-assisted chemical etching by some groups (4-6) with Pt particles as a catalyst and they obtained porous GaN with superior properties of cathode luminescence and photoresponse.

On the other hand, an investigation on metal-assisted chemical etching has just recently been carried out for GaAs and the utilization of the etching method on GaAs was confirmed by our group (7, 8). We fabricated GaAs column arrays through Ag-/Pd-assisted chemical etching deposited by electroless plating as metal catalysts and revealed that noble metal sources have been effectively enhanced etching rate for *n*-GaAs (100) and (111) substrates. However, a problem in terms of Ag-assisted chemical etching was slow etching rate, *i.e.*, ~0.6 nm/s. A considerable side etching in the Pd-assisted chemical etching was also raised as a negative problem.

Recently, we have confirmed the utilization of polystyrene (PS) spheres forming the self-organized structure as an etching mask, *e.g.*, fabrication of Si hole arrays (9), dot arrays (9), disk arrays (10), pillar arrays (10), porous alumina possessing 2D/3D composite structures (11) and the control of pit initiation sites on aluminum (12).

Therefore, we describe here the effectiveness of Au-assisted chemical etching for GaAs, as a function of crystal-face orientations, (100) and (111) with a resistivity level of 10^{-3} Ω cm order by adopting a templating technique of self-organized PS spheres. Au was chosen as the metal catalyst in this study.

Experimental

Patterning of *n*-GaAs Substrate Using Ion-Sputtered Au as the Etching Catalyst

A GaAs wafer with a resistivity level of 10^{-3} Ωcm order was used as a substrate. Before forming a mask, the substrate was degreased by ultrasonic cleaning in acetone, and the native-oxide film was removed by immersing the substrate in 46 wt% HF solution for 15 min. The present experimental procedure is schematically explained in Fig. 1. A solution with PS spheres of 3 μm diameter was adjusted to a suspension concentration of 0.25 %, added dropwise onto the substrate, and then dried in air. After the evaporation of the solvent, a mask consisting of PS spheres with a close-packed structure was obtained (Fig. 1(a)). Deposition of Au fine particles was performed by ion sputtering (Hitachi E-1010) by controlling the discharge current of 25 mA for 50 s resulting in Au-layer thickness of ~6 nm (Fig. 1(b)). After deposition of Au particles on the substrate, an ultrasonic cleaning in toluene was carried out to remove the mask (Fig. 1(c)). Finally, the chemical etching was conducted in analogy to our previous reports on chemical etching of GaAs (7, 8), *i.e.*, in a mixture of 5 mol dm^{-3} HF and 1 mol dm^{-3} H_2O_2 solutions, at room temperature for various periods (Fig. 1(d)).

The obtained surface morphologies and the etching depths of the substrate were evaluated by field-emission scanning electron microscopy (SEM, Hitachi FE-SEM S-4200) and atomic force microscopy (AFM, Digital Instrument Nano Scope IIIa).

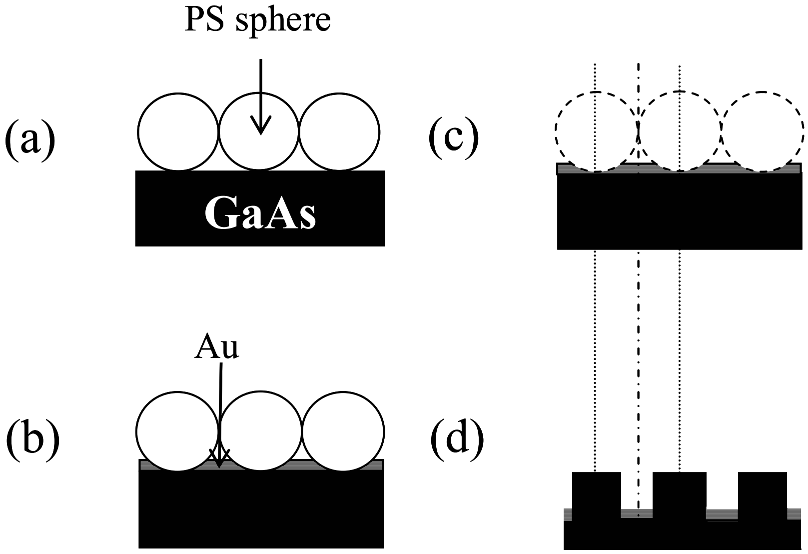

Figure 1. Schematic explanation of site-selective chemical etching of GaAs. (a) Colloidal crystals formed on substrate as a mask, (b) formation of Au layer, (c) removal of the PS mask, and (d) obtained GaAs column arrays using Au catalyst.

Results and discussion

Au Deposition on GaAs Substrate by Ion Sputtering

Although metal-assisted chemical etching proceeds only in the metal-coated substrate surface, the etching structure and rate are affected by the amount and the distribution of noble-metal deposition (13). Thus, preliminary to Au-assisted chemical etching of GaAs, appropriate thickness of Au-sputtered layer for the present metal-assisted chemical etching was searched. In the present study, Au-layer thickness was tested from 6 to 30 nm for Au-assisted chemical etching and it was revealed that the appropriate thickness of Au layer was determined to be ~6 nm. After Au sputtering on the substrate with the film thickness of ~6 nm by adjusting the ion current and sputtering time, the surface morphology was observed by AFM to evaluate the exact thickness of Au layer.

Fundamental Chemical Etching Behavior for (100) and (111) Substrates Using a Au Catalyst

Before fabricating GaAs column arrays, the effect of Au-assisted chemical etching on the (100)- and (111)-oriented substrates without use of the mask was confirmed, as shown in Figs. 2(a) and (b), respectively. Au-assisted chemical etching effectively acted for both substrates and an influence of the crystal-face orientation on the chemical etching of the GaAs substrate was clarified. Traces of the etching showed anisotropic etching configurations for both substrates but (111) substrate underwent relatively less anisotropic etching. Previously, we confirmed the conventional chemical etching, etching without a mask or catalytic metal particles, on the (100)- and (111)-oriented substrates (8). The results revealed that the crystal-face orientation affected the chemical etching of GaAs as well; for the (100) substrate, traces of the etching were seen in the horizontal direction to the substrate surface, resulting in the transverse line etching of the substrate but the (111) substrate showed somewhat circular anisotropic etching structures compared with that of (100). The fundamental chemical etching behavior for both substrates mentioned above in the previous work is reflected to the present etching structures formed by Au-assisted chemical etching as seen in Figs. 2(a) and (b).

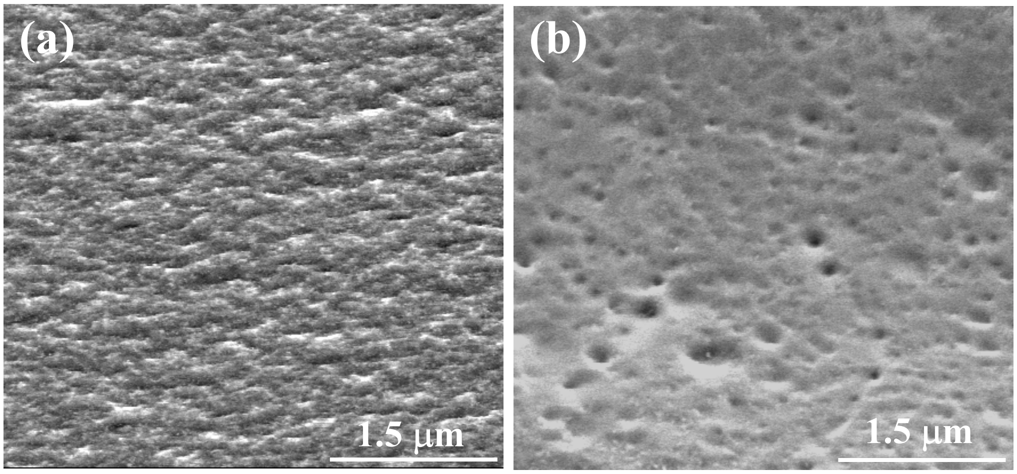

Figure 2. SEM images of (a) *n*-GaAs (100) and (b) *n*-GaAs (111) substrates after Au-assisted chemical etching for 60 s without using an etching mask. The images were taken at 45° to the surface.

Patterning of *n*-GaAs (100) and (111) Substrates by Au-Assisted Chemical Etching

Metal-assisted chemical etching with Au catalyst was investigated aiming for the microfabrication of GaAs. The Au sputtered substrate was immersed in an etching solution for up to 120 s after removing the etching mask. It was clarified that etching time of 20 s was the most optimized condition. Figures 3(a) and (b) show *n*-GaAs (100) substrates after Au sputtering and subsequent etching for 20 s. Au particles were deposited selectively in the interspaces among PS spheres and a Au honeycomb pattern was formed. Afterwards, the substrate was etched into column arrays through Au-assisted chemical etching. The contact areas between the PS spheres and the substrate were not etched because Au particles had not been deposited, resulting in the formation of convex structures. Anisotropic GaAs column arrays were formed through the Au-assisted chemical etching reflecting the structures of the etched specimens shown in Fig. 2(a). The etched structure originates from the PS spheres with 3 μm diameter but the resultant patterns exhibited non-spherical shape. Anisotropic etching configurations of the substrates generated by the present etching were enhanced with increasing the etching time from 20 s to 60 s, as shown in Figs. 3(c) and (d). Enhancement of the anisotropic etching structure for elongated etching period was due to the anisotropic dissolution of the apex of the convex portions. An AFM measurement for obtained GaAs microarrays showed that the average etching height was estimated to be 160 nm, suggesting the average etching rate of approximately 8.1 nm/s for a specimen etched for 20 s.

Chemical etching using patterned Au particles was also performed on the (111) substrate to examine the effect of crystal-face orientation on the etching morphology. Figures 4(a) to (d) show the GaAs surfaces after chemical etching using Au honeycomb patterns formed by ion sputtering. When the etching time was 20 s (Figs. 4(a) and (b)), column structures were observed with less anisotropy, i.e., less transverse compared with that of the (100) substrate etched for the same period (Figs. 3(a) and (b)). Not only Au-assisted chemical etching structures but also considerable dissolution of the apex of column arrays was enhanced by longer etching time, as seen in Figs. 4(c) and (d). An evaluation of etching height on a basis of AFM measurement of the GaAs (111) substrate revealed the average etching height was ~250 nm for a specimen etched for 20 s. Thus, the average etching velocity was calculated approximately 12.7 nm/s indicating 1.6 times faster etching rate of (111) than (100).

Etching heights obtained for (100) and (111) increased in proportion to the etching time for both substrates. In the present investigation however, three different types of etching ought to act upon GaAs when the metal-assisted chemical etching was conducted for long period; (1) metal-assisted chemical etching with a Au catalyst, (2) side etching, *i.e.*, etching progressing parallel to the substrate surface due to the Au catalyst and (3) chemical etching of the substrate generated by the etchant itself, *i.e.*, etching without a use of the catalytic ability of Au. Although longer etching time enhances the effect of Au-assisted chemical etching and side etching, an influence of chemical etching on the substrate becomes remarkable as well. It is because the PS mask was removed before Au-assisted chemical etching in the present experimental condition.

In the previous study, we reported the formation of GaAs column arrays by means of Ag- and Pd-assisted chemical etching throughout electroless plating (7, 8). However, one of the biggest problems concerning the wet process was found to be inhomogeneous sizes of metal particles. On the other hand, ion sputtering enables us to deposit much smaller metal particles with relatively similar size. This improves controllability and accuracy of the structures of the resultant GaAs microarrays. In fact, a diameter of each GaAs column obtained by the present study showed more uniform diameter compared with that of Pd-assisted chemical etching.

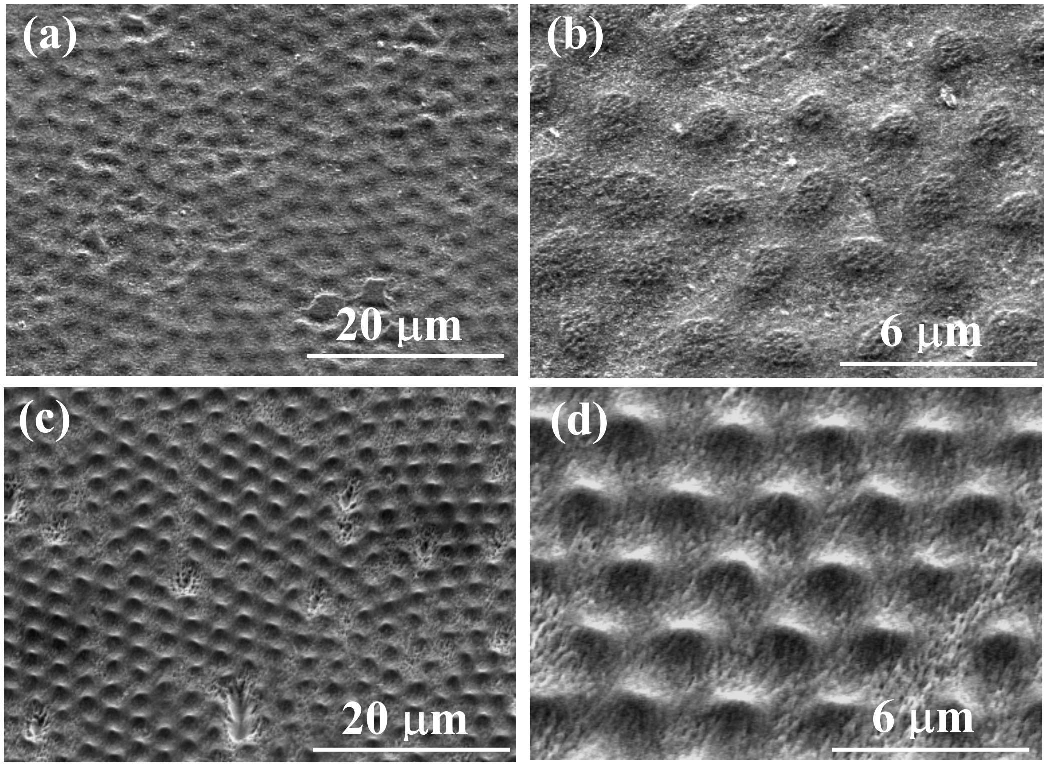

Figure 3. Surface structures of GaAs obtained by a combination of self-organized structural mask consisting of PS spheres (ϕ 3 μm), Au sputtering and metal-assisted chemical etching for (100). (a) low- and (b) high-magnification views etched for 20 s. (c) and (d) represent low- and high-magnification views obtained by the etching for 60 s. All the images were taken at 45° to the surface.

Conclusion

Microarrays of *n*-GaAs were fabricated for both (100) and (111) by colloidal crystal templating, ion sputtering and chemical etching using nanosized Au particles as the etching catalyst. The crystal-face orientation had a considerable effect on the resulting structures formed and etching rate. Since self-organized polystyrene spheres were used as a mask, Au particles were selectively deposited at the sites resulting in the formation of Au honeycomb pattern on GaAs. Microsized GaAs column arrays were achieved by chemical etching of GaAs, where the honeycomb-patterned Au metals were deposited. Although ordered column structures were obtained for both planes, different anisotropic etching patterns were obtained by Au-assisted chemical etching between *n*-GaAs (100) and (111).

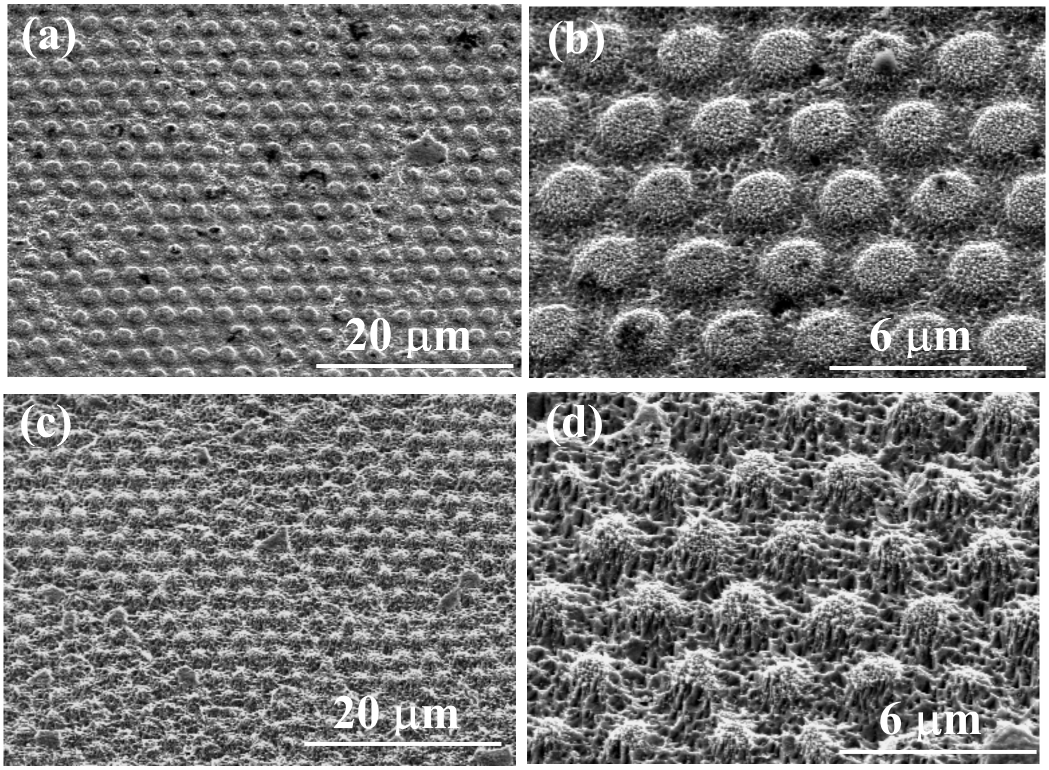

Figure 4. SEM images of *n*-GaAs (111) substrate after Au-assisted etching for 20 s ((a), (b)) and 60 s ((c), (d)). (a) and (c) show low-magnification views, whereas (b) and (d) are results of high-magnification observation. Images were taken at 45° to the surface.

References

1. S. Yae, Y. Kawamoto, H. Tanaka, N. Fukumuro, and H. Matsuda, *Electrochem. Commun.*, **5**, 632 (2003).
2. X. Li and P.W. Bohn, *Appl. Phys. Lett.*, **77**, 2572 (2000).
3. K. Tsujino and M. Matsumura, *Electrochim. Acta*, **53**, 28 (2007).
4. J. Bardwell, J. Webb, H. Tang, J. Fraser, and S. Moisa, *J. Appl. Phys.*, **89**, 4142 (2001).
5. X. Li, Y.-W. Kim, P.W. Bohn, and I. Adesia, *Appl. Phys. Lett.*, **80**, 980 (2002).
6. X.Y. Guo, T.L. Williamson, and P.W. Bohn, *Solid State Commun.*, **140**, 159 (2006).
7. Y.Yasukawa, H. Asoh, and S. Ono, *Electrcochem. Commun.*, **10**, 757 (2008).
8. Y.Yasukawa, H. Asoh, and S. Ono, *ECS Transactions*, **13**, 83 (2008).
9. H. Asoh, A. Uehara, and S. Ono, *Jpn. J. Appl. Phys.*, **43**, 5667 (2004).
10. H. Asoh, A. Oide, and S. Ono, *Electrochem. Commun.*, **8**, 1817 (2006).
11. H. Asoh and S. Ono, *Appl. Phys. Lett.*, **87**, 103102 (2005).
12. H. Asoh, K. Nakamura, and S. Ono, *Electrochim. Acta*, **53**, 83 (2007).
13. H. Asoh, F. Arai, and S. Ono, *ECS Transactions*, **6**, 431 (2007).

CHAPTER 5

TUESDAY: POSTER SESSION

ECS Transactions, 16 (3) 261-266 (2008)
10.1149/1.2982564 ©The Electrochemical Society

Dye-sensitized TiO_2 nanotubes with Ag nanoparticles

Y. Shinkai, H. Tsuchiya, and S. Fujimoto

Division of Materials and Manufacturing Science, Graduate School of Engineering, Osaka University

The present work examines the deposition of Ag nanoparticles on anodic TiO_2 nanotubes in order to improve solar energy conversion by increasing the optical absorption of dye. Ag nanoparticles are successfully deposited on TiO_2 nanotube layers. The size of nanoparticles is increased when amorphous TiO_2 nanotubes are crystallized and the tube diameter is increased. Photocurrent for dye-sensitized TiO_2 nanotubes is increased by the deposition of Ag nanoparticles, but the increment is decreased during dye-sensitization. This may be ascribed to the dissolution of Ag nanoparticles during the sensitization and the decreased plasmon resonance effect by thickening the dye layer on Ag nanoparticles.

INTRODUCTION

Since Zwilling et al. reported that tubular TiO_2 layers were formed by anodization of metallic Ti-based substrate in a fluoride containing electrolyte (1), the tubular layers have attracted much attention due to the fact that TiO_2 is one of the most promising functional materials and have numerous interesting properties such as solar energy conversion, photocatalysts of decomposition of organic compounds, wettability control and biocompatibility. Schmuki et al. have reported how tailoring electrochemical parameters can affect resulting morphology of electrochemically formed TiO_2 layers and achieved nanotubes with a length of a few hundred micrometers, nanotubes with hexagonal arrangement etc. (2).

The applications of TiO_2 nanotubes are based on their large surface area (3). Dye-sensitized solar cells are one of the most investigated applications of TiO_2 nanotubes (4, 5). Recently, Wen et al. reported that photoresponse in the visible light region increased when TiO_2 electrode was covered with very tiny Ag particles and concluded that the improved photoresponse is attributed to the enhancement of the optical absorption of dye by Ag plasmon resonance effect (6). In the present work, we attempt to deposit Ag nanoparticles on TiO_2 nanotube layers with different morphologies and evaluate photoresponses of dye-sensitized Ag-loaded TiO_2 nanotube layers.

EXPERIMENTAL

Samples used were titanium (99.6 % purity) in the form of foils with a thickness of 0.1 mm. Prior to anodization, the samples were degreased by sonicating in acetone, isopropanol and methanol, successively, rinsed with deionized (DI) water and dried with nitrogen stream.

For the anodization, an electrochemical cell with a three-electrode arrangement was used. The samples were contacted by a Cu plate and then pressed against an O-ring in the electrochemical cell, exposed to an electrolyte. Platinum plate served as a counter electrode and Ag/AgCl as a reference electrode. The anodization was carried out with a high-voltage potentiostat. The electrolyte used for tubular layer formation was 1M H_2SO_4 + 0.15 wt.% HF. The experiments were performed at room temperature under aerated non-stirred conditions. All solutions were prepared from chemical reagents of a high purity and deionized water. The anodization consists of a potential ramp from open circuit potential (OCP) to desired potentials, followed with holding the potentials for several hours.

To deposit Ag nanoparticles on TiO_2 layers, anodized samples were soaked in 1M $AgNO_3$, then slightly rinsed with DI water and dried in air stream. The samples were exposed to UV irradiation to induce photocatalytic reduction of Ag^+ to metallic Ag in the form of nanoparticles. For dye-sensitization, the samples were sensitized for several hours in N3 dye dissolved in ethanol with a concentration of 300 μM. After soaking, photocurrent spectra were recorded at 0.5 $V_{Ag/AgCl}$ with a step of 10 nm in the range from 500 nm to 800 nm. The electrolyte for all photocurrent measurements was acetonitrill containing 15 mM KI and 1.5 mM I_2.

For morphological characterization of the samples, a field-emission scanning electron microscope and transmission electron microscope were used. The cross-section images were taken from cracked layers after scratching the sample surface.

RESULTS AND DISCUSSION

Figure 1(a) and 1(b) show top-view and cross-sectional SEM images of anodic TiO_2 layer formed by anodization in 1M H_2SO_4 + 0.15 wt.% HF. As apparent from the figure, tubular TiO_2 layer with a length of approximately 450 nm and a diameter of 100 nm was formed by the anodization. Pores are open at the top surface and closed at the interface between the oxide and Ti substrate with a barrier layer. Anodization voltage dependence of diameter and length is summarized in Fig. 1(c). Evidently, tube diameter and tube length exhibit linear dependence with the anodization voltage. The diameter increases from approximately 20 nm at 5 V to 100 nm at 20 V and the length is varied from 100 nm at 5 V to 450 nm at 20 V. These results are in line with the previous works in acidic electrolytes containing a small amount of HF (7).

It is well know that anatase-type of TiO_2 shows higher conversion efficiency than the others. In literature, as-anodized TiO_2 nanotubes are in amorphous state and can be converted to anatase by annealing. Therefore, samples were annealed in air at 450 °C for 3 hours to form anatase-type TiO_2 nanotube layers. Figure 4(a) shows photocurrent spectra of annealed TiO_2 nanotube layers sensitized with Ru-dye for different time. In all photocurrent measurements, maximum photocurrents were achieved at around 570 nm. As it is reported that typically sensitization longer than 12 hours does not change the amount of chemisorbed dye molecules (8), we examine the effect of sensitization time up to 12 hours also in the present work. In this time scale, the photocurrent increases with sensitization time. Figure 2(b) shows effect of tube morphology on the maximum photocurrent. The maximum photocurrent has a trend to increase with anodization voltage – increase tube length and tube diameter. As the geometrical surface areas of the tubes formed at different voltages are almost same, there may be difference in the amount of active sites for chemisorption of the dye.

Figure 3 shows SEM images of as-anodized and annealed TiO_2 nanotube layers after Ag deposition. It is clear from Fig. 3(a) that Ag nanoparticles with a diameter of approximately 10 nm are deposited on the nanotube surface. From cross-sectional TEM observations, the nanoparticles are not only on the top of the tubes but also within the tubes. Therefore, it is found that Ag nanoparticles can be successfully deposited on TiO_2 layer by the treatment. The size of Ag nanoparticles increases by annealing – conversion of crystal structure of TiO_2 nanotubes from amorphous to anatase – and also by increasing tube diameter. For further experiments, therefore, we used the annealed nanotubes formed at 20 V.

Figure 4(a) shows photocurrent spectrum for Ag-nanoparticle loaded TiO_2 nanotube layer. Spectrum obtained for nanotube layer without Ag nanoparticles is also included as comparison. Both layers were dye-sensitized for 12 hours. The photocurrent is slightly enhanced by loading Ag nanoparticles. Increment of maximum photocurrent is plotted as a function of dye-sensitization time. It is obvious that the increment drastically decreases at the short time of sensitization and then become almost constant. The reason may be attributed to dissolution of Ag nanoparticles during sensitization. Increased amount of chemisorbed dye during sensitization may also result in thickening the dye layer on Ag nanoparticles, leading to the decrease of Ag plasmon resonance effect.

CONCLUSIONS

In the present work, we measured photocurrent spectra for dye-sensitized TiO_2 nanotube layers with different morphologies (length and diameter) and attempt to deposit Ag nanoparticles in order to enhance the optical absorption of dye by Ag plasmon resonance effect. Anodization voltage affects the morphology of TiO_2 nanotube layer – increasing anodization voltage leads to the increase of tube diameter and tube length. Photocurrent obtained for dye-sensitized nanotube layers is increased with anodization voltage for tube formation. Ag nanoparticles can be deposited independent of crystallinity and morphology of nanotube layers, but the better crystallinity and the larger the tube diameter, the larger the average diameter of Ag nanoparticles. The presence of Ag nanoparticles can enhance photocurrent by the enhanced optical absorption of dye, but the enhancement is decreased during dye-sensitization.

ACKNOWLEDGEMENTS

This work was supported by Priority Assistance for the Formation of Worldwide Renowned Centers of Research – The Global COE Program (Project: Center of Excellence for Advanced Structural and Functional Materials Design) from the Ministry of Education, Culture, Sports, Science and Technology (MEXT), Japan. A part of the present experiments was carried out by using a facility in the Research Center of Ultrahigh Voltage Electron Microscopy, Osaka University.

REFERENCES

1. V. Zwilling, E. Darque-Ceretti, A. Boutry-Forveille, D. David, M.Y. Perrin, and M. Aucouturier, *Surf. Interface Anal.*, **27**, 629 (1999).
2. J.M. Macak, H. Tsuchiya, A. Ghicov, K. Yasuda, R. Hahn, S. Bauer, and P. Schmuki, *Curr. Opin. Sol. State Mater. Sci.*, **11**, 3 (2008).

3. B. O'Regan, and M. Grätzel, *Nature*, **35**, 37 (1991).
4. J.M. Macak, H. Tsuchiya, A. Ghicov, and P. Schmuki, *Electrochem. Commun.*, **7**, 1133 (2005).
5. M. Paulose, K. Shankar, O.K. Varghese, G.K. Mor, and C.A. Grimes, *J. Phys. D: Appl. Phys.*, **39**, 2498 (2006).
6. C. Wen, K. Ishikawa, M. Kishima, and K. Yamada, *Sol. Eng. Mater. Sol. Cells*, **61**, 339 (2000).
7. S. Bauer, S. Kleber, and P. Schmuki, *Electrochem. Commun.*, **8**, 1321 (2006).
8. A. Fillinger, D. Soltz, B.A. Parkinson, *J. Electrochem. Soc.*, **149**, A1146 (2002).

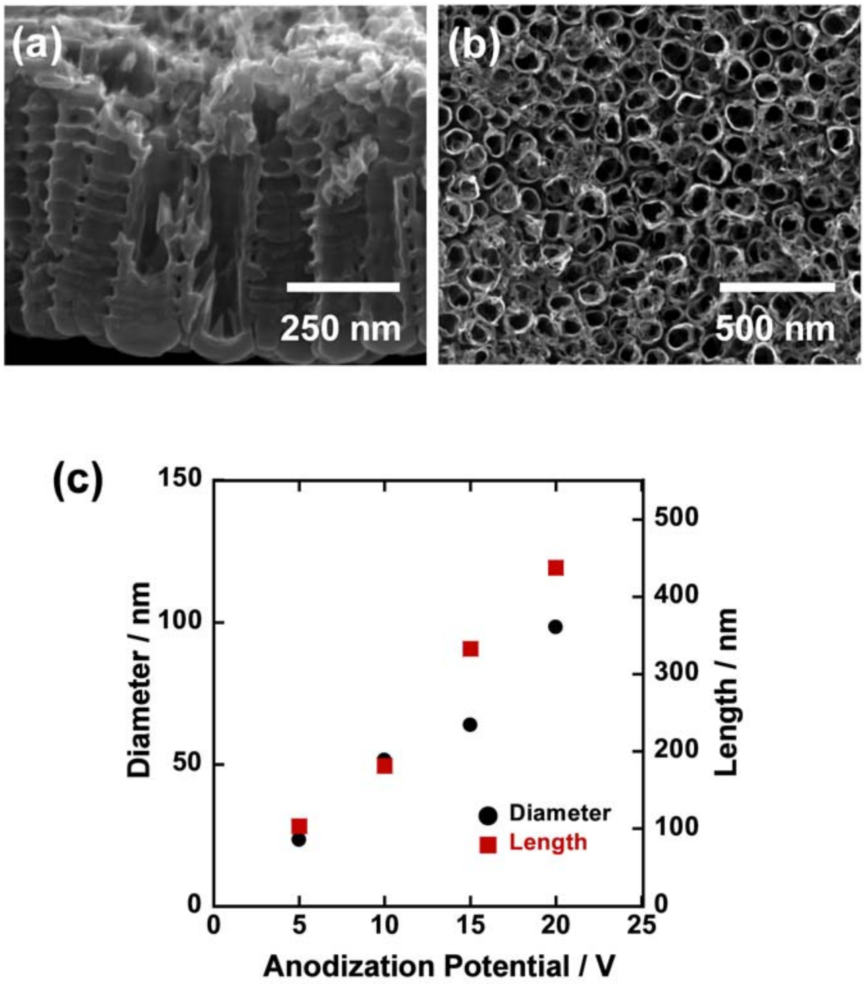

Figure 1. (a) Top-view and (b) cross-sectional SEM images of TiO_2 nanotube layer formed in 1M H_2SO_4 + 0.15 wt.% HF. (c) Diameters and thickness of nanotube layers in 1M H_2SO_4 + 0.15 wt.% HF at different potentials.

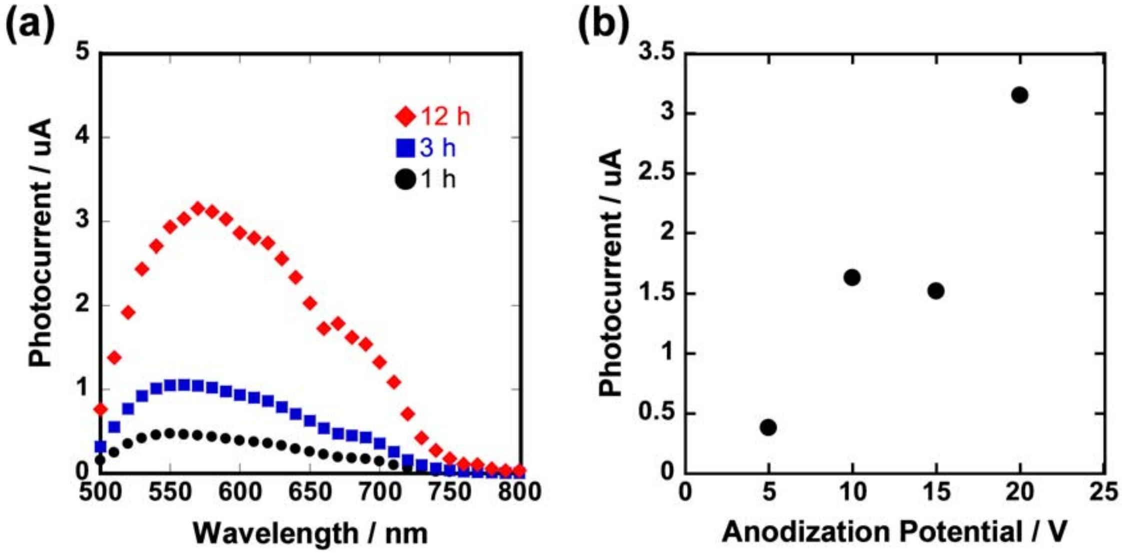

Figure 2. (a)Photocurrent spectra for TiO_2 nanotube layers formed at 20 V. The layers were soaked in Ru-dye solution for different time. (b) Maximum photocurrent as a function of anodization potentials. The maximum photocurrents were obtained at a wavelength of 570 nm.

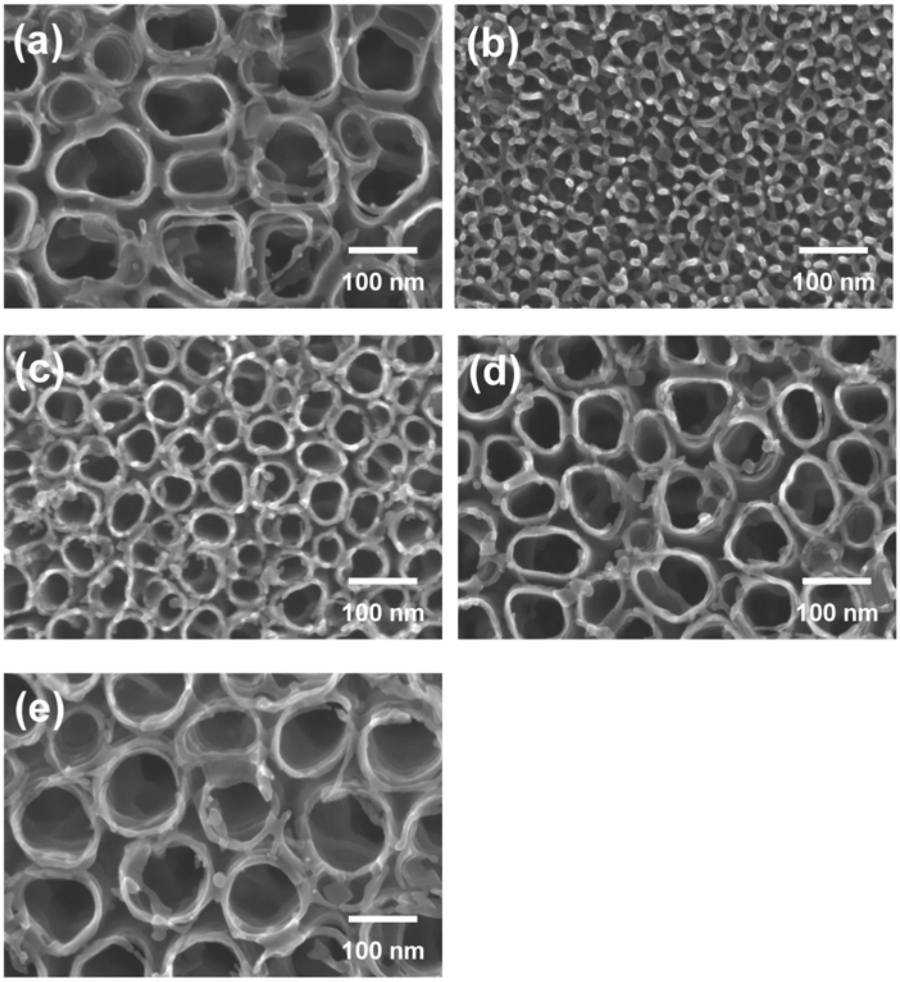

Figure 3. (a) Ag deposition on as-anodized TiO_2 nanotube layer. Ag-loaded annealed nanotubes formed at (b) 5 V, (c) 10 V, (d) 15 V and (d) 20 V.

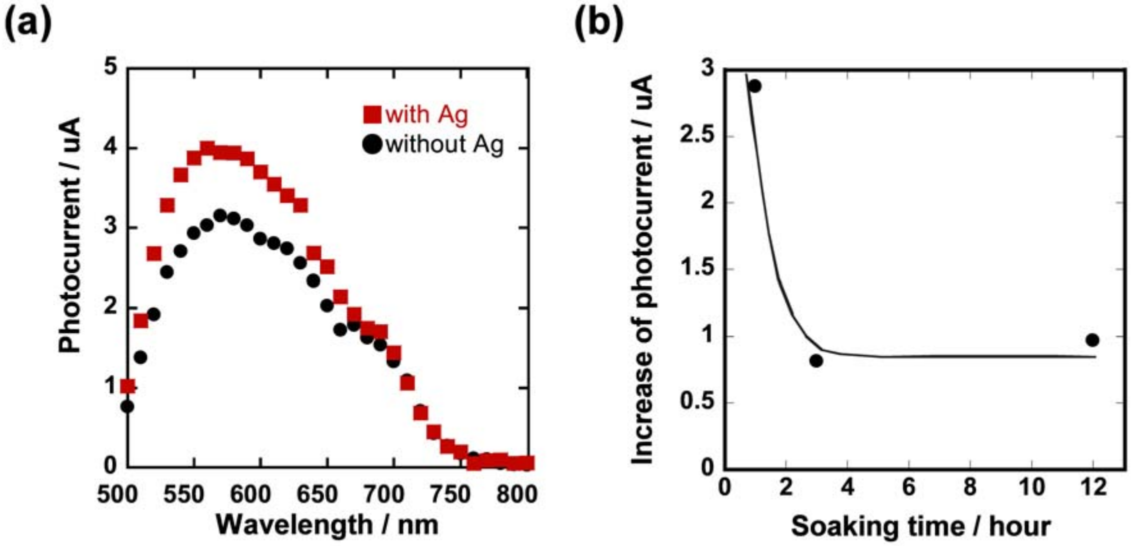

Figure 4. (a) Effect of Ag-nanoparticles on photocurrent spectrum obtained for dye-sensitized TiO_2 nanotube layer. (b) Increase of photocurrent as a wavelength of 570 nm as a function of dye-sensitization time.

ECS Transactions, 16 (3) 267-276 (2008)
10.1149/1.2982565 ©The Electrochemical Society

Resonant Energy Transfer from Porous Silicon to Iodine Molecules

T. Nakamura[a], T. Ogawa[a], T. Kubota[a], S. Adachi[a], and M. Fujii[b]

[a] Department of Electronic Engineering, Faculty of Engineering, Gunma University, Kiryu, Gunma 376-8515, Japan
[b] Department of Electrical and Electronics Engineering, Faculty of Engineering, Kobe University, Rokkodai, Nada, Kobe 657-8501, Japan

The electronic excitation energy transfer between excitons in porous silicon and iodine molecules in an organic solution is studied. From the time-resolved photoluminescence the rate of the energy transfer is increased with approaching a wavelength region where the photoluminescence spectrum of porous silicon overlaps the absorption spectrum of iodine molecules, and with increasing the radiative recombination rate of porous silicon. We show that the dependence of the rate is well explained by Förster type dipole-dipole interaction mechanism in which the diffusion of the assemblies and molecules is taken into consideration. Furthermore, it is found that the efficiency of the energy transfer strongly depends on the emission wavelength at low iodine concentration.

Introduction

Silicon (Si) nanocrystal is a promising material for opt-electronic devices because of their strong visible and near infrared photoluminescence (PL) at room temperature. The efficient luminescence is due to the recombination of quantum confined excitons (1)-(3). The typical system that contains luminescent Si nanocrystal assemblies is porous Si. Because Porous Si is easily prepared by the anodic electrochemical etching in a hydrofluoric acid based solution and has high luminescent efficiency, the structural and optical properties of porous Si are intensively investigated (4).

The radiative lifetime of Si nanocrystals is rather long (~ μs range) because of the inheritance of indirect bandgap nature of bulk Si. Then, it is difficult to realize the light emitting devices based on the Si nanocrystal assemblies. It is demonstrated that Si nanocrystals used as efficient photosensitizer for rare earth ions (5)-(6), molecular oxygen (7). Particularly, in the photosensitized effect for the molecular oxygen, the long lifetime of Si nanocrystals is an important role since the decay time of excitons is smaller than the transfer time of electronic excitation energy to molecular oxygen. Additionally the large surface area in porous Si is an advantage for the energy transfer.

Si nanocrystals can be used as the photosensitizer for other materials such as organic molecules. Recently, the energy transfer from Si nanocrystals to organic molecules is demonstrated (8). In that work, the energy transfer takes place via the direct electron exchange interaction, Dexter process, which is the same mechanism as that between Si nanocrystals and molecular oxygen. Basically, the electronic excitation energy of donor can non-radiatively transfer to acceptor via the dipole-dipole Columbic interaction, Förster process (9), in addition to Dexter process. In colloidal semiconductor nanocrystals such as CdSe quantum dots, the excitation energy transfer to organic dye molecules or nearby quantum dots via Förster process is observed (10)-(11). Then, Si nanocrystals also expect for use of the energy donor in Förster type energy transfer. It is important to investigate Förster process in Si nanocrystals, because Si nanocrystals have a longer lifetime compared to direct bangap semiconductor quantum dots, the size tunable PL spectra allowing the excitation of an acceptor at a specific wavelength, and the broad absorption band in an ultraviolet region. However, there are a few works on the process in Si nanocrystals (12).

In this work we demonstrate that the excitation energy of the porous Si transfers to acceptor molecules via Förster type dipole-dipole interaction in an organic solution. The iodine molecules are chosen as the energy acceptor because of small influence on the PL of Si nanocrystals due to low intrinsic dipole moment of the iodine and a large spectral overlap between absorption of iodine and PL of Si nanocrystals (12). We show that the rate and efficiency of energy transfer strongly depend on the emission wavelength i.e., the size of porous Si. Furthermore, the dependences are strongly modified by increasing the concentration of iodine molecules.

Experimental

We used porous Si powder as nanocrystal assemblies. The porous Si was prepared by a stain-etching process (13). Metallurgical-grade polycrystalline Si powder (Vesta Ceramics, with mean diameter 3-11 μm) was immersed in a HF, H_2O solution, and in the solution HNO_3 was added gradually up to 4:1:20 of HF:H_2O:HNO_3 for 20 minutes. After etching, the powder was collected from etching solution and dried at ambient condition for 24 hours. The as-prepared sample shows efficient orange emission illuminated by ultraviolet light. The as-prepared porous Si powder has H-terminated surface. As a comparison purpose, we prepared the porous Si with oxygen terminated surface by thermal annealing method. The as-prepared sample is annealed in air ambient at 900 ^{o}C for 30 s. By x-ray electron spectroscopy, it is confirmed that the SiO_2 overlayer is formed on the surface of the porous Si (14).

For PL measurement, porous Si powder was dispersed in a quartz cell filled with trichloroethylene for as-prepared and with ethanol for annealed samples. Then iodine molecules are gradually mixed in solutions. During optical measurements, the solution was permanently mixed using a magnetic stirrer.

The excitation sources for steady-state and time-resolved PL measurements were 325 nm line of He-Cd laser and 355 nm light from the third harmonic of a Neodium:Yttrium-Aluminum-Garnet (Nd:YAG) laser (pulse width 5 ns, and repetition frequency 20 Hz). The steady-state PL spectra were measured by using a grating spectrometer and a Peltier-device-cooled photomultiplier tube (Hamamatsu R375), and for time-resolved PL spectra a spectrometer equipped with a gated Charge Coupled Device (PI-Max, Princeton Instrument, 5 ns response time) was used. In a time-resolved PL measurement the delay time after excitation pulse is 20 nm and the gate width was 60 ns. All measurements were performed at room temperature.

Results and Discussion

Figure 1 shows steady-state PL spectra of porous Si powder for as-prepared and annealed samples dispersed in a solution (solid line, left axis). We can see that the PL peak wavelength shifts to longer wavelength and the intensity is decreased by annealing porous Si. This is due to the formation of the SiO_2 overlayer on the surface of porous Si (14). The absorption spectrum of iodine solution is also shown in Fig.1 (dashed line, right axis). An absorption band at around 500 nm is seen due to the $1u(^1\Pi) \leftarrow X$ and $B \leftarrow X$

electronic transitions for iodine molecule (15). It is found that PL spectrum for as-prepared sample overlaps absorption spectrum of iodine molecules very well in the range from 500 to 600 nm, while that for the annealed sample does not overlap. Therefore, it is expected that the energy transfer from porous Si to the iodine molecules occurs efficiently for the as-prepared sample.

In Fig. 2, PL spectra of porous Si for (a) as-prepared and (b) annealed samples with iodine molecules are shown. The concentration of the iodine is varied (a) from 0.6 to 10 and (b) from 6 to 14 × 10^{-4} mol/l. In both samples, the intensity decreases with increasing the concentration of the iodine. In addition, the red shift of PL peak wavelength with increasing the concentration for the as-prepared sample is observed.

In order to investigate the degree of the PL quenching by adding the iodine quantitatively, we estimate the strength of the quenching which is defined as the PL intensity for the sample without iodine divided by that with iodine. Figure 3 shows the strength of the quenching at various iodine concentrations as a function of the emission wavelength for (a) as-prepared and (b) annealed samples. It should be noted that the scale of vertical axis in Fig. 3(b) is the same as that in Fig. 3(a). For the as-prepared sample the strength strongly depends on both iodine concentration and emission wavelength. The PL quenching is efficient at shorter wavelength region, and the strength shows peak at around 550 nm. The feature is more pronounced with increasing the iodine concentration. The dependence of the quenching on the emission wavelength indicates that the resonant energy transfer from porous Si to iodine molecules occurs, since the spectral overlap between porous Si and iodine is larger at around 550 nm. For the annealed sample, the PL quenching does not depend on the emission wavelength. Moreover, the strength of the PL quenching is much smaller than that for the as-prepared sample.

The possible mechanisms of the PL quenching are as follow (9). One is the radiative energy transfer; the photon emitted by the excited energy donor is absorbed by the energy acceptor. Another one is the non-radiative energy transfer, which is transferring the excited energy of the donor to acceptor via Columbic interaction or electron exchange. To clarify the mechanism of the quenching of the PL intensity by adding iodine, we measured the temporal behavior of the PL for porous Si. If the mechanism for the energy transfer is non-radiative one, the modification in the decay dynamics of porous Si should be observed.

Figure 4(a) shows time-resolved PL spectra of porous Si dispersed for the as-prepared sample in the solution with iodine (dashed line) and without iodine (solid line). The iodine concentration is 5.4 × 10^{-4} mol/l. The gate width is 60 ns, and the delay time with respect to the excitation pulse is varied from 0.02 to 6 μs. The PL intensity is quenched by adding the iodine molecules, and the degree of the quenching is larger as the delay time is increased and emission wavelength approaches the absorption peak of iodine molecules. The PL decay curves of porous Si detected at 567 (open square) and 700 nm (closed square) are plotted in Fig. 4(b). It is clearly seen that by adding iodine molecules the lifetime becomes shorter. The degree of the shortening depends on the emission wavelength, i.e., the modification of PL decay curve detected at 567 nm by adding iodine is much stronger than that detected at 700 nm. The shortening of lifetime suggests that the non-radiative energy transfer from excitons confined in Si nanocrystals to iodine molecules occurs. For the annealed sample, a clear change in temporal spectral behavior by adding iodine is not observed (data are not shown). This result implies that the PL quenching for the annealed porous Si by adding iodine is due to the radiative energy transfer or the absorption of the excited light by the iodine molecules.

To discuss the degree of the lifetime shortening quantitatively, we estimate the PL lifetime by fitting the PL time transients of porous Si with a stretched exponential function. In Fig. 4(b) examples of the fitting are plotted (solid lines). We can see that the curves are well fitted. Figure 5 shows estimated PL lifetime of porous Si for (a) as-prepared and (b) annealed samples as a function of the emission wavelength. For the as-prepared sample, the clear features depending on the emission wavelength and iodine concentration are observed. At the 1.6×10^{-4} mol/l the lifetime is shortened in the shorter wavelength region. On the other hand, the lifetime of porous Si with iodine is the almost the same as that without iodine. At the 5.4×10^{-4} mol/l the lifetime is shortened in a whole wavelength range. The shortening of the rate are the clear evidence of the non-radiative energy transfer from porous Si to iodine molecules. Compared to the as-prepared sample, the overall feature is not modified by adding the iodine for the annealed sample as shown in Fig. 5(b), and this result supports that the non-radiative energy transfer does not occur.

In the presence of iodine molecules in the solution dispersed porous Si powder the decay rate (the reciprocal value of lifetime) of excitons measured by PL decay curve consists of three components, the radiative recombination rate k_r, non-radiative one k_{nr} and the rate of energy transfer to the iodine k_{et}. If the increase in the decay rate by the presence of iodine molecules is caused only by the energy transfer, the rate of the energy transfer can be estimated by subtracting the decay rate without iodine ($k_r + k_{nr}$) from that with iodine ($k_r + k_{nr} + k_{et}$). In Fig. 6(a), the energy transfer rate estimated by this procedure is plotted as a function of emission wavelength at 1.6×10^{-4} and 5.4×10^{-4} mol/l. As shown in Fig. 6(a) the energy transfer rate strongly depends on the emission wavelength and iodine concentration. The energy transfer rates are increased to shorter wavelength side for both iodine concentrations. At low iodine concentration, the increase in the rate is observed in the range from 500 to 650 nm, and in the other region the rates are nearly zero, i.e., the energy transfer does not occur. In contrast, at highest concentration the rate starts to increase at around 700 nm, and the energy transfer takes place in the whole wavelength range.

A possible mechanism of non-radiative energy transfer from excitons in the porous Si to iodine molecules can be accounted for the Förster type dipole-dipole interaction (12). The rate of Förster type energy transfer depends on the oscillator strength of donor and acceptor and the separation between donor and acceptor (9). From the Förster theory for energy transfer in a single donor-acceptor pair, the rate of energy transfer k_{et} is given by $k_{et} = k_r(r/R_0)^{-6}$, where R_0 is the Förster distance in which the transfer is 50% efficient, k_r is the decay rate of a donor, and r is the distance between a donor and an acceptor. In our case, the energy transfer occurs for donors (excitons in Si nanocrystals) and acceptors (iodine molecules) randomly distributed in a three dimensional solution. Therefore, we should take the situation into account for the calculation of the energy transfer rate. In addition, the diffusion of donors and acceptors affects the rate of energy transfer because the lifetime of excitons (~μs) is much longer than that of typical fluorescent organic molecules (17). To consider these conditions, the rapid diffusion limit (18) is assumed. The rapid diffusion limit is adopted in a system where a mean distance diffused by donor and acceptor is sufficiently smaller than the diffusion distance during the lifetime of donor. The energy transfer rate in this limit is

$$k_{et} = 4\pi\rho(R_0)^6 k_r/3a^3, \qquad [1]$$

where, a and ρ are the distance of closest approach between donor and acceptor and the density of acceptor, respectively. In previous work, to verify the validity of this assumption, we fitted the Eq. (1) to the dependence of energy transfer rate obtained experimentally on the acceptor concentration and the dependence is well reproduced by the calculation (19). In this work, we calculate the dependence of the rate on the emission wavelength by the same procedure. In the calculation, a is 4.5 Å is estimated by the fitting procedure in previous work, and the value of k_r is used for the porous Si without iodine molecules. R_0 in Å is given by (17) $R_0 = 0.211(\kappa^2 n^{-4} Q_0 J(\lambda))^{1/6}$, where κ is a factor describing the relative orientation in space of the transition dipoles of the donor and acceptor. Q_0 is the quantum yield of donor in the absence of acceptor. n is the refractive index of the medium. $J(\lambda)$ is the overlap integral, i.e., the spectral overlap between donor emission and the acceptor absorption. In the calculation of R_0, κ^2 is assume to be 2/3, which is the value for a random distribution of interacting dipoles, n equals 1.48, and $J(\lambda)$ is calculated by using experimentally obtained spectra. We assume that the value of Q_0 is 1, because an individual nanocrystalline Si has a large PL quantum efficiency (20) although the value for an assembly of nanocrystalline Si reported is several percent (21). The calculation result of R_0 is 21.8 Å.

In Fig. 6(a) the calculated energy transfer rate as a function of the emission wavelength is plotted at 1.3×10^{-4} (open circle) and 5.4×10^{-4} mol/l (open square). A good agreement between the calculation and experiments is obtained in spite of a simple assumption for the calculation except in the longer wavelength range. The agreement indicates that the energy transfer between excitons and iodine is caused by the Förster type dipole-dipole interaction. Noted that at low iodine concentration the calculation in shorter wavelength range slightly deviates from the experimental result. This is due to the breaking the rapid diffusion limits (19).

The rate of Förster type energy transfer strongly depends on the oscillator strength of donor and spectral overlap between PL of donor and absorption of acceptor. Therefore, the origin of the emission wavelength dependence of energy transfer rate as shown in Fig. 6(a) can be explained as follows. The increase in the energy transfer rate in shorter wavelength region results from two factors. First is the larger spectral overlap between PL of porous Si and absorption of iodine in longer wavelength region. Second one is the dependence of the radiative recombination rate on the size of Si nanocrystals. With decreasing the size of Si nanocrystals the oscillator strength is increased due to the quantum confinement effect, and then the radiative recombination rate is enhanced as shown in Fig. 5(a). The enhancement of the rate results in the increase in the energy transfer rate.

For the annealed sample, the energy transfer does not occur as shown in Fig 5(b). This is partly due to the lower spectral overlap between porous Si and iodine. Furthermore, the formation of the SiO_2 overlayer, which is a few nanometers in thickness, results in the decreasing the energy transfer rate because of increasing the mean distance between porous Si and iodine molecules.

It should be noted that large deviations of the calculation from experimental data are observed in longer wavelength region i.e., the calculation increases with increasing the wavelength while the experimental results are nearly constant. This results from the overestimation of the radiative recombination rate k_r of porous Si. The experimentally obtained recombination rate consists of radiative rate and non-radiative one. If the value of non-radiative rate competes the radiative one, the calculated energy transfer rate is larger than a real value. In fact, as shown in Fig. 6(a), the calculated result is much larger than that for experimental results in longer wavelength region.

Finally, in Fig. 6(b) we plotted the energy transfer efficiency η_{et}, which is defined as

$$\eta_{\mathrm{et}} = (k_{\mathrm{et}}) / (k_{\mathrm{r}} + k_{\mathrm{nr}} + k_{\mathrm{et}}), \qquad [2]$$

as a function of the emission wavelength at 1.6×10^{-4} and 5.4×10^{-4} mol/l. In Fig. 6(b), we can see that the efficiency at low iodine concentrate strongly depends on the emission wavelength, while at high concentration the efficiency is nearly constant in the whole wavelength. Furthermore, the value at high concentration is larger than that for low concentration. The increase in the efficiency with increasing the iodine concentration corresponds to the result in the steady state measurement. However, the wavelength dependence of the efficiency is not explained by the calculation model used above; the energy transfer efficiency does not depend on the emission wavelength. In the present work, the dependence experimentally obtained is not fully understood. The wavelength dependence probably relates inhomogeneous PL broadening due to the size distribution of Si nanocrystals, and then to explain the result we should modify the calculation model.

Conclusion

The energy transfer from excitons in Si nanocrystals to iodine molecules was studied by using the time-resolved PL spectroscopy. The shortening of the lifetime due to the non-radiative energy transfer were observed and the degree of the shortening depended on the emission wavelength for as-prepared sample, while for the annealed porous silicon the shortening was not show. The energy transfer rates were increased with increasing the emission wavelength. These results imply that efficient energy transfer takes place under the resonant condition where the spectral overlap between the PL of porous Si and the absorption of iodine molecules, and the large radiative recombination rate of porous Si. The dependence of the rate was well explained by the Förster model in which the diffusion of the porous Si powder and iodine molecules is taken into consideration in shorter wavelength. The present result suggests that the porous Si can be act as a donor in the energy transfer via dipole-dipole interaction.

Acknowledgments

This work was supported by a Grant-in-Aid for Scientific Research from the Japan Society for the Promotion of Science and Hosokawa Powder Technology Foundation.

References

1. L. T. Canham, *Appl. Phys. Lett.*, **57**, 1046 (1990).
2. C. Delerue, M. Lannoo, G. Allan, and E. Martin, *Thin Solid Films* **255**, 27 (1995).
3. D. Kovalev, H. Heckler, G. Polisski, and F. Koch, *Phys. Stat. Sol (b)* **215**, 871 (1999).
4. A. G. Cullis, L. T. Canham, and D. J. Calcott, *J. Appl. Phys.* **82**, 909 (1997).
5. A. J. Kenyon, P. F. Trwoga, M. Federighi, and C. W. Pitt, *J. Phys.: Condens. Matter* **6**, L319 (1994).
6. M. Fujii, M. Yoshida, S. Hayashi, and K. Yamamoto, *J. Appl. Phys.* **84**, 4525 (1998).

7. D. Kovalev, E. Gross, N. Künzner, F. Koch, V. Y. Timoshenko, M. Fujii, *Phys. Rev. Lett.* **89**, 137401 (2002).
8. B. Goller, S. Polisski, and D. Kovalev, *Phys. Rev. B* **75**, 073403 (2007).
9. Nicholas. J. Turro, *Modaern Molecular Photochemistry*, University Science Books, Sausalito, CA (1991).
10. I. L. Medintz, A. R. Clapp, H. Mattoussi, E. R. Goldman, B.Fisher, and J. M. Mauro, *Nat. Mater.* **2**, 630 (2003).
11. S. A. Crooker, J. A. Hollingsworth, S. Tretiak, and V. I. Klimov, *Phys. Rev. Lett.* **89**, 186802 (2002).
12. V. A. Karavanskii, A. A. Chistyakov, G. E. Kotokovskii, M. B. Kuznetsov, and K. V. Zakharchenko, *Phys. Stat. Sol. (a)* **197**, 403 (2003).
13. S. Limaye, S. Subramanian, B. Goller, J. Diener, and D. Kovalev, *Phys. Stat. Sol. (a)* **204**, 1597 (2007).
14. T. Nakamura, T. Ogawa, and S. Adachi, in preparation.
15. J. Tellinghuisen, *J. Che. Phys.* **58**, 2821 (1973).
16. M. Fujii, D. Kovalev, B. Goller, S. Minobe, S. Hayashi, V. Y. Timoshenko, *Phys. Rev. B* **72**, 165321 (2005).
17. J. R. Lakowicz, *Principles of Fluorescence Spectroscopy*, Springer, New York, NY (2006).
18. Y. Elkana, J. Feitelson, and E. Katchalski, *J. Chem. Phys.* **48**, 2399 (1968).
19. T. Nakamura, T. Kubota, T. Ogawa, S. Adachi, and M. Fujii. submitted.
20. S. Miura, T. Nakamura, M. Fujii, M. Inui and S. Hayashi, *Phs. Rev. B* **73**, 245333 (2006).
21. W. L. Wilson, P. F. Szajowski, and L. E. Brus, *Science* **262**, 1242 (1994).

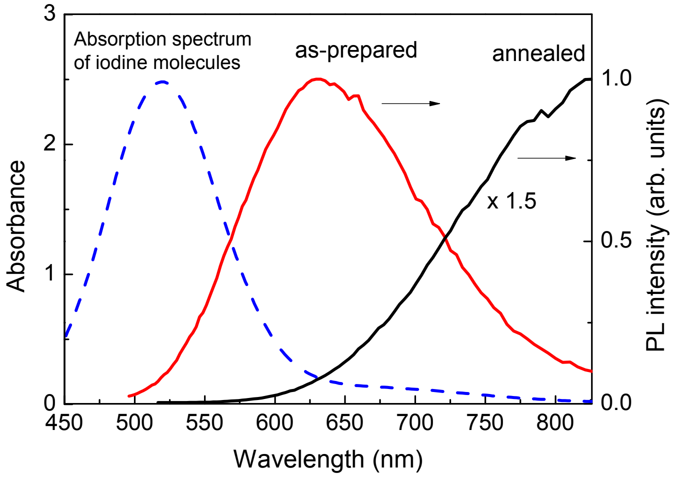

Figure 1. PL spectra of porous Si powder for as-prepared and annealed samples dispersed in a solution (right axis). Absorption spectrum of iodine molecules in a solution is also shown (left axis).

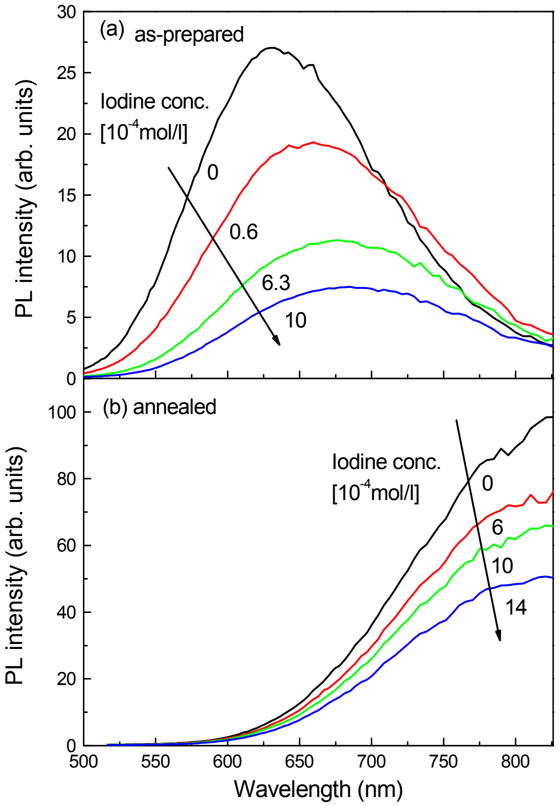

Figure 2. PL spectra of porous Si powder for (a) as-prepared and (b) annealed samples for various iodine concentrations.

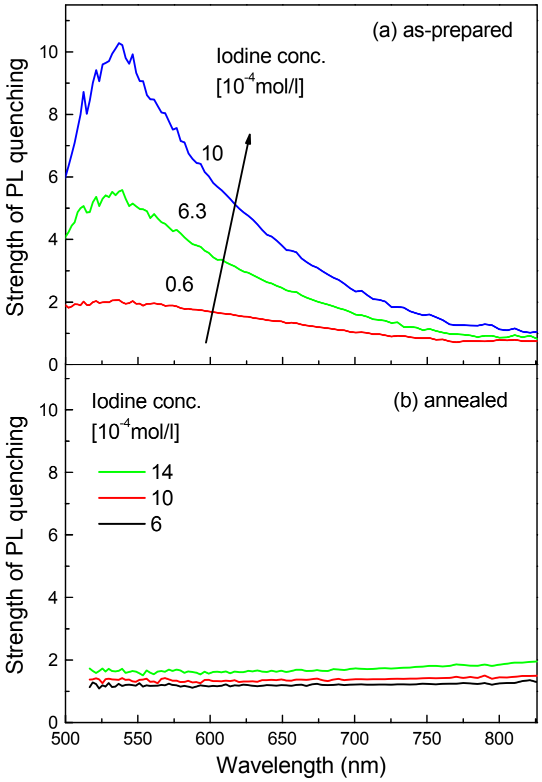

Figure 3. Strength of PL quenching for (a) as-prepared and (b) annealed samples at various iodine concentrations as a function of emission wavelength.

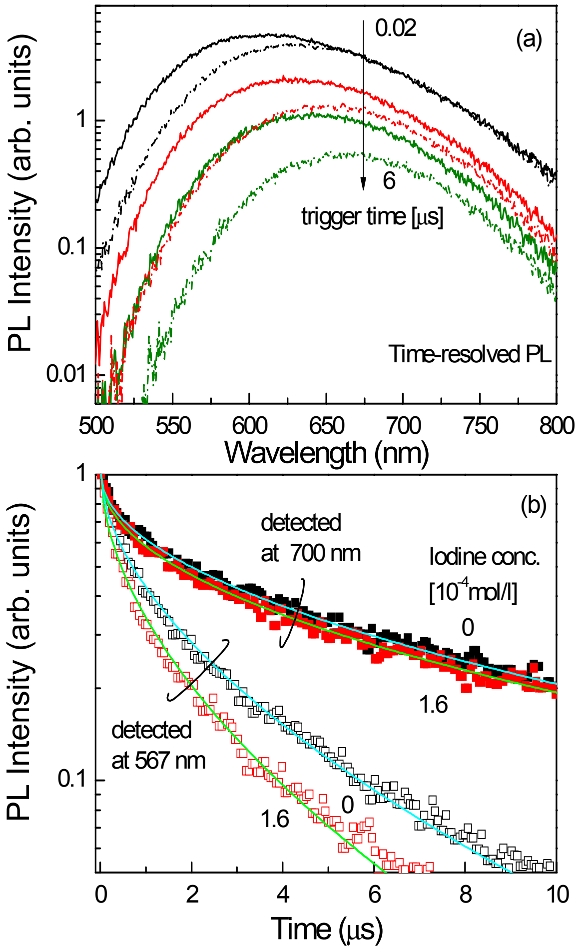

Figure 4. (a) Time-resolved PL spectra of a porous Si powder dispersed in a solution with iodine molecules (solid lines) and without iodine molecules (dashed lines). The measurement gate time is 60 ns. The data for the measurement with respect to the excitation pulse of 0.08, 2, 6µs are shown. (b) PL decay curves detected at 567 nm (open symbols) and at 700 nm (closed symbols). The concentration of iodine solutions is1.6 × 10^{-4} mol/l.

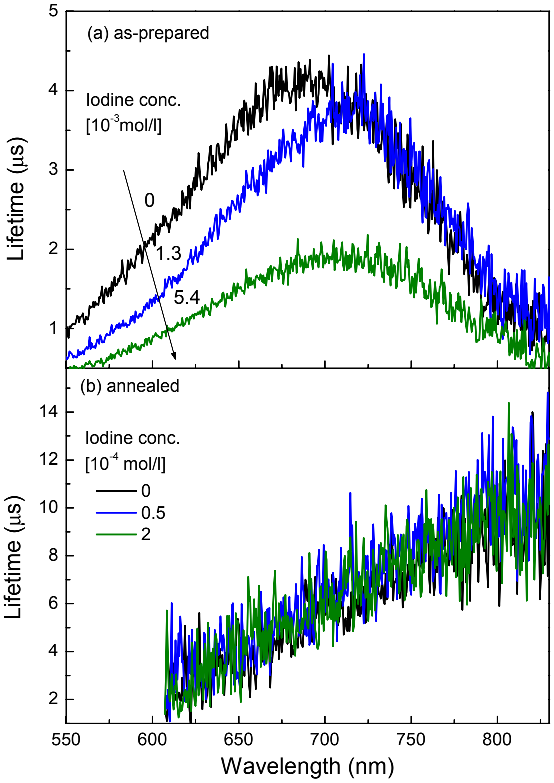

Figure 5. PL lifetime of porous Si for (a) as prepared and (b) annealed sample at various iodine concentrations as a function of emission wavelength.

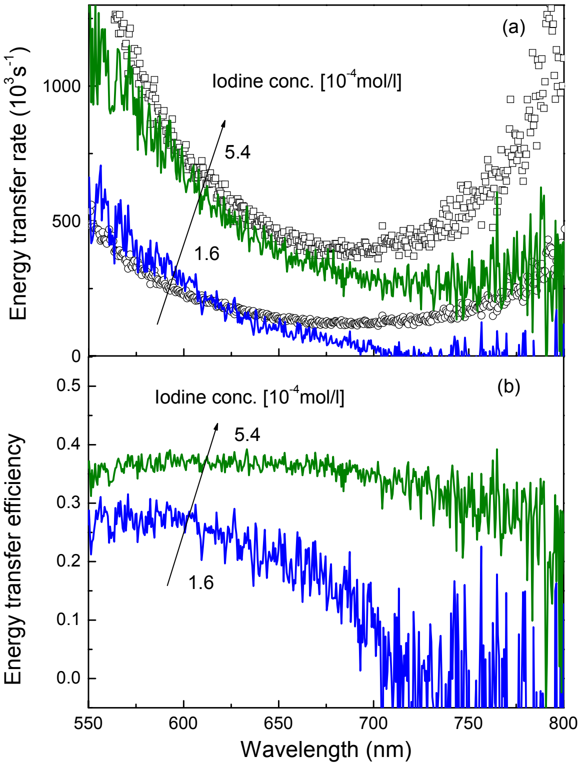

Figure 6. (a) Energy transfer rate and (b) energy transfer efficiency for as prepared sample at 1.6×10^{-4} and 5.4×10^{-4} mol/l as a function of emission wavelength.

ECS Transactions, 16 (3) 277-283 (2008)
10.1149/1.2982566 ©The Electrochemical Society

Macropore Formation in p-type Silicon and Si/SiGe/Si/SiGe/p-type Silicon

J. H. Kim[a], H. S. Seo[b], K. P. Kim[a], H. K. Lyu[a], S. H. Woo[a], and J. H. Lee[b]

[a] Division of Nano & BioTechnology, Daegu Gyeongbuk Institute of Science & Technology, Daegu, 704-230, Korea
[b] Department of Materials and Chemical Engineering, Hanyang University, Ansan, Kyounggi 426-791, Korea

Random and ordered macropore formation in p-type silicon substrate (10 ~ 20 Ω·cm) by electrochemical anodization in various HF-containing electrolytes was investigated under different operating conditions. The effect of electrolyte composition controlling the macropore formation both for random and periodically arranged pores is reported. The role played by etch pit for ordered macropore formation was investigated. The results revealed that the nature of constituents of solution plays very important roles in determining pore formation and morphology and the stable ordered macropore growth is not possible without etch pit. By using Si/SiGe/Si/SiGe/p-type silicon structure, ordered pillar structures were fabricated without etch pit formation process. The possible role of two sets of Si/SiGe layer for pillar formation is proposed.

Introduction

Electrochemical etching of silicon in hydrofluoric acid is a widely established technique for producing porous silicon (1). It is also emerging as an alternative technique for micromaching due to its low cost, fast etching process, and its compatibility with standard microelectronic processes. Especially, the macropores of very high aspect ratio-up to 250 μm with smooth surfaces can be obtained compared with deep reactive ion etching (DRIP or ICP) where surfaces are damaged and wavy. Macropore formation on n-type silicon is well documented and understood in terms of the space charge region effect, which results in a collection of the charge carriers at the tip of the macropores (2). The various three-dimensional microstructures have been produced mainly in n-type silicon, based on well established electrochemical etching mechanism of n-type silicon (3,4). However, a few experimental groups have produced experimental data on the macropore formation in p-type silicon. The interpretation of the current results is possible not using a unified theory but a number of theoretical models (5-9).

To get a deeper understanding of the electrochemical processes taking place during the macropore formation in p-type silicon materials, more reliable experimental data are required about random and ordered macropore formation.

Many organic solvents have been usually mixed with HF during the macropore formation in p-type silicon. Of these, DMSO (dimethylsulfoxide), DMF (dimethylformamide) are the most frequently investigated and of similar chemical characteristics. Further, isopropanol and EtOH except for DMF have different physicochemical properties and hence, different effects during pore formation are expected. The other challenge especially for ordered macropore formation is using other layers at the top of p-type Si, in which very interesting experimental results are also expected to take place.

In this paper, their effect on both random and ordered macropore formation of p-type silicon, changing the current density in the various content of the organic component (DMF) in HF etching solution. The effect of etch pits on the ordered macropore formation are also investigated in DMF:HF solutions. For random macropore formation, data for DMF:HF etching were compared with them for HF:EtOH:H_2O. The ordered macropore formation phenomena are also studied in two different HF etching solutions; DMF:HF based and HF:H_2O:$(CH_3)_2CHOH$ based. Finally, the results are presented when electrochemical etching of two set of Si/SiGe layers on p-type silicon are performed.

Experimental

An array of macropores was prepared in p-type Si(100) wafers with a resistivity of 10 ~ 20 Ω·cm (a boron doping density of ~ 10^{15} cm^{-3}) by anodic oxidation. In order to make periodically arranged pores with high aspect ratio, the wafer surface must be structured prior to the etching. This is usually done by a standard photolithography followed by an alkaline etching to form pyramidal notches that act as nuclei for the pore growth.

For the preparation of mixed solutions, 49% HF acid was used. Various ratio of DMF:HF electrolyte are used for random and periodically arranged pore formation. HF:EtOH:H_2O (15:600:200) and HF:H_2O:$(CH_3)_2CHOH$ (5:9:26) are also used for random and ordered macropore formation, respectively.

Scanning electron microscopy (SEM) has been used to analyze the plain and cross-sectional morphologies of macropores.

Results and Discussion

Random macropore formation

Several experimental dependencies have been investigated in this part of the work. First, a dependency of the macropore morphology on the ratio of HF and DMF together with current density has been revealed. The observed structures of all samples under various conditions (3 ~ 30 mA/cm^2 and DMF:HF = 7:1, 10:1) were nanowires instead of macropores. Figure 1 shows the SEM image of specimen after electrochemical etching at 7.5 mA/cm^2 in DMF:HF (10:1) electrolyte. The diameter of nanowires decreases and their length increases with increasing current density at each composition of electrolyte, resulting in high aspect ratio. The nanowires in DMF:HF (7:1) has higher aspect ratio than them in DMF:HF (10:1) as shown in Table 1.

Second, The electrolyte are changed to HF:EtOH:H_2O (15: 600:200). Morphological features are shown in Fig. 2. Macropores were not formed in the investigated current range (3 ~ 20 mA/cm^2).

The observation does not contradict with the results of p-type silicon in F. A. Harraz et al (10). This means that the porous silicon is still formed and no passivation is detected under this condition in this ethanol-based solution. The possible cause for the dissolution observed in solution with this low HF content is the high oxygen amount in the sample surfaces and modification of hydrogen termination (11). SiO_xF_y is the dissolved form of silicon in HF solution. The SiO_xF_y surface is less stable due to larger amount of weaker

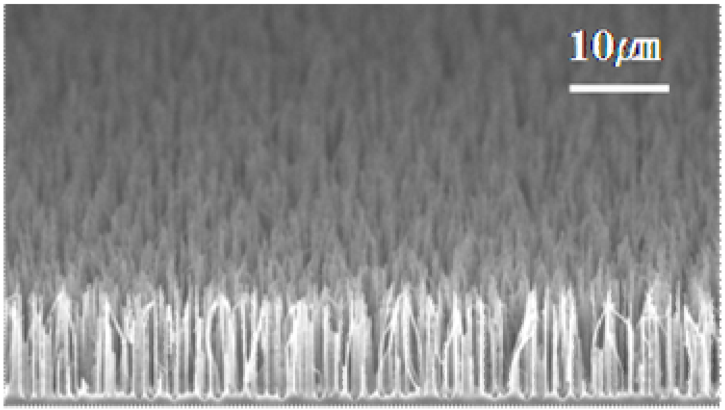

Figure 1. SEM images of nanowires formed by an electrochemical etching at at 7.5 mA/cm^2 in DMF:HF(10:1) electrolyte.

TABLE I. The summary of nanowires formation in DMF:HF solutions.

	DMF:HF = 10:1			**DMF:HF = 7:1**	
	3 mA/cm^2	25 mA/cm^2	30 mA/cm^2	20 mA/cm^2	25 mA/cm^2
Diameter (nm)	300	250	200	200	150
Height (μm)	6	12	22	18	24
Aspect ratio	20	48	110	90	160

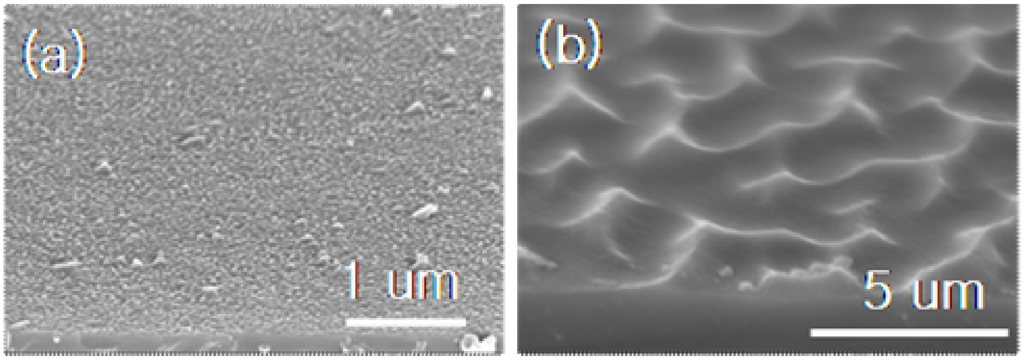

Figure 2. SEM view of sample after anodization in HF:EtOH:H_2O (15: 600:200) at (a) 3 and (b) 20 mA/cm^2) for 20 min.

bonds when it contains more oxygen. Oxygen can bond to two silicon atoms, while fluorine can bond only to one. Fluorine atoms are removed when the silicon atom to which they are attached is dissolved. On the other hand, an oxygen atom in a back-bond position may remain at the surface when one of its two neighbor silicon atoms is dissolved. Therefore, the remaining silicon bonded to the oxygen atom can be a favorable target for attack by HF, resulting in homogeneous dissolution of silicon. The high content of oxygen on the surface also causes a decrease of hydrogen terminations. Modification of terminations could reduce passivation properties of the hydrogen terminations and also

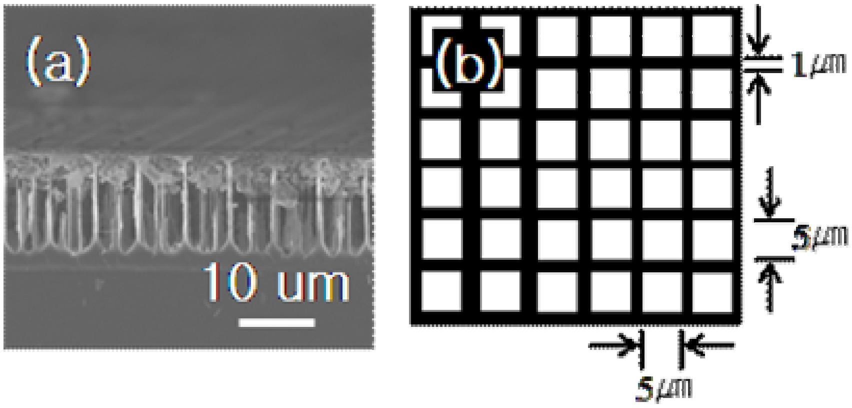

Figure 3. (a) Cross-sectional SEM image of p-Si processed in DMF:HF(7:1) at 10 mA/cm^2 for 30 min, (b) used mask pattern for macropore formation.

explains higher dissolution rate.

Ordered macropore formation

The two kinds of experiments of ordered macropores growth have been conducted to know the effect of etch pits on the macropore formation. One has just open square areas that are not covered with SiN_x by photolithography and etch pits of exact inverse pyramid type are not made. The other has well defined etch pits.

We have first investigated macropore formation in the current range from 2 to 15 mA/cm^2 for solutions (DMF:HF = 5:1, 7:1, 10:1) when the etch pits of inverse pyramid type by KOH is not defined. Figure 3 (a) shows a general representative morphology among all the samples observed. The patterned macropores are not empty but filled with several other pores and this kind of morphological trends are the same for all the other investigated specimens.

Second, exact inverted pyramids are created and then electrochemical etching has been conducted in the electrolyte (DMF:HF = 10:1). The image taken from DMF:HF (10:1) etching is shown in Fig. 4. Contrary to the experimental results done without etch pits, macropores with very rough interface of walls are formed. This type of porous silicon is morphologically analyzed as macropores having branches shorter than diameter according to Ref.12.

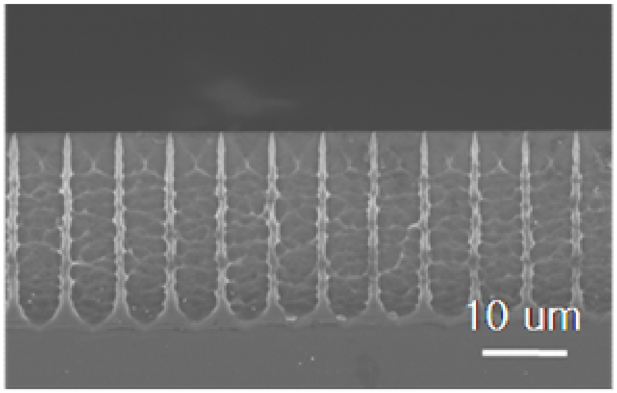

Figure 4. Cross-sectional SEM image of p-Si processed in DMF:HF (10:1) at 3 mA/cm^2 for 120 min.

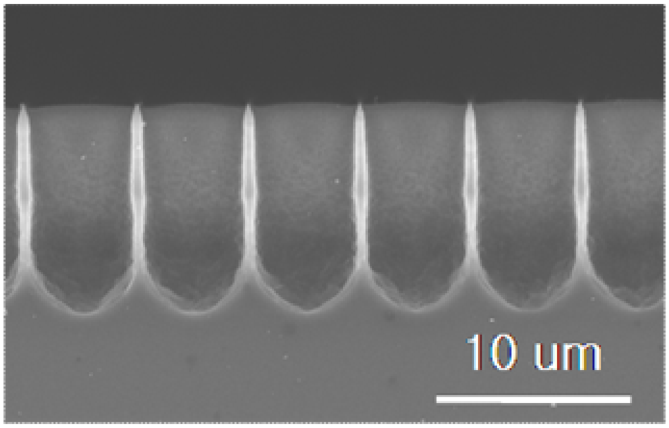

Figure 5. Cross-sectional SEM image of p-Si processed in HF:H_2O:$(CH_3)_2CHOH$ (5:9:26) at 1.75 mA/cm^2 for 120 min.

Based on the above results, it is confirmed that etch pits are indispensible to uniform shapes of macropore formation. Its main cause may be explained by the concentration of holes at the tip of etch pits. The pits favor macropore formation as the collection of the holes is enhanced at the tip of the pits, inducing active dissolution of silicon in the vertical direction of silicon substrate.

Finally we have performed anodization in HF:H_2O:$(CH_3)_2CHOH$ (5:9:26) solution (13) to investigate solution effect on macropore formation.

Cross-sectional view of SEM image after the galvanostatic treatment of the sample in a HF:H_2O:$(CH_3)_2CHOH$ (5:9:26) is shown in Fig. 5. The lattice constant of etch pits is 5 μm and the interval between orthogonally aligned etch pits is 1 μm. The macropores have 10 μm in depth with current density J = 1.75 mA/cm^2 for 2 hours. The etching rate of 5 μm/hr are very slow compared with 20 ~ 25 μm/hr in Ref. 14.

The slow pore formation rate may result from lower current density than that in Ref. 14 (J = 13 mA/cm^2) in the current range of porous silicon formation. The observed walls of macropores are thick at the center and gets thinner near top and bottom, different from maintaining constant thickness of walls except for tapering only near the surface of macropores as was observed in the results of Kobayashi et al (14).

The distinct difference in morphologies between HF:H_2O:$(CH_3)_2CHOH$ (5:9:26) and DMF:HF (10:1) based electrolyte can be understood by the chemical role played by the organic solvent in the dissolution reaction at the silicon/electrolyte interface. DMF is very good solvents for positive ions, which is called protophilic property (15), as compared to $(CH_3)_2CHOH$. The dissociation constant of HF may be increased, leading to dissolution of silicon. The another effect of DMF is less solvation of the anions(F-, HF_2^-) and much more reactive due to its aprotic characteristics (16).

Electrochemical etching of Si/SiGe/Si/SiGe/p-type silicon

Two sets of Si/SiGe layers on p-type silicon substrate have been deposited. The thickness of each layer is 100 nm. In this case, etch pits were not defined and just open areas of square pattern which is not deposited by SiN_x were formed for electrochemical etching. The type of mask is identical with that of Fig. 3 (b). The very interesting phenomena are the formation of the pillar-like structures as shown in Fig. 6. The pore

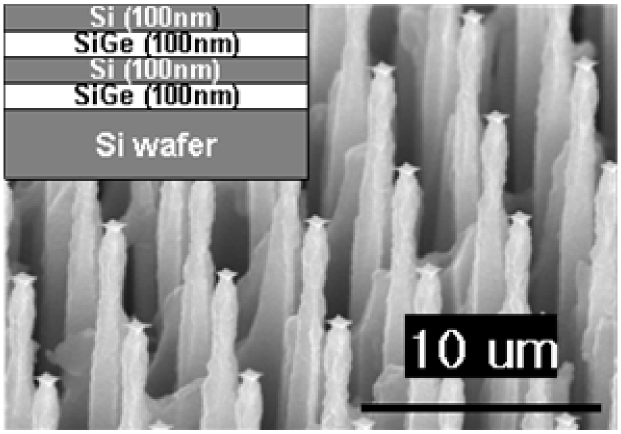

Figure 6. SEM images of ordered pillar structure prepared in two sets of Si/SiGe layers on p-type silicon substrate by anodization in HF:H_2O:$(CH_3)_2CHOH$ (5:9:26) at 0.75 mA/cm^2 for 120 min. The inset shows the schematic of used wafer.

walls are dissolved by the anodization and only the wall cross points are left. Each pillar has very thin plate of concaved square type. It needs further analysis such as TEM to confirm that that the top Si/SiGe/Si/SiGe layers on p-type silicon still remain. Vyatkin et al. observed that germanium redistribution occurs across an epitaxial layer during a porous layer formation in the silicon-germanium epitaxial structure (17). Because a solid-state reaction cannot occur in room temperature electrochemical etching process, it can be predicted that germanium atom dissolves in liquid electrolyte and transport to pore walls by diffusion or mass transport, and finally deposited at pore walls, inducing acceleration of pore wall dissolution by a kind of electrochemical reaction.

Conclusion

Nanowires have been fabricated by electrochemical etching on un-patterned p-type silicon in DMF:HF (7:1, 10:1) solutions. While neither macropores and nanowires are not observed in HF:EtOH:H_2O (15: 600:200) electrolytes. The etch pit definition for ordered macropore formation is shown to be decisive factor for ordered macropore formation. The reactive nature of DMF organic solvent results in very rough interface of pore walls compared with non-DMF containing HF:H_2O:$(CH_3)_2CHOH$ (5:9:26) solution. The new method for pillar formation is illustrated using Si/SiGe/Si/SiGe/p-type silicon without etch pit formation steps in photolithography process.

Acknowledgments

This work was supported by Korea Ministry of Education, Science and Technology (MEST) basic research fund

References

1. H. Föll. M. Christophersen, J. Carstensen, G. Hasse, *Mater. Scien. Eng.*, **R 39**, 93, (2002).
2. P. C. Searson, J. M. Macaulay, and F. M. Ross, *J. Appl. Phys.*, **72**, 253 (1992).
3. K. J. Chao, S. C. Kao, D. M. Yang, M. S. Hseu, and T. G. Tsai, *Electrochem,*

Solid-State Mater, Adv. Technol., **69**, 1 (2000).

4. G. Barillaro, P. Bruschi, A. Diligenti, and A. Nannini, *Phys. Stat. Solidi. (c)* **2**, 3198 (2005).
5. V. Lehmann and S. Rönnebeck, *J. Electrochem. Soc*., **146**, 2968 (1999).
6. E. A. Ponomarez and C. Lévy-Clément, *Electrochem. Solid-State Lett*., **1**, 42 (1998)
7. R. B. Wehrspohn, J.-N. Chazalviel, and F. Ozanam, *J. Electrochem. Soc*., **145**, 2958 (1998).
8. J. Carstensen, M. Christophersen, and H. Föll, *Mater. Sci. Eng., B*, **69**, 23 (2000).
9. E. S. Kooij and D. Vanmaekelbergh, *J. Electrochem. Soc*., **144**, 1296 (1997)
10. F. A. Harraz, K. Kamada, K. Kobayashi, T. Sakka, and Y. H. Ogata, *J. Electrochem. Soc*., **152**, C213 (2005).
11. D. Hamm, J. Sasano, T. Sakka, and Y. H. Ogata, *J. Electrochem. Soc*., **149**, C331 (2002).
12. X. G. Zhang, *J. Electrochem. Soc*., **151**, C69 (2004).
13. A. Vyatkin, V. Starkov, V. Tzeitlin, H. Presting, J. Konle, and U. König, *J. Electrochem. Soc*., **149**, G70 (2002).
14. K. Kobayashi, F. A. Harraz, S. Izuo, T. Sakka, and Y. H. Ogata, *J. Electrochem. Soc*., **153**, C218 (2006).
15. J. F. Tyler, G. N. Patey, *J. Chem. Phys*., **110 (22)**, 10937 (1999).
16. J._N. Chazalviel, R. B. Wehrspohn, and F. Ozanam, *Mater. Sci. Eng., B*, **69-70**, 1 (2000).
17. A. F.Vyatkin, J. Linnros, N. Lalic, and M. Rosler, *Phys. Low-Dimens. Semicond. Struct*., **5/6**, 89 (1997).

ECS Transactions, 16 (3) 285-289 (2008)
10.1149/1.2982567 ©The Electrochemical Society

High Catalytic Activity of Palladium for Metal-Enhanced Hydrofluoric Acid Etching of Silicon

S. Yae, M. Tashiro, T. Hirano, M. Abe, N. Fukumuro, and H. Matsuda

Department of Materials Science and Chemistry, Graduate School of Engineering,
University of Hyogo, Himeji, Hyogo 671-2280, Japan

Metal-enhanced HF etching of Si is an electroless method to produce porous Si. Such etching generally uses not only metal-modified Si but also an oxidizing agent, such as hydrogen peroxide. Pd exhibits high activity for enhancing the HF etching of Si without an oxidizing agent, even under dissolved oxygen free and dark conditions. Electrolessly deposited Pd particles on n-Si enhance the HF etching of Si, but produce no porous layer. Patterned Pd films localize the etching under and the boundary of the Pd deposited areas, and thus Pd can produce a micro-etch pattern on Si with simple immersion in the HF solution. This etching reaction is explained by electron injection into the conduction band of Si due to Pd-enhanced anodic oxidization of Si with water.

Introduction

Porous silicon (Si) is usually prepared by electrochemical etching under anodic bias in a fluoride-containing solution (1,2). Metal-enhanced hydrofluoric acid (HF) etching of Si has attracted considerable attention as a new electroless method that can produce porous Si by immersing metal-modified Si in an HF solution without bias (3-14). Such etching generally uses not only metal-modified Si but also an oxidizing agent, such as hydrogen peroxide (4,9,11-13), peroxodisulfate (7), permanganate (7), or metal ions (6). We reported the preparation process (5,8,10,14) and solar cell application (5,8,15) of porous Si using metal-particle-enhanced HF etching of Si without a particular oxidizing agent. This etching generally proceeds by local galvanic cell mechanism requiring photoillumination or dissolved oxygen. Recently, we found that palladium (Pd) exhibits high activity for enhancing etching under dissolved oxygen free and dark conditions (14,16). In this paper, we describe the unique behavior of Pd on the HF etching of Si and micro-pattern formation.

Experimental

Single-crystalline n-type Si wafers (Yamanaka Semiconductor, (100), ca. 1 Ω cm) were washed with acetone and etched with CP-4A (a mixture of HF, nitric acid, acetic acid, and water) and a 7.3 M (M = mol dm^{-3}) HF solution. Metal particles were deposited on Si wafers by electroless displacement deposition from a 1 mM metal-salt solution containing 0.15 M HF (17). Pd thin films were deposited onto n-Si wafers by the electron-beam evaporation method. The thickness of the deposited films was measured using a quartz crystal microbalance (ULVAC, CRTM-5000) adjusted by gravimetry. The Pd films were patterned by attaching a mask (85-μm square holes and 40-μm space) to the n-Si wafers during deposition. The metal deposited n-Si wafers were immersed in a 7.3 M HF aqueous solution under dark conditions. The etching time was 24 h unless otherwise specified. Argon gas (>99.9999% purity) bubbling was applied to the HF solution before and during etching to remove the dissolved oxygen from the solution. The average etch rate of Si was measured using a gravimetric procedure with an analytical balance (Mettler Toledo XS105DU). Surface and cross-sectional inspections of the Si wafers were performed with a scanning electron microscope (SEM, Hitachi, S-900) and a tapping-mode atomic force microscope (TM-AFM, Digital Instruments Nanoscope IIIa).

Results and Discussion

Pd-Particle-Enhanced HF Etching of Si

Figure 1 shows typical SEM images of Pd- and Pt-particle-deposited n-Si after immersion in an oxygen-containing HF solution. With the Pd particles, the n-Si was polish etched at a rate of 4.5 μm/h to accompany hydrogen evolution. With the Pt particles, pores, whose diameters resembled the Pt particles, were formed on the n-Si. The Pt particles were present on the bottoms of the pores. The Ag and Au particles produced micro pores with diameters corresponding to particle sizes much smaller than the Pt particles (17). Under the oxygen free and dark conditions, Pd particles yielded an etch rate of 0.05-0.9 μm/h, and Pt, Ag, and Au yielded etch rates lower than 0.01 μm/h (14).

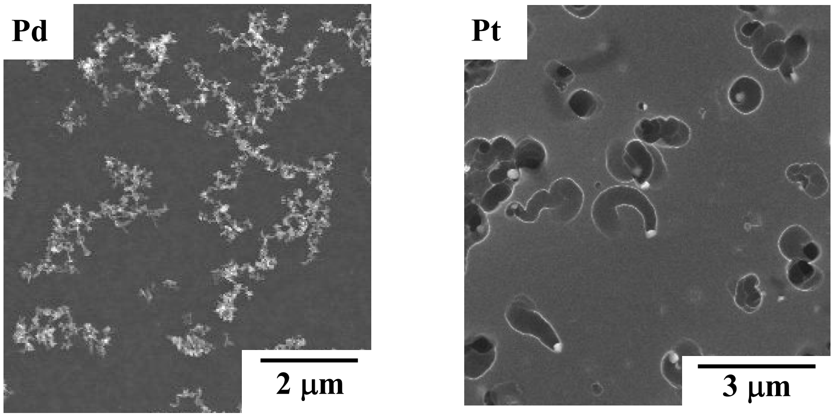

Figure 1. SEM images of Pd- and Pt-particle-deposited n-Si wafers after immersion in oxygen containing HF solution.

The mechanism of metal-particle-enhanced HF etching of Si under the presence of dissolved oxygen in the HF solution is explained by the hole injection to the Si valence band with cathodic reduction of oxygen on the metal particles (8,10,14). Only Pd strongly promotes the etching of Si under dark conditions and the absence of dissolved oxygen. Since the potential of proton reduction exists between the conduction band and the valence band edges of n-Si, this etching mechanism is explained by electron injection into the conduction band of Si due to two possible anodic reactions: the oxidization or the dissolution of Si (14). The anodic oxidation of Si proceeds with water and produces silicon oxide that is chemically etched to SiF_6^{2-} with HF. The anodic dissolution of Si proceeds with fluoride species such as HF_2^- and F^- and directly changes Si to SiF_6^{2-} (1). Table I summarizes the change of the contact angle of pure water on the n-Si by immersion in a 1 M $HClO_4$ aqueous solution under oxygen free and dark conditions for 1 h. The contact angle of the water on the Pd-particle-deposited n-Si was decreased to below 20° by immersion. The contact angle of the water on the bare and Pt-particle-deposited n-Si was higher than 50° after immersion. The lowering of the contact angle indicates the production of hydrophilic silicon oxide on the n-Si. These results show that the Pd particles catalyze the oxidation of Si with water under such conditions. Thus, the local anode reaction of the Pd-particle-enhanced HF etching of Si, i.e., the process of electron injection into the conduction band of Si, is the oxidation of Si with water. The etching is expressed with the following equations:

$$\text{Local anode} \qquad Si + 2H_2O \longrightarrow SiO_2 + 4H^+ + 4e^- \qquad [1]$$

$$\text{Chemical dissolution} \qquad SiO_2 + 6HF \longrightarrow SiF_6^{2-} + 2H_2O + 2H^+ \qquad [2]$$

$$\text{Local cathode} \qquad 2H^+ + 2e^- \longrightarrow H_2 \qquad [3].$$

TABLE I. Contact angle of pure water on n-Si wafers before and after immersion in 1 M $HClO_4$ aqueous solution under oxygen free and dark conditions for 1 h. Average values and standard deviation are indicated.

Modification of n-Si	**Contact angle/°**	
	Before immersion	**After immersion**
Bare	79 ± 2.1	72 ± 1.3
Pt-particle-deposited	60 ± 5.8	54 ± 6.3
Pd-particle-deposited	46 ± 4.0	16 ± 5.2

Pattern Etching of Si using Pd Thin Film

Figure 2 shows an SEM image of Pd-film (29-nm thick)-deposited n-Si after HF immersion under the oxygen free and dark conditions. The etching formed square holes, which are consistent with the pattern of the Pd film, and indicate that Pd can produce micro-etch patterns on Si with simple immersion in the HF solution.

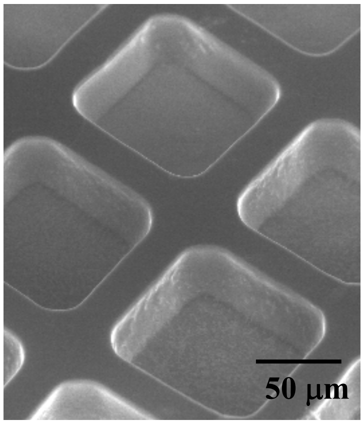

Figure 2. SEM image of Pd-film (29-nm thick)-deposited n-Si wafer after immersion in HF solution under oxygen free and dark conditions. Sample was inspected at a 40° tilt.

The size of the holes is ca. 100 μm, which is larger than the Pd-pattern of 85 μm. The etch rate is determined at 1.4 μm/h with a hole depth of ca. 35 μm. The etching pattern of Si is changed with the pattern size and the thickness of the Pd films. Figure 3a shows an SEM of 4-nm-thick Pd film deposited n-Si after etching. The almost same etching pattern as the 29-nm case (Fig. 2) was produced. A 58-nm-thick Pd film (Fig. 3b), twice as thick as Fig. 2, produced a much shallower etching pattern, whose center kept almost the same height of the non-etched area of the Si surface. Figure 4 shows SEM and TM-AFM images of Pd-film (29-nm thick)-deposited n-Si after etching for 5 min. At the early stage of etching, the dissolution area of Si was localized at the boundary between the Pd-film-deposited and non-Pd-deposited areas of the Si surface. These results are consistent with our previously reported results about another size of a Pd pattern and indicate that etching proceeds where Si, Pd, and the HF solution have contact with each other (16). To confirm this contact requirement for etching, we formed a double layer pattern of Pt and Pd on n-Si, such as Pt/Pd/n-Si and Pd/Pt/n-Si. Only the Pt/Pd/n-Si sample was etched by immersion in the HF solution under the same conditions as Fig. 2, indicating that direct contact between Pd and Si is necessary for etching and the local cathode reaction of the hydrogen evolution on Pd does not dominate the etching. These results support the previously proposed etching mechanism expressed by Eqs. [1], [2], and [3].

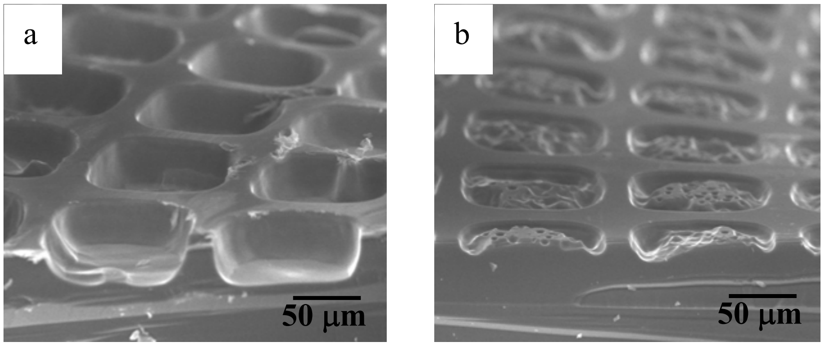

Figure 3. SEM images of Pd-film-deposited n-Si wafers, whose Pd-film thicknesses were 4 (a) and 58 nm (b), after immersion in the HF solution under oxygen free and dark conditions. Cleaved samples were inspected at a 70˚ tilt.

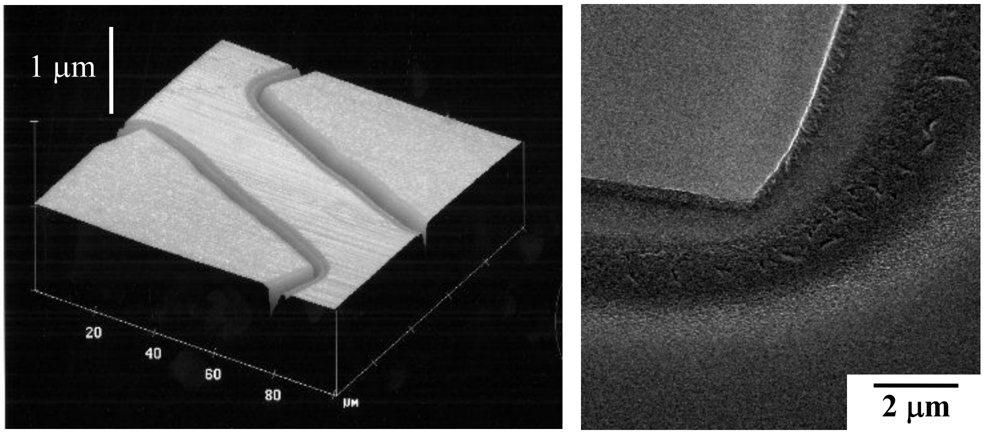

Figure 4. TM-AFM (left) and SEM (right) images of Pd-film (29-nm thick)-deposited n-Si after immersion in HF solution under oxygen free and dark conditions for 5 min. Scan size of TM-AFM is 100 μm. For SEM inspection, sample was at 40˚ tilt.

The following results, which remain unexplained, were obtained in this study: the Pd-particle-deposited Si was polish etched and the holes produced by etching with the Pd-film-pattern were larger than the size of the Pd-film-pattern; that is, the etched area extended toward the non-Pd-deposited area of Si. We obtained preliminary results where Pd was detected on a bare-like Si surface between Pd particles after electroless deposition by scanning Auger electron microscopy, and Pd particles were observed on the non-Pd-deposited area of the pattern etched Si surface by SEM and energy dispersive X-ray spectroscopic analysis. The spread of Pd on the Si surface should be correlated to the polish etching and the extension of the etching area of Si.

Acknowledgments

The present work was partly supported by CREST and Research for Promoting Technological Seeds from JST, and Grants-in-Aid for Education and Research from Hyogo Prefecture and for Scientific Research (C) (17560638 and 20560676) from JSPS.

References

1. V. Lehmann, *Electrochemistry of Silicon*, Wiley-VCH, Weinheim (2002).
2. C. Lévy-Clément, in *Encyclopedia of Electrochemistry 6*, S. Licht, Vol. Editor, A. J. Bard and M. Stratmann, Series Editors, p. 185, Wiley-VCH, Weinheim (2002).
3. K. W. Kolasinski, *Current Opinion in Solid State & Materials Science*, **9**, 73 (2005).
4. X. Li and P. W. Bohn, *Appl. Phys. Lett.*, **77**, 2572 (2000).
5. S. Yae, Y. Kawamoto, H. Tanaka, N. Fukumuro, and H. Matsuda, *Electrochem. Comm.*, **5**, 632 (2003).
6. K. Peng, Y. Yan, S. Gao, and J. Zhu, *Adv. Funct. Mater.*, **13**, 127 (2003).
7. T. Hadjersi, N. Gabouze, E. S. Kooij, A. Zinine, A. Ababou, W. Chergui, H. Cheraga, S. Belhousse, and A. Djeghri, *Thin Solid Films*, **459**, 271 (2004).
8. S. Yae, H. Tanaka, T. Kobayashi, N. Fukumuro, and H. Matsuda, *Phys. Stat. Sol. (c)*, **2**, 3476 (2005).
9. K. Tsujino and M. Matsumura, *Electrochem. Solid-State Lett.*, **8**, C193 (2005).
10. S. Yae, T. Kobayashi, T. Kawagishi, N. Fukumuro, and H. Matsuda, in *Pits and Pores III: Formation, Properties and Significance for Advanced Materials*, P. Schmuki, D. J. Lockwood, Y. H. Ogata, M. Seo, and H. S. Isaacs, Editors, PV2004-19, p. 141, The Electrochemical Society Proceedings Series, Pennington, NJ (2006).
11. H. Asoh, F. Arai, and S. Ono, *Electrochem. Comm.*, **9**, 535 (2007).
12. K. Tsujino and M. Matsumura, *Electrochim. Acta*, **53**, 28 (2007).
13. C. Chartier, S. Bastide, and C. Lévy-Clément, *Electrochim. Acta*, **53**, 5509 (2008).
14. S. Yae, M. Abe, T. Kawagishi, K. Suzuki, N. Fukumuro, and H. Matsuda, *Trans. Mater. Res. Soc. Jpn.*, **32**, 445 (2007).
15. S. Yae, T. Kobayashi, T. Kawagishi, N. Fukumuro, and H. Matsuda, *Solar Energy*, **80**, 701 (2006).
16. S. Yae, M. Abe, N. Fukumuro, and H. Matsuda, *Electrochemistry,* **72**, 144 (2008).
17. S. Yae, N. Nasu, K. Matsumoto, T. Hagihara, N. Fukumuro, and H. Matsuda, *Electrochim. Acta*, **53**, 35 (2007).

ECS Transactions, 16 (3) 291-297 (2008)
10.1149/1.2982568 ©The Electrochemical Society

Macropore Formation in Prepatterned p-type Silicon

J. H. Kim[a], K. P. Kim[a], H. S. Seo[b], H. K. Lyu[a], S. H. Woo[a], and J. H. Lee[b]

[a] Division of Nano & BioTechnology, Daegu Gyeongbuk Institute of Science & Technology, Daegu, 704-230, Korea
[b] Department of Materials and Chemical Engineering, Hanyang University, Ansan, Kyounggi 426-791, Korea

The formation of ordered macropores in a prepatterned p-type silicon wafer by electrochemical anodization in HF:H_2O:DMSO (dimethyl sulfoxide) and HF:DMSO solutions was investigated. The pore wall thickness in the solutions was found to be reduced with increasing current density. The pore growth rate was compared using two kinds of etch pit; one is for 2 μm lattice spacing, the other is for 5 μm. The growth rate of the macropores for 2 μm size revealed a saturation behavior, while that of 5 μm corresponded to a linear increase in the same range of current density. The big difference in morphologies of macropores between HF:H_2O:DMSO and HF:DMSO solutions was accounted for based on the chemical nature of DMSO

Introduction

Various types of porous structures can be easily formed in Si wafers by electrochemical etching process. Porous silicon formed in silicon is generally classified into three categories according to pore sizes: microporous structures with pores below 2 nm in size, mesoporous structures with ones of 2−50 nm, and macroporous structures with pores greater than 50 nm. Among them, macropores have been a subject of great attention for both theory and practice because new areas of macropore silicon applications have been developed from micromachining (1), membrane techniques (2), solar cells (3), sensors (4), photonic crystals (5). Especially, micromachining application of macropore silicon has superior merits such as low cost, fast rate of etching, and excellent compatibility to the standard microelectronic processes.

High-aspect-ratio (HAR) structures have easily been developed by forming deep macropores or trenches in an n-type silicon substrate as described by Lehmann (6). However, such a deep macropore formation in p-type silicon is more difficult than in n-type silicon because there are some ambiguities in space-charge region to control the diffusion of holes towards the pore tips for anisotropic dissolution of silicon, and in passivation of pore walls against dissolution. Several mechanisms have been proposed to explain the macropore formation in p-type silicon. Of particular importance in suggested models are based upon the depletion and field effects (7), the chemical passivation (8), the linear stability (9), the current burst (10), and the pure chemical (11), however, the macropore formation in silicon still has remained unclear to date. Further understanding based on more universal nature of the electrochemical process for macropore formation is required.

In order to produce the periodically arranged pores, the wafer surface must be structured prior to etching. This is usually done by standard optical photolithography followed by an alkaline etching for forming the pyramidal notches that act as nuclei for pore growth. Although there have been several reports about random macropore formation, few results concerning the HAR macropore formation with a smooth surface morphology of sidewalls have been reported. Usually, the ordered array of macropores that have a smooth morphology of sidewalls has been mainly formed in the non-organic electrolytes such as HF: deionized water: 2-propanol with a ratio of 5:6:29 in volume (12, 13).

In the present study, we show the solvent effects in mixtures of HF with various composition of dimethyl sulfoxide (DMSO) on the macropore formation in monocrystalline p-type silicon. We will clarify the roles played by the organic solvent in the dissolution reaction at the silicon/electrolyte interface and in the limiting conditions of macropore formation.

Experimental

The macropore arrays were prepared in p-type Si(100) wafers with a resistivity of 10–20 Ω·cm (boron doping ~10^{15} cm^{-3}) by anodic oxidation. Prior to anodizing, etch pits were purposely defined on the Si surface using a lithographical patterning technique followed by KOH etching. The etch pits that showed the shape of inverted pyramids were typically 2–5 μm in size with the pattern interval of 2 μm. 49 % HF acid was used for preparing the mixed solutions. Two different compositional ratios in mixed electrolytes were used, i.e., HF:H_2O:DMSO = 1:5:5 and HF:DMSO = 7:43. The current density was applied at the range of 5–15 mA/cm^2. Scanning electron microscopy (SEM) has been used for analyzing the morphologies of macropores.

Results and Discussion

A typical current density-potential curve with a current peak corresponding to the critical current density was obtained in HF:H_2O:DMSO (1:5:5) electrolytes used, which indicates that porous silicon formation took place at current density below 20 mA/cm^2. Dependencies of the macropore etching rate in p-Si(100) on the current density for two different rectangular pores with sides of 2 μm and 5 μm in the electrolyte (HF:H_2O:DMSO) are shown in Fig. 1. The growth rate of patterned silicon with a 5 μm-sides shows almost a linear dependence on current density while saturation in the growth rate of p-type macropores after a linear dependence with the current density is observed in sample of etch pit of 2 μm size within the range of applied current. It is necessary to understand factors inducing the different behaviors in the two samples at the same measured current density. The linear increase and the leveling in growth rate are observed in two different electrolytes of HF/DMF and HF/H_2O/$(CH_3)_2CHCO$, respectively in the results of Vyatkin and co-workers (12). They considered the leveling in the etch rate as a evidence that the charge transfer process is not a limiting process over a specific value of current density. A chemical reaction controls the pore growth rate above a certain limiting current density. Our observed pore growth behaviors illustrate that the size of rectangular etch pits can also affect pore formation rate, that is again closely related with the chemical reaction. This may be closely related with the easiness of transport of chemical species in the interface of silicon. The linear growth rate of pore with size of 5 μm etch pits without saturation can be ascribed to smooth supply of reactants and removal of reaction products for dissolution of silicon due to its large pore diameter when compared with that of 2 μm.

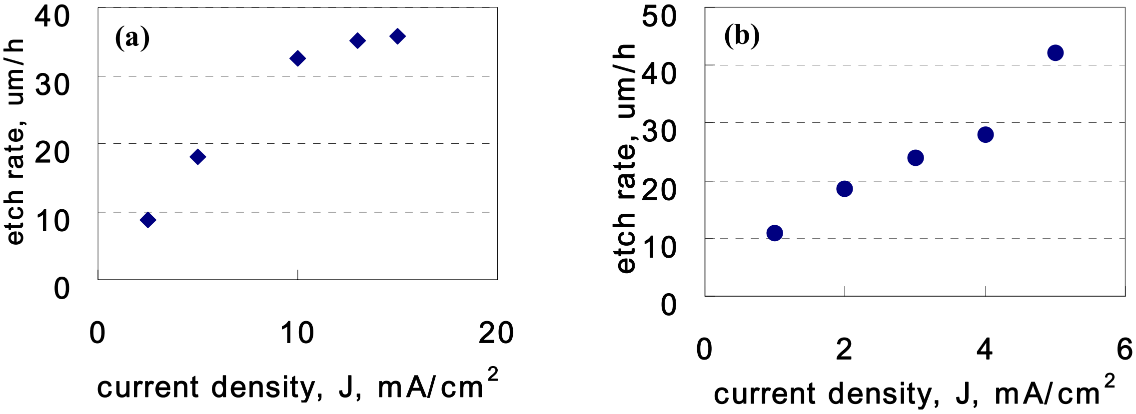

Figure 1. Macropore etching rate dependence on the current density in (a) 2 µm and (b) 5 µm lattice constant.

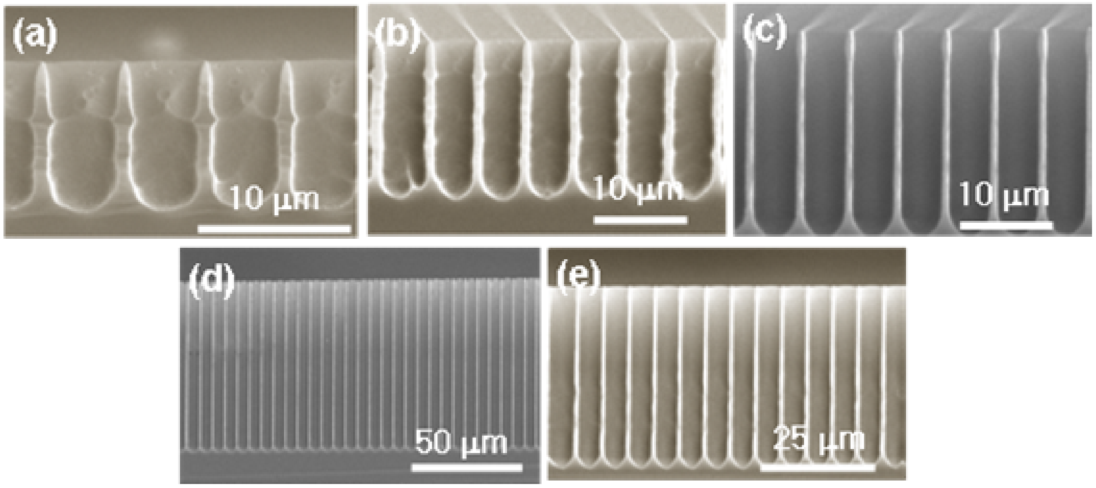

Figure 2. Cross-sectional SEM images of ordered macropores formed at (a) 2.5, (b) 5, (c) 10, (d) 12.5, (e) 15 mA/cm^2. The etching time is 60 min except for sample (d) which is 180 min.

Figure 2 (a) shows cross-sectional SEM images of macropores prepared in p-type silicon with a spacing of etch pits of 5 µm in current density ranging from 2.5 to 15 mA/cm^2. The pores grows perpendicularly to the substrate surface in the <100> direction and have a very uniform diameter and same depth at each current density. The pore bottom shape is a rounded upside-down pyramid. The fact that the pore diameter is constant from top to bottom indicates that dissolution of silicon proceeds only at the pore tip toward the depth direction. The result that the pore wall thickness keeps constant from the surface to the bottom is different from the previous report which shows a tapering in the pore-wall thickness towards the top surface (13,14). This means that the applied process condition is better method to fabricate uniform macropores of constant wall thickness.

When the distance between the edges of two neighboring inverse pyramids becomes more than pyramid width, random nucleation takes place in the areas between the inverted pyramids as was called as proximity effect in Ref. 15. Such a result is not observed in the Fig. 2 (a) because the etch pit width of 5 μm is over 2 μm which is a spacing of inverted pyramids (12). The random nucleation of pores is not also detected in the case, in which the lattice constant of a etch pit is 2 μm and its interval is 2 μm as shown in Fig. 3 (a). This condition is considered as the limit for random nucleation in proximity effect. Further experiments reducing the lattice constant of square etch pit below interval of etching pyramid is under conducting.

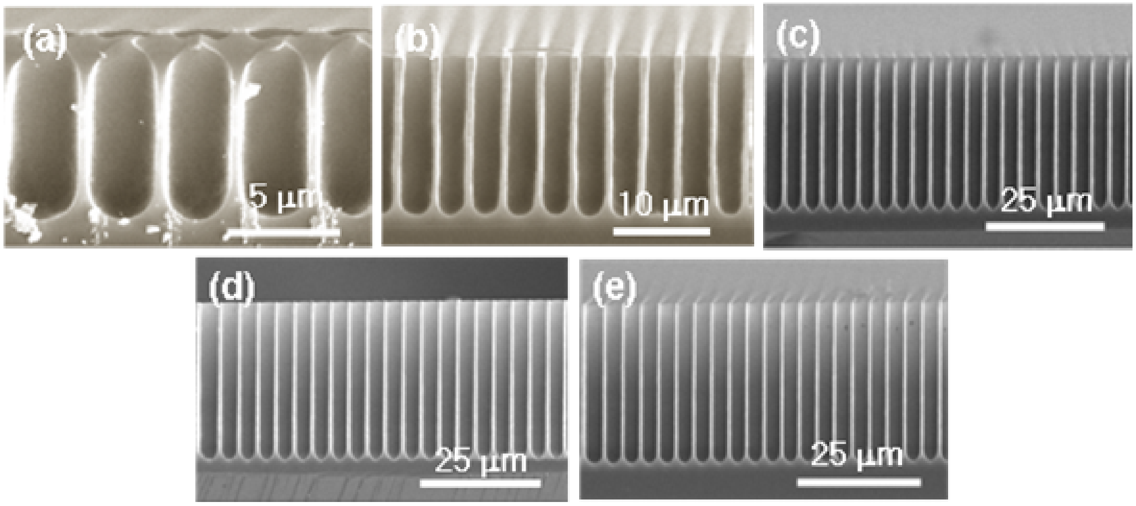

Figure 3. Cross-sectional SEM images of ordered macropores formed at (a) 2.5, (b) 5, (c) 10, (d) 12.5, (e) 15 mA/cm^2 for 60 min.

It is accepted as a rule that the pore diameter is proportional to the wall thickness (7). According to Lehmann's theory, the wall thickness is determined by the width of the SCR and the width of the SCR is proportional to the doping concentration. So, when the width of the SCR increases, the pore wall thickness increases as well. This statement can be used to account for the random nucleation that does not use the periodic patterns. Such behavior does not explain the present experimental data about ordered macropore formation as shown in Table I. The table shows that the wall thickness significantly decreases when the current density increases, although the doping concentration and the pore diameter are being constant, contrary to Lehmann's theory.

The data of Ref. 13 shows that ordered macropores are obtained when etch pits at 3 ~ 8 μm intervals are employed, while two small etch-pit spacing of 2 μm results in collapse of pore walls. This phenomenon was explained by the development of the resistance distribution in the silicon substrate during the macropore formation. Figure 3 (a) shows that macropores with a very smooth interface can grow even if the size of etch-pit is 2 μm, which is in contradiction to the previous result (13). The main discrepancy may be originated from different chemical composition of electrolytes. The electrolyte of HF:H_2O:DMSO is used in present study, while K. Kobayashi and co-workers used HF:H_2O:$(CH_3)_2CHCO$ solution.

TABLE I. The pore wall thickness dependence on the current density.

Current density (mA/cm^2)	5	10	15
Pore wall thickness (μm)	2.7	0.5	0.2

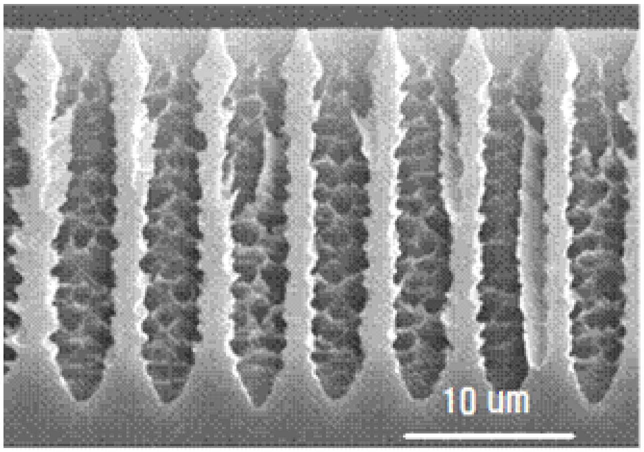

Figure. 4 Cross-sectional SEM micrograph of macropores formed by an electrochemical etching in HF:DMSO (7:43) for 60 min, current density equal to 8 mA/cm^2.

Figure 4 shows that the cross-sectional view of the macropores obtained in HF:DMSO (7:43) electrolyte. The interface of wall in the macropore is very rough and has branches shorter than pore diameter. This is a striking different morphology in comparison with the macropores observed in HF:H_2O:DMSO solution. These results seem to come from the relative amount of DMSO content which cause unstable pore growth with a very rough wall interface in the electrolyte.

It is evident that the electrochemical reaction associated with the pore formation is not only dependent on current density and semiconductor properties but also on the electrolyte composition. This is an example that shows that the simple addition of water in HF electrolyte containing DMSO can change the morphologies of macropores drastically. Analysis of the experimental data presented above is done here, starting from taking into consideration the reaction mechanism proposed by Gerischer et al (15).

$$(\equiv Si)_2SiH_2 + F^- + h_{VB}^+ \rightarrow (\equiv Si)_2Si{\cdot}H + HF, \quad (A)$$
$$(\equiv Si)_2Si{\cdot}H + F^- \rightarrow (\equiv Si)_2SiFH + e_{CB}^- \quad (B)$$
$$(\equiv Si)_2SiFH + 2\,HF \rightarrow 2\,(\equiv SiH) + HSiF_3 \quad (C)$$
$$HSiF_3 + HF \rightarrow SiF_4 + H_2 \quad (D)$$

The hole is captured in a Si-H surface state, resulting in the leaving of a proton and the formation of a Si dangling bond (Step A). After the nucleophilic attack of a fluoride ion (Step B), this Si surface atom becomes sufficiently positively polarized, such that in a next step HF can be added across the Si-Si back bonds (Step C). F^- is added to the more positively polarized Si; therefore, the Si surface stays hydrogen terminated. The leaving group $HSiF_3$ reacts with HF to form the final product H_2SiF_6 and a molecular of hydrogen (step D).

DMSO does not stabilize nucleophilic anions (e.g. fluoride) by hydrogen bonding because it is dipolar aprotic solvent, i.e., strong hydrogen-bond accepter. This means that the anions, e.g., F^- and HF_2^- are very mobile in the solvent and consequently enhance the silicon dissolution rate. DMSO also has a protophilic characteristics, which is proton acceptor property. Protons, and in general cations, are more easily solvated in DMSO and the dissociation constant of HF may be increased. To dissolve silicon, F^- need a hole. When the content of DMSO is high in HF solution in respect to HF:DMSO solutions, the very reactive F^- and HF^-_2 seem to combine easily and fast with holes in uniformly and abundantly distributed in p-type silicon, resulting in rough walls with many short branches. The reactivity of ions are reduced with relatively decreased amount of DMSO content by the addition of water, so that there is enough time for holes to get together at the pore tips in response to applied electric field, resulting in one directional growth of macropore with very smooth interface of pore wall.

Conclusion

In this work, a nice two dimensional periodical macropores with pore size from 2 ~ 5 μm have been obtained in HF:H2O:DMSO electrolyte by electrochemical etching. The uniform wall thickness of macropores has been formed from top to bottom without the pore-wall thinning towards the top surface. The 2 and 5 μm in etch pit size show a saturated and linear growth rate, respectively. The change of growth rate according to etch pit size is accounted for taking into consideration the easiness of chemical reaction. The macropores obtained in HF:H_2O:DMSO electrolyte shows very smooth wall interface, while the morphology of pore wall interface in HF:DMSO solution is very rough. It is a good experimental data that the relative of amount of DMSO in the solutions can change chemical reactivity and finally the morphologies of macropores in ordered pore formation.

Acknowledgments

This work was supported by Korea Ministry of Education, Science and Technology (MEST) basic research fund.

References

1. V. Lehmann, W. Honlein, R. Reisinger, A. Spitzer, H. Wendt, and J. Willer, *Thin Solid Films*, **276**, 138 (1996).
2. K. J. Chao, S. C. Kao, C. M. Yang, M. S. Hseu, and T. G. Tsai, *Electrochem. Solid-State Lett.*, **3**, 489 (2000).
3. I. Kuzma-Filipek, F. Duerinckx, K. Van Nieuwenhuysen, G. Beaucarne, J. Poortmans, and R. Mertens, *Phys. Stat. Sol. (a)*, 204, 1340 (2007).
4. R. Angelucci, A. Poggi, L. Dori, G. C. Cadinali, A. Parisini, A. Tagliani, M. Mariasaldi, and F. Cavani, Sens. *Actuators A*, **74**, 1 (1999).
5. A. Chelnokov, K. Wang, S. Rowson, P. Garoche, and J. –M. Lourtioz, *Appl. Phys. Lett.*, **77**, 2943 (2000).
6. V. Lehmann and H. Föll, *J. Electrochem. Soc.*, **137**, 653 (1990).
7. V. Lehmann and S. Rönnebeck, *J. Electrochem. Soc.*, **146**, 2968 (1999).
8. E. A. Ponomarez and C. Lévy-Clément, *Electrochem. Solid-State Lett.*, **1**, 42 (1998).
9. R. B. Wehrspohn, J.-N. Chazalviel, and F. Ozanam, *J. Electrochem. Soc.*, **145**, 2958 (1998).
10. J. Carstensen, M. Christophersen, and H. Föll, *Mater. Sci. Eng. B*, **69**, 23 (2000).
11. E.S. Kooij and D. Vanmaekelbergh, *J. Electrochem. Soc.*, **144**, 1296 (1997).
12. A. Vyatkin, V. Starkov, V. Tzeitlin, H. Presting, J. Konle, and U. König, *J. Electrochem. Soc.*, **149**, G70 (2002).
13. K. Kobayashi, F. A. Harraz, S. Izuo, T. Sakka, and Y. H. Ogata, *Phys. Stat. sol. (a)*, **204**, 1321 (2007).

14. K. Kobayashi, F. A. Harraz, S. Izuo, T. Sakka, and Y. H. Ogata, *J. Electrochem. Soc.*, **153**, C218 (2006).
15. H. Gerischer, P. Allingue, and V. Costa-Kieling, *Ber. Bunsenges. Phys. Chem.*, **97**, 753 (1993).

ECS Transactions, 16 (3) 299-303 (2008)
10.1149/1.2982569 ©The Electrochemical Society

The Effect of N_2 in Vapor Detectors Based on Porous Silicon Layers

E. Rucavado, J.P. Badilla, and A. Ramírez-Porras

Escuela de Física and Centro de Investigación en Ciencia e Ingeniería de Materiales
(CICIMA), Universidad de Costa Rica, San Pedro de Montes de Oca 2060, Costa Rica

Porous Silicon sensing devices have been developed and tested in air and pure nitrogen atmospheres containing organic vapors in order to study their electric response. It has been found differences in the electrical behavior of the sensors when subjected to both atmospheres. Possible explanations are proposed.

Introduction

Porous silicon has been extensively studied since photoluminescence was discovered (1). Its high reactivity to external agents has been prompted for the production of sensing devices for chemical species in gas or liquid phase (2-4) and for biological and biomedical applications (5,6). Several attempts to build devices approaching the commercial requirements in stability, reproducibility and cost-benefit variables have been reported by various groups (7). Some applications have been developed as humidity sensors (8-10). The sensing principle is the fact that the water molecules infiltrate the porous media and change the surface reactivity of the pores. The change is expected to be amplified with respect to the non-treated crystalline samples because of the surface area increment. One interesting point to study is the effect of air and nitrogen on these kind of devices. This is the subject of the present report.

Experimental Setup

Nanostructured silicon surfaces have been produced from commercial available crystalline boron-doped silicon with a resistivity in the 30–50 Ohm-cm range. The wafer has a thickness of 300 mm and a (1 0 0) crystallographic surface orientation. A back contact of aluminium was deposited by sputtering means and heated thereafter for 20 min at 400 ºC to form an ohmic contact. The electrochemical etching process was performed in presence of an ethanoic solution of 12.5% hydrofluoric acid at room temperature with two distinct current densities: Sample A of 53 mA/cm^2 and Sample C of 26 mA/cm^2. The etching time was set to 20 min. Immediately after this process, the samples were washed with pure ethanol and deionised water and let dried by evaporation in ambient air.

Two Indium contacts were soldered to the samples as illustrated in Figure 1(a). The samples were introduced successively in a chamber for exposure to the different vapors, as shown in Figure 1(b). The electrical contacts were driven to the exterior for resistance measurements.

High purity nitrogen gas was inserted by rubber tubing to the chamber. Humid nitrogen was obtained by bubbling the gas through a glass balloon containing either deionised water, ethanol or acetone. The resistance measurements were performed by the use of programmable multimeter in ohmmeter function in parallel with the sample contacts. The data were recorded by a computer system.

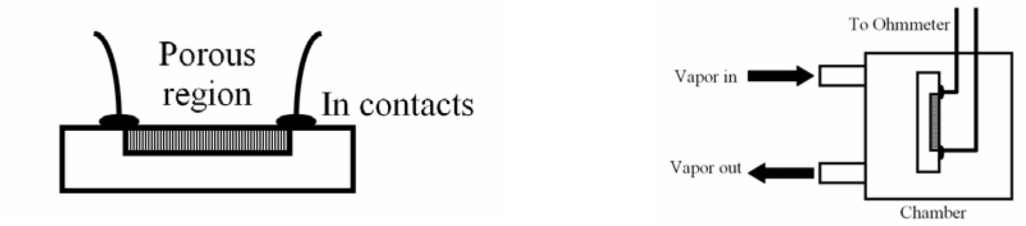

(a) (b)

Figure 1. (a): Cross section of the sensing device. Indium contacts have been soldered to the porous edge regions. (b): Sketch of the sensing chamber.

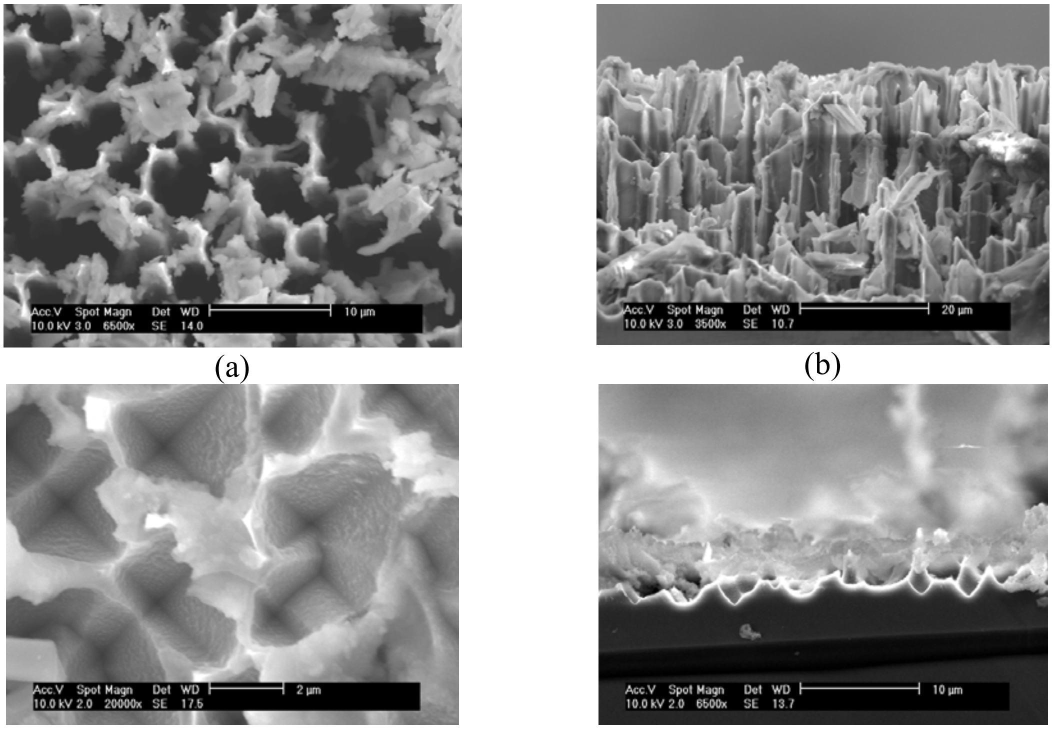

(a) (b)

(c) (d)

Figure 2. Microphotographs of samples A [(a) and (b)] and C [(c) and (d)] taken by SEM. (a) and (c): Surface views. (b) and (d): cross sections.

Results and Discussion

Figure 2 shows microphotographs of the two kinds of samples. For Sample A, the pores have typical diameters of 2 – 8 µm in diameter, whereas Sample C has pore diameters in the 2 – 5 µm range. The shape of the pores in Sample A is cylindrical, but in Sample C is conical, as seen in Figure 1 (b) and (d) where cross sections are shown. For the latter, the shape might be due to preferential directions in the crystal surface orientation when the etching takes place (7). By gravimetric measurements, the porosities found for both samples are: 90% for Sample A and 50% for Sample C.

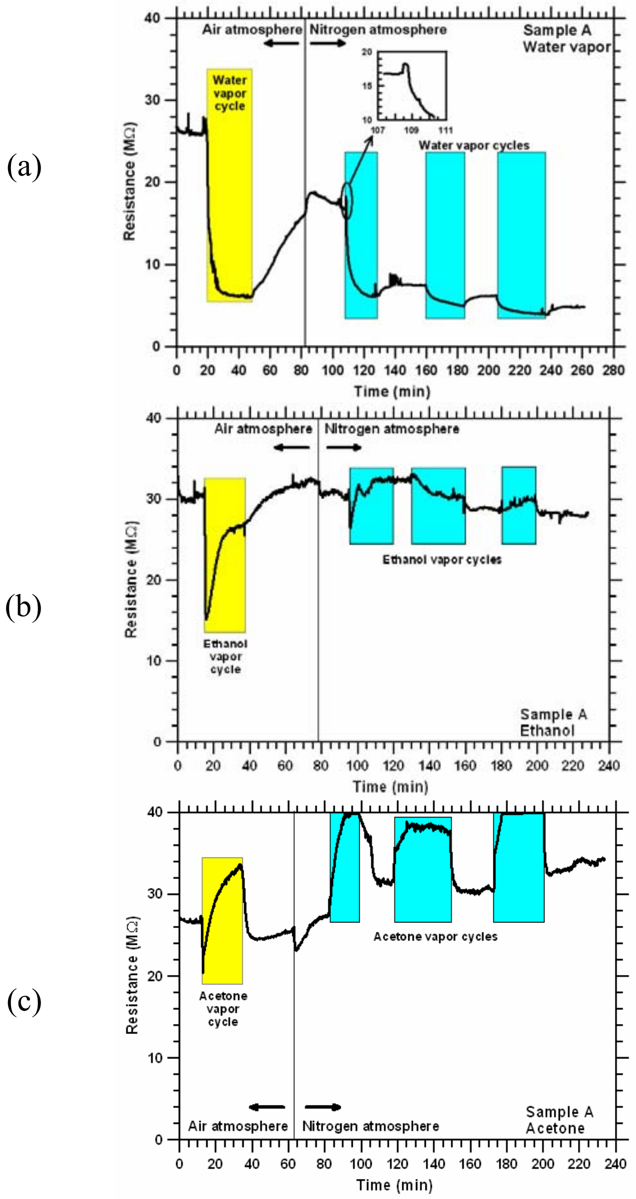

Figure 3. Electrical response of Sample A. (a): Water vapor. (b): Ethanol vapor. (c): Acetone vapor. The inset in (a) shows a possible Gibbs phenomenon.

Figures 3 and 4 show the device response of Sample A and C, respectively, to water, ethanol and acetone vapors in the two atmospheres (air and nitrogen). The initial resistance value lied in the 26 – 30 MΩ range for Sample A, and 4 – 6 MΩ for Sample C, corresponding to aged surfaces where oxidation must be present (11). The differences in the initial resistance can be related to porosity of surfaces: more porosity means more blocked paths for the charge to circulate from one electrode to the other.

An interesting feature to observe is a behavior that resembles a Gibbs phenomenon usually when the vapor cycle sets in. The inset in Fig. 3(a) shows a zoom of this feature for one case. This phenomenon was previously observed by others (2,12) and is explained in terms of charge injection by vapor molecules on the porous surface (13,14).

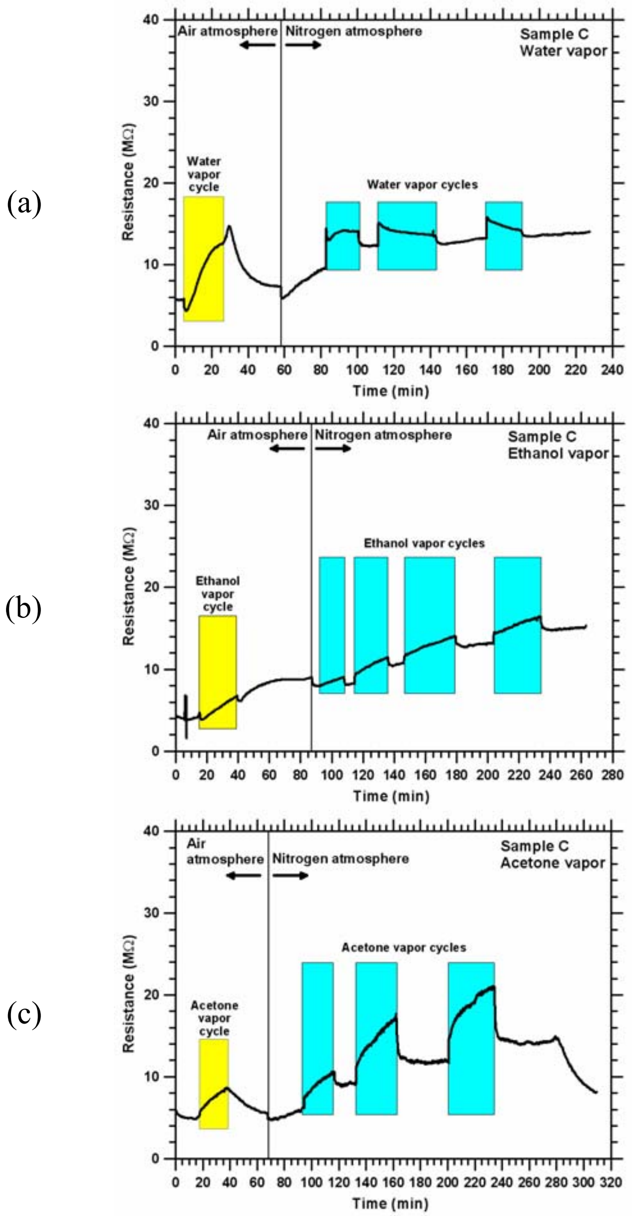

Figure 4. Electrical response of Sample C. (a): Water vapor. (b): Ethanol vapor. (c): Acetone vapor.

For Sample A, the change in resistance when vapor enters the chamber is stronger in air than in nitrogen, except for the case of acetone vapor. Ethanol sensing is not evident in nitrogen ambient, but is clearly observed for water and acetone. After removing the vapor, the signal tends to recover their original level both in air and in nitrogen. Nevertheless, the recovering seems to be faster in nitrogen than in air, as can be seen by the presence of "plateaux" where the resistance is kept essentially constant with time. The same occurs for Sample C, but having those plateaux increased resistance values. This can be an indication of hysteresis effect in the electric response (15).

The curves obtained in vapor cycles resemble the shape of transient charge or discharge of an equivalent RC circuit. This sort of behavior has been already studied proposing such an equivalent model (2). When the vapor cycle ends, a relaxation signal is observed. The corresponding time constant in air atmosphere in general is higher than in nitrogen atmosphere (this is particularly notable for Sample A with water and ethanol vapors, and for Sample C with water and acetone vapors). Therefore, it is plausible to attribute the slower responses in air ambient to the presence of Si-O bonds which increase capacitive effects on charge storage (11). It is proposed therefore that the effect of nitrogen is to decrease this kind of bonds. Such hypothesis must be tested in a near future.

Comparing the performances of both devices, Sample C does not have such a large change in resistance in air that shows up for Sample A, although the former has a better sensing capacity for Ethanol vapor in nitrogen.

Conclusions

The effect of nitrogen ambient in two sensor devices has been reported. The general performance of the devices in a nitrogen atmosphere seems to increase with respect to the air ambient where oxygen is present, perhaps due to the replacement of Si-O bonds that slower the time constants corresponding with changes in resistance. The sensing capability in nitrogen ambient is not lost in spite the aging of the samples. This can also be a support of the idea of reduction of Si-O bonds in nitrogen atmosphere.

Acknowledgments

This work has been supported by the Vicerrectoría de Investigación of the Universidad de Costa Rica, by the project numbers P816-A5-018 and P816-A8-086.

References

1. L.T. Canham, *Appl. Phys. Lett.*, **57**, 1046 (1990).
2. M. Archer, M. Christophersen, and P.M. Fauchet, *Sensors and Actuators B*, **106**, 347 (2005).
3. G. García Salgado, T. Díaz Becerril, H. Juárez Santiesteban, and E. Rosendo Andrés, *Optical Materials*, **29**, 51 (2006).
4. J. Mizsei, *Thin Solid Films*, **515**, 8310 (2007).
5. V. Vrkoslav, I. Jelínek, G. Broncová, V. Král, and J. Dian, *Materials Science and Engineering C*, **26**, 1072 (2006).
6. Joon-Hyung Jin, Nam Ki Min, and Suk-In Hong, *Appl. Surf. Sci.*, **252**, 7397 (2006).
7. O. Bisi, S. Ossicini, and L. Pavesi, *Surf. Sci. Rep.* **38**, 1 (2000).
8. P. Fürjes, A. Kovács, Cs. Dücsö, M. Ádám, B. Müller, and U. Mescheder, *Sensors and Actuators B*, **95**, 140 (2003).
9. M. Björkqvist, J. Salonen, and E. Laine, *Appl. Surf. Sci.*, **222**, 269 (2004).
10. M. Björkqvist, J. Paski, J. Salonen, and V.-P. Lehto, *Phys. Stat. Sol. (a)*, **202**, 1653 (2005).
11. M.V. Wolkin, J. Jorne, and P.M. Fauchet, *Phys. Rev. Lett.*, **82**, 197 (1999).
12. F. Razi, F. Rahimi, and A. Iraji zad, *Sensors and Actuators B*, **132**, 40 (2008).
13. I. Schechter, M. Ben-Chorin, and A. Kux, *Anal. Chem.*, **67**, 3727 (1995).
14. M. Chiesa, G. Amato, L. Barino, E. Garrone, F. Geobaldo, and E. Giamello, *J. Electrochem. Soc.*, **152**, G329 (2005).
15. T. Islam and H. Saha, *Sensors and Actuators B*, **114**, 334 (2006).

CHAPTER 6

WEDNESDAY: MORNING SESSION

ECS Transactions, 16 (3) 307-321 (2008)
10.1149/1.2982570 ©The Electrochemical Society

Porous Multilayers as a Dielectric Host for Photons Manipulation

M. Ghulinyan[a] and L. Pavesi[b]

[a] Micro-Technology Laboratory, Fondazione Bruno Kessler, via Sommarive 18, 38100 Povo (Trento), Italy
[b] Nanoscience Laboratory, Department of Physics, University of Trento, via Sommarive 14, 38100 Povo, Italy

Porous silicon multilayers are a suitable tool to modify the photon mode density in one dimension. In this way, new phenomena such as photon Bloch oscillations, Zener tunneling of light, slow light, photon Anderson localization, necklace light states and optical bistability may occur. A review of these phenomena and their actual demonstration is here reported.

Introduction

Transport phenomena of charge carriers in solids have several analogies with the propagation of light waves in dielectric materials. Electronic crystals have an analogue in the form of *photonic crystals* which are artificial materials, where a periodic variation of dielectric constant leads to the formation of bands where the propagation of photons is allowed or forbidden. As the photons do not interact with each other, a light wave packet remains coherent for much longer times than charged particles. This means that dynamic interference effects could be isolated and studied much easier with light than with electrons. But since both have a wave nature the same phenomena could be observed for both. In the past years we have developed one dimensional complex dielectric systems based on porous silicon multilayers with the aim of studying in depth the photon propagations in these complex systems (1-13). Here we review how it is possible to handle photons in a complex dielectric host.

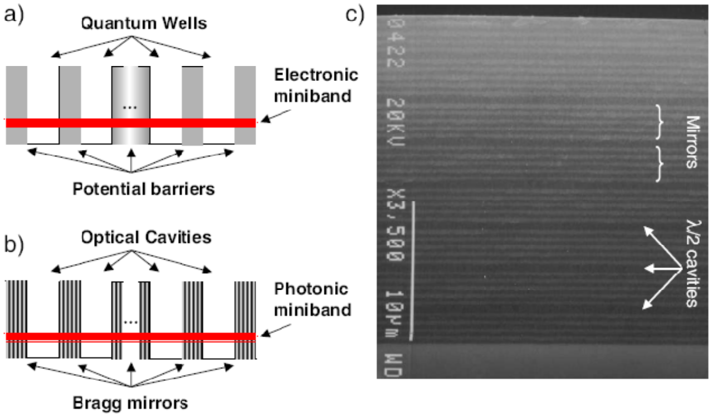

Figure 1. In analogy to the electronic coupling of separate quantum wells in a semiconductor superlattice (a) an optical superlattice can be realized when optical cavities are brought together (b) resulting to the formation of a miniband of extended photonic states. (c) A SEM micrograph of a 1D optical superlattice.

Porous Silicon Microcavities

In a close analogy to the formation of an electronic superlattice when several semiconductor quantum wells are brought together (Fig. 1(a)), an optical superlattice is made by coupling degenerate optical resonators (cavities) within the same photonic structure (Fig. 1(b)). Optical coupling between the various cavities yields a degenerate mode repulsion and a formation of a miniband of optical states, which are densely packed around the resonant wavelength. In one dimension, an optical superlattice can be formed by stacking two dielectric layers A and B with different refractive indices and quarter-wave thickness in a way to form identical cavities separated by Bragg reflectors (Fig. 1(c)). In particular, we choose the following sequence of layers: $BABABABAB$ $(AA)_1$ $BABABABAB$ $(AA)_2$: : : $(AA)_m$ $BABABABAB$. This structure is essentially a series of m microcavities $(AA)_m$ coupled to each other through the $BABABABAB$ Bragg reflectors.

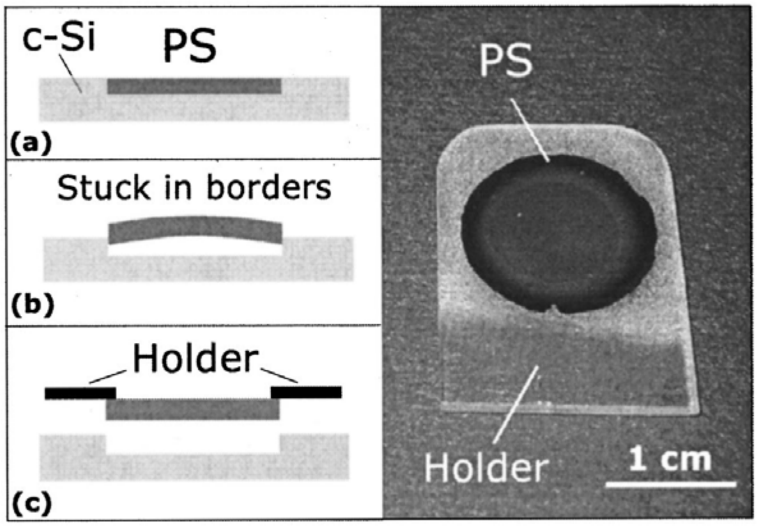

Figure 2. Schematic diagram of free-standing PS microcavity sample fabrication. (a) before the high current step, (b) after the high current step, and (c) taking PS off the substrate after drying. (right) A photograph of a free-standing PS coupled microcavity.

We have grown the optical superlattices by controlled electrochemical etching of heavily doped p-type (100)- oriented silicon (2,3,8). The electrolyte was prepared mixing a 30% volumetric fraction of aqueous HF (48 wt.%) with ethanol. A magnetic stirrer was used to improve electrolyte exchange. The applied current density defined the porosity of the layer (the latter is related to the effective refractive index of the layer). We applied 7 mA/cm^2 for the low porosity layer A (refractive index $n_A = 2.1$) and 50 mA/cm^2 for the high porosity layer B ($n_B = 1.4$). The physical thickness of the layers was controlled by adjusting the duration of the etch times. The superlattice structures were made free-standing by applying an electropolishing current pulse at the end of the growth process (Fig. 2).

Alternating these currents, we grew a superlattice structure with a single (Fig. 3) and up to ten coupled cavities (Fig. 4) (3). Particular care was taken to control the anodization conditions which usually drift as the total sample thickness increases. Moreover, the natural refractive index drift was compensated by changing the etching times of the layers.

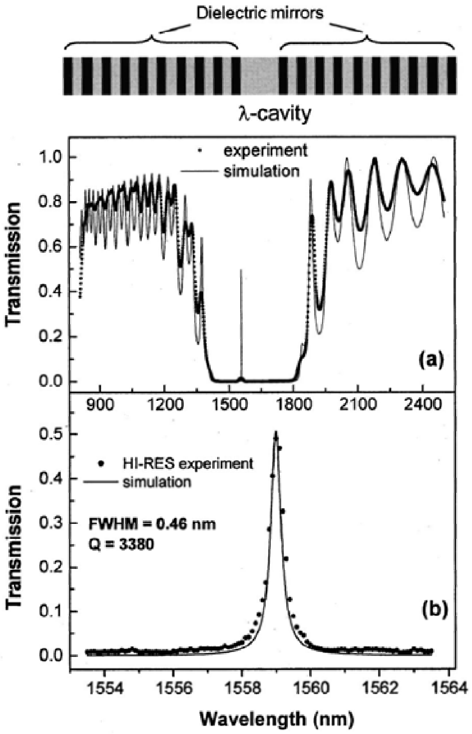

Figure 3. Transmission spectra of a single $\lambda/2$ microcavity: Solid dots are the experimental data and the lines are the simulations: (a) Measurements with 1 mm spot in a wide wavelength range, (b) measurements with 35 μm spot with a high-resolution tunable laser source. The top diagram shows the structure of the microcavity.

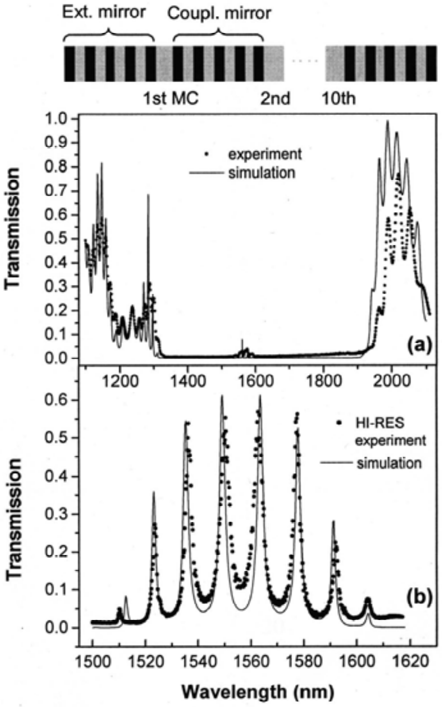

Figure 4. Transmission spectra of a ten coupled microcavity structure, with $\lambda/2$ cavities sandwiched between 4.5 period external DBRs (dots) and numerical calculations (lines). (a Wide range measurements with 1 mm spot size and (b) high-resolution measurement

Bloch oscillation of light-waves

Bloch oscillations of electrons is a phenomena for which a constant electric field causes an oscillating current. This is a consequence of Bragg reflections of electrons at the Brillouin zone boundaries. In fact, if an external bias is applied to a crystal, electrons are accelerated by the electric field F in the first half of the Brillouin zone, while in the second half they move against the field. This oscillatory motion is known as electronic Bloch oscillations and has a characteristic period of $T_B = h/eFd$ (d is the lattice constant). Also, the energy spectrum of a biased crystal is changed and the energy bands are substituted by a Wannier-Stark ladder (WSL) of equidistant energy levels, with an energy separation proportional to the inverse of T_B. The experimental study of electronic Bloch oscillations has been an issue for a long time because electrons loose their coherence on a time scale shorter than the oscillation period T_B. Only with the advent of electronic superlattices and their long lattice constants, electronic Bloch oscillations have been observed.

Optical superlattices have been proposed as a potentially ideal system to observe Bloch oscillations for light (4). An optical path gradient, $\Delta\delta$, *parallel* to the light propagation direction was suggested to mimic the optical equivalent of an external force (the static electric field in the electron case). In fact, multilayer structures with a linearly increasing/decreasing refractive index have a tilted photonic crystal band in close analogy to the tilted electronic miniband of a biased semiconductor superlattice. The light intensity distribution inside this structure can be calculated using a transfer matrix (TM) formalism. Figure 5(a) shows the appearance of a miniband of extended optical states (bright lines) in the photonic stop band (dark regions) in the conditions of a unique optical path throughout the structure. If a gradient in the optical thickness of the layers is introduced, a spatial tilting of the miniband is observed (Fig. 5(b)) with the formation of an optical Wannier- Stark ladder.

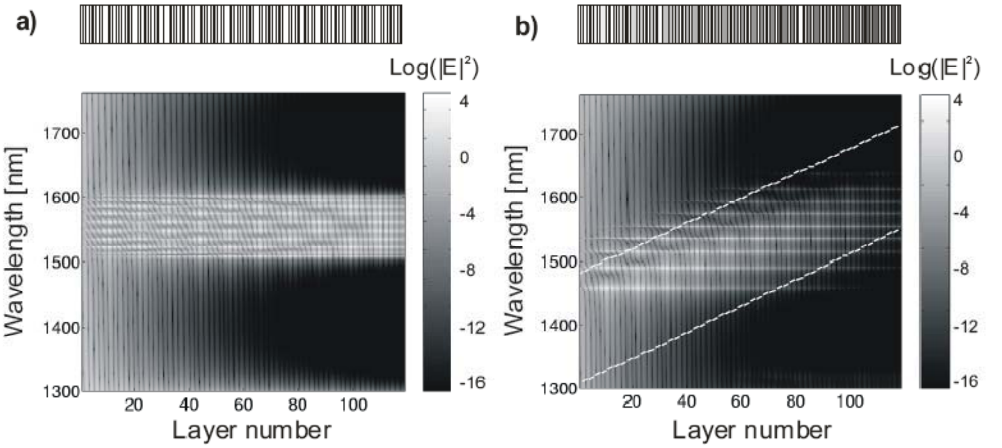

Figure 5. Scattering state calculation of the distribution of the energy spectrum inside the multilayer. The parameters used in the calculations correspond to samples used in the actual experiment. Panel a) flat band situation, $\Delta\delta = 0\%$. Panel b) tilted band situation, $\Delta\delta = 14\%$. The dashed lines indicate the theoretical tilting of the miniband. Above each panel the coupled microcavity structure is schematically shown; the grey scale refers to the refractive index variation along the depth in the sample (the darker the larger *n*).

Actually these structures were produced by using the etching techniques and parameters discussed above (4). The optical path gradient in the growth direction of the structure was achieved by changing the duration of the etch stop current, which controlled the refractive index and hence the variation in the optical thickness of each layer. We produced samples with gradient values in the range from $\Delta\delta = 2$ to 14% (values that were extracted from the best fit parameters to the transmission spectra). Figure 6 compares a series of transmission spectra for sample with growing $\Delta\delta$. The formation of a WSL structure manifests itself as a series of narrow equidistant transmission peaks with a frequency separation of the peaks that depends on the strength of $\Delta\delta$ and defines the period T_B of the Bloch oscillations. The resonances become thinner and less intense for the large gradient values (Fig. 6(b-d)). This is a clear signature of the strongly inclined miniband, which also means that in order to be transmitted the photons now need to overcome a thicker tunneling barrier. More interestingly, if a short resonant optical pulse is sent through the sample, a series of pulses appears in transmission (Fig. 6 right). The oscillation period (Fig. 6 and 7) decreases as $\Delta\delta$ increases. This a direct evidence of the Bloch oscillations that the photons suffer while propagating in the tilted optical superlattice. One can see how the amplitude of the transmitted intensity decreases as the gradient increases: as a result of an increased tilt of the photonic miniband the oscillating photon wave packet has to tunnel out through a thicker barrier.

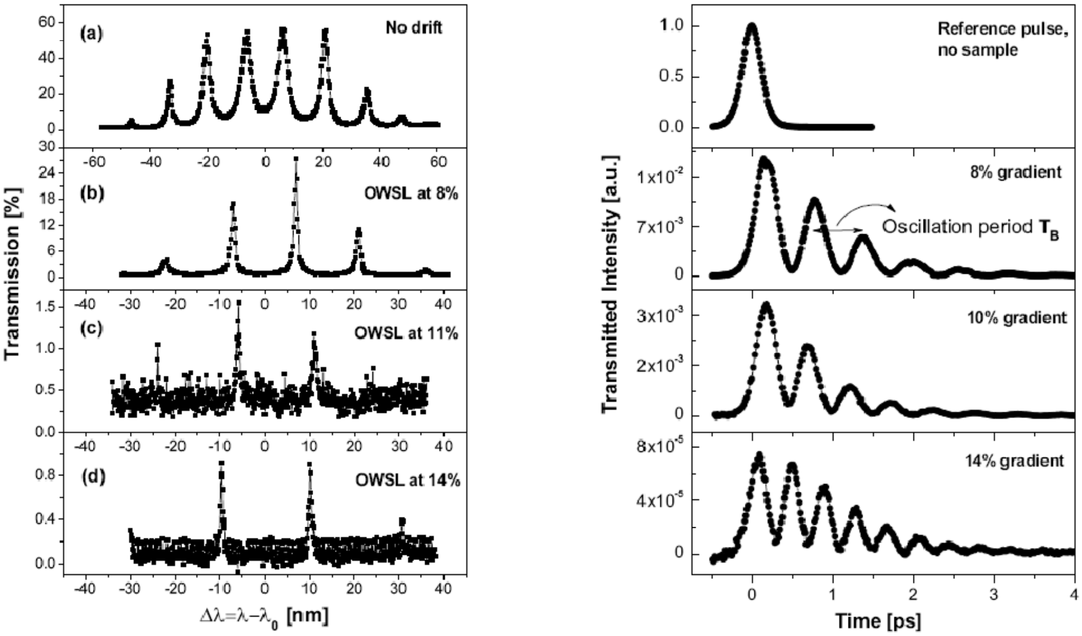

Figure 6. (left) Transmission spectra of the optical superlattice with different gradients of the optical thickness of the layers (λ_0 =1.55 μm is the central wavelength). Spectrum (a) corresponds to non drifted sample (spatially flat miniband), while (b), (c), (d) show the occurrence of the optical Wannier-Stark ladder with equidistant resonances: the energy separation of the states increases with the increase of the miniband tilt. (right) Temporal response of the system for various values of the optical path gradient Δδ. The period of the oscillations and the total transmission decrease while increasing Δδ. The top panel shows the undisturbed probe pulse without sample.

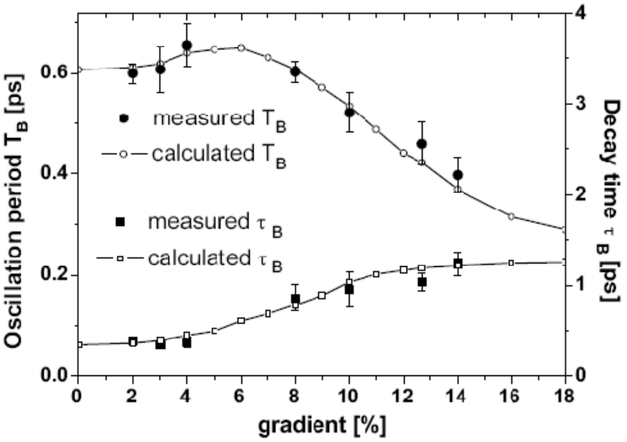

Figure 7. Experimentally observed oscillation period T_B and decay time τ_B as a function of the gradient Δδ. The error bars are the standard deviations obtained from various measurements on several positions on the sample and represent therefore the effect of lateral sample inhomogeneities. The solid lines are the predicted behaviours of T_B and τ_B from transfer matrix calculations.

Zener Tunneling of light-waves

The Bloch oscillations are closely related to another phenomenon, known as electrical breakdown or *nonresonant* Zener tunneling, which becomes effective as the electric field increases. At high enough electric fields the electron can tunnel from one band to the continuum of states of another upper energy band without gaining extra energy. With the increasing escape probability of the electron to the other energy band the Bloch oscillations are damped strongly. Another kind of tunneling is possible which is called *resonant* Zener tunneling and occurs at high electric fields between charge carriers in WSL formed from different energy bands.

To be able to observe Zener tunneling of photons we have grown optical superlattices with two minibands within the unique stop band (7). This will allow to use relatively small optical path gradients. For this, one should couple within the same structure two sets of cavities of *C* and *D* type, which are centered at different wavelengths. The appropriate sequence of layers looks like the following: $BABABAB\ (CC)_1\ BABABAB\ (DD)_1$: : $(CC)_m\ BABABAB\ (DD)_m\ BABABAB$, where we have used m=6. The refractive indices for this type of structures were determined to be $n_A = n_C = n_D = 1.5$ and $n_B = 2.12$. We produced samples with controlled gradient values in the range from $\Delta\delta$= 0 to 18%. The light intensity distribution inside this structure in the absence of optical path gradient (Fig. 8(a)) shows the formation of two flat minibands MB1 and MB2. The two minibands are separated by a photonic minigap (dark region), which shows an negligible transmission of 0.43%. The corresponding calculated transmission spectrum of the structure (Fig. 8(b)) is compared with the experimental one (Fig. 8(c)).

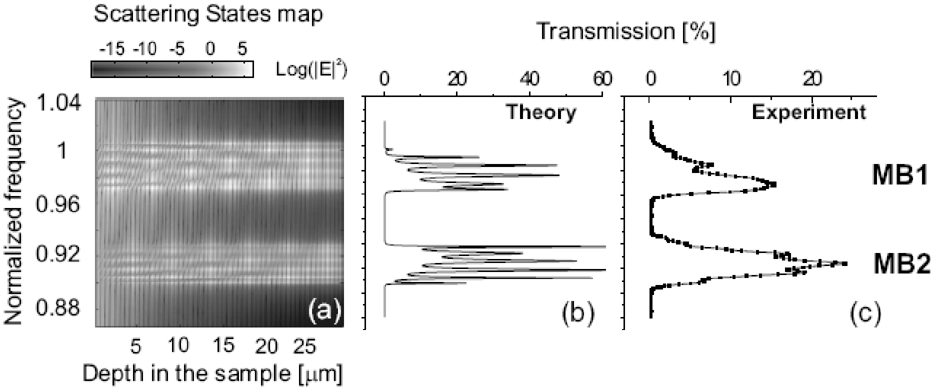

Figure 8. The calculated intensity distribution of the light inside the sample plotted as a color scale versus the normalized frequency $\omega=\omega_0$, where ω_0 is the minigap central frequency, and depth inside the sample. (a) Flat miniband situation, $\Delta\delta$= 0%. Two minibands MB1 and MB2, separated by a minigap region are seen in the calculated (b) and measured transmission spectrum (c).

An introduction of 6.7% of negative optical path gradient tilts the photonic band structure and results in the formation of optical WSLs in both minibands (Fig. 9(a)). Now the spatial confinement of localized states causes a decrease of absolute transmission from 50% in the flat band case (delocalized states) down to 2% (Fig. 9(b)). In Fig. 9(c) we plot the measured transmission spectrum of the superlattice with tilted minibands, where the WSLs can be appreciated.

We go on further with increasing the optical path gradient and look at the evolution of photonic miniband picture. At a critical degree of band tilting ($\Delta\delta$~ 10.3% in our case) the WSLs in two minibands couple within the extension of the structure. Coupling induced delocalization of two anticrossing states takes place, which appears as an intense resonant tunneling channel (Fig. 10(a)). The resonant Zener tunneling manifests as an enhanced transmission peak in both calculated (Fig. 10(b)) and measured transmission spectra (Fig. 10(c)) .

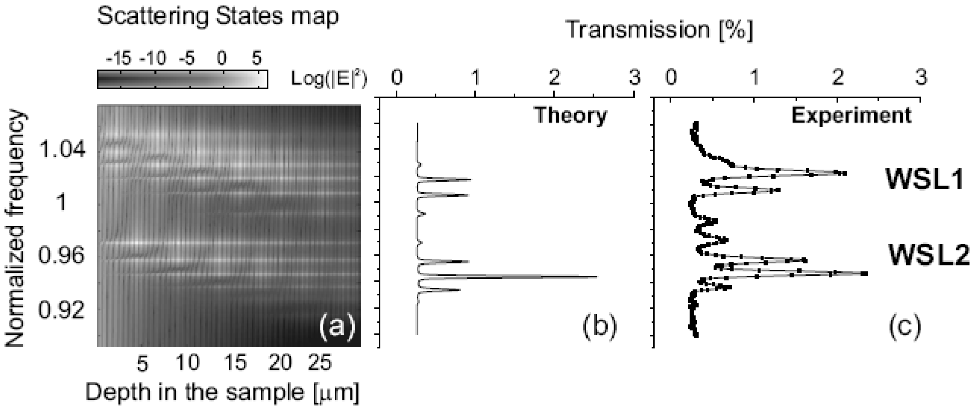

Figure 9. (a) Optical WSLs of localized modes are formed in two minibands at Δδ=6.7%. Light transmission drops down to 2%: TM-calculations (b) and experiment (c).

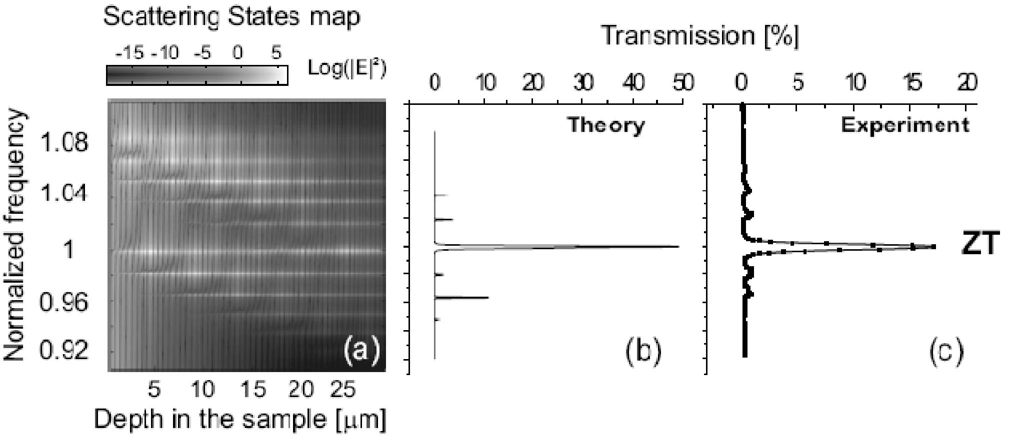

Figure 10. (a) The two WSLs couple at Δδ = 10.3% and form a resonant tunnelling channel through the sample. Resonant Zener tunnelling is predicted by theory (b) and confirmed experimentally (c) as an enhanced transmission peak in the center of the minigap.

Up to now, the measurements have been performed on different samples for each value of Δδ. In order, to measure a single sample kinetically we have developed a technique based on vapour condensation in the pores which change the refractive index of the layers and hence causes a time dependent Δδ (10). Fig. 11, bottom panel shows the experimental idea: the Zener structures are blown with ethanol vapors and driven in or out of the resonant tunnelling conditions. The tuning of the photonic bands towards resonant coupling has an effect on light transmission that closely resembles the Zener tunneling of charge carriers in semiconductor diodes. In Fig. 12 we report the peak amplitude of the photon transmission at the resonant Zener tunneling wavelength as a function of the gradient of the refractive index. The plot shows a threshold-like character, staying almost constant over a range of gradients and undergoing an enhancement once the critical gradient value of $\Delta\delta$=10.1% is reached. This observation points to a close analogy between the light transmission in a photonic crystal and the reverse current of electrons in a semiconductor diode, where a threshold reverse bias results in a rapidly growing current over its saturation value .

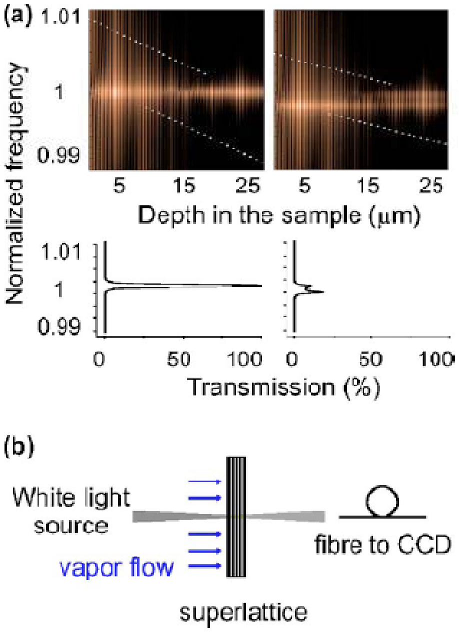

Figure 11. The calculated light intensity distribution inside the optical superlattice, plotted around the normalized frequency ω/ω_{ZT} and versus depth in the sample. Below the corresponding transmission spectra for two cases of resonantly coupled (left-hand panels) and decoupled WS states (right-hand panels) are shown. The dotted lines are a guide for the eye and show the minibands tilting. (b) The sketch of the experimental setup.

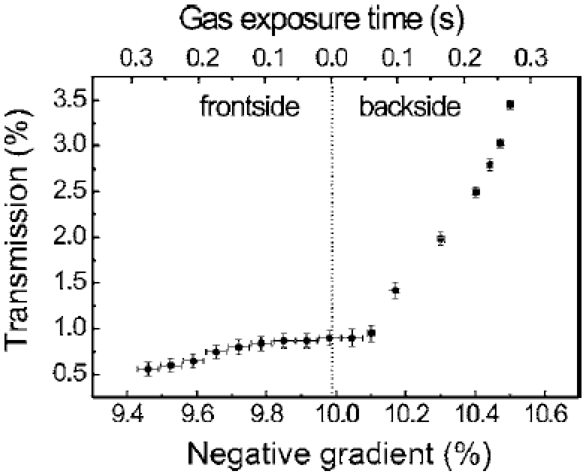

Figure 12. Resonant Zener breakdown of the optical superlattice. With an increase in the optical path gradient along the sample, the light transmission shows a threshold-like behaviour, in a close analogy to the tunnelling current of electrons in a reverse-biased solid-state diode.

Slowing down light

Stopping or slowing down of the light is achieved in photonic crystals by varying the photon mode dispersion to a flat dispersion and hence reducing the group velocity v_g to values that can be two to three orders of magnitude smaller than the vacuum speed of light c. Coupled resonator optical waveguides (CROW), in which a resonant suppression of group velocity of optical pulses occurs, have been suggested as reliable photonic systems to slow down light propagation. From the point of view of device application, it is desirable to maintain the propagating signal lineshape along with small group velocities. High-finesse 1D Fabry-Perot cavities offer very low group velocities at the resonant frequencies, while they strongly distort optical pulses. It is possible to design a finite size coupled cavity system with optimized coupling to the environment (impedance matching), which results in an almost flat dispersion in the center of the wide and high transmission miniband of photonic states (9).

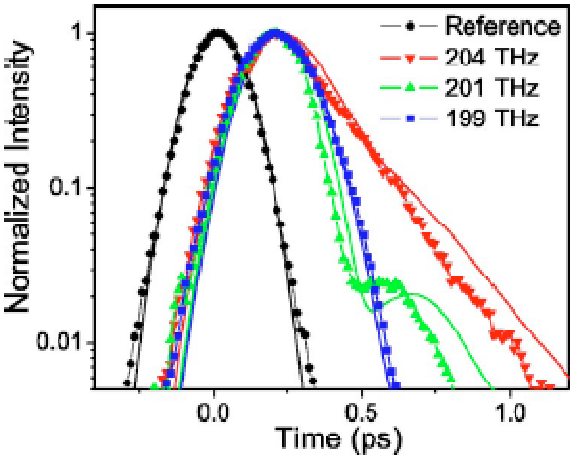

Figure 13. Measured (scatter) and calculated (solid lines) time resolved ultrashort pulse propagation through impedance matched optical superlattice. The reference Gaussian pulse is transmitted with negligible distortion (199 THz) when it fits the wide transmission miniband. Long exponential decays or oscillatory behaviour is observed when the input pulse excites the edge states (204 THz) or two maxima (201 THz) of the miniband.

An optical superlattice is built up by using porous silicon multilayers with similar cavities and coupling mirrors, while the external mirrors have been chosen such that a good coupling condition to the environment (impedance matching) was fulfilled (Fig. 4 defined the various mirrors). In particular the external mirror had period number was halved with respect to the internal mirrors. The transmission spectrum of this superlattice is characterized by a single wide band. Pulse transmission experiments are shown in Fig. 13. One can see, that the transmitted signals are delayed with respect to the reference pulse. In addition, the signals present different lineshapes depending on the probe frequency of the input pulses. When the ultrashort pulse at 199 THz is fitting perfectly in the broad part of the miniband, it is similarly delayed, while the input Gaussian lineshape remains almost undisturbed. We note, that the highest absolute transmission value is measured for the non-distorted signal.

White-light interferometry was performed to measure the phase-delay of the light transmitted through samples using a Mach-Zehnder interferometer coupled to a Fourier-transform spectrometer (9). In particular, the group velocity has been obtained from the measured phase ϕ using the relation $1/v_g = 1/L \times d\phi/d\omega$, where L is the physical extension of the sample. Values so obtained are compared with those deduced by direct pulse transmissions experiments in Fig. 14. Quite good correspondence is found between the data derived from two different measuring techniques and the numerical results. The group velocity is found to be around v_g=c/0.2.

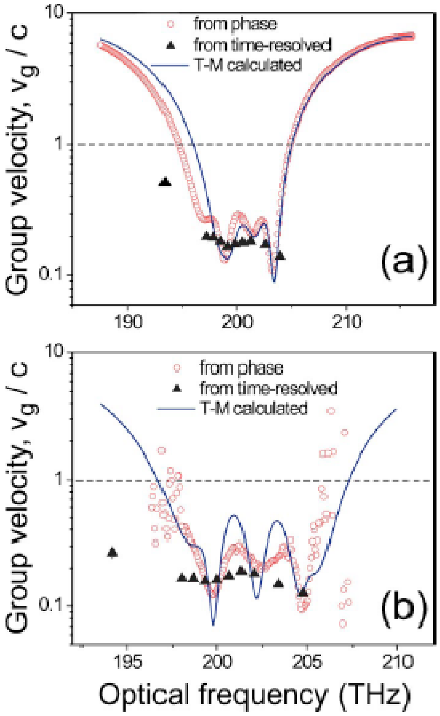

Figure 14. The group velocity obtained from phase (open circles) and from time-resolved measurements (full triangles). (a) Four cavity (S2) and (b) five cavity sample (S3) cases. Transfer matrix calculations are plotted in both graphs as solid lines. A group velocity reduction by a factor of 5 is observed in both samples.

Anderson localization of light waves

Anderson localization of light is a pure interference phenomena that happens when a sufficient amount of disorder is introduced into a dielectric system. In the localized regime light diffusion comes to a halt and localized states, which trap the light, appear. Anderson localization was originally discovered for electron transport, where the diffusion of electrons was found to disappear upon increasing the disorder inside a conductor. The transmission spectra of localized 1-D systems exhibit many randomly distributed high transmission peaks. These high transmission peaks originate from resonances created inside the sample by localized modes and result in big fluctuations in the transmission coefficient T. The localized modes decay exponentially and, as a consequence, the ensemble average of $\ln T(\lambda)$ over all possible realization of the disorder decays linearly with the sample thickness L.

We studied samples composed of *many* dielectric layers of two types (A and B) (6). The disorder was introduced by giving each layer a 50% probability to be of type A or B. We have grown 9 disordered samples of various thicknesses in the range from 60 to 350 layers (i.e. with physical thickness between 13 and 78 μm). In Fig. 15 examples of measured transmission spectra are shown for three values of the sample thickness. The high transmission peaks are typical for a localized system and are due to internal resonances inside the sample. Upon increasing sample thickness, on average, the spectral width of the peaks narrows, as is expected for localized modes.

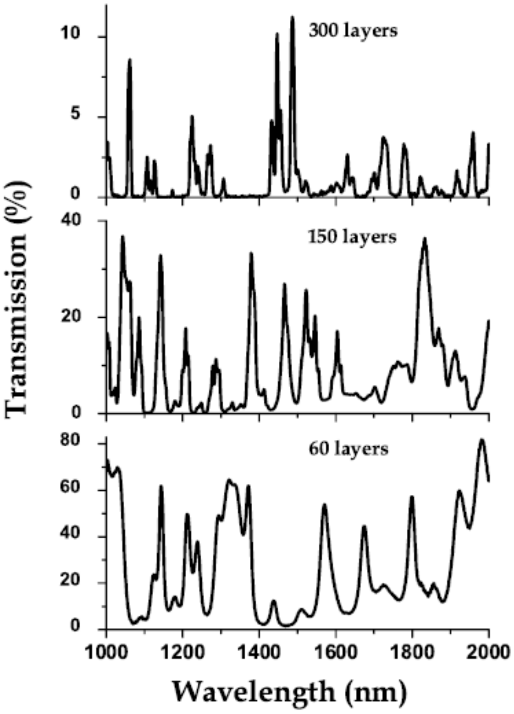

Figure 15. Measured transmission spectra for three values of the sample thickness *L*. The spectra contain narrow high transmission peaks that, on average, become narrower upon increasing *L*.

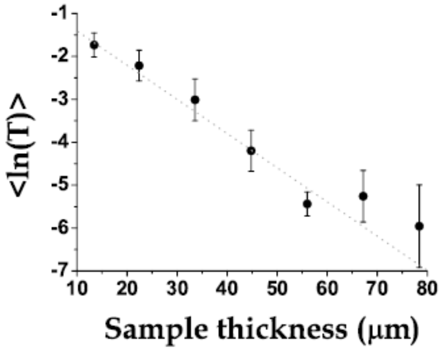

Figure 16. Spectral average of the logarithm of the measured transmission versus sample thickness. The error bars are obtained by repeating the measurement in various spots on the sample and therefore reflect lateral sample inhomogeneities.

The localized modes decay exponentially over a typical length scale called the localization length ξ. The transmission coefficient is therefore related to the localization length via: $\langle \ln T \rangle = -L/\xi$, where the brackets denote an average over realizations of the disorder. To determine the localization length in our samples we have calculated the wavelength-average of the logarithm of the transmission coefficient for each measured spectrum. The results are plotted in Fig. 16. The dashed line is a linear fit to the data. Taking into account propagation losses of the light due to the composite nature of porous silicon of 100 cm^{-1}, we found a ξ of 14.9±2.4 μm. This confirms that the physical sample thickness L exceeds the localization length, and hence that our samples are in the Anderson localized regime.

Necklace states in random systems

One of the fascinating property of the Anderson regime is the coexistence of localized and extremely rare non-localized states, called necklace states, that were theoretically predicted but never actually shown experimentally. We experimentally observed these necklace states in one-dimensional dielectric system, consisting in binary disordered multilayers made of porous silicon, through their peculiar time behaviour (6). While the time evolution of a laser pulse in a localized state is characterized by an exponential decay, meaning the light is trapped into the resonance, for a necklace state the exponential decay is washed out by its non-localized nature while the time decay is strong due to multiple resonance scattering. The necklace is a multi-resonance non-localized mode and the distribution of light intensity inside the system appears as a "shining bright necklace" (11).

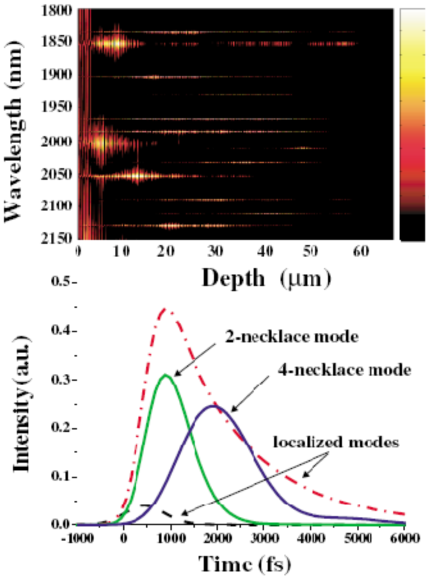

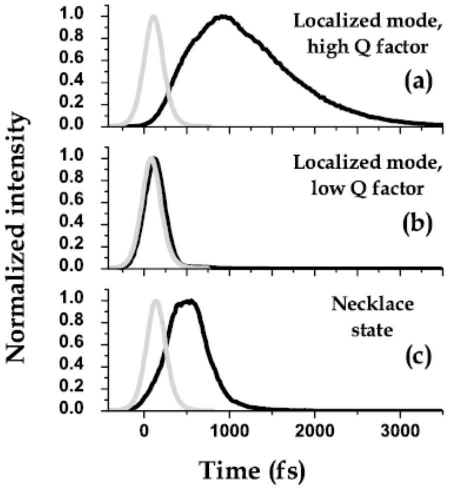

Figure 17. Top panel: calculated intensity distribution inside the sample. The internal resonances are localized modes. In rare occasions multiple resonances couple and lead to extended necklace modes. A 4-resonance necklace state can be observed around λ=1855 nm. Bottom panel: Transfer-matrix calculation of the transmission of a short laser pulse. Dashed curves: localized modes with high (dot-dashed) and low (dashed) Q factor. Solid lines: necklace states, with two and four resonances. The refractive indices and pulse duration were taken equal to the experimental values.

Figure 18. Time-resolved transmission data. In (a) and (b) a localized mode is probed, with high, respectively, low Q factor. In (c) a nearly symmetric pulse shape is observed that exhibits a fast decay time and a relatively large delay, typical for a multiple-resonance necklace state. Sample thickness: 250 layers. Gray curves: instrumental response (cross correlation between probe and gate), corrected for the trivial delay introduced by the effective refractive index $n_{eff}=(d_A n_A + d_B n_B)/(d_A+d_B)$ of the sample.

The necklace transmission peaks are non-Lorenzian since they are inhomogeneously broadened. Transmission peaks due to localized modes, on the other hand, are spectrally narrow and have a Lorenzian lineshape. A clear signature of necklace states can be expected in time-resolved experiments. The Lorenzian line-shape associated to a localized mode will give rise to an asymetric time-response with exponentially decaying tail. This is the typical time-response of a single resonance and its quality factor (Q-factor) will determine the delay of the pulse and exponential decay time (Fig. 17 and 18). The time-response of a necklace state will be different since the mode consists of several coupled resonances. This leads to a time response that is symmetric and strongly delayed, with a delay time determined by the number of resonances (Fig. 17 and 18).

Optical bistability

Capillary condensation of vapour into the pores of an optical superlattice can be used as a mechanism to induce optical bistability (12). The idea is sketched in Fig. 19. An optical superlattices is grown with a Δδ such that resonant Zener tunneling of the light can be observed. A weak probe beam is measuring the transmission spectrum of the sample exposed to a vapor flow. Capillary condensation of the vapor in the pores occurs which causes a detuning out of the resonance condition of the optical superlattice (Fig. 19 a). Transmission is low due to the decoupling of the two WSL structures. Once an energetic laser is used (Fig. 19b), the light is absorbed by the porous silicon, this heats up the sample and causes the evaporation of the condensed gas from the pores which in turn changes the refractive index of the layer recovering the resonant Zener tunneling situation. Transmission is now high.

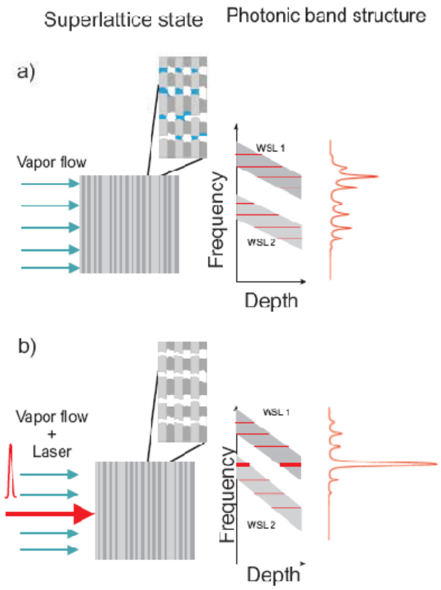

Figure 19. Environment-dependent optical modulation of the photonic band structure in porous optical superlattices. (a) Under vapor exposure, capillary condensation induces the formation of a liquid phase in the pores. The resulting refractive index modification prevents the Wannier-Stark ladders (WSL 1 and 2) to couple, leading to low transmission. (b) Laser-induced evaporation restores the resonant coupling between the Wannier-Stark states and allows to recover the Zener transmission channel.

If a signal light is finely tuned to the wavelength of the Zener resonance and its intensity is increased while the sample is exposed to a vapor flow, the curve shown in Fig. 20 is measured. For low input power, the transmission power is low since the condensation of vapor detuned the Zener structure. At a given power (P_{th1}), heating is so high that evaporation occurs and the Zener resonance conditions is recovered. Transmission power is now high and increases for further increase of the input power. If the input power is now gradually decreases from high values, the sample stays in a high transmission state down to a given power threshold (P_{th2}) where condensation of the vapor occurs. At this threshold the structure is detuned and transmission turns down to low values (Fig. 20). Since the two thresholds for evaporation and condensation occur at different input power levels, the in-out power transmission show an hysteresis, i. e. the behavior is bistable (12,13).

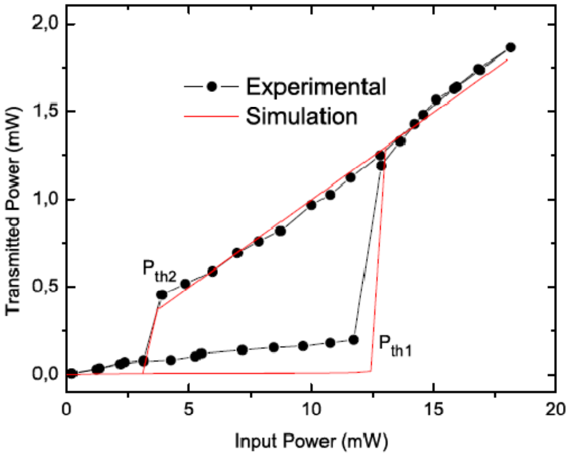

Figure 20. Bistable transmission of a porous optical superlattice exposed to an organic vapor flow. At low power the incident laser being is mainly reflected. Above a certain power threshold (P_{th1}), the transmitted power abruptly increases. This high transmittivity state is stable upon decreasing the incident power. Under a second threshold (P_{th2}), the superlattice switches back to the low transmission state. (line) Simulated bistable transmission curve.

Conclusions

In this paper we have demonstrated that porous silicon coupled microcavities are a suitable tool to study several new phenomena where the light propagation in one dimension is strongly affected by the variation of the photon mode density. Porous silicon has thus other interesting applications in addition to the more standard one in light emission and sensing.

Acknowledgments

We acknowledge a number of friends who collaborate with us in this fascinating research, their names appear in the literature. In particular we wish to acknowledge collaboration and friendship with L. Dal Negro, C. J. Oton, Z. Gaburro, D. Wiersma and L. C. Andreani.

References

1. L. Dal Negro, C. J. Oton, Z. Gaburro, L. Pavesi, P. Johnson, A. Lagendijk, R. Righini, M. Colocci, and D. S. Wiersma, *Phys. Rev. Lett.* **90**, 055501 (2003)
2. M. Ghulinyan, C. J. Oton, Z. Gaburro, P. Bettotti, and L. Pavesi, *Appl. Phys. Lett.* **82**, 1550 (2003).
3. M. Ghulinyan, C. J. Oton, G. Bonetti, Z. Gaburro, and L. Pavesi, *J. Appl. Phys.* **93**, 9724 (2003).
4. R. Sapienza, P. Costantino, D. Wiersma, M. Ghulinyan, C. J. Oton and L. Pavesi, *Phys. Rev. Lett.* **91**, 263902 (2003).
5. M. Ghulinyan, C. J. Oton, L. Dal Negro, L. Pavesi, R. Sapienza, M. Colocci, and D. Wiersma, *Phys. Rev. B* **71**, 094204 (2005).
6. J. Bertolotti, S. Gottardo, D. S. Wiersma, M. Ghulinyan, and L. Pavesi *Phys. Rev. Lett.* **94**, 113903 (2005)
7. M. Ghulinyan, C. J. Oton, Z. Gaburro, L. Pavesi, C. Toninnelli and D. Wiersma *Phys. Rev. Lett*. **94**, 127401 (2005).
8. E. Lorenzo, C. J. Oton, N. E. Capuj, M. Ghulinyan, D. Navarro-Urrios, Z. Gaburro, L. Pavesi, *Appl. Optics* **44**, 5415 (2005).
9. M. Ghulynian, M. Galli, C. Toninelli, J. Bertolotti, S. Gottardo, F. Marabelli, D. S. Wiersma, L. Pavesi and L. C. Andreani, *Appl. Phys. Lett.* **88**, 241103 (2006).
10. M. Ghulinyan, Z. Gaburro, D. S. Wiersma and L. Pavesi, *Phys. Rev. B* **74**, 045118 (2006)
11. J. Bertolotti, M. Galli, R. Sapienza, M. Ghulinyan, S. Gottardo, L. C. Andreani, L. Pavesi, and D. S. Wiersma *Phys. Rev. E* **74**, 035602 (R) (2006).
12. P. Barthelemy, Mher Ghulinyan, Z. Gaburro, C. Toninelli, L. Pavesi, and D. S. Wiersma Nature Photonics **1**, 172 (2007).
13. Z. Gaburro, M. Ghulinyan, L. Pavesi, P. Barthelemy, C. Toninelli, and D. Wiersma, *Phys. Rev. B***77**, 115354 (2008).

ECS Transactions, 16 (3) 323-328 (2008)
10.1149/1.2982571 ©The Electrochemical Society

Stain Etching with Ferric Ion to Produce Thick Porous Silicon Films

M. E. Dudley [a, b] and K. W. Kolasinski [a]

[a] Department of Chemistry, West Chester University, West Chester, PA 19383 USA
[b] Current address: Department of Chemistry and Biochemistry, University of California
San Diego, La Jolla, CA 92093, USA

Stain etching of silicon in aqueous solutions composed of $FeCl_3$ + HF + concentrated (HCl, $HClO_4$ or H_2SO_4) leads to brilliantly luminescent porous Si with a unique dual layer structure. The upper layer (~2 µm or more thick) exhibits bluer luminescence (peaked at 520–590 nm). The lower layer exhibits redder luminescence (peaked at 630–660 nm). The peak PL wavelength and the PL intensity both depend strongly on the excitation wavelength. Photoluminescence excitation (PLE) spectroscopy indicates that the upper and lower layers are distinct because the PLE spectra of the two layers are different. Additionally, we demonstrate that two completely new stain etchants can produce visibly luminescent microporous silicon: V_2O_5 dissolved in HF(aq) and CeF_4 dissolved in H_2SO_4(aq). In all cases bubble formation is suppressed and layer homogeneity greatly exceeds that obtained with nitrate based stain etchants.

Introduction

Stain etchants are composed of an oxidant in an acidic fluoride solution (1). Nahidi and Kolasinski (2) proposed that the role of the oxidant is to initiate etching by injection of a hole into the silicon valence band rather than to oxidize the surface as proposed by Turner (3). The first requirement for an oxidant, therefore, is that it has a sufficiently positive electrochemical potential so that it is lies below the valence band maximum and can accept electrons from (inject holes into) the valence band. Based on this premise they predicted that a number of oxidants should be usable in stain etchants and demonstrated that both permanganate and the ferric ion (Fe^{3+}) are capable of facilitating the formation of visibly photoluminescent porous silicon (por-Si) thin films. Furthermore, since these oxidants do not release a gas upon reduction (unlike nitric acid), the films they produce are highly uniform in both thickness and porosity. The ferric ion was found to be particularly adept at making uniform films; however, the solutions used often exhibited a long initiation time before the onset of film growth.

In this report we demonstrate that Fe^{3+}/HF stain etchants are stabilized and enhanced by the addition of concentrated acids such as HCl, $HClO_4$ and H_2SO_4. Addition of these acids significantly reduces both the duration and variability of the initiation time. They also (when air is excluded from the etchant) allow for the formation of thick (approaching and sometimes exceeding 10 µm) photoluminescent layers with a unique new structure. Etch times exceeding 3 h can lead to green photoluminescence (PL) rather than the red/orange PL normally associated with stain etching. In addition, we demonstrate that two of the other oxidants predicted to work by Nahidi and Kolasinski do indeed form uniform por-Si films. V_2O_5/HF solution form visibly photoluminescence films extremely rapidly with essentially no initiation time. CeF_4 dissolved in H_2SO_4 forms film more slowly. Bubble formation is suppressed in both cases and films with mirror finishes and uniform color are produced in both cases. The films produced with the ceric ion (Ce^{4+}) are the most uniform observed yet. However, with short etching times (≤ 45 min) these films are not luminescent. Only with extended etching times (several hours) or prolonged exposure to air do these films become photoluminescent.

Experimental

All solutions were aqueous and all etching for Fe^{3+} and V^{5+} was performed at room temperature. Etching with Ce^{4+} was performed at temperatures between 0° and 75°C. The three oxidants were introduced by the addition of (i) $FeCl_3 \bullet 6H_2O$ to provide Fe^{3+}, (ii) V_2O_5 to produce V^{5+}, or (iii) CeF_4 dissolved in H_2SO_4 to produce both Ce^{4+} as well as fluoride species such as F^-, HF and HF_2^-. For etchants (i) and (ii) fluoride is supplied from 48% HF. When added, concentrated $HClO_4$, HCl, and H_2SO_4 were used. All etchants are aqueous. We only tested the effects of concentrated acid on the Fe(III) based etchants. Therefore, to simplify our notation we refer to $FeCl_3 \bullet 6H_2O$ + 48% HF as the Fe(III) etchant; $FeCl_3 \bullet 6H_2O$ + 48% HF + concentrated $HClO_4$ as Fe(III) + $HClO_4$ or simply $HClO_4$ etchants, etc. The etchant to which V_2O_5 was added is referred to as the V-based etchant and the etchant made from CeF_4 is the Ce-based etchant. After etching the samples are rinsed several times, first in water then methanol or ethanol. Critical point drying is performed in a Tousimis AutoSamDri 815 critical point drier with ethanol as the initial liquid solvent being replaced by a supercritical fluid of ethanol and CO_2. For long etch durations, the sample is placed in a Teflon jig, which only exposes the front side of the crystal to the solution. Si(001) wafers (*p*-type) were cleaved into 1 cm^2 pieces and then ultrasonically cleaned in acetone and methanol before being rinsed in water and then etched.

Scanning electron microscopy (SEM) was performed with an FEI Quanta 400 ESEM, at a voltage of 2–15 kV with a working distance of 8–15 mm. The highly porous upper layer exhibits strong charging effects; therefore imaging was usually performed in a background of ~100 Pa of water in an environmental SEM mode. The SEM operates with integrated Oxford INCA energy dispersive X-ray spectroscopy (EDS). Photoluminescence (PL) and PL excitation (PLE) spectroscopies were performed on a Cary Eclipse fluorescence spectrometer, with slit widths set for 5 nm resolution and filtering on both the emission and excitation. PL peak position are determined by fitting the top of the peak to a Gaussian profile and are reported as the center of the resulting Gaussian fit. While PL spectra were observed to change over the course of several hours of air exposure or several minutes of UV exposure, they do not change over the course of the time scale of a minute or so required to acquire a single spectrum.

Results and Discussion

Etchants Containing Fe^{3+}

The standard electrochemical potential, E_0, (4) of the ferric/ferrous ion couple is

$$\mathrm{Fe}^{3+} + e^- \rightarrow \mathrm{Fe}^{2+} \qquad E_0 = 0.770\ \mathrm{V}\,. \tag{1}$$

This value, of course, depends on the ionic strength and composition of the solution and can only be used as a rough guide in the highly concentrated solutions used here. Nonetheless, we expect that only redox couples with E_0 close to or more positive than this value are good candidates for the formation of efficient stain etchants. As an example,

E_0 of Fe^{3+} in 1 molar H_3PO_4 is only +0.438 V and we have found that the addition of concentrated phosphoric acid to Fe^{3+} + HF leads to little if any por-Si production.

Stain etching of silicon in solutions composed of $FeCl_3$ + HF + concentrated (HCl, $HClO_4$ or H_2SO_4) leads to highly luminescent por-Si with a unique dual layer structure and shown in Fig. 1. This structure is only observed if the etch duration is extended to ≥3 h. This dual layer structure can also be obtained in Fe(III) + HF; however, it develops much more slowly and requires several more hours to form.

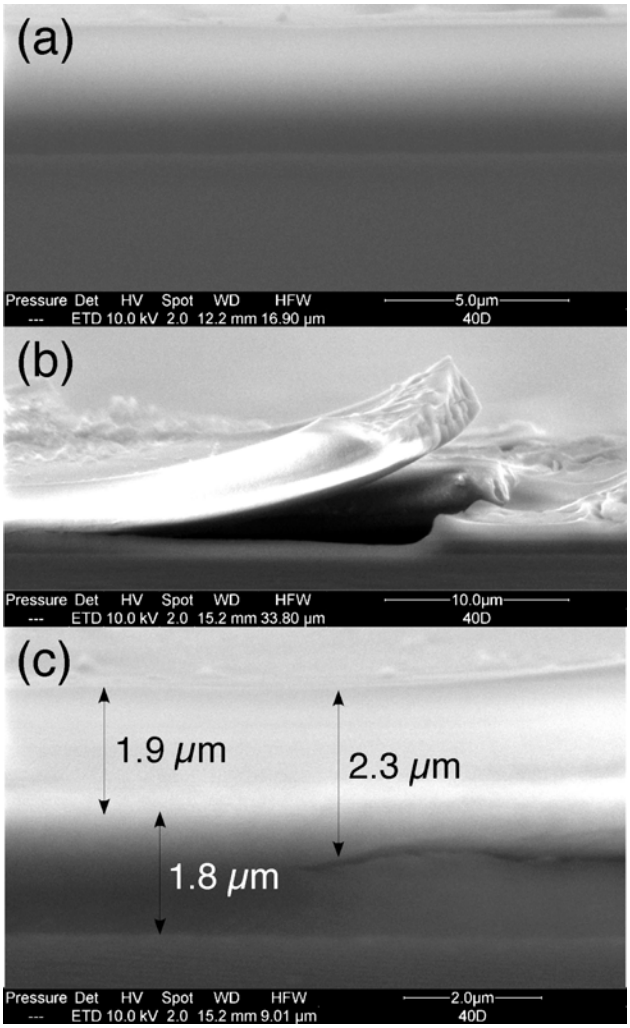

Figure 1. Cross sectional scanning electron micrographs of a por-Si film produced by etching in 1.37 g $FeCl_3 \bullet H_2O$ + 3 mL $HClO_4$ + 7 ml HF for 27 h. (a) After critical point drying in CO_2/ethanol mixture. (b) Exfoliation of top layer caused by soaking the sample in ethanol/water mixture and then drying in air. (c) Expanded view of the cracked region where exfoliation terminates.

Figure 1(a) exhibits a cross sectional micrograph of a film etched in the $HClO_4$ etchant and then processed with critical point drying. The film has a shiny bronze appearance before and after drying. Next in Fig. 1(b) we see the result of placing a drop of water/ethanol mixture on the film and allowing it to drying in air. Ethanol was added to the water to facilitate the infusion of water into the pores. The capillary forces formed in the nanopores upon drying cause the film to exfoliate. In Fig. 1(c), we follow the crack back to its origin and can see that the entire film is not exfoliated. Instead, the top 2.3 µm have separated from the bottom 1.4 µm. We suggest that the upper layer of the film is mechanically less stable because it has a higher porosity than the bottom layer. Preliminary TEM images indicate that the nanopores may be as small as 3 nm in diameter. Based on the work of Canham and Bellet (5) for determining the critical thickness for cracking during drying, we can estimate that the minimum porosity of the upper layer is above 80%.

Film uniformity (as indicated by the uniformity of film color observed with white light as well as the homogeneity of PL intensity and color under UV irradiation) is greatly enhanced by exclusion of air by filling the etch container with Ar. For these very long etch times, bubble formation is observed at the cleaved edges of the crystal and the unpolished backside of the crystal (if exposed to the solution) but very few if any bubbles form on the front face of the crystal. All three acids (HCl, $HClO_4$ and H_2SO_4) lead to more stable and reproducible etchants than Fe^{3+} in HF alone; however, a precipitate tends to form when etching is carried out for ≥4 h in $HClO_4$. Upon addition of any of these three acids, the initiation time is reduced below 5 min. Of the three, H_2SO_4 has the shortest induction period, usually <1 min. Frequently, the initiation of por-Si formation in H_2SO_4 etchants is remarkable uniform across the entire surface as demonstrated by a uniform color change across the whole wafer. More commonly and especially in the other etchants, a color change begins in one part of the crystal and then sweeps across the remainder.

As shown in Fig. 2, the top and bottom layers are optically distinct, exhibiting different PL spectra. Consistent with the proposition that the top layer has a higher porosity, the PL from the upper layer is blueshifted compared to the PL of the bottom layer. As the etch duration is extended beyond 3 h, the PL of the top layer continues to blueshift until its peak value gets as low as 520–530 nm, at which point the blueshift saturates. Green PL is stable (at least for a period of 2–3 days) as long as the sample remains in water. However, upon exposure to air, the green PL fades over a matter of tens of minutes. A short burst of ultrasonic radiation or wiping with a tissue efficiently removes the upper layer to reveal the red-orange emitting lower layer. The red-orange PL is more robust and some samples remain brightly photoluminescent for months.

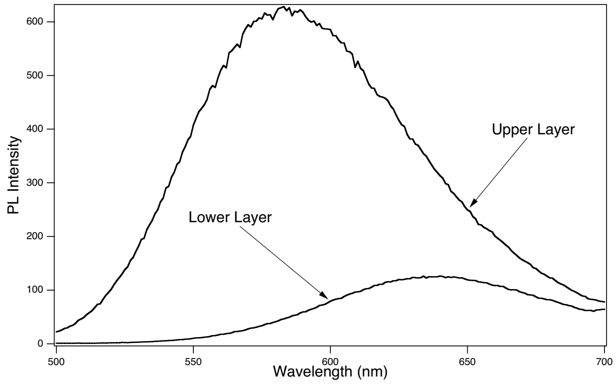

Figure 2. Photoluminescence excited with 350 nm light from the upper and lower porous layers. The film was produced by etching in 1.65 g $FeCl_3 \bullet H_2O$ + 3 mL $HClO_4$ + 7 ml HF for 5 h, dried in Ar.

The PL peak from the lower layer behaves much like what is observed at shorter etch times. Thus, we speculate that there are two reactions occurring in the stain etchant. The first is the conventional stain etching reaction, which forms por-Si as described by Nahidi and Kolasinski (2). The second reaction is a much slower chemical reaction that gradually increases the porosity and blueshifts the PL spectrum. The second reaction is similar to the reaction suggested by Canham (6) in his original report of visible PL from high-porosity por-Si. Canham used a 6 h quiescent reaction in 40% aqueous HF to obtain visible PL in anodically etched por-Si. If the mechanism of dual layer structure formation is that of two competing reactions with different rates and with the ability to produce correspondingly different minimum size silicon nanostructures, then our films might possess a porosity gradient from low at the bottom to high at the top. It is unclear whether this gradient is abrupt, as suggested by Fig. 1, or whether it is gradual. Nonetheless, the mechanical instability of the upper layer lends itself to facile production of copious quantities of photoluminescent, nanocrystalline porous silicon powder.

Etchants Containing V^{5+}

The standard electrochemical potential (4) for the VO_2^+ redox couple is

$$\mathrm{VO_2^+} + 2\mathrm{H}^+ + e^- \rightarrow \mathrm{VO}^{2+} + \mathrm{H_2O} \qquad E_0 = 1.00\ \mathrm{V}. \tag{2}$$

Vanadium pentoxide dissolves in HF to form the V(V) oxidation state as VO_2^+. By adding 0.14 – 0.28 g of V_2O_5 to 10 ml HF, we created extremely active stain etchants. Initiation was essentially instantaneous and uniform films in the absence of bubble formation were produced in 5 – 45 s. The PL spectrum in Fig. 3(a) has a peak at 595 nm. The PL from samples etched in V-based etchants was extremely robust and the spectrum changed little over the course of months. The samples had mirror finishes and rather uniform color and PL when etched for short times. Etching for longer times (>45 s), the films seemed to overetch, becoming thinner and less uniform.

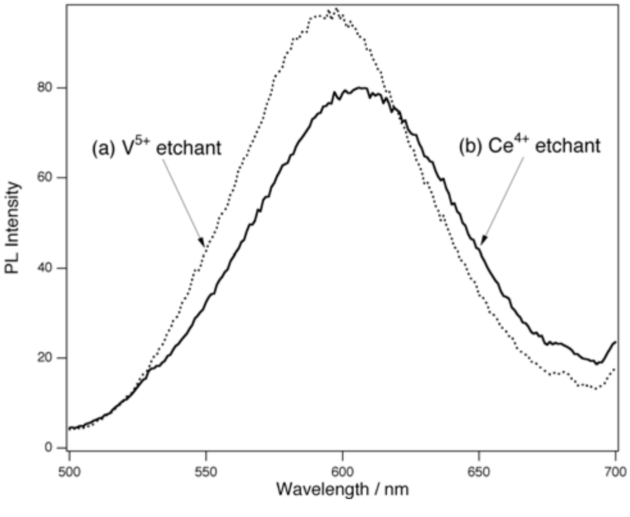

Figure 3. (a) PL spectrum observed from a film etched in 0.25 g V_2O_5 in 10 ml HF for 30 s. The spectrum was taken 2 months after the film was produced and was excited by 250 nm light. (b) PL spectrum of a film etched for 18 h in 0.5 g CeF_4 + 5 ml H_2SO_4 + 5 ml H_2O. The spectrum was excited by 350 nm light.

Etchants Containing Ce^{4+}

The standard electrochemical potential (4) for the Ce^{4+}/Ce^{3+} redox couple is

$$\mathrm{Ce}^{4+} + e^{-} \rightarrow \mathrm{Ce}^{3+} \qquad E_0 = 1.44\ \mathrm{V}. \tag{2}$$

Thus, cerium in its IV oxidation state has a sufficiently positive electrochemical potential to inject holes into Si. However, it precipitates as an insoluble fluoride when added to HF. Therefore, we added 0.5 g CeF_4 to 5 ml H_2SO_4 + 5 ml H_2O. The yellow color formed upon mixing is an indication that Ce^{4+} is liberated into solution. The acidity of the solution forms a range of fluoride species from the liberated F^- ions, which must provide the driving force for dissolution. Very little of the CeF_4 dissolves and some solid remains on the bottom of the beaker. We investigated etching with the solution held in an isothermal bath at 0°, 25°, 35°, 45°, 55°, 65° and 75°C. Etching was observed at all temperatures. It is somewhat slower at 0°C and the range 25 – 55°C appears to be optimum. Even for etch durations as long as 45 min no evidence of bubble formation is seen on the front face of the crystal.

The resulting films for etch times of 5 – 45 min are the most uniform with the deepest, richest colors of any that we have seen. The upper surface has a mirror finish. The color even tends to be quite uniform on the back (unpolished) side of the crystal, which is in contact with the undissolved CeF_4. For these short etch times the samples are not photoluminescent after drying. Samples develop PL after being exposed to air for a day or more. When the samples are left to etch overnight, the samples exhibit robust photoluminescence. The PL spectrum in Fig. 3(b) has a peak at 605 nm.

Conclusions

New formulations of stain etchants can lead to a variety of more reproducible outcomes than can be had with standard nitric acid based stain etchants. For thick films and porous powder formation, long duration etching in Fe^{3+}/HF/(HCl or H_2SO_4) is preferred. These can also lead to green photoluminescent films. The fast film formation with robust visible PL is found with V-based etchants. The most uniform films are created with Ce-based etchants.

Acknowledgments

This work was supported by West Chester University, the Center for Microscopy Research and Training at WCU and the expert technical assistance of Frederick Monson.

References

1. K. W. Kolasinski, *Curr. Opin. Solid State Mater. Sci.* **9**, 73 (2005).
2. M. Nahidi and K. W. Kolasinski, *J. Electrochem. Soc.* **153**, C19 (2006).
3. D. R. Turner, *J. Electrochem. Soc.* **107**, 810 (1960).
4. R. C. Weast (Ed.), *Vol. 60*, CRC Press, Boca Raton, Florida, 1980.
5. D. Bellet and L. Canham, *Adv. Mater.* **10**, 487 (1998).
6. L. T. Canham, *Appl. Phys. Lett.* **57**, 1046 (1990).

ECS Transactions, 16 (3) 329-336 (2008)
10.1149/1.2982572 ©The Electrochemical Society

Electrical Properties of Meso-Porous Silicon: from a Surface Effect to Coulomb Blockade and More

L. Boarino, S. Borini and G. Amato

Electromagnetic Division, Nanotechnology and Quantum Devices Laboratory,
Istituto Nazionale Ricerca Metrologica
Strada delle Cacce, 91 – 10135 Turin, Italy

Since the Volker Lehmann’s paper “Resistivity of Porous Silicon: a surface effect” published in 1995, a great deal of effort has been produced in understanding the basic mechanisms ruling the electron transport in Si mesostructures and how these phenomena are affected by external environment. After more than 10 years, new experimental evidences and physical insights have been obtained, like gas sensitivity, chemisorptions phenomena, Coulomb blockade and glassy dynamics at room temperature, but reading that former paper, the feeling of an extraordinary comprehension and intuition of the physical phenomena occurring in this fascinating material is continuously accompanying the reader.
A review of these major results in studying electronic transport in mesoporous silicon will be reported, starting from the still valid intuitions of Volker Lehmann in his paper.

Introduction

In the first half of the ‘90s, the most studied porous silicon morphology was from high resistivity p-type wafers, because of the high luminescence efficiency. The former studies on electrical and transport properties of nano[i] and mesoporous[ii] silicon (mesoPS), revealed a resistivity of the porous layer of few orders of magnitude higher than the original substrate. The models proposed to explain these first results were based on quantum confinement[iii] and on the dielectric constant variation[iv], but they where strictly applicable to luminescent, confined structures, rather than to mesoporous silicon from highly doped silicon. The Lehmann’s paper on electrical properties of porous silicon from p+ doped wafers, addressed few unanswered crucial questions regarding resistivity, impurity role, carrier freeze out and surface conditioning, proposing a microscopic model of transport in mesoPS, in which also in a broader size distribution, typically a log-normal between 4 and 12 nm[v], where quantum confinement is not observed, the effect of trapped charges at surface and the interaction of single charges result in a blocking of conduction mechanisms.

High resistivity of mesoPS

One of the most inspiring idea of the Lehmann’s paper is the analogy of mesoporous silicon structures to submicron channels of CMOS devices, whose figures of telegraph noise are due to single charge trapping at the oxide-semiconductor interface. Telegraph noise is a screening effect manifesting in submicron CMOS channels, ascribable to the capture and emission from a trap at the silicon-oxide interface in gate region, so blocking part of the channel to electrical conduction. A parallel with silicon nanowires in a mesoporous structure was proposed, in which charged surface traps could block conduction pathways by Coulomb repulsion.

Another evidence in support of this hypothesis was the almost complete transparence to IR light of the material after etching, while in the original form the highly doped substrates are opaque, due to the absorption from free carriers. So, an interesting question was, like Polissky et al.[vi] titled in one of their papers: “Boron in mesoporous Si - Where have all the carriers gone?”

In this work the authors proposed, on the basis of detailed ERDA and SIMS studies, that despite the electrical and optical evidence of complete absence of free carriers, the Boron is still present after etching, the electrochemical process does not selectively remove these impurities, (vice versa at high porosities the boron content increases respect to silicon atoms) so the most plausible explanation resides in the presence of saturated dangling bonds. These centers, also called Pb centers[vii] have been observed by Electron Spin Resonance (ESR) by different groups[viii,ix] and could be the responsible of the high resistivity of mesoporous silicon. These authors also proposed a mechanism affecting the PS formation and morphology, in which boron impurities remain passivated in near-surface sites, while the etching proceeds removing silicon atoms not in vicinity of impurities. This picture could also justify the different size distribution of crystallites in mesoPS.

Surface effects

To validate his model, Lehmann also focused his attention on the interaction between mesoPS and environment, in particular in polar gases and liquids, like water and ethanol[iv,x]. The condensation of these two vapors or the direct immersion in these two liquids give origin to an increase of conductivity, explained by Tsu and Babic[xi] in terms of an increase of effective dielectric constant. The interaction with liquid ethanol was then addressed by a detailed study of Timoshenko[xii].

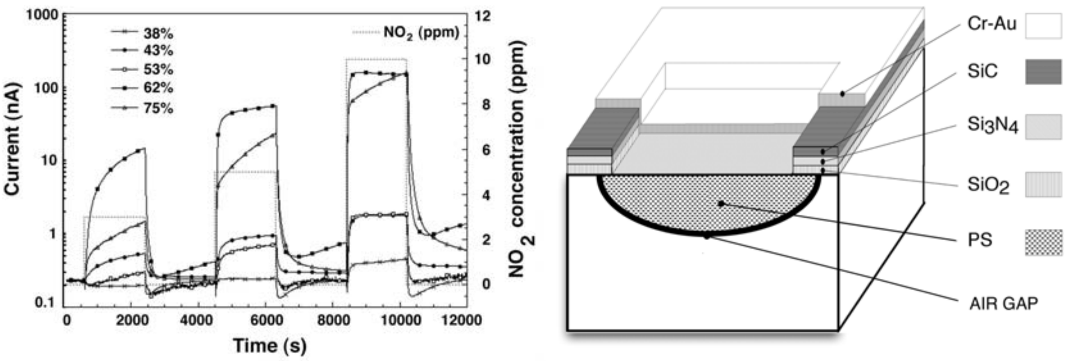

Figure 1. Left: electrical response to controlled concentrations of NO_2 (3, 5, 10 ppm) of one of the former group of mesoPS sensors as a function of time and plotted for increasing porosities. Right: the fabrication scheme of a front-side micromachined mesoPS sensor.

In the same period, the first report of a sensitivity of PS to NO_2 appeared in literature, by Harper and M.J. Sailor[xiii]. They were using n type nanoporous silicon obtained by front illumination, but the effect of exposure to nitrogen dioxide was not reversible.

MesoPS and nitrogen dioxide

In 1999, a strong interaction between mesoporous p+ silicon was announced in Strasbourg, EMRS by our group[xiv]. Volker Lehmann was chairman of that session, and he was sincerely interested in the electrical and infrared striking response of this material to nitrogen dioxide.

In Fig.1 (left) the current response of different porosity samples of mesoPS, contacted by chromium gold pads in planar configuration, is shown, plotted versus exposure time. The right axis reports the NO_2 concentration, and the thin continuous line refers to the different gas dosage in the chamber. The samples were constantly biased at 5 V.

The response appears to be related to specific surface through porosity, with a maximum around 62%, as reported by previous studies[xv], but our feeling already in that period was that structures dimension are more meaningful than porosity. The response to gas was anyway impressive, more than one order of magnitude in current variation for 1 ppm of NO_2, a sensitivity never reported with any other gas or liquids. Another striking feature of the data was the response time, composed of a sharp and quick response on the rising front, and a slower component, never reaching stability or saturation in the flat part of the step. Also during gas evacuation, a peculiar and undesired drift in response was observed on the visualized time scale.

While a technological CMOS compatible process was easily proposed in 2001[xvi] for the front-side fabrication of a porous silicon NO_2 sensor, with a new record in sensitivity obtained by means of a self-suspended membrane of PS (Fig. 1, right), the origin of such a high sensitivity, was still unclear. The active element, mesoPS, was obtained opening a window in the passivation layers, then performing electrochemical etching for mesoPS formation, and stopping the etching with few seconds of high

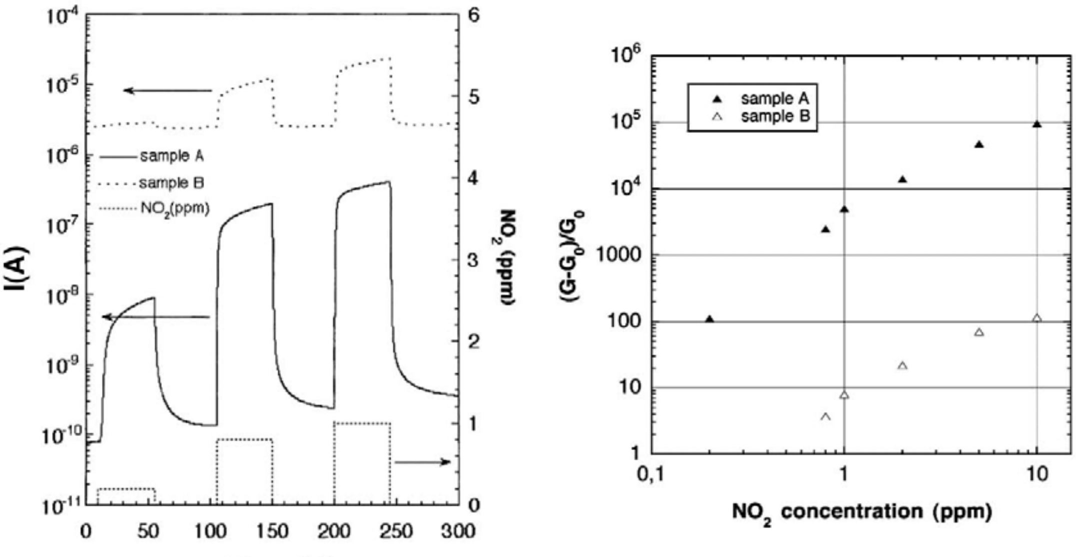

Figure 2. Left: electrical response vs time of a front-side micromachined NO_2 sensor for NO_2 dosage of 200, 800 ppb and 1 ppm. Right: comparison between the electrical response of a suspended membrane PS sensor and a PS layer still attached to crystalline substrate is shown, for NO_2 concentrations ranging from 200 ppb (alarm level for EU legislation) to 10 ppm.

current density, working in electropolishing regime. A mesoporous membrane was so obtained, sustained by the passivation layers, also thanks to the under-etching.

In Fig.2, the electrical response of a front-side micromachined NO_2 sensor is presented. The comparison between the electrical response of a suspended membrane PS sensor and a PS layer still attached to crystalline substrate is shown, for different NO_2 concentrations ranging from 200 ppb (alarm level for European legislation) to 10 ppm.

More than two orders of magnitude in relative conductance $(G-G_0)/G_0$ in presence of 1 ppm of NO_2 are obtained respect to the normal configuration. These first indications on the response of freestanding and electrically insulated structures were important to improve the device performances, but the origin of the reactivity was still unclear.

FTIR studies

In conjunction with the investigation on the electrical properties, in-situ IR spectroscopy was carried out, revealing another impressive feature of the interaction phenomenon. The FTIR spectra of freshly prepared mesoPS have been widely reported in literature[xvii], and the major characteristics were well known, but a study on the spectral evolution in controlled environment was still lacking. The first FTIR measurements of fresh meso PS in presence of NO_2 were impressive, since a featureless absorption, characteristic of a loss of transparency of the sample, occurred at NO_2 exposure, with an almost fully reversible effect during gas evacuation. The typical spectral features related to $Si-H_x$ stretching and SiO-H modes were not apparently affected by this dramatic optical response. The behavior is visible in Fig. 3, where the solid line 1 is the spectrum of the fresh sample in vacuum, the dashed line 2 is the spectrum in presence of 1 Torr of pure NO_2, and the dotted line 3 has been acquired after gas evacuation. It is interesting, and not yet understood, the complete return to initial conditions (curve 1) only after exposure to air.

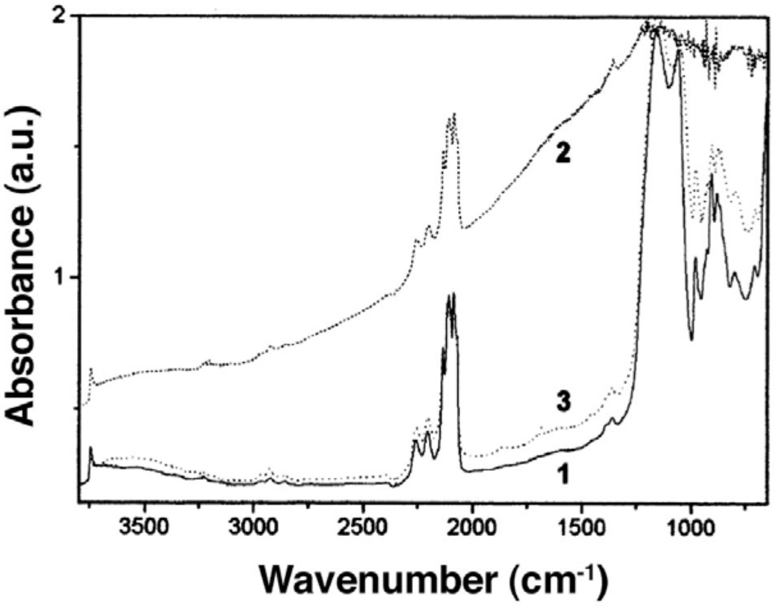

Figure 3. FTIR spectra of mesoPS exposed to nitrogen dioxide. The solid line 1 is the fresh sample in vacuum, the dashed line 2 is in presence of 1Torr of pure NO_2, and the dotted line 3 has been acquired after gas evacuation.

This loss of transparency was immediately attributed to the optical absorption of free carriers, in some way reactivated by interaction with nitrogen dioxide, whose electron affinity is rather high (2.2 eV) respect to other gases and molecules.

Then, the following years were devoted to a fundamental study of mesoporous silicon in interaction with gas, by means of IR spectroscopy[xviii][xix], ESR[xx], NMR and ab-initio calculations,[xxi][xxii] in order to understand the basic mechanisms at the origin of such an impressive optical and electrical response to nitrogen dioxide and also ammonia, another probe gas capable to easily donating an electron, and the role of impurities and morphology in these phenomena.

Other techniques and results

Since our former paper of 1999, other groups contributed to study the NO_2 interaction with detailed papers on IR spectroscopy and Drude effect due to free carriers restored by nitrogen dioxide[xxiii] and obtaining new records of sensitivity[xxiv] (15 ppb in dry air).

The main results of this period of fundamental investigations were the following[21]:

- meso Porous Silicon is by the electrical point of view, a near-insulator and becomes either a p- or an n-type semiconductor upon gas adsorption (NO_2 and NH_3)
- the interaction with these two probe gases is stronger than those typical of polar gases and liquids, and it can be well represented by an adsorption isothermal characteristic of a chemisorption mechanism
- The effect of free carriers deactivation/reactivation is reversible at low concentration of these two gases, and it's not due to a changing in coordination of the boron impurities at the mesostructure surface.

Electrical anisotropy and Coulomb Blockade

Since 2005, our work continued focusing the investigation on electron transport phenomena in mesoPS in interaction with probe gases. Thanks to new experimental set-ups, new aspects of the complex phenomena were understood and demonstrated.

The experimental setup shown in the inset of Figure 4, allowed the demonstration of electrical anisotropy in p+ mesoPS morphology[xxv], only demonstrated, in the same period, for (110) wafers by Timoshenko et al.[xxvi], and always given as an assumption, but never measured and separated in two different contributions, longitudinal (I_L) and transversal (I_T) to the (100) direction.

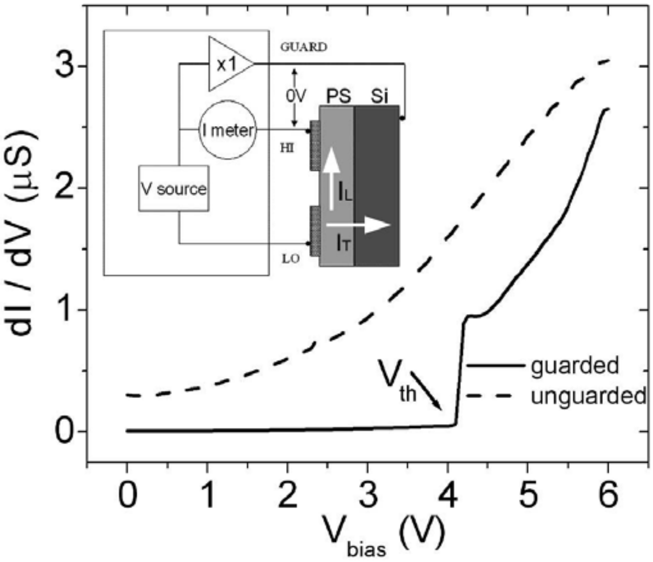

Figure 4. Differential conductance of a mesoPS sample (60% porosity). A gap characterized by a threshold voltage is clearly visible. When the guard is removed, the gap disappears.This is related to the structural anisotropy of mesoPS. The inset shows the measurement configuration.

As depicted in the scheme of Fig. 4, when a bias voltage is applied between the coplanar contacts, the measured current I is given by the sum of the longitudinal current I_L crossing mesoPS from one pad to the other, i.e., parallel to the (100) plane and the leakage current I_T, unless the backside contact is used as guard electrode. In the latter case, the same potential is kept on the backside contact and on one planar contact, so that no current flow occurs between them.

Measuring the samples in both the configurations is possible to separate the different conductivity contributions in the case of a strongly anisotropic material like p+ mesoporous silicon.

The room temperature conductivity in the transverse direction appears to be already percolated, while the longitudinal direction appears to be strongly inhibited. This difference disappears with increasing the temperature, with a longitudinal conductivity rise of orders of magnitude. The strong electrical anisotropy measured in this material gives a further confirmation of the former results of increased sensitivity in the suspended PS membranes of 2001[xvi].

Furthermore, all the mesoPS samples under investigation showed, in guard electrode configuration, the presence of a sharp threshold voltage V_{th} in the current–voltage (I–V) characteristics at RT. The typical gap in the conductance observed for a sample of 60 % porosity is shown in Figure 4. As the guard contact is removed, the threshold disappears, since the conductive pathways are restored again along the transversal direction, already percolated, and the bottlenecks constituted by small nanoconstrictions are easily bypassed.

Investigating the shape and dependence of the threshold voltage with temperature variation from room temperature to 200 K, it's been possible to understand the origin of the conductivity gap, identifying an increasing of the threshold values with decreasing temperature, and a power-law behavior for $V>V_{th}$ common to other metallic or semiconducting nanoparticle systems like Co nanocrystal superlattices[xxvii], Au nanocrystal arrays[xxviii][xxix], GaAs quantum dots[xxx], PbSe quantum dots[xxxi], C nanoparticle chains[xxxii], and polymer nanofibers[xxxiii].Moreover, such a behavior was theoretically predicted by Middleton and Wingreen (MW)[xxxiv] for the collective transport in arrays of small metallic dots.

Therefore, it was concluded that the conductivity gap could be due to the localization of positive charges in nanoconstrictions, which can inhibit , by Coulomb interaction, the hole current in the longitudinal direction, where the Si nanocrystals are poorly interconnected. Both T and NO_2 are able to detrap holes, thus opening conductive pathways. Such interpretation is strictly connected to the surface effect scenario proposed by Lehmann. Moreover, Coulomb blockade effects in the electrical transport in PS were taken into accoungt by Hamilton[xxxv] and coworkers in 2000, but never demonstrated before.

Finally, the most recent chapter of the story is the experimental observation of intriguing time-dependent charge transport phenomena, such as slow conductivity relaxation, nonergodicity, and simple aging at room temperature[xxxvi]. These phenomena have a deep impact on transport in mesoPS, and may affect the electrical response of the material to gases.

Conclusions

From the first electrical measurements in nitrogen dioxide atmosphere to now, a basic research activity on mesoporous silicon, its interaction with gases and its transport properties has been carried out. Chemisorption mechanisms, free carriers reactivation and doping by gaseous species, electrical anisotropy of <100> p+ porous silicon have been evidenced and demonstrated, and moreover, Coulomb blockade effects have been identified.

The Lehmann's deep intuitions, after 13 years from his paper on these topics, and 2 years from his early departure, still hold true, and new areas of investigation are emerging thanks to the deeper comprehension gained also thanks to his first indications.

References

---

i. T. Unagami, *J. Electrochem. Soc.* **127**, **476** (1980).

ii. M. I. J. Beale, J. D. Benjamin, M. J. Uren, N. G. Chew and A. G. Cullis, *J. Cryst. Growth*, **73**, 622 (1985).

iii. A. J. Read, R. J. Needs, K. J. Nash, L. T. Canham, P. D. J. Calcott and A. Qteish, *Phys. Rev. Lett.*, **69**, 1232 (1992).

iv. R. Tsu and D. Babic, *Appl. Phys. Lett.*, **64** 1806 (1994).

v. L.T. Canham, *Properties of Porous Silicon*, p. 106., edited by L. T. Canham, EMIS Data review series, INSPEC, (1997)

vi. G. Polisski, D. Kovalev, G. Dollinger, T. Sulima, F. Koch, *Physica B*, **273** 951 (1999)

vii. E.H. Poindexter, P.J. Caplan, B.E. Deal, R.R. Razouk, *J. Appl. Phys.* **1981**, 52, 879.

viii. H.J. von Bardeleben, D. Stievenard, A. Grosman, C. Ortega, J. Siejka *Phys. Rev. B* **1993**, 47, 10899.

ix. F. C. Rong, J. F. Harvey, E.H. Poindexter, G.J. Gerardi, *Appl. Phys. Lett.* **1993**, 63, 920.

x. M. Ben-Chorin, A. Kux and I. Schechter, *Appl. Phys. Lett.*, **64** 481 (1994).

xi. R. Tsu, D. Babic, *Appl. Phys. Lett.*, **64** 1806 (1994)

---

xii. V. Yu. Timoshenko, T. Dittrich, V. Lysenko, M. G. Lisachenko, and F. Koch, *Phys. Rev. B*, **64**, 085314 (2001)

xiii. J. Harper and M. Sailor, *Anal. Chem.*, **68**, 3713, (1996)

xiv. L. Boarino, C. Baratto, F. Geobaldo, G. Amato, E. Comini, A. M. Rossi, G. Faglia, G. Lérondel, G. Sberveglieri, *Materials Science and Engineering B*,**69-70**, 210 (2000)

xv. Lavoro superficie specifica-porositaà, Halimaoui Les Houches o INSPEC

A. Halimaoui, in *Porous silicon: material processing, properties and applications*, Les Houches, J.C. Vial, J. Derrien Eds., Les editions de physique Springer, pp. 33 (1994)

xvi. C. Baratto, G. Faglia, G. Sberveglieri, L. Boarino, A. M. Rossi, and G. Amato, *Thin Solid Films*, **391-392**, 261 (2001).

xvii. Y. Ogata, H. Niki, T. Sakka, M. Iwasaki, *J. Electrochem. Soc.*, **142**, 1595 (1995)

xviii. P. Rivolo, F. Geobaldo, M. Rocchia, et al., *Physica Status Solidi A*, **197**, 217 (2003).

xix. F. Geobaldo, P. Rivolo, M. Rocchia, et al., *Physica Status Solidi A,* **197,** 458 (2003) ,

xx. M. Chiesa, G. Amato, L. Boarino, E. Garrone, F. Geobaldo, and E. Giamello, *Angewandte Chemie Int. Ed.*, **42**, 5031 (2003)

xxi. S. Borini, P. Ugliengo, *Physica Status Solidi A-Applied Research*, **197** 436 (2003)

xxii. E. Garrone, F. Geobaldo, P. Rivolo, G. Amato, L. Boarino, M. Chiesa, E. Giamello, R. Gobetto, P. Ugliengo, A. Viale, *Advanced Materials*, **17,** 528 (2005)

xxiii. V.Y. Timoshenko, T. Dittrich, V. Lysenko, et al., *Physical Review B*, **64**, 8 (2001).

xxiv. L. Pancheri,C. J. Oton, Z. Gaburro Z, et al., *Sensors and Actuators B-Chemical*, **89**, 3, 237 (2003)

xxv. S. Borini, L. Boarino, and G. Amato, *Applied Physics Letters*, **89**, 132111 (2006)

xxvi. P.A. Forsh, M.N. Martyshov, V. Y. Timoshenko, et al., *Semiconductors,* **40**, 471, (2006)

xxvii. C. T. Black, C. B. Murray, R. L. Sandstrom, S. Sun, *Science*, **290**, 1131. (2000)

xxviii. H. Fan, K. Yang, D. M. Boye, T. Sigmon, K. J. Malloy, H. Xu, G. P. Lopez, C. J. Brinker, *Science*, **304**, 567. (2004)

xxix. R. Parthasarathy, X.-M. Lin, K. Elteto, T. F. Rosenbaum, H. M. Jaeger, *Phys. Rev. Lett.*, **92**, 801, (2004)

xxx. C. I. Duruoz, R. M. Clarke, C. M. Marcus, J. S. Harris, *Phys. Rev. Lett.*, **74**, 3237 (1995)

xxxi. H. E. Romero, M. Drndic, *Phys. Rev. Lett.*, **95**, 801, (2005)

xxxii. A. Bezryadin, R. M. Westervelt, M. Tinkham, Appl. Phys. Lett., 74, 2699 (1999)

xxxiii. A. N. Aleshin, H. J. Lee, S. H. Jhang, H. S. Kim, K. Akagi, Y. W. Park, *Phys. Rev. B*, **72**, 202 (2005)

xxxiv. A. A. Middleton, N. S. Wingreen, *Phys. Rev. Lett.*, **71**, 3198 (1993)

xxxv. B. Hamilton, J. Jacobs, D.A. Hill, et al., *Nature*, **393**, 443 (1998)

xxxvi. S. Borini, L. Boarino, G. Amato, *Phys. Rev. B*, **75**, 165205 (2007)

ECS Transactions, 16 (3) 337-344 (2008)
10.1149/1.2982573 ©The Electrochemical Society

Photoexcited Silicon Nanocrystals as Multifunctional Spin-Flip Activator

B. Goller[a], S. Polisski[a], A. Moskalenko[a], K. Loponov[b], and D. Kovalev[a]

[a] Department of Physics, University of Bath, Bath BA2 7AY, UK
[b] Department of Chemical Engineering, University of Bath, Bath BA2 7AY, UK

Nano-sized silicon crystals have entirely new physical properties which do not occur in its bulk form. Investigation of its photoluminescence properties can explain the mechanism of transferring energy from photoexcited excitons confined in silicon nanocrystals to energy accepting substances via electron exchange mechanism. This excitation process changes the electronic spin structure of the acceptor molecule, which is forbidden in the dipole approximation, and therefore it requires the involvement of photosensitizers.

Introduction

The production of nano-sized solid state structures is usually realised by two approaches: growth from atomic or molecular precursors in gas or liquid phase, or alternatively, reduction of the size of bulk materials to nano-sizes, by means of e.g. electron beam lithography and various etching techniques. Nanostructured silicon was first realised by Ingeborg and Arthur Uhlir at Bell Labs in the 1950's (1): porous silicon (PSi) formed by electrochemical etching. However, significant scientific interest in nanosilicon containing systems arouse only after publications on visible light emission at room temperature by Canham (2) and blue shift of the light absorption by Lehmann and Gösele in 1990 (3).

Si nanocrystal assemblies can be prepared in different ways, including aerosol procedures (4) and thermal precipitation of Si atoms implanted in SiO_2 (5) or Si–SiO_2 superlattices (6) and laser-pyrolysis techniques yielding relatively narrow size distribution of Si nanocrystals (7). Due to the simplicity of the production method, PSi prepared via anodization of bulk Si wafers in HF based etchants, is the most widely used and discussed nano Si based system. Thin PSi films can be prepared via stain etching of Si (8): due to successive oxidation of Si and removal of the grown oxide in HF:HNO_3:H_2O solutions PSi can be formed. Detailed spectroscopic studies demonstrated that all these systems show strong near infrared and visible photoluminescence (PL) with very similar characteristics (9).

The excitation of molecules in the first energetically higher lying electronic states involves, in most cases, a change of their spin configuration. Absorption of photons can not change electronic spin states, therefore intermediate light absorbing substances are used to sensitize this process. As prepared PSi seams to fulfil all optical and structural requirements to be a very good sensitisation agent.

Experimental details

For our studies on the transfer of energy, stored in photoexcited excitons, from Si nanocrystals to surrounding acceptor substances we used PSi layers and powders prepared via electrochemical and stain etching procedures, respectively.

Nano PSi layers have been prepared via electrochemical etching of B-doped Si (100) substrates with a typical resistivity of 1–10 Ω•cm. The electrochemical etching was done in a Teflon cell containing the etchant, and using a Pt wire as cathode. The etching solution was a 1:1 by volume mixture of hydrofluoric acid (49 wt. % in water) and ethanol. The etching current density was 30–50 mA/cm^2. The porosity of the 15–30 μm thick samples, determined gravimetrically, was ~70 %.

To prepare nanocrystalline PSi powder (see Fig. 1) we used standard metallurgical grade polycrystalline Si powder having a mean particle size of 4 μm. The powder was immersed in a solution of HF and water, then HNO_3 was added gradually until the ratio of used chemicals was about 4:1:20 of $HF:HNO_3:H_2O$. The etching was finished when the initially metallic colour of the powder was changed to brown-yellow and an efficient red-orange photoluminescence (PL) under illumination by ultraviolet light appeared.

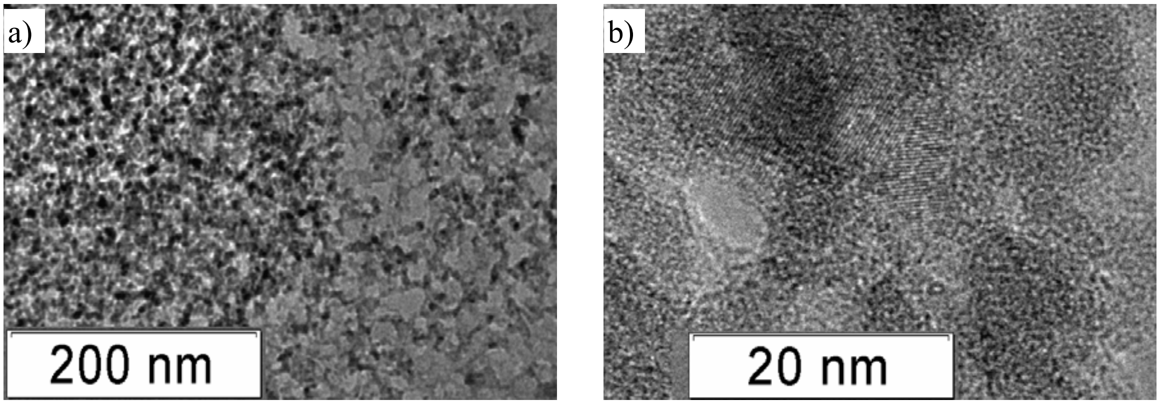

Figure 1. Low a) and High b) resolution transmission electron microscopy: images of stain-etched Si powder. Lattice fringes in b) correspond to the (111) atomic planes of Si nanocrystals.

Due to nanometer-sized remnant Si fragments, nanoporous PSi is characterised by an enormously large (up to 500 m^2/cm^3 (9)) hydrogenated internal surface area. Si-H, Si-H_2 and Si-H_3 groups have been identified as the dominating surface groups using infrared absorption spectroscopy (9-11). Soon after the invention of nanoporous Si (1) it has been realized that for specific applications the as prepared H-terminated surface is unstable, and different surface termination has been investigated (9, 12). Nanocrystals having a layer of back-bonded oxygen or especially surface oxides have much more stable surface configurations.

In bulk silicon non-radiative decay channels dominate, due to the indirect band-gap nature of Si, the recombination processes of electron hole pairs, and therefore bulk Si is an extremely poor light emitter. For nanostructured Si however, quantum size effects, i.e.

geometrical confinement of excitons inside the crystal, result in atomic-like electronic states (13). By varying the nanocrystals size the confinement energy, i.e. the excitons energy can be tuned, which means that the photoluminescence (PL) band of an assembly of nanocrystals is dependent on the particle size distribution. Alongside this effect, the probability for zero phonon assisted optical transitions increases in small Si nanocrystals (14). It is important to note that by choosing the particle size the exciton energy can be tuned from the band-gap of bulk Si (1.12 eV) to up to 2.5 eV for small nanocrystals. But still, contrary to low-dimensional direct band-gap semiconductors where the exciton lifetime is in the nanosecond range, photo excitations persist in Si nanocrystals, dependent on the temperature, from microseconds to milliseconds (14). Due to the exchange interaction the exciton states split in a higher lying and optically active spin single state (S=0) and an optically passive and energetically lower spin triplet (S=1) state. Photoexcitation takes place via the optically allowed transition to the excitons singlet state which then relaxes into the long lived dipole forbidden triplet state (15). The long exciton lifetime is limiting the application of Si nanocrystals in optical devices, due to low repetition frequencies (16). On the other hand this long exciton lifetime ensures that photogenerated electronic excitations can transfer the stored energy to another medium before radiative decay processes become predominant. For energy transfer processes it is important to bring donor and acceptor substances in close proximity. Samples containing a monolayer of oxygen back bonded to the silicon surface exhibit a drastically reduced sensitization efficiency, due to an about 3 times larger spacing between the nanocrystals core and the energy acceptor, therefore all described experiments have been carried out on PSi samples having their large accessible surface terminated with hydrogen. The above mentioned properties seam to make Si nanocrystals a good candidate in photosensitizing applications.

Results and discussion

Generally, the energy transfer from excitons to an acceptor can take place via dipole-dipole interaction (Förster process) (17), or direct electron exchange mechanism (Dexter process) (18). Due to the fact that spin-flip processes can not be caused by dipole-dipole interactions, exchange of electrons having mutually opposite spins has to take place between energy donor (silicon nanocrystals) and acceptor substance. Possible candidates for excitation in their higher lying electronic state need to have a singlet-triplet (or triplet-singlet) splitting energy within or below the PL energy of Si nanocrystals. Then, independently from the spin structure of their ground state (singlet or triplet state), an electronic excitation having matching spin orientation and energy can be found, within Si nanocrystals, for the exchange process.

To demonstrate the unique character of the interaction we used molecular oxygen having its lowest excited singlet spin state ($^1\Delta$) at 0.98 eV and its second excited singlet state ($^1\Sigma$) at 1.63 eV above the triplet ground ($^3\Sigma$) state. Depending on the band-gap energies of Si nanocrystals participating in the energy transfer they can transfer energy to form different singlet oxygen states. Since the formation of the lowest singlet state requires a change of the angular momentum of O_2 ($\Delta L=2$), also multiple phonons have to be emitted to match resonant energy transfer conditions. This process is out of the above reasons much less efficient than the excitation of the $^1\Sigma$ state (see Fig. 2). The energy transfer efficiency strongly depends on the radiative exciton lifetime, which increases with decreasing temperatures, but also on the overlap of the electronic wavefunctions of excitons confined in PSi and O_2 molecules, which increases with decreasing temperature due to longer contact time of O_2 on the nanocrystals surface. Out of that reason, we can see that the PL of silicon nanocrystals is much stronger suppressed at low temperatures (see Fig. 2). The inset of Fig. 2 shows the PL suppression spectrum (the ratio of the PL intensity measured in vacuum divided to that measured in O_2 ambient) at 50K. It represents the energy dependent coupling strength of excitons and oxygen molecules.

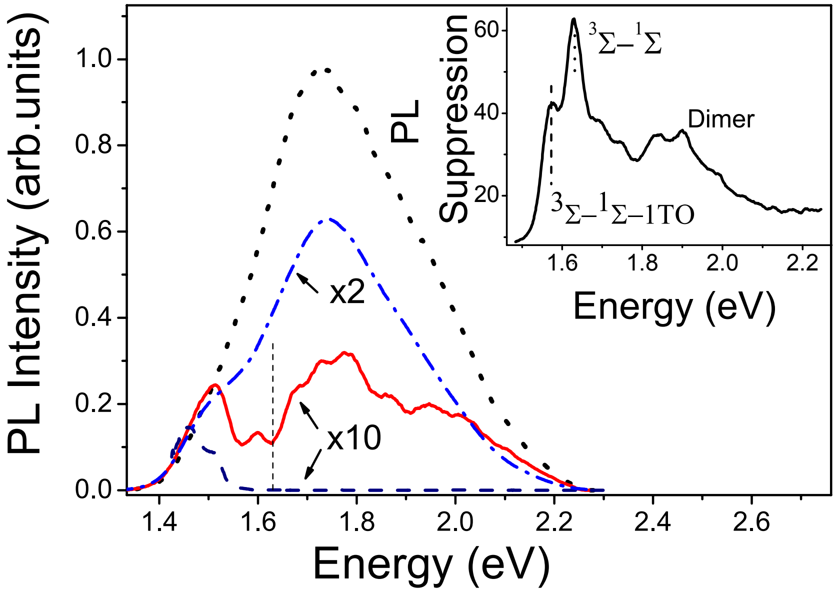

Figure 2. PL spectrum of Si nanocrystals in vacuum (dotted curve). PL spectrum of PSi at room temperature with 1 bar of oxygen ambient (Dashed dotted curve). PL spectrum of PSi with a small amount of oxygen physisorbed to the Si surface: at 50 K (solid curve) and at 30 K (dashed curve), respectively. Scaling factors are indicated. Inset: PL suppression spectrum at 50 K. The formation of singlet oxygen dimers can be seen. The singlet-triplet splitting energy of oxygen molecules is indicated. $E_{ex.}$=2.54 eV, I=20 mW/cm^2

At low temperatures almost all excitons having energies above 1.63 eV transfer their energy to oxygen molecules, so that the energy transfer efficiency is close to 100 %. The spectral onsets seen above the energy of the O_2 $^1\Sigma$ state result from efficient energy transfer to O_2 when the exciton matches 1.63 eV plus the energy of a integer number of TO(Γ) phonons. The PL quenching at 1.57 eV results from the fact that most excitons, having an energy of 1.63 eV would luminesce, in absence of oxygen, only after emission of a TO(Δ) phonon (19). It is seen that, by exciting dimers, one photon can initiate the formation of two singlet oxygen molecules. We would like to mention that the efficiency of the energy transfer, from PSi to an acceptor, depends amongst others on the starting Si material. For PSi powder prepared via stain etching of metallurgical grade polycrystalline Si powder the room temperature PL in one bar of oxygen ambient, is due to energy transfer to oxygen commonly more than 6 times smaller than in vacuum. For electrochemically or stain etched B-doped monocrystalline Si wafers however PL suppression levels of about 1.5 are typical. This means, that the energy transfer efficiency is much higher for stain etched polycrystalline Si powder than for PSi prepared from B-doped Si wafers, and therefore we assume that the mean distance between the core of Si nanocrystals and oxygen molecules is larger for the latter case.

To prove the formation of singlet oxygen by other means, we measured the fluorescence of photosensitized singlet oxygen being in its ($^1\Delta$) state and decaying radiatively into its ground $^3\Sigma$ state (see Fig. 3). PSi powder (1.5 mg) was dispersed in 1 ml Hexafluorobenzene (C_6F_6), which was continuously bubbled with molecular oxygen. Under illumination by an Ar^* ion laser, a distinct fluorescence line of singlet oxygen can be seen, on the top of a broad PL background from surface Si dangling bonds. The sensitised reactive oxygen was used to oxidise α-terpinene molecules and form ascaridole. α-terpinene was used because of its high chemical reaction rate with singlet oxygen ($k_{\text{(in chloroform)}} = 1.0 \times 10^8$ (L mol^{-1} s^{-1}) (20)). Adding 0.025 µl of α-terpinene quenches the singlet oxygen luminescence, mainly due to quick chemical deactivation. Illuminating the PSi powder for about 40 minutes leads to an almost full recovery of the singlet oxygen luminescence. This means that no efficient chemical quenching is realised, therefore we conclude that nearly all the added α-terpinene is oxidised after that time.

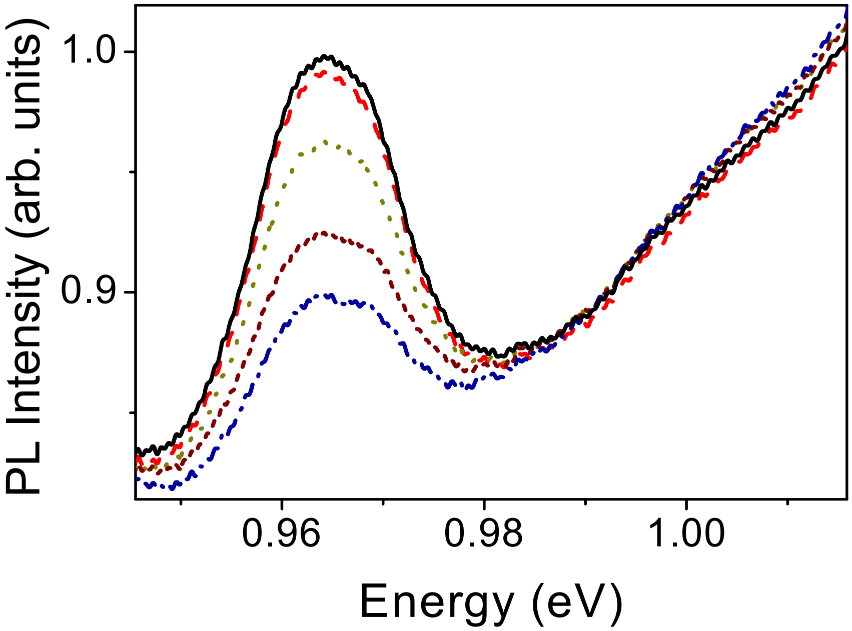

Figure 3. Fluorescence of singlet oxygen photogenerated by 1.5 mg of PSi powder in one ml of C_6F_6: without α-terpinene (solid line), suppression of the fluorescence after adding 0.025 µl α-terpinene (dashed doted line). Short dashes, dots and dashes: recovery of singlet oxygen fluorescence after illumination for 12, 21 and 39 minutes, respectively. $E_{ex.}$=2.54 eV, I=500 mW/cm^2

Aromatic molecules belong to the group of molecules which, principally, can be excited by photosensitization. They have a spin structure which is different to oxygen: their ground state is singlet and the first excited electronic spin state is triplet. The nature of the excitation process is identical to that of oxygen: photoexcited excitons transfer, via exchange of electrons having mutually opposite spins, energy to the acceptor molecules.

For energy transfer experiments molecules were dissolved in organic solvents (up to 1 %wt.). PSi was filled with this solution, and after evaporation of the solvent PL measurements were performed in an optical cryostat. PSi samples having energy accepting molecules inside their pores exhibit a strong PL quenching (21). We would like to note again, that this excitation process is only possible if the exciton energy is equal or larger than the singlet-triplet splitting energy of the acceptor molecule. Two of the possible candidates are β-carotene and anthracene. β-carotene has its first triplet state 0.8 eV above its singlet ground state (22), and it is supposed to have its second triplet state at about 1.9 eV. The lowest triplet state of anthracene lays 1.84 eV above the ground singlet state (22). In Fig. 4 it is shown, that indeed the PL quenching coincides with the singlet-triplet splitting energies of the investigated molecules: anthracene, oxygen and β-carotene. The fact that we do not achieve complete suppression of the PL above the singlet-triplet splitting energy of organic molecules arises to our opinion from a non sufficient pore filling. In the case of β-carotene we cannot see resonant PL quenching which corresponds to the sensitisation of the first excited triplet state, since it lies energetically below the band-gap of Si nanocrystals. For substances having their singlet-triplet splitting energy above the band-gap of silicon nanocrystals, e.g. naphthalene (2.56 eV) (22), no PL quenching could be observed.

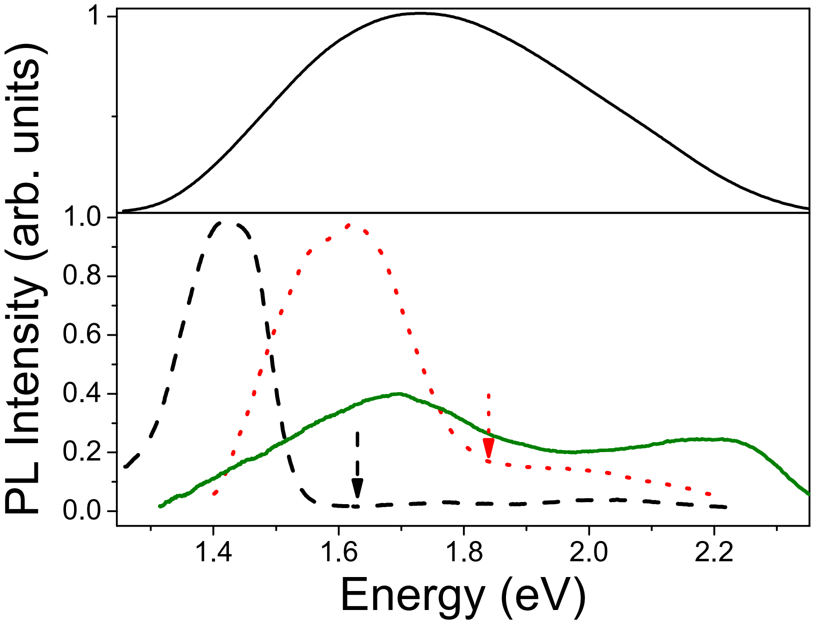

Figure 4. Top: PL spectrum of PSi powder in vacuum. Bottom: the PL of PSi samples incorporated with various energy accepting molecules is quenched at their singlet-triplet splitting energies: PSi in 1 bar of O_2 (dashed curve, arrow indicates triplet-singlet energy splitting), PSi impregnated with anthracene molecules (dotted line, arrow indicates singlet-triplet energy splitting) and β-carotene (solid line) this spectrum is not normalised to unity to show that excitons of all energies participate efficiently in the energy transfer process. $E_{ex.}$=2.54 eV, T=80 K

Conclusions

We investigated the energy dependent PL quenching of Si nanocrystals, caused by energy transfer to acceptor molecules. The results show, that independently from the spin structure of ground and first excited states, singlet or triplet, photoexcited silicon nanocrystals can efficiently transfer energy to acceptor molecules. As long as the first excited state of the energy acceptors lies below the exciton energy PSi seems to be a multifunctional spin-flip activator. These kinds of processes, involving spin-flip activation of substances, are becoming more and more important in photochemistry and biology.

Acknowledgments

A part of this work was supported by the Commission of the European Community, 6th Framework Pro-gram (STRP 013875). We acknowledge Vesta Sciences for support.

References

1. A. Uhlir, *Bell Syst. Tech. J.*, **35**, 333 (1956).
2. L. T. Canham, *Appl. Phys. Lett.*, **57**, 1046 (1990).
3. V. Lehmann and U. Goesele, *Appl. Phys. Lett.*, **58**, 856 (1991).
4. L. Brus, in *Semiconductors and Semimetals* (Ed: D. J. Lockwood), Academic, New York (1996).
5. M. Fujii, M. Yoshida, Y. Kanzawa, S. Hayashi and K. Yamamoto, *Appl Phys. Lett.*, **71**, 1198 (1997).
6. G. F. Grom et al., *Nature (London)*, **407**, 358 (2000).
7. F. Huisken, G. Ledoux, O. Guillois, C. Reynaud, *Adv. Mater.*, **14**, 1861 (2002).
8. A. J. Steckl, J. Xu and H. C. Mogul, *Appl. Phys. Lett.*, **62**, 2111 (1992); G. Anaple, R. Burrows, Y. Wu and P. Boolchand, *J. Appl. Phys.*, **78**, 4273 (1995).
9. O. Bisi, S. Ossicini and L. Pavesi, *Surf. Sci. Rep.*, **38**, 1 (2000).
10. K. Beckman, *Surf. Sci.*, **3**, 314 (1965).
11. Y. Ogata, T. Tsuboi, T. Sakka and S. Naito, *J. Porous Mater.*, **7**, 63 (2000).
12. R. Smith and S. Collins, *J. Appl. Phys.*, **71**, R1, (1992).
13. I. Sychugov, R. Juhasz, J. Valenta and J. Linnros, *Phys. Rev. Lett.*, **94**, 087405 (2005); I. Sychugov, R. Juhasz, J. Valenta, A. Zhang, P. Pirouz and J. Linnros, *Appl. Surf. Science*, **252**, 5249 (2006).
14. M. S. Hybertsen, *Phys. Rev. Lett.*, **72**, 1514 (1994).
15. P. D. J. Calcott, K. J. Nash, L. T. Canham, M. J. Kane and D. Brumhead, *J. Phys. Condens. Matter*, **5**, L91 (1993).
16. P. M. Fauchet et al., *IEEE J. Sel. Top. Quantum Electron.*, **1**, 1126 (1995).
17. F. Förster, *Ann. Phys.* (Paris), **437**, 55 (1948).
18. D. L. Dexter, *J. Chem. Phys.*, **21**, 836 (1953).
19. E. Gross, D. Kovalev, N. Künzner, J. Diener, F. Koch, V. Yu. Timoshenko and M. Fujii, *Phys. Rev. B*, **68**, 115405 (2003).
20. B. M. Monroe, *J. Am. Chem. Soc.*, **103**, 7253 (1981).
21. J. H. Song and M. J. Sailor, *J. Am. Chem. Soc.*, **119**, 7381 (1997).

22. S. Murov, I. Carmichael and G. Hug, *Handbook of Photochemistry*, 2nd ed. Marcel Dekker, New York (1993).

ECS Transactions, 16 (3) 345-351 (2008)
10.1149/1.2982574 ©The Electrochemical Society

Growth of Porous Anodic Films on Niobium in Hot Phosphate-Glycerol Electrolyte

Y. Oikawa, K. Fushimi, Y. Aoki and H. Habazaki

Division of Materials Chemistry, Graduate School of Engineering, Hokkaido University,
N13-W8, Kita-ku, Sapporo 060-8628, Japan

Porous anodic films have been developed on niobium at constant formation voltages between 5 and 50 V in glycerol electrolyte containing 0.8 mol dm^{-3} dibasic potassium phosphate at 433 K. Except at the formation voltage of 5 V, at which the current density is approximately constant during anodizing, the current shows the minimum and then maximum. After the current maximum, the current density decreases gradually, which follows the Cottrell equation. Thus, diffusion of some species in the pores should control the growth rate of the anodic films. The porous films developed are practically Nb_2O_5 with a small amount of carbon contamination. Incorporation of phosphorus species, which often occurs in aqueous electrolytes, is negligible at all the formation voltages in the present electrolyte. Based on the results obtained, the growth process of the porous anodic films on niobium in this hot organic electrolyte is discussed.

Introduction

In addition to the well-known porous anodic alumina films with cylindrical pores arranged normal to the metal/film interface, it is now possible to form self-organized porous anodic oxides on a range of valve metals, including niobium, tantalum, titanium, tungsten and zirconium, in fluoride-containing electrolytes (1-6). These porous anodic oxides have attracted much attention concerning their formation mechanisms and potential widespread applications.

Recently, it has been found that porous anodic oxides can also be formed on aluminium, niobium, tantalum and Ti-Si alloys in fluoride-free, hot glycerol electrolyte containing phosphate (7-9), although initially the films formed in this electrolyte were considered to be of a barrier-type (10). The film morphologies closely resemble that of the well-known porous anodic alumina produced in aqueous acid electrolytes; an outer layer, containing nano-scale, almost cylindrical, parallel-sided pores, is developed above a thin barrier layer that separates the porous layer and the metal substrate (11). The anodic films formed in the glycerol electrolyte consist of the oxides of the respective valve metals, with negligible incorporation of phosphorus species, although the oxides developed in aqueous electrolytes are usually contaminated with species derived from electrolyte anions (12). The anodic films formed in the glycerol electrolyte were thin, generally less than 500 nm, due to the low formation voltages.

In the present work, niobium has been anodized at a constant formation voltage of 5 to 50 V in glycerol electrolyte containing 0.8 mol dm^{-3} dibasic potassium phosphate at 433 K. Thick anodic films of several micrometers have been developed in this work. Further, the current transients have been analyzed and the developed films were characterized using FE-SEM and GDOES, to get insight into the growth mechanism of the anodic films in the present organic electrolyte.

Experimental

The specimens used for anodizing were cut from 99.9% niobium sheet, of 0.2 mm thickness; individual specimens were ultrasonically degreased in acetone. The electrolytes employed for anodizing were stirred 0.8 mol dm^{-3} K_2HPO_4 in glycerol containing 0.65 mass% water at 433 K. The water concentration in the electrolytes was measured by Karl Fischer titration using a Hiranuma Sangyo, AQV-7S instrument. The specimens, masked with silicone resin to define the exposed surface area, were anodized at several formation voltages of 5 to 50 V for 3.6 ks. A two-electrode cell with a platinum counter electrode was used.

Surfaces and fracture sections of the anodized specimens were observed using a JEOL JSM6500 scanning electron microscope operated at 10 kV. Depth profiles of the anodized specimens were obtained by GDOES, using a Jobin-Yvon 5000 RF instrument, in an argon atmosphere of 650 Pa with application of RF of 13.56 MHz and power of 30 W. Light emissions of characteristic wavelengths were monitored throughout the analysis with a sampling time of 0.1 s to obtain depth profiles. The wavelengths of the spectral lines used were 416.477, 178.287, 130.217, 165.701 and 121.567 nm for niobium, phosphorus, oxygen, carbon and hydrogen, respectively. The signals were detected from a circular area of approximately 4 mm diameter.

Results

Fig. 1 shows the current transients of niobium during anodizing at constant formation voltages between 5 and 50 V in 0.8 mol dm^{-3} K_2HPO_4 in glycerol at 433 K. At the formation voltage of 5 V, the current density is approximately constant, being 0.7 mA cm^{-2} during anodizing for 3.6 ks. At the other formation voltages, a minimum current density appears after an initial steep current decrease. The minimum current density tends to increase and appear at shorter time with increasing the formation voltage. The presence of the current minimum in the current transients resembles that for porous anodic alumina formation in aqueous acid electrolytes. However, a difference of the current transients between the present niobium in organic electrolyte and aluminum in aqueous acid electrolytes appears after the current minimum. During anodizing of aluminum in acid electrolytes, the current density becomes finally almost constant. In contrast, a current maximum appears in the present case, and then the current decreases gradually. Again, the maximum current density increases and it appears at shorter time with increasing the formation voltage. The current transient at the formation voltage of 50 V becomes almost the same as that at 30 V, after the current maximum.

The gradual current decrease after the current maximum at the formation voltages of 10 to 50 V is associated with a diffusion-controlled reaction process. If an charge-transfer reaction is high enough to cause deficiency of reactive species at the surface, a diffusion layer is developed and thickens with increasing anodizing time. Then, the current density decreases gradually. Under such a diffusion-controlled film growth, the current density follows the Cottrell equation:

$$i^{-1} = \frac{1}{nFc_0}\left(\frac{\pi t}{D}\right)^{1/2} \qquad [1]$$

in which D is a diffusion coefficient, c_0 is the bulk concentration of reactive species, n is the number of electron and F is Faraday constant. Thus, the reciprocal of the current density increases linearly with a square root of anodizing time. The current transients at the formation voltages of 20, 30 and 50 V are re-plotted for the Cottrell equation (Fig. 2), showing that there is a linear correlation between the reciprocal of the current density and the square root of anodizing time after the current maximum. Similar slope for the formation voltages of 30 and 50 V indicates that diffusional transport of matter controls the overall rate of film growth at these high voltages. The reduced slope at 20 V may be some contribution of the migration rate of ions in the barrier layer between the porous layer and the metal substrate under the high electric field to the overall growth rate. Thus, a diffusion layer is developed, possibly in the cylindrical pores of the anodic films, during anodizing in this organic electrolyte.

The formation of porous films has been examined by SEM observations (Fig. 3). Obviously, pores are developed in the anodic films formed at all the formation voltages, and the pore size increases from 7-10 nm at 5 V to ~20 nm at 30 V. The pores are cylindrical and approximately normal to the film surface. At the formation voltage of 50 V, larger pores of ~100 nm were also developed, but only in the film region close to the film surface.

Thickening of the anodic film with the formation voltage is obvious from the cross-sectional SEM observations (Fig. 3(d)-(f)). As shown in Fig. 4, there is a linear correlation between the film thickness and the charge passed during anodizing, indicating that no significant chemical dissolution of the anodic films occurs during anodizing. The slope is 0.46 μm C^{-1} cm^2, which is ~20% lower than the calculated value of 0.59 μm C^{-1} cm^2 for the barrier-type anodic Nb_2O_5 with a density of 4.7 g cm^{-3}. This is roughly in agreement with the porosity of the porous anodic films of ~15%, measure from the SEM observations (Fig. 3(a)-(c)).

Elemental depth profiles obtained by GDOES (Fig. 5) disclose that the anodic films are mainly composed of niobium oxide. The intensity of phosphorus in the anodic films is at the background level except in the outermost film region; hence, the incorporation of phosphorus species into these anodic films is negligible (Fig. 5(c)). The relatively high background level of the phosphorus signal may be due to overlapping with an emission line from argon (178.258 nm) (13). Hydrogen signal decreases with increasing the depth, and a peak appears at the metal/film interface. The origin of hydrogen enriched in metal substrate immediately beneath the anodic film is hydrogen impurity of niobium substrate, which accumulates the metal surface during anodizing (14). Carbon species are also present in the anodic films, probably derived from glycerol.

Discussion

Film Composition

Findings indicate that the anodic films formed in hot glycerol electrolyte containing dibasic potassium phosphate is porous, with cylindrical pores developing normal to the metal/film interface, and are composed mainly of niobium oxide, probably Nb_2O_5. In contrast to a relatively high level of incorporation of phosphorus species (~10 %) in anodic oxides formed in aqueous electrolytes containing phosphate at an ambient temperature, the incorporation of phosphorus species is negligible in the present anodic films. The negligible incorporation of phosphorus species may be related to the field strength in the barrier layer present between the porous layer and the metal substrate. It is known that an increase in anodizing temperature results in the reduction of the field strength in the barrier layer, and hence the phosphorus concentration in the anodic films is reduced (15). In a separated paper (16), we have reported that the reduced water content in the present electrolyte increases the field strength, leading to the increased incorporation of phosphorus species. Thus, it is likely that the field strength in the barrier layer play a crucial role in incorporation of phosphorus species.

Recently, SIMS depth profiling analysis of the anodic films formed on niobium in the phosphate-glycerol electrolytes containing ~0.4 mass% water with and without $H_2{}^{18}O$ enrichment was carried out, in order to examine the origin of oxide ions in the anodic films (16). The profiles disclosed that the oxygen species in the anodic films formed in hot K_2HPO_4-glycerol electrolyte are derived predominantly from water in the electrolyte, not from glycerol itself. A gradual decrease in hydrogen concentration in the anodic films to the direction of the metal/film interface may be related to the reduction of water concentration at the pore base due to its consumption to form anodic oxide.

Growth Kinetics

It is obvious from Fig. 2 that the diffusional transport of matter controls the growth rate of the porous films at the formation voltages of 30 and 50 V in the present organic electrolyte. A film material is formed at the metal/film interface by inward migration of oxide ions. For porous film formation, no film material is formed at the film/electrolyte interface of the pore base, and cation species migrating in the barrier layer to the pore base are directly ejected into the electrolyte. Findings suggest that diffusion of species, which act as a source of oxide ions in the anodic films, to the pore base may control the growth rate. One of the possible diffusing species is water, since water in the electrolyte is a predominant source of oxide ions in the anodic films. However, we have also found that the reduction of water content in the electrolyte results in the increase in the current density (16). Thus, it is unlikely that simply water in the electrolyte is diffusing species in the pores of the anodic films. The addition of K_3PO_4 to the K_2HPO_4-glycerol electrolyte increased the current density. The hydroxide ions in the electrolyte, therefore, are possible diffusing species. Further study to elucidate the diffusing species is now in progress.

Conclusions

Porous anodic films, several micrometers thick, are formed on niobium in hot glycerol electrolyte containing 0.8 mol dm^{-3} K_2HPO_4. The pore size increases from 7-10 nm at 5 V to ~20 nm at 50 V. Even in the organic electrolyte, the films developed are composed mainly of niobium oxide with negligible incorporation of phosphorus species. After a certain period of anodizing, the film growth is controlled by diffusion of some species, possibly in the pores of the anodic films, not by migration of anions and cations in the barrier layer under the high electric field.

Acknowledgments

The present work was supported by a Grant-in-Aid for Exploratory Research, No. 19656184 from the Japan Society for the Promotion of Science, and also by the Global COE Program (Project No. B01: Catalysis as the Basis for Innovation in Materials Science) from the Ministry of Education, Culture, Sports, Science and Technology, Japan.

References

1. R. Beranek, H. Hildebrand and P. Schmuki, *Electrochem. Solid State Let.*, **6**, B12 (2003).
2. I. Sieber, H. Hildebrand, A. Friedrich and P. Schmuki, *Electrochem. Commun.*, **7**, 97 (2005).
3. H. Tsuchiya and P. Schmuki, *Electrochem. Commun.*, **7**, 49 (2005).
4. H. Tsuchiya, J. M. Macak, I. Sieber, L. Taveira, A. Ghicov, K. Sirotna and P. Schmuki, *Electrochem. Commun.*, **7**, 295 (2005).
5. H. Tsuchiya and P. Schmuki, *Electrochem. Commun.*, **6**, 1131 (2004).
6. W. Wei, J. M. Macak and P. Schmuki, *Electrochem. Commun.*, **10**, 428 (2008).
7. Q. Lu, G. Alcala, P. Skeldon, G. E. Thompson, M. J. Graham, D. Masheder, K. Shimizu and H. Habazaki, *Electrochim. Acta*, **48**, 37 (2002).
8. Q. Lu, T. Hashimoto, P. Skeldon, G. E. Thompson, H. Habazaki and K. Shimizu, *Electrochem. Solid-State Let.*, **8**, B17 (2005).
9. H. Habazaki, Y. Oikawa, K. Fushimi, K. Shimizu, S. Nagata, P. Skeldon and G. E. Thompson, *Electrochim. Acta*, **53**, 1775 (2007).
10. B. Melody, T. Kinard and P. Lessner, *Electrochem. Solid State Let.*, **1**, 126 (1998).
11. J. P. O'Sullivan and G. C. Wood, *Proc. R. Soc. London, A*, **317**, 511 (1970).
12. G. C. Wood, P. Skeldon, G. E. Thompson and K. Skeldon, *J. Electrochem.Soc.*, **143**, 74 (1996).
13. R. Payling, D. G. Jones and A. Bengtson, *Glow Discharge Optical Emission Spectrometry*, John Wiley & Sons, UK (1997).
14. H. Habazaki, K. Fushimi, H. Konno, K. Shimizu, K. Asami, P. Skeldon and G. E. Thompson, *J. Surf. Finish. Soc. Jpn.*, **57**, 676 (2006).
15. Q. Lu, S. Mato, P. Skeldon, G. E. Thompson, D. Masheder, H. Habazaki and K. Shimizu, *Electrochim. Acta*, **47**, 2761 (2002).
16. H. Habazaki, Y. Oikawa, K. Fushimi, Y. Aoki, K. Shimizu, P. Skeldon and G. E. Thompson, *Electrochim. Acta*, submitted.
17. Y. Yamamoto and N. Baba, *Thin Solid Films*, **101**, 329 (1983).

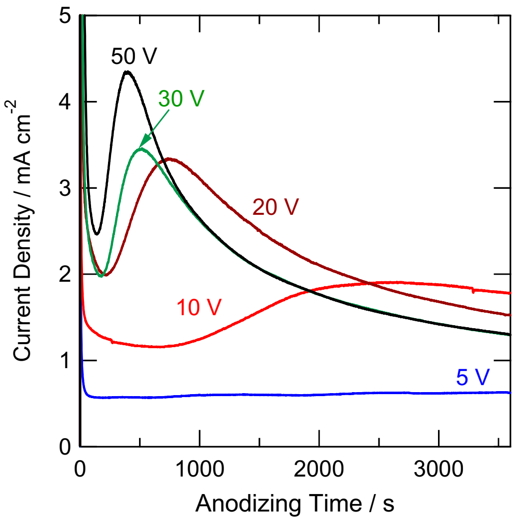

Fig. 1 Current transients of niobium during anodizing at several formation voltages in 0.8 mol dm^{-3} K_2HPO_4 in glycerol at 433 K.

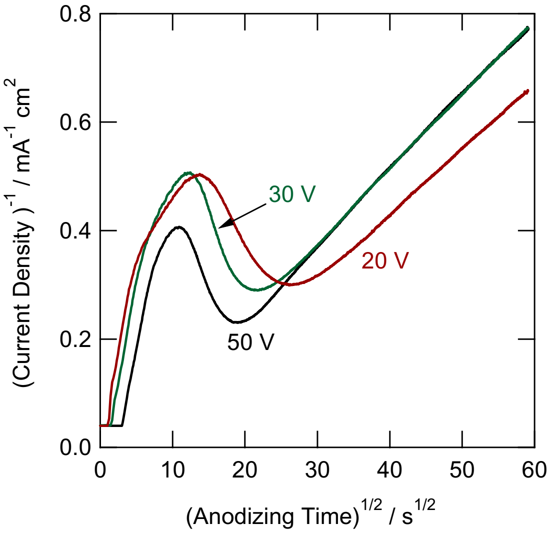

Fig. 2 Cottrell plot of the current transients of niobium during anodizing at several formation voltages in 0.8 mol dm^{-3} K_2HPO_4 in glycerol at 433 K.

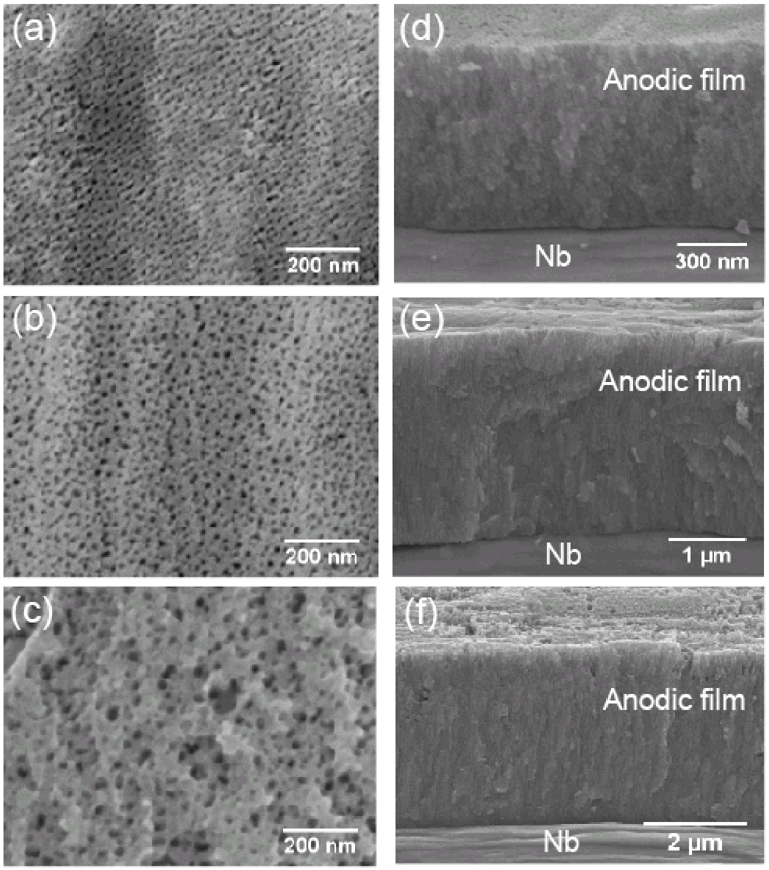

Fig. 3 SEM images of surfaces and cross-sections of niobium anodized at (a), (d) 5 V, (b), (e) 10 V and (c), (f) 30 V in 0.8 mol dm^{-3} K_2HPO_4 in glycerol at 433 K for 3.6 ks.

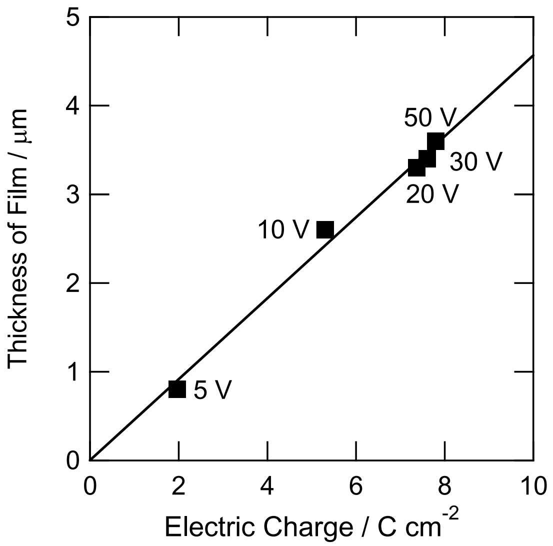

Fig. 4 Change in thickness of the anodic films as a function of the charge passed during anodizing.

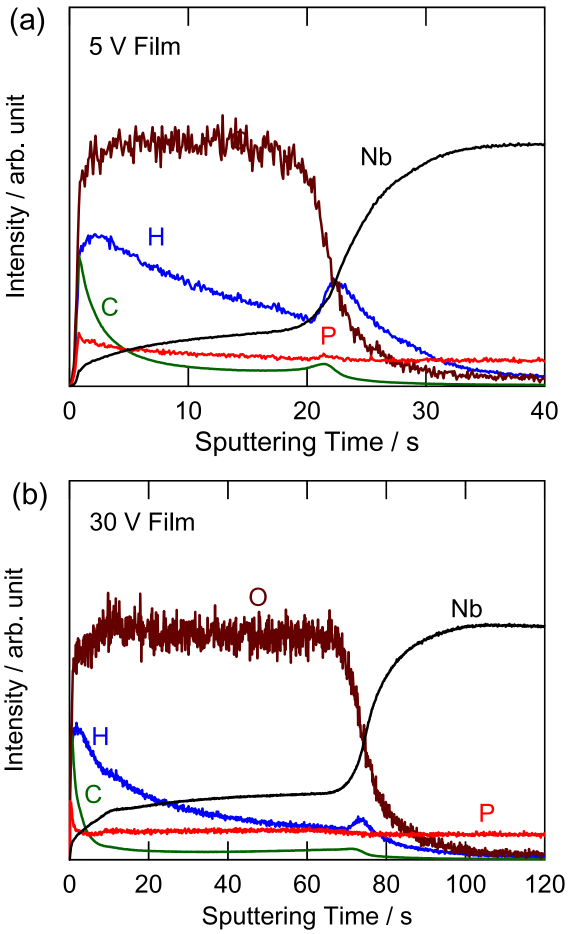

Fig. 5 GDOES depth profiles of the anodic films formed at (a) 5 V and (b) 30 V in 0.8 mol dm^{-3} K_2HPO_4 in glycerol at 433 K for 3.6 ks.

ECS Transactions, 16 (3) 353-358 (2008)
10.1149/1.2982575 ©The Electrochemical Society

Fabrication of Self-Organized Nanoporous Oxide Semiconductors by Anodization

Sachiko Ono, Yuta Kobayashi, Ryohei Kobayashi and Hidetaka Asoh

Department of Applied Chemistry, Faculty of Engineering, Kogakuin University
2665-1 Nakano, Hachioji, Tokyo 192-0015, Japan

Self-organized nanoporous semiconductors such as ZnO and SnO_2 having high aspect ratio was prepared by a simple, high throughput and non-costly wet electrochemical process without use of catalyst. By using anodization of metal plate of zinc in sodium hydroxide solution, tubular oxide with a pore interval of 10-20 nm and the thickness up to several ten microns was obtained. Photocatalytic activity of anodic film on zinc was improved by increasing annealing temperature up to 400 ^{o}C associated with increasing crystallinity, although the specific surface area of the oxide film decreased as a result of decreasing grain size caused by sintering. Anodic film formed on tin in sodium hydroxide solution showed cellular structure with the size of 50 nm consisted of microcrystal and the thickness up to 60 μm in only 1 h. Photo catalytic activity of the anodic SnO_2 was ascertained by a methylene blue degradation test under UV irradiation. If sulfuric acid was used as an anodizing electrolyte for tin, a peculiar tubular film composed of mixture of crystalline SnO, SnO_2 and $Sn_3O(OH)_2SO_4$ was found.

Introduction

Fabrication technology of nanoholes has been significantly developed due to the demand in the application fields such as magnetic recording media, photonic and opto-electronic devices, patterning, photo catalyst and dye-sensitized solar cells. Among various fabrication techniques, chemical wet processes to produce self-assembled porous oxide by anodization are most promising because of their size controllability, high specific area, simplicity and high throughput. It is well known that self-organized porous anodic alumina (1-3) has significant potential application as a template for the nanofabrication of various devices (4).

Recently, fabrication of porous anodic oxide films formed on various metals such as titanium, zirconium, hafnium and tungsten other than aluminum has been received growing interest because of their exploitation in the fields of photo catalyst, die-sensitized solar cells and chemical sensors. Nanostructured TiO_2 and ZnO have been receiving particular attention in recent years due to its great potential applications in electronic, optoelectronic and sensing devices (5-9). Great interests have been focused on controllable synthesis and application of tubular anodic oxides owing to a high porosity and a large surface area, which are required to fulfill the demand of high efficiency and activity (5, 6, 10-13). In addition, high degree of regularity and alignment are important to control the properties, which are crucial for the fabrication of nanodevices. We have reported the fabrication process of nanoporous ZnO by anodization having high specific area, which are required to fulfill the demand of high efficiency and activity (14). However, in contrast to the case of anodic porous alumina, detailed film growth mechanism of porous oxide semiconductors by anodization has not been well understood (15, 16). In these circumstances, we have studied growing behavior of nanoporous oxide semiconductors on zinc and tin plates by anodization with focusing on their structure and photocatalytic activity as well as a film growth mechanism. Such type of semiconductor is also expected as a plate catalyst because of its specific shape directly attached to a metal plate.

Experimental

Preparation of anodic films

Pure zinc (99.5 %) and tin (99.9 %) rolled plates were polished by buffing and degreased in acetone under ultrasonic treatment before anodization. Anodization was carried out in different electrolytes, i.e., 0.3 mol dm^{-3} oxalic acid, 0.01 mol dm^{-3} sulfuric acid and 0.1 mol dm^{-3} sodium hydroxide. Ethylene glycol was added to improve the film property and current efficiency of anodization. Anodic oxide films were heated to improve the crystallinity.

Evaluation of anodic film structure and property

Thin film X-ray diffraction analysis (MXP18VACE, Mac Science), field-emission scanning electron microscopy (FESEM, Hitachi-S4200) combined with cross section polisher (JEOL-SM09010), specific surface area / pore size distribution analyzer (ASAP 2010, Shimadzu) and spectrophotometer (CS-9000, Shimadzu) were used for the analysis of the structure and properties of ZnO film.

Results and Discussion

Anodic films formed on Zinc

Figure 1 indicates the cross section of porous ZnO film in the thickness of approximately 45 μm obtained by anodization in a solution of sodium hydroxide with the addition of ethylene glycol at 10 V for 8 h. As shown in a high magnification image of the bottom layer (Fig.1c), the film is composed of straight cells similar to the Keller's model of cylindrical anodic porous alumina, though the cell wall appears to be granular at the surface (Fig.1 b). Since the film is identified as polycrystalline ZnO, the granular appearance would be caused by dissolution of amorphous oxide or hydroxide as a result of long anodization time. Whereas, at the bottom layer, newly formed cells appear to be tubular in the average size of 30 nm are observed. After prolonged anodization time, we could obtain a film with the thickness more than 90 μm. Thus, the film growth is unlimited because of the low solubility of nanoporous anodic oxide arisen from its high crystallinity. It is noteworthy that the barrier layer between porous oxide layer and substrate must be amorphous because it is highly soluble into the electrolyte under the high electric field. Thereafter, crystallization starts to take place when the barrier layer transforms to a porous layer.

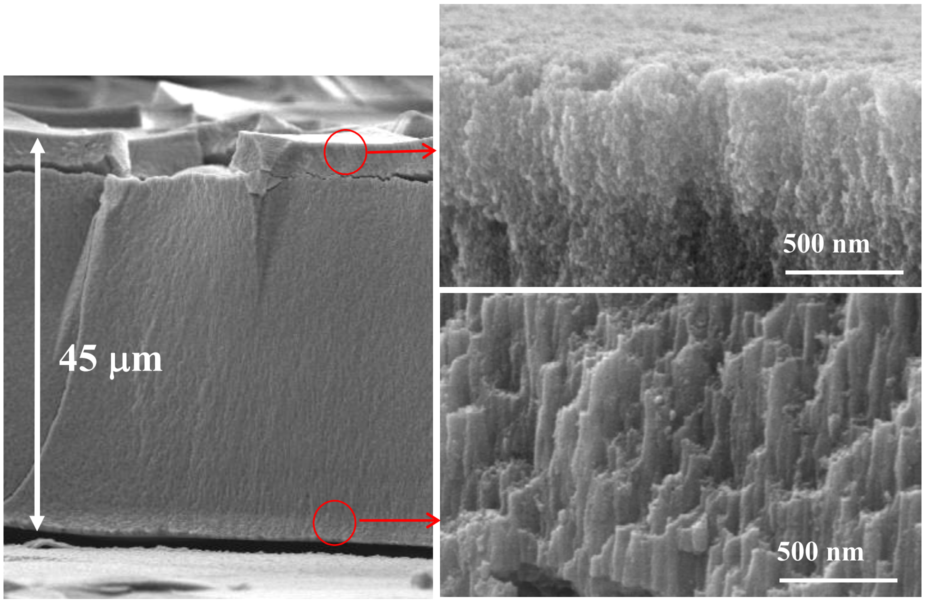

Fig. 1 SEM images of cross section of nanoporous ZnO prepared by anodization in a solution of sodium hydroxide with the addition of ethylene glycol at 10 V for 8 h..

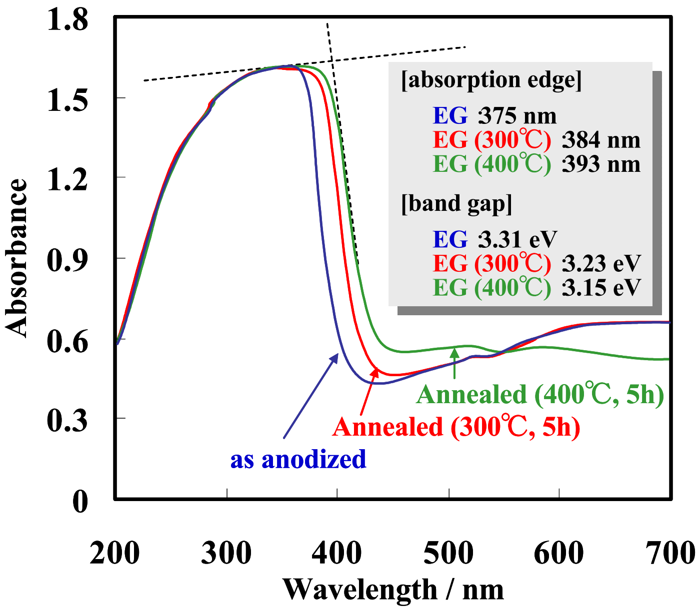

Fig. 2 UV and visible light optical absorption spectra of anodic ZnO with the effect of annealing temperature.

As revealed in absorption spectra shown in Fig. 2, absorption edge and corresponding band gap of as anodized ZnO is 375 nm and 3.31 eV respectively. The band gap energy decreased with increasing annealing temperature down to 3.15 eV. Photo catalytic activity of the nanoporous anodic ZnO after annealing was ascertained to be equivalent as TiO_2 (P25) by methylene blue degradation test under UV irradiation at the wavelength of 365 nm.

However, if the annealing temperature increased form 300 ^oC to 400 ^oC, specific surface area measured by ASAP decreased to a half value and crystal grain size increased. It is caused by sintering of metal at a high temperature. In fact, photo degradation rate of methylene blue was almost same to that annealed at 300 ^oC although crystallinity increased considerably.

Anodic films formed on Tin

As seen in Fig.3, TEM and SEM images of cross section of anodic porous tin oxide formed in NaOH at 5V revealed self-organized porous structure with the pore interval of approximately 50 nm. The porous cells are not tubular different from the cases of anodic TiO_2 and ZnO. The film thickness reached to 10 μm by anodization for 10 min. Micro-diffraction pattern indicates that the anodic SnO_2 film is composed of nano-crystallites. In fact, as anodized SnO_2 film revealed sufficient photocatalytic activity. When anodization was conducted for 1 h, the film thickness increased up to 60 μm as shown in Fig. 3b. It would be noteworthy that the efficiency of oxide film growth on Sn is significantly high in comparison with the cases of Zn, Al, Ti, and Nb.

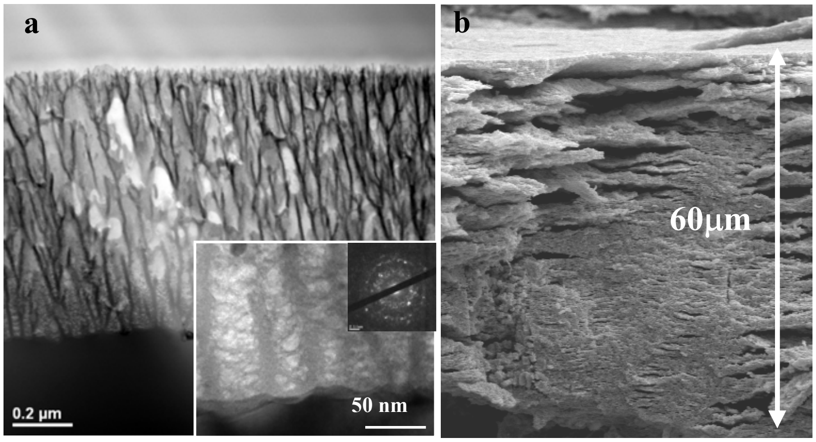

Fig.3 (a) TEM images of cross section of anodic porous anodic film formed on tin in NaOH at 5V for 1 min and (b) at 10V for 1 h.

Figure 4 indicates SEM images of anodic tin oxide films formed in sulfuric acid at various constant voltages for 10 min in connection with current density and temperature. When formation voltage was 20V, an aggregated film structure of rock like cubic crystals in the size of 3-4 μm was observed. XRD analysis indicated that the rock like film was composed of SnO, SnO_2 and $Sn_3O(OH)_2SO_4$. When formation voltage increased higher than 40V, which was associated with current density increase, the film structure changed to a peculiar tubular shape though the crystal structure was the same to the rock like film.

Conclusions

We have demonstrated the fabrication method of highly ordered nanoporous crystalline ZnO and SnO_2 without use of catalyst possessing straight channels with extremely high aspect ratio and high specific surface area by a simple, high through put wet electrochemical method such as anodizing of metal plates. The proposed process with use of anodization of metal could be expanded to other metals to prepare various nanoporous oxides, and has potential technological applications in the fields of catalysis, supports, and sensors.

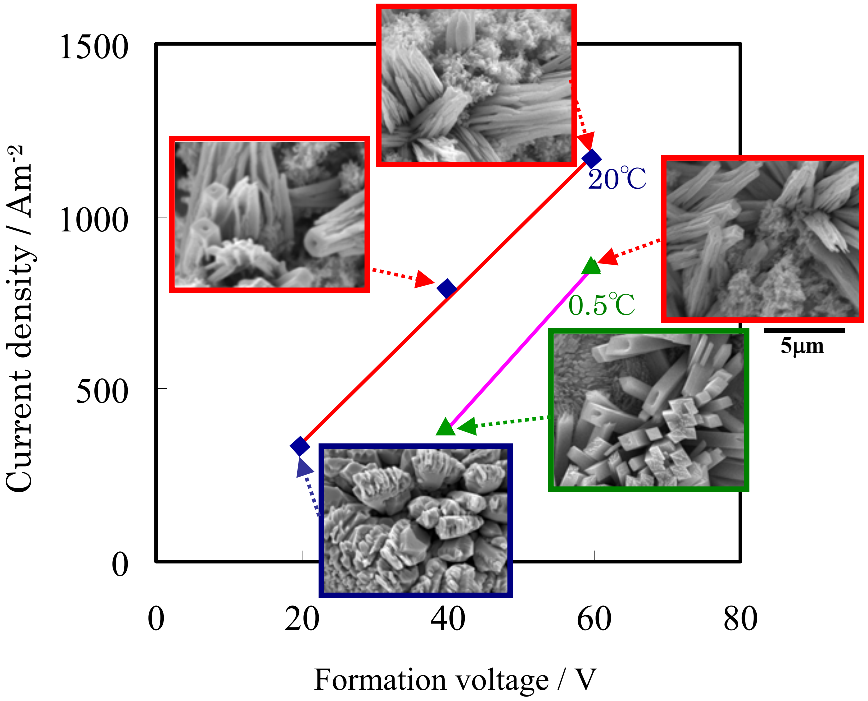

Fig. 4 SEM images of anodic oxide films formed on tin in sulfuric acid at various constant voltages for 10 min in connection with current density and temperature.

Acknowledgments

Parts of this work were financially supported by a Grant-in-Aid for Scientific Research from the Japan Society for the Promotion of Science. Thanks are also due to the "High-Tech Research Center" Project for Private Universities: matching fund subsidy from the Ministry of Education, Culture, Sports, Science and Technology.

References

1. H. Masuda and K. Fukuda, *Science,* **268**, 1466 (1995).
2. H.Masuda, F.Hasegawa and S.Ono *J.Electrochem.Soc.*, **144,** L127 (1997).
3. S. Ono, M. Saito, M. Ishiguro, H. Asoh, *J. Electrochem. Soc.* 151, B473 (2004).

4. H. Asoh and S. Ono, *in Electrocrystallization in Nanotechnology*, Chap. 7, p138, Wiley-Vch, Weinheim (2007).
5. A. Ghicov, H. Tsuchiya, J. M. Macak, P. Schmuki, *Electrochem. Commun.*, 7, 505 (2005).
6. J.M. Macak, M. Zlamal, J. Krysa, P. Schmuki, *Small,* **3**, 303 (2007).
7. Y. D. Wang,_K. Y. Zang, and S. J. Chua, C. G. Fonstad, *Appl. Phys. Lett.*, **89**, 263116 (2006).
8. L. E. Greene, M. Law, D. H. Tan, M. Montano, J. Goldberger, G. Somorjai, and P. D. Yang, *Nano Lett.*, **5**, 1231 (2005).
9. W. I. Park, G. C. Yi, M. Kim, and S. J. Pennycook, *Adv. Mater.,* **14**, 1841 (2002).
10. C. Yan, D. Xue, *Electrochem. Commun.*, **9**, 1247 (2007).
11. J. Zhang, L.D. Sun, C.S. Liao, C.H. Yan, *Chem. Commun.*, **3** (2002).
12. G. She, X. Zhang, W. Shi, X. Fan, J. C. Chang, *Electrochem. Commun.*, **9,** 2784 (2007).
13. C. Liu, J. A. Zapien, Y. Yao, X. Meng, C. S. Lee, S. Fan, Y. Lifshitz, and S. T. Lee, *Adv. Mater.,* **15**, 838 (2003).
14. S. Ono, Y. Kobayashi and H. Asoh, *ECS Trans*. **13**, 183 (2008).
15. H-C. Shin, J. Dong, and M. Liu, Advanced Materials 16, 237, (2004).
16. S.Kusakari, K.Shinozaki, K.Higa, Y.Yamaguchi, S.Yoshihara and T.Shirakashi, *DENKI KAGAKU*, 66, 594 (1998).

ECS Transactions, 16 (3) 359-367 (2008)
10.1149/1.2982576 ©The Electrochemical Society

Anodic Porous and Tubular Oxide Layers on Ti Alloys

H. Tsuchiya[a], J. Nakata[a], S. Fujimoto[a], S. Berger[b], and P. Schmuki[b]

[a] Division of Materials and Manufacturing Science, Graduate School of Engineering, Osaka University
[b] Department of Materials Science, Institute for Surface Science and Corrosion(LKO), University of Erlangen-Nuremberg

The present work investigates anodic oxide layers on Ti-Zr, Ti-Ta and Ti-Al alloys, focusing on how chemical compositions of the alloys and metallurgical textures can affect the resulting morphology of anodic oxide layers. The formation of porous and tubular oxide layers is achieved on all alloys The homogeneity of anodic oxide layers strongly depends on metallurgical textures of the alloys – on binary $\alpha + \beta$ Ti-Ta alloys, anodic oxide layers are not uniform while on single phase alloys such as Ti-Zr and Ti-Al, uniform oxide layers are formed. On the other hand, pore (tube) diameter and length are varied with the chemical compositions of the alloys. Emphasis is that on Ti-Al alloy, the morphological transition from pore morphology to tubular morphology can be observed depending the chemical compositions of the alloy.

Introduction

Anodizing self-organization have been reported for many metals in two different morphologies – highly ordered parallel-aligned porous structures and ordered arrays of tubes. The most established example of ordered porous structure achieved by anodization can be observed on Al. Since Masuda et al. reported aluminum oxide layers with highly ordered pores in hexagonal configuration (1), the structures have attracted much attention due to a wide range of applications. To obtain highly ordered pore arrays, optimized anodization process in suitable acidic electrolytes is required. Recently, it was reported that anodization in a neutral fluoride containing electrolyte can also lead to the formation of highly ordered porous aluminum oxide layers (2) and ordered anodic porous oxides can be achieved also on W (3), Ta (4) and Nb (5) using fluoride containing electrolytes. In contrast to these metals, anodization of other metals such as Ti (6), Zr (7) and Hf (8) in fluoride containing electrolytes results in highly ordered arrays of tubes.

Self-ordered tubular layers have been reported also on biomedical Ti-based alloys such as Ti6Al4V (9), Ti6Al7Nb (9), Ti28Zr8Nb (10) and Ti29Nb13Ta4.6Zr (11, 12). However, how compositions of alloys affect resulting morphology of anodic oxide layers has not been considered. In the present work, we examine the effect of alloy compositions on the structures of anodic oxide layers using Ti-Zr, Ti-Al and Ti-Ta alloys. Ti-Zr alloys consist of metals that can form tubular oxide layers while in the case of Ti-Al and Ti-Ta alloys, one element forms a tubular oxide and the other forms a porous oxide.

Experimental

Samples used were Ti-xTa(x= 13, 25, 50, 80 %) alloys, Ti-yZr(y= 20, 50, 80 wt.%) alloys, Ti_3Al, TiAl and $TiAl_3$ alloys. The samples were ground with SiC abrasive papers and mirror-finished with diamond paste. Prior to anodization, the samples were degreased by sonicating in acetone, isopropanol and methanol, successively, then rinsed with deionized (DI) water and dried with nitrogen stream.

The samples were contacted by a Cu plate and then pressed against an O-ring in an electrochemical cell, leaving 1 cm^2 exposed to the electrolyte. The electrochemical measurements were carried out in a classical three-electrode configuration with a Ag/AgCl (1 M KCl) electrode as a reference electrode and a platinum grid as a counter-electrode. The Ti samples were anodized using a high-voltage potentiostat. 1 M $(NH_4)_2SO_4$ + 0.5 wt.% NH_4F was used for Ti-Zr and Ti-Al alloys and 1M H_2SO_4 + 0.15 wt.% HF was for Ti-Ta alloys. The experiments were performed at room temperature under aerated non-stirred conditions. All solutions were prepared from chemical reagents of a high purity and deionized water.

The anodization consists of a potential ramp from open circuit potential (OCP) to 20 V, followed with holding the potential at 20 V for several hours.

For morphological characterization of the samples, a field-emission scanning electron microscope and transmission electron microscope were used. The cross-section images were taken from cracked layers after scratching the sample surface.

Results and discussion

Effect of Zr Content on Morphology of Anodic Oxide Layers

Figure 1 shows top-view and cross-sectional SEM images of anodic oxide layers on Ti-Zr alloys. The layers were formed by anodization at 20 V for 1 hour in 1M $(NH_4)_2SO_4$ + 0.5 wt.% NH_4F. It is clear from the figure that all anodic oxide layers formed on the alloys show tubular structures and the length and diameter of the tubes were varied with Zr content. The length and diameter variations are summarized in Fig. 2. As apparent, the tube length increases with increasing Zr content and on the other hand, the tube diameter decreases with Zr content. The tube diameter and tube length variations against Zr content in the alloys may be ascribed to the differences in growth rate of compact oxide layers and in chemical etching rate during anodization, respectively (13, 14). As-anodized TiO_2 nanotubes were reported to be amorphous while as-anodized ZrO_2 showed crystalline nature (15, 16). Figure 3 shows cross-sectional TEM images of anodic oxide layers on Ti-Zr alloys. Corresponding selected area diffraction (SAD) patterns are included in the figure. The TEM images also support anodic oxide layers on Ti-Zr alloys consist of arrays of nanotubes. It is apparent from the SAD patterns that all nanotubes are in amorphous state. Interesting is that even on high Zr content Ti-80wt.%Zr(Ti-68at.%Zr), the crystal structure of the layer reflects the nature of anodic TiO_2 layer.

Anodic Oxide Layers on Ti-Ta and Ti-Al Alloys

On Ti-Ta and Ti-Al alloys, compared to Ti-Zr alloy, different behaviors can be expected due to the morphologically different oxide layers on Ti and Ta (or Al). Figure 4 shows SEM images of anodic oxide layers formed on Ti-Ta alloys in 1M H_2SO_4 + 0.15 wt.% HF for 3 hours. It is clear that inhomogeneous oxide layers were formed on Ti-

13Ta and Ti-25Ta alloys. The alloys consist of α and β phases due to the relatively large two-phase region. In literature (11), for binary alloys, anodic oxide layers are not uniform and consist of two regions with different features. This can be the reason for the inhomogeneity observed on the alloys. However, the inset pictures in Fig. 4(a) and 4(b) reveal that anodic oxide layers on Ti-13Ta and Ti-25Ta consist essentially of nanotubes although the layers are not uniform. On Ti-50Ta that also has binary phases, as shown in Fig. 4(c), the layer consists of two regions – black and white regions (black and white regions are marked as "B" and "W", respectively, in Fig. 4(c)). At some locations, nanoporous structures can be observed as shown in Fig. 4(e). At the other locations, as apparent from Fig. 4(f), nanotubular structures are formed. However, nanotubes were formed underneath the nanoporous structures as shown in Fig. 4(g). Therefore, it can be deduced that on Ti-50Ta, a nanoporous layer was formed on the surface in the beginning stage of anodization and then, the formation of regular nanotube arrays underneath the top porous layer occurred. During the tube formation, the top porous layer was slowly dissolved, but the dissolution rate was strongly dependent of metallurgical phases of the alloy – α phase or β phase. As a result, after certain time of anodization, on some locations, nanotubes can be observed from the top while on other locations, nanotube layer is still covered with nanoporous layer. On Ti-80Ta alloy, a nanoporous layer was formed and the pore diameter and the thickness of the layer were totally similar to that on pure Ta (4). Therefore, it is concluded that morphological transition from tubular to porous morphology occurs with increasing Ta content, that is, chemical composition affects the morphology of anodic oxide layers on the Ti alloys. Figure 5 shows cross-sectional TEM image of nanotubes formed on Ti-50Ta alloy and corresponding SAD pattern. It is clear that on Ti-Ta alloys, as-formed nanotubes have amorphous structure.

In order to confirm that chemical compositions can affect the morphology of anodic oxide layer, Ti-Al alloys are examined. In contrast to Ti-Ta alloys, as Ti-Al alloy system has several intermetallic compounds where single phase can be obtained by heat treatments, only chemical compositions can be considered. Figure 6 shows top-view and cross-sectional SEM images of anodic oxide layers on pure Al, $TiAl_3$, TiAl and Ti_3Al formed at 20 V in 1M $(NH_4)_2SO_4$ + 0.5 wt.% NH_4F. On Al, regular pore arrays can be observed, consisting of nanopores with an average pore diameter of approximately 50 nm. Increasing Ti content in the intermetallic compounds, the porous features turn into a tubular structure. The transition from one morphology to another occurs between TiAl and Ti_3Al. The compositional threshold for the transition is anodization voltage controlled – when anodized at lower voltage such as 10 V, the threshold is between Ti_3Al and Ti while at 40 V, transition takes place between $TiAl_3$ and TiAl (14). The tube separation behavior can be attributed to increased stress that occurs within growing oxides due to increasing volume expansion. The present work clearly demonstrates that chemical compositions of alloys can affect morphology of anodic oxide layers.

Conclusions

In the present work, we examine how the chemical compositions and metallurgical textures of substrates affect the formation and morphology of anodic oxide layers using Ti-Zr, Ti-Ta and Ti-Al alloys. On binary Ti-Ta alloy where two phase structure is established in a wide range of chemical composition, tubular oxide layers can be obtained below 50 wt.% Ta, but the tubular structures are not uniform due to chemical etching of formed nanotubes by fluoride. The inhomogeneity is attributed to two phase structure. Ti-

Zr alloy system exhibits a solid solution behavior over the entire composition range. Therefore, as one can expect, uniform oxide layers are formed consisting of arrays of nanotubes. On the alloy, tubular structures can be observed on the entire composition range. The diameter of the tubes decreases with increasing Zr content while the length increases with Zr content. Morphological transition is achieved on Ti-Al alloy – increasing Ti content in the alloy results in a tube separation. The tube separation is attributed to increased stress by volume expansion.

Acknowledgements

This work was supported by Priority Assistance for the Formation of Worldwide Renowned Centers of Research – The Global COE Program (Project: Center of Excellence for Advanced Structural and Functional Materials Design) from the Ministry of Education, Culture, Sports, Science and Technology (MEXT), Japan. A part of the present experiments was carried out by using a facility in the Research Center of Ultrahigh Voltage Electron Microscopy, Osaka University.

References

1. H. Masuda, and K. Fukuda, *Science*, **268**, 1466 (1995).
2. H. Tsuchiya, S. Berger, J.M. Macak, A. G. Muñoz, and P. Schmuki, *Electrochem. Commun.*, **9**, 545 (2007).
3. H. Tsuchiya, J.M. Macak, I. Sieber, L. Taveira, A. Ghicov, K. Sirotna, and P. Schmuki, *Electrochem. Commun.*, **7**, 295 (2005).
4. I. Sieber, B. Kannan, and P. Schmuki, *Electrochem. Solid-State Lett.*, **8**, J10 (2005).
5. I. Sieber, H. Hildebrand, A. Friedrich, and P. Schmuki, *Electrochem. Commun.*, **7**, 97 (2005).
6. J.M. Macak, H. Tsuchiya, A. Ghicov, K. Yasuda, R. Hahn, S. Bauer, and P. Schmuki, *Curr. Opin. Sol. State Mater. Sci.*, **11**, 3 (2008).
7. H. Tsuchiya, J.M. Macak, L. Taveira, and P. Schmuki, *Chem. Phys. Lett.*, **410**, 188 (2005).
8. H. Tsuchiya, and P. Schmuki, *Electrochem. Commun.*, **7**, 49 (2005).
9. J. M. Macak, H. Tsuchiya, L. Taveira, A. Ghicov, and P. Schmuki, *J. Biomed. Mater. Res.*, **75A**, 928 (2005).
10. X.J. Feng, J.M. Macak, S.P. Albu, and P. Schmuki, *Acta Biomaterialia*, **4**, 318 (2008).
11. H. Tsuchiya, J.M. Macak, A. Ghicov, and P. Schmuki, *Small*, **2**, 888 (2006).
12. H. Tsuchiya, J.M. Macak, A. Ghicov, Y.-C. Tang, S. Fujimoto, M. Niinomi, T. Noda, and P. Schmuki, *Electrochim. Acta*, **52**, 94 (2006).
13. A. Ghicov, S. Aldabergenova, H. Tsuchiya, and P. Schmuki, *Angew. Chem. Int. Ed.*, **45**, 6933 (2006).
14. S. Berger, H. Tsuchiya, and P. Schmuki, *Chem. Mater.*, **20**, 3245 (2008).
15. J. M. Macak, H. Tsuchiya, L. Taveira, S. Aldabergerova, and P. Schmuki, *Angew. Chem. Int. Ed.*, **44**, 7463 (2005).
16. H. Tsuchiya, J.M. Macak, L. Taveira, and P. Schmuki, *ECS transactions*, **1**, 351 (2006).

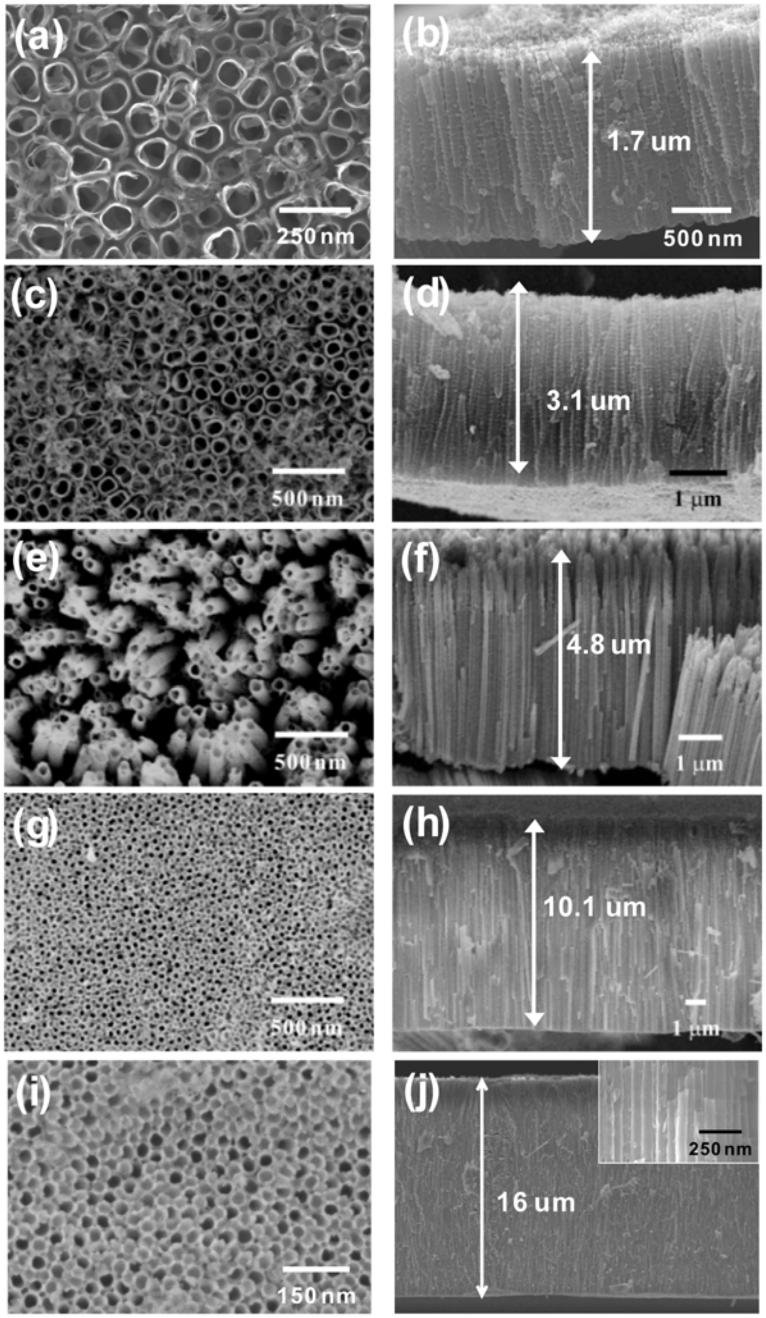

Figure 1. Top-view (a, c, e, g, i) and cross-sectional (b, d, f, h, j) SEM images of anodic oxide layers formed on Ti (a, b), Ti-20Zr (c, d), Ti-50Zr (e, f), Ti-80Zr (g, h) and Zr (I, j), respectively.

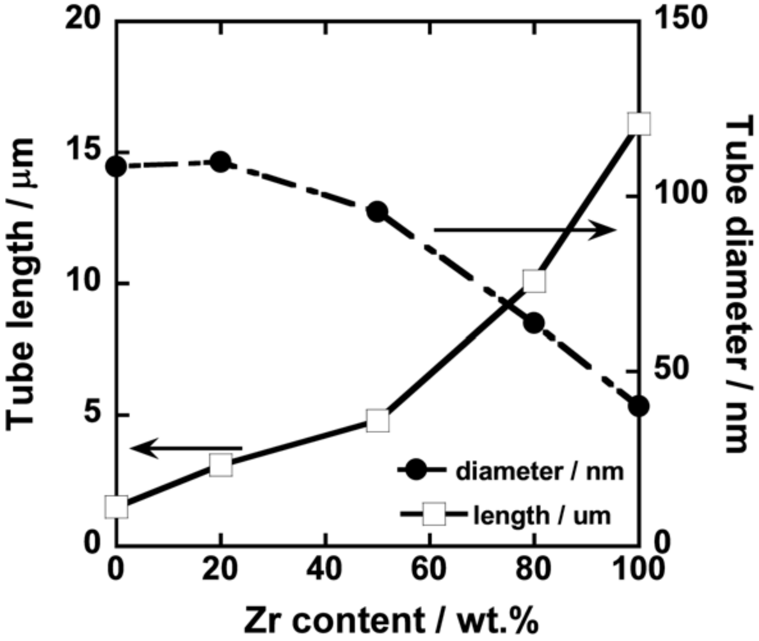

Figure 2. Effect of zirconium content on tube diameter and tube length.

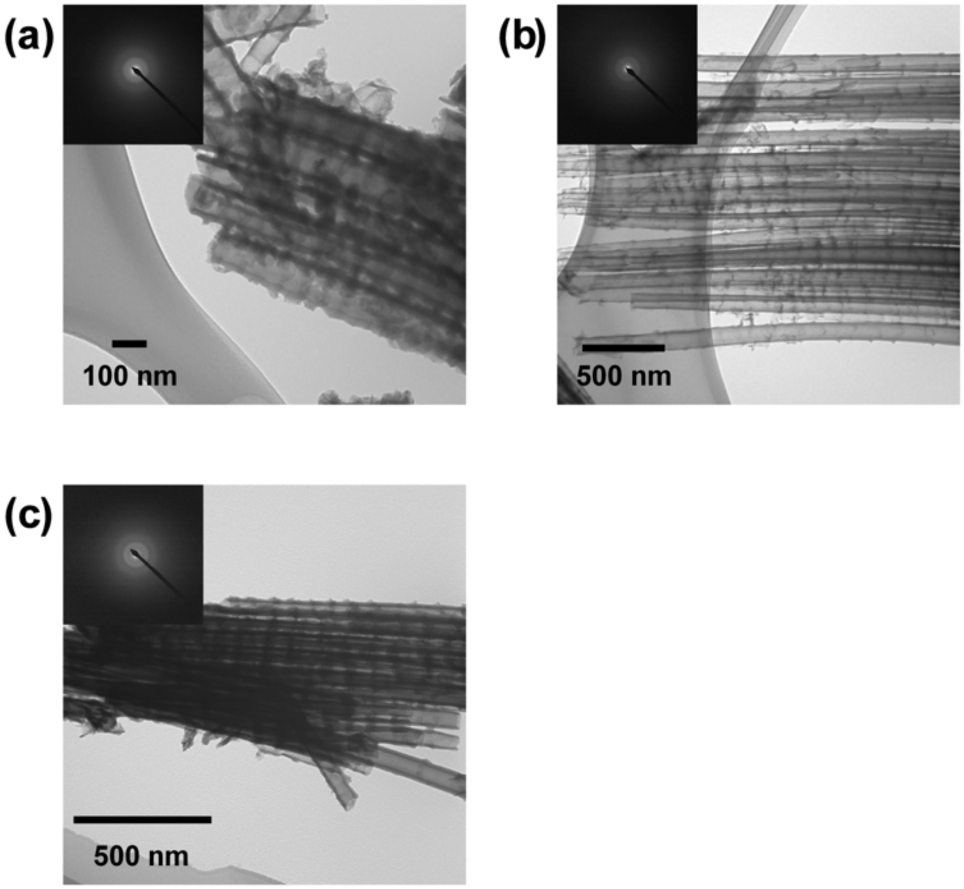

Figure 3. TEM images of anodic tubular layers on Ti-20Zr (a), Ti-50Zr (b) and Ti-80Zr (c). The insets show corresponding SAD patterns.

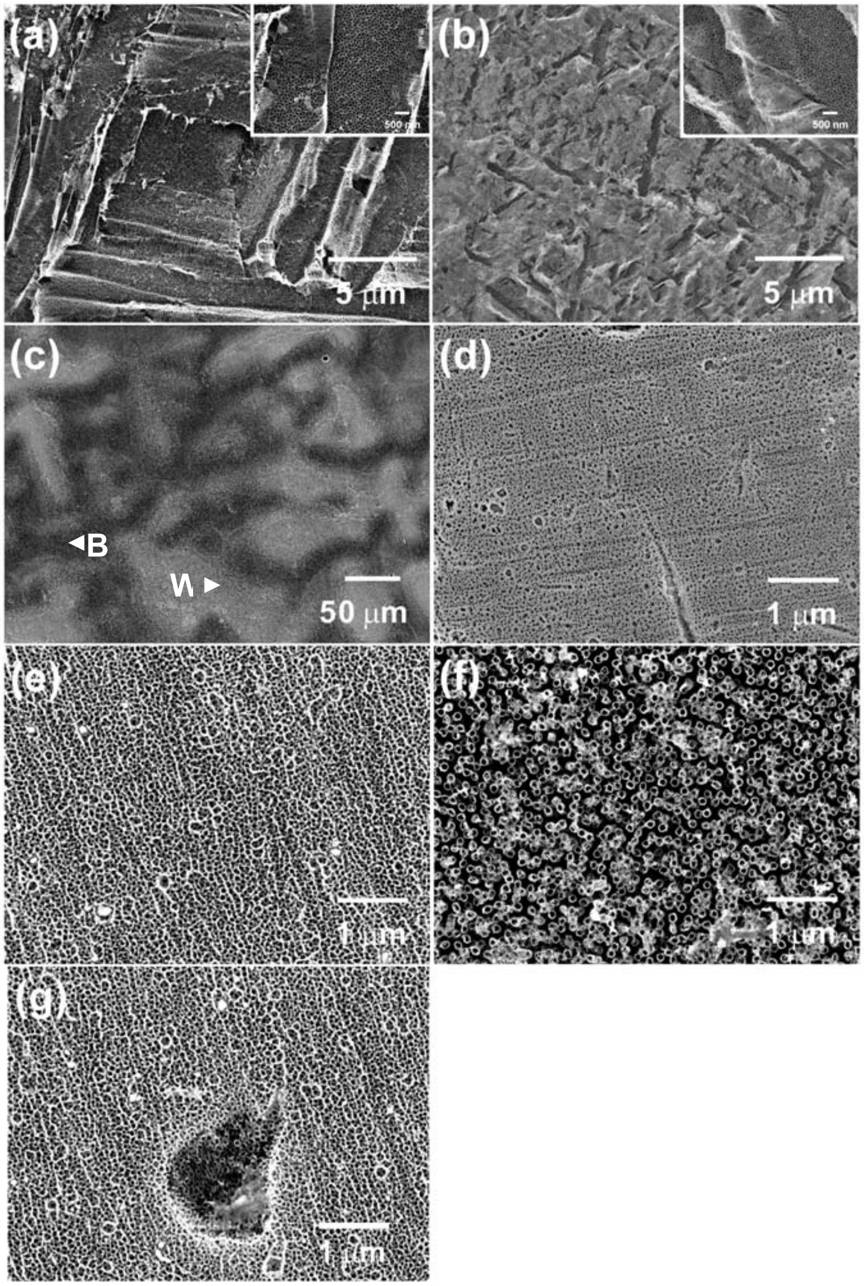

Figure 4. Top-view SEM images of anodic oxide layers formed on Ti-Ta alloys in 1M H_2SO_4 + 0.5 wt.% HF; (a) Ti-13Ta, (b) Ti-25Ta, (c) Ti-50Ta, (d) Ti-80Ta. Higher magnification for the black (f) and white (e, g) regions in the image (c).

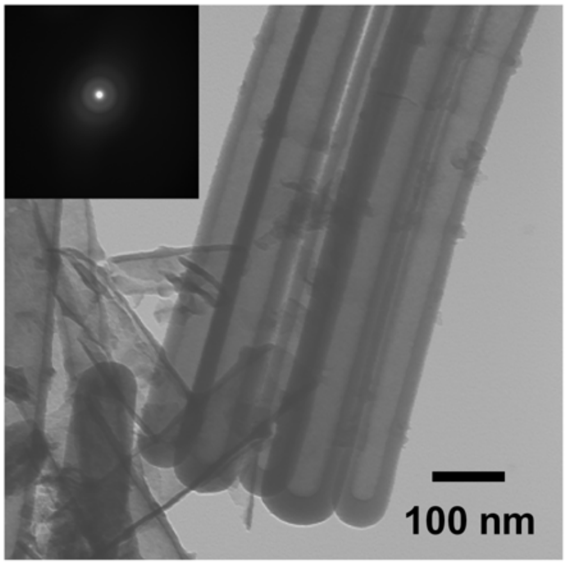

Figure 5. TEM image of anodic oxide nanotubes formed on Ti-50Ta alloy. The inset shows selected area diffraction (SAD) pattern of corresponding tubes.

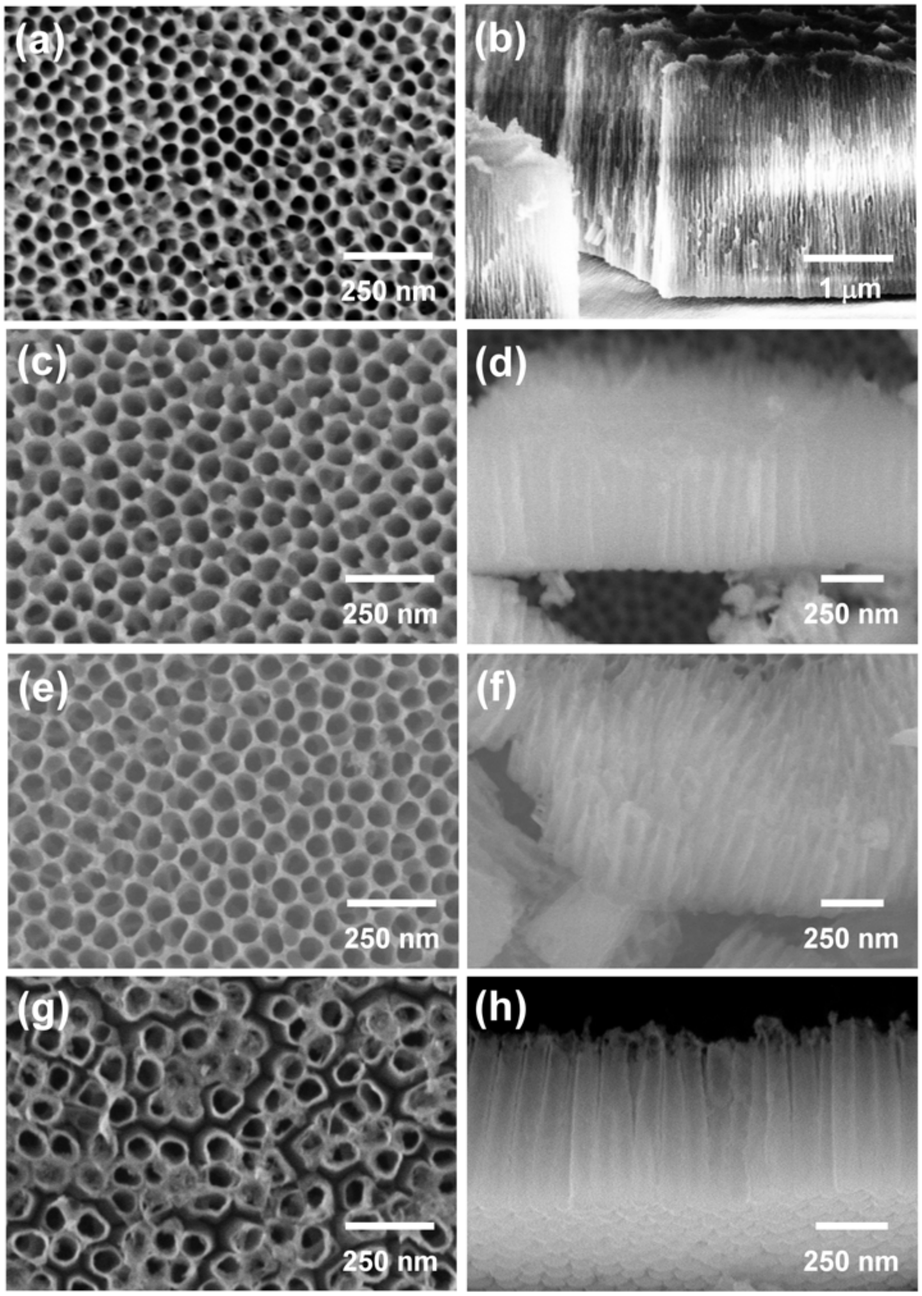

Figure 6. Top-view (a, c, e, g) and cross-sectional (b, d, f, h) SEM images of anodic oxide layers formed on Al (a, b), $TiAl_3$ (c, d), TiAl (e, f) and Ti_3Al (g, h), respectively.

ECS Transactions, 16 (3) 369-373 (2008)
10.1149/1.2982577 ©The Electrochemical Society

Self-organized Anodic TiO_2-nanotubes in Fluoride Free Electrolytes

R. Hahn, H. Lee, D. Kim, S. Narayanan, S. Berger, P. Schmuki*

Department of Materials Science and Engineering, WW4-LKO, University of Erlangen-Nuremberg, Martensstrasse 7, D-91058 Erlangen, Germany

* Corresponding author: e-mail address: schmuki@ww.uni-erlangen.de

The conventional approach for the formation of highly self-organized nanotube layers is based on anodization of titanium in fluoride containing electrolytes. In the present work we demonstrate that also chloride ions in a suitable organic electrolyte can be used to grow organized nanotube layers. The results show, that under specific electrochemical conditions the growth process can change from a previously reported rapid breakdown anodization mechanism (that leads to disordered nanotube bundles) to a self-organized nanotubular growth mechanism. Under these conditions the nanotubes exhibit the key characteristics of self-ordered tubes (closed tube bottoms, regular dimple structures on the metallic substrate and a linear dependence of the tube diameter on the applied potential).

Introduction

Since Zwilling et al. (1) reported in 1999 on the possibility to grow self organized TiO_2-nanotubes by anodization of titanium in diluted HF electrolytes, several steps of progress towards enhanced nanotubular morphology were reported based on ever optimized growth conditions. The focus of research was to achieve higher aspect ratios by diminishing the TiO_2 dissolution rate in the presences of fluoride ions. Significant breakthroughs were the tailoring of the pH profile in the solution (2,3) and the use of more viscous or non aqueous electrolytes (4,5). This enabled the growth of highly hexagonal ordered nanotubes with super high aspect ratios (6), similar to nanoporous Al (7). An overview of achievements in nanotubular growth and their usage towards electrochromic, photocatalytic, medical and solar energy conversion applications is given in (8).

Stimulated by abstracts of Nakayama et al. (9) that anodic nanotubular growth on titanium may not exclusively be induced by fluoride ions, reports showed that nanotubes can also be grown in perchlorates (10), chlorides (10,11) or newly bromide containing electrolytes (12). Although these nanotubes lack order - they grow in disordered bundles - a significant advantage is the extremely rapid growth process, i.e. within seconds, nanotubes of tens of micrometers can be grown. Recent work of Ishibashi et al. (13) describes a more homogeneous growth of the TiO_2-nanotubes using perchloric acid in ethanolic electrolytes. Overall, this fast production makes the nanotubes very attractive for their use in applications such as dye-sensitized solar cells (13,14).

The key deficit of these tubes is, however, that they do not grow in ordered arrays-while, except for the rapid growth the key advantage is their production in fluoride free media. In the present work we show though that in organic chloride containing electrolytes the electrochemical conditions can be tuned to form ordered high aspect ratio arrays of TiO_2 nanotubes.

Experimental Part

Ti samples (Advent, 99.6% purity) were cleaned by sonicating in pure ethanol and dried with a nitrogen stream prior to electrochemical experiments. For anodization, a constant voltage source (Voltcraft, VLP-2403) with Pt as counter electrode was used. The distance between counter and working electrode was adjusted to 1cm. The electrolyte used consisted of glycerol/formamide mixtures (volume ratio 50:50) with 0.3M HCl. One parameter under study was the applied voltage (10-40V). After anodization the samples were carefully dipped into pure ethanol for 1h and then dried in air. For characterization of the sample morphology a field-emission scanning electron microscope Hitachi FE-SEM S4800 was used.

Results and Discussions

Figure 1A) shows a typical current transient for the anodization of titanium in an electrolyte of formamide/glycerol mixture containing hydrochloric acid. Using formamide/glycerol mixtures as electrolyte system is based on surface tension effects as demonstrated by Dörfler in 1979 (15). Interestingly, the obtained I-t curve is in shape and values very similar to those obtained for the anodization of titanium in fluoride containing electrolytes when growth of self-organized TiO_2 nanotubes is established. In analogy, the transient can be divided into three steps: I) high field assisted oxide growth, II) contribution of anion species in the field aided process and III) diffusion limitation of the tube growth. In the case of the organic chloride ion containing electrolyte after 10 min of anodization a yellow jellylike layer is forming on the surface which is most likely associated with the precipitation of titanium-hydroxy species.

Figures 1B) and 1C) depict the corresponding SEM tilted top and a cross sectional views on the TiO_2 nanotubes formed by an anodization process in 0.3M HCl in glycerol/formamide (50:50) at 20V for 6200s. Clearly, smooth TiO_2 nanotubes with a diameter of ~100nm and lengths of up to 2.2 μm are formed on the surface. Prolonged anodization (up to 12 hours) leads to much longer tubes (12μm) but due to their smooth character and the bad adherence, these nanotube layers lift off from the surface.

Figure 2A) shows SEM of the closed bottoms of these nanotubes and the resulting dimple imprint structure remaining on the metallic titanium surface. These observations are in line with work done using fluorides and demonstrate that not only disordered RBA-TiO_2 nanotubes (RBA stands for rapid breakdown anodization) (10) can be formed in chloride containing solutions but also ordered arrays.

The biggest difference to the RBA type nanotubes, where only a small dependence of the tube diameter on the applied potential is found (13), is plotted in Figure 3. Under the used electrochemical conditions a clear linear dependence of the tube diameter on the applied potential is visible. The tube diameter could be varied between ~45 and 200 nm by applying 15 to 40V. In contrast to fluoride ions where nanotubes were observed at 1V (3), it seems that for chlorides at least 10V needs to be applied to observe nanotubular growth. On the one hand, due to the bigger ion size of chlorides a higher field needs to be applied to initiate tube growth. Another explanation may be the higher chemical stability of TiO_2 against chlorides. Nevertheless, this dependency on the tube radius of ~2.9nm/V is in line with work done on fluoride where values of 2.5nm/V are reported (16). The insets are SEM pictures of nanotubes obtained at 15 and 20V applied potential.

In contrast to fluoride electrolytes where nanotubes can be observed over a broad range of electrochemical conditions (concentrations, electrolyte compositions,…) the presented system is much more sensitive to small changes. The most critical factor seems to be the water content, as at too high water content the growth process easily changes back to RBA type nanotubular growth. In our case the remaining water content was determined by the use of 37% aqueous HCl. A remaining challenge is to achieve thicker nanotubular layers by improving the adherence to the Ti substrate. Homogeneous nanotubular growth can be optimized by using polished titanium substrates and by stepping the potential to 20V to overcome the critical nanotube formation boarder of approx. 10V in chloride based electrolytes (otherwise only irregular compact films are formed or strong localized surface attack takes place).

Conclusions

In the present work we demonstrate self-organized, anodic growth of high aspect ratio TiO_2 nanotubes in an organic electrolyte containing only chloride ions. We show that by optimization of the electrochemical conditions the usual growth of RBA-nanotubes can be significantly slowed down and self-organized ordering takes place. Under these conditions nanotubes could be grown with diameters of ~45nm and up 200nm depending on the applied potential (15-40V) and tube lengths of up to 2.2μm. Additionally these results imply new concepts regarding mechanisms leading to self-organized nanotubular growth, as it is demonstrated that fluorides lost their privilege on being the prerequisite for the formation of ordered, high aspect ratio TiO_2 nanotubular arrays.

Acknowledgments

The authors gratefully acknowledge the Staedtler-Stiftung, the DFG and the European Union within the FP6 program for financial support.

References

1. V. Zwilling, E. Darque-Ceretti, A. Boutry-Forveille, D. David, M.Y. Perrin, M. Aucouturier, *Surf. Interface Anal.*, **27**, 629 (1999).
2. J. M. Macak, H. Tsuchiya, P. Schmuki, *Angew. Chem., Int. Ed.*, **44**, 2100 (2205).
3. S. Bauer, S. Kleber, P. Schmuki, *Electrochem. Commun.*, **8**, 1321 (2006).
4. J. M. Macak, H. Tsuchiya, L. Taveira, S. Aldabergerova, P. Schmuki, *Angew. Chem., Int. Ed.*, **44**, 1 (2005).
5. S. P. Albu, A. Ghicov, J. M. Macak, P. Schmuki, *phys. stat. sol. (RRL)*, **1**, R65 (2007).
6. J. M. Macak, S.P. Albu, P. Schmuki, *phys. stat. sol. (RRL)*, **1**, 181 (2007).
7. H. Masuda, K. Fukuda, *Science*, **268**, 1466 (1995).
8. J. M. Macak, H. Tsuchiya, A. Ghicov, K. Yasuda, R. Hahn, S. Bauer, P. Schmuki, *Curr. Opin. Solid State Mater. Sci.*, **11**, 3 (2007).
9. K. Nakayama et al. in: *208th ECS Meeting*, California, Abstract #819 and Abstract # 843 (2005).
10. R. Hahn, J. M. Macak, P. Schmuki, *Electrochem. Commun.*, **9**, 947 (2007).

11. C. Richter, Z. Wu, E. Panaitescu, R. Willey, L. Menon, *Adv. Mater.*, **19**, 946 (2007).
12. Q. A. Nguyen, Y. V. Bhargava, T. M. Devine, *Electrochem. Comm.*, **10**, 471 (2008).
13. K. Ishibashi, R. Yamaguchi, Y. Kimura, M. Niwano, *J. Electrochem. Soc.*, **1**, K10 (2008).
14. R. Hahn, T. Stergiopoulos, J. M. Macak , D. Tsoukleris, A. G. Kontos, S. P. Albu, D. Kim, A. Ghicov, J. Kunze, P. Falaras, P. Schmuki, *phys. stat. sol. (RRL)*, **1**, 135 (2007).
15. H.-D. Dörfler, *Colloid Polym. Sci.*, **257**, 882 (1979).
16. K. Yasuda, J. M. Macak, S. Berger, A. Ghicov, P. Schmuki, *J. Elctrochem. Soc.*, **154**, C472 (2007).

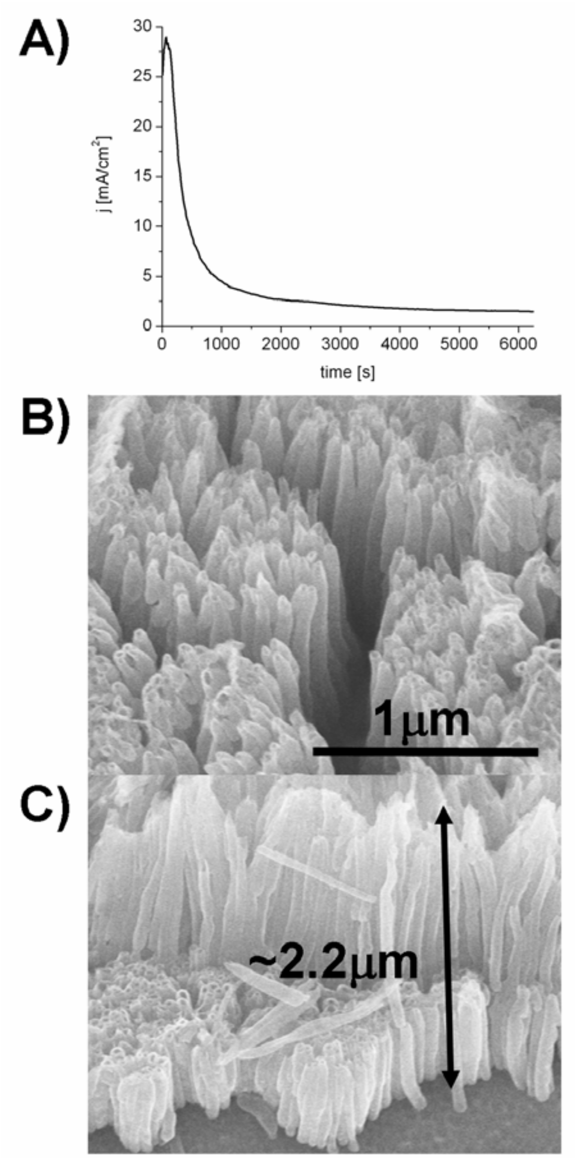

Figure 1. A) A typical current transient for the anodization of Ti in 0.3M HCl in formamide/glycerol mixtures (50:50) at 20V. 1B) and 1C) are the corresponding SEM

tilted top and cross sectional views of TiO_2 nanotube layers obtained after the anodization process in A).

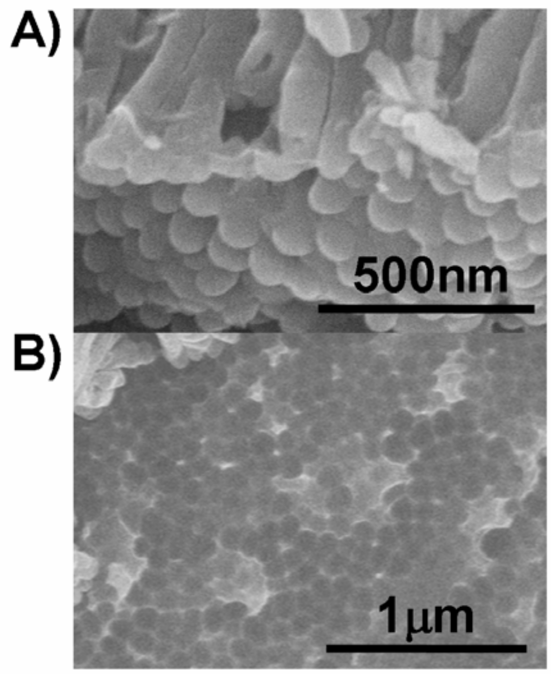

Figure 2. SEM images of the bottom of TiO_2 nanotubes A) and the imprinted dimple structure left in the metallic Ti surface after removal of the nanotube layer B).

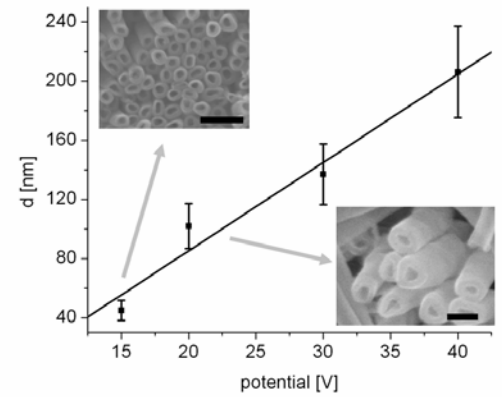

Figure 3. Linear dependence of the tube-diameter on the applied potential. The insets show nanotubes obtained at 15V and 20V in 0.3M HCl in formamide/glycerol mixtures (50:50). The scale bars are 100nm.

ECS Transactions, 16 (3) 375-389 (2008)
10.1149/1.2982578 ©The Electrochemical Society

Efficient Solar Cell Structure Prepared by Electrodeposition into Oscillation-Induced Nanoporous Silicon Oxide

H. J. Lewerenz, T. Stempel

Division of Solar Energy, Helmholtz Zentrum Berlin, Germany

A silicon-based nanoemitter solar cell is described that operates in the photovoltaic mode of a photoelectrochemical solar cell (PECS). Low temperature scalable processing uses current oscillation-induced nanoporous oxide matrices as templates for noble metal nanocontacts prepared by electrodeposition. Light-to-electricity conversion efficiencies of $\eta > 10\%$ have been obtained if the nanopores in the passivating oxide layer are deepened into the silicon substrate by electro-etching in alkaline solution. In synchrotron radiation photoelectron spectroscopy (SRPES) investigations on model surfaces that were H-terminated, oxide formation during Pt deposition is observed while Pt is present in its elemental state. The influence of the oxidic film that is also present underneath the Pt nanoislands on the electronic properties of the cell is discussed and optimization routes for increased efficiencies are outlined.

1. Introduction

The advent of nanoscience has resulted in the discovery of novel properties and features of nano-dimensioned matter that have important implications for solar energy conversion. Besides the discovery of novel excitation processes such as multiple exciton generation (1), alternative excitation energy transfer mechanisms such as Dexter exciton hopping (2) and (multichromic) Förster resonant energy transfer (3) have been found increasing interest in the recent past, resulting in detailed theoretical understanding (4,5). Inspection of the principles in excitation energy funnelling and in spatial arrangement of photosynthesis systems also led to the preparation of nanocomposite structures for light-induced energy conversion (6,7).

In the field of non-linear dynamics, oscillatory phenomena have been analyzed since long (8)and in solution chemistry, the spatial-temporal behaviour of the Belusov-Zhabotinski reaction is the most known example (9). More recently, oscillating (photo)electrochemical systems have found increasing attention (10-14). In photoelectrochemistry, modern theories have been advanced, in particular to understand and describe the oscillatory behaviour of silicon electrodes in fluoride containing solutions (15-17) A main feature in the explanation of silicon photoelectrode oscillations has been the postulation and the experimental observation of nano-sized pores in the oxide that covers Si during oscillation (18-19).

In solid state photovoltaics, point contact solar cells have been introduced about two decades ago (20,21). The so-called point contacts were diffused highly doped n- an p-regions within float zone Si with diffusion determined sized of the order of 5-10µm. Despite this rather large size of the contacts, the principle operation of such solar cells

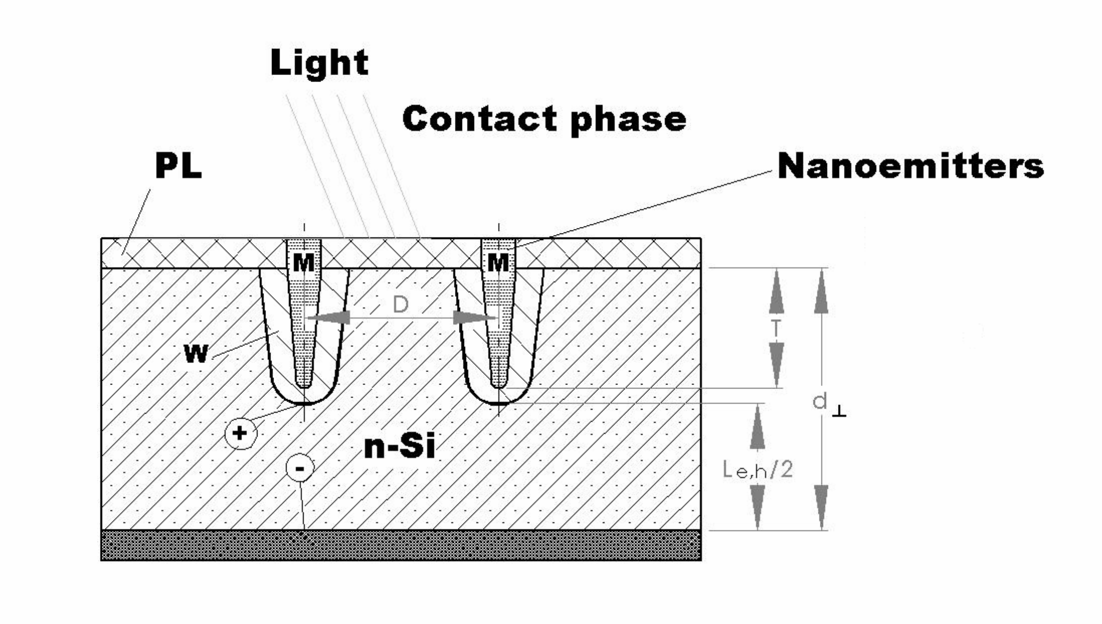

Figure1. Schematic of the concept of a nanoemitter solar cell; nano-dimensioned pores in a passivating layer (here silicon oxide) that have been deepened by etching are filled with a material that forms a rectifying contact with the absorber such as Pt for n-Si. At these contacts, diffusing and then drifting excess minority carriers are collected and emitted to the front contact; W: space charge region; D: distance between nanoemitters; $d_\perp$: thickness of the absorber; T: depth of pores within silicon; M: metal nanoemitter in wire-type/rod shape; cross-hatched area: passivating layer (PL); full grey area: ohmic back contact; $L_{e,h}$: minority carrier diffusion length.

where light-induced excess carriers diffused and were deflected to their respective contacts allowed fabrication of high efficiency solar cells for concentrator applications.

In the present approach, we present a nano-composite Si-based structure that has been prepared by photocurrent oscillations of Si in dilute ammonium fluoride solutions at larger anodic potential. The structure is based on the spatially selective filling of the nanopores that occur during current oscillations with a metal that forms a Schottky barrier with the underlying Si substrate. These metal contacts serve as nanoemitters for the light-induced excess carriers and Fig.1 shows a schematic of the corresponding solar cell geometry where the conditions for efficient charge carrier collection can be deduced from the lateral distance of the nanoemitters, the extension of the space charge layer and the depth of the nanopores that become metallized for improved red sensitivity. It should be emphasized that this concept allows adjustment of the emitter spacing to the material quality as given by the minority carrier diffusion length and that the small size of the contacts leads to negligible shading of the incoming light. Besides metals, many other materials that can form rectifying junctions with the absorber and that can be conformally deposited either chemically or electrochemically can be employed, thus offering new avenues for low cost efficient solar cells where the absorber is protected by passivating films from the reactive interface in photoelectrochemical solar energy converting devices (22-24). As a first application, the develoment of an efficient photoelectrochemical solar cell (PECS) that operates in the photovoltaic will be described below.

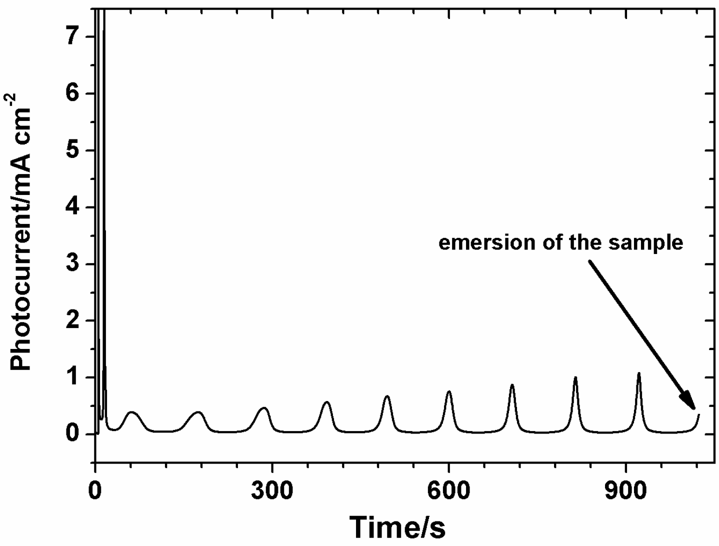

Figure 2. Photocurrent versus time in 0.1 M NH_4F, pH 4, illumination intensity 20 mWcm^{-2}, electrode potential V= 6V (SCE).

2. Experimental procedures

Electrolytes were prepared from the highest available purity grade, either in analytical grade or ultrapure quality. High purity 18MΩ water was used. As Si substrates, n-type (100) oriented wafers from CrysTec with 0° nominal miscut, P-doped to $5\cdot10^{15}$ cm^{-3} were used. (Photo)electrochemical experiments were performed in the standard three-electrode configuration with a Pt or C counter- and a saturated calomel reference electrode (SCE). All potentials are referred to SCE. Prior to oscillations, the samples were chemically H-terminated using an established procedure that results in extended atomically flat terraces (25). Photocurrent oscillations were induced as shown in Fig.2: the sample was immersed in a dilute ammonium fluoride solution (0.1 M, pH 4) and a potential of +6V was applied in the dark where n-Si still shows blocking behavior. Upon illumination with white light, two initial current peaks are observed which indicate an hitherto unknown two-step passivation and after about 30s have elapsed, regular oscillations set in. After 6-8 oscillatory cycles, the sample is emersed from the solution and submitted to further processing as will be described in the results section.

For electrodeposition into nanopores, the standard electrochemical arrangement described above has been used. The solution consisted of a 10^{-3} M H_2PtCl_6 and 0.1 M K_2SO_4 with pH 2.8.

Model experiments on Pt electrodeposition onto (1x1) H-terminated n-Si(111) samples were done in a combined electrochemistry-surface analysis system where electrochemical processing can be done in inert N_2 atmosphere (26) with subsequent transfer into an outgasing chamber and then into the analysis chamber of the Solid-Liquid Analysis System (SoLiAS) at the U49/2 beamline at the synchrotron storage ring Bessy II.

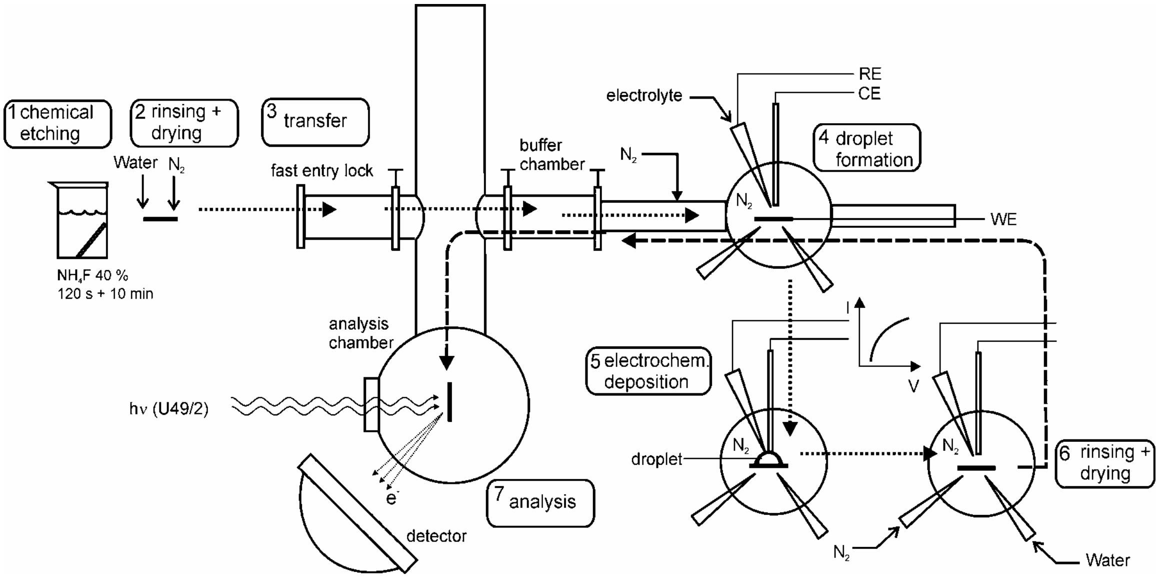

Figure 3. Chemical, electrochemical and surface analytical procedures in the combined electrochemistry/surface analysis system SoLiAS; 1: chemical pretreatment; 2: preparation for insertion of the sample into the analysis system; 3: sample transfer to the electrochemistry vessel on the upper right where electrolyte is supplied as droplets onto the horizontally aligned sample (step 4); 5: electrodeposition model experiment showing also schematically the I-V characteristicfollwed by rinsing and drying (step 6) and then by UHV surface analysis in the analysis chamber (step 7) after outgasing in the buffer chamber.

The SoLiAS and the glass vessel where (photo)electrochemical experiments were performed are schematically shown in Fig.3.

3. Results and Discussion

After sample emersion following the protocol given in Fig.2, HRSEM images show nano-dimensioned pores within the approximately 10 nm thick oxide layer that is formed upon electrode oscillation (27). The area density and the average pore sizes can be influenced rather easily by the solution pH and the light intensity. The dynamic competition between oxide formation due to light induced holes and oxide etching which increases with lowering the pH according to the overall reaction

$$SiO_2 + 6HF \rightarrow SiF_6^{2-} + 2H_{aq}^{+} + 2H_2 \qquad [1]$$

$$SiO_2 + 3HF_2^{-} \rightarrow SiF_6^{2-} + H_2O + OH^{-}. \qquad [2]$$

Despite the statement of Judge [28] that the F$^-$ ion is not actively participating in the dissolution of silicon oxide, Kikuyama has more recently found (29) that F$^-$ ions can contribute to oxide etching if their concentration is sufficiently large. The ions react via the consumption of protons with the oxide according to

$$SiO_2 + 6F^{-} + 4H_{aq}^{+} \rightarrow SiF_6^{2-} + 2H_2O. \qquad [3]$$

Compared to the rate for the etch processes in eqns.[1,2], this third mechanism is slow and can be neglected in the determination of the contributing factors to the etch rate which is then given by (28)

$$k_e = a[HF] + b[HF_2^-] + c\,. \qquad [4]$$

The concentrations $[HF]$ and $[HF_2^-]$ are given by the dissociation constants

$$K_1 = \frac{[H^+][F^-]}{[HF]} \quad ; \quad K_1 = 1.3 \cdot 10^{-3} \qquad [5]$$

$$K_2 = \frac{[HF][F^-]}{[HF_2^-]} \quad ; \quad K_2 = 0.104 \qquad [6]$$

The dependence of k_e on pH is then given by

$$k_e = \left(\frac{a}{K_1} + \frac{b}{K_1 K_2}[F^-] \right) [H^+][F^-] + c\,, \qquad [7]$$

where the concentration $[F^-]$ can be determined from an according quadratic equation deduced from the condition

$$[F_{total}] = [F^-] + [HF] + 2[HF_2^-]\,. \qquad [8]$$

Eqn. [7] shows that the etch rate increases with decreasing pH in these dilute NH_4F solutions. The oxide formation rate is dependent on the surface concentration of light-induced holes, h_s, which react to form silicon oxide:

$$Si_s + 2H_2O + 4h_{VB}^+(h\nu) \rightarrow SiO_2 + 4H_{aq}^+ \qquad [9]$$

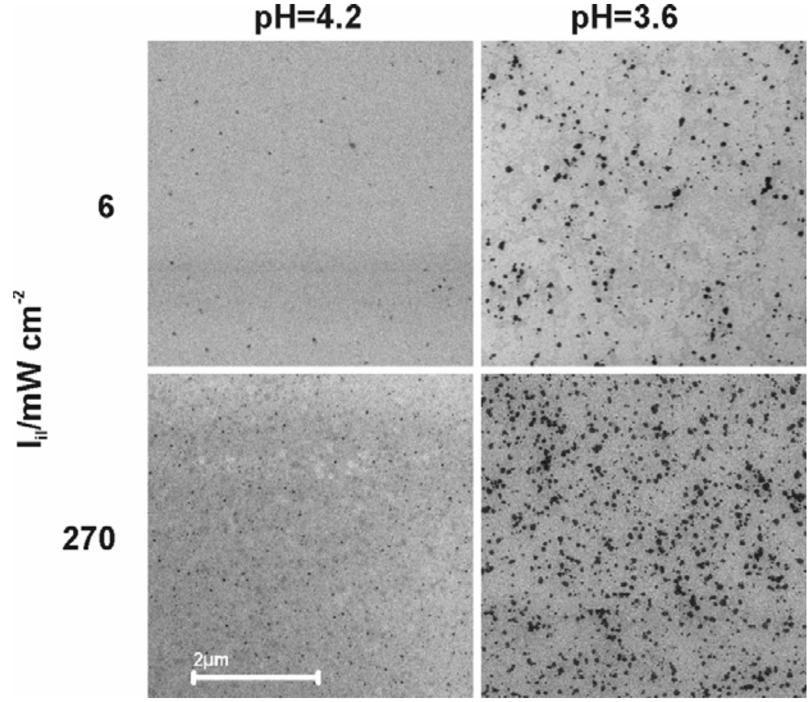

Figure 4. HRSEM images of n-Si(100) after oscillatory treatment (see text and Fig.2) for two light intensities given on the ordinate (6mWcm^{-2} and 270 mWcm^{-2}) and for pH 3.6 and 4.2 as indicated; 0.1 M NH_4F, V = +6V).

As can be seen from Fig.2 upon inspection of the initial photocurrent signal and in the related literature on anodic oxidation of silicon (27), the oxidation is a fast process compared to the period of the oscillations. A typical result is shown in Fig.4 where it can be seen that at lower pH and low light intensity, only a few small pores with diameters below 10 nm are formed. Increasing the light intensity at the same pH (lower left part of the figure) produces a larger number of these small pores and an indication of an increased roughness of the oxide layer is seen in the HRSEM material contrast. At lower pH and increased k_e (upper right image), a considerably larger number of pores with increased diameters is found and a rather large size dispersion exists. Some of the pores have been grown into each other thus forming larger entities. It should also be noted that some pore shapes exhibit the twofold C_{2v} symmetry of the Si(001) substrate surface. A drastic increase of the light intensity at this pH (lower right image) results in even larger pores, more pore coalescence and almost exclusively rectangular shaping according to the substrate symmetry. The influence of the light intensity and the oxide etch rate on oscillatory behavior can be seen in the chronocoulometric profiles displayed in Fig.5. Whereas at fixed pH, the influence of the light intensity I_{il} does not induce a change of the charge Q(t) passed with time (Fig.5b), the pH has a distinct effect on Q(t). Between pH 3.6 and pH 4.2, the average slope changes from 0.53 mC cm^{-2}s^{-1} to 0.14 mCcm^{-2}s^{-1}, i.e. it is reduced by a factor of ~3.7. The relative etch rate according to eqns.(4, 7) is reduced by a smaller factor of about 2.5, resulting in a slower oxidation and etching process at pH 4.2 as is also indicated by the lower oscillation frequency: the periodicity with I_{il} shows periods in the upper part of Fig.5 of 140-150s for pH 4.2 and of ~ 20s for pH 3.6. The more dynamic system at pH 3.6 is characterized by faster oxide growth and dissolution which in turn produces more stress at the interface between the growing oxide and the silicon substrate. Thus, the overproportional charge flow increase can be understood by the increased surface roughness of the electrode. In our general model (16,17,30), the volume mismatch induced stress between Si and its oxide has been identified as cause for the generation of cracks in the oxide that eventually develop into pores in the oxide etching solution. Faster oxide growth and etching is believed to produce a larger number of oxide islands within two successive cycles resulting in a larger area density of so-called high- and low quality oxides (31). This then results in the formation of a larger number of pores as can be seen in the lower part of Fig.4. This also obviously results in the coalescence of adjacent pores whose distances have become considerably smaller and also, larger pores can be seen in the lower part of Fig.4. Presently, with the experimental data that are available, this is a working hypothesis and, in addition, it is not clear why the nano-dimensioned pores in the amorphous oxide exhibit the crystal symmetry of the underlying Si substrate plane. This topic will be investigated by a combination of HRSEM and AFM structure analysis.

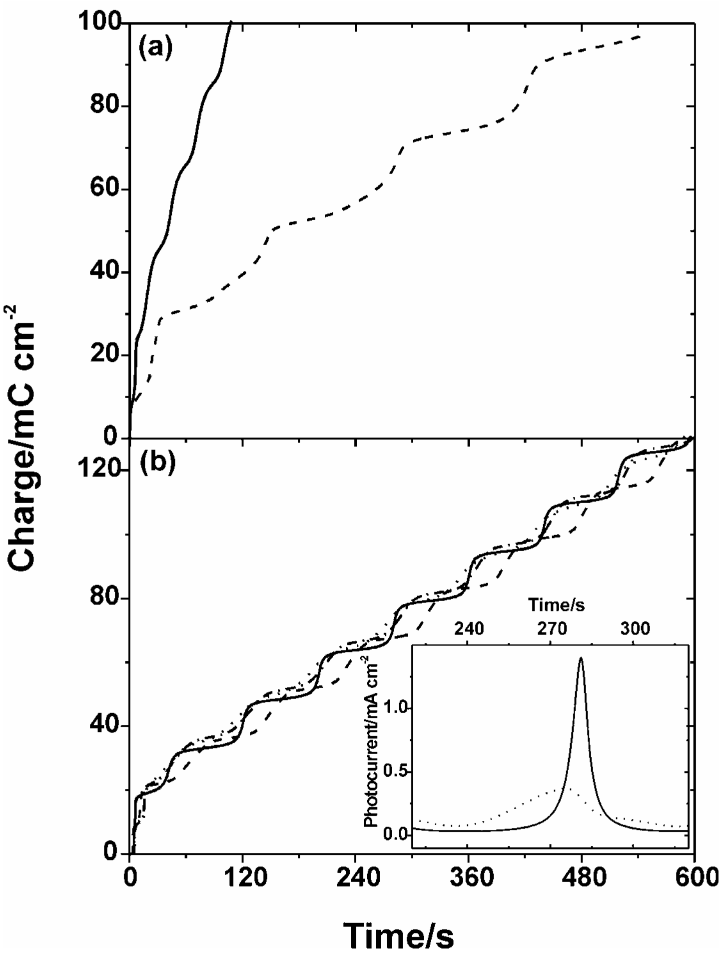

Fig.5: Chronocoulometric profiles of n-Si(100) in 0.1M NH_4F at V = +6V; (a) light intensity 270mWcm^{-2}, full line pH 3.6, dashed line pH 4.2; (b) pH 4.0, light intensity 80mWcm^{-2}(full line), 40mWcm^{-2} (dashed line), 20mWcm^{-2} (dashed-dotted line) and 10mWcm^{-2} (dotted line). The insert shows one oscillations cycle for two light intensities.

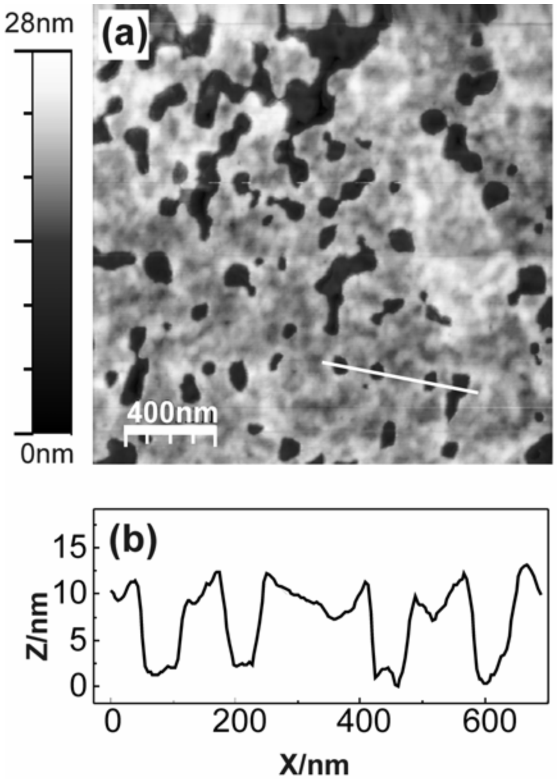

Fig.6: Contact mode AFM images of n-Si(100) after (i) photocurrent oscillation in 0.1 M NH_4F (see also Fig.2), (ii) 10 min. electrochemical etching in 4 M NaOH at -0.85V(SCE) and (iii) 10s immersion into 25% HF and subsequent UPW rinsing and drying.

The data in Fig.5b show the independence of the charge passed and of the oscillation frequency on illumination intensity for a fixed pH of 4 thus supporting the concept that has been the basis of our theoretical modeling that the etching process is dominating the oscillatory behavior. The integral charge flow is equal for different illumination intensities but the full width at half maximum (FWHM) of the single current peaks decreases with increasing light intensity, as can be seen in the insert, indicating a higher level of synchronization of the oxide domains. As the current has to pass through the pores in the oxide layer, this explains the higher porosity of the oxide for higher light intensities.

In the processing sequence for preparation of a PEC nanoemitter solar cell, the next step consists of pore deepening by *electrochemical* etching which ensures that specifically those Si substrate areas that have electrical contact to the electrolyte are etched in the alkaline solution used for selective Si etching (32). A typical result, obtained by contact mode AFM, is shown in Fig.6. The samples used have been conditioned following the procedure given in Fig.2. The electrochemical treatment consisted of a 10 min. etch in 4 M NaOH at -0.85V(SCE) followed by a 10s dip in 25% HF. This procedure has two effects: first, the Si substrate is attacked through pores in the oxide which make electrolytic contact to Si. Secondly, the HF dip removes the remaining oxide from the surface and thus allows investigation of the influence of the treatment by CM-AFM. It can be seen that the procedure creates a series of round pits but also, rather extended lake-like features are found that are considerably larger than the original oxide pores, suggesting an extended etching underneath the oxide by the electrochemical procedure. Fig.6b shows that the pits have depths of about 10nm but the overall topography seen in Fig.6a indicates that the height modulation reaches about 20nm.

In the fabrication of the solar cell, the procedure is as follows: after oscillation and emersion of the samples, the alkaline etching procedure as described in the caption of Fig.6 is carried out but the oxide is left on the surface, i.e. the HF dip is omitted. Then, the metallization of the pores that penetrate into the Si substrate is done by electrodeposition of Pt following the protocol given in Fig. 7.

Fig.7a shows the dark I-V characteristic of the electrochemically pitted Si/nanoporous oxide matrix in the Pt plating solution. It is characterized by a pronounced maximum near -0.8V. In separate C-V measurements, we have determined the flatband potential in the Pt electrodeposition solution from Mott-Schottky plots to be located at -0.55V (33). Therefore, at a potential of -0.8V as used here, the semiconductor surface is in an accumulation condition where a high electron concentration in the conduction band prevails (34). From the doping concentration, the energetic distance between Fermi level and conduction band is 0.2x eV and at -0.25V vs. flatband, the Fermi level would be located at the conduction band edge at the surface.

Generally, the deposition process can follow three routes: (i) via hole injection from the Pt(II/IV) and Pt(II/0) redox potential at +0.54V and +0.71V, respectively, into the Si valence band, (ii) via hole injection into surface states at the Si/silicon oxide interface that have been found in C-V measurements and (iii) via direct reduction of the $PtCl_6^{2-}$ anions by electrons from the conduction band. Processes (i) and (ii) are chemical in nature although the hole injection into the surface states is revealed by an electrode potential dependence in the depletion region (potentials below -0.55V) that stems from the inhomogeneous distribution of the surface state density with energy (35). Here, we have used the direct reduction route but it should be kept in mind that already upon sample immersion into the plating solution, chemical deposition takes place. This effect will be discussed further below in conjunction with improvements of the solar cell.

The Cottrell equation (36) describes the chronoamperometric profile of an electrochemical reaction on a planar electrode, where time t, diffusion coefficient D and concentration of the solution species c_R are interrelated.

$$I = nF\frac{Ac_R D^{1/2}}{\pi^{1/2}t^{1/2}}. \tag{9}$$

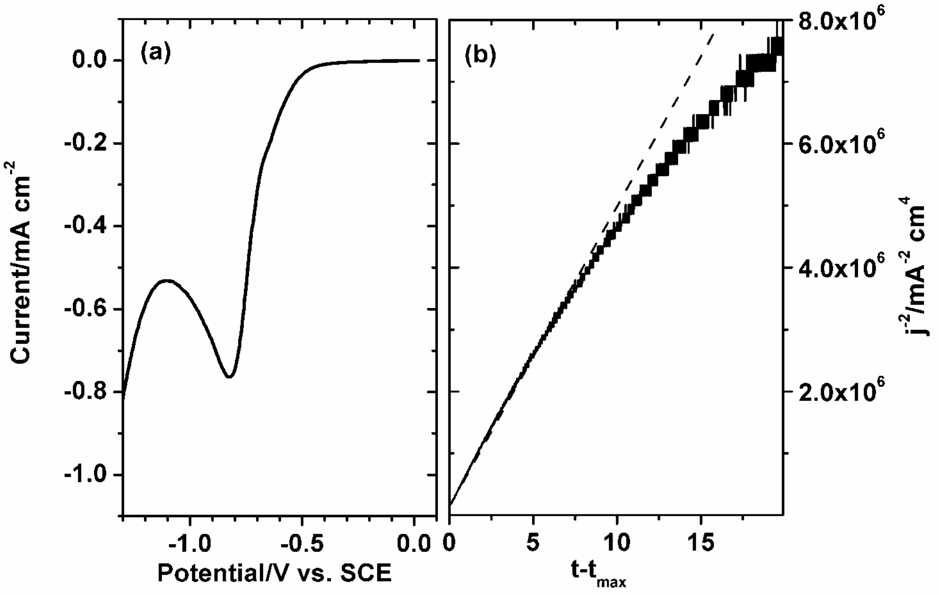

Fig.7: Pt electrodeposition into silicon oxide nanopores that have been extended by electrochemical etching (see Fig.6) into the Si(100) substrate at –0.8 V for 30 s, the integral charge flow was 13.7 mQ cm^{-2}; solution: 10^{-3} M $H_2[PtCl_6]$, 0.1 M K_2SO_4, pH=2.8; (a) potential dependence of the reduction current; (b) evaluation of the temporal behavior of the electrodeposition current according to the Cottrell equation where t_{max} is the moment of the current peak (see text).

Fig.7b shows an according evaluation of the Pt deposition into the nanoporous matrix. The time-axis is shifted by the time of the deposition peak because the deposition process is initially determined by the nucleation process. It can be seen that the behavior after the deposition peak follows, in the first 4s, quite well the Cottrell behavior, indicated by the dashed line, but deviates for increased time. The customary 3D nucleation and diffusion modells do not fit the measured data well because $PtCl_{4/6}^{2-}$ reduction can only occur at the pores, which represent only a small part of the electrode surface. Thus, after overlapp of the rather narrow diffusion zones of the single pores we observe a quasi planar diffusion towards the surface. Basically, the initial process appears to be diffusion controlled, but for t > 4s, deviations that are related to either non-planar geometry or to chemical changes at the reacting surface occur. In conjunction with photoelectron spectroscopy model experiments on Pt electrodeposition onto H-terminated Si surfaces, shown in Fig.10, the deviations are believed to be predominantly influenced by oxide film formation underneath the Pt nanoislands.

Fig.8 shows the output power characteristic of the photoelectrochemical n-Si/oxide/Pt-iodine-iodide-HI/C solar cell. At 100mWcm^{-2} irradiation from a W-I lamp, an efficiency of 10.7% is obtained. All solar cell parameters are not yet close to their expected limiting values. The short circuit current is reduced due to the reflectivity of silicon, the fill factor and the open circuit voltage should be considerably improved for high efficiency cells. The latter losses can be attributed to the influence of surface/interface states at the silicon/silicon oxide interface where the electrode is passivated and excess minority carriers can be trapped and recombine subsequently. The effect of interface states can be seen in Fig 9, where the photovoltageshift versus redox potential is analyzed. The photovoltage increase $\Delta V_{\text{photo}} / \Delta V_{\text{red/ox}}$ of 0.45 shows partial fermi level pinning due to interface states at the solid-liquid interface (35). Still, a detailed analysis of the distributions of interface states from these data is difficult as the variation of ions in the different electrolytes induce unequal interface conditions, such as e.g. surface dipoles.

SRPES in Fig.10 shows that silicon is oxidized during Pt deposition. The Si2p core level photoemission shows a pronounced peak at 103.3 eV binding energy, refering to the Si^{4+} oxidation state and thus to the presence of SiO_2. This result is confirmed by the energetic position of the O1s line at 532.7 eV. It should be emphasized that spectra taken prior to Pt deposition do not show any SiO_2. The presence of Pt is proven by the appearance of the Pt4f peak, which shows the usual asymmetric line shape due to screening effects of the d-band electrons. Recent TEM (transmision electron microscopy) images show that this film also exists underneath the Pt nano-islands. Therefore, two more interfaces have to be considered with respect to their influence on the electronic properties, i.e. the interface between oxide and Pt and that between Si and the oxidic film uner the Pt islands which might be different in thickness and composition compared to the analysis by SRPES on the open surface areas. Obviously, this film does not much reduce the current collection efficiency as can be inferred from the value of the short circuit current. Also, the interfacial layer can have a positive electronic effect due to the spatial decoupling of metal induced gap states from the semiconductor [37]. Nevertheless, the remaining interface recombination processes clearly limit the cell performance and strategies have to be developed to overcome these limitations.

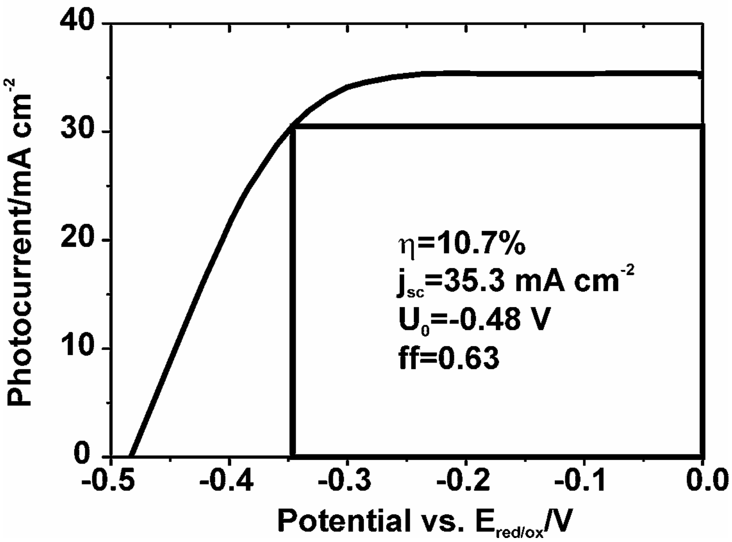

Fig.8: Output power characteristic of a nanoemitter n-Si(100)/oxide/Pt-I_3^-/I^-/HI-C photoelectrochemical solar cell; illumination intensity 100mWcm^{-2} (W-I lamp); solution: 2.5 M KI, 2M HI and 50 mM I_2.

Consequently, experiments will be designed to improve the composition and structural properties of the anodic oxide that passivates the surface and to study the influence of the oxidic film under the Pt islands on electronic properties of the device, for instance, by AFM using conductive tips which allows recording of local dark- and photo I-V characteristics. This will provide information about the barrier height of the Si/oxide/Pt junction and on possible local recombination channels by analysis of the forward and reverse I-V curve. Another aspect entails to the process of pore deepening which is not yet established and optimized. Here, empirical work has to be done to analyze the influence of depth, size and shape on device performance.

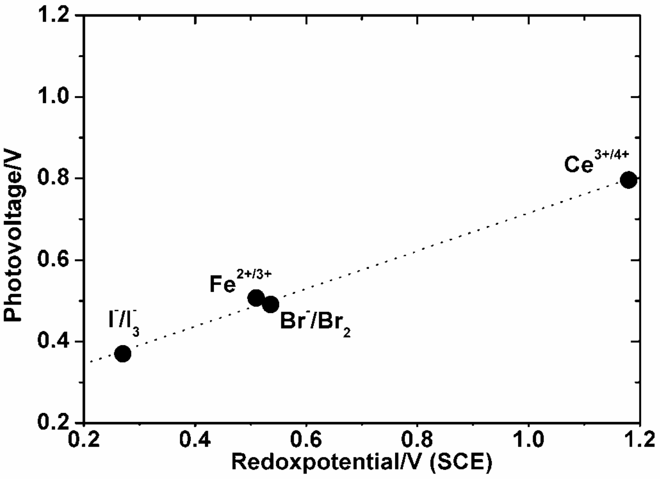

Fig.9: Photovoltage of the nano emitter PECS in different redox electrolytes (I^-/I_3^- : 2.5 M KI, 50 mM I_2; $Fe^{2+/3+}$: 50 mM $FeCl_3$, 50 mM $FeCl_2$, 0.1 M HCl; Br^-/Br_2: 8.6 M HBr, 25 mM Br_2; $Ce^{3+/4+}$: 25 mM $Ce(SO_4)_2$, 25 mM $Ce2(SO_4)_3$, 4M H_2SO_4. A linear fit to the data yields a photovoltageshift of 0.45.

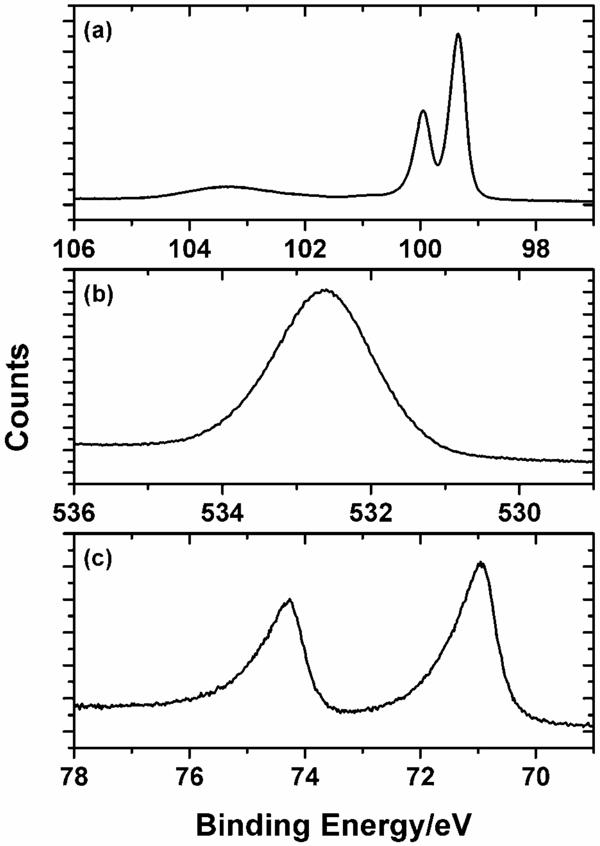

Fig 10: SRPE core level spectra of a n-Si (111) sample after potential scanning from 0 V to –0.6V in 10^{-3} M H_2PtCl_6, 0.1 M K_2SO_4, 900eV excitation energy: (a) Si2p, (b) O1s, (c) Pt4f.

4. Conclusions

The realization of a novel nanoemitter solar cell as an electrochemical light-to-electricity converting cell was described. Pore deepening by alkaline electro-etching was identified as a crucial step in the achievement of efficiencies above 10%. Model experiments using SRPES allowed the assessment of fundamental aspects of the surface chemistry of crystalline silicon upon electrodeposition in a $H_2[PtCl_6]$ electroplating electrolyte. The interfacial oxidic film results in a spatial separation of the Pt islands from the Si substrate that has the advantage that metal induced gap states can not dominate the electronic behavior of the nanocontacts. Nevertheless, the still limited performance of the devices has been attributed to recombination at the various interfaces in the structure.

Acknowledgements

The authors are grateful to M. Lublow and J. Grzanna for enlightening discussions and to K. Skorupska, M. Kanis, A. G. Muñoz and P. Hoffmann for their contribution to the SRPES measurements.

Literature

1. J. E. Murphy, M. C. Beard, A. G. Norman, S. P. Ahrenkiel, J. C. Johnson, P. R. Yu, O. I. Micic, R. J. Ellingson, A. J. Nozik, *JACS*, **128**, 3241 (2006)
2. D.L. Dexter, *J. Chem. Phys*., **21**, 836 (1953)
3. Th. v. Förster, *Ann. D. Phys*., **2**, 55 (1948)
4. S. Jang, M. D. Newton, R. J. Silbey, *Phys. Rev. Lett*., **92**, 218304 (2004)
5. G. R. Fleming, G. D. Scholes, *Nature*, **431**, 256 (2004)
6. N. Lewis, *J. Electroanal. Chem.*, 508, 1 (2001)
7. S. E. Gledhill, B. Scott, B. A. Gregg, *J. Mat. Res.*, **20**, 3167 (2005)
8. M. T. M. Koper, *J. Chem. Soc., Faraday Trans.*, **94**, 1369 (1998)
9. P. Belusov, *Sb. Ref. Radiats Med.*, 145 (1959)
10. K. Krischer, in *Modern Aspects of Electrochemistry*, Vol. 32, p. 1, B. E. Conway, J. o'M. Bochris, R.E. White, Editors, Plenum Press, New York (1999)
11. E. Foca, J. Carstensen, H. Föll, *J. Electroanal. Chem.*, **603**, 175 (2007)
12. J. Grzanna, H. Jungblut, H. J. Lewerenz, *Phys. Stat. Sol. A*, **204**, 1245 (2007)
13. J. N. Chazalviel, F. Ozanam, *J. electrochem. Soc.*, **139**, 2501 (1992).
14. V. Parkhutik, E. Rayon, E. Pastor, E. Matveeva, J. Sasano, Y. Ogata; *Phys. Stat. Sol. A*, **202**, 1586 (2005)
15. J. Carstensen, R. Prange, H. Föll, *J. Electrochem. Soc.*, **146**, 1134 (1999)
16. J. Grzanna, H. Jungblut, H. J. Lewerenz, *J. Electroanal. Chem*, 486, 181 (2000)
17. J. Grzanna, J. Jungblut, H. J. Lewerenz, *J. Electroanal. Chem.*, 486, 190 (2000)
18. H. J. Lewerenz, M. Aggour, *J. Electroanal. Chem.*, **351**, 159 (1993)
19. M. Aggour, M. Giersig, H. J. Lewerenz, *J. Electroanal. Chem*., **383**, 67 (1994)
20. R. A. Sinton, Y. Kwark, S. Swirhun, R. M. Swanson, *IEEE Electr. Dev. Lett.*, **6**, 405 (1985)
21. M. A. Green, A. W. Bladers, J. Zhao, A. M. Milne, A. Wang, X. Dai, *IEEE Trans. Electron. Dev.*, **37**, 331 (1990)
22. H. J. Lewerenz, German patent DE 10347401A1 (2005)
23. M. Aggour, K. Skorupska, T. Stempel Pereira, H. Jungblut, J. Grzanna, H. J. Lewerenz, *J. Electrochem. Soc.*, **154**, H794 (2007)
24. K. Skorupska, M. Aggour, M. Kanis, M. Lublow, H. Jungblut, H. J. Lewerenz, *ECS Trans.*, **2**, 1 (2007)
25. M. Lublow, H. J. Lewerenz, *Surface Science*, **601**, 1693 (2007)
26. H. J. Lewerenz, H. Jungblut, in *Semiconductor Micromachining*, Vol. 1, p. 217, S. A. Campbell, H. J. Lewerenz, Editors, Wiley, Chinchester (1997)
27. H. J. Lewerenz, *J. Phys. Chem. B*, **101**, 2421 (1997)
28. J. S. Judge, *J. Electrochem. Soc.*, **118**, 1772 (1971)
29. H. Kikuyama, M.Waki, I. Kawanabe, M. Miyashita, T. Yabune, N. Miki, J. Takano, T. Ohmi, *J. Electrochem. Soc.*, 139, 2239 (1992)
30. J. Grzanna, J. Jungblut, H. J. Lewerenz, *Phys. Stat. Sol. A*, **204**, 1245 (2007)
31. V. Lehmann, *J. Electrochem. Soc.*, **143**, 1313 (1996)
32. S. A. Campbell, S. N. Port, D. J. Schiffrin, in *Semiconductor Micromachining*, Vol. 2, p. 1, S. A. Campbell, H. J. Lewerenz, Editors, Wiley, Chinchester (1997)
33. A. G. Muñoz, H. J. Lewerenz, *J. Elecrochem. Soc.*, **55**, D527 (2008)
34. K. Skorupska, M. Lublow, M. Kanis, *APL*, **87**, 263101 (2005)
35. H. J. Lewerenz, *J. Electroanal. Chem.*, **356**, 121 (1993)

36. A. J. Bard, L. R. Faulkner, in *Electrochemical Methods: Fundamentals and Applications*, Wiley, New York
37. J. Tersoff, *Phys. Rev. Lett.*, **52**, 465 (1984)

CHAPTER 7

WEDNESDAY: AFTERNOON SESSION

ECS Transactions, 16 (3) 393-404 (2008)
10.1149/1.2982579 ©The Electrochemical Society

Preferential <111>A Pore Propagation Mechanism in n-InP Anodized in KOH

R. Lynch[a], C. O'Dwyer[a], N. Quill[a], S. Nakahara, S. B. Newcomb[b], and D. N. Buckley[a]

Materials and Surface Science Institute, University of Limerick, Ireland

[a] *Department of Physics, University of Limerick, Ireland*
[b] *Glebe Scientific Limited, Newport, Co. Tipperary, Ireland*

This paper describes the formation of pores during the anodization of n-InP in aqueous KOH. The pores propagate preferentially along the <111>A crystallographic directions and form truncated tetrahedral domains. A model is presented that explains preferential <111>A pore propagation and the uniform diameters of pores. The model outlines how pores can deviate from the <111>A directions and from their characteristic diameters. It also details the effect of variation of carrier concentration on the dimensions of the porous structures.

Introduction

Porosity in electrochemically etched semiconductors has been extensively investigated in the case of silicon (1) and to a lesser extent in the case of III-V compounds such as GaAs (2,3) and InP (4,5). Anion type and concentration can play a significant role in affecting the pore growth and morphology (6,7). The depth of porous layers and their preferential crystallographic growth directions have been shown to be affected by the substrate type (8), orientation (9) and doping density (10).

We have previously investigated (11,12) the early stages of anodic formation of porous InP in 5 mol dm^{-3} KOH and reported transmission electron microscopy (TEM) and scanning electron microscopy (SEM) evidence that clearly shows individual nanoporous domains. From this work we concluded that pore propagation was preferentially along the <111>A direction and that the resulting nanoporous domains that initially form have triangular $(01\bar{1})$ cross-sections, 'dove-tail' (011) cross-sections and rectangular profiles when (100) planes are viewed in parallel to the electrode surface. It was also observed by our group (13,14) that these structures are obtained when InP is anodized in KOH at concentrations of 2 mol dm^{-3} or above. Pores originating from pits in the surface create porous domains beneath a thin (~40 nm) dense near-surface layer and eventually these domains merge to create a continuous porous layer (15). However, at concentrations of 1 mol dm^{-3} or less, no porous layers were observed and between 1.8 mol dm^{-3} and 1.0 mol dm^{-3} a transition region of highly porous growth (without the presence of a near surface layer) was observed (16).

This paper describes an investigation by SEM and TEM of pore propagation in n-InP anodized in KOH and presents a model for the preferential propagation and branching of pores along the <111>A direction.

Experimental

The working electrode consisted of polished (100)-oriented monocrystalline sulfur-doped n-type indium phosphide (n-InP). An ohmic contact was made to the back of the InP sample and isolated electrically from the electrolyte by means of a suitable varnish. The electrode area was typically 0.5 cm^2. InP wafers with carrier concentrations from 3.4-6.7 $\times 10^{18}$ cm^{-3} and etch pit densities <500 cm^{-2} were used. Anodization was carried out in aqueous KOH electrolytes of 5 mol dm^{-3}. Each experiment involved a linear potential sweep (LPS) at 2.5 mV s^{-1} from 0.0 V (SCE) to an upper potential. A conventional three-electrode cell configuration was used employing a platinum counter electrode and saturated calomel reference electrode (SCE) to which all potentials were referenced. Prior to immersion in the electrolyte, the working electrode was dipped in an etchant (3:1:1 H_2SO_4:H_2O_2:H_2O) for 4 minutes and then rinsed in deionized water. All of the electrochemical experiments were carried out in the absence of light at room temperature.

A CH Instruments Model 650A Electrochemical Workstation interfaced to a Personal Computer was employed for cell parameter control and for data acquisition. Cleaved {011} cross-sections were examined using a HITACHI S-4800 field emission SEM operating at 5 kV. Electron transparent sections for cross-sectional TEM were prepared using standard focused ion beam milling (FIB) procedures (17) in a FEI 200 FIB workstation. The TEM characterization was performed using a JEOL JEM 2010 TEM operating at 200 kV.

Results and Discussion

Cross-Sectional Microscopy

Fig. 1 shows an SEM image of a porous layer (011) cross-section. In this image, two primary pores that have grown all the way through the porous layer from a pit in the electrode surface are clearly visible.

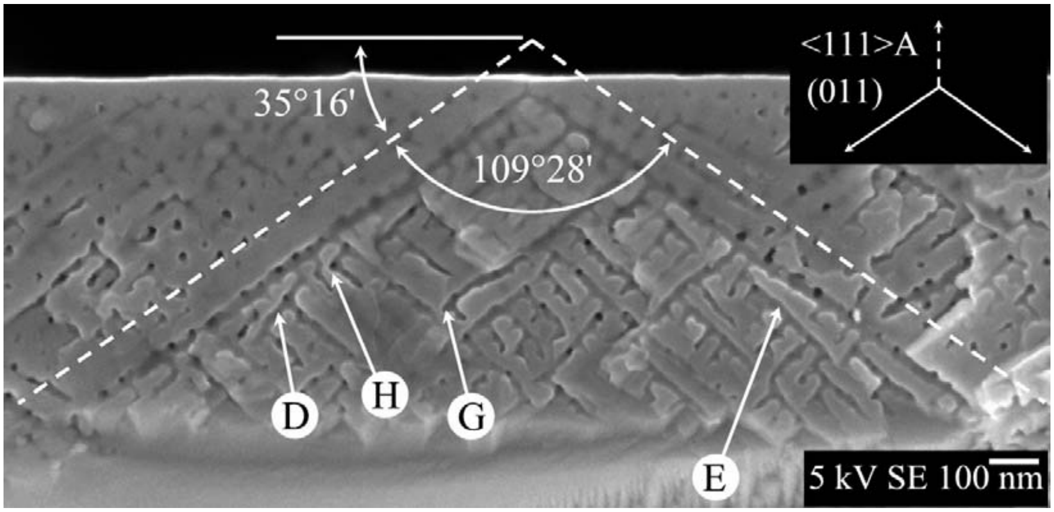

Fig. 1 Cross-sectional (011) SEM micrograph of InP following an LPS from 0 to 0.46 V (SCE) at 2.5 mV s^{-1} in 5 mol dm^{-3} KOH. The current peak in the LSV is at 0.46 V (SCE). The <111> directions are superimposed on the image as white, dotted lines. Two primary pores extending from a pit in the surface are clearly along <111>A. Pores that deviate from these directions are indicated at D and E and pores that have avoided crossing each other are indicated at G and H.

It is clear from the superimposed lines representing the <111> directions that these two primary pores have propagated preferentially along the <111>A directions.

Measurement of the pore width shows that the pore has the same width for its entire length except where it narrows near the surface pit and pore tip. Other (shorter) pores are also visible. They are generally along the <111> directions but deviate somewhat from these directions in places. Where pores are in close proximity to each other they have diverged (e.g. at D and E), and when growing towards each other they have avoided crossing (e.g. at G and H). This tendency of pores to grow around obstacles is frequently observed in micrographs and will be discussed later in the context of the proposed pore propagation model. The pores appear to have a uniform width: there is no evidence that the pores are wider closer to the surface. This suggests that pore growth occurs only at the pore tips with no subsequent widening due to etching at pore walls in the electrolyte-filled pores.

Fig. 2 shows an SEM micrograph of the cleavage plane orthogonal to that shown in Fig. 1. Also, during anodization the potential sweep was stopped at a lower potential, before the domains had time to fully merge together. Therefore, the characteristic triangular $(01\bar{1})$ cross-sections associated with these domains (11) are visible. Two types of pores are evident: those passing through the plane of the image (Type 1) and those in the plane of the image (Type 2). The Type 1 pores appear as round cross-sections in Fig. 2 and are in (011) planes (such as that in Fig. 1) orthogonal to the $(01\bar{1})$ plane of the image. Each of the Type 2 pores can be seen to have originated at a Type 1 pore and to have grown along <111>A towards the surface (*i.e.* upwards at ~35^{o} to the horizontal in Fig. 2). Where pores come close to the near-surface layer they deviate (F) from their preferred propagation direction leaving the near-surface layer intact. Indeed, most Type 2 pores in Fig. 2 deviate from the <111>A direction due to the proximity of Type 1 pores.

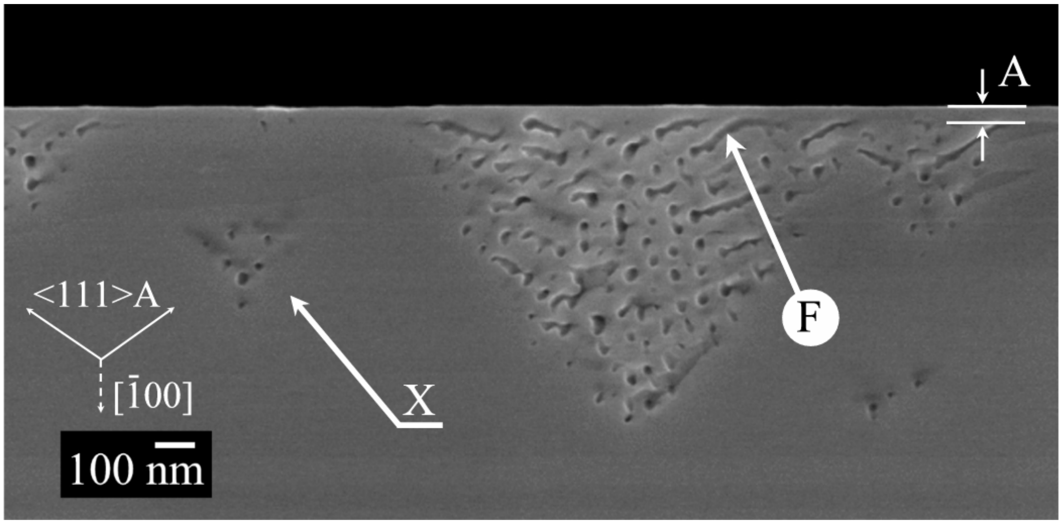

Fig. 2 Cross-sectional SEM image of InP cleaved along the $(01\bar{1})$ plane (orthogonal to Fig. 1) following an LPS from 0 to 0.44 V (SCE) at 2.5 mV s^{-1} in 5 mol dm^{-3} KOH. The pores shown in Fig. 1 (Type 1) appear as round cross-sections in this figure. The near-surface layer at A is also visible. Pores in the plane of the image (Type 2) propagate upwards at ~35^{o} to the horizontal along the <111>A directions. A pore that has deviated from <111>A as it approaches the near-surface layer is indicated at F. The apex of an adjacent domain is shown at X.

Pore Cross-Section and Tip Shape

Fig. 3 shows two TEM images where the sample has been tilted to the <111>B direction so as to observe the pore cross-sections as viewed along a pore axis. The cross-section in Fig. 3a passes close to the apex of a porous domain and intersects a pore very close to its tip (at G). The light-grey triangular area at G appears to define three facets. The sides of this triangle are approximately parallel to the intersections of the {111} planes with the image plane as shown in the inset. Thus, the internal surface of the tip of a pore appears to consist of {111}A facets (the arrows in the inset represent the <111>A directions). The cross-section shown in Fig. 3b intersects pores far from their tips. It is clear that, in contrast with Fig. 3a, these cross-sections are quasi-circular.

The observation of a uniform pore width in Fig. 1 is also consistent with the fact that no particular crystallographic facets have been observed at the pore walls; as far as can be determined, the pore cross-sections are round with no facets apparent except near the tip. If etching occurred at the pore walls as well as at the pore tip, it might be expected that the walls would be faceted, giving a characteristic pore shape such as a triangular cross-section. For example, Osaka *et al.* (18) reported that pores formed along the <100> directions during etching of silicon in HF solution had square cross-sections. However, in that case the pores were tapered, being wider close to their points of origin at the surface. This suggests that some etching occurred at the walls, enabling crystallographic faceting. Spiecker *et al.* (19) also reported faceting of pore walls for InP in acidic solution; the pore cross-sections were triangular but, as in the case of silicon, pore width increased with distance from the pore tip. In the present case of anodic anodization of InP in KOH, the etching process occurs only in a very small region near the pore tip and this region of reaction is constantly advancing. Therefore, the etching process does not delineate pore wall facets.

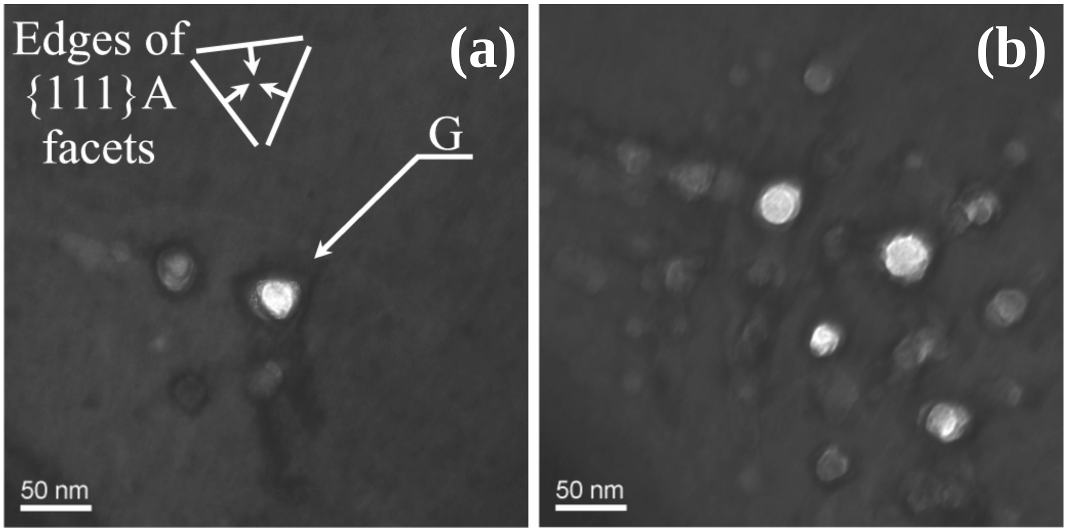

Fig. 3 TEM images, viewed along <111>B direction, of a $(01\bar{1})$ slice of InP. The cross-section in (a) passes through a pore close to its tip (at G) while the cross-section in (b) passes through pores far from their tips. The electrode had experienced a LPS from 0 to 0.44 V (SCE) in 5 mol dm^{-3} KOH at 2.5 mV s^{-1}. The FIB-milled InP slice is ~100 nm thick.

In III-V semiconductors the {111}B planes (*e.g.* the phosphorus planes in InP) are commonly found to be fast-etching both in electrochemical pore formation (19,20) and in wet etching of trenches (21). Therefore the direction of etching (*i.e.* the direction in which an etch front moves) is the <111>A direction. Gatos and Levine (22,23) have proposed a model for the {111} surfaces of III-V semiconductors with a zinc-blende structure. According to this model the etch rates of these surfaces are dependent on the relative reactivity of the terminating atoms. The {111}A plane is terminated by weakly reacting Group III (metallic) atoms and the {111}B plane is terminated by strongly reacting Group V (non-metallic) atoms. Subsequent work by Holt (24) on the behavior of these surfaces in InSb supports this model, showing a strong reactivity for the Sb and a weaker reactivity for the In. Research on the behavior of GaAs (25,26) and InP (27,28) in a range of etchants, such as Piranha (H_2SO_4-H_2O_2-H_2O mixtures) and bromine-methanol, has identified the {111}A planes as the slow etch planes that are revealed during chemical etching. Similar results for photo-electrochemical etching (29,30) and thermal decomposition (31) of InP have also shown the {111}A planes to be revealed due to the preferential removal of phosphorus.

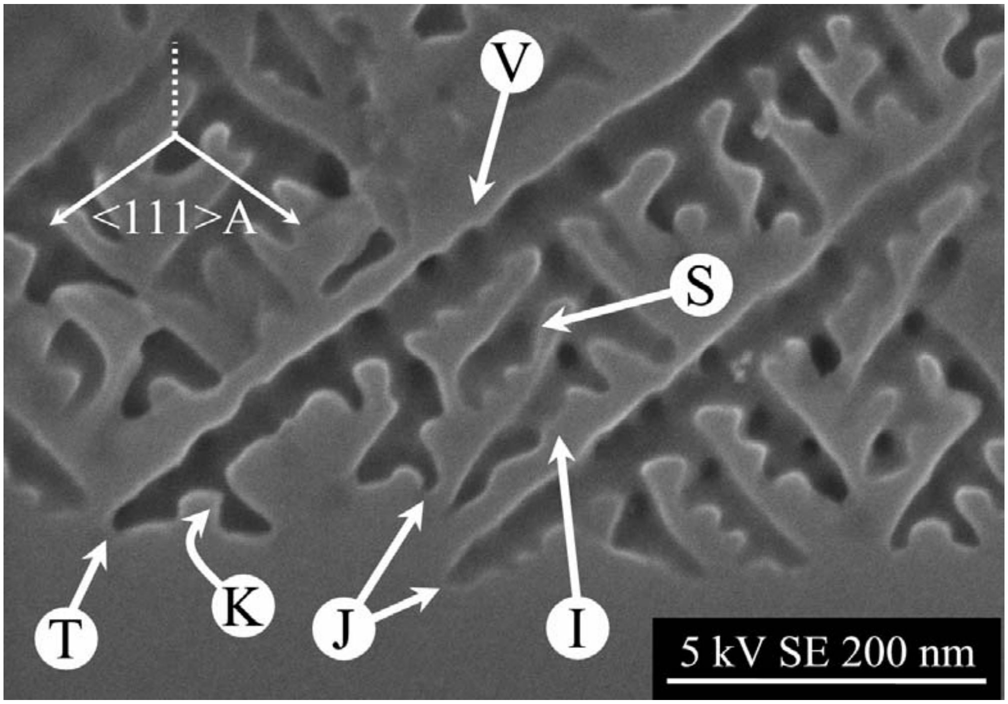

Fig. 4 Cross-sectional (011) SEM image of InP after an LPS from 0 to 0.383 V (SCE) in 5 mol dm^{-3} KOH at 2.5 mV s^{-1}.

Fig. 4 shows an SEM image of a (011) cross-section through a porous domain. Several interesting features of the pores can be observed in this image. As in Fig. 1 a primary pore can be seen at V. The pore has propagated along a <111>A direction and has rough but parallel edges. The parallel edges of this pore can be seen to end at a tip with a rounded point at T. Again, it can be seen that not all of the pores are exactly along the <111>A directions. This is especially the case where pores are branching from a primary pore and are in close proximity to regions that are depleted of carriers by the presence of nearby pores. An example can be observed at S, where a pore has diverged from the primary pore at V. Also, at I a pore that is restricted by several neighboring pores (*e.g.* at J) has propagated into a bottle-neck resulting in a tapered shape. Again, at K restriction of the development of a branching pore at V has resulted in narrowing, presumably due to the proximity of other pores not visible in the micrograph. Despite this narrowing, the pore has later re-established a normal width.

Thus, pores propagate preferentially along the <111>A crystallographic directions and have both a characteristic pore width but may change direction and width so as to navigate past restricted regions. As shown in the next section, such behavior can be understood if it is assumed that the etching at the pore tip is controlled both by the high electric field (32), and by preferential etching of the {111}B phosphorus planes.

Pore Propagation Mechanism

Pore propagation is controlled both by the availability of charge carriers at the pore tips and by the strength of the electric field that enables transport of these carriers across the depletion layer surrounding the tips. The faster etch rate of InP {111}B faces is considered to be due to the full dangling bonds that extend from the surface phosphorus atoms (22,33). Near the pore tips the electric field is sufficiently high to enable substantial quantum tunneling of carriers (34) and these dangling bonds facilitate a higher etch rate resulting in the propagation of pore tips.

Modeling of the relationship between pore-tip shape and electric field in silicon by Zhang (32) showed that the electric field is dependent on the radius of curvature of the internal surface of a pore. He concluded that the electric field ξ at the surface is a function of the ratio of the radius of curvature r_o and the space-charge layer thickness x_{sc}, *i.e.* $\xi = \xi(r_o/x_{sc})$. Since a threshold electric field ξ_{th} must be attained for etching to occur, a corresponding threshold value Λ of r_o/x_{sc} must also exist. Thus, a reduction in x_{sc} corresponds to a reduction in the value of r_o at which the threshold values of Λ and ξ_{min} are attained.

A related mechanism of chemical etching has been described by MacFayden (35) where it was proposed that chemical etching progresses through the removal of the most loosely bound atoms from the crystal faces. In the case of III-V semiconductors, the {111}B atoms (e.g. phosphorus) are the most loosely bound. Atomic ledges on {111}A surfaces represent quasi-{111}B planes. Since these are the fast-etching planes, we propose that the ledges etch, revealing a fresh {111}A plane one monolayer beneath the original. Where such a {111}A plane has been revealed, there are no {111}B atoms remaining, but where a indium atom is removed from such a plane, a triangular-shaped void, one atom deep, surrounded by a ledge of {111}B phosphorus atoms is created. The phosphorus atoms on this ledge can then be etched, revealing loosely bound indium atoms which in turn can be easily etched to reveal a similar, but widened, triangular-shaped void in the {111}A surface surrounded by a ledge of {111}B phosphorus atoms. Therefore an indium vacancy in a {111}A surface allows a layer of atoms to etch quickly, in a zip-like fashion. This rapid etching occurs in a two-dimensional manner, outwards from the initial indium vacancy, exposing the next {111}A plane; the crystal can be considered to consist of layers like an onion that are removed one at a time.

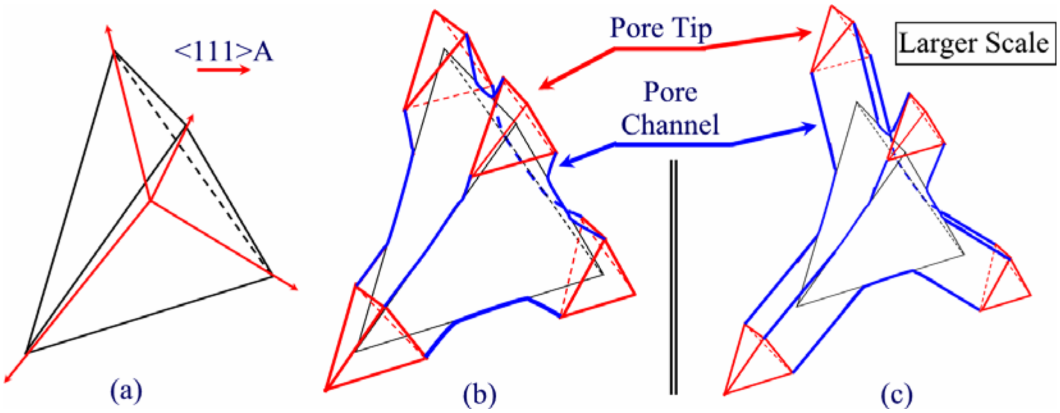

Fig. 5 Schematic representation of the widening of a hypothetical electrolyte-filled void in the bulk of the semiconductor. (a) Initially the etching leads to a tetrahedral shape. (b) As the void becomes larger, suitable conditions for etching continue to exist only at the vertices. Therefore (c) the void stops expanding while four pore tips grow outwards from the vertices along the <111>A directions.

Consider now an electrolyte-filled void in a semiconductor. At the semiconductor-electrolyte interface, under suitable conditions of electric field, carrier concentration and electrolyte composition, the zip-like propagation of etching described above will occur to reveal {111}A facets. These facets will enlarge until they meet, creating a tetrahedral shape as shown in Fig. 5a. As etching continues, the tetrahedron will increase in size. The electric field across the interface will vary with position on the surface of the tetrahedron, being greatest at the apexes and decreasing towards the centers of the faces. It follows that, as the tetrahedron grows, the electric field will eventually become too small to maintain etching near the centers of the four {111}A facets and etching will cease in that region while the remainder of the void will continue to etch. This situation is shown in Fig. 5b, where continued etching of void walls has resulted in the formation of four pore tips that point outwards from the vertices.

Zip-like etching will occur on the {111}A facets near the pore tips but the vertex of each tip will be maintained. If carriers are equally available at the three facets, etching progresses at the same rate at each facet with the result that the pore tip propagates along the <111>A direction. In the direction away from the tip, etching will occur until the electric field becomes too small to sustain it. In the wake of the propagation of the tip, a channel is therefore created, the walls of which do not etch because of the lack of a suitable electric field (see Fig. 5c).

To the rear of the growing tip structure, the availability of carriers is limited due to the proximity of the depletion region surrounding the void. Once the pore tip has progressed some distance from the starting point, carriers become available that allow the formation of a fourth <111>A facet to the rear of the propagating tip so that the tip structure now has three additional apexes (a total of four corresponding to the four <111>A directions as shown in Fig. 6a). Thus, the tip structure now has a tetrahedral shape which expands until the electric field near the centers of its facets becomes too small to sustain further etching while etching continues near the apexes (Fig. 6b). This results in the formation of tetrahedral tip structures at each of the four vertices, as depicted in Fig. 6c. Thus, a porous structure is formed by pores that propagate and branch along the <111>A directions.

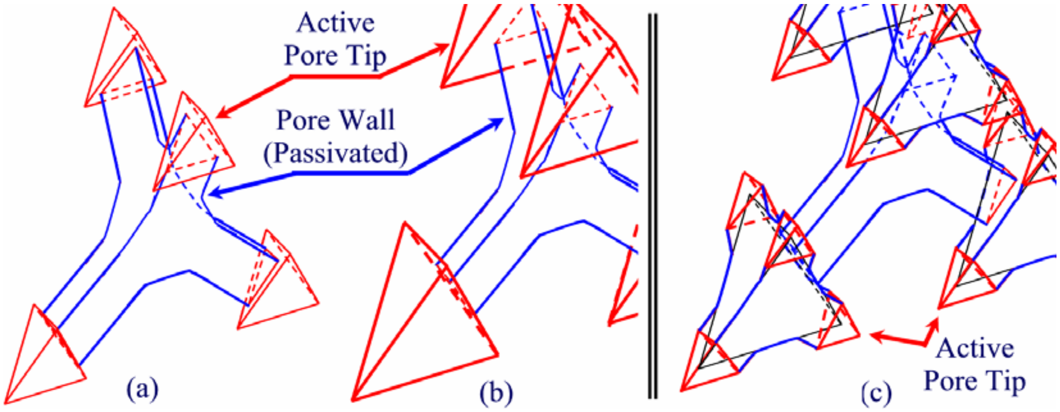

Fig. 6 Schematic representation of the widening of pore tips (a) after the tip has extended past the depletion region of the void from which it originated, followed by (b) the expansion of these tips into tetrahedral voids until their radii of curvature match the characteristic radius of curvature. This expansion of the pore tips leads (c) to branching of the pores along the <111>A directions.

As shown in Fig. 5c, a pore propagates along the <111>A direction because the {111}A facets near the tip are etched at equal rates when the two factors that enable etching (electric field and carrier availability) are present to equal degrees at all three {111}A facets.

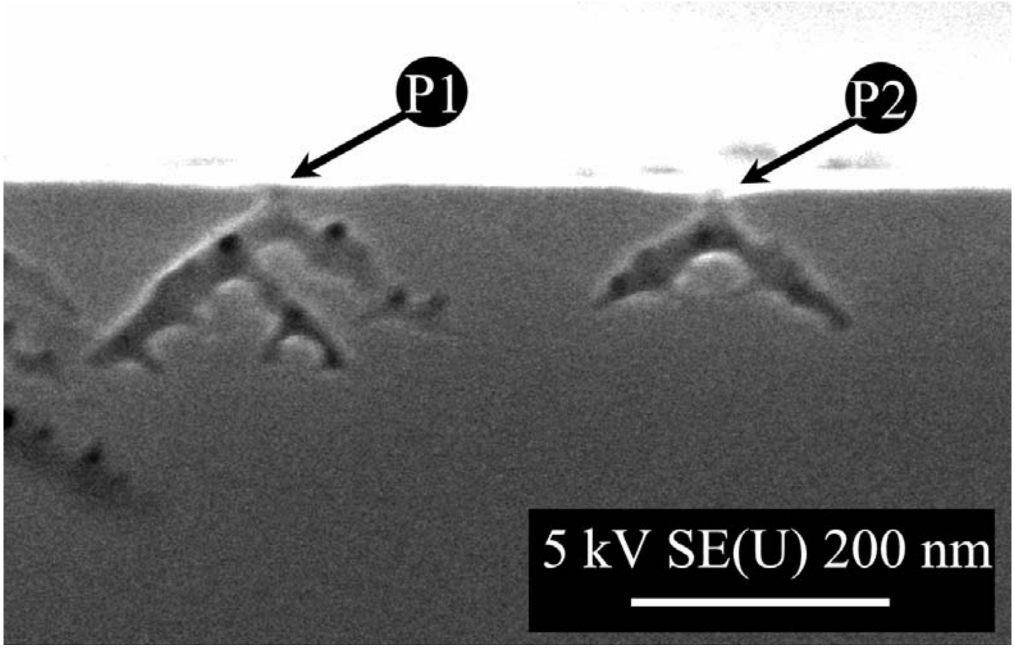

Fig. 7 Cross-sectional (011) SEM image showing pits at P1 and P2 that connect the surface to two primary pores. The n-InP electrode was anodized in 5 mol dm^{-3} KOH by a LPS from 0 to 0.245 V (SCE) at 2.5 mV s^{-1}.

If either of these factors is diminished at any of the three tip facets, the etch rate at that facet decreases, causing the propagation of the pore tip to deviate away from that facet. Thus, when a pore tip is close to an existing pore, the absence of carriers due to the overlapping of the depletion layers around the pore results in the pore tip been redirected away from it. The outcome from such a process can be seen at S in Fig. 4 where the pore tip has veered away from the pre-existing pore channel at V.

A similar situation arises at the surface pits. The cross-section in Fig. 7 shows two sets of pores and the surface pits from which they originate. Such pits (channels) along the $[\bar{1}00]$ direction connect the surface (electrolyte) to the underlying porous domains, through the near-surface layer as depicted in Fig. 8. Once a surface pit has formed, its preferred shape is, like that of any void, a tetrahedron. However, carriers are available only by tunneling through the depletion layer at the surface and this can occur only at small angles to the surface normal as shown at x and y in Fig. 8b. Thus, the surface pit is initially constrained to grow only along the normal to the surface causing the formation of a very narrow channel as shown in Fig. 8c. Once a channel has grown a certain distance through the depletion layer, the availability of carriers at the sides of the channel tip allows the formation of tetrahedrally oriented facets as shown in Fig. 8c and 8d. This truncated tetrahedron continues to expand (Fig. 8e) until the electric field near the centers of its facets becomes insufficient to sustain etching while etching continues near the apexes. This results in the formation of two primary pores as shown in Fig. 8f. As observed in Fig. 7, this process results in the channels (shown at P1 and P2 in Fig. 7) that form pits in the surface layer along the $[\bar{1}00]$ direction leading to the formation of two primary pores at each pit. Similarly, the channel formed during the restricted growth of the pore at K in Fig. 4 is due to the propagation of a tip through a similarly wide depletion region that exists between two pre-existing pores that are not parallel to the propagation direction of the pore tip.

Effect of Carrier Concentration on Porous Domain Dimensions

The carrier concentration of the InP has a major effect on the electrochemical process resulting in changes in the magnitude and position of current peaks and in the overall shape of linear sweep voltammograms (LSVs) (11).

Table 1 shows how several porous layer parameters vary with carrier concentration for three highly doped InP electrodes. With increasing carrier concentration, surface pit diameter increases and both the near-surface layer thickness and the pore width decrease. Although the variation of these parameters is not large, this is a very interesting result since it suggests a relationship between the mechanisms that determine, respectively, the thickness of the near-surface layer and the pore width while also suggesting that the surface pit diameter and the pore width are not directly related.

To explain the variation of the parameters in Table 1, it is useful to consider the width x_{sc} of the depletion layer at the semiconductor solution interface. For a given potential difference across the interface, the depletion layer decreases with increasing carrier concentration. This variation in x_{sc} can help explain the results of Table 1 because the pore growth mechanism is dependant on the tunneling of carriers across the depletion layer. Thus, as x_{sc} decreases, the widths of the near-surface layer, inter-pore walls and pores, respectively, should also decrease. The explanation for the observed increase in pit diameter with increasing carrier concentration is not obvious. It may simply be due to a geometrical effect that causes the surface pits to widen as the thickness of the near-surface layer decreases.

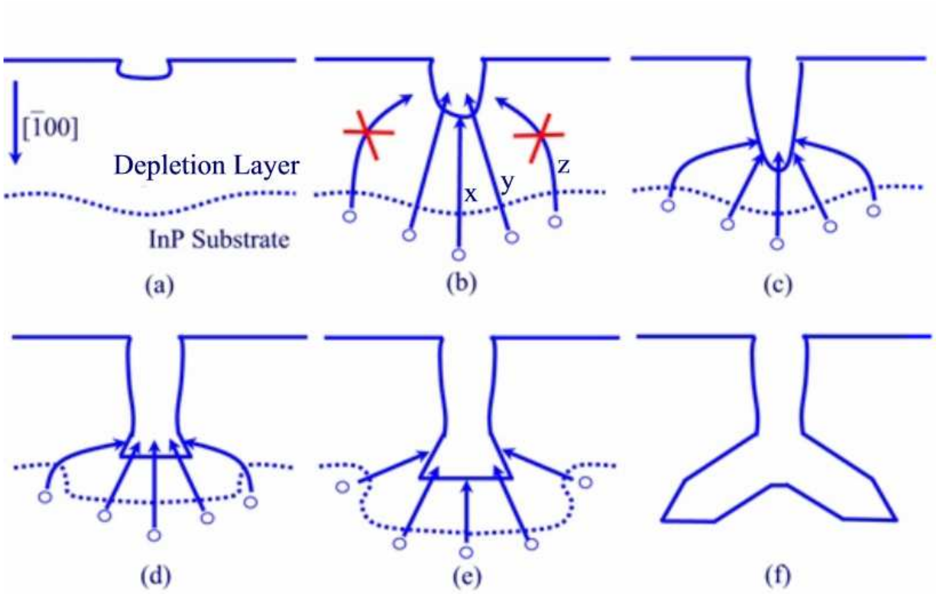

Fig. 8 Schematic representation of the progression of etching from (a) a pit in the surface. (b) The lower surfaces of this pit etch vertically downwards due to decreasing availability of carriers with increasing angle to the surface normal (from x to z). This etching results in the formation (c) of a long, narrow channel in the [$\bar{1}$00] direction. Once the channel is deep enough, the availability of carriers to the sides allows some lateral etching. (d) This etching widens the end of the channel into (e) a truncated tetrahedral void that produces (f) two primary pores when the void is sufficiently large.

The pore wall and near-surface layer thicknesses are influenced by the redirection of pore growth away from regions of limited carrier availability. As discussed earlier, this process occurs where the depletion layers of two neighboring regions overlap. The pores etch faster in directions where carriers are available, with the result that tips propagate away from, or around, existing pores. Therefore, at higher carrier concentrations the depletion layer is thinner and consequently pores can grow much closer together, decreasing the thickness of both the inter-pore walls and the near-surface layer.

Table 1 Variation, due to carrier concentration of InP, of average values for three porous layer parameters: surface pit diameter, near-surface layer thickness and pore width.

Carrier Concentration / 10^{18} cm^{-3}	Surface-Pit Diameter / nm	Near-Surface Layer-Thickness / nm	Pore Width / nm
3.4	14	45	30
5.3	17	39	28
6.7	22	34	19

As explained earlier, a minimum electric field $\xi_{\min}$ is required for quantum tunneling across the depletion layer at the pore tip to occur and the value of $\xi_{\min}$ is dependent on the ratio r_o/x_{sc}. Since a threshold electric field ξ_{th} must be attained for etching to take place, a corresponding limiting value Λ of r_o/x_{sc} also exists. Therefore a decrease in x_{sc} must be matched by a proportionate decrease in r_o so as to maintain the value of Λ. Since the value of x_{sc} at a given potential decreases with increasing carrier concentration, the radius of curvature of the pore must also decrease resulting in a decrease in pore width.

Conclusions

Observations of pore cross-sections, using SEM and TEM images, suggest that pore tips are pyramidal in shape with {111}A internal faces. Despite the tip shape, the pore cross-sections are round and the pore width is constant with respect to distance from the tip, *i.e.* the pores are cylindrical in shape. The {111}A faces near the tip are revealed due to fast etching of loosely bound {111}B phosphorus atoms. This process results in removal of planes of atoms parallel to the {111}A facets beginning with an indium vacancy in a {111}A face. A vertex is therefore maintained where the three {111}A facets, intersect; this, in turn, maintains the electric field near the tip due to the high surface curvature in this region. To the rear of the tip, the electric field decreases below the threshold value required for etching and the locus of the threshold electric field on the {111}A facets is such that the resulting pore cross-section is approximately circular.

Where the availability of carriers is reduced near one of the facets at a pore tip, etching is reduced at the facet causing pore growth to deviate from the <111>A direction. This also results in changes in the shape of a tip and the channel that is left in its wake. Such reductions in the availability of carriers can occur where the depletion region surrounding the tip overlaps another region that is depleted of carriers, *e.g.* during the formation of a pit in the electrode surface or when a pore tip is close to an existing pore or to the near-surface layer.

References

1. R. L. Smith and S. D. Collins, *J. Appl. Phys.*, **71**, 8 (1992).
2. S. Langa, J. Carstensen, M. Christophersen, H. Föll, and I. M. Tiginyanu, *Appl. Phys. Lett.*, **78**, 1074 (2001).
3. G. Oskam, A. Natarajan, P. C. Searson, and F. M. Ross, *Appl. Surf. Sci.*, **119,** 160 (1997).
4. S. Langa, J. Carstensen, I. M. Tiginyanu, M. Christophersen, and H. Föll, *Electrochem. Solid-State Lett.*, **4**, G50 (2001).
5. S. Langa, I. M. Tiginyanu, J. Carstensen, M. Christophersen, and H. Föll, *Electrochem. Solid-State Lett.*, **3**, 514 (2000).
6. P. Schmuki, J. Fraser, C. M. Vitus, M. J. Graham, H. S. Isaacs, *J. Electrochem. Soc.*, **143,** 3316 (1996).
7. P. Schmuki, D. J. Lockwood, J. Fraser, M. J. Graham, H. S. Isaacs, *Mater. Res. Soc. Symp. Proc.*, **431,** 439 (1996).
8. M. Christopherson, J. Cartensen, A. Feuerhake, and H. Föll, *Mater. Sci. Eng. B,* **69,** 70, 194 (2000).
9. S. Rönnebeck, J. Carstensen, S. Ottow, and H. Föll, *Electrochem. Solid-State Lett.*, **2**, 126 (1999).
10. P. Schmuki, L. E. Erickson, D. J. Lockwood, J. W. Fraser, G. Champion, H. J. Labbé, *Appl. Phys. Lett.*, **72**, 1039 (1998).

11. R. Lynch, C. O'Dwyer, D. Sutton, S. Newcomb, and D. N. Buckley, *ECS Trans.*, **6**, 355 (2007).
12. C. O’Dwyer, D. N. Buckley, D. Sutton, M. Serantoni, and S. B. Newcomb, *J. Electrochem. Soc.*, **154**, H78 (2007).
13. D. N. Buckley, C. O’Dwyer, R. Lynch, et al., Proceedings of the 41st State-of-the-Art Program on Compound Semiconductors, PV 2004-05, p.103 (ECS, 2004).
14. C. O’Dwyer, D. N. Buckley, D. Sutton, and S. B. Newcomb, *J. Electrochem. Soc.*, **153**, G1039 (2006).
15. R. Lynch, M. Dornhege, P. Sánchez-Bodega, H. H. Rotermund, and D. N. Buckley, *ECS Trans.*, **6**, 331 (2007).
16. R. Lynch, C. O’Dwyer, D. N. Buckley, D. Sutton, and S. B. Newcomb, *ECS Trans.*, **2**, 131 (2006).
17. L. A. Giannuzzi and F. A. Stevie, *Micron.*, **30**, 197 (1999).
18. T. Osaka, K. Osgasawara, and S. Nakahara, *J. Electrochem. Soc.*, **144**, 3750 (1991).
19. E. Spiecker, M. Rudel, W. Jäger, M. Leisner and H. Föll, *phys. stat. sol. (a),* **202,** 2950 (2005).
20. S. Langa, J. Carstensen, I. M. Tiginyanu, M. Christophersen, and H. Föll. *Electrochem. Solid-State Lett.,* **5**, C14 (2002).
21. M. Kappelt and D. Bimberg, *J. Electrochem. Soc.*, **143**, 3271 (1996).
22. H. C. Gatos and M. J. Lavine, *J. Electrochem. Soc.*, **107**, 427 (1960).
23. H. C. Gatos, *J. Appl. Phys.,* **32**, 1232 (1961).
24. D. B. Holt, *J. Appl. Phys.*, **31**, 2231 (1960).
25. Y. Tarui, Y. Komiya and Y. Harada, *J. Electrochem. Soc.*, **118**, 118 (1971); S. Iida and K. Ito, *J. Electrochem. Soc.,* **118**, 768 (1971).
26. S. Adachi and K. Oe, *J. Electrochem. Soc.,* **130**, 2427 (1983).
27. P. H. L. Notten, *J. Electrochem. Soc.,* **138**, 243 (1991).
28. I. E. Vermeir, W. P. Fomes, and P. van Daele, *J. Electrochem. Soc.,* **142**, 3226 (1995).
29. D. Soltz and L. Cescato, *J. Electrochem. Soc.,* **143**, 2815 (1996).
30. M. M. Carrabba, N. M. Nguyen, and R. D. Rauh, *J. Electrochem. Soc.,* **134**, 1855 (1987).
31. S. N. G. Chu, C. M. Jodlauk, and W. D. Johnston, Jr., *J. Electrochem. Soc.,* **130**, 2399 (1983).
32. X. G. Zhang, *J. Electrochem. Soc.,* **138**, 3750 (1991).
33. M. Nishida, *J. Phys. C,* **12**, 535 (1981).
34. X. G. Zhang, *J. Electrochem. Soc.,* **151**, C69 (2004).
35. D. N. MacFayden, *J. Electrochem. Soc.,* **130**, 1934 (1983).

ECS Transactions, 16 (3) 405-410 (2008)
10.1149/1.2982580 ©The Electrochemical Society

Complete Removal of Irregular Top Layer for Sensor Applications of InP Porous Nanostructures

Taketomo Sato, Akinori Mizohata, Naoki Yoshizawa, and Tamotsu Hashizume

Research Center for Integrate Quantum Electronics, Hokkaido University,
North 13, West 8, Sapporo 060-8628, Japan

The photo-electrochemical (PEC) process was developed to remove the irregular top layer of InP porous nanostructures for the application to amperometric chemical sensors. The PEC etching rate of the pore surface was associated with their structural properties, resulting in the complete removal of the irregular layer by monitoring and controlling the anodic photo-currents. The porous electrode prepared by PEC process gave higher sensitivity for detecting H_2O_2 due to the enlarged openings of all pores with complete removal of irregular top layer.

Introduction

In recent years, the demand for biological and chemical sensors has increased in the field of blood-sugar monitoring, antibody and DNA testing, virus screening and so on. One present challenge in biochemical sensor research is to utilize conductive nanomaterials with a large surface area (1-3). Among various nanomaterials, the semiconductor porous nanostructures formed by electrochemical anodization are one of the more promising candidates for the building blocks of biochemical sensors due to their extremely large surface areas and superior electrical properties of semiconductor materials.

The direct formation of semiconductor porous structures has been investigated for Si (4,5), GaAs (6,7), GaP (8,9), InP (10,11), GaN (12), CdSe (7) and so on. Up to the present, various crystal orientations and electrochemical conditions have been investigated to reveal structural properties and their tunability. We have recently succeeded in the anodic formation of arrays of straight nanopores on n-InP (001) substrates (13–15). The nanopores were laterally separated by InP nanowalls with a thickness of several 10nm, and straightly formed in a vertical direction greater than several 10μm. However, the disordered irregular layer has been usually formed at the initial stage of pore formation and it has partly remained on the top of the ordered porous layer. Since the irregular layer has a thickness in the range from a hundred nanometer to a several micrometer, it exerts a harmful influence on the electrical and optical properties.

In this study, we report the amperometric chemical sensors based on the InP porous nanostructures prepared by the photo-electrochemical (PEC) process. In the PEC process, the photo-electrochemical etching can be continuously conducted after the anodic formation of porous structures in the same electrolyte (16). Hence, our present approach should be of great advantage to process simplicity and controllability as compared with other methods such as a dry etching and a conventional chemical etching. After optimization of the PEC process for complete removal of the irregular top layer, we demonstrated the direct detection of H_2O_2 amperometrically by using InP porous nanostructures. The current sensitivities for detecting H_2O_2 were investigated using various porous electrodes with different structural properties.

Experimental

The experimental procedure and the applied waveform used in this study are schematically shown in Figs. 1(a) and (b), respectively. The porous structures were first formed by an anodic reaction in the dark, and then, the photo-electrochemical (PEC) etching of the porous surface was performed in the same electrolyte under illumination. A series of electrochemical processes was conducted using a standard cell with three electrodes, i.e., a (001) n-type InP electrode (n=1x10^{18}cm^{-3}) as a working electrode (WE), a Pt counter electrode (CE), and a saturated calomel electrode (SCE) for a reference. The potential of WE, V_s, with respect to SCE was precisely controlled by a pontentiostat with a function generator. The electrolyte consisting of 1 M HCl (200 ml) with HNO_3 (3 ml) was used throughout the experiment.

The constant bias was firstly applied to the semiconductor electrode to obtain high-density porous structures. After the porous formation, the PEC etching was carried out to remove the irregular top layer under illumination using a tungsten lamp with an intensity of 10mW/cm^2. The anodic bias was applied in ramped mode in order to control the etching depth by cycle number of the ramped bias, as shown in Fig. 1(b). V_s was swept at a rate of 50mV/s starting from 0V to 1V in the positive direction first, and then turning in the negative one.

Samples with a different pore depth, d, were prepared in this study by changing the anodization time. The current sensitivities for detecting H_2O_2 were compared using amperometric measurements in 100 ml of phosphate buffer solution (PBS) with a pH of 7.4. The V_s was set at +0.65V in the dark to enable the H_2O_2 to be directly detected. After the background current had stabilized at the WE, amperometric measurements were carried out by successively adding 35% H_2O_2 into a PBS electrolyte stirred at 200 rpm using a magnetic stirrer. The concentration of H_2O_2 is corresponding to 1.14mM when 100μl of H_2O_2 was added in 100ml of electrolyte.

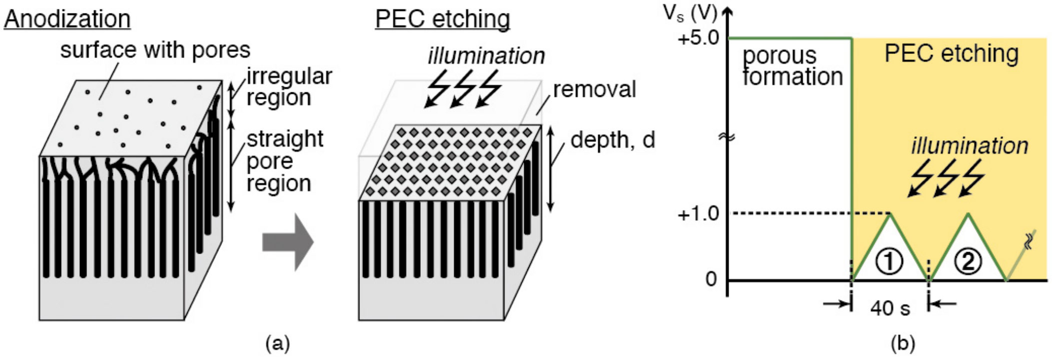

Figure 1. (a) Schematic illustrations of experimental procedure and (b) applied waveform used in this study.

Results and Discussion

Photo-electrochemical (PEC) Etching of Pore Surface

Figure 2 shows plan-view scanning electron microscope (SEM) images of the template porous sample formed at V_s = 5V for 60s, the samples after the ramped bias applied with 3 cycles and 6 cycles. The average pore diameter of the present template was about 30nm, as shown in Fig. 2. After the PEC process, the surface morphology was changed and the pore diameter increased. As shown in Fig. 2, the pore shape became a square defined by four equivalent {100} planes, whose feature is very similar to the case of the porous structures after the cathodic decomposition process (15). This is because the etching rate of the InP was strongly dependent on crystal orientation, where the {100} planes preferentially appeared on the wall surface due to their slow etching rate. After the ramped bias applied with 6 cycles, the lateral thickness of the InP nanowalls was bellow 20nm near the surface, which was thinner than the initial value of the template porous sample. These results indicate that the etching of the porous surface has been developed by the photo-electrochemical reaction.

From the cross-sectional SEM observation, it was found that the straightness in vertical direction was improved after the PEC process. Figure 3 compares the cross-sectional SEM images of the template porous sample and the sample after the ramped bias applied with 6 cycles. As previously reported (14), the array of straight nanopores was formed over 10 μm in depth, but the irregular layer partially remained on the top of the ordered porous structure. After the PEC process, the irregular top layer was completely removed and the regular array of straight pores appeared on the surface, as shown in Fig. 3. The initial thickness of the porous structure was 27.6 μm including the irregular top region with a thickness of 4.1 μm. After the ramped bias applied with 6 cycles, the thickness of porous layer decreased to 22.9 μm due to the PEC etching developed on the surface.

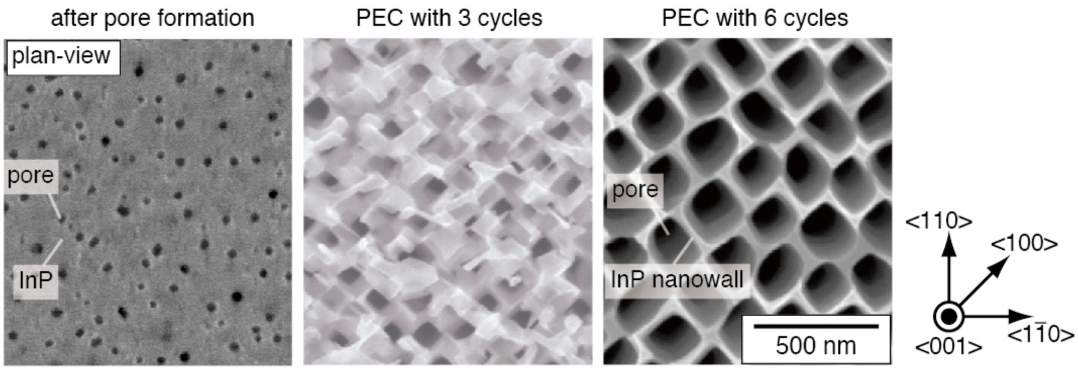

Figure 2. Plan-view SEM images of porous samples before and after PEC etching.

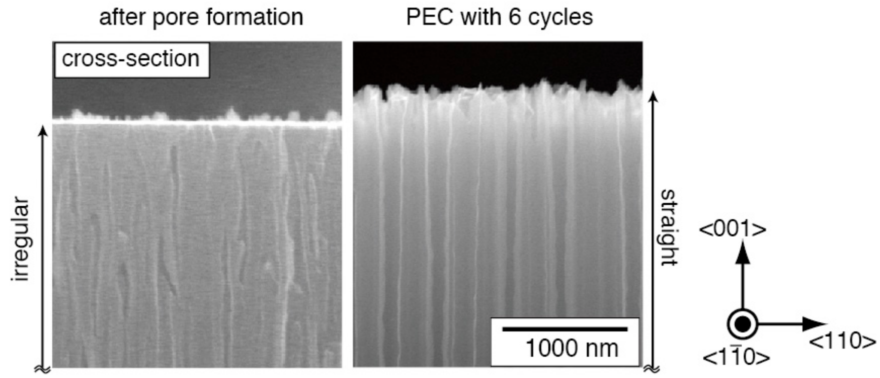

Figure 3. Cross-sectional SEM images of porous samples before and after PEC etching.

The etching rate of the InP porous nanostructures was investigated from the SEM observation. Figure 4 shows the plot of the pore depth, *d*, measured as a function of the cycle number of the ramped bias applied during the PEC process. The measured anodic current obtained on the InP porous electrode is also shown as a solid curve. It was found that the surface of the InP porous structure started to be etched at the rate of 1.2 μm/cycle and later in a gradual decline. This behavior is very consistent with the current transition, as shown in Fig. 4. It appears certain that the etching rate became lower and lower along with the anodic currents contributing the electrochemical dissolution of InP porous surface. In this study, the irregular top layer with a thickness of 4.1 μm was completely removed after the ramped bias applied with 5 cycles.

The decline of the etching rate can be explained by the fact that the amount of anodic photo-currents was strongly associated with the surface morphology of the InP porous electrode (16). At the beginning of the PEC process, the surface etching started with a large photo-current due to the hole generation efficiently caused by the illumination in the irregular pore region. As the PEC etching proceeds, the pore diameter increased and the thickness of InP nanowalls decreased, as shown in Fig. 2. In that case, the etching rate declined because the effective area subjected to illumination became very small on the surface with InP nanowalls. In addition to this, the etching rate of the surface further declined as the {100} facets appeared on the wall surface during the PEC process. This model qualitatively explains the observed behavior on the PEC etching of the InP porous nanostructures. These results indicate that the irregular top layer can be completely removed from the surface of InP porous nanostructures by the PEC process controlling and monitoring the anodic photo-currents.

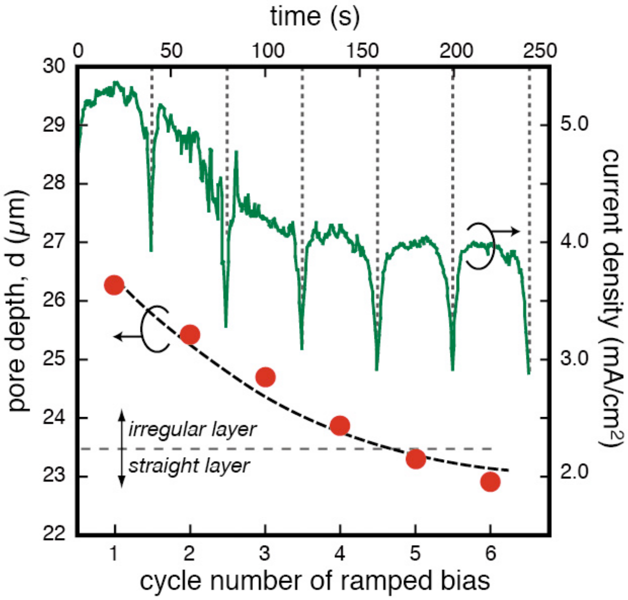

Figure 4. Relationship between average pore depth, *d*, and cycle number of ramped bias applied to sample. Anodic currents measured during PEC etching is also shown as a solid curve.

Amperometric Detection of H_2O_2

In order to clarify the electrochemical activity of the InP porous nanostructures, the amperometric measurements for detecting H_2O_2 were performed on various samples having different pore depth and different surface morphology. Figure 5(a) plots the transient curves for anodic currents obtained on a porous electrode with d = 5.4μm after the PEC process. The surface area used for the calculation of the current density is only the geometric surface area not including the wall inside. As expected, the measured current density was strongly dependent on the amount of H_2O_2. From the results of cyclic voltammetry, the anodic current started to increase at around 0.5V, which is comparable with the potential of the following reaction.

$$H_2O_2 \rightarrow O_2 + 2H^+ + 2e^- \qquad [1]$$

This indicates that the observed response currents on the porous electrodes were due to the oxidation of H_2O_2 described by eq. [1].

Figure 5(b) shows the calibration plots for detecting H_2O_2 obtained at various electrodes with different structural properties. The values for current density were measured at t = 20s after H_2O_2 was added, as indicated by the dashed line in Fig. 5(a). All electrodes exhibit good linearity between the current signal and H_2O_2 concentration in a range from 0 to 2 mM. As for the sample prepared with the PEC process, three kinds of porous structures with different d's of 5.4, 8.1, and 10.2μm were compared in Fig. 5(b). Samples with large d's had higher sensitivity than those with small d's. This is most probably because the effective surface area available for detecting H_2O_2 increased with the pore depth. In this study, the highest value of 1.670μA/mM·cm^2 was obtained on a sample with d = 10.2μm.

It is also interesting to note that the PEC process after pores had formed extremely effectively improved the sensing properties of the InP porous electrodes, in spite of reduction of total surface area. One explanation for this is that the diffusion coefficient was increased inside the nanopores after the PEC process because the diffusion of reactants into and out of nanopores was enhanced due to the enlarged openings of all pores after the PEC process. Further experimental and theoretical discussions are necessary to clarify the complicated current response observed in the porous electrodes.

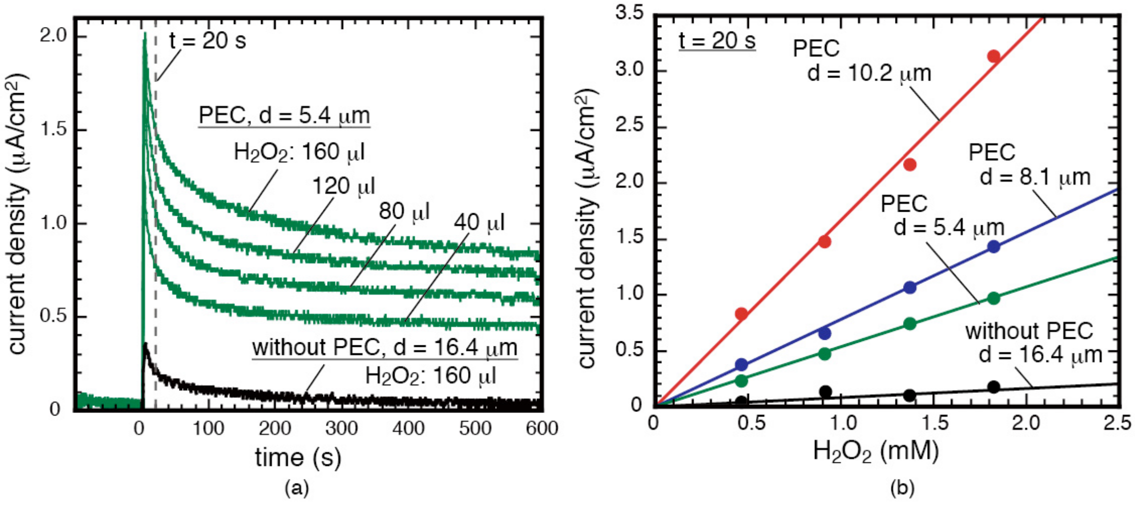

Figure 5. (a) Transient curves of anodic currents obtained on porous electrode with H_2O_2 only added once. (b) Calibration plots of anodic currents versus concentration of H_2O_2.

Conclusion

The PEC process was first optimized for the complete removal of the irregular top layer from the InP porous nanostructures. The PEC etching rate of the pore surface was associated with their structural properties, being larger in the irregular top layer. Thus, the complete removal of the irregular layer was realized by monitoring and controlling the anodic photo-currents in the ramped bias mode. The electrochemical activity of the InP porous nanostructures was strongly dependent on their structural properties. The current sensitivity for detecting H_2O_2 dramatically improved on the sample prepared by the PEC process as well as the samples with a larger pore depth.

Acknowledgments

The work reported here was supported in part by the Ozawa and Yoshikawa Memorial Electronics Research Foundation and by a Grant-in-Aid for young scientists, (B)-19760208, from the Japanese Ministry of Education, Culture, Sports, Science, and Technology.

References

1. Y. Cui, Q. Wei, H. Park, and C. M. Lieber: *Science*, **293**, 1289 (2001).
2. Y. Lin, F. Lu, Y. Tu, and Z. Ren: *Nano Lett.*, **4**, 191 (2004).
3. Z. W. Zhao, X. J. Chen, B. K. Tay, J. S. Chen, Z. J. Han, and K. A. Khor: *Biosens. Bioelectron.*, **23**, 135 (2007).
4. R. L. Smith, S.-F. Chuang, and S. D. Collins, *J. Electron. Mater.*, **17**, 533 (1988).
5. L. T. Canham, *Appl. Phys. Lett.*, **57**, 1046 (1990).
6. P. Schmuki, J. Fraser, C. M. Vitus, M. J. Graham, and H. S. Isaacs, *J. Electrochem. Soc.*, **143**, 3316 (1996).
7. I. M. Tiginyanu, V. V. Ursaki, E. Monaico, E. Foca, and H. Föll, *Electrochem. Solid-State Lett.*, **10**, D127 (2007).
8. A. Anedda, A. Serpi, V. A. Karavanskii, I. M. Tiginyanu, and V. M. Ichizli, *Appl. Phys. Lett.*, **67**, 3316 (1995).
9. K. Kuriyama, K. Ushiyama, K. Ohbora, Y. Miyamoto, and S. Takeda, *Phys. Rev. B*, **58**, 1103 (1998).
10. T. Takizawa, S. Arai, and M. Nakahara, *Jpn. J. Appl. Phys.*, **33**, L643 (1994).
11. T. Baba, and M. Koma, *Jpn. J. Appl. Phys.*, **34**, 1405 (1995).
12. M. Mynbaeva, A. Titkov, A. Kryganovskii, V. Ratnikov, K. Mynbaev, H. Huhtinen, R. Laiho, and V. Dmitriev, *Appl. Phys. Lett.*, **76**, 1113 (2000).
13. H. Fujikura, A. Liu, A. Hamamatsu, T. Sato, and H. Hasegawa, *Jpn. J. Appl. Phys.*, **39**, 4616 (2000).
14. T. Sato, T. Fujino, and H. Hasegawa, *Appl. Surf. Sci.*, **252**, 5457 (2006).
15. T. Sato, T. Fujino, and T. Hashizume, *Electrochem. Solid-State Lett.*, **10**, H153 (2007).
16. T. Sato, and A. Mizohata, *Electrochem. Solid-State Lett.*, **11**, H111 (2008).

ECS Transactions, 16 (3) 411-416 (2008)
10.1149/1.2982581 ©The Electrochemical Society

COMMENT ABOUT THE MECHANISM OF POROUS LAYER GROWTH : CASE OF INP

L. Santinacci, I. Gérard, M. Bouttemy, M. Marques
& A. Etcheberry

Institut Lavoisier UMR CNRS 8180 Université de Versailles

45 Ave des Etats Unis 78035 Versailles France
etcheber@chimie.uvsq.fr

Porous InP layer are obtained in HCl. Kinetic aspect associated to the growth are considered. XPS shows that specific Cl chemistry seems to be linked to the porous layer growth. Dosage of dissolution product by atomic spectroscopy demonstrated that a very interesting delay phenomenon for the observation of the final In concentration in solution is observed. This phenomenon can be understood as the consequence of the presence of a confined medium at the time of the porous layer inside the pore. This situation seems to generate a dissolution process with strong electron injection.

Introduction

Growths of porous layers, on III-V or II-VI semiconductor occur on a specific atomic network which include “A” and “B” types of atom. Consequently they can differ for a chemical point of view from the ones obtained on the silicon as anodic dissolution is. Number of charges consumed, injection of charge by corrosion intermediates can influence the global process [1]. So the nature of the processes is a very interesting thing for fundamental semiconductor electrochemistry. Particularly the problems, of, the mechanism related or not to the final morphology, have focused a lot of attention [2]. The experimental conditions as nature of the solvent, nature of the material, the use of galvanostatic or potentiostatic conditions, chosen values of the current intensity or the electrode polarization are parameters that govern the final network of pores. When it considers compound semiconductors as III-V or II-V very different pore repartitions or morphologies are reported, with very interesting crystallographic or columnar features [2,3,4]. Literature proposed explanation for these specific behaviors but the nature of the electrochemical mechanism is often marginally considered.

Our contribution will help to clarify the question of the actual mechanism associated to a porous layer growth for InP described for the first time in HCl, by P. Kohl in 1983 [5].On this material, initial step for the very important dissolution phenomenon which follows is always an opened question. The question of the surface chemistry of the interface that undergone the dissolution is not well established with the very difficult question of an eventual specific surface layer that trigger the initiation of pores. Another interesting question is related to the becoming of the very large amount of matter released into the solution for process that happen often during short time typically<1 min. In opposition to what happens for classical dissolution, pore growth confined amount of cationic or anionic species which behavior are poorly investigated. SEM Cross sectional image refers only to the final situation. The dynamic aspect which associates the evacuation of the dissolution products outside le layer zone is poorly considered.

In this paper, using InP in 1M HCl, which gives rise to very reproducible shape feature Two mechanistic aspects will be discussed. The first consider the initiating step using *ex situ* XPS analysis. The second consider the question of the behavior of the corrosion products. Dosage of corrosion products, outside the layer zone inside the bulk solution, allows complement of information obtained often by the analysis of cross section views of the layers. Taking working solution sample at different time after a porous layer growth we dosed the amount of In^{3+}, released outside the layer.

Experimental Section

Sn-doped *n*-InP (100) wafers ($N_D = 10^{18}$ at·cm^{-3}) are purchased from InPact Inc.. Prior to use, samples are chemomechanically polished with a solution of bromine in methanol (2%), rinsed with methanol and dried under argon stream. In order to remove residual oxides, samples are dipped for a few minutes in 2M HCl and finally rinsed with ultra-pure water.

The electrochemical setup is a classical three electrode cell. All anodic galvanostatic treatments are performed in the dark with a PAR EG&G 273 The current density is set at $J = 100$ mA·cm^{-2}. The surface modifications are examined using a scanning electron microscope (SEM) in top view and cross-section using a JEOL JSM 5800LV.

XPS chemical analyses are performed with a Thermo-VG Escalab 220i XL spectrometer. X excitation is performed with the Al line of a twin-anode (Al, Mg). The constant analyzer energy mode is used with pass energy of 20 eV.

Indium quantities dissolved were measured with a Thermo-Fisher M6-SOLAAR atomic-absorption spectrometer. The flame quantification mode (air-acetylene) was used in the concentration range 1-30 mg/L although graphite furnace mode was employed in the 1-50 µg/L one. Background corrections on flame and furnace spectra acquired were provided respectively by a deuterium lamp and a Zeeman effect system. Calibration solutions were prepared freshly from 20 mg/L In(III) absorption standard solution (CaPurAn standards from A.C.S.D.) diluted in acidified high purity water (flame : HCl 1.0 M and furnace : HCl 0.3 M). Furnace experiments were realized with an Extended Lifetime Cuvette (ELC), a working volume of 20 or 40 µL and the following optimised operating parameters : 60 s drying at 110°C, 20 s ashing at 800°C, 3 s atomization at 2300°C and finally a 3 s cleaning at 2500°C. A manual pre-dilution of sample solutions was made when the dilution factor exceeded 1/40. Before furnace analysis a first matrix modifier solution, composed with 2.5 % (w/v) EDTA ammonium salt dissolved in 3 % aqueous ammonia [6], was directly incorporated in each reference and sample solution in 5 % volume proportion. A second matrix modifier solution, $Mg(NO_3)_2$ 10 g/L and $Pd(NO_3)_2$ 2 g/L, was automatically added during the humid stage in a ratio of 3 µL for a 20 µL working volume.

Results and discussion

The porous layer was obtained under constant current conditions fixed at 100mA.cm^2. A classical growth with columnar aspect is obtained the thickness of the layer being set by the time of treatment or the same thing the electric charge. A specific cross sectional view of the layer was given in figure 1. The time evolution of the electrode potential was shown in figure 2. Both are classical and in agreement with a lot of results given in the literature.

The initial stage of the layer growth was characterized by XPS. Surfaces corresponding to the initial stage of the growth typically 0.1-0.5 C.cm^{-2} was analyzed. After anodic treatment the surface is dipped into ultra pure water immediately after stopping the current flow. In this condition an eventual thick oxide would be partially conserved even in 1M HCl.

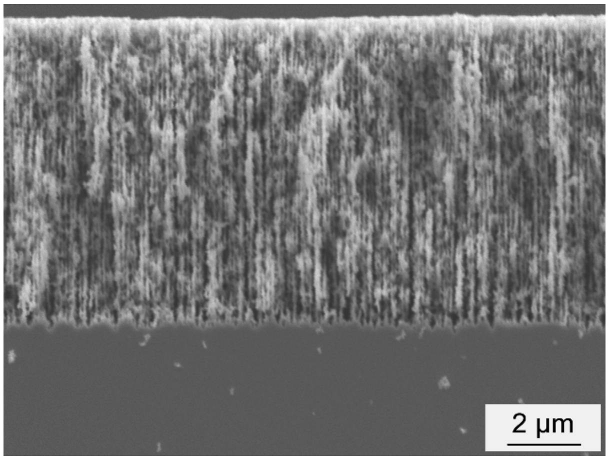

Figure 1. SEM cross sectional view of a porous layer obtained on n$^+$- InP; j: 100mA.cm^2

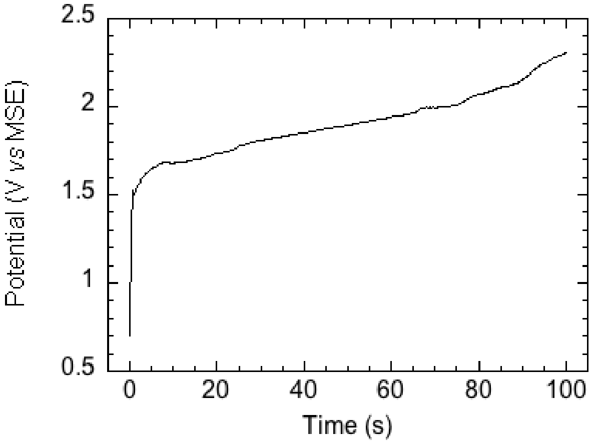

Figure 2 Variation of the electrode potential during the growth of the porous layer on n$^+$-InP; j: 100mA.cm^2

The XPS analysis gives rise to a very reproducible response typical of a well desoxidized surface with a classical tedious carbon contamination. The typical values of the XPS parameter are summarized in the tableIx

InP porous	*P2p*	*P2p*	*O1s*	*In3d5*	*Cl2p*	*C1s*
Peak BE	*132,97*	*128,69*	*532,59*	*444,43*	*198,46*	*284,94*
Height CPS	*61,5*	*5823,49*	*3382,47*	*91055,24*	*670,94*	*6131,76*

FWHM eV	*1*	*0,72*	*2,68*	*0,8*	*1,3*	*1,38*
At, %	*0,36*	*19,35*	*12,06*	*23,41*	*3,69*	*41,13*

The important point is the presence of a Cl signal with a typical binding energy lower than 200eV. The amount seems reproducible even if the rising procedure has not be completely. A typical ratio Cl/(In+P) close to 0.1 is obtained. If we look at the ratio between In and P which is slightly elevated we can suggest an adsorbed Cl layer on surface In sites. But it is a preliminary remark. The Cl_{2p} signal was shown in figure 3 with a specific double contribution in addition to the spin orbit splitting 2p1/2, 2p3/2 structure

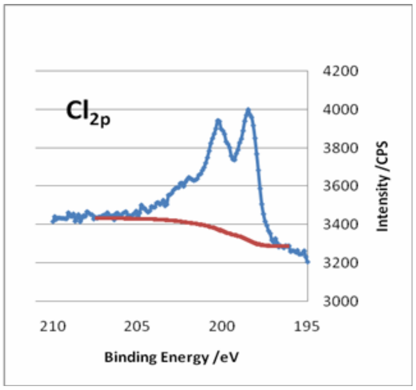

Figure 3: Cl2p signal on porous layer

The second part of the paper presents results about the porous layer growth observed by its actual dissolution aspect. Idea is to follow the kinetic aspect of the process in the solution side.

The figure 4 shows how the amount of dissolved In change when the galvanostatic treatment is stop. One minute after the controlled current flow stops very small sequential removals of solution are taken in the bulk of the solution and dosed by AAF spectrometry. It is perfectly pointed out that a very reproducible variation of In amount is observed with a regular increase of the concentration in the working solution during times that are large compared to the time of anodization.

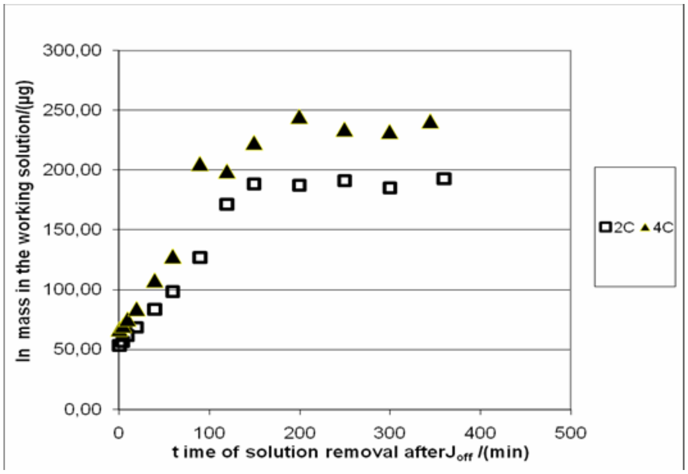

Figure 4: Evolution of the amount of In, into the working solution after the end of the porous layer growth, The variations are given for two amounts of charge.

It is demonstrated that matter is realized long time after the porous growth event. So a delay before observation of the final concentration is always observed. The second important point is that the amount of matter detected just after the growth is important and very far from zero. So, dissolution products are present just after the porous growth stopped and increase by approximatively by a factor 3.5 to 4 to reach their final and very stable concentration over immersion time of several hours.

This very reproducible increase of In concentration, long time after the end of the porous growth can have both origins. One could be the dissolution of the porous layer for long immersion time in HCl. In this condition the factor 4 would be in agreement with the total dissolution of a porous layer at 25% of porosity. Dissolution of bare InP in 1M HCl is almost null. However nanometric feature can have different behaviors and dissolution of pore walls is not impossible. Nevertheless as the porous layer is well observed until the end of the experiment, this assumption can be considered as limited. So the only one possibility is that the porous layer releases, dissolved species, long time after their creation inside the pores during the anodic treatment. This result is original and implies that a confined dissolution mixture is present inside the pores at the time of their creation. The electrochemical conditions for the dissolution process are then very different as the one of a planar surface. The local electric field is demonstrated in the literature as very important for the pore tip progression, our experiment asks the question of the influence of the local concentration into the solution. At this time the question of the concentration in the solution just after the end of the current flow becomes important. It is very reproducible and close to a value deduced by the faraday law, assuming that the number of dissolved InP moles is $n=Q/6F$, F being, the Faraday constant. Indeed, the dissolution of bare InP in a classical process is known as consuming 6 holes by InP equivalent “molecule” [7]. This is also a very surprising result which gives a second very important feature, with a very significant initial value. So the global observation which set the final In concentration four time over the prediction of the Faraday law with a six holes process suggests that a specific dissolution mechanism occurs. Strong electron injection [1,8,9] by corrosion intermediates must be supposed even at the very high dissolution rate used to obtain the porous layer. This very specific mechanism would be understood as the consequence of the local solution condition inside the pore at the time of the porosification. It must be pointed out that this observation implied that a complex mass balance must be considered.

Conclusions

The kinetic aspect associated to the growth of porous InP has been considered in this paper.Using XPS on porous layer and dosage of dissolution products into the solution at different times after the end of the porous growth we try to bring new information about the mechanism of the porous layer growth. XPS brings few information suggesting only that a Cl network must be present at the surface during the process. At this time the conclusion is premature and needs still works particularly during the emersion step. The information obtained on the evolution of the dissolution product concentration is more clear. Due to the high sensitivity of elemental atomic absorption methods a kinetic evolution was demonstrated. It appears that strong time dependency of the In concentration is observed showing that a large amount of dissolution product is kept inside the pores during the progression of the dissolution stage. So the liquid environment at the interface differs strongly from the situation observed for a classical anodic dissolution performed for example under illumination. It is a confined medium that changes the dissolution process and implies strong injection phenomenon from corrosion intermediates at high dissolution levels.

References

1. J.Jaume, C Debiemme-Chouvy, J.Vigneron, M.Herlem, E.M Khoumri, J.L Sculfort, D.LeRoy, A.Etcheberry, *Journal de Physique III,4, 273 (1994)*
2. H. Föll, S. Langa, J. Carstensen, M. Christophersen, I.M Tiginyanu, *Adv.Mater. 15, 183(2003)*
3. B. Erne, A. Million, J. Vigneron, C. Mathieu, C. Debiemme-Chouvy, A. Etcheberry *Electrochemical Solid State Letters* **2,** *619, (1999)*
4. H. Erné, C. Mathieu, J. Vigneron, A. Million, A. Etcheberry, *J. Electrochem. Soc . 147 (2000) 3759- 3767*
5. P. Kohl, C. Wolowodiuk, and J. Ostermayer, *J. Electrochem. Soc.*, **130**, 2288 (1983).
6. Yansheng Zheng and Yuqi Wang, Talanta, Vol. 42, N°3, 361 (1995).
7. S.Preusser, M.Herlem, A.Etcheberry, J.Jaume,***Electrochemica Acta,37,289 (1992)***
8. E.M Khoumri, A.Etcheberry ,C.Debiemme-Chouvy, D.Le Roy, O.Poliakoff, J.L Sculfort *J.Electroanal.Chem.,312,301(1991)*
9. E.M Khoumri, A.Etcheberry, O.Poliakoff, C.Debiemme-Chouvy, J.L Sculfort *J.Electrochem.Soc.,138,L65 (1991)*

ECS Transactions, 16 (3) 417-424 (2008)
10.1149/1.2982582 ©The Electrochemical Society

Growth of a porous layer on InP in liquid ammonia: a specific interfacial behavior

A .Eb, A-M Gonçalves, C. Mathieu & A. Etcheberry

Institut Lavoisier UMR CNRS8180 Université de Versailles
45 Ave des Etats Unis 78035 Versailles France etcheber@chimie.uvsq.fr

InP in liquid ammonia presents specific pore growth. The first stages of this process are studied with electrical, XPS and microscopy characterizations. We points out that an overlayer associated to typical phosphorus-nitrogen chemistry seem to acts as the precursor stage before the porosification starts.

Introduction

Since the first electrochemical pore formation on *n*-InP in HCl by P. Kohl in 1983 [1], numerous studies have been carried out and revealed an influence of the electrolyte in the porosification processes [2]. The question of the pore initiation is always opened. For example on III-Vs, the presence of a superficial film as initial step is very difficult to appreciate due to the instability of oxides layers at the pH of the solution used for the porous layer growths.

Liquid ammonia (NH_3 *liq*., T = -55°C) gives a very different medium to perform semiconductors electrochemistry. It provides electrochemical reactions under true water free and oxygen free conditions [3]. In addition to both conditions, NH_3 *liq*. exhibits chemical and physical properties obviously different from water and other non-aqueous media: a wide range of pH (33 units), low liquid temperature domain (195 K to 240 K) at atmospheric pressure, and very low viscosity coefficient and dielectric constant [4].

Recently, we established two main results about the anodization of InP in acidic liquid ammonia. On one hand, a surface passivation phenomenon has been reported [5]. This process leads to a phosphazene like "$NH{=}P{-}NH_2$" film formation, which is close to a monolayer. The formation of this film has been associated to a concomitant oxidation of the solvent (NH_3 *liq*.) and InP. It gives rise to a reproducible voltamogramm with a unique oxidation wave that can be understood as resulting from a perfect passivation process. On the other hand, anodic galvanostatic treatments performed at current density higher than 1 $mA \cdot cm^{-2}$ [6-8] lead to very specific porous network. The interesting fact in these results is that is possible to obtain in the same medium stable nanometric passivation layer and porous structure. So the question is about an eventual relation between these both phenomena.

So, in this paper we present a study which focuses on the first stages of a galvanostatic porous layer growth. This study has been performed in order to detect if a chemical modification of the surface is able to generate the initiation of the anodic porosification.

Experimental Section

Sn-doped *n*-InP (100) wafers ($N_D = 10^{18}$ at·cm^{-3}) are purchased from INPact Inc. and cleaved in 10 mm^2 rectangles. Prior to use, samples are chemomechanically polished with a solution of bromine in methanol (2%), rinsed with methanol and dried under argon stream. In order to remove residual oxides, samples are dipped for a few minutes in 2M HCl and finally rinsed with ultra-pure water. Liquid ammonia from gaseous ammonia ("electronic grade" from Air Liquide) is condensed and maintained at 223 K in a cryostat [6]. Anhydrous 0.1M NH_4Br (purest available quality from Aldrich) is used as a conducting salt and leads to a strongly acidified solution: pH = 1 in liquid ammonia pH scale (pH = - log [NH_4^+]).

The electrochemical setup is a classical three electrode cell. Pt and Ag wires serve, respectively, as counter and reference electrodes (Silver Reference Electrode SRE, E° = 0.79 V/NHE [9]). All anodic galvanostatic treatments are performed in the dark with a PAR EG&G 273 potentiostat & galvanostat. The current density is set at $J = 2$ mA·cm^{-2}. The surface modifications are examined using a scanning electron microscope (SEM) in top view and cross-section using a JEOL JSM 5800LV.

XPS chemical analyses are performed with a Thermo-VG Escalab 220i XL spectrometer. X excitation is performed with the Al line of a twin-anode (Al, Mg). The constant analyzer energy mode is used with pass energy of 20 eV. All experiments are performed by using the same procedure: anodization is performed in acidic liquid ammonia and at constant current. Samples are dipped in pure NH_3 *liq*. solution prior to the transfer in the XPS chamber. To achieve the transfer, a pending drop ammonia drop sheltering is used [5].

Results and discussion

Electrochemical evolution

The evolution of the interfacial electrode potential (E) against the amount of coulometric charge (Q) is reported in figure 1. A main result is the highly reproducible E *vs*. Q variation which suggests a well established anodic process with at least three characteristic domains. The figure 1 shows a very nice reproducibility of eleven distinct samples.

The electrode potential features can be described as followed according to Q. At short time, an initial step corresponding to $Q \sim 10$ mC is detected. It is associated to a steeply increase of E from *ocp* to ~1.7 V which is followed by a sharply decrease of E to ~1.5 V. This initial spike consumes an electric charge that is similar to the one associated to the anodic wave observed by cyclic voltammetry, which is in this case unambiguously correlated to a surface passivation process [5]. As demonstrated elsewhere the phenomenon observed by cyclic voltammetry leads to a phosphazene film formation.

For the time duration corresponding to the following 90 mC consumption, the electrode potential reaches slowly again 1.7 V with a characteristic shape. Afterwards, the electrochemical behavior shows a steep increase of E from 1.7 V (Q ~100 mC) to 2.8 V (Q ~ 200 mC). For higher amount of coulometric charge, an oscillatory electrochemical behavior is triggered. This last step is associated unambiguously to a thick porous layer growth [7, 8].

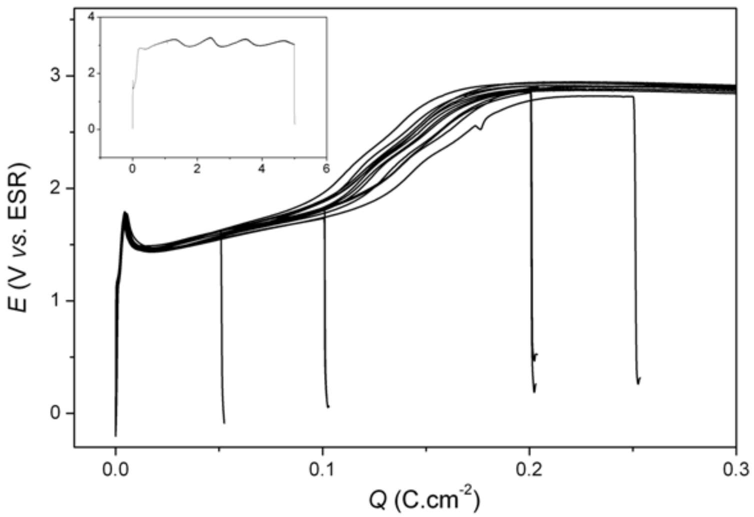

Figure 1. Electrode potential *vs*. anodic charge of *n*-InP in acidic liquid ammonia ([NH_4Br] = 0.1M), T = 223 K, *J* = 2 mA·cm^{-2}.

Surface analysis

Surface chemistry evolution is studied by XPS analysis for increasing amount of charge at each characteristic stage described in the electrochemical part. The sheltering drop of NH_3 *liq*. evaporates at atmospheric temperature under inert atmosphere. Then, the resulting anodized electrodes are transferred toward an XPS analyzer using a procedure minimizing air contamination.

Characteristic core level peaks are observed. Atomic levels of phosphorus, indium, bromine and nitrogen are clearly detected on surface with also additional carbon and oxygen contributions. The analysis are performed using the P_{2p}, In_{3d}, Br_{3d}, N_{1s}, O_{1s} and C_{1s} levels. As reported on the *E-Q* curves (fig. 1), specific stages are also observed for the XPS responses according to different anodization time of InP samples.

Figure 2 presents the P_{2p} XPS spectra evolution according to the coulometric charge. The detected components are P_{InP} at 129 eV and a P_{2p} peak at 133.5-134 eV. Their respective ratios clearly depend on the consumed charges. The low binding energy component at 129 eV decreases while the high binding energy at 133.5-134 eV increases. Moreover, the high binding energy component is observed as soon as the anodic process is triggered. This new component at high binding energy is close to the one observed after the anodic wave performed under cyclic voltammetry [5]. It exhibits the same binding energy and the same full-width at half maximum (*fwhm*), and the ratio between the high and low binding components is similar (~0.6). Then, we can assume that this high energy contribution is assimilated to the $P_{phosphazene}$ which was obtained by voltammetry.

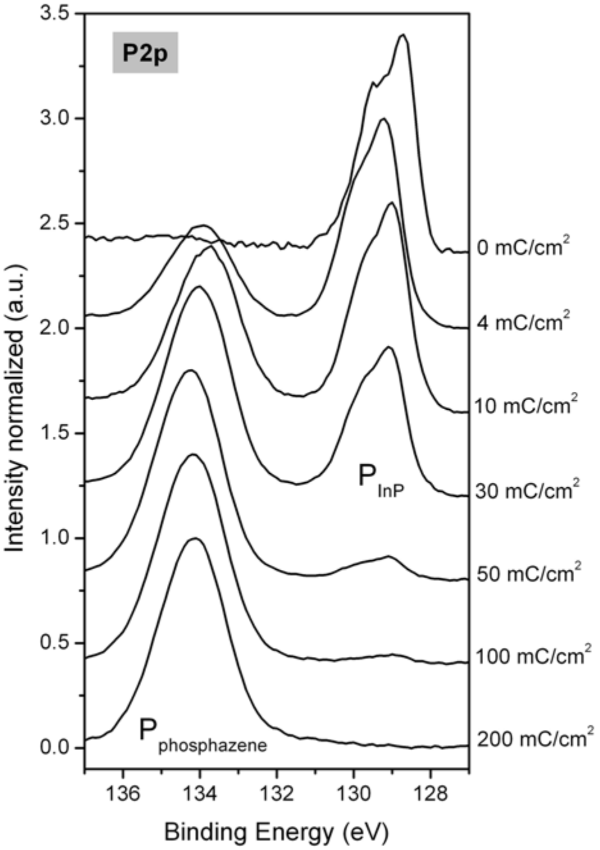

Figure 2. Normalized P_{2p} XPS spectra evolution according to the amount of coulometric charge achieved by anodic treatment ($J = 2$ mA·cm^{-2}) in acidic NH3 *liq*.

For higher Q, binding energy and *fwhm* remain constant for both P peaks. The ratio between them evolutes until Q reaches 200 mC·cm^{-2}. Then, the P_{InP} component decreases progressively to zero. The phosphazene-like layer seems to thicken on the whole surface.

Figure 3 presents the In_{3d5} XPS spectra evolution according to the coulometric charge. The binding energy of In_{InP} component is close to 445 eV. Such as P_{InP} evolution, the In bulk component decreases as Q increases. It is not discernible for $Q > 200$ mC·cm^{-2}. In addition, another component at higher energy (446-446.5 eV) appears clearly from $Q = 50$ mC. This peak is not nowadays expressly attributed. Its binding energy is however very close to $InBr_3$ even if this attribution cannot be directly proposed. In seek of clarity, this component is noticed “In(III)”.

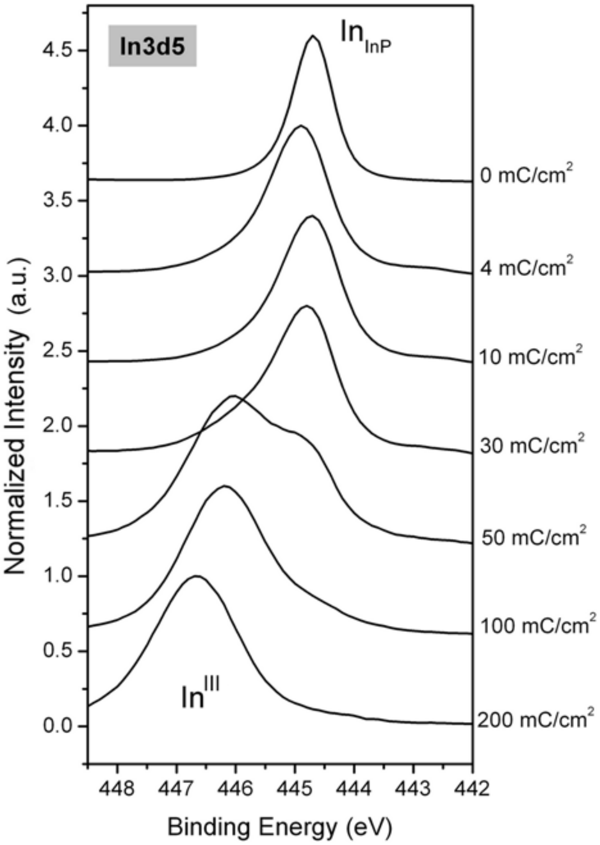

Figure 3. Normalized In_{3d5} XPS spectra evolution according to the amount of coulometric charge achieved by anodic treatment ($J = 2$ mA·cm^{-2}) in acidic NH_3 *liq*.

N_{1s} XPS spectra and associated fits for increasing Q are shown in figure 4. Again specific peak shapes are observed which depend on the consumed charges. The peak can be fitted with three components. The two lower energy components present same binding energy and *fwhm* as both N_{1s} components of phosphazene obtained by cyclic voltammetry. Moreover, the ratio N_{400} / N_{398} (~1.4) is close but slightly higher than the one observed after voltammetric treatment (~1.1) for a same amount of charge. Thus, as observed for P levels, the chemical composition and the covering of the surface are very close in both anodic treatments for the same low *Q* values.

For higher *Q*, binding energy and *fwhm* for each N_{1s} component remain constant. Moreover analysis of ratio between components, points out an evolution in three phases according to *Q* (fig. 5). At short time of anodic treatment (for $Q \leq 30$ mC), the ratio remains constant close to 1.4. It increases gradually to 3.3 for 30 mC < *Q* < 500 mC. For higher amount of charge (*Q* > 500 mC) this ratio remains constant. So, an evolution of the surface chemistry is observed for an intermediate domain of *Q*. This domain corresponds to a stage for which the InP response decreases strongly indicating the thickening of a superficial film.

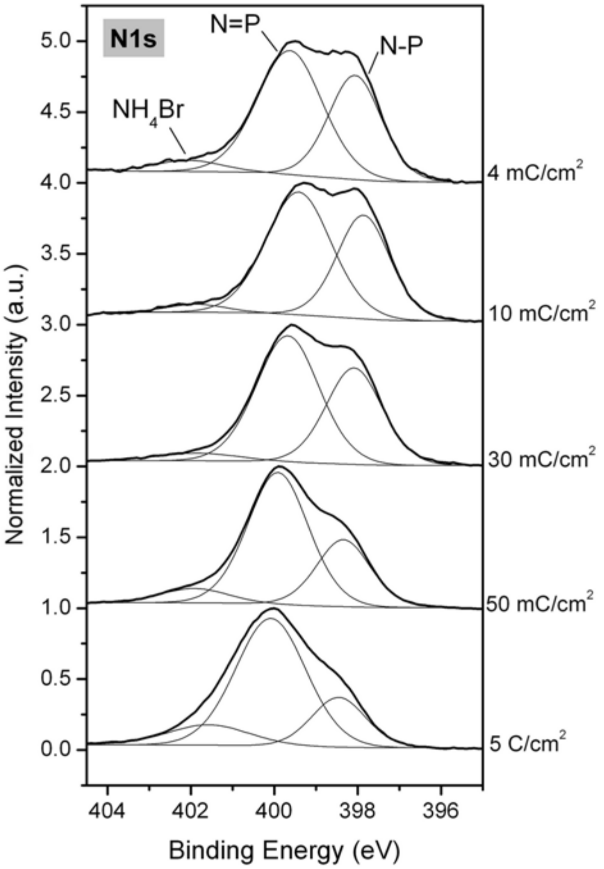

Figure 4. Normalized N_{1s} XPS spectra and fits evolution according to the amount of coulometric charge achieved by anodic treatment ($J = 2$ mA·cm^{-2}) in acidic NH_3 *liq*.

The literature [10, 11] suggests that $N_{400\ eV}$ and $N_{398\ eV}$ can be associated respectively to $N_{N=P}$ and to N_{N-P} in phosphazene or polyphosphazene compounds. In our case, the ratio $N_{400\ eV} / P_{phosphazene}$ remains constant, close to 1.1, whatever Q. That suggests the presence of a "P=N" core.

The third component is associated to nitrogen provided by the conducting salt (NH_4Br). In spite of dipping in pure NH_3 *liq*. solution, some conducting salts remain on the sample.

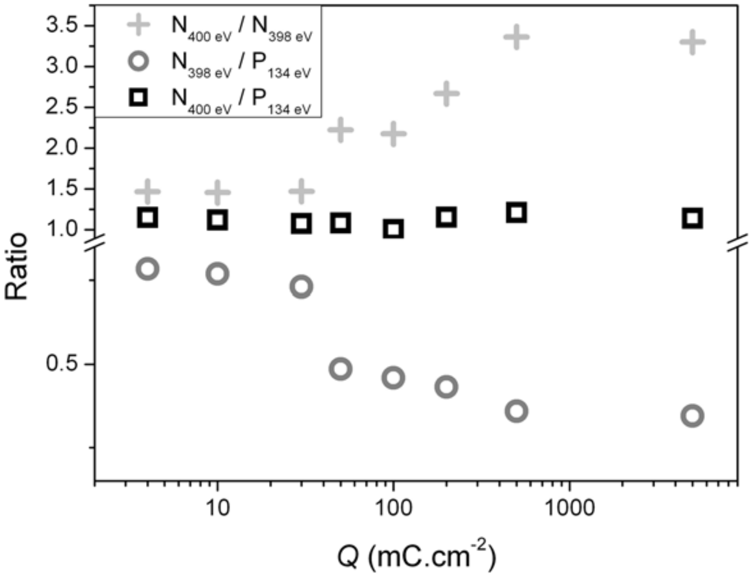

Figure 5. Evolution of the ratios between $N_{400\ eV}$, $N_{398\ eV}$ and $P_{134\ eV}$ according to the amount of coulometric charge achieved by anodic treatment ($J = 2$ mA·cm^{-2}) in acidic NH_3 *liq* (% at. determined by XPS analysis).

Morphology evolution

Figure 6 shows the cross-section of two *n*-InP samples treated by anodic treatments (for $Q = 400$ and 800 mC). As detailed in a previous work [8], a porous nucleation layer grows during the first step of porosification process (for $Q = 150$-200 mC). This layer is surlined in figure 6a and presents a maximum thickness of 80 nm. It can be also observed by SEM from $Q = 50$ mC.

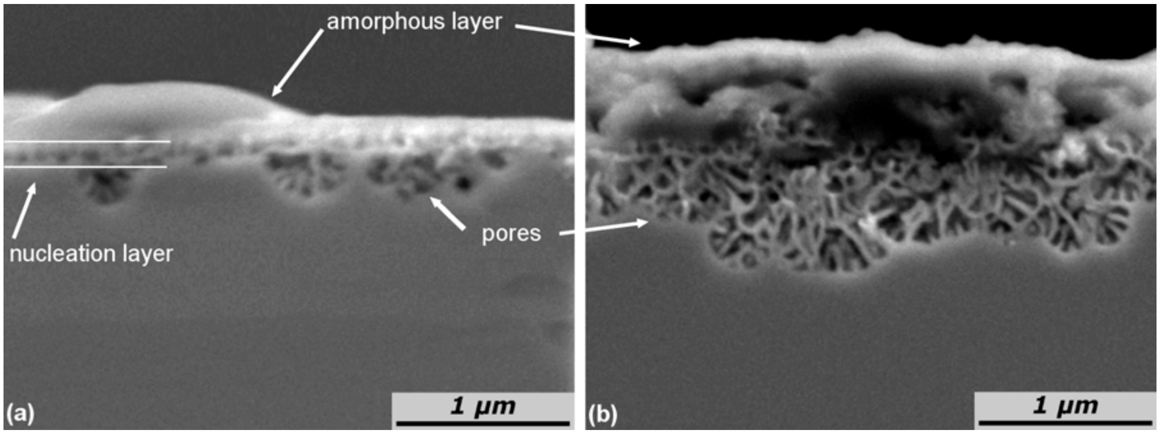

Figure 6. SEM cross section pictures after an anodic galvanostatic process on *n*-InP with $J = 2$ mA·cm^{-2} in NH_3 *liq*. ([NH_4Br] = 0.1M), T = 223 K, (a) for $Q = 400$ mC·cm^{-2}, (b) for $Q = 800$ mC·cm^{-2}.

Considering a 6 holes dissolution mechanism [12], the thickness of dissolved bulk material is of 80 to 100 nm for $Q = 150$ to 200 mC. Since the nucleation layer is porous, it could be thicker: a calculated thickness of 300 to 400 nm would have been expected (with the same porosity of the porous layer of ~25 %). In this way, a secondary reaction must occur during the anodic porosification process. In addition to nucleation layer growth, a growing overlayer is observed in figure 6. Preliminary analysis by X-ray diffraction has shown the amorphous nature of this coated overlayer [7].

Studying porous growth for higher amount of charges, the observed porosity is in agreement with a 6 holes dissolution mechanism. Then, all coulometric charges are consumed by the material dissolution for $Q > 200$mC. Besides, the amorphous overlayer grows together with the porous layer until $Q \sim 1$ C·cm^{-2} (fig. 6b).

Conclusions

The comparison of the evolution observed on *E-Q*, XPS spectra and cross-sectional SEM views suggests that the porous growth appears with a delay compared to the growth of the "P_N" overlayer. This delay supports that the "P_N" overlayer acts as a precursor stage of the pore initiation. Note that the atomic balance needs a phosphorus and nitrogen. This implies that the global InP dissolution must occurs whatever the step of the process. Moreover, the reproducibility of the *E-Q* evolution and that observed by XPS analysis demonstrates that the process with its sequential stages is perfectly established. Thus, the notion of precursor before porosification is strongly comforted

References

1. P. Kohl, C. Wolowodiuk, and J. Ostermayer, *J. Electrochem. Soc.*, **130**, 2288 (1983).
2. M. Christophersen, J. Carstensen, K. Voigt, and H. Foll, *Phys. Stat. Sol. (a)*, **197**, 34 (2003).
3. A. Etcheberry, A. M. Gonçalves, C. Mathieu and M. Herlem, *J. Electrochem. Soc.,* **144**, 928 (1997).
4. Jochen Jander and Volker Doetsch, in *Anorganische und allgemeine Chemie in flüssigem Ammoniak*, edited by Friedr. Vieweg und Sohn, Vol. 1, Braunschweig (1966).
5. A. M. Goncalves, O. Seitz, C. Mathieu, M. Herlem and A. Etcheberry, *Electrochem. Comm.*, **10**, 225 (2008).
6. A. M. Goncalves, L. Santinacci, A. Eb, I. Gerard, C. Mathieu and A. Etcheberry, *Electrochem. Solid St. Lett.*, **10**, D35 (2007).
7. A. Eb, A. M. Goncalves, L. SantinacciC. Mathieu and A. Etcheberry, *Comptes Rendus Chimie,* in press, doi:10.1016/j.crci.2008.02.002 (2008).
8. A. Eb, A. M. Goncalves, L. Santinacci, C. Mathieu and A. Etcheberry, *Phys. Stat. Sol. (c)*, in press (2008).
9. D. Guyomard, C. Mathieu and M. Herlem, *J. Electroanal. Chem.*, **246**, 29 (1988).
10. L. L. Fewell, *J. Appl. Polymer Sci.,* **41**, 391 (1990).
11. P. Vassileva, V. Krastev, L. Lakov, and O. Peshev, *J. Mat. Sci.,* **39**, 3201 (2004).
12. A. M. Goncalves, L. Santinacci, A. Eb, C. David, C. Mathieu, M. Herlem and A. Etcheberry, *Phys. Stat. Sol. (a)*, **204**, 1286 (2007).

Author Index